Hosted by:
ASOSIASI PANASBUMI INDONESIA (API)
INDONESIAN GEOTHERMAL ASSOCIATION (INAGA)

Supported by:
KEMENTERIAN ENERGI DAN SUMBER DAYA MINERAL
REPUBLIK INDONESIA

ISSN 2829-9671
Volume 5, 2022

IIGC

DIGITAL INDONESIA INTERNATIONAL GEOTHERMAL CONVENTION 2021

21 - 24 SEPTEMBER 2021

ADVANCEMENT THROUGH CREATIVE TECHNOLOGY INNOVATION

PROCEEDING BOOK

ISSN 2829-9671
Volume 5, 2022

Proceeding Book

DIGITAL INDONESIA INTERNATIONAL GEOTHERMAL CONVENTION (DIIGC) 2021

September 21-24, 2021

Advancement Trough
Creative Technology Innovation

Editors:

Abadi Poernomo Doddy Astra
Suryantini Ali Ashat

Reviewers:

Doddy Astra Suryantini
Ali Ashat Khasani
Hendra Grandis Rudi Rubiandini
David Pambudi Sahara

Indonesian Geothermal Association

2022

This page is intentionally left blank

DIGITAL INDONESIA INTERNATIONAL GEOTHERMAL CONVENTION (DIIGC) 2021

September 21-24, 2021

COMMITTEE

ADVISOR
Dadan Kusdiana *(DG NREEC)*

STEERING COMMITTEE
Harris Yahya *(Geoth. Dir NREEC)*
Prijandaru Effendi *(API)*
Abadi Poernomo *(API)*
Sanusi Satar *(API)*
Paul Mustakim *(API)*
Tafif Azimudin *(API)*
Heribertus Dwiyudha *(API)*
Yudistian Yunis *(PLN)*

CHAIRMAN DIIGC
Ahmad Yuniarto *(PGE)*

SECRETARIAT
Andry Sutanto *(API)*
Panggih Akbar *(API)*

TECHNICAL PAPER
Doddy Astra *(SOL)*
Suryantini *(ITB)*
Ali Ashat *(ITB)*
Khasani *(UGM)*
Aquardi Suminar *(SEG)*
Ashadi *(KS Orka)*
Christovik Simatupang *(KS Orka)*
Drestanta Yudha *(SOL)*
Fatah Gunawan *(PGE)*
Harry Nurcholis *(PLN)*
Marino Christiano Baroek *(SUPREME)*
M. Andhika *(ECOLAB)*
Mulyanto *(PGE)*
Mulyadi *(SEG)*
Rio Marza *(GDE)*
Tavip Dwikorianto *(PGE)*
Yayan Sofyan *(WJEC)*

This page is intentionally left blank

SPEAKERS

Arifin Tasrif, Minister of Energy and Mineral Resources *(Represented by **Ego Syahrial**, Secretary General Ministry of Energy and Mineral Resources)*

Bahlil Lahadalia, Minister of Investment/ Chairman of Indonesia Investment Coordinating Board (BKPM) *(Represented by **Nurul Ichwan**, Deputy Chairman for Investment Planning)*

Tri Handoko, Head of National Research and Innovation Agency, Ministry of Research Technology *(Represented by **Barman Tambunan**, Head of National Laboratory for Energy Conversion Technology)*

A. Octavian, Rector Indonesia Defense University

Dadan Kusdiana, Director General of New Renewable Energy and Energy Conservation, Ministry of Energy and Mineral Resources

Febrio Nathan Kacaribu, Head of Fiscal Policy Agency, Ministry of Finance *(Represented by **Noor Syaifuddin**, Associate Policy Analyst)*

Ruandha Agung Sugardiman, Director General of Forestry Planning and Environmental Management, Ministry of Environment and Forestry *(Represented by **Roosy Tjandrakirana**, Director of Plan, Use and Establishing of Forest Management Area)*

Jarot Widyoko, Director General of Water Resources, Ministry of Public Works and Public Housing *(Represented by **Iriandi Azwartika**, Director of Groundwater and Raw Water)*

Dicky Fahnudi, Digital & Integration Division Manager Schlumberger Indonesia

Paul Hultzsch, Digital Subsurface Consulting Manager Schlumberger Indonesia

Darwin Abas, Director of Commercial PT Sucofindo (Persero)

Maria Wongsonagoro, President Director of IPM Public Relations

Wiluyo Kusdwiharto, Director of Mega Project and New Renewable Energy PT PLN (Persero) *(Represented by **Cita Dewi**, EVP New and Renewable Energy)*

Brian Carey, Geothermal Applications and Industry Specialist Institute of Geological & Nuclear Sciences

Ahmad Yuniarto, President Director of PT Pertamina Geothermal Energy *(Represented by **Eko Agung Bramantyo**, Director Operation of PT Pertamina Geothermal Energy)*

Riki F. Ibrahim, President Director of PT Geo Dipa Energi (Persero)

Hendra Soetjipto Tan, Chief Executive Officer of Star Energy Geothermal *(Represented by **Suharsono Darmono**, Deputy Power Plant Operations Officer)*

Nisriyanto, President & CEO of Supreme Energy

Riza Pasikki, Chief Technical Officer of KS Orka Renewables

Published by:

Asosiasi Panasbumi Indonesia (API)

ISSN 2829-9671
Volume 5, 2022

FOREWORD PRESIDENT OF INAGA

Indonesian Geothermal Association (INAGA) has been proud to host the Indonesia International Geothermal Convention & Exhibition (IIGCE) as well as the Digital Indonesia International Geothermal Convention (DIIGC), both of which were a huge success.

The 2nd DIIGC 2021 was successfully held virtually on September 21-24, 2021, and attended by more than 800 people from all over the world.

This year, the PIT (*Pertemuan Ilmiah Tahunan*) Committee received 42 abstracts and selected 32 papers focusing on Earth Science, Engineering, General, Resources Management, and Special Topics as part of the DIIGC event.

I would like to take this opportunity to offer my gratitude and appreciation to the Technical Paper Committee, the Technical Session Chairperson and Co-Chair, Authors, Presenters, and all others who contributed to the success of the 2021 Technical Papers Session.

I believe that all of the articles were wonderful and excellent in terms of content and quality, with a variety of interesting topics. As a result, I am pleased to provide these documents to our geothermal community on behalf of INAGA.

Yours truly,

Prijandaru Effendi
President of INAGA

This page is intentionally left blank

ISSN 2829-9671
Volume 5, 2022

CONTENTS

Committee iii
Speakers v
Foreword President of INAGA vii

ENGINEERING	1
EARTH SCIENCES	99
RESOURCE AND MANAGEMENT	179
SOCIAL, POLITICS, ECONOMICS, AND COMMUNITY	213

ENGINEERING

Shaped PDC Cutter with High-Density Impreg's Element Deliver Superior Performance in Sorik Marapi Geothermal Power, Indonesia 1
Sentanu W. Reksalegora, Triadi Herwasto Aribowo, Candra Budhi Prasetyo, Ashadi, and Juliana Phan

Implementation of Acid Stimulation Job to Significantly Improve Injection Capacity at Sorik Marapi Geothermal Field 7
Junior Setiawan, M. Ramos Suryanta Lubis, Rudy Yahya Sophian, Riza G. Pasikki, Muhammad Gusti Bastisya, and Andhika Pratama

Pressure Transient Analysis of Injection/Fall-off Tests in the Fractured Geothermal Reservoir 13
Gitta A. Septiani, Eylem Kaya, and Daniel W. Adityatama

Design Improvement in 17-1/2" Hybrid Drill Bit Successfully Improved Drilling Performance in Sorik Marapi Geothermal 25
Sentanu W. Reksalegora, Ariatama Yustisia, Ashadi, Kiki Yustendi, Mohammad Khairanto Nugroho, and Jake Drew

Drilling Digitalization to Enhance and Optimize Geothermal Drilling Operation – Road to Single Digit Well 31
Sentanu W. Reksalegora, Redha B. Putra, Fadhil Rhisnanda, Ashadi, Arya Dwipangestika, and Dicky Alamsyah

Design of Geothermal Brine Energy Dryer as Alternative Thermal Energy Source 37
Febri Rizki Dwi Satriyo Pamungkas, Khasani, and Wahyu Hartono

Real Time Steam Dryness Monitoring by Integration with DCS 45
Abdul Halim F., Edwin Ardiansyah, and Wahyu Firmansyah

Progress in Research and Development (R&D) of Geothermal Binary Plant in Indonesia 49
Cahyadi, Suyanto, Riza, and Agus Nurrochim

Unit 2 and Unit 3 Interface Header Separation Optiramp Simulation 55
Agus Riyadi, Dian Katriya Hadi, Albert Lukman, Asfaari Raasyidah, and Tito Juliasmi

Grounding and Lightning Protection Issues and Solutions in Darajat Geothermal Power Plant 63
Nixon Manik, Muhammad Ichsan, Agustiawan, Achmad Arbi, and Muhamad Reyhan Savero

Enhancing Geothermal Power Generation with Binary Technology in Brine Recovery: Exergy's case study in the Philippines, Mindanao 3 Power Plant 69
Nicola Frascella, Marco Frassinetti, and Chee Aun Kok

Success Story of Scaling Silica Treatment in Brine ORC (Study Case Sorik Marapi Geothermal Field) 77
Nugraha Y. Arifpin and Ryan Hidayat

Managing Sulfur Deposition and Microbiofouling in Geothermal Power Plant Cooling Tower 81
Yohannes N. Arifpin, Tomy Suryatama, Fajar M. Rahman, and Fritz Monterozo Earwin

Real Time Monitoring of Steam Chemical Composition in Geothermal Plant 87
Ahmad Marzuki and Ruben Lalamentik

Analysis of Cooling Water Flow in the Condenser to Improve the Performance of Dieng Geothermal Power Plant 93
Arief Surachman

EARTH SCIENCES

Spatial Identification and Structure Control on the Distribution of Manifestation in Mountain Ungaran, Semarang, Central Java, Indonesia 99
Pius Artdanno Bernaldo, Nazwa Khoiratun Hisan, Alviani Permatasari, Ludovicus Damardika Jasaputra, Arhananta, Aditya Rizky Wibowo, and Agung Prayoga

Fracture Characterization on the Great Sumatera Fault Zone at Sorik Marapi Geothermal Field 109
Dhani Sanjaya, Wishnu Triananda, Radhitya E. Pradipta, Haris Siagian, M. Ramos Suryanta Lubis, Christovik H. Simatupang, and Riza G. Pasikki

The Important Role of Wairakite at Sorik Marapi Geothermal Field 121
Ridha Hendri, Stephen Simamora, Haris Siagian, Tio Ferdinan, Junior Setiawan, Christovik Simatupang, and Riza Pasikki

The Characteristic of 320˚C Geothermal Wells at Sorik Marapi Geothermal Field 131
Ryan Hidayat, Christovik H. Simatupang, M. Ramos Suryanta Lubis, Junior Setiawan, Haris Siagian, and Riza G. Pasikki

Subsurface Structure Identification from Gravity Modelling of Silangkitang Geothermal Field for Future Injection Well Targeting 139
Rizal Abiyudo, Yunus Daud, and Drestanta Yudha Satya

New Insight into Geothermal System in Field X Based on Reprocessing and 3D Inversion Magnetotelluric Data 147
Sri Mulyani, Yunus Daud, Riza G. Pasiki, Haris Siagian, and Wambra Aswo

2-Dimensional Modeling of Subsurface Structures Based on Gravity Data Using Multilayer Perceptron Neural Network (MPNN) Method 161
Supriadi R. Ferrianggoro

Application of Multi-Level Second Vertical Derivative (ML-SVD) Method to Identify Subsurface Structure in Mount Endut Geothermal Prospect Area, Indonesia 171
William Jhanesta and Supriyanto

ISSN 2829-9671
Volume 5, 2022

RESOURCE AND MANAGEMENT

Initiation of Low Temperature Geothermal System Development in Indonesia: The Potential Challenges 179
Muhammad Ikhwan, Nova Mutiara, Asep Purnama, Saeful Ghofar Z P, and Rendy Maylana P

Managing a Drilling Rig – A KS Orka Experience 189
Kiki Yustendi, Ashadi, Sentanu W. Reksalegora, Dicky Alamsyah, and Huda N. Ilham

Geothermal Power Plant is Moving to Governor Free Operation, Case Study from Darajat 55 MW Geothermal Power Plant 193
Sugeng Triyono and Danu Sito Purnomo

Improving The Quality of Preventive Maintenance (PM) Work For FCRS And GPP Equipment With "At Cost Based-Annual Maintenance Contract (AMC) Innovation" at PT PGE Area Lumut Balai 201
Raka Kautsar Lahia, Azhari Surya Adiputro, Firman Johannes Simanulang, and Angga Hendrawardhana

SWOT Analysis for Geothermal Enhanced System (EGS) As New Technology for Geothermal Development in Indonesia 205
Sulistyorini Widi Hastuti, Andi Novita Mama Anugrah, Konita Nafista, and Ashabul Kahfi Ilham

SOCIAL, POLITICS, ECONOMICS, AND COMMUNITY

Opportunity of Geothermal Energy Direct Use for Agriculture in Indonesia 213
Rizki Edi Nugroho, Iqbal Ipmawan Yogatama, and Andri Wibowo

This page is intentionally left blank

Shaped PDC Cutter with High-Density Impreg's Element Deliver Superior Performance in Sorik Marapi Geothermal Power, Indonesia

Sentanu W. Reksalegora[1], Triadi Herwasto Aribowo[2], Candra Budhi Prasetyo[2], Ashadi[1], and Juliana Phan[2]

[1]KS ORKA, Recapital Building 5th Floor, Jakarta
[2]National Oilwell Varco, Kawasan Taman Tekno Blok C No.1, Tangerang Selatan

Sentanu.wisnuwardhana@ksorka.com, Triadi.Aribowo@nov.com, CandraBudhi.Prasetyo@nov.com, Ashadi@ksorka.com, Juliana.Phan@nov.com

Keywords: PDC technology, drill bits, drilling performance, fixed cutter bits

ABSTRACT

With the increase in geothermal drilling activities in Indonesia, the challenge of continuous improvement in drilling operations are always being tackled – one of the challenges is improvement through drilling bits. To tackle the challenges faced by conventional roller cone bits in geothermal drilling, NOV ReedHycalog have developed PDC bit with advanced cutter technology, called Fusetek. The bit combines shaped PDC cutters and High-Density Impreg (HDI) elements technology in order to increase the efficiency of cutting action to be able to increase the average ROP in hard volcanic rock. Recently, the bit was utilized in Sorik Marapi geothermal field with great success. The bit was able to drill long interval with 56% ROP improvement substituting an estimate of 3-4 traditional roller cone bits and eliminating multiple bit trips. The use of advanced shaped cutter technology and High-Density Impreg (HDI) Elements successfully delivered superior drilling performance in geothermal well and have reduced the overall drilling cost in Sorik Marapi. This paper will present the result and performance of the new technology bit and how it will improve for further application.

1. INTRODUCTION

Indonesia has 40% of the world's potential geothermal resources estimated at 28,000 megawatts (MW) (Allard, 2010). Aligning with the government's goal to exploit this potential, the increase in geothermal drilling activities can be seen nationwide. One of the challenges in geothermal drilling is drilling through volcanic rock with high unconfined compressive strength (UCS). Currently, geothermal drilling bits are dominated by the utilization of roller cone bits. However, these bits have shown several weaknesses. To overcome the shortcoming of roller cone bits, PDC bits acts as an alternative to improve the performance and economics of drilling activities. However, in certain situation, conventional PDC bits still fail to achieve this goal. NOV ReedHycalog has developed a PDC bit which uses High-Density Impreg (HDI) Elements combined with shaped PDC cutters in order to overcome this challenge in conventional PDC bit. The first run of NOV Fusetek in geothermal drilling was in Sorik Marapi project and have showed promising result. This paper will discuss the design aspects of the bit, enabling cutter technology, and rock failure mechanisms specific to this application. It will conclude with the lessons learned and best practices from this project that are transferable to similar applications.

2. OVERVIEW OF SORIK MARAPI GEOTHERMAL FIELD

Sorik Marapi Geothermal Field is one of the largest developing geothermal projects in Indonesia operated by PT Sorik Marapi Geothermal Power. This project is located in Mandailing Natal Regency, North Sumatera Province. KS Orka acquired majority shares of the company in mid-2016 and since then the project has completed drilling program for 18 wells and confirmed at least 55 MW proven resources. Geographically, Sorik Marapi Geothermal Field is also located between two geothermal fields are still being developed Sarulla (SOL) and Muara Laboh (Supreme Energy). Figure 1 shows the field location.

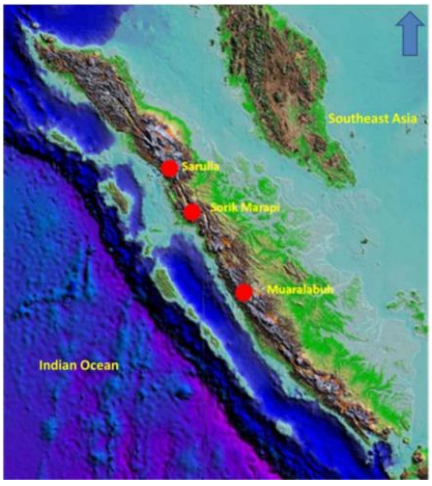

Figure 1: Map of Sorik Marapi Geothermal.

3. FIELD APPLICATION

The typical geothermal big bore well consists of four hole-section. The topmost section is a 36" hole with 30" conductor pipes, normally set between 30-40 m from the surface The second section is a 26" open hole with 20" casing down to 450 mMD. Followed by the third section, a 17 ½" open hole with 13 ⅜" casing down to 1100-1400 mMD. The last section is a 12 ¼" open hole with 10 ¾" casing that can go down to 2400-2500 mMD. The main objective of the first field test will be in the 12 ¼" hole section where the operators typically need several bits to finish the typically long section. This section is drilled with the smallest bit size hence it has the lowest roller cone bearing life. By improving the interval drilled from each bit runs, operation hours will be shortened since bit trips will be eliminated.

The potential drilling hazard that might be encountered would be severe lost circulation (blind drilling) and stuck pipe. The second drilling hazard would be drilling hard formation of high silicification and metamorphic rock. The formation drilled in the 12-1/4" section is dominated by meta sediment (quartzite and phyllite), felsic porphyries, and high silicified rock. High temperature mineral such as epidote, chlorite calcite, wairakite, sericite prehnite is also found in this section. The quartzite found in this section was strongly altered, dominated by abundant silica replacement, rare chips show as milky quartz, moderate calcite as matrix replacement, minor to moderate disseminated pyrite embedded in silica matrix and some as vein, moderate to abundant illite widespread in silica matrix, rare chlorite replacing grains, incipient epidote embedded in matrix decreasing to depth. The phyllite was dark grey, moderate hard, foliated, interlayered with quartzite.

Sorik Marapi is one of the few fields to first run the Fusetek bit in Indonesia. The bit was first used back in 2018 in Lumut Balai field in the 9-7/8" hole section drilling 1,021 m interval with 13.6 m/hr ROP (Andika et al., 2018). It was also used most recently in New Zealand geothermal field in Tauhara field, having an overall performance improvement of 20% compared to roller cone bits (Lock, et al., 2020).

3.1 Prism shaped PDC cutter

In this drilling application where hard formation is expected, cutter selection is very important. Two aspects in regard to cutter selection: physical properties and cutter shape. Cutter physical properties is related to resistance. There are two types of resistances, abrasion and impact resistance. In the case of dealing with hard formations like igneous or metamorphic rock, impact resistance is the most important. Conventional PDC bit with standard round cutter (Figure 2) run in hard formation typically end up with severe broken cutters only after drilling a short interval in hard formation. In this case standard round cutter will typically less efficient in rock failure mechanism in hard formation, resulting drilling at low depths of cut (DOC) and potentially increased lateral vibration. Hence, the bit will typically end up with severe broken cutters.

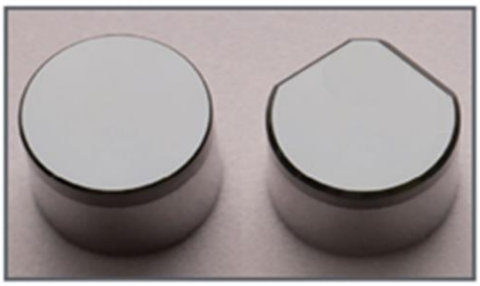

Figure 2: Standard round cutter on the left and prism shaped cutter on the right.

To improve cutter engagement into formation associated with rock failure mechanism, the cutter shape in this application will be strongly recommended. In such drilling through metamorphic rock with hard and brittle physical properties, drilling bits will require crushing action rather than shearing action. Because of the formation hardness drilled, it will be difficult to get enough engagement into the formation with conventional PDC cutter. The V-shaped or called as prism shaped PDC cutter will give a benefit of point loading to crack the formation and then improve cutter engagement into formation. This prism shaped cutter also helps giving the effect of crushing effect into formation, improving its efficiency. The prism cutter has been well proven to increase rate of penetration (ROP) since its introduction in 2015. The resilience of this cutter is also superior to the traditional round cutter as shown in SPE-199598 (Rahmani et al., 2020).

Figure 3 illustrates how the prism shape cutter will help getting better cutter engagement and how it will increase drilling efficiency by propagating to the rock surface instead of below the surface, making an efficient use of energy.

3.2 High-Density Impreg (HDI) Elements

The second bit design strategy for this application is to focus on impact durability. Drilling in hard formation will often cause some impact to the bit. Once one or two cutters is broken, it will affect the whole cutting structure and the rest of the cutting structure will deteriorate exponentially. HDI Elements play an important part on the PDC drill bit design for this geothermal well.-HDI elements combine the toughness of carbide with the hardness of diamond to provide a flexible element that is tough yet wear resistant. These elements enhance drill-bit durability, stability, and impact resistance. Figure 4 shows where HDI Elements bring an additional option to secondary elements. Carbide is a great option for impact and low wear applications, PDC is excellent in high wear low impact, but there was no high impact high wear solution. HDI Elements close that gap bringing element with higher wear and impact resistance than carbide.

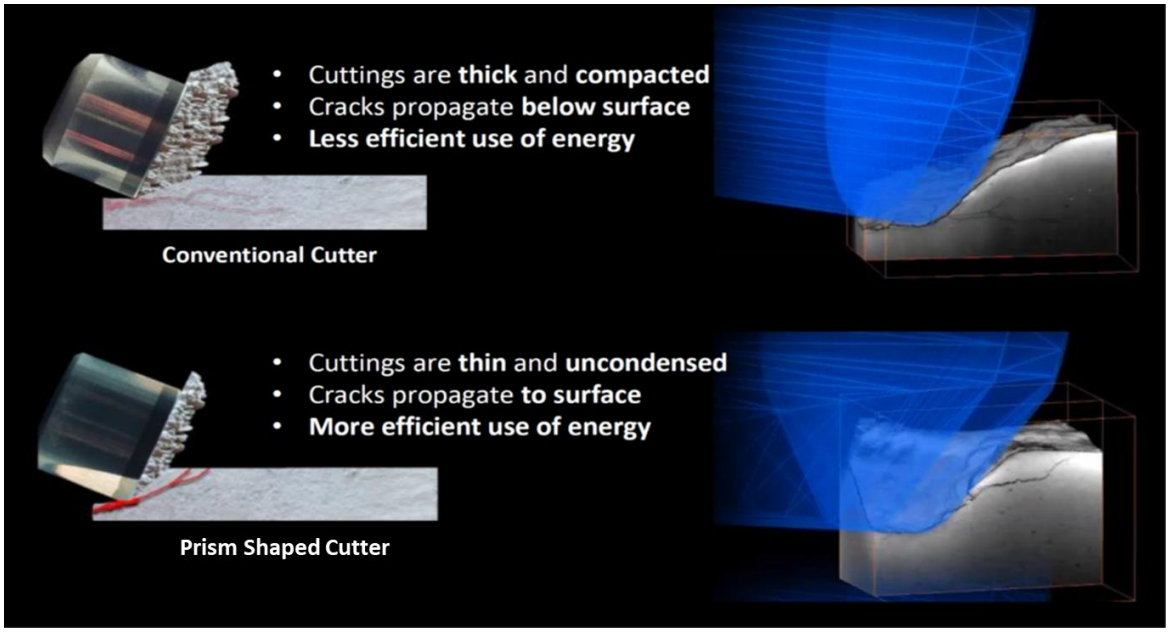

Figure 3: Cutting mechanism of conventional vs. prism shaped cutters.

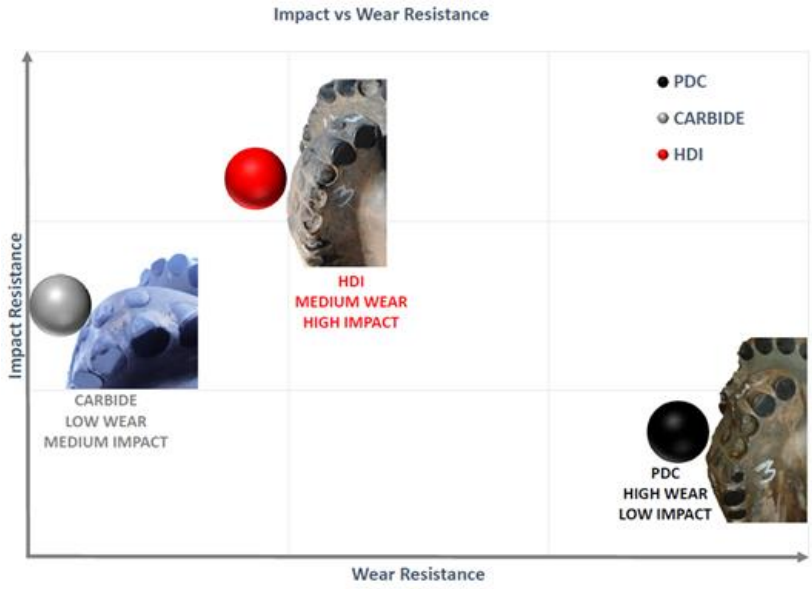

Figure 4: Physical properties of HDI Elements in comparison with Carbide and PDC.

Secondary cutting element can be utilized in two forms, as a secondary cutting element itself or as an impact arrestor component. In this case the HDI Elements was utilized as impact arrestors component. These HDI Elements were placed and positioned behind the primary cutters that will act as vibration dampener (Figure 5). Should the bit be exposed to an impact, most of the load will be dampened by the HDI Elements so the primary cutters do not break. This will reduce the overall impact overload damages to the primary cutting structure.

Replacing the HDI Elements with conventional PDC cutters would not be possible in this case because HDI physical properties are completely different from conventional PDC cutters. Conventional PDC cutters might help improve the primary cutter endurance during the first few impacts, however it will break quicker than HDI component and once these secondary PDC cutters got broken, the primary cutters would follow.

4. RESULT

Well 04 is a J-shaped well. The 26" hole section was drilled vertically. The kickoff point is at the beginning of the 17 ½" hole section with a final inclination of 30 degrees tangent to section TD. The inclination angle was also held in the 12 ¼" hole section to TD at around 2400 mMD/2046mTVD. The 12 ¼" hole section was drilled using directional motor BHA with 0.78 bent housing setting.

In the offset wells, the 12 ¼" hole section is drilled with Roller Cone (RC) TCI Bit with IADC 437 or 537. Based on the bit record (Table 1), on average, each RC bit run could drill for approximately 300 meters. The average on bottom ROP from the same well pad in the 12 ¼" hole section drilled with this RC bit is 7.1 mph. The reason for running TCI RC bit in the past was because the formation is considered hard, while standard PDC has not shown significant benefits in terms of economics and performance. Considering the 12 ¼" hole interval is around 1300 m, it would need at least 4 RC bit trips with 4 new bits to drill the well to TD. The 12 ¼" PDC

with prism shaped cutter and HDI Elements or can call as *Special* bit was selected for this well to eliminate the need for the time-consuming bit trips. As bearing failure was seen in the offset wells, the use of PDC bit will also eliminate the risk of bearing failure or costly lost in hole cones as well as majority of poor dull condition needs to be improved.

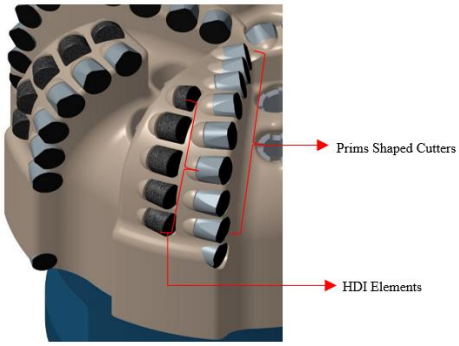

Figure 5: the placement of HDI Elements and the prism shaped cutters.

Table 1: Bit record of 12 ¼" Offset runs on the same well pad.

Well Name	Bit Type	Depth In m	Depth Out m	Interval Drilled (meter)	Hours	ROP m/hr	Dull Grading
01	RC IADC 437	1042	1087	45	13.1	3.4	1-1-WT-A-E-I-NO-CSG/TD
01	Standard PDC	1087	1427	340	29.20	11.64	2-2-WT-A-X-3-LT-CP
01	RC IADC 437	1436	1731	295	31.7	9.3	1-1-WT-A-X-I-NO-BHA
02	RC 437	1060	1531	471	75.60	6.23	2-3-WT-A-E-I-BT-BHA
02	RC 537	1531	2000	469	71.38	6.57	3-7-BT-S-E-1/16-CT-BHA
03	RC IADC 437	1085	1136	51	5.6	9.1	-------
05	RC IADC 437	1076	1168	92	30.0	3.1	2-3-WT-A-E-2/16-NO-BHA
05	RC IADC 537	1168	1721	553	65.4	8.5	2-6-WT-A-F#3-2-BT-BHA
05	RC IADC 537	1721	2142.5	421.5	43.6	9.7	2-4-WT-A-F#1-1-BT-CP
05	RC IADC 437	2147	2235	88	12.7	6.9	3-6-WT-A-E-I-CT-TD

The *Special* bit utilized in this well is a 7 bladed PDC bit with majority 16mm cutters equipped with HDI Elements as vibration dampener in secondary cutting elements. The bit design strategy for this run was based on the experience on drilling hard geothermal formation in Indonesia. Design-wise, a 6-bladed bit will compromise the number of cutters installed, while an 8-bladed design will sacrifice speed for durability. A 7-bladed design was selected because the bit has just enough cutters count and diamond volume. In addition, the HDI is in the position as back up cutters to lessen impact to the primary cutters. Related to rock failure mechanism, as expected from offset wells the lithology found in this section was quartzite and phyllite. In this aspect, the prism shaped PDC cutters played an important role on getting firm cutter engagement into formation on a lithology as hard as Quartzite and Phyllite.

Figure 6: The dull condition of the 12 ¼" PDC bit used on subject well. Most cutters were still in good condition. Some cutter on the gauge was damaged. The bit was undergauged 3/16".

The 12 ¼" FTKC76 ran was the first *Special* bit ran in Sorik Marapi well. Figure 6 shows the bit dull condition that was pulled out after indication of sudden pressure increase and suspect that the mud motor has reached its running hours. The bit came out in relatively good condition (1-1-BT-A-X-3-PN-BHA). Observed, several damaged gauge cutters have caused the bit to become 3/16" undergauged and the bit was decided not be rerun. Most of the cutters are in good condition and observed several gauge cutters was damaged. This proves that the HDI Elements are effective in maintaining and protecting the cutting structure as seen in the 1-1 overall cutter dull grading, allowing effective cutting mechanism of the prism-shaped cutters throughout the interval.

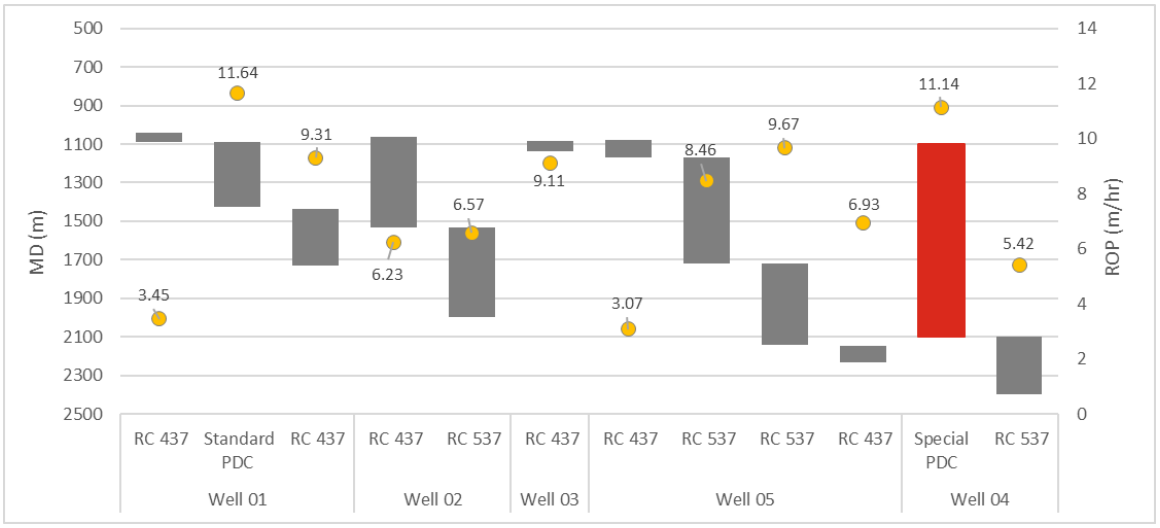

Figure 7: Performance comparison of Special PDC bit compared to offset wells.

The S*pecial* bit that uses of prism shaped cutter technology and HDI Elements has shown an increase of interval drilled (Figure 7). This performance is equivalent to 3 runs of TCI RC bits in the offset wells, setting a field record for the longest interval drilled (1000 m). For drilling 1000m interval, the ROP improvement was also significant with an average on-bottom ROP of 11.14 mph or 56% improvement compared to the average ROP of the offset well runs. In the final output, the utilization of this bit has saved approximately 3 rig operation days.

5. FUTURE PLANS AND IMPROVEMENTS

The way forward for performance improvement will vary. From bit design standpoint, testing more shaped cutters type and position specific for drilling hard formation or focus on impact resistance will be required. The base design change in the future might be needed as well. The gauge cutter damage seen after the bit was pulled out showed an indication of metal-metal contact possibly during drilling the float equipment. Metal shaving on the surface was also seen while drilling this interval. Since 13-3/8" casing plays an important part in well integrity, this shows room for improvement in terms of design to enable the 12-1/4" bit to safely drill out the float equipment and cement and withstand the gauge area. The standard 7 bladed – 16mm cutters design may also be changed in the future if the current design runs will consistently result a good dull condition and increase in ROP is desired.

REFERENCES

Allard T: Indonesia's hot terrain set to power its future, The Sydney Morning Herald (2010).

Andika, F., Sutan, M., Krisnanto, W., Roza, E., Setiawan, B., Malau, F., and Putradi, R.: Hybrid Drill Bit Improves Drilling Efficiency in Geothermal Application in Lumut Balai Field Indonesia, *Proceedings*, The 6th Indonesia International Geothermal Convention and Exhibition (IIGCE), Jakarta (2018).

Lock, E., Tipples, R., Ching, B., and Victor, P.: Custom PDC Bits Significantly Increase Drilling Performance in Tauhara Geothermal Drilling Project, *Proceedings*, 42nd New Zealand Geothermal Workshop in Waitangi, New Zealand (2020).

Rahmani, R., Pastusek, P., Yun, G., and Roberts, T.: Investigation of Geometry and Loading Effects on PDC Cutter Structural Integrity in Hard Rocks, Proceedings, IADC/SPE International Drilling Conference and Exhibition held in Galveston, Texas (2020).

This page is intentionally left blank

Implementation of Acid Stimulation Job to Significantly Improve Injection Capacity at Sorik Marapi Geothermal Field

Junior Setiawan[1], M. Ramos Suryanta Lubis[1], Rudy Yahya Sophian[1], Riza G. Pasikki[1], Muhammad Gusti Bastisya[2], and Andhika Pratama[2]

[1]KS Orka, Jakarta 12160, Indonesia
[2]Halliburton Indonesia, Banten 15314, Indonesia

junior.setiawan@ksorka.com, ramos.lubis@ksorka.com, rudy.sophian@ksorka.com, riza.pasikki@ksorka.com, muhammadgusti.bastisya@halliburton.com, andhika.pratama@halliburton.com

Keywords: Sorik Marapi Geothermal Field, coiled tubing acidizing

ABSTRACT

Sorik Marapi geothermal field is currently generating 90 MW, and is continuously developing production and generation facilities to meet target of 240 MW. Besides providing sufficient steam and brine for the generation, field injection capacity is also a key parameter to the development. To meet the challenge, it is required to have a robust injection management system and routine monitoring of injection performance.

An acid stimulation campaign has been conducted in four injection wells, which is mainly driven by the evidence of declining injection performance. The damage is strongly suspected due to solid particle deposition which has been carried over by the injection fluid and plugged the near-wellbore formation. Series of analysis and testing were conducted to formulate the appropriate chemical formula to treat the damaged zone.

Application of acid stimulation in injection wells have proven to restore the permeability of the damaged wells. In all of the treated wells, post-acid injectivity is higher than its initial state, by a factor up to four times. This phenomenon shows that acid treatment had removed skin damage not only from solid deposition, but also from cuttings and mud during drilling phase. It is also possible that insitu permeability has been enhanced due to the dilution of filling materials by acid. The success of this campaign positively supports the Sorik Marapi's plan to meet the generation target.

1. INTRODUCTION

Declining injection capacity at Sorik Marapi geothermal field was observed after no more than one year of continuously put in service. Normally in early stage of geothermal field operation, such decline is due to either transient effect, near-wellbore formation damage, reservoir pressure dynamic, or the combination of those parameters. During shut-down and turn-around activities when injection wells are put on standby, surveys were conducted at each well. The surveys were conducted while the wells were not connected to the system, to eliminate the effect of surface interference. Based on the characterization of updated well data, declining well performance is mainly caused by decreasing permeability due to formation damage. To improve the wells' injection capacity, a well intervention program using acid solution was planned.

2. WELL SELECTION CRITERIA AND CHARACTERIZATION

2.1 Declining Performance of Injection Wells

In the early months after Unit 1 power plant being commissioned in late 2019, degrading injection performance was observed. Total injected flow rate declined while operating pressure was increasing. The most common problem of geothermal injection wells is usually due to scaling deposition in the wellbore, creating friction along the pathway which will limit the injection capacity. Other possible causes of injectivity degradation are reduced II (injectivity index) of feedzone, or increased reservoir pressure.

Characterization processes were conducted to analyze the main cause of the decline. This will aid future studies on the field. If II reduction is the main cause of the degrading injectivity, it is more likely that damage occurs at near-wellbore formation, which involves local fractures that are intersected by the well. In this case, the well is still connected to the larger fracture network, however it is clogged due to mineral or other carried-over material. On the other hand, increasing reservoir pressure would suggest the injected reservoir section is compartmentalized with limited connectivity to the main fracture network.

Figure 1 shows the historical injection data (flow rate and wellhead pressure, at certain injection temperature) of Well 9. The figure portrays rapid decline of injection capability in the first months of 2020. After a prolonged injection period, injectivity recovered (the rebound in May-June 2020), however to the level lower than initial injectivity. This phenomenon explains that injection wells are actually connected with the fracture network and the main reservoir. The decline in early stage of injection could be due to the transient effect of commencing the continuous mass extraction and injection processes, while the rebound in the later months indicates more stable system. This theory is supported by the evidence of balanced pre-exploitation pressure between production and injection wells, as seen in Figure 2. The tracer test conducted later during the year showed tracer returns from injection wells to production wells. These explain that the degrading injection capacity is unlikely to be caused by reservoir pressure dynamic.

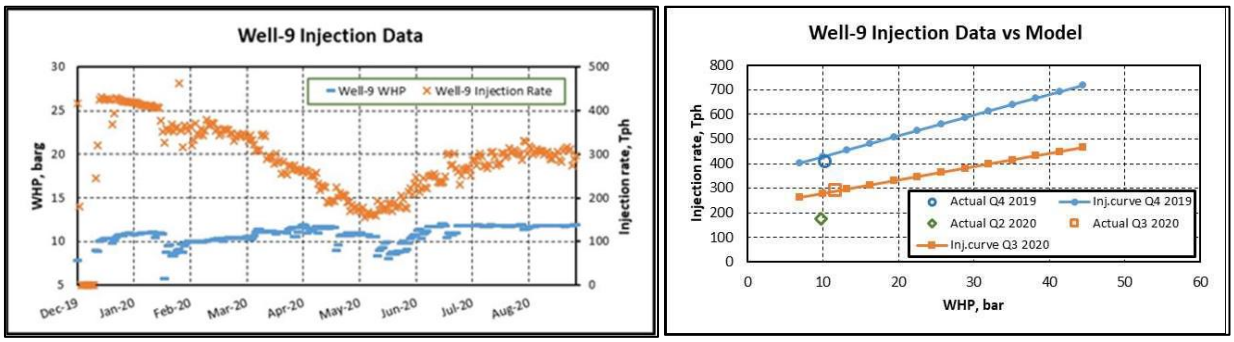

Figure 1: Injection data history of Well-9.

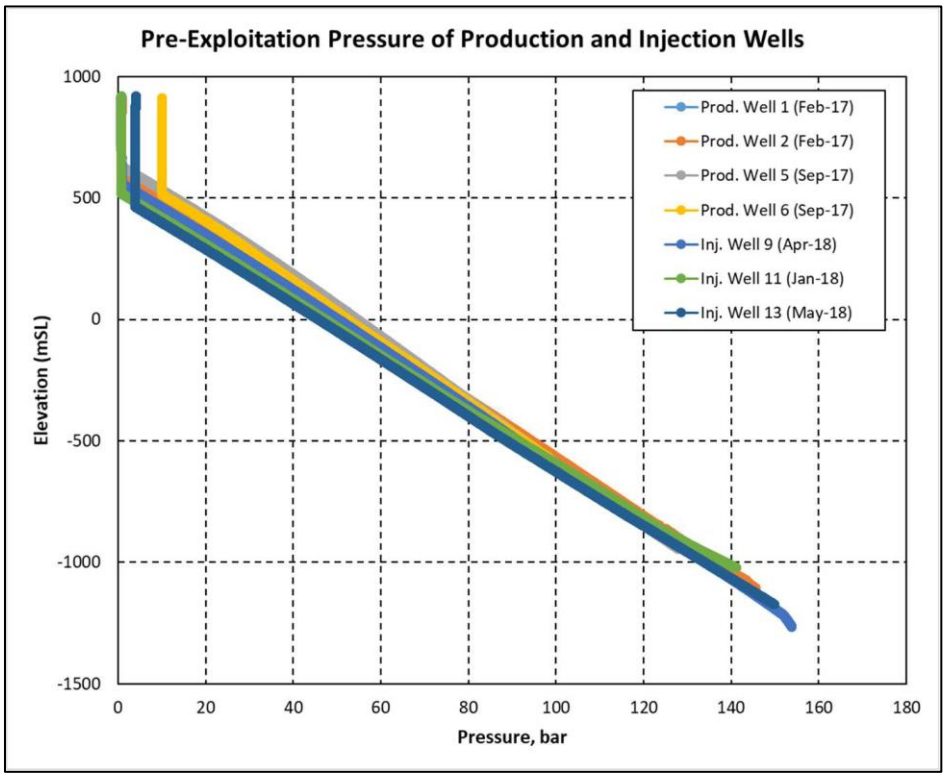

Figure 2: Static pressure of production and injection wells during pre-exploitation phase.

In September 2020, a series of well testing was conducted in injection wells. The surveys were part of routine well monitoring, utilizing the time window during shut-down and turn-around program. Careful review and analysis on the data shows reducing II in four injection wells, namely Well 9, 11, 13, and 14. In some wells, trend of II reduction has been observed since the wells being operated for injection several months before the Unit-1 commissioning.

Table 1: Evolution of injectivity index at Well-14.

No	Well Test Type	Date of Test	II (kg/s/bar)
1	Multirate II Test	Mar-18	6.6 – 9.8
2	Multirate II test	May-19	2.4
3	Injection PTS	Nov-19	1.2
4	Injection PTS	Mar-20	0.7
5	Injection PTS	Jan-21	1.1

To further investigate the cause of reducing II in the injection wells, operational lookback was conducted. It is later found that during the injection process, main injection line was frequently bypassed due to operational reason. In the past, the bypass line does not have strainer properly installed yet. Brine sample was taken and sent to the laboratory for further analysis. It was reported that three filtering

stages were required to purify 500 ml brine sample from carried-over solid material. From this evidence, it is clearly shown that solid particle has been carried-over to the wellbore and plug the permeable zone, hence reducing the II and injection capacity.

All four wells with reducing II (Well 9, 11, 13, and 14) are located in the same wellpad and are connected to the main injection line. Based on the study and damage evidence, these four wells are selected to be acidized to restore its permeability.

2.2 Pre-Treatment Test

Prior to conducting acid treatment, series of tests were conducted to all of wells candidate. The result of this pre-treatment test will be set as the baseline and compared with the post-treatment test. Tests include Pressure-Temperature-Spinner (PTS) during injection, multirate II test, and static Pressure-Temperature survey. The tests were conducted after well being dismantled from the injection system. It is essential to provide a standalone test facility for the well, enabling the test to examine individual properties of the well, eliminating the potential surface interference.

3. COILED TUBING ACIDIZING TREATMENT

3.1 Solubility Test

The near-wellbore formation damage occurred in Well 9, 11, 13, and 14 was strongly suspected due to the solid particle carried-over by the brine. To formulate the appropriate chemical formula for treatment, team conducted analysis of brine sample and cutting from drilling activities. Laboratory analysis indicates sample consist dominant silica, clay mineral, and plagioclase with less than ten percent calcite and insignificant iron content.

The mineralogy of the formation has restricted the use of the more popular conventional hydrochloric (HCl) acid since silica is not HCl acid-soluble. For this reason, further laboratory analysis was done to investigate the solubility of the sample in several acid system. Based on the laboratory analysis, a selected acid mixture with the highest solubility was chosen for the treatment. It is a Hydrofluoric (HF) acid-based system that effectively remove formation damage. However, high HF acid concentrations usually result in secondary precipitation in the near-wellbore region, resulting in failures or limited short-term successes which generally caused by calcareous minerals. Calcareous minerals can form damaging precipitates when reacting with HF acid (Pasikki and Gilmore, 2006). These minerals can eventually cause even the aluminum to precipitate in the matrix at the end of the tertiary reaction. Aluminum fluorides will continue to react with alumino silicates until all the acid is consumed. The resulting high aluminum can lead to aluminum precipitation. To overcome this situation, planning must be done beforehand to reduce the risk of precipitation.

To minimize precipitation, two different acid system was used. 20% HCl acid stage minimizes local damage and helps to dissolve the carbonate minerals which followed by 9% HCl – 6% HF mixture that should further enhance the conductivity of the formation. Based on the solubility test conducted at laboratory, combination of HCl preflush and main HCl-HF treatment could dissolve up to 94% solid particle contained in the injection brine.

Table 2: Solubility test results.

Test No.	Sample	Chemical	Initial sample weight (gr)	Temperature (°F)	Time (hours)	Paper weight (gr)	Last weight (gr)	Solubility (%)
1	Sample A	HCl followed by HCl-HF	1.97	300	1	1.03	1.14	94.42
2	Sample B	HCl followed by HCl-HF	1.96	300	1	1.05	1.14	80.10

3.2 Depth of Interest for Treatment

Acid treatment zone is determined by considering several aspects: permeable zone indicated from PTS survey, break and loss evidence during drilling, and mineralogy considerations. There is a plan in the future to convert some injection wells into production wells, hence reservoir temperature is also considered on the treatment zone selection.

Since the wellbore will be exposed directly to the acid system, temperature plays an important part in designing an acid treatment. A larger coiled tubing size is required to maximize acid delivery rate, which increase success rate and decrease treatment duration. The use of coiled tubing is preferred, rather than conducting bullhead injection from wellhead. Beside requiring longer duration of treatment, bullhead injection has its own setback due to corrosion and leakage potential at dosing pump and along the injection pipe. Moreover, the acid mixture will induce rapid corrosion process at wellhead and casing. Corrosion inhibitor will potentially fail to protect the system due to high temperature and long duration (Pasikki et al., 2010). The use of coiled tubing will also help in diverting the stimulation fluids mechanically where bullhead treatments fail to provide. This will allow the treatment fluid enters the target zone effectively and avoid thief zones.

Another factor to be considered is corrosion loss. To mitigate an excessive corrosion loss during treatment, corrosion inhibitor was added to the acid systems. A corrosion test was conducted in the laboratory to determine the maximum exposure time to keep the corrosion loss within the limitation. The corrosion loss for both acid systems are below 0.05 lb/ft^2 which is used as industry standard.

Table 3: Corrosion test results.

Test No.	1	2	3	4	5	6
Fluid System	**HCl**			**HCl-HF**		
Temperature (ºF)	235	235	300	225	300	300
Duration (hr)	6	3	4	8	3	2
W1 (gr)	33.280	33.930	35.640	98.470	33.330	33.920
W2 (gr)	33.180	33.850	35.020	97.080	32.820	33.700
W3 (gr)	0.099	0.077	0.622	1.390	0.511	0.220
Corrosion Loss (lb/ft^2)	0.0071	0.0055	0.0442	0.0330	0.0363	0.0156

Figure 3: Corrosion test coupon upon completion of the test.

3.3 Acid Treatment

The selected interval for acid treatment is approximately 650 ft for each well. For the first step, all designated zone is pre-flushed using 20% HCl. In each interval of treatment zone, coiled tubing was run in a reciprocating direction. Pre-flush solution amount is set at 50 gallon per foot.

The next step is the main treatment, in which acid was pumped through 2-3/8" coiled tubing from the deepest treatment zone. Average pumping rate is 3.5 bpm (through the coiled tubing) and not more than 40 lps of fresh water through the annulus as backside injection. The backside injection is meant to keep the downhole temperature to satisfy the optimum range of corrosion inhibitor, while keeping the rate low enough to not add dilution factor to the acid mixture. Pumping more water will result in lower temperature environment, however acid concentration will be reduced due to dilution, which is contra-productive to the program success.

4. TREATMENT RESULTS AND ANALYSIS

The acid job campaign was executed from mid of April to early May 2021 safely and incident free. Waste management, secondary containment is applied for spill protection and chemical wastes was handled in-house hence no environmental issue from the start of the equipment mobilization, during execution and after demobilization. Fit for purpose community engagement and local workers involvement was applied and therefore no community issues were encountered.

Acid treatment in Sorik Marapi injection wells achieved 100% success ratio. Of the four treated wells, all exhibited significant II increase. The post-treatment test conducted after the acid treatment shows very encouraging result in the wells' injectivity. As shown in Figure 4, lower downhole pressure during post-acid test is exhibited at certain injection rate. Figure 4 also shows II has increased from 1.78 to 7.03 kg/s/bar. Feedzone interpretation from the spinner analysis also shows consistent depth location, but with greater II.

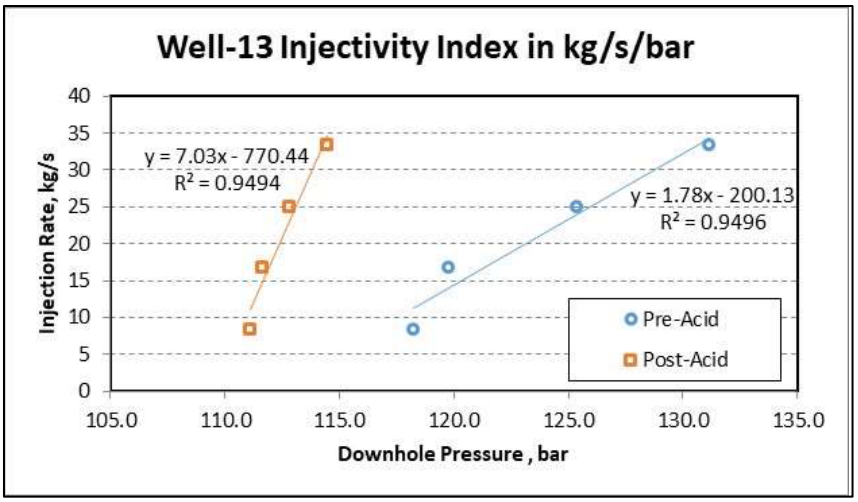

Figure 4: Injectivity index of Well-13.

The acid job execution was performed simultaneously with the other on-going activities, namely make-up well drilling campaign in the other two well pad locations. Fresh water supply is one of the key challenges that cause some of the other wells did not have the multi-rate II test. However, historically in Sorik Marapi field, individual II measured from PTS Injection analysis generally showed agreement. The Figure 5 below showed one example of the well that did not have multi-rate II test data, which show its individual II.

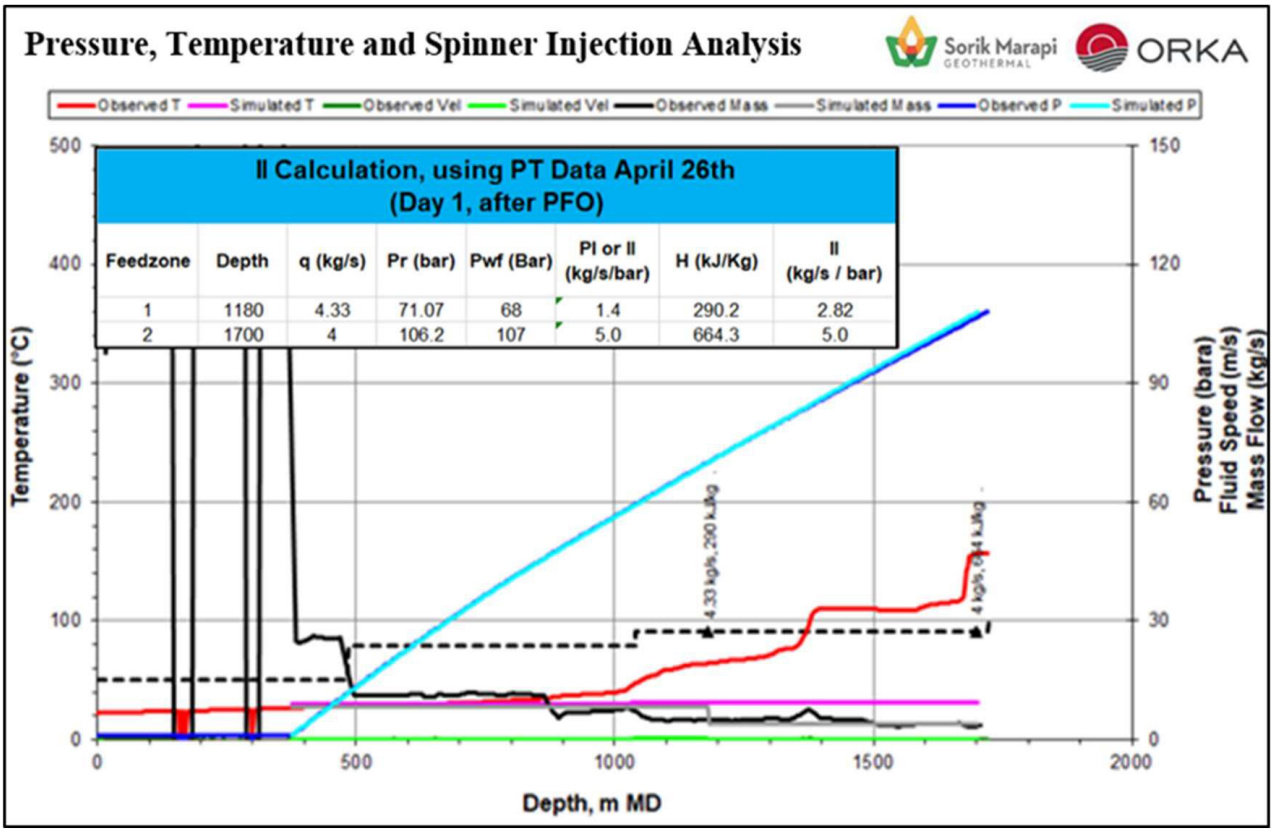

Figure 5: Injectivity index of Well-14 from Water Loss Test (PTS-Injection).

As previously mentioned in table 1, the Injectivity Index of Well-14 before acid stimulation treatment was between 0.7 to 1.1 kg/s bar. The Figure 5 shows the post-stimulation total II is 7.82 kg/s bar. This is more than seven times improvement of the pre-acid condition and furthermore this is also higher than the II obtained when this well was initially drilled in 2018. Total incremental injection capacity is shown by Figure 6 below. Based on Figure 6, it can be inferred that the team is successful to obtain total increasing injection capacity by 2600 tph. Two out of four treated wells were decided to be assigned as production wells for upcoming power plant unit III, hence it is disconnected from the injection facility line and currently in the process of heating up. From the remaining two injection wells, the team is successful to add 500 tph of injection capacity. This increment, combined with the potential gain from the two soon-to-be production wells, was successfully achieved at a fraction of the price to drill one new well.

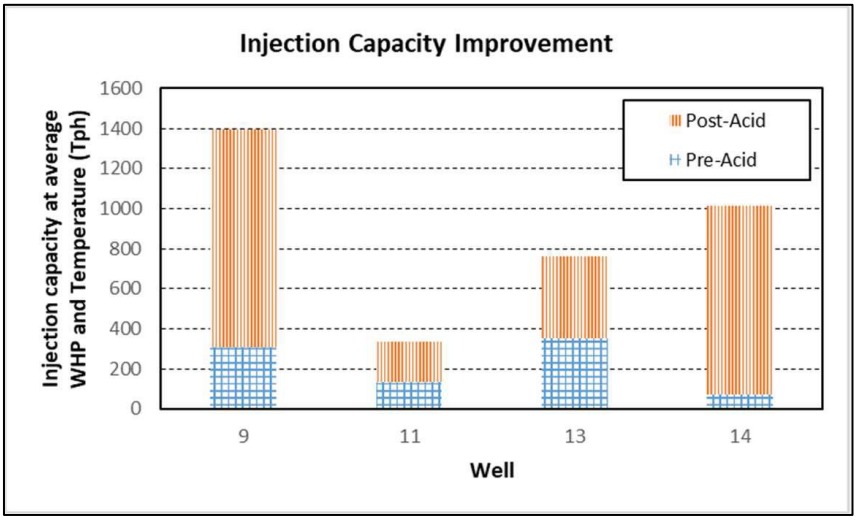

Figure 6: Injection capacity improvement calculated at average wellhead pressure and temperature.

Another interesting result of the acid treatment is that the final II is even higher than its initial state, as shown in Figure 7. This phenomenon confirms that acid stimulation is not only successful to remove the skin damage from the solid deposition during operation, but also remove the skin previously caused by the plugging of the drilling cuttings and muds during drilling in the

feedzones. It is also possible that the permeability of the in-situ fracture has been enhanced due to dilution of the filling materials by the acid solution.

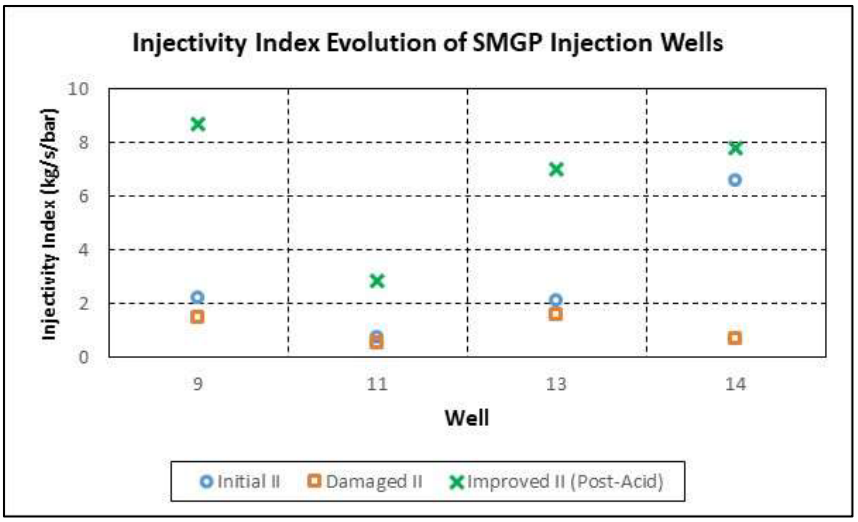

Figure 7: Injectivity index improvement in acid-treated wells.

5. CONCLUSION

Acid stimulation using a mixture of HCl and HF acid was conducted to restore permeability of injection wells at Sorik Marapi geothermal field, due to declining injectivity after being put online as injector. Analysis on wellbore characterization and operational method revealed such decline is caused by carried-over solid particles which causing near-wellbore formation damage. Acid solution was delivered to the designated treatment zone through 2-3/8" coiled tubing. Evaluation on wells' performance following the acid stimulation shows very encouraging results in terms of permeability increase. The final injectivity index is higher than its initial state, showing an enhancement of in-situ permeability of the injection wells at Sorik Marapi geothermal field.

REFERENCES

Malate, R.C.M., Austria, J.J.C., Sarmiento, Z.F., Di Lullo, G., Sookprasong, P.A., and Francia, E.S.: Matrix Stimulation Treatment of Geothermal Wells Using Sandstone Acid, *Proceedings*, 23rd Workshop on Geothermal Reservoir Engineering, Stanford University, Stanford, CA (1998).

Pasikki, R., Libert, F., Yoshioka, K., and Leonard, R.: Well Stimulation Techniques Applied at the Salak Geothermal Field, *Proceedings*, World Geothermal Congress 2010, Bali, Indonesia (2010).

Pasikki, R.G. and Gilmore, T.G.: Coiled Tubing Acid Stimulation: The Case of Awi 8-7 Production Well in Salak Geothermal Field, Indonesia, *Proceedings*, 31st Workshop on Geothermal Reservoir Engineering, Stanford University, Stanford, CA (2006).

Pressure Transient Analysis of Injection/Fall-off Tests in the Fractured Geothermal Reservoir

Gitta A. Septiani[1,2], Eylem Kaya[1], and Daniel W. Adityatama[1,3]

[1]Department of Engineering Science, The University of Auckland, Private Bag 90210, Auckland, New Zealand
[2]PT Sarana Multi Infrastruktur, Jakarta, Indonesia
[3]PT Geoenergi Solusi Indonesia, Jakarta, Indonesia

gsep095@aucklanduni.ac.nz, e.kaya@aucklanduni.ac.nz, daniel.adityatama@geoenergis.com

Keywords: Pressure transient analysis, numerical models, injection/falloff, fractured geothermal reservoir, free CO_2 phase geothermal reservoir.

ABSTRACT

Early analytical methods for pressure transient analysis (PTA) commonly assume uniform rock properties over a large reservoir. However, geothermal systems are not homogeneous and often consist of natural fissures and fractures, allowing fluid transport. With the standard PTA methods, it is difficult to represent a fractured reservoir adequately or determine the sharp gradients in fluid temperature, pressure, or saturation that may occur very close to the fracture during the well test. Thus, in this study, numerical modelling in PTA with dual-porosity approach is used to simulate a fractured geothermal reservoir.

A set of numerical models were developed using the TOUGH2 simulator to obtain the reservoir pressure response during injection/fall-off tests in the fractured single-phase pure-water reservoir and fractured reservoir with free-CO_2 phase. Python script from the PyTOUGH library is used in the model setup and automation. Several other parameters were also investigated namely injectate temperature, skin factor value, and boundary conditions to determine the accuracy of estimated values and evaluate the adequacies and limitations of the numerical models.

The results demonstrated that the pressure response in a log-log pressure derivative plot follows a half slope line, and the S-shaped transition appears in the fractured single-phase pure water while in the fractured reservoir with the free-CO_2 phase, the decline in the derivative pressure is observed before reaching the infinite-acting radial flow (IARF). The reservoir parameters estimated using Horner and semilog methods were compared with the actual value inputted to TOUGH2 to identify variables that may leads to the wrong interpretation of the reservoir characteristic. Thus, the results may be used as the groundwork for future use of PTA in the fractured geothermal reservoir.

1. INTRODUCTION

Pressure transient analysis (PTA) is used to analyse the pressure response data from the well testing. In early times, the PTA theory is based on the analytical models which have been mainly developed for groundwater hydrology and petroleum engineering applications. The basic assumptions of the analytical models developed for PTA contradict the nature of geothermal reservoirs which include complex non-isothermal, non-uniform situations and phase changes (McLean and Zarrouk, 2017; O'Sullivan and McKibbin, 1989). Therefore, the need for a numerical model for PTA has been recognised as the analytical models would not be able to handle the complex geometries, a broader range of model types, the high nonlinearity on diffusion processes and thermodynamic conditions, particularly in the presence of phase changes (Houzé et al., 2012).

As geothermal systems are often fractured and consist of natural fissures to transport the fluid, in this study dual-porosity approach is used to model this complex system. In this approach, the reservoir consists of rock matrix blocks and natural fissures. The rock matrix blocks have high storativity and high permeability, whereas the fractures have low storativity and high permeability connected to the well. The fluid transport to the wellbore mainly takes place in the high-permeability fracture. The matrix blocks act as the source of the fluids to the fracture. Thus, at first, the production fluid flows from the fracture system as if this system was there alone and no pressure change happens inside the matrix blocks. Once the pressure in the fracture decreases, the fluid from the matrix blocks starts to flow to the fracture system. It provides pressure support and slows down the drawdown (Houzé et al., 2012).

This study investigates the numerical PTA of injection/fall-off test under the various conditions of a fractured geothermal reservoir such as single-phase pure water and reservoir with free CO_2 phase. The effect of fracture spacing and matrix permeability is also investigated in this study to identify how the change of these parameters affects the results of PTA. Moreover, the injectate temperature and the boundary conditions that control the reservoir pressure response (closed or no-flow boundary and constant pressure boundary) are being examined in this study. Therefore, the results of this study may be used in an attempt to identify any undesirable sensitivities and interpret the real pressure transient data from the geothermal fields more accurately.

The need for numerical modelling for PTA has been recognised for a long time. This is because the analytical models are based on the diffusivity equation which does not match the geothermal datasets (Earlougher, 1977). There are many factors of geothermal reservoirs that violate the assumption of analytical models due to the high temperature and complexity of geothermal reservoirs. Geothermal reservoirs are non-isothermal, which incorporates non-uniform and non-linear fluid properties and non-horizontal flow. Numerous studies utilised the numerical modelling of PTA using TOUGH2 (Adityatama et al., 2018; Guerra and O'Sullivan, 2018; McLean and Zarrouk, 2017; Septiani et al., 2021). In addition, TOUGH2 and its various equation of states (EOS) have been widely used in simulating the non-isothermal flows of multicomponent, multiphase fluids in one-, two-, and three-dimensional porous and fractured media (Pruess et al., 1999).

This study uses the AUTOUGH2 simulator for numerical modelling of non-isothermal flows of multicomponent, multiphase fluids in porous media (Yeh et al., 2012). The PyTOUGH scripting library was used for the automation of TOUGH2 setup and simulation

(Croucher, 2011). The TIM graphical tool was utilised for assisting in visualising the results from TOUGH2 simulations (Yeh et al., 2012). The analytical PTA methods used in this study are manual calculations and plotting of Horner and semilog plots, log-log plots of pressure (Bourdet et al., 1989; Onur and Al-Saddique, 1999; Zarrouk and McLean, 2019).

2. NUMERICAL MODEL SET UP

2.1 Model Geometry

The fractured reservoir is represented by 1D-radial model grid design using dual-porosity approach. Logarithmic radial block spacing is used to have very fine grid structure in the region close to the well block. Refer to previous numerical modelling of PTA work (McLean and Zarrouk, 2017; Septiani et al., 2021), the pressure response is insensitive to the number of skin zone block and reservoir zone block. The blocks setup is divided using the MINC method into fracture and nested matrix blocks. The key parameters of the 1D radial model of infinite reservoir and reservoir with boundary are shown in Table 2. The fractured reservoir model's schematic illustration can be seen in Figure 1, which visualised the infinite reservoir. MINC partitioning method is applied for the first 50 blocks located from the origin up to 322 m (Figure 1a), and a reservoir with only a single fracture zone with MINC discretisation approach is used for 10 blocks with a total size of 20 m and located 10 m away from the origin point (Figure 1b). Lastly, in the closed and constant pressure-boundary reservoir, the MINC partitioning method was applied to all blocks.

In this study, we chose not to include the wellbore as part of porous media because the early time behaviour obtained from the numerical model results is sensitive to the parameters used in the well block (porosity, permeability, volume, compressibility values). Also, geothermal systems are usually fractured, and the permeability of these fractures is very high. Unless it is a vapour-dominated system, we do not expect the wellbore storage period to be long in geothermal PTAs. Thus, a well radius of 0.1 m was used to represent the empty space in the volume occupied by the wellbore. The skin zone has a high-resolution area immediately outside the wellbore at r direction. Outside this, the block sizes increase logarithmically until the radius of the region (skin, reservoir, or boundary) is achieved.

Table 1: Key parameters for 1D radial model.

	Infinite Reservoir (Single Phase Pure Water Model and Two-Phase with Free CO_2 Model)	**Enclosed with Boundary (Single Phase Pure Water Model)**	**Enclosed with Boundary (Two-Phase with Free CO_2 Model)**
Skin Zone	• Radius = 3.875 m • Number of blocks = 14 blocks • Porosity = 0.1 • Permeability = 2 mD (positive skin); 100 mD (negative skin) • Skin factor = 14.63 (positive skin); -3.29 mD (negative skin)	• Not applied	• Not applied
Reservoir Zone	• Radius = 132000 m • Number of blocks = 85 blocks • Porosity = 0.1 • Permeability = 10 mD (base) • Layer thickness = 600 m • Relative permeability = Linear; S_l = 0.3, S_v = 0.05 • Number of MINC blocks = - Infinite reservoir: 50 blocks from origin up to 322 - Reservoir with single fracture zone extending infinitely: 10 blocks with total size of 20 m located 10 m from the origin	• Radius = 303.875 m • Number of blocks = 99 blocks • Porosity = 0.1 • Permeability = 10 mD (base) • Layer thickness = 600 m • Relative permeability = Linear; S_l = 0.3, S_v = 0.05 • Number of MINC blocks = all reservoir blocks	• Radius = 53.875 m (closed boundary); 33.875 m (constant pressure bounday) • Number of blocks = 99 blocks • Porosity = 0.1 • Permeability = 10 mD (base) • Layer thickness = 600 m • Relative permeability = Linear; S_l = 0.3, S_v = 0.05 • Number of MINC blocks = all reservoir blocks
Boundary Zone	• Not applied	<u>Closed or No Flow Boundary</u> • No additional block <u>Constant Pressure Boundary</u> • Number of blocks = 1 block • Aquifer zone extent = 100 m • Volume aquifer = 1 x 10^{99} m^3 • Nodal distance between reservoir and boundary blocks = 10^{-9} m	<u>Closed or No Flow Boundary</u> • No additional block <u>Constant Pressure Boundary</u> • Number of blocks = 1 block • Aquifer zone extent = 100 m • Volume aquifer = 1 x 10^{99} m^3 • Nodal distance between reservoir and boundary blocks = 10^{-9} m

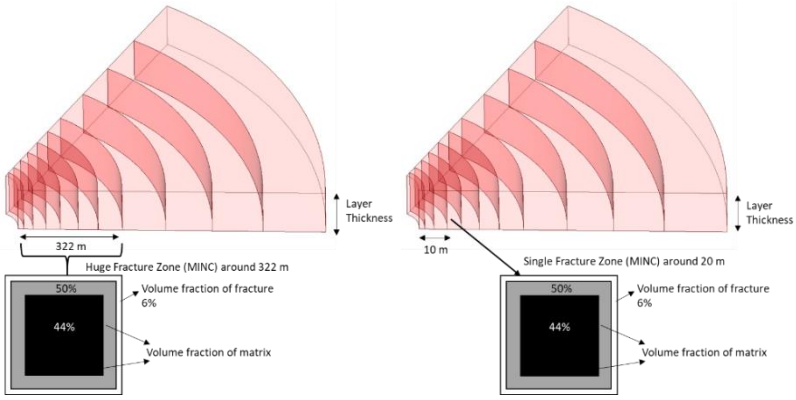

a. **b.**

Figure 1: Block layout for the dual-porosity MINC model; a. infinite reservoir; b. reservoir with a single fracture zone.

2.2 Base Model Parameters

The key parameters used for setting up the base dual-porosity model are shown in Table 2.

Table 2: MINC model parameters.

Total number of multiple interacting continua	3
Type of proximity function	ONE-D
Volume fraction of the fracture continuum	6%
Volume fraction of the matrix continuum	50%, 44%
Matrix porosity	0.048937
Fracture porosity	0.9
Matrix permeability	0.1 mD
Fracture permeability	10 mD
Fracture spacing	10 m

Number of MINC blocks

The number of MINC blocks describes the active grid blocks that undergo the partitioning MINC process. Hence, the selected blocks or active grid blocks will be divided into fracture and matrix continuum, whereas the inactive grid blocks are left unchanged as single porosity blocks (Pruess et al., 1999). The python script from PyTOUGH library is used to create the MINC blocks and connections in the grid for simulating the flow in the fractured reservoir. This has the same capability as the GMINC program or the MINC part of TOUGH2's MESHMAKER (Croucher, 2015).

The volume fraction of fracture and matrix continuum

In a dual-porosity model using the MINC method, the fracture permeability is retained from the single porosity model. The permeability of matrix blocks is usually tighter, at least two orders of magnitude lower than fracture permeability (Austria, 2014). The fracture porosity is mostly larger than the matrix blocks porosity. However, the total porosity of both fracture continuum and matrix blocks continuum is constrained by making the total pore volume equivalent to the pore volume of the grid blocks in single porosity. Generally, the fracture volume fraction is smaller than the volume occupied by the matrix blocks (Austria, 2014). Hence, the effective porosity of the dual-porosity model can be calculated as:

$$\theta_{effective} = \theta_f V_f + \theta_m (1 - V_f) \quad (1)$$

where θ is porosity and V is volume, whereas the subscripts f and m indicate fracture and matrix blocks. In this model, the fracture continuum is set to have a 6% volume portion while the rest is for the matrix blocks, divided into 50% and 44%. By using the combination of porosity and volume, as stated in Table 2, the effective porosity of the model is:

$$\theta_{effective} = (0.9 \times 0.06) + (0.048937 \times 0.5) \times (0.048937 \times 0.44) = 0.1$$

Proximity function (fracture type)

The proximity function expresses for a given reservoir domain V_o, the total fraction of matrix material within x distance from the fracture (Pruess et al., 1999). The fracture type used in this study is the one-dimensional option which uses a set of planes parallel to infinite fractures.

Fracture spacing

In MINC formulation, fracture spacing is an input parameter to the MESH generator to produce the active grid of the dual-porosity model. The fracture spacing is the measure of the average perpendicular distance between fractures in physical terms. The fracture spacing can be determined from the average number of fractures found within a standard distance normal to a fracture (Austria, 2014).

Equation of State (EOS) TOUGH2

EOS modules of TOUGH2 were used to state the thermophysical properties of fluid mixtures in governing the mass and energy balance equation. For the single-phase reservoir model, EOS 1 module of TOUGH2 is used with primary variables inputted are reservoir temperature and reservoir pressure, which are 250°C and 80 bar, respectively.

EOS 2 module of TOUGH2 is used to simulate the initial condition of a two-phase reservoir with CO_2 content. The primary variables input for this condition are gas-phase pressure (80 bar); gas saturation, Sg (3%); and CO_2 partial pressure (40.197 bar). The CO_2 partial pressure is calculated based on Henry's Law, given by:

$$P_{CO_2} = \frac{18}{44} K_h X_{CO_2} \quad (2)$$

Where Henry's Constant, K_h is calculated using a correlation from Battistelli et al. (1997), which extends the temperature range of Henry's constant correlation up to 350°C.

2.3 Sensitivity Analysis of Model Set-Up

Dual-porosity models using the MINC method have been conducted for several years. The important model parameters of fracture spacing and matrix permeability are incorporated differently. Thus, the manual sensitivity of these parameters is investigated to know the effect of different parameter values on the pressure derivative.

2.3.1 Fracture spacing

The sensitivity analysis of fracture spacing is investigated from small to large fracture spacing. The analysis is conducted in the infinite reservoir zone with an injectate temperature of 250°C. The effect of changing fracture spacing during the fall-off period is plotted in the pressure derivative shown in Figure 2. At first, by comparing the dual-porosity model to the single porosity model, it is apparent that the dual-porosity model has an S-shaped transition, while in the single porosity model, the zero-slope straight line appears from the transition time until late times. This is because the S-shaped transition in the dual-porosity model indicates the pressure difference between the fracture and matrix blocks where the fracture zone is present.

For the 1 m fracture spacing case, the time start of S-shaped transition is the earliest among other cases. This is due to the small fracture spacing indicating that the grid consists of many fractures with smaller apertures, making the pressure differential between fracture and matrix occur early. In addition, the small fracture spacing results in a large surface area between the fractures and matrix. Therefore, as soon as the fracture system starts to produce, the exchange of fluid and heat between the fracture and matrix continuum will also start due to the large surface area. In contrast, the large fracture spacing represents a smaller number of fractures with a large aperture. Thus, the pressure differential between fracture and matrix continuum appears late due to the small number of fractures in the system. The large fracture spacing also causes the fluid and heat exchange between the fracture and matrix to be limited.

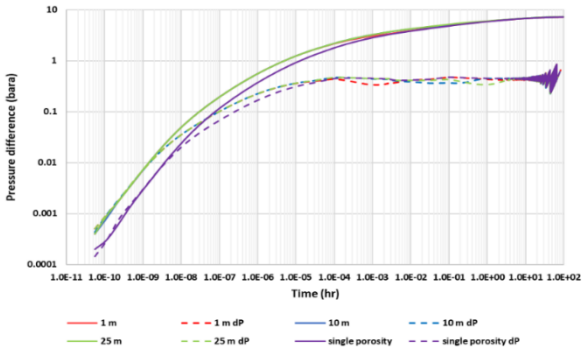

Figure 2: Effect of changing fracture spacing on the pressure derivative plot.

2.3.2 Matrix permeability

The base model uses a matrix permeability of 0.1 mD, which is two orders of magnitude lower than the fracture permeability, which is 10 mD. A smaller matrix permeability 0.01 mD is tested to know the sensitivity of this parameter. The pressure derivative plot result is shown in Figure 3.

Changing the matrix permeability affected the start of the transition and the depth of the dip. A smaller matrix permeability causes the matrix response to the global flow in the fracture to appear late. In addition, the small matrix permeability also causes the depth of the dip to be more apparent as the exchange of fluid and heat between fracture and matrix blocks is limited.

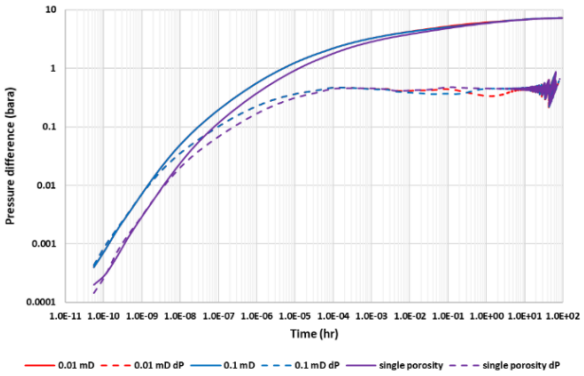

Figure 3: Effect of changing matrix permeability on the pressure derivative plot.

2.4 Model Test Set-Up

The injection/fall-off test is conducted with a single injection rate at the mass flow rate for 24 hours and the fall-off period lasting for 96 hours. To obtain accurate and realistic predictions for PTA problems, different reservoir parameters and various aspects of model design were investigated which are the effect of injectate temperature, negative and positive skin, and boundary conditions: no flow or closed and constant pressure. The following model schemes were examined:

- Reservoir zone (no-skin) extending infinitely
- Reservoir zone (no-skin) with a single fracture zone, extending infinitely
- Skin zone (positive and negative) and a reservoir zone, extending infinitely
- Reservoir zone (no-skin) with closed boundary
- Reservoir zone (no-skin) with constant pressure boundary

The range model parameters tested are summarised in Table 3.

Table 3: Range tested for the injection/fall-off test.

Parameter and description	Range tested
Injectate temperature	57ºC, 250ºC
Skin zone permeability (skin factor)	2 mD (14.63), 100 mD (-3.29)
Boundary condition	No flow (closed) boundary, constant pressure boundary

3. SINGLE-PHASE PURE WATER MODEL

The PTA of fractured reservoirs with single-phase initial conditions is investigated in this section. The pressure derivative is plotted to illustrate the reservoir pressure response during the fall-off period. Furthermore, the IARF flow regime is identified and used to derive the reservoir properties using the manual calculation method (Horner and semilog plots). Δk represents the difference of permeability value between AUTOUGH2 inputs and the analytical model result; ΔSkin represents the difference in skin value between AUTOUGH2 inputs and the analytical model result.

3.1 Effect of Injectate Temperature

In an injection/fall-off test, the injectate fluid used is mostly a low-temperature surface fluid. The injection temperature used makes a difference in fluid properties and affects the result of analytical PTA. Temperature-dependent properties that affect the pressure transient data are dynamic viscosity, density, and fluid compressibility. Grant and Bixley (2011) suggest using the same water injectate temperature as the reservoir temperature. In this study, we will run our models with two different temperatures; 57ºC (cold water) and 250ºC (the same as reservoir temperature), to investigate the sensitivity of model results to the injectate temperature in PTA analysis.

3.1.1 Infinite reservoir with no skin

In this section, the effect of injectate temperature is simulated in the reservoir that extends infinitely. This simulation aims to know the pressure response of the reservoir only without any other parameters that will affect the PTA result, such as skin zone or boundary. The pressure response of the dual-porosity model is compared to the single porosity model and plotted in the derivative plot shown in Figure 4.

At the early time of the fall-off period (Figure 4a), half a slope line which is illustrated by the green line has occurred after the unit slope line. As the well deflects a dominant fracture, the pressure response follows half a slope line because the standard well test analysis is based on the assumption of a uniform porous reservoir (O'Sullivan and McKibbin, 1989). A derivative hump due to the cold-water injection is observed for both single and double porosity models (Figure 4b). As the cold water invaded the reservoir during injection, it travels further than in the single porosity model (Figure 5). Thus, the effect of cold water is more persistent in the fall-off period for the dual-porosity model, and the response of dual-porosity reaches the IARF region later.

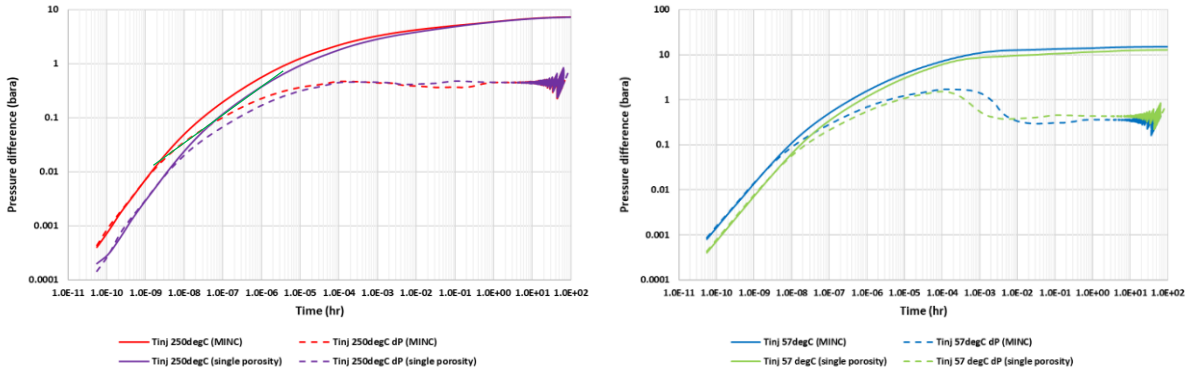

a. **b.**

Figure 4: Effect of injectate temperature on the pressure derivative plot in a fractured reservoir (no-skin) extending infinitely; a. injectate temperature of 250ºC; b. injectate temperature of 57ºC.

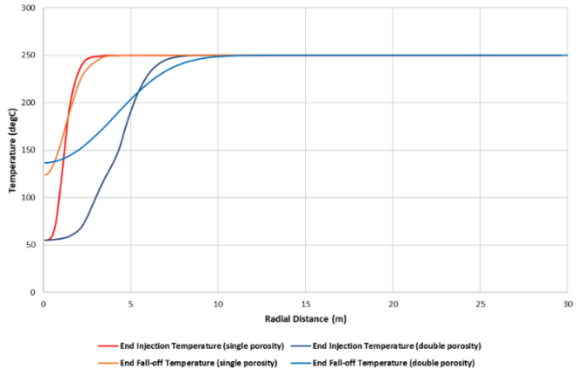

Figure 5: Radius of condensation front between single and double porosity in cold water injection case.

The global flow in the fracture system causing the pressure difference between a fracture and the matrix blocks because when the pressure in the fracture system is at P_{wf}, the matrix block is still in the initial pressure (P_i). Hence, the matrix blocks will start to provide fluid to the fracture system and maintain the pressure support, creating the transitional dip. The dip in the cold-water injection (Figure 4b) is deeper than the hot-water injection, which is likely due to the storativity ratio, ω. The pressure dip also occurs in the single porosity model, which is likely due to the temperature difference between injectate fluid and reservoir fluid. The second radial flow indicates the total system radial flow (the flow in the fracture and matrix blocks). The reservoir parameter is then derived using the slope of the second radial flow in the fall-off period. From Table 4, the reservoir permeability estimated for both injectate temperatures has a small quantified error, while the skin factor value estimated for the injectate temperature of 57ºC is overestimated and resembles positive skin.

Table 4: Reservoir parameters estimated for different injectate temperature in a fractured reservoir (no-skin) extending infinitely.

Injectate Temperature (ºC)	k (mD)	Δk (mD)	Skin	ΔSkin
57	12.19	2.19	11.96	11.96
250	9.81	0.19	0.93	0.93

3.1.2 Infinite reservoir with single fracture zone and no skin

At this section, we assumed that the reservoir has only one single fracture zone with a radial length of 20 m, located 10 m away from the wellbore. The presence of this small fracture zone during the injection/fall-off test is investigated, and the pressure derivative results are shown in Figure 6. The estimation of reservoir properties is summarised in Table 5.

Table 5: Reservoir parameters estimated for different injectate temperature in a single fractured reservoir (no-skin) zone extending infinitely.

Injectate Temperature (ºC)	k (mD)	Δk (mD)	Skin	ΔSkin
57	10.33	0.33	7.65	7.65
250	10.16	0.16	0.39	0.39

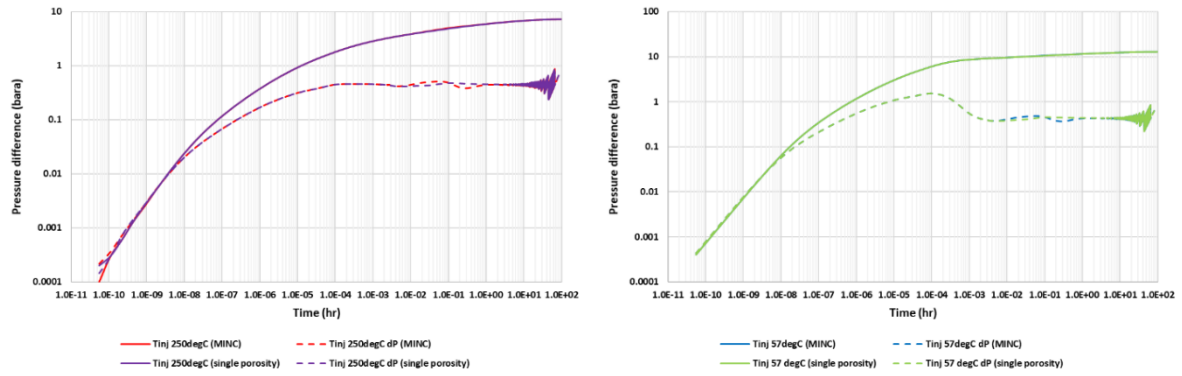

a. **b.**

Figure 6: Effect of injectate temperature on the pressure derivative plot in a single fractured reservoir (no-skin) zone extending infinitely; a. injectate temperature of 250ºC; b. injectate temperature of 57ºC.

At the early times, the pressure difference in the dual-porosity model is the same as in the single porosity model, which indicates that the flow has not reached the fracture zone (Figure 6). In the intermediate times, the S-shaped transition has appeared due to the presence of fractures, resulting in the pressure difference between the fracture and matrix blocks. The reservoir permeability estimated for all cases has a small difference with the actual value inputted to TOUGH2. However, the skin factor value estimated for the cold-water injection case is higher than the actual value, which resembles a positive skin.

3.2 Effect of Skin Factor Value

The presence of the skin zone in the fractured reservoir is simulated by changing the fracture permeability in the skin zone while the reservoir zone permeability is retained at 10 mD. The skin factor values tested are varied, as summarised in Table 3. The pressure derivative results for the positive skin model are shown in Figure 7a, while Figure 7b is referred to the negative skin model result.

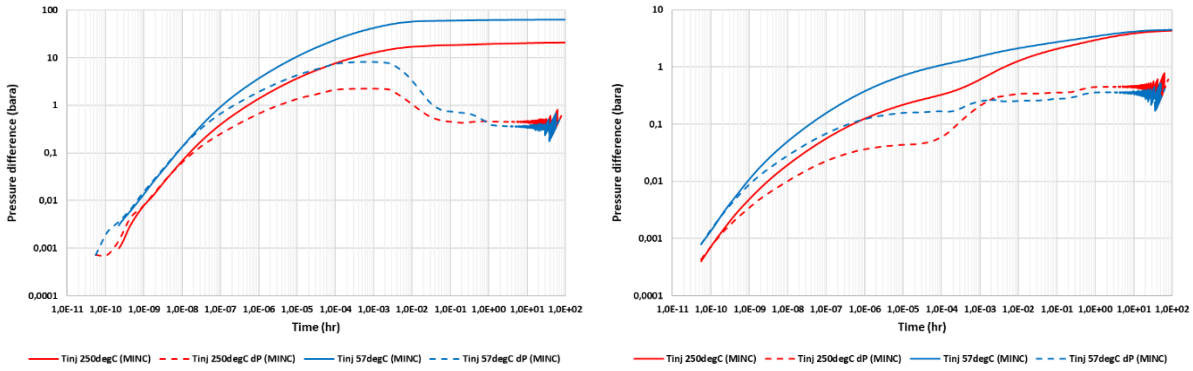

a. **b.**

Figure 7: Effect of skin factor value on the pressure derivative plot in a fractured reservoir with skin zone extending infinitely; a. positive skin; b. negative skin.

The pressure derivative results illustrate a hump in the positive skin model for both injectate temperatures (Figure 7a). However, a bigger hump is apparent in the cold water injection case due to the temperature difference between injectate water and reservoir fluid. In the negative skin model, the pressure derivate plot shows two humps for both injectate temperatures (Figure 7b). This might be the effect of negative skin as the permeability near the wellbore is higher than the reservoir permeability, resulting in the first hump being smaller than the second hump. The zero-slope straight line observed in the long-term period after the second hump is used for parameter estimation. The reservoir parameter estimation (see Table 6) has an acceptable range of error except for the 57ºC injectate temperature case. The skin factor value estimated during the fall-off period is greatly exaggerated.

Table 6: Reservoir parameters estimated for different injectate temperature and skin factor value in the fractured reservoir with skin zone extending infinitely.

Actual skin factor value	Injectate temperature (ºC)	k (mD)	Δk (mD)	Skin	ΔSkin
14.63 (positive skin)	57	11.82	1.82	73.96	59.33
	250	9.7	0.3	15.16	0.53
-3.29 (negative skin)	57	12.31	2.31	-1.42	1.87
	250	9.8	0.2	-2.99	0.3

3.3 Effect of Boundary Condition

The presence of a closed boundary in the fractured reservoir zone is investigated by reducing the reservoir radius to 300 m and implementing MINC partitioning to all of the blocks. The effect of a constant pressure boundary is investigated by adding one block representing a huge volume of aquifer results in the reservoir pressure supported by natural fluid influx from an aquifer. The MINC

partitioning process was applied to the blocks in the reservoir zone, while the aquifer block remained the same as a single porosity model. The reservoir pressure response during the injection/fall-off test is illustrated in the pressure derivative plot shown in Figure 8a for the closed boundary condition and Figure 8b for the constant pressure boundary condition. Furthermore, the derived reservoir parameter is tabulated in Table 7.

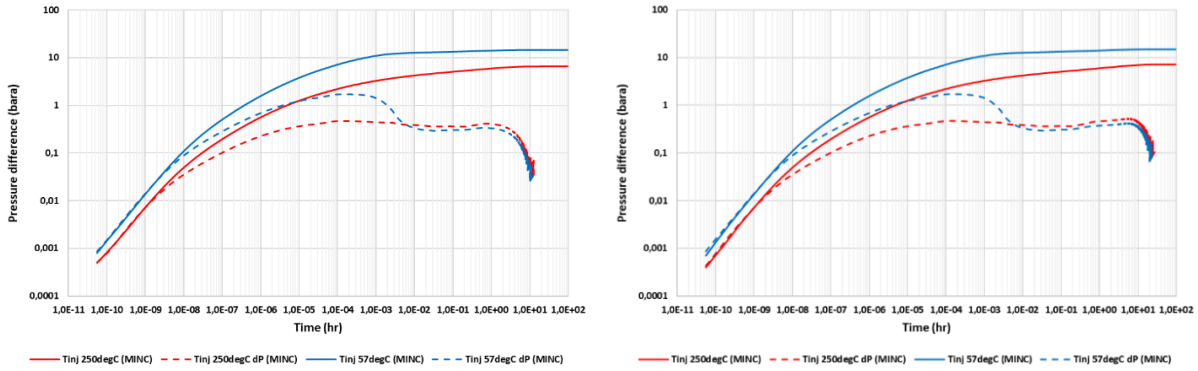

a. **b.**

Figure 8: Effect of boundary condition on the pressure derivative plot in a fractured reservoir zone; a. closed or no flow boundary; b. constant pressure boundary.

Table 7: Reservoir parameters estimated for different injectate temperature and boundary condition in the fractured reservoir zone.

Boundary condition	Injectate temperature (°C)	k (mD)	Δk (mD)	Skin	ΔSkin
Closed boundary	57	13.08	3.08	14.84	14.84
	250	10.74	0.74	1.18	1.18
Constant pressure boundary	57	11.46	1.46	12	12
	250	9.13	0.87	0.34	0.34

The presence of a closed boundary was represented by the pressure dip towards zero during the fall-off period (Figure 8a). This condition is known as pseudo-steady state flow because when the well is shut-in during the fall-off period, there will be a fluid transfer back to the well zone until the pressure is stabilised back to the average reservoir pressure. The rate of pressure decrease is equal to zero, then enters the pseudo-steady state flow (Houzé et al., 2012). The derivative plot of the fall-off period in the reservoir with a constant pressure boundary (Figure 8b) has a similar pattern to the reservoir that encounters the closed boundary. However, in the constant pressure boundary case, the derivative of pressure that dips down towards zero at the late times illustrates that the boundary pressure is stabilised at the initial reservoir pressure (80 bar) due to pressure support from the aquifer. For both boundary conditions, the S-shaped transition is only apparent in the injectate temperature of 250°C.

The reservoir parameter estimated has a small quantified error from the actual value for the hot-water injection case, whereas in the cold-water injection case, the error is quite significant, especially for the skin factor value estimation. As expected, the derived skin factor value is overestimated, especially in the cold-water injection case. Also, the reservoir permeability estimated in the cold-water injection case has a significant error with a deviation ranging from 3% to 30%.

4. TWO-PHASE WITH FREE CO_2 MODEL

The presence of free CO_2 in the two-phase reservoir complicates the PTA in geothermal applications. Adityatama et al. (2018) investigated the effect of dissolved CO_2 during an injection/fall-off and drawdown build-up with initial reservoir pressure and temperature being 80 bar and 250°C, respectively. As the boiling point pressure of water is 250°C at 39.759 bar, the maximum CO_2 content to be dissolved in the water is calculated as ~1.98% by weight. Furthermore, they investigated a reservoir with a CO_2 content of 2% wt; the reservoir conditions represented in their work encompass 100% gas saturation. This is due to the total sum of CO_2 partial pressure and water boiling pressure exceeding 80 bar.

In this study, the numerical models will be set for a geothermal reservoir that initially has free CO_2 gas with gas saturation (S_g) of 3%, linear relative permeability of S_l = 0.3; S_v = 0.05, and same initial reservoir pressure and temperature, which are 80 bar and 250°C. TOUGH2 has calculated that the CO_2 content that was initially present in the reservoir is 2.11% (above 1.98% by weight). Similar to the single-phase pure water model, the range model parameters that will be investigated are summarised in Table 3 but specific for fracture geothermal reservoir that initially has free CO_2 gas.

4.1 Effect of Injectate Temperature

4.1.1 Infinite reservoir with no skin

The effect of injectate temperature using the dual-porosity model to indicate the fractured reservoir zone that extends infinitely is investigated in this section. With the initial reservoir condition being two-phase with free CO_2, the pressure response during the fall-off period is shown in Figure 9. The estimation of reservoir parameters is tabulated in Table 8.

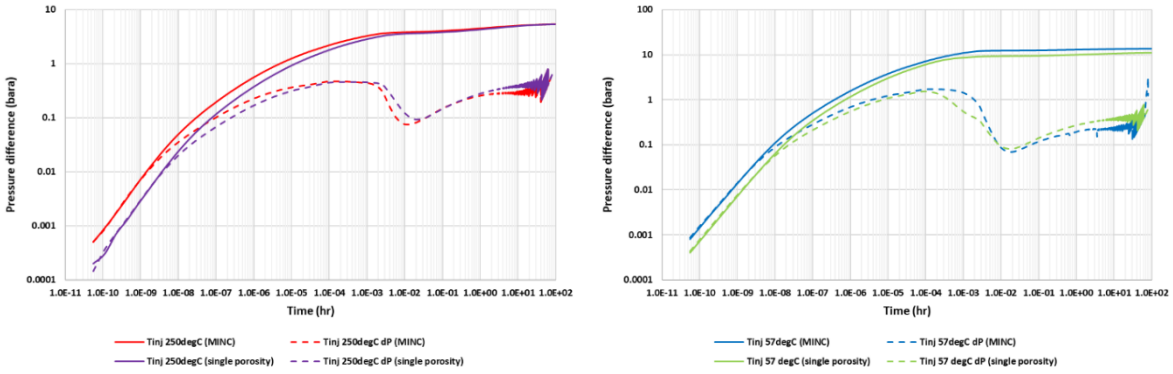

a. **b.**

Figure 9: Effect of injectate temperature on the pressure derivative plot in a fractured reservoir (no-skin) extending infinitely with free CO_2 gas; a. injectate temperature of 250°C; b. injectate temperature of 57°C.

Table 8: Reservoir parameters estimated for different injectate temperature in a fractured reservoir (no-skin) extending infinitely with free CO_2 gas.

Injectate Temperature (°C)	k (mD)	Δk (mD)	Skin	ΔSkin
57	21.5	11.5	4.34	4.34
250	10	0	0.84	0.84

It is apparent that the pressure difference in the dual-porosity model is higher than in the single porosity model for all injection temperature cases. Moreover, due to the MINC partitioning, the pressure derivative is shifted to the right. However, both injectate temperatures follow a similar trend at which the pressure derivative drops between 0.01 and 0.1 log hour. This indicates that the cooling effects of cold-water injection do not exhibit any significant difference in the diagnostic plot at the early times of the fall-off period. Also, because the injected water has a different phase from the reservoir fluid, it results in the formation of a moving thermal front. As shown in Kaya et al., (2019), cold water injection makes the steam condense (or CO_2 dissolves in water), resulting in a pressure drop. The S-shaped transition that indicates the flow of fracture and matrix blocks is not significantly apparent in the derivative plot. However, it shows that the derivative pressure dip due to the gas condensation in the dual-porosity model is deeper than in the single porosity model. The estimation of reservoir properties results in a closer match for injectate temperature 250°C. In contrast, for injectate temperature of 57°C, the reservoir properties estimated are significantly different from the actual value.

4.1.2 Infinite reservoir with single fracture zone and no skin

The presence of a single fracture zone in the fractured reservoir with a free CO_2 phase is observed. The result of the pressure derivative plot during the fall-off period is illustrated in Figure 10, while the estimated reservoir properties are shown in Table 9. Figure 10 show that the early time response of both the derivative and the pressure difference is the same between the double and single porosity models. Towards the late times, the S-shaped transition is apparent in the dual-porosity model. The first radial flow indicates the global flow in the fracture system, causing the pressure to drop, and is then supported by the flow from the matrix blocks. The reservoir permeability and skin factor value estimated for the hot-water injection case have a small difference in value compared with the actual value inputted to TOUGH2. In contrast, the reservoir properties estimated in the cold-water injection significantly deviate from the actual value.

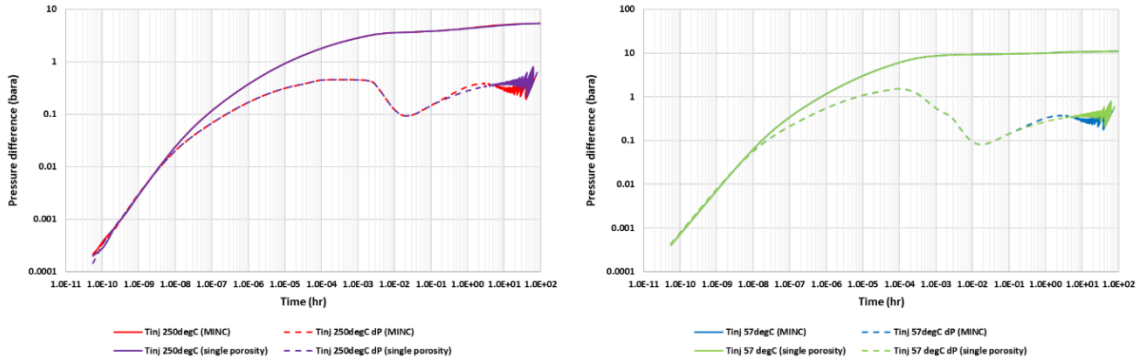

a. **b.**

Figure 10: Effect of injectate temperature on the pressure derivative plot in a single fractured reservoir (no-skin) zone extending infinitely with free CO_2 gas; a. injectate temperature of 250°C; b. injectate temperature of 57°C.

Table 9: Reservoir parameters estimated for different injectate temperature in a single fractured reservoir (no-skin) zone extending infinitely with free CO_2 gas.

Injectate Temperature (°C)	k (mD)	Δk (mD)	Skin	ΔSkin
57	12.61	2.61	7.38	7.38
250	10.06	0.06	0.41	0.41

4.2 Effect of Skin Factor Value

The impact of adding positive and negative skin in the fractured reservoir with the free CO_2 phase is examined in this section. The pressure derivative plot results during the fall-off period are illustrated in Figure 11**,** and the estimation of reservoir properties is shown in Table 10.

In the positive skin case, low permeability in the skin zone causing a hump in the derivative plot for both injectate temperatures with a bigger hump in the cold-water injection case. The pressure derivative drops due to free CO_2 gas compressed into the reservoir fluid occur in the same time frame for both injectate temperatures between 0.01 and 0.1 log hour. After that, the derivative plot follows transitional dip as it reached fracture zone with a dip in the cold-water injection is deeper due to storativity ratio and temperature difference. The overall system radial flow appears in the derivative plot at the late times with the IARF of 57°C injectate temperature seems to intersect with IARF of 250°C injectate temperature.

In the negative skin case, it should be noted that the skin zone has higher permeability than the reservoir, resulting in a lower pressure difference during the transitional zone. After that, while the injectate fluid reaches the reservoir zone, the gas condensation occurs between 0.001 and 0.01 log hour, causing the derivative pressure to decrease. The overall system radial flow then appears at the late times. However, in the cold-water injection case, the IARF region is not observed, and the derivative plot oscillations were more apparent. Figure 11b shows that the early time response of the derivative and the pressure change is distorted, causing the slope line representing the early time behaviour to not appear in the derivative plot. The derived reservoir permeability and skin factor value shown in Table 10 are significantly different from the actual value.

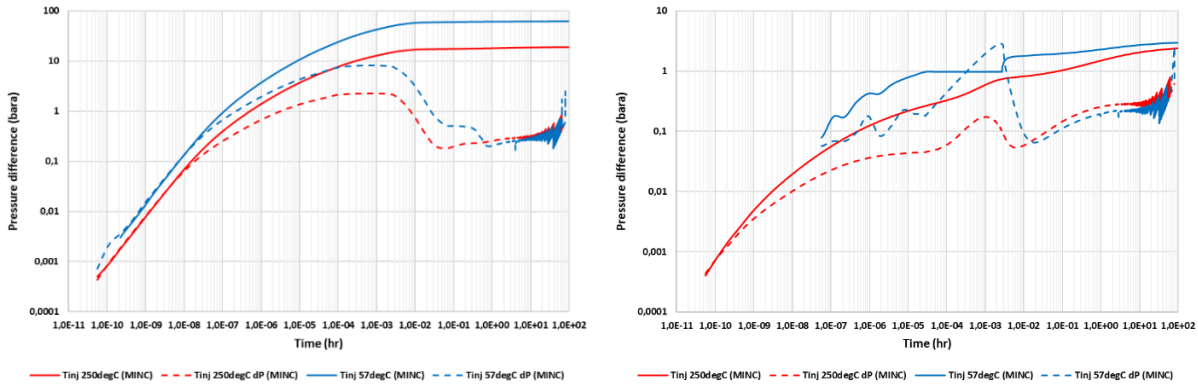

a. **b.**

Figure 11: Effect of skin factor value on the pressure derivative plot in a fractured reservoir with skin zone extending infinitely with free CO_2 gas; a. positive skin; b. negative skin.

Table 10: Reservoir parameters estimated for different injectate temperature and skin factor value in the fractured reservoir with skin zone extending infinitely with free CO_2 gas.

Actual skin factor value	Injectate temperature (°C)	k (mD)	Δk (mD)	Skin	ΔSkin
14.63 (positive skin)	57	17.58	7.58	28.08	13.45
	250	16.34	6.34	25.92	11.29
-3.29 (negative skin)	57	23.32	13.32	-0.33	2.96
	250	16.56	6.56	-3.54	0.25

4.3 Effect of Boundary Conditions

The PTA of a fractured geothermal reservoir with free CO_2 phase and boundary condition is investigated in this section. The MINC partitioning was applied to all blocks in the reservoir to make the pressure changes spread fast in the reservoir. The presence of boundary is simulated by reducing the reservoir to a smaller radius than the single-phase pure water model as the two-phase diffusivity is very small, and the pressure changes spread extremely slowly in the reservoir. The result of the pressure derivative plot during the fall-off period is shown in Figure 12a for closed boundary and Figure 12b for constant pressure boundary. Table 11 summarises the estimation of the reservoir permeability and skin factor value.

Table 11: Reservoir parameters estimated for different injectate temperature and boundary conditions in the fractured reservoir zone with free CO_2 gas.

Boundary condition	Injectate temperature (°C)	k (mD)	Δk (mD)	Skin	ΔSkin
Closed boundary	57	21.71	11.71	24.34	24.34
	250	17.54	7.54	2.1	2.1
Constant pressure boundary	57	19.64	9.64	21.5	21.5
	250	9.97	0.03	0.78	0.78

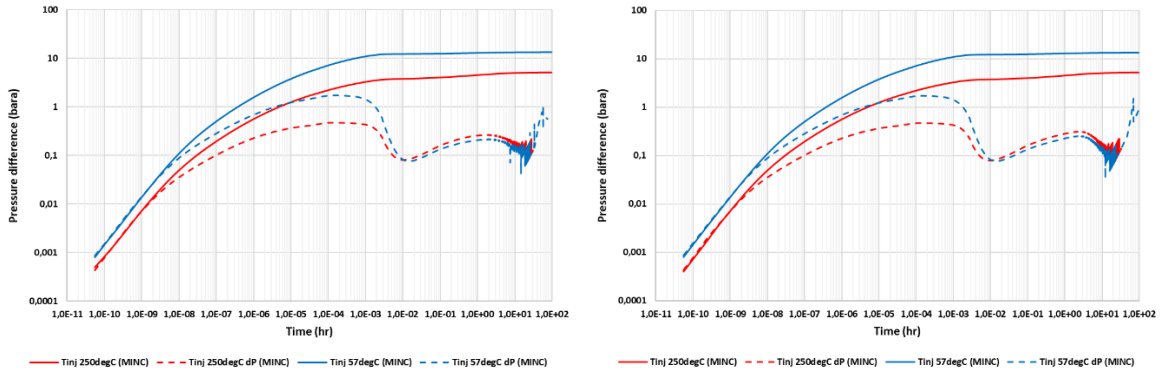

a. **b.**

Figure 12: Effect of boundary condition on the pressure derivative plot in a fractured reservoir zone with free CO_2 gas; a. closed or no flow boundary; b. constant pressure boundary.

The result shows that the injection fluid in the fractured free CO_2 phase reservoir reaches the boundary zone. As all the blocks were partitioned to fracture and matrix continuum, the S-shaped transition appears at the intermediate times and is followed by pressure dip towards zero for both injectate temperatures in the closed boundary model. For the constant pressure boundary model, the S-shaped transition and the pressure derivative dives towards zero at the late times, which represents the boundary pressure is stabilised at the initial reservoir pressure due to pressure support from the aquifer. For both injectate temperatures, the derived reservoir permeability is overestimated compared to the actual value. In terms of skin factor, the value estimated in the cold-water injection case is greatly exaggerated, while in the hot-water injection case, the estimated value has a small quantified error.

5. CONCLUSIONS

Numerical models were utilized to investigate the PTA of injection/fall-off test under the various conditions of a fractured geothermal reservoir, such as single-phase pure water and reservoir with free CO_2 phase. Several parameters were tested, for sensitivity and the accuracy of analytical models. Also, several models structures were tried to observe the effect of the dual-porosity and boundary effect on the diagnostic plot and their impact on the estimation of the reservoir parameters. Thus, the results of this study may be used in an attempt to identify any undesirable sensitivities and interpret the real pressure transient data from the geothermal fields more accurately. The key findings in this study are as follows:

Fracture spacing

According to the experiments of different fracture spacing tried, the smaller fracture spacing will cause the transition to start early. This is because the pressure differential between fracture and matrix blocks continuum significantly occurs as small fracture spacing indicates the large surface area between these two continuums.

Matrix permeability

Changing the matrix permeability affects the start of transition and the depth of the dip. A smaller matrix permeability causes the matrix response to the global flow in the fracture to appear late and the depth of the dip to be more apparent as the exchange of fluid and heat between fracture and matrix blocks is limited.

Characteristic in pressure derivative plot

According to the comparison between single porosity and MINC models, fractured reservoirs demonstrate a delayed response for the fall-off period due to the travel time and diffusion of cold reinjection fluid. In the case of a single fracture zone, the S-shaped transition of the dual-porosity model is apparent in the intermediate times when the fluid encounters the single fracture zone. Aside from that, the pressure response is the same as with the single porosity model.

Injectate temperature

The difference between injectate temperature and reservoir temperature will cause the derivative hump to resemble a positive skin. Moreover, the cold-water injection causing the pressure dip is deeper than the hot-water injection. This is due to the cold water that invaded the reservoir during injection travelling a further distance in the MINC model. As a result, the effect of cold water is more persistent in the fall-off period for the dual-porosity model, and the response of dual-porosity reaches the IARF region later.

Skin effect

Adding positive skin does not have a significant effect on the S-shaped transition of the dual-porosity model, thus no diagnostic feature is lost. However, adding negative skin distorts the early time response of the pressure derivative plot, especially in the reservoir with the initial condition of two-phase with free CO_2. An unrecognised pressure derivative plot was observed in the 57°C injectate temperature case. The derived skin factor value in the MINC model is overestimated.

Closed or no flow boundary

In a fractured single-phase and free CO_2 phase reservoir, the presence of a closed boundary is causing the derivative pressure to dip towards zero during the fall-off period. The S-shaped transition is also apparent in the derivative pressure due to the MINC partitioning. However, the reservoir radius extent in the free CO_2 phase reservoir is smaller than the single-phase reservoir to make the boundary condition detected.

Constant pressure boundary

The constant pressure boundary is also apparent in the fractured single-phase and free CO_2 phase reservoir, as with a closed boundary effect. The presence of a constant pressure boundary causes the derivative of pressure in the injection and fall-off period to dip down towards zero at the late times. Due to the MINC partitioning, the S-shaped transition is apparent in the derivative pressure.

REFERENCES

Adityatama, D.W., Kaya, E., and Zarrouk, S.J.: Investigation of pressure transient analysis methods for single and multiphase geothermal reservoirs, *Proceedings*, 40th New Zealand Geothermal Workshop, November, 1–8, (2018).

Austria, J.J.C.: Dual porosity numerical models of geothermal reservoirs, The University of Auckland (2014). https://researchspace.auckland.ac.nz/handle/2292/27115

Battistelli, A., Calore, C., and Pruess, K.: The simulator TOUGH2/EWASG for modelling geothermal reservoirs with brines and non-condensible gas, *Geothermics*, 26(4), (1997), 437–464. https://doi.org/10.1016/S0375-6505(97)00007-2

Bourdet, D., Ayoub, J.A., and Pirard, Y.M.: Use of pressure derivative in well-test interpretation, SPE Formation Evaluation, 4(02), (1989), 293–302. https://doi.org/10.2118/12777-pa

Croucher, A.: Pytough: a python scripting library for automating tough2 simulations, *Proceedings*, New Zealand Geothermal Workshop, November, 1–6, (2011).

Croucher, A. E.: Recent developments in the PyTOUGH scripting library for TOUGH2 simulations, *Proceedings*, 37th New Zealand Geothermal Workshop, (2015). http://www.geothermalworkshop.co.nz/wp- content/uploads/NZGW2015_Programme_1511_17Nov.pdf

Earlougher, R.C.: Advances in well test analysis, Henry L. Doherty Memorial Fund of AIME, (1977).

Grant, M.A. and Bixley, P.F.: Geothermal reservoir engineering (2nd ed.), Academic Press (2011).

Guerra, R.J.A. and O'Sullivan, J.: Investigating the effects of non-isothermal reservoir conditions on pressure transient analysis of an injection/fall-off test using numerical modelling, *Proceedings*, 40th New Zealand Geothermal Workshop, November, 1–8, (2018).

Houzé, O., Viturat, D., Fjaere, O., and Trin, S.: Dynamic data analysis, In Kappa Engineering. Kappa Engineering (2012).

Kaya, E., Adityatama, D., and Zarrouk, S. J.: Investigation of pressure transient analysis methods for single-phase and CO2-rich geothermal reservoirs, *Renewable Energy*, 141, (2019), 162–180. https://doi.org/10.1016/j.renene.2019.03.140

McLean, K. and Zarrouk, S.J.: Pressure transient analysis of geothermal wells: A framework for numerical modelling, *Renewable Energy*, 101, (2017), 737–746. https://doi.org/10.1016/j.renene.2016.09.031

O'Sullivan, M.J. and McKibbin, R.: Geothermal reservoir engineering, University of Auckland (1989). https://doi.org/10.1016/C2010-0-64792-4

Onur, M. and Al-Saddique, M.: Comparison of derivative algorithms used in pressure transient analysis, *The Arabian Journal for Science and Engineering*, 24(1B), (1999), 59–78.

Pruess, K., Oldenburg, C., and Moridis, G.: TOUGH2 User's Guide, Version 2.0 (No. LBNL-43134) (Issue November) (1999).

Septiani, G., Adityatama, D.W., Kaya, E., and Zarrouk, S. J.: Numerical Pressure Transient Analysis of CO 2 -Containing Geothermal Reservoirs during Draw-Down Buildup Testing, October, 1–10, (2021).

Yeh, A., Croucher, A.E., and Sullivan, M.J.O.: Recent developments in the AUTOUGH2 simulator, *Proceedings*, TOUGH Symposium, 8, (2012).

Zarrouk, S.J. and McLean, K.: Geothermal well test analysis (1st ed.), Elsevier Inc (2019). https://doi.org/https://doi.org/10.1016/C2017-0-02723-4

Design Improvement in 17-1/2" Hybrid Drill Bit Successfully Improved Drilling Performance in Sorik Marapi Geothermal

Sentanu W. Reksalegora[1], Ariatama Yustisia[2], Ashadi[1], Kiki Yustendi[1],
Mohammad Khairanto Nugroho[2], and Jake Drew[2]

[1]PT Sorik Marapi Geothermal Power, Recapital Building 5th Floor, Jakarta Selatan, Jakarta, Indonesia
[2]Baker Hughes Indonesia, South Quarter Level 18 and 19 Tower B Jl. RA. Kartini Kav. 8, Kel. Cilandak Barat, Kec. Cilandak Jakarta Selatan 12430, Indonesia

Sentanu.wisnuwardhana@ksorka.com, Ariatama.CitraAgungYustisia@bakerhughes.com, ashadi@ksorka.com, kiki.yustendi@ksorka.com, Mohammad.KhairantoNugroho@bakerhughes.com, Jake.Drew@bakerhughes.com

Keywords: Geothermal drilling, Hybrid drilling bit, Sorik Marapi, New Technology Bit

ABSTRACT

Geothermal drilling bit selection has been dominated by roller cone bits utilizing a crushing mechanism. To reduce the overall drilling time and cost related to the lifetime and rate of penetration of roller cone bits, new drill bit technology such as the hybrid drilling bit was developed. The hybrid drilling bit attempts to gain the best of roller cone and PDC bits by combining them into one bit. Like other new drill bit technologies, it still has various challenges. Since it was first used in 2018 in Sorik Marapi Geothermal, the 17-1/2" hybrid drill bit has gone through several design changes such as additional blades, new generation cutters, insert placement, and additional protection. These design changes have successfully improved the bit performance and has reached a record-breaking ROP at Sorik Marapi. This paper describes the changes in design and the reason behind them as lessons learned for the future development of drilling bits.

1. INTRODUCTION

Roller cone bits have dominated the geothermal drilling market considering its crushing mechanism in the hard volcanic formation. However, to reduce the overall drilling time and cost related to these bits, new bit technologies were developed. The hybrid bit is a combination bit intended to obtain the benefits of roller cone and PDC bits while drilling hard formation. Similar to other new technologies, changes were made along the way to apply lessons learned and ultimately improve overall performance of the drilling bit. The 17-1/2" Hybrid Bit has evolved since it was first used in the Sorik Marapi drilling campaign in 2018. In the most recent run, it has successfully reached a record-breaking ROP. Changes to the bit design include additional blades, new generation cutters, insert placement, and additional hard facing. The improvement in design was also able to reduce risks concerning the roller cone failures. This paper will highlight the design changes in the Hybrid bit throughout its drilling performance in Sorik Marapi and explain the main principle of the changes that enabled the bit to improve its overall performance and provide cost savings to the drilling operation.

2. BIT DESIGN

TCI bits implements a crushing rock failure mechanism which are commonly used in geothermal drilling for its low and smooth torque. However, due to low aggressiveness they penetrate the rock slowly and consequently are only able to drill short intervals due to bearing revolution limits. In contrast, a PDC bit has an aggressive shearing cutting mechanism which allows higher ROP. This high aggressiveness however, can lead to unstable tool face and higher torsional vibration causing operational challenges. Furthermore, minor cutter damage can drastically reduce the efficiency of PDC bits and deteriorate the bit condition exponentially in hard rock environments. By combining roller cone and fixed cutter elements into one bit, the hybrid drill bit design not only benefits from both types, but also synergizes their best attributes (Figure 1). In a hybrid bit, the intermittent crushing of roller cone bit is combined with continuous shearing and scraping of a fixed blade bit (Pessier and Damschen, 2010). Figure 2 illustrates the drilling mechanics of hybrid bits. The hybrid drill bit is able to deliver several benefits in challenging applications such as:

- Low ROP applications with TCI,
- Torque or weight-on-bit limited applications with large diameter PDC or TCI,
- Applications with high torque fluctuation causing premature bit and bottom hole assembly failure,
- Directional applications with bent motors facing limited drilling parameters, poor tool face control and/or low steerability.

The hybrid drill bit technology has been introduced to the drilling industry and have shown good performances in the oil and gas industry around the world. The earliest size being applied in the industry was the 12.25". In 2011, Thomson et al. utilized hybrid drill bit to reduce drilling time by 35%-44% (Thomson et al., 2011), while in Turkey it saved the operator more than USD 100k (Pasquale et al., 2013). In 2015 Holub et al. also showed that the hybrid bit generated smoother rotation and lower vibration in hard formation offshore of Ireland, extending the bit life and constant ROP (Holub et al., 2015).

The larger diameter hybrid drill bit, such as the 17.5", have also been utilized in the drilling industry such as in the Timor Sea, where the drilling bit went through several changes such as in the insert geometry in order to gain durability (Bone et al., 2018). These changes are also present in the current design.

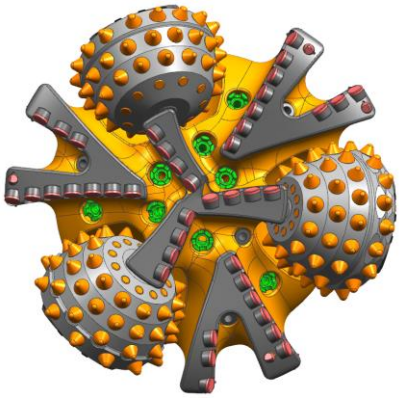

Figure 1: Example of a top view of a hybrid bit.

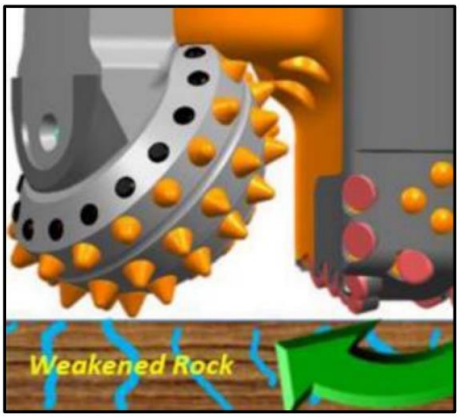

Figure 2: Illustration of hybrid bit cutting action.

3. DESIGN EVOLUTION OF 17.5" HYBRID BIT IN SORIK MARAPI

Sorik Marapi Geothermal field is located in North Mandailing, North Sumatra. The power plant has been commissioned in 2019 and is currently actively producing 90 MW to the North Sumatra power grid. The drilling campaign traces back to 2016, when the first exploration well was drilled and 2018 when the first development drilling was done.

3.1 First Run – Well D 2018

The first time the hybrid bit was run in Well D it showed promising performance levels. However, the consequent runs yielded less than desirable results. The runs are summarized in Table 1. After the final run, the bit was pulled out due to poor ROP and was found to be rung out with failed bearings.

Table 1: Bit record summary of hybrid bit run in Well D.

Run	BHA	Bit Size	Depth In, m	Depth Out, m	Depth Drilled (m)	Hours	ROP, m/hr	Grade Out
1 - New	Motor	17 1/2	502	805	303	29.3	10.34	TCI: 1-1-WT-A-E-1/16-NO-HP PDC: 1-1-CT-N-X-I-NO-HP
2 - RR#1	Rotary	17 1/2	805	864.7	59.7	13.1	4.56	TCI: 1-1-WT-A-E-1/16-NO-HP PDC: 1-1-WT-A-X-I-BT-HP
3- RR#2	Motor	17 1/2	864.7	1099	234.3	31.27	7.49	TCI: 1-6-WT-A-F-16-RO-PR PDC: 1-8-WT-A-X-16-RO-PR

3.1.1 Challenges

- Heavy damage on the outer rows of cutting structure
- Failed bearings

3.1.2 Changes

To tackle the challenges encountered from the run in Well D, the bit went through the following modifications:

- 3 additional PDC blades to increase diamond volume in the shoulder area for improved shoulder and gauge durability (Figure 3)
- Change cutter geometry from standard single chamfer to dual chamfer to improve impact resistance and wear resistance
- Denser insert placement on cone cutting structure for durability, but sharper insert shape to maintain aggressiveness

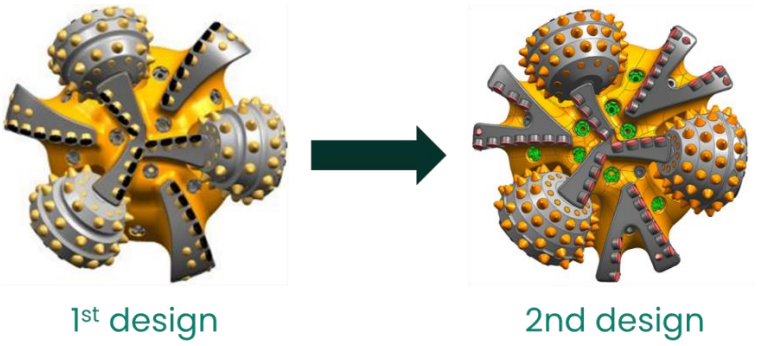

Figure 3. Design changes of 17.5" Hybrid bit after well D.

3.2 Second Run – Well T7 2020

After modifying the design from the first run, the second hybrid bit design was able to exceed the target and successfully delivered performance with 44% improvement from average offset penetration rate (7.41 m/hr) that were drilled with IADC 435 TCI roller cone bits. Furthermore, this run drilled 32% longer compared to average offset well intervals, and is 26% longer than the longest offset (Figure 4). This design was also utilized in another field in South Sumatra, saving 29 hours of drilling time (Nugroho and Pham, 2019).

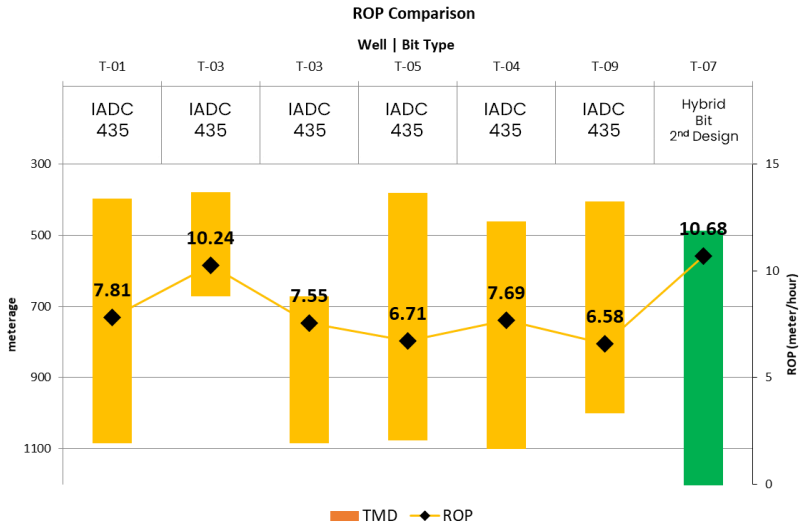

Figure 4: Hybrid bit 2nd design performance compared to TCI bits on offset wells.

3.2.1 Challenge

Despite the good performance, severe wear was observed on the shirttail and leg areas of the bit – the leg became significantly tapered. The bit dull grade was TCI: 1-2-SD-A-F-2-WT-TD, PDC: 1-3-WT-S-X-2-CT-TD. Wear markings on upper leg area indicate damage from upward rotating movement (back reaming) through abrasive lithology. This is a challenge the bit has to address as back reaming can be unavoidable. The pressure compensator (the component that equalizes pressure in the bearing assembly) is located in that area. After investigation, it was concluded that the bearing failure is the result of damage to the gauge/shirttail area and not due to bearing reliability (Figure 5).

Figure 5: Condition of leg and shirttail after run in Well T7.

3.2.2 Changes

To address the leg wear from the T7 run, more coverage of tungsten carbide hard facing was added to the new design to improve the overall wear resistance in abrasive formations. Tungsten carbide hard facing was also added to the pressure compensation area to protect these critical parts, illustrated on Figure 6.

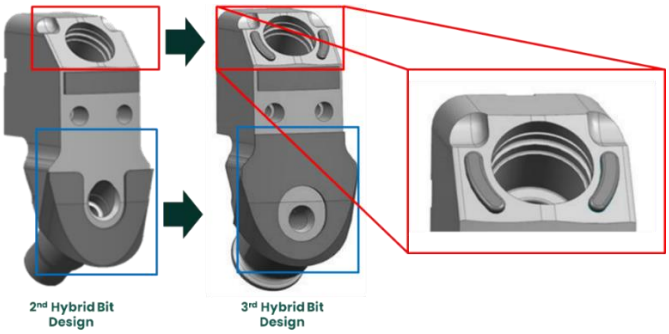

Figure 6: Leg protection addition to the 2nd design.

The PDC gauge pads extend further on the new design, so that they are positioned slightly higher above the cone leg hence the PDC gauge pad will come into contact with the formation first during back reaming, preventing damage to the cone legs. More importantly the new design is equipped with up-drill PDC cutters, which will significantly improve the protection when back reaming (Figure 7).

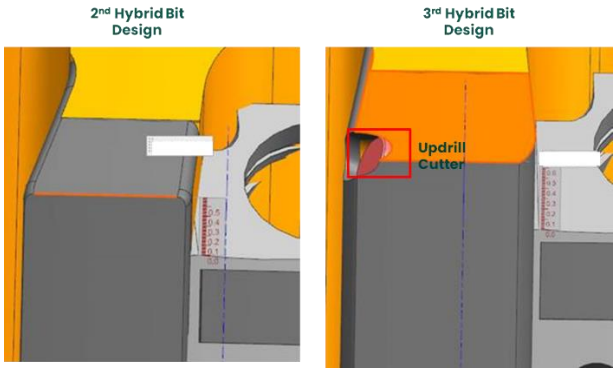

Figure 7: Raising the gauge pad above the cone legs and additional back reaming cutters.

Several modifications were also done to the main cutting structure of the PDC to improve the durability and aggressiveness (Figure 8). The changes are:

- Cutters changes to next generation of dual chamfer cutter, with sharper main edges to add aggressiveness while maintaining impact resistance due to better material in the next gen cutters.
- Engineered placement of PDC cutters on the shoulder/gauge area for improved durability
- Cutter size combination between 19mm and 16mm. 19m cutters on cone-nose area; 16mm cutters from nose-shoulder area. Improved durability due to significantly increased cutter density, 12 additional cutters (25% increase)

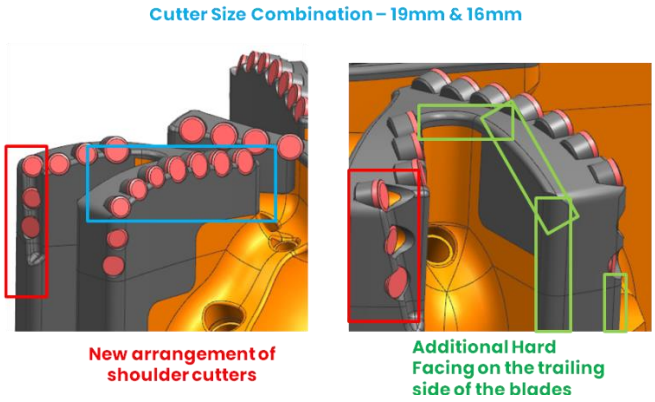

Figure 8: Modification to the cutting structure to add durability.

3.3 Runs of the 3rd Hybrid Bit Design, well T10, A1, A2 and A5 2020-2021

The 3rd hybrid bit design was subsequently used in four wells with positive results. All four runs managed to complete the 17.5" interval in one run to TD with satisfying ROP. The first three runs were successful in breaking the 17.5" ROP record in Sorik Marapi Field. At the time this paper is written, well A2 holds the record for the fastest 17.5" bit run in Sorik Marapi Field with an ROP of 15.36 meters/hour. The performance summary illustrated on Figure 9.

The durability of this new design also shows positive results. All four runs pulled out with effective bearings, and more importantly, the leg durability issue that occurred at well T7 was not present. All bit dull grades observed the leg protection to be in good condition as shown in Figure 10.

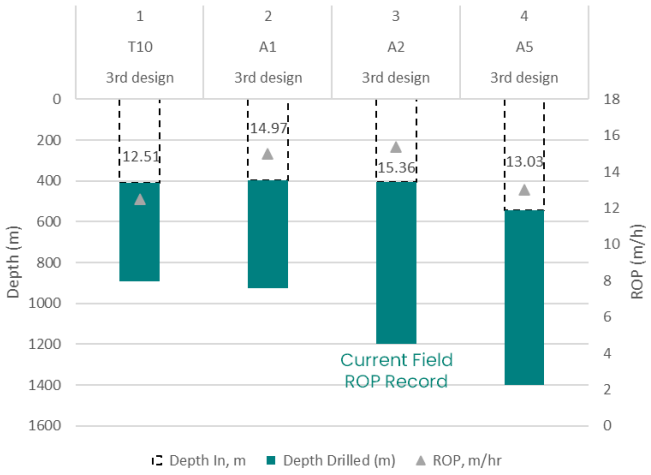

Figure 9: Performance summary of the 3rd hybrid bit design at Sorik Marapi.

Figure 10: Cone leg protection condition after run of 3rd hybrid bit design.

Table 2: Summary of challenges and design changes of 17.5" hybrid bit.

Design	Bit Design Challenges	Bit Design Improvements	Results
1st design	Durability issues in shoulder and gauge.	Baseline design	TD with one bit
2nd design	Shirttail and leg durability issues during backreaming, leading to cone bearing failure.	Additional PDC blades, change cutter type, modify cutter placement	TD in one run, 44% ROP improvement.
3rd design		Additional leg protection, gauge pad modification, cutting structure modification	TD in one run at record ROP. Excellent dull condition.

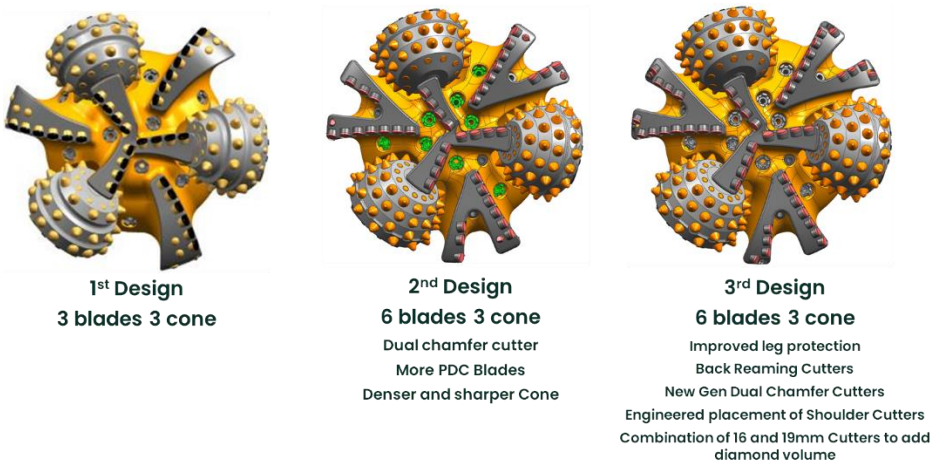

Figure 11: Design evolution summary of 17.5" hybrid bit.

4. CONCLUSION

Hybrid drill bit technology has been utilized in the oil and gas industry and has evolved to also be utilized in the geothermal industry, addressing the challenge of drilling hard formations. Throughout its drilling campaign, to date, the operator has utilized a total of six 17.5" Hybrid bits. The first 17.5" hybrid bit was utilized in well D in 2018. The bit was re-run three times at the same well with different pull-out reason. After the final run, the bit came out in a ring out condition and had poor overall ROP. After this performance, the bit design was then re-evaluated together with lesson learned from other Geothermal Fields. The next design of 17.5" hybrid bit was then used in Well T7. The bit was used to drill a long interval and successfully drilled with above 10 meter per hour ROP. However, the bit came out in poor condition where the leg area was damaged causing bearing failure. From Well T7, the bit was used again in T10, after the previous issue was addressed. The ROP increased by 20% compared to the previous run up to 12.5 m/hr with a shorter depth interval. After T10, the bit was utilized in A1 where the ROP increased to almost 15 m/hr with a slightly longer interval. Most recently, the bit was used in A2 and A5 well with good performance. These improvements were achieved by addressing the issues and continuously improving the bit design.

The 17.5" hybrid bit had gone through several design changes as summarized in Table 2 and Figure 11. These changes were based on the data evaluation of each run such as dull grades and drilling data. With these design evolutions, data shows that performance of the bits significantly improved after each change, with the latest design successfully becoming one of the best performing 17.5" drill bits in this specific application. In general, the design changes done are part of perfecting the hybrid bit design to be more suitable for Geothermal Drilling in Indonesia.

5. ACKNOWLEDGEMENT

The authors wish to express gratitude to Sorik Marapi Geothermal Power and Baker Hughes for permission to release the field performance, data validation, and bit development process outlined in this paper.

REFERENCES

Bone, K., Kerimofski, R., and Gauld, J.: Large Diameter Hybrid Bit with Sharp and Dense Inserts Drills Hard Carbonate Formation with Exceptional ROP, *Offshore Technology Conference*, Kuala Lumpur (2018).

Holub, C.M., Chiniwala, B., Montgomery, J., and Buske, R.J.: Innovative Hybrid Bit Delivers Breakthrough in a Deepwater Exploration Well on the West Coast of Ireland, *SPE/IADC Drilling Conference and Exhibition*, London (2015).

Nugroho, M.K. and Pham, S.N.: Hybrid Drill Bit Technology, Improved ROP, Drilled Interval and Contributed to 96 hours Cumulative Saving in One Geothermal Well in South Sumatera Operation, *The 7th Indonesia International Geothermal Convention and Exhibition (IIGCE)*, Jakarta (2019).

Pasquale, M.D., Calvaresi, E., and Pecantet, S.: A Breakthrough Performance for an Inland Application with a Hybrid Bit Technology, *SPE/IADC Drilling Conference and Exhibition*, Amsterdam (2013).

Pessier, R., and Damschen, M.: Hybrid Bits Offer Distinct Advantages in Selected Roller Cone and PDC Bit Applications, *IADC/SPE Drilling Conference and Exhibition*, New Orleans (2010).

Thomson, I., Krasuk, R., Silva, N., and Romero, K.: Hybrid Drill Bit Improves Drilling Performance in Heterogeneous Formations in Brazil, *Brasil Offshore Conference and Exhibition*, Macae: Society of Petroleum Engineers, (2011).

Drilling Digitalization to Enhance and Optimize Geothermal Drilling Operation – Road to Single Digit Well

Sentanu W. Reksalegora, Redha B. Putra, Fadhil Rhisnanda, Ashadi, Arya Dwipangestika, and Dicky Alamsyah

PT Sorik Marapi Geothermal Power, Recapital Building 5th Floor, Jakarta Selatan

Sentanu.wisnuwardhana@ksorka.com, Redha.putra@ksorka.com, Fadhil.rhisnanda@gmail.com, Ashadi@ksorka.com, aryadwipangestikapriyono@gmail.com, dicky.alamsyah@ksorka.com

Keywords: Data Management, Data Visualization, Drilling Digitalization, Sorik Marapi

ABSTRACT

With the rapid advancement of digitalization, the geothermal drilling industry in Indonesia still has room for improvement in this particular field compared to the oil and gas industry. Using digitalization, the huge influx of drilling data from various sources, can be effectively utilized by engineers, which is critical in the agile and dynamic drilling environment. Through identifying the goal, the current condition of the operation, the activities with room for improvement, and providing accessibility to enable quick decision-making during operation, optimization can be done. Drilling digitalization has successfully improved and optimized the geothermal drilling operation at Sorik Marapi Geothermal. Through digitalization the drilling team was able to continuously improve towards a full length well drilled in single digit days and broke its previous drilling records in a short amount of time.

1. INTRODUCTION

In the drilling industry, the long-distance relationship between the head office and drilling site often limits the amount of information that can be delivered. Recently, the pandemic has further limited the face-to-face interaction between engineers. The internet however is able to bridge this gap by allowing, data transmission, collaboration, and communication through online means. With various sources of digital data flowing from the rig site to the head office, it has become important to process these data quickly and accurately. The classic Microsoft Excel, which all drilling engineers rely on to process and present data sometimes are unable to handle the huge amount of data. The use of commercially available data visualization software or business intelligence (BI) tool is one of the solutions to tackle this big data influx and optimize drilling operations. This type of software enables drilling engineers to process and compare large amount of data quickly and clearly – critical in a fast-paced drilling operation environment with a small team. On the spot-decision is also assisted through the dashboard visualization. This paper will discuss the digitalization in Sorik Marapi Geothermal (SMGP) drilling where it has successfully made an impact on the drilling performance. It will share the journey of turning data into meaningful insight for the current drilling team and how it improved its performances.

2. DRILLING DIGITALIZATION IN GEOTHERMAL

In the 21st century, digitalization is not as simple as turning sheets of paper into a Word or Spreadsheet file. This type of digitalization has been going on for many years and brings little insights unless processed. Today digitalization can be defined more accurately as creating value from data. The most basic form of data digitalization is data structure, which is shaping the data into a database format. The second form is data visualization, which turns the data into a form that can be analyzed. The final form is data forecast, which predicts the data based on past history. The geothermal drilling industry is still a bit behind in digitalization compared to oil and gas. In the oil and gas industry, drilling digitalization has been widely discussed with various software available to be utilized. Such transformation has been successful in cutting drilling cost for example in Oman where digitalization saved 7% of total well time (Al-Aufi et al., 2018). The available data in geothermal drilling is also different compared to oil and gas as less tools and less sensors are utilized on the field.

2.1 Data Structure

As previously mentioned, turning sheets of paper into a digital file brings little operational insights other than easy file access. Data structuring involves extracting valuable data into database formats that can easily be processed and stored. There are many discussions and publications on establishing a data architecture system for drilling. For example, Jing, et al discussed how establishing a drilling data warehouse can provide effective data decision analysis and other technical project support (Jing et al., 2012). Other than DDRs, other reports are also structured in similar manner with a common primary key, well name for example. By doing this, these data can be joined together with other databases and easily related. As drilling operation involve many parties and services, working together with them and creating a set template for them to input the required data saves time in data gathering – making collaboration critical. Furthermore, the use of online sharing tools enables quick and live file synchronization.

2.2 Data Visualization

The most common form of visualization drilling engineer will see is the drilling parameters from logging companies. This real time data helps the engineer to monitor what is happening downhole. However, often these data are stored only at the logging company unless requested or are only submitted as PDF reports, which are difficult to analyze side-by-side. The next step to fully utilize the structured data is to visualize the data. Excel can be said to be the most basic data visualization tool. However, visualizing drilling parameters of multiple offset wells with Excel will require a huge processor and will take a lot of time – inefficient if a quick decision has to be made. Imagine the time it will take to import hundred thousand of time-based or depth-based drilling parameter from the mud logging companies into a spreadsheet and plotting into a scatter plot. With a structured data, data visualization with a BI tool can be done faster than conventional spreadsheet. In the past few years, the study of utilization of BI tool has been discussed in the oil and gas industry such as in the published article by Thomson and Vulgamore (2011) and Chen et al. (2018) where BI tool was used on Gulf of Mexico and Permian Basin data set. The main purpose for data visualization is to tell a story or what is normally

known as “storyboarding”, to quickly explain data from a large database as discussed by Saini et al, where once a template is available, it can be applied to multiple datasets (Saini et al., 2018).

3. SMGP ROAD TO SINGLE DIGIT WELL

Reflecting on the history of geothermal drilling in Indonesia where a single digit day well was achieved in one of the geothermal fields in Salak completing 1630 meters in 9.6 days in 2010 (Prihutomo and Arianto, 2010), the team sets out on a journey to improve the performance of the current drilling operation. As many have said, “you can only improve what you measure”, brings the team to its first step: measuring its current performance and comparing it to the best performing well.

SMGP has been drilling since 2016 and has just recently completed its 90 MW power plant commissioning. The 2020 drilling campaign started with a small new drilling team, which faces the challenge of having years of data to analyze in order to optimize the current drilling operation; as of April 2020, SMGP has completed a total of 28 wells.

The fast and agile nature of the drilling operation requires the team to quickly gather the data from both the past and the present to be utilized in the current drilling campaign. Gathering data to identify the current performance is one thing, but presenting it in a meaningful way to tell a story and highlight inefficiencies is another. This is where digitalization plays a critical role. Various drilling software used in oil and gas are available in the market and are also available to the geothermal drilling industry. However, apart from the fact that geothermal drilling has different approach from oil and gas drilling, they are often not suitable to the geothermal drilling budget which are relatively lower than that of oil and gas wells. To overcome these challenges, the drilling team created an in-house digitalization campaign starting from applying two of the basic form: data structure and data visualization to improve its performance.

3.1 Data Structuring in SMGP

Structuring the offset well data from 2016 to 2020 took a significant amount of time as the sources are scattered and are in different formats.

To start off, the most basic data that needs to be restructured are the DDRs. To do this the DDR files are collected and extracted into a form that can be read with BI tool. Figure 1 shows the format that the DDR was transformed into.

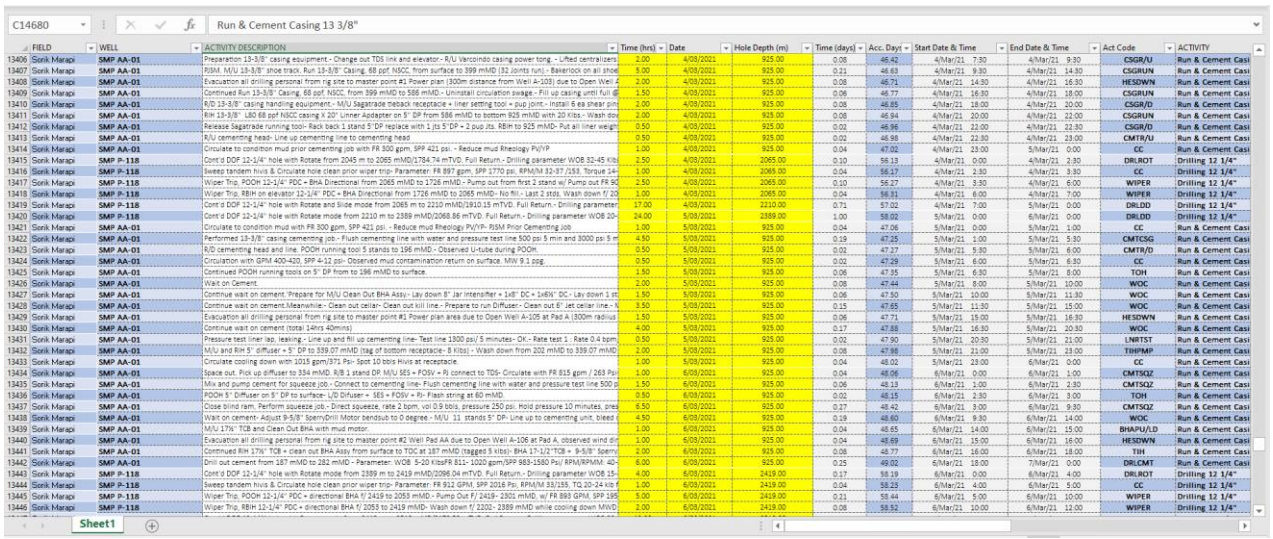

Figure 1: Example of DDR database.

Other than the DDRs, the next data that needs to be structured and standardized is the drilling parameters. The team worked together with the mud logging company to make sure the data are provided in the format shown in Figure 2. As drilling continues, the amount of data continues to grow. For example, the Excel workbook in Figure 2 with 465,125 rows of data is sized at 148 MB. Trying to further process this data in Excel is limited and will increase the size of the file significantly, moreover the need for the processing capacity. To overcome this, the team decided to make the update direct from the field using storage sharing online in separate small files and the data is then exported further to SQL to save time and storage space by using a custom-made exporter. To further enhance the drilling monitoring, the team also coordinated with relevant services to gather data in similar way. Table 1 shows some of the parameters gathered along with the relevant parties and formats.

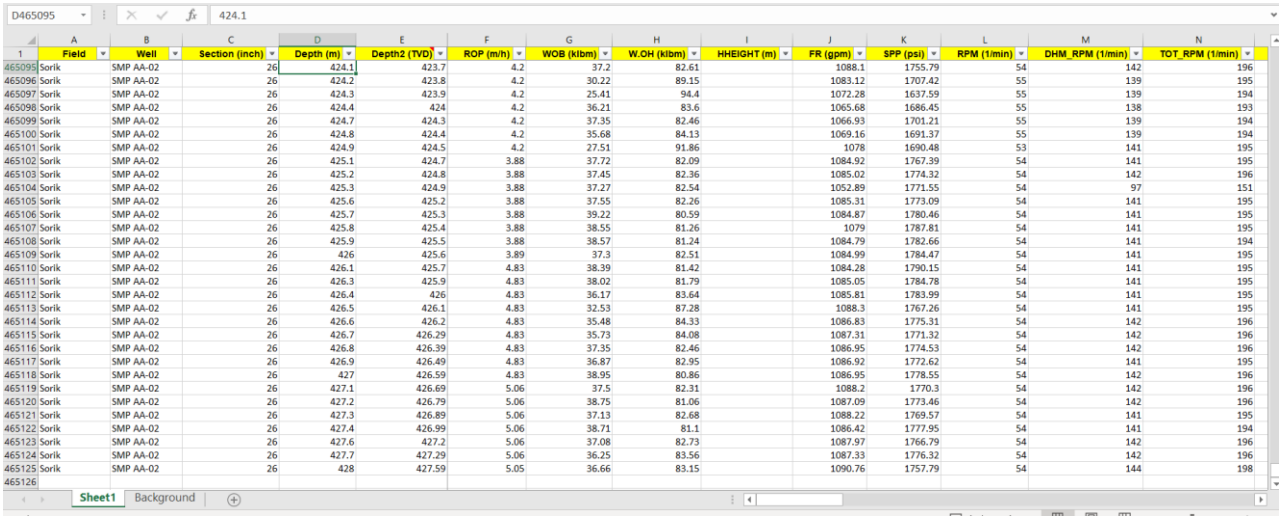

	A	B	C	D	E	F	G	H	I	J	K	L	M	N
1	Field	Well	Section (inch)	Depth (m)	Depth2 (TVD)	ROP (m/h)	WOB (klbm)	W.OH (klbm)	HHEIGHT (m)	FR (gpm)	SPP (psi)	RPM (1/min)	DHM_RPM (1/min)	TOT_RPM (1/min)
465095	Sorik	SMP AA-02	26	424.1	423.7	4.2	37.2	82.61		1088.1	1755.79	54	142	196
465096	Sorik	SMP AA-02	26	424.2	423.8	4.2	30.22	89.15		1083.12	1707.42	55	139	195
465097	Sorik	SMP AA-02	26	424.3	423.9	4.2	25.41	94.4		1072.28	1637.59	55	139	194
465098	Sorik	SMP AA-02	26	424.4	424	4.2	36.21	83.6		1065.68	1686.45	55	138	193
465099	Sorik	SMP AA-02	26	424.7	424.3	4.2	37.35	82.46		1066.93	1701.21	55	139	194
465100	Sorik	SMP AA-02	26	424.8	424.4	4.2	35.68	84.13		1069.16	1691.37	55	139	194
465101	Sorik	SMP AA-02	26	424.9	424.5	4.2	27.51	91.86		1078	1690.48	53	141	195
465102	Sorik	SMP AA-02	26	425.1	424.7	3.88	37.72	82.09		1084.92	1767.39	54	141	195
465103	Sorik	SMP AA-02	26	425.2	424.8	3.88	37.45	82.36		1085.02	1774.32	54	142	196
465104	Sorik	SMP AA-02	26	425.3	424.9	3.88	37.27	82.54		1052.89	1771.55	54	97	151
465105	Sorik	SMP AA-02	26	425.6	425.2	3.88	37.55	82.26		1085.31	1773.09	54	141	195
465106	Sorik	SMP AA-02	26	425.7	425.3	3.88	39.22	80.59		1084.87	1780.46	54	141	195
465107	Sorik	SMP AA-02	26	425.8	425.4	3.88	38.55	81.26		1079	1787.81	54	141	195
465108	Sorik	SMP AA-02	26	425.9	425.5	3.88	38.57	81.24		1084.79	1782.66	54	141	194
465109	Sorik	SMP AA-02	26	426	425.6	3.89	37.3	82.51		1084.99	1784.47	54	141	195
465110	Sorik	SMP AA-02	26	426.1	425.7	4.83	38.39	81.42		1084.28	1790.15	54	141	195
465111	Sorik	SMP AA-02	26	426.3	425.9	4.83	38.02	81.79		1085.05	1784.78	54	141	195
465112	Sorik	SMP AA-02	26	426.4	426	4.83	36.17	83.64		1085.81	1783.99	54	141	195
465113	Sorik	SMP AA-02	26	426.5	426.1	4.83	32.53	87.28		1088.3	1767.26	54	141	195
465114	Sorik	SMP AA-02	26	426.6	426.2	4.83	35.48	84.33		1086.83	1775.31	54	142	196
465115	Sorik	SMP AA-02	26	426.7	426.29	4.83	35.73	84.08		1087.31	1771.32	54	142	196
465116	Sorik	SMP AA-02	26	426.8	426.39	4.83	37.35	82.46		1086.95	1774.53	54	142	196
465117	Sorik	SMP AA-02	26	426.9	426.49	4.83	36.87	82.95		1086.92	1772.62	54	141	195
465118	Sorik	SMP AA-02	26	427	426.59	4.83	38.95	80.86		1086.95	1778.55	54	142	196
465119	Sorik	SMP AA-02	26	427.1	426.69	5.06	37.5	82.31		1088.2	1770.3	54	142	196
465120	Sorik	SMP AA-02	26	427.2	426.79	5.06	38.75	81.06		1087.09	1773.46	54	142	196
465121	Sorik	SMP AA-02	26	427.3	426.89	5.06	37.13	82.68		1088.22	1769.57	54	141	195
465122	Sorik	SMP AA-02	26	427.4	426.99	5.06	38.71	81.1		1086.42	1777.95	54	141	194
465123	Sorik	SMP AA-02	26	427.6	427.2	5.06	37.08	82.73		1087.97	1766.79	54	142	196
465124	Sorik	SMP AA-02	26	427.7	427.29	5.06	36.25	83.56		1087.33	1776.32	54	142	196
465125	Sorik	SMP AA-02	26	428	427.59	5.05	36.66	83.15		1090.76	1757.79	54	144	198
465126														

Sheet1 Background

Figure 2: Example of drilling parameter database in Excel.

Table 1: Sample data taken for monitoring.

No	Data	Source	Type
1	Survey	Directional drilling company	Csv, txt, Excel
2	Cutting volume	Solid control/management company	Excel
3	Mud properties	Drilling fluid company	Excel
4	Torque and drag	Directional drilling company	Csv, txt, Excel
5	DDRs	Operator	Excel report
6	Drilling parameters	Mud logging company	Csv, txt, Excel
7	Cutting lithology	Geologist	Excel table

3.2 Data Visualization in SMGP

With the data gathered and structured in a way it can be read by BI tool, the team started to set the benchmark performance of its past wells. As mentioned previously, this storyboarding method allows the team to quickly identify parts that needs improvements – after all a picture is worth a thousand words. Figure 3 shows the flow chart for the data management system done as part of the digitalization process. The first step to improve is to determine the end goal or best performance. Fortunately, the team had access to the data of one of the fastest geothermal well in Indonesia and decided to use this as the end goal or the single digit well.

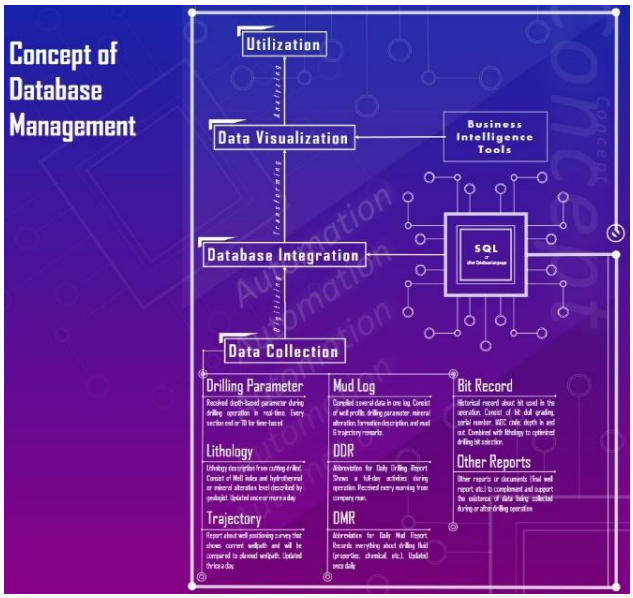

Figure 3: Flow chart of database management applied.

Although the main goal is clear, there are many small targets that needs to be achieved. One of the parameters that is identified from the start is the on bottom ROP. Figure 4 shows the visualization of ROP when compared to the target. Another is the weight-to-weight connection time that is still far from the target time (Figure 5). These visualizations allow the engineer to determine the current performance quickly. With the BI tool and structured data, these data can also be filtered and sorted quickly to gain different perspective.

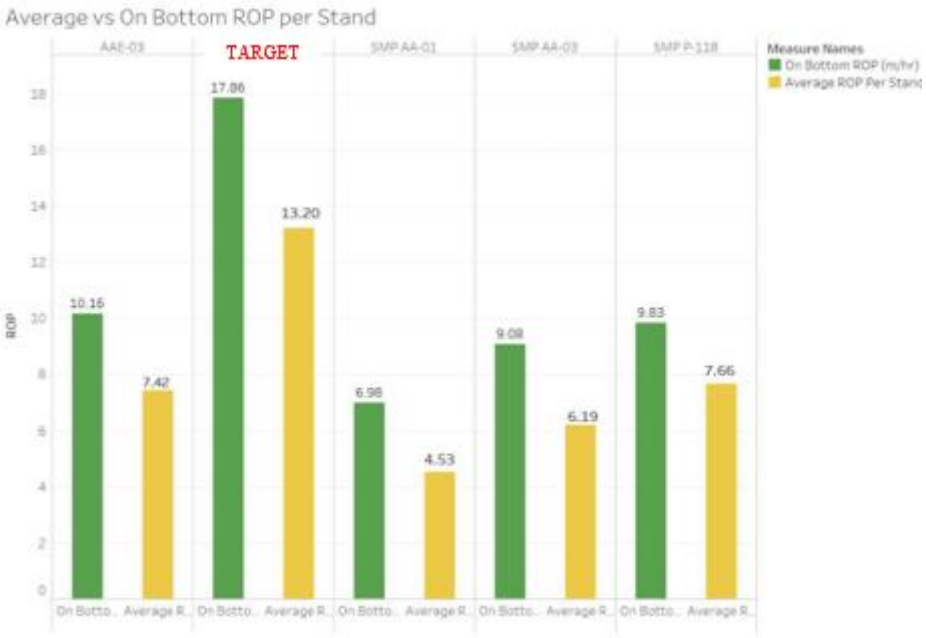

Figure 4: ROP visualization.

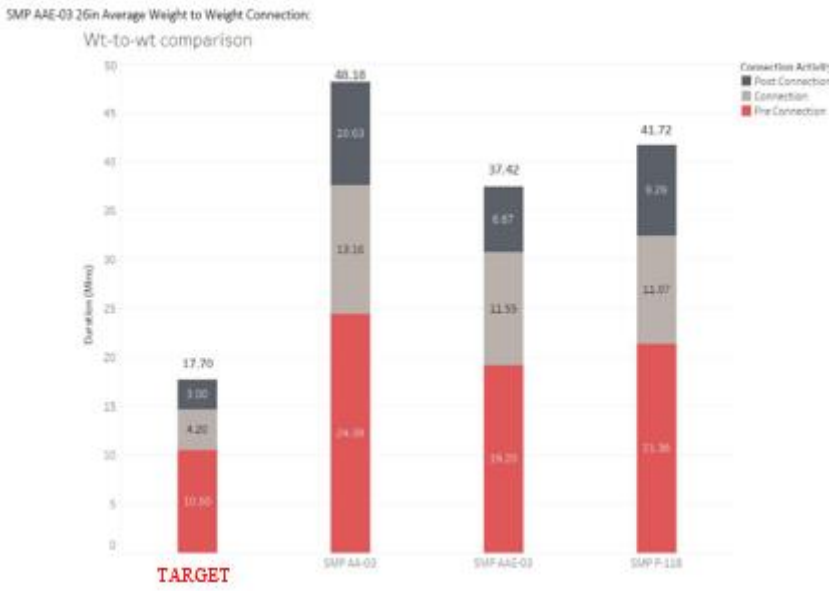

Figure 5: Weight to weight visualization.

Other than performance comparison that is done after drilling operation, visualization also allows monitoring while drilling. The most common tool used in most drilling activities is the real time operation monitor, displaying time-based drilling parameter. Visualization can act as a support to this by allowing engineers to compare depth-based drilling parameter that can be configured to update periodically such as shown in Figure 6. Such tools allow the engineer to further optimize the drilling parameter on site as they can avoid mistakes made or repeat successful runs.

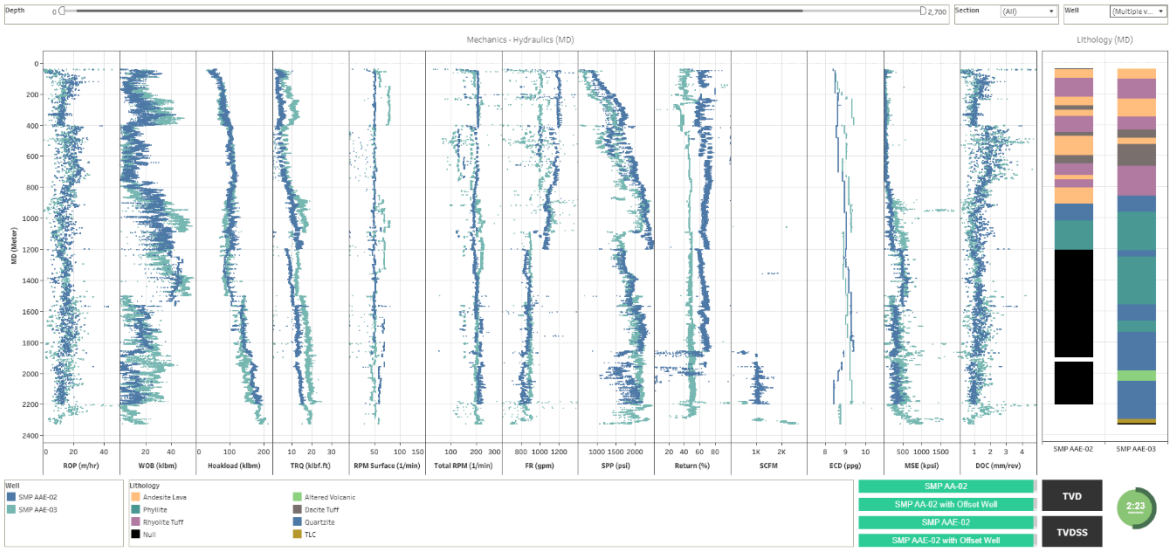

Figure 6: Depth-based drilling parameter visualization in comparison to offset wells.

Lastly, the visualization allows the engineers to get past records in a different perspective such as viewing bit records in an interactive dashboard as shown in Figure 7. The BI tool also allows tooltips to be shown to further enhance the data analysis process. Good performance bit can easily be identified and be planned to be utilized again to maintain or improve performance in the next wells.

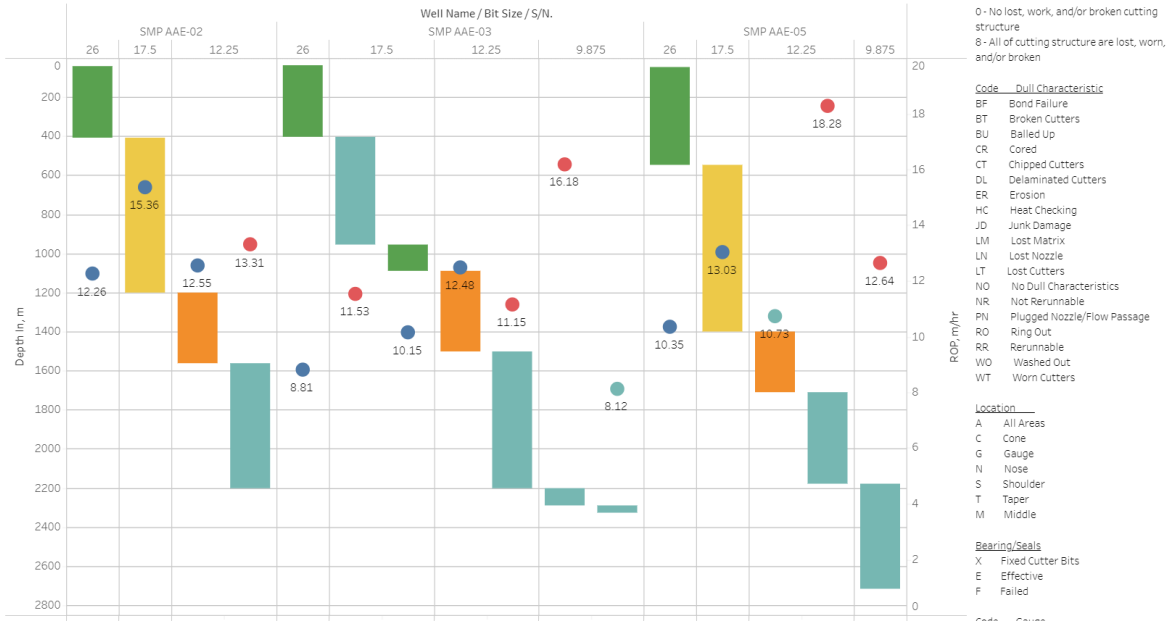

Figure 7: Interactive drilling bit dashboard and database.

3.3 SMGP Performance Improvement

The recent performance improvement in SMGP was achieved through the following steps with the aid of drilling digitalization:

a) Determining the performance goals
b) Understanding our current performance
c) Identify the gaps between the performance goals and current performance
d) Create the plan to reduce the gap and incorporate them in the drilling program
e) Monitor the execution during drilling operation.

As mentioned previously, the team decided to put the performance of one well drilled in pad 2 in Gunung Salak as the performance goal. The drilling operation to 1630 meters was completed within 9.6 days. The detail of time required to complete drilling 26" Hole Section, 17-1/2" Hole Section, 12-1/4" Hole Section, casing running, cementing, and all others activities were identified. Additionally, what and how they were done were analyzed.

Other than the well drilled in 9.6 days, with the data of the 28 wells drilled since 2016, data visualization really help to identify which well has the best performance on each drilling activities and what were done on these wells. These data then became the team's guide to better performance.

The third step was to identify the correct gap by using the visualization and asking following questions: What has been done in the performance goal? Can it be repeated? What would be the additional risk? Can it be mitigated? Does the current drilling equipment have the same technical limit?

Afterward, the plan on what to be done for the next drilling operation is created. This plan needs to be detailed and communicated to the related parties who will be executing it on the field.

Lastly, during drilling operation, with the live monitoring and live comparison to the best performance, the team ensure the plan is executed properly. Challenges that came up and hinders the improvement are captured and is subject to the next well improvement.

With all these five activities, AAE-02 as the 35th wells drilled in SMGP, was able to complete the 2200 meters within 23 days, including 2 days of completion test. The drilling speed of 94 meter / day broke SMGP previous record of 65 meter / day and it also broke the record drilling cost to USD 1179/meter (previous best well was USD 1426/meter) – a huge leap on a single well. Figure 8 shows the time versus depth chart of the AAE-02 compared to the wells in Sorik Marapi.

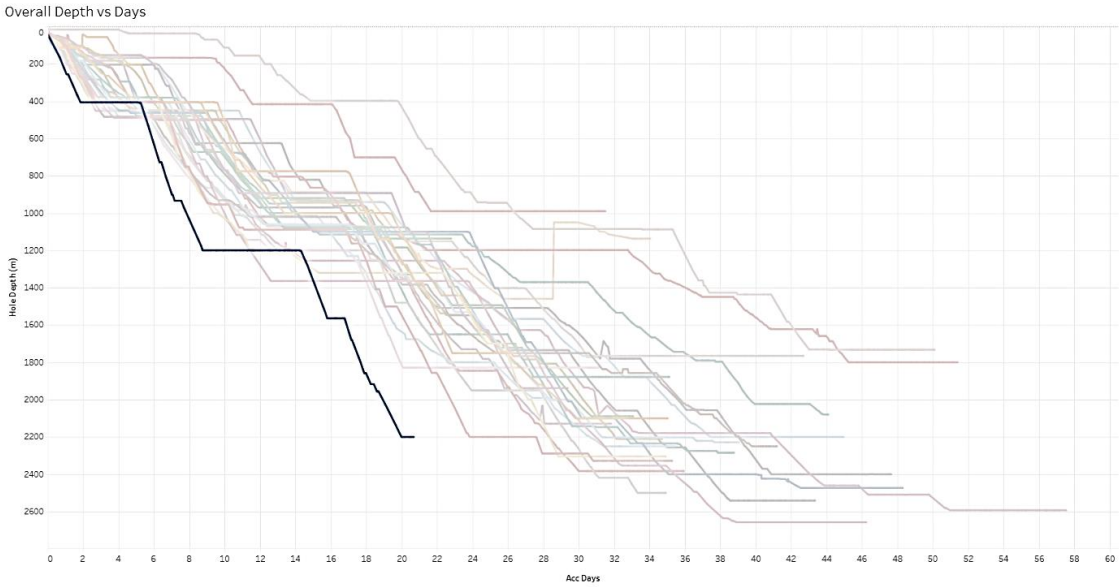

Figure 8: Time vs depth chart of SMGP wells.

4. FUTURE WORKS

The SMGP drilling team continue to explore drilling digitalization to identify possible operation improvement in order to reach the single digit well. The various data tools available to use also opens up various possibility to develop the digitalization further. An example that is available in the market, but yet to be utilized here, is the identification of drilling activities from drilling parameters using algorithm to further accurately identify drilling activities. New data visualization templates are also being explored in order to be able to "story tell" drilling performances. The drilling digitalization field, especially in geothermal drilling, still have a lot to improve and will definitely help in achieving efficient geothermal wells in Indonesia, making the geothermal industry much more attractive.

REFERENCES

Al-Aufi, Y., Al Sulti, A.M., Arnaout, A., Bakhti, S., Thonhauser, G., and Leoben, M.: The Impact of Digital Transformation on Cutting Drilling Costs - A Case Study from Oman, *Abu Dhabi International Petroleum Exhibition and Conference*, Society of Petroleum Engineers, Abu Dhabi (2018).

Chen, Z., Lo, A., Carrasquilla, M.N., Zhao, Z., and Shahid, T.: Using a Business Intelligence Tool for Drilling Data Analysis in the Permian Basin, *SPE Asia Pacific Oil and Gas Conference and Exhibition*, Society of Petroleum Engineers, Brisbane (2018).

Jing, N., Fan, H., Zhai, Y., and Liu, T.: Data Warehouse Design and Optimization for Drilling Engineering, *The Open Petroleum Engineering Journal*, (2012), 124-129.

Prihutomo, M.J. and Arianto, S.: Drilling Performance Improvements of Salak Geothermal Field, Indonesia 2006-2008, *Proceedings*, World Geothermal Congress 2010, Denpasar (2010).

Saini, G., Chan, H., Ashok, P., Van Oort, E., and Isbell, R.M.: Automated Large Data Processing: A Storyboarding Process to Quickly Extract Knowledge from Large Drilling Database, *IADC/SPE Drilling Conference and Exhibition*, Society of Petroleum Engineers, Fort Worth (2018).

Thomson, I.J. and Vulgamore, D.J.: The Quest for Drilling Optimization Improvement by Using Business Intelligence Methods, *SPE Digital Energy Conference and Exhibition*, Society of Petroleum Engineers, The Woodlands (2011).

Design of Geothermal Brine Energy Dryer as Alternative Thermal Energy Source

Febri Rizki Dwi Satriyo Pamungkas, Khasani, and Wahyu Hartono

febripamungkas04@gmail.com, khasani@ugm.ac.id

Keywords: Geothermal, Brine, Alternative Energy, Fluid

ABSTRACT

Pertamina Geothermal Energy (PGE), is a subsidiary of PT Pertamina (Persero) which has 14 Geothermal Working Areas in Indonesia, one of which is the PLTP Karaha area. Generally, geothermal systems in Indonesia are hydrothermal systems that have high temperatures (>225 ˚C) with only a few of them have moderate temperatures (150-225 ˚C). The output brine from separator is channeled into the holding pond and injected into the reinjection well directly. The data shows that the temperature of geothermal waste or brine, the output of the cluster 3 well separator shows 164.8˚C and has a pressure of 6.19 barg and a flow rate of 63.10 tons per hour or 17.527 kg/s (statistical average). The data has the potential to be used as an alternative heat energy in the use of agriculture, horticulture, fisheries and tourism sectors. The data is used as a design calculation of the dryer to determine the relationship between the air flow velocity (V) produced by the air blower and the drying temperature (T_o). The dryer is designed using a heat exchanger which is modeled on the pipe arrangement in a staggered manner. Where the air from the atmosphere flows through the heat exchanger using a blower to the drying room using trays. In this experiment, calculations were carried out to calculate various heat transfer rates and air flow velocities for varying drying temperatures using a geothermal liquid at a fixed temperature of 164.84 ˚C. Experimental calculations using geothermal fluid flow with a heat transfer rate of 1000 to 7000 Watt, an air flow velocity 3 to 9 m/s, and heat exchanger input temperature of 20˚C and 30˚C, resulted in an output drying temperature vary between 35.21˚C to 32.69˚C and 44.31˚C to 41.93˚C, the temperature range is sufficient for drying purposes, with drying energy (heat) produced about 29.88 to 74.78 kW per meter length and 27.18 to 67.94 kW per meter length of heat exchanger. From the above calculations, it can be concluded that the most important parameters that affect the temperature of the air entering the drying chamber are the geothermal fluid, the fluid flow velocity entering the pipe and the air velocity. The brine produced by the separator still has potential for uses such as alternative thermal energy for agriculture, horticulture, and aquaculture (fish farming). While the direct use of geothermal energy sources with low enthalpy as hot springs and swimming pools.

1. INTRODUCTION

Based on the records of the Geological Agency of the Ministry of Energy and Mineral Resources (ESDM) as of December 2020, Indonesia's geothermal resources reached 23,965.5 megawatts (MW) or about 24 giga watts (GW). But unfortunately, the magnitude of this geothermal reserve has not been utilized optimally. This can be seen from the installed capacity of geothermal power plants in Indonesia. Until 2020, Indonesia's PLTP installed capacity has only reached 2,130.7 MW. This means that the utilization is only 8.9% of the existing resources. Until today, the application of direct utilization of geothermal energy in geothermal fields has not been developed. Local communities cannot maximize geothermal energy for direct use applications. So, there is no significant economic benefit for them.

In general, geothermal systems in Indonesia are hydrothermal systems that have high temperatures (>225 ˚C) and only a few have moderate temperatures (150-225 ˚C). The heat contained in the liquid can still be extracted to supply equipment or machinery to produce fresh water vapor, to supply heating or drying equipment for planting media sterilization, drying agricultural and livestock products and other direct uses. The existence of geothermal energy sources that are widely available in mountainous and inland areas has its own advantages. In mountainous and inland areas of Indonesia, there are agricultural, plantation and forestry areas whose products require processes such as drying, preservation, heating, sterilization, pasteurization, etc. Processing of agricultural and plantation products that require heat are for example: drying rice, coffee, and tea, potato seeding, mushroom cultivation, pasteurization of milk, etc.

Based on the development of direct use of geothermal energy in Indonesia, grains and beans drying equipment using heat in geothermal fluids has been carried out around power plants in the Kamojang area, West Java by Sumotarto (2007). In this tool, it uses a heat exchanger fluid and air is flowed using a fan. Then the use of geothermal energy as a means of planting mushrooms in Kamojang, West Java by Surana et al. (2010). The worldwide application of geothermal energy for direct utilization by Lund (2010). Utilization of thermal energy extracted from brine for fish farming as a local direct use application by Purwaningsing and Abdurrahman (2016).

This study will discuss a model for utilizing geothermal brine energy to be implemented in the Karaha geothermal field, West Java, Indonesia. Geothermal fluid waste from the well separator cluster 3 will be used to supply the dryer. The heat from the brine fluid will be extracted and used in this case to dry agricultural and plantation crops. Other applications can be used to produce room drying, heating, bathing media, swimming pools, heating fish ponds etc.

2. METHODOLOGY AND DESIGN

Traditionally, drying of agricultural and plantation crops such as rice, coffee, beans, grains, tea, and copra in Indonesia is done by heating the product under sunshine (solar drying). The product will be affected by seasons and weather changes, thus preventing the drying process from continuing. This will result in the product cracking, fracturing and incomplete drying. To improve the process, drying must be carried out continuously, requiring a continuous supply of heat. This can be achieved by using a sustainable supply of energy resources such as geothermal fluid flows.

This research was conducted by analytical calculations using energy and heat transfer equations. These equations are formed in a calculation model using Microsoft Excel to facilitate calculations. This research was conducted in well separator cluster 3 in Karaha

geothermal field. Literature studies were conducted to collect information about heat transfer data analysis and heat transfer process. The cluster 3 well separator data is used as an input parameter in the heat transfer model for the dryer built in this study.

2.1 Equipment Design

The dryer used will be made with a fluid-air heat exchanger to produce hot air which will be blown into a drying chamber filled with agricultural and plantation products. The brine fluid output from the separator will be flowed through a 2 inch pipe from the main pipe to the cooling pool. From this 2 inch pipe the brine fluid will enter the dryer. The Figure 1 shows the design of the geothermal brine energy dryer in 3D and Figure 2 shows the design from longitudinal cross section. After from the dryer, the geothermal waste brine fluid is flowed into the drain pool, and the air is blown outside the pipe to extract heat from the geothermal waste brine fluid inside the tube for the drying process.

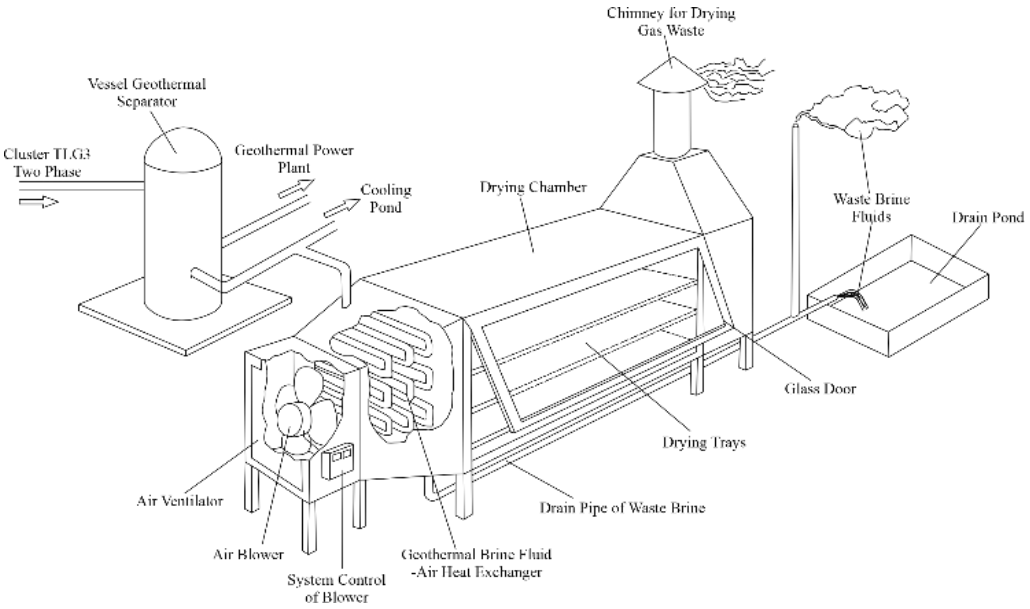

Figure 1: The design of geothermal brine energy dryer in 3D.

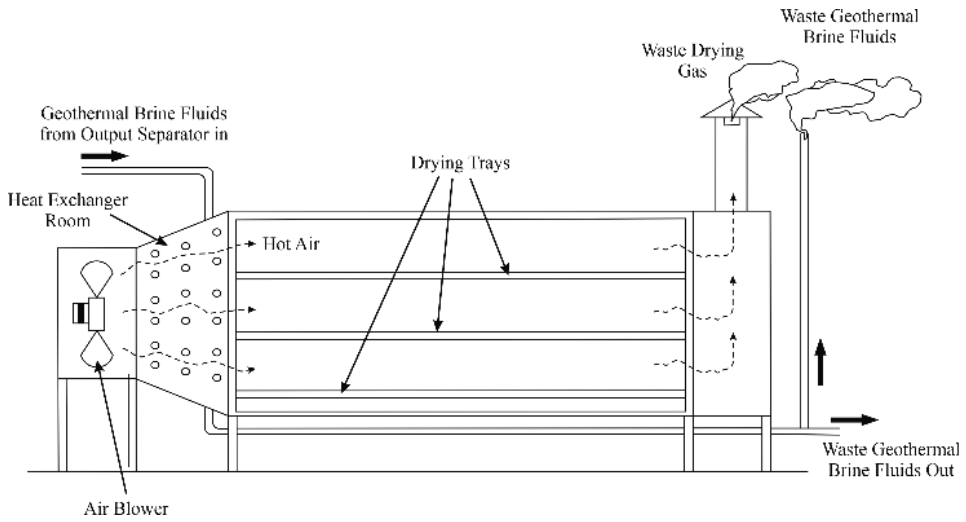

Figure 2: The longitudinal cross section of geothermal brine energy dryer.

The only device that moves is the blower. Blowers are used to transfer heat from the brine fluid in the heat exchanger chamber. Meanwhile, agricultural and plantation products are placed in trays in the drying room. The drying duration depends on the original moisture of the product which the blower can be adjusted by the control system depend on drying duration. By conducting several drying experiments, an ideal drying time can be found for a completely dry product. This Dryer is designed simply to assist the technical feasibility of direct utilization of thermal energy from brine.

2.2 Heat Transfer

The law of conservation of energy shows that heat exchangers can be divided into two parts. The first part is the heat transfer from the geothermal fluid inside the pipe to the outside of the pipe. The second part is the heat transfer that occurs outside the pipe that enters the drying room.

2.2.1 Heat Transfer in the First Part

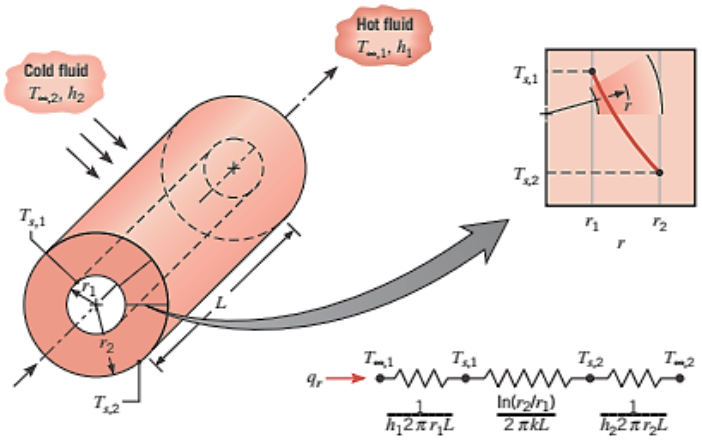

Figure 3: Hollow cylinder with convective surface conditions (Incropera et al., 2011).

Calculation of heat transfer in this section is carried out with steady state assumptions. The calculation is based on the phenomenon where the heat flows across the cylindrical pipe (Figure 3). Outside of the heat exchanger, air is assumed to flow convectional into the drying chamber at a certain speed from the fan. At this time, it is assumed that there is no radiation heat transfer. This is caused by the speed of air flowing through the pipe.

For simple calculation, this part can be modeled as hollow cylinder whose inner and outer surfaces are exposed to fluids at different temperatures. For steady-state conditions with no heat generation, the appropriate form of the heat equation is

$$\frac{1}{r}\frac{d}{dr}\left(kr\frac{dT}{dr}\right) = 0 \tag{1}$$

Where r is radius of cylinder (in m), k is the thermal conductivity of the material (in W/m.K) and $\frac{dT}{dr}$ is temperature gradient (in ℃/m).

According to Fourier's Law, energy (heat) flow rate by conduction through solid cylindrical surface can be expressed as

$$q_r = -kA\frac{dT}{dr} = -k(2\pi rL)\frac{dT}{dr} \tag{2}$$

Where q_r is heat transfer rate (in Watt), A = $2\pi rL$ is the area normal to the direction of heat transfer (in m^2), r is radius of cylinder pipe (in m), L is length of cylinder pipe (in m), k is the thermal conductivity of the material (in W/m.K) and $\frac{dT}{dr}$ is temperature gradient (in ℃/m). The heat transfer rate q_r is a constant value in radial direction.

Assuming the value of k to be constant, Equation 1 may be integrated twice to obtain the general solution

$$T(r) = C_1 \ln r + C_2 \tag{3}$$

Where $T(r)$ is temperature distribution (in ℃), r is radius of cylinder pipe (in m), C_1 and C_2 are constant.

To obtain the constants of integration C_1 and C_2, with boundary conditions: $T(r_1) = T_{s,1}$ and $T(r_2) = T_{s,2}$. Applying these conditions to the general solution

$$T_{s,1} = C_1 \ln r_1 + C_2 \text{ and } T_{s,2} = C_1 \ln r_2 + C_2$$

C_1 and C_2 can be found as

$$C_1 = \frac{T_{s,1} - T_{s,2}}{\ln(r_1/r_2)} \text{ and } C_2 = T_{s,2} - \left(\frac{T_{s,1} - T_{s,2}}{\ln(r_1/r_2)}\right)\ln r_2$$

Substituting C1 and C2 into the general equation of temperature for the system as follows

$$T(r) = \frac{T_{s,1} - T_{s,2}}{\ln(r_1/r_2)} \ln\left(\frac{r}{r_2}\right) + T_{s,2} \tag{4}$$

Where $T(r)$ is temperature distribution (in ℃), $T_{s,1}$ and $T_{s,2}$ are inner and outer surface temperature (in ℃), and r_1 and r_2 are inner and outer radius of cylinder pipe (in m), respectively.

Note that the temperature distribution associated with radial conduction heat flow through a cylindrical wall is logarithmic, not linear such as on a plane wall under the same conditions.

Further, Equation 4, is now used with Fourier's law, Equation 2 results for the heat transfer rate as follows

$$q_r = \frac{2\pi Lk(T_{s,1} - T_{s,2})}{\ln(r_2/r_1)} \quad (5)$$

Where q_r is heat transfer rate (in Watt), L is length of cylinder pipe (in m), k is the thermal conductivity of the material (in W/m.K), $T_{s,1}$ and $T_{s,2}$ are inner and outer surface temperature (in °C), and r_1 and r_2 are inner and outer radius of cylinder pipe (in m), respectively.

So, the thermal resistance of radial conduction in a cylindrical wall is of the form

$$R_{t(cond)} = \frac{\ln(r_2/r_1)}{2\pi Lk}$$

The heat flow from the center of the cylindrical tube to the inside wall of the tube and from the outer side of the tube into the open air is a convection flow. For the whole system from $T_{\infty,1} \rightarrow T_{s,1} \rightarrow T_{s,2} \rightarrow T_{\infty,2}$, the heat transfer rate may be expressed as

$$q_r = \frac{T_{\infty,1} - T_{\infty,2}}{\frac{1}{2\pi r_1 Lh_1} + \frac{\ln(r_2/r_1)}{2\pi Lk} + \frac{1}{2\pi r_2 Lh_2}} \quad (6)$$

Which can also be expressed in heat rate equations for each portion of the entire flow as

$$q_{r,1} = 2\pi r_1 Lh_1(T_{\infty,1} - T_{s,1}) \quad (6.a)$$

$$q_{r,2} = \frac{2\pi Lk(T_{s,1} - T_{s,2})}{\ln(r_2/r_1)} \quad (6.b)$$

$$q_{r,3} = 2\pi r_2 Lh_2(T_{s,2} - T_{\infty,2}) \quad (6.c)$$

Where q_r is heat transfer rate (in Watt), L is length of cylinder pipe (in m), k is the thermal conductivity of the material (in W/m.K), $T_{\infty,1}$ and $T_{\infty,2}$ are temperature of cylinder pipe's center and temperature of open air (in °C), and r_1 and r_2 are inner and outer radius of cylinder pipe (in m), h_1 and h_2 are inner and outer convection heat transfer coefficient (in W/m^2.K), respectively.

Those three equations (6.a, 6.b, and 6.c) can be used to calculate $T_{s,1}$ and $T_{s,2}$ because $q_r = q_{r,1} = q_{r,2} = q_{r,3}$

2.2.2 Heat Transfer in the Second Part

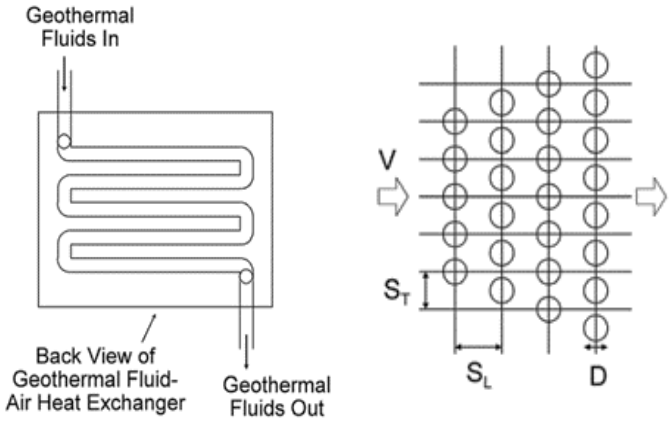

Figure 4: Hollow cylinder with convective surface conditions (Sumartono, 2006).

As heat leaves the outer side of the pipes, the governing air convection flow equations can be modeled through a bank of tubes in the heat exchanger (Figure 4). The tube rows in this heat exchanger are staggered in the direction of fluid velocity *(V)*. The configuration is characterized by the tube diameter *(D)* and by the transverse pitch *(S_T)* and longitudinal pitch *(S_L)* measured between tube centers. Flow conditions within the bank are dominated by boundary layer separation effects and by wake interactions, which in turn influence convection heat transfer (Incropera et al., 2011), describes such phenomena with the following equations.

The amount of heat transfer can be calculated by, first calculating the Reynolds number as:

$$Re_{D,max} = \frac{V_{max} D_o}{v} \quad (7)$$

Where $Re_{D,max}$ is Reynolds number, V_{max} is maximum fluid velocity (in m/s), D_o is outer diameter tube (in m), and v is kinematic viscosity of the air (m^2/s).

The Reynolds number ($Re_{D,max}$) for the foregoing correlations is based on the maximum fluid velocity (V_{max}) occurring within the tube bank. For the staggered configuration, the maximum velocity may occur at either the transverse plane or the diagonal plane. If the rows are placed such that

$S_D = [S_L^2 + (S_T/2)^2]^{1/2} > (S_T + D)/2$, then

$$V_{max} = \frac{S_T}{S_T - D} V \quad (8.a)$$

Otherwise,

$$V_{max} = \frac{S_T}{2(S_D - D)} V \quad (8.b)$$

Where S_D is diagonal pitch (in m), S_T is tranverse pitch (in m), S_L is longitudinal pitch (in m), D is diameter tube (in m), and, V is fluid velocity (in m/s), and V_{max} is maximum fluid velocity (in m/s).

Then air-side Nusselt number can be calculated as follows

$$Nu_D = C\, Re_{D,max}^{m} \mathrm{Pr}^{0,36} \left(\frac{Pr_\infty}{Pr_s}\right)^{1/4} \quad (9)$$

$$Pr = \frac{v}{a} = \frac{\mu/\rho}{k/\rho Cp} = \frac{c_p\, \mu}{k}$$

Where Nu is Nusselt number, C and m are that depend on tube configuration (tabulated in Table 1), Re is Reynolds number, Pr is Prandtl number, c_p is gas (air) specific heat at constant pressure (J/kg.K), μ is dynamic viscosity of the air (m^2/s), and k = gas (air) thermal conductivity (W/m.K).

By knowing the number of $Re_{D,max}$, the value of C and m can be determined.

Table 1: Constants C and m in Equation 9.

Configuration	$Re_{D,max}$	C	m
Aligned	$10 – 10^2$	0.80	0.40
Staggered	$10 – 10^2$	0.90	0.40
Aligned	$10^2 – 10^3$	0.51	0.50
Staggered	$10^2 – 10^3$	0.51	0.50
Aligned ($S_T/S_L > 0.7$)	$10^3 – 2 \times 10^5$	0.27	0.63
Staggered ($S_T/S_L < 2$)	$10^3 – 2 \times 10^5$	$0.35(S_T/S_L)^{1/5}$	0.60
Staggered ($S_T/S_L > 2$)	$10^3 – 2 \times 10^5$	0.40	0.60
Aligned	$2 \times 10^5 – 2 \times 10^6$	0.021	0.84
Staggered	$2 \times 10^5 – 2 \times 10^6$	0.022	0.84

The average convection heat transfer coefficient (h) can be calculated using the following equation

$$\bar{h} = \overline{Nu}_D \frac{k}{D} \quad (10)$$

Where $\bar{h}$ is average convection heat transfer coefficient ($W/m^2.K$), Nu is Nusselt number, k is gas (air) thermal conductivity (in W/m.K), and D is diameter tube (in m).

The heated air temperature produced from the heat exchanger can be calculated using a log-mean temperature difference

$$\Delta T_{lm} = \frac{(T_s - T_i) - (T_s - T_o)}{ln\left(\frac{T_s - T_i}{T_s - T_o}\right)} \quad (11)$$

Where ΔT_{lm} is log-mean temperature difference (in ˚C), T_i and T_o are temperatures of the fluid as it enters and leaves the bank (in ˚C), respectively, and T_s is tube outside surface temperature (in ˚C).

The outlet temperature T_o, which is needed to determine ΔT_{lm} may be estimated from

$$\frac{T_s - T_o}{T_s - T_i} = \exp\left(-\frac{\pi D N \bar{h}}{\rho V N_T S_T c_p}\right)$$

Where T_i and T_o are temperatures of the fluid as it enters and leaves the bank (in ˚C), respectively, T_s is tube outside surface temperature (in ˚C), D is diameter tube (in m), N is total number of tubes in the bank, $\bar{h}$ is average convection heat transfer coefficient ($W/m^2.K$), ρ is air mass density (in kg/m^3), V is fluid velocity (in m/s), N_T is number of tubes in transverse plane, S_T is transverse pitch (in m), and c_p is gas (air) specific heat at constant pressure (J/kg.K).

Finally, the amount of heat transfer per unit length of the tubes can be determined using the equation

$$q' = N(\bar{h}\pi D \Delta T_{lm})$$

Where q' is heat transfer per unit length (in W/m), N is total number of tubes in the bank, $\bar{h}$ is average convection heat transfer coefficient ($W/m^2.K$), D is diameter tube (in m), and ΔT_{lm} is log-mean temperature difference (in ˚C).

3. CASE STUDY

The scheme shows (Figure 5) that the output of geothermal waste or brine from the cluster 3 well separator, have a temperature of 164.8˚C, a pressure of 6.19 barg and a flow rate of 17.527 kg/s. Systematically, the output brine from separator is distributed to cooling pond before injected to the reinjection well. Unfortunately, this waste brine is not used to direct use. Therefore, the heat from the brine fluid will be extracted and used to dry agricultural and plantation crops in Geothermal brine energy dryer.

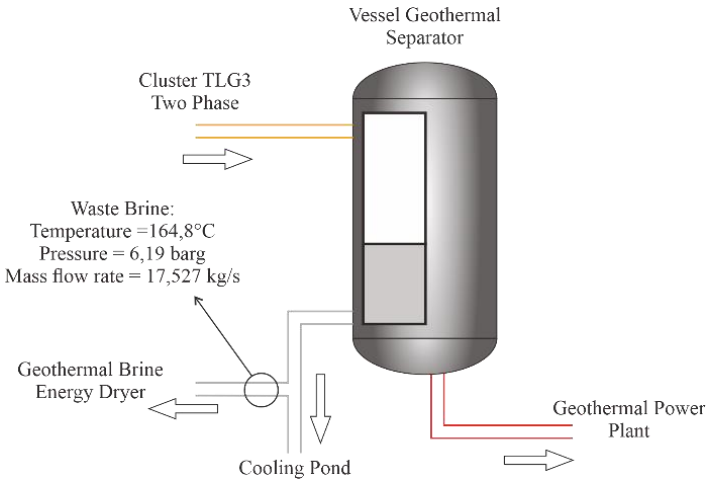

Figure 5: Output of geothermal waste or brine from the cluster 3 well separator.

Geothermal brine energy dryer has certain specifications of the components that has been designed. The specifications of Geothermal brine energy dryer consist of the geothermal fluid heat convection coefficient, heat exchanger pipe thermal conductivity, geothermal fluid temperature, mass flow rate, HE input temperature, HE transverse pitch and longitudinal pitch, total number of tubes in the HE bank, HE number of the tubes in the transverse plane, velocity of Air of Blower. The specification of Geothermal brine energy dryer is shown in Table 2.

Table 2: Parameters used in the simulation and calculation of the geothermal brine energy drying equipment.

Parameters			Unit
Geothermal Fluid heat convection coefficient (h_1)	1000		$W/m^2.K$
Heat Exchanger pipe thermal conductivity (k)	10		W/m.K
Geothermal Fluid Temperature (Tb)	164.8		^oC
Flow Rate (ṁ)	17.53		kg/s
He Input Temperature (Ti)	20	30	^oC
Air kinematics viscosity (ν)	$1.516*10^{-5}$	$1.608*10^{-5}$	m^2/s
Air dynamic viscosity (μ)	$1.825*10^{-5}$	$1.872*10^{-5}$	kg/m.s
Gas (air) thermal conductivity (K_{air})	0.02514	0.02588	W/m.K
Air mass density (ρ)	1.204	1.164	kg/m^3
Prandtl numer Pr and Prs	0.7309, 0.69	0.7282, 0.69	
Gas (air) specific heat at constat pressure (C_p)	1.007		J/kg.K
Constants in Nusselt number calculation (C&m)	0.022, 0.84		
HE transverse pitch (S_T) and longitudinal pitch (S_L)	0.09, 0.12		m
Tota number of tubes in the HE bank (N)	26		
HE number of the tubes in the transverse plane (N_T)	6		
HE pipe inner and outer diameter and total length	0.043, 0.0508, 29.3		m
Velocity of Air of Blower	3 to 9		m/s

4. RESULTS AND DISCUSSION

Using the equations described in the above section, it can be determined the relation between the air flow velocity (V) produced by the air blower, the drying temperature (T_o), and the heat transfer per unit length of the tubes (q'). Depending on the drying temperatures that are specific to each product, the air flow velocity (V) can be adjusted accordingly. The calculation and simulation are conducted as follows:

1. Write a formula in Microsoft Excel for the calculation according to the equations described in previous sections.
2. Prepare parameters and constants needed in the calculation such as geothermal brine fluid temperature inside the tube, mass flow rate, heat transfer convection coefficients, etc. Table 2 shows parameter and constants needed for the calculation.
3. Using the proper data and calculation procedure, it can be calculated the parameter needed for the drying process.
4. Tables and charts showing various relations can be made according to the calculation results.

Using the above parameters in Table 2 it is found that at a geothermal fluid temperature of 164.8˚C and heat exchanger input temperature 20˚C and 30˚C, by using simulation procedure there can be calculated various heat transfer rate and drying temperature at various air flow velocity produced from the air blower, 3 to 9 m/s. Tables 3, 4 and chart Figure 6, 7 show the results of the calculations and the relations between air flow velocity to heat transfer rate and drying temperature.

Table 3: Relationship between geothermal brine heat flow rate, q_r (Watt), inside the HE tubes and outside pipe surface temperature, $T_{s,1}$, $T_{s,2}$ (˚C) for a constant geothermal fluid temperature, $T_{\infty,1}$ (˚C) of 164.8 (˚C).

q_r (Watt)	$T_{s,1}$ (˚C)	$T_{s,2}$ (˚C)
1000	164.55	164.46
2000	164.29	164.11
3000	164.04	163.77
4000	163.79	163.43
5000	163.54	163.08
6000	163.28	162.74
7000	163.03	162.40

Table 3 shows that at various geothermal fluid flows with heat transfer rate (q_r) of between 1000 to 7000 W, the outside surface temperature of the heat exchanger pipes would reach as high as 164.48 to 162.40˚C

Table 4: Output (drying) temperature, T_o (˚C) and heat transfer rate per length of HE, q_{rate} (kW/m) according to heat exchanger input temperature, T_i (˚C) of 20˚C and 30˚C and at various outside surface temperature of the HE, $T_{s,2}$ (˚C).

$T_{s,2}$ (˚C)	T_i 20˚C		T_i 30˚C	
	T_o (˚C)	q_{rate} (kW/m)	T_o (˚C)	q_{rate} (kW/m)
164.46	35.21	29.88	44,31	27.18
164.11	34.53	38.06	43,67	34.60
163.77	34.01	45.88	43,18	41.70
163.43	33.60	53.42	42,78	48.55
163.08	33.25	60.73	42,46	55.19
162.74	32.95	67.84	42,17	61.64
162.40	32.69	74.78	41,93	67.94

Further, Table 4 shows that at the above various heat transfer rate, the output temperature (T_o) of the HE would reach 32.69 to 35.21˚C (at T_i 20˚C) and 41.39 to 44.31˚C (at T_i 30˚C), from which we can have enough temperature for drying purposes.

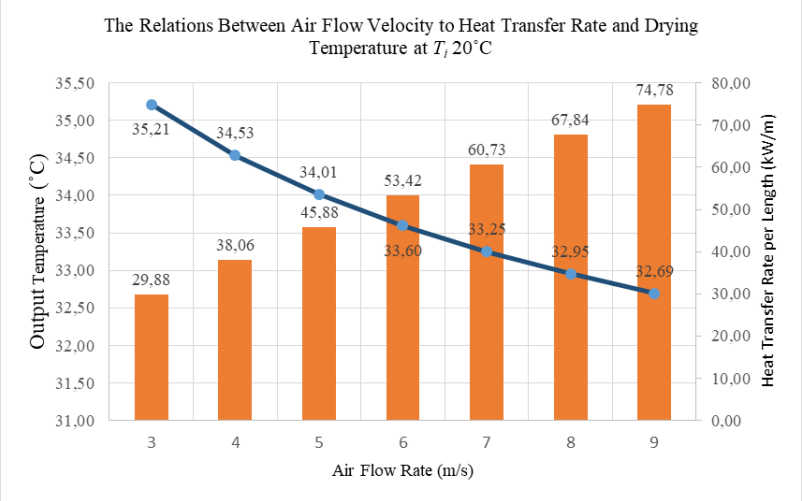

Figure 6: Output (drying) temperature, T_o (˚C) and heat transfer rate per length of HE, q_{rate} (kW/m) at HE input temperature, T_i 20˚C and various air flow rate, V (m/s) from the air blower.

Eventually, it can be seen in Figure 6 and 7 that for various air flow velocities from the air blower of between 3 to 9 m/s, the drying temperature would vary between 35.21 to 32.69˚C and 44.31 to 41.93˚C, respectively, which will produce drying heat transfer rate of 29.88 to 74.78 kW per meter length and 27.18 to 67.94 kW per meter length of the HE, respectively.

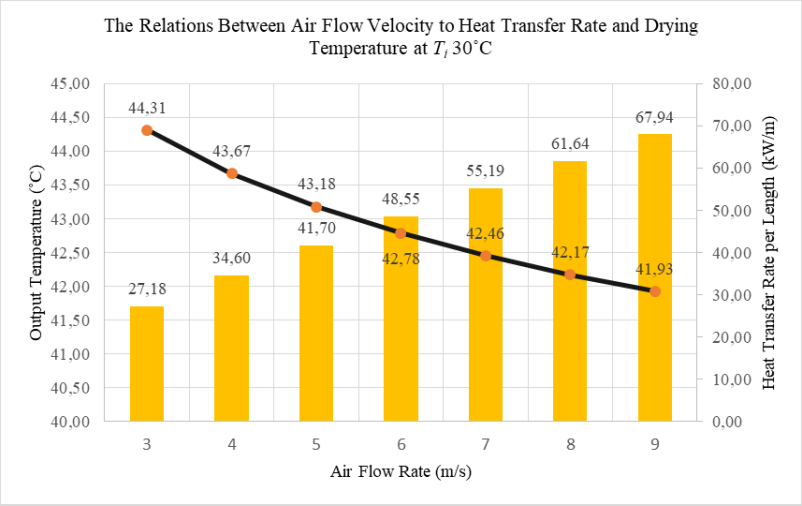

Figure 7: Output (drying) temperature, T_o (˚C) and heat transfer rate per length of HE, q_{rate} (kW/m) at HE input temperature, T_i 30˚C and various air flow rate, V (m/s) from the air blower.

5. CONCLUSION

As the design of the geothermal brine energy dryer and equations model needed for the design there can be calculated various parameters needed for the drying process. From the calculation and simulation performed in this research it can be concluded the following:

a) The dryer equipment designed in this research uses a fluid-air heat exchanger that can be modeled as staggered pipes bank in which air from the atmosphere is flowed through the fluid-air heat exchanger using an air blower into a drying chamber filled with trays of agricultural and plantation crops product to be dried.
b) In this study, the phenomenon of heat transfer is divided into two parts. The first part is heat transfer in from geothermal brine fluids inside the 2 inch pipes to the outer side of the 2 inch pipes in heat exchanger room where heat is transferred through convection and conduction modes. The second part is heat transfer from the outer side of the pipe into the drying room where heat is mainly transferred by (forced) convection mode.
c) The drying temperature can be set according to product being dried to find a proper air flow velocity from the air blower. In this experiment, calculation is performed to compute various heat transfer rate, air flow velocity, and heat exchanger input temperature for varying drying temperature using a fixed geothermal brine fluids temperature of 164,8˚C.
d) The result from calculation using geothermal fluid flow with heat transfer rate of between 1000 to 7000 Watt, an air flow velocity 3 to 9 m/s, and heat exchanger input temperature of 20˚C and 30˚C, resulted in an output drying temperature vary between 35.21˚C to 32.69˚C and 44.31˚C to 41.93˚C, respectively, the temperature range is sufficient for drying purposes, with drying energy (heat) produced about 29.88 to 74.78 kW/m length and 27.18 to 67.94 kW/m length of heat exchanger, respectively.
e) Geothermal Power Plant or PLTP Karaha has potential thermal to direct use of geothermal system. The heat from the system can be extracted and used for activities to dry agricultural crops, plantation corps, bathing, swimming pools, hearing fish ponds, and so on. This research use data from the cluster 3 well separator as input parameter in the heat transfer model.

6. RECOMMENDATON

This research was carried out by developing the heat transfer model by considering the design of geothermal brine dryer and the parameters. This research has to be followed up with more detail experiments and calculations in order to find a complete and thorough design of the equipment that can work optimally.

REFERENCES

Incropera, F. P., Bergman T. L., Lavine A. S., and DeWitt D. P.: Introduction to Heat Transfer, New Jersey, John Wiley & Sons, Inc. (2011).

Lund, J. W.: Direct Utilization of Geothermal Energy, *Energy* 3(8), (2010), 1443-1471.

Purwaningsing, F. P. and Abdurrahman, G.: Geothermal Brine, From Waste to Alternative Thermal Energy, *Proceedings*, 41st Workshop on Geothermal Reservoir Engineering, Stanford University, Stanford, California (2016).

Sumotarto, U.: Design of a Geothermal Energy Dryer for Beans and Grains Drying in Kamojang Geothermal Field, Indonesia, *GHC Bulletin*, 28, (2007), 13-18.

Surana, T., Atmojo J. P., Suyanto, and Subandriya A.: Development of Geothermal Energy Direct Use in Indonesia, *GHC Bulletin*, (2010), 11-15.

Real Time Steam Dryness Monitoring by Integration with DCS

Abdul Halim F., Edwin Ardiansyah, and Wahyu Firmansyah

PT Pertamina Goethermal Energy, Jl. Muara Dua, Kec. Ulubelu, Kab. Tanggamus, Lampung 35379

abdul.hfauzi@pertamina.com

Keywords: Steam Dryness, Automatic Monitoring, Dryness Measurement

ABSTRACT

Dryness of steam must be equals to 99% or higher before enter the steam turbine. The lower percentage of dryness can be harmful for the turbine due to the maximum allowable condensate on the blade of turbine. Monitoring of dryness is needed to ensure the dryness meet the requirement or to determine action that should be done to maintain the dryness. Measurement of dryness is essential but only held once a week because the system of measurement. Equipment called Ellison throttling calorimeter is used to measure the dryness. This equipment needs operators to stay on the spot of measurement to observe the value from the thermometer and calculate the dryness using that value to determine the dryness and impossible for the operator to stay 24 hours for monitoring.

Automatic monitoring can be done by modification of measurement system. The thermometer that used on the measurement was changed to temperature sensor and connected to temperature transmitter so the reading of the sensor can be transmitted to DCS (Distributed Control System) and specific program was installed on the DCS so the calculation can be automatically operated on DCS and value of dryness can be monitored and trended on DCS on the center control room. The specific program is development from the equation of Ellison throttling calorimeter. Calculation of dryness needs chemical properties (enthalpy) but it was hard to enter the steam table into DCS, so the specific program was made to find the enthalpy using linear regression.

After the modification was held, Real time monitoring is possible now. By doing monitoring and made trending from DCS, the operator can maintain the dryness of steam by doing several actions based on the result of real time monitoring and trending. The system also completed by alarm which will give a sign (sound) if the dryness decreasing to ensure faster action to solve the problem. Another benefit of this modification is operator have bank data of dryness that can be used for analysis performance of equipment related to the steam above ground system.

1. INTRODUCTION

PT Pertamina Geothermal Energy Area Ulubelu delivers steam to power plant of PT PLN to produce electricity. Based on the agreement, the steam supplied must meet the specific requirements. One of the parameters required is the level of steam dryness which must be equals to 99% or higher. The lower percentage of dryness is widely known to be doubly-damaging, leading to both loss of efficiency and to mechanical damage of the machine components (Hesketh and Walker, 2005). The turbine will experience a trip as a form of protection / security for the turbine.

The loss due to trip of the turbine are quite large. For example, the loss experienced by PT Pertamina Geothermal Energy Area Ulubelu due to trip of the turbine, unit 1, power plant of PT PLN because of wet steam (dryness 98.3%) are Rp. 164,650,865. Wet steam that supplied to the power plant should be prevented. A series of efforts need to be taken to ensure the dryness meets the criteria, the earliest effort is to measure the dryness. The measurement of dryness only held once a week so the data is not enough to describe the change of dryness and cannot show the value of dryness every single time which is needed for determine action that should be taken to solve the problem.

2. STEAM DRYNESS MEASUREMENT

Dryness is measured using an equipment called Ellison Throttling Calorimeter. The basic principle of the throttling calorimeter is that dry saturated steam, in passing through an orifice to a lower pressure, becomes superheated. The enthalpy dry saturated steam and the superheated steam are equals. After temperature and pressure of superheated steam measured, the dryness fraction or percentage of steam can be determined (equation. 1)

$$SQ = 100 - (100 \times (\frac{H-h-K(T-t)}{L})) \quad (1)$$

where *SQ, H, h, K, T, t , L* are steam quality, total heat of steam at line pressure at saturated condition , total heat of steam at calorimeter pressure at saturated condition, specific heat of superheated steam, temperature of superheat in calorimeter, temperature due to the pressure in calorimeter, latent heat on steam line.

H can be determined using two parameters, pressure and temperature of steam line. On PT Pertamina Goethermal Energy, temperature of steam line can be monitored from Supervisory Control and Data Acquisition (SCADA) but temperature superheated in calorimeter should be measured on spot of the equipment. The measurement need operator to observe it manually. After that, operator use the value of the temperature to calculate the percentage of dryness using Microsoft excel. This is the reason why measurement of dryness cannot be measure continuously for 24 hours.

3. REAL TIME STEAM DRYNESS MONITORING

Real time dryness monitoring will be possible if the method of measurement changed from manual to auto. Modification on dryness measurement system have been made. The purpose of modification is to collect all the variables that used in calculation then calculate it on Distributed Control System (DCS) so the dryness can be show on faceplate of DCS or monitored (live or historical) using application called “Trend” which is part of DCS itself.

3.1 The Modification of Measurement

First step of achieving real time steam dryness monitoring is substitution of thermometer that used in throttling calorimeter. Temperature superheated steam in calorimeter was measured using portable thermometer. The portable thermometer changed by the temperature sensor and connected to temperature transmitter so the reading of the sensor can be transmitted to DCS (Distributed Control System). The cable that used are installed underground for safety purpose. By this substitution, the operator did not need to stay on the spot of measurement to observe the temperature because the value of the temperature is sent directly to the DCS for calculation

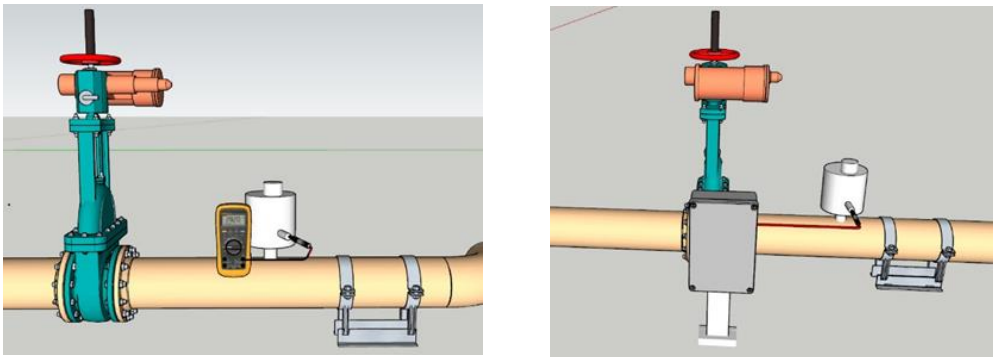

Figure 1: The Substitution from portable thermometer to temperature transmitter.

Other parameters required to finish the calculation of dryness on DCS are temperature at steam line and pressure at saturated condition are parameters. The temperature at steam line can be provided on DCS by change the direction of transmission from SCADA to DCS. For the pressure at saturated condition, it is assumed to be usually equal to the ambient air pressure and can be monitor on faceplate weather station ambient on DCS.

The steam tables is used to determine total heat or enthalpy but hard to enter it to the DCS. Entering the steam table also need more space in memories which is slowing the process of calculation on DCS. The solution of this problem is interpolation using linier regression. Linier regression had been made using Microsoft excel equipped by steam tables. The result of this linier regression is specific equation for each variable (*H, h, K, t, L)*. The more data used on finding equation of linier regression, the more accurate the result.

$$H = 1.0819\,a + 2594.6312 \quad (2)$$
$$h = 0.1 \times 0.421b + 2626.9218 \quad (3)$$
$$K = 0.1 \times 0.011b + 1.9633 \quad (4)$$
$$t = 0.1 \times 0.3024b + 69.4275 \quad (5)$$
$$L = -3.3526\,a + 2618.5386 \quad (6)$$

Where *a* and *b* are temperature of steam line at saturated condition and pressure of ambient air pressure. All the equations above are input to the equation.1 to determine the dryness of steam without using steam table. The program which contains this calculation are created and on DCS by Ovation Developer so dryness can be directly and continuously calculated after all the parameters are available. All the operation are mathematic operation only.

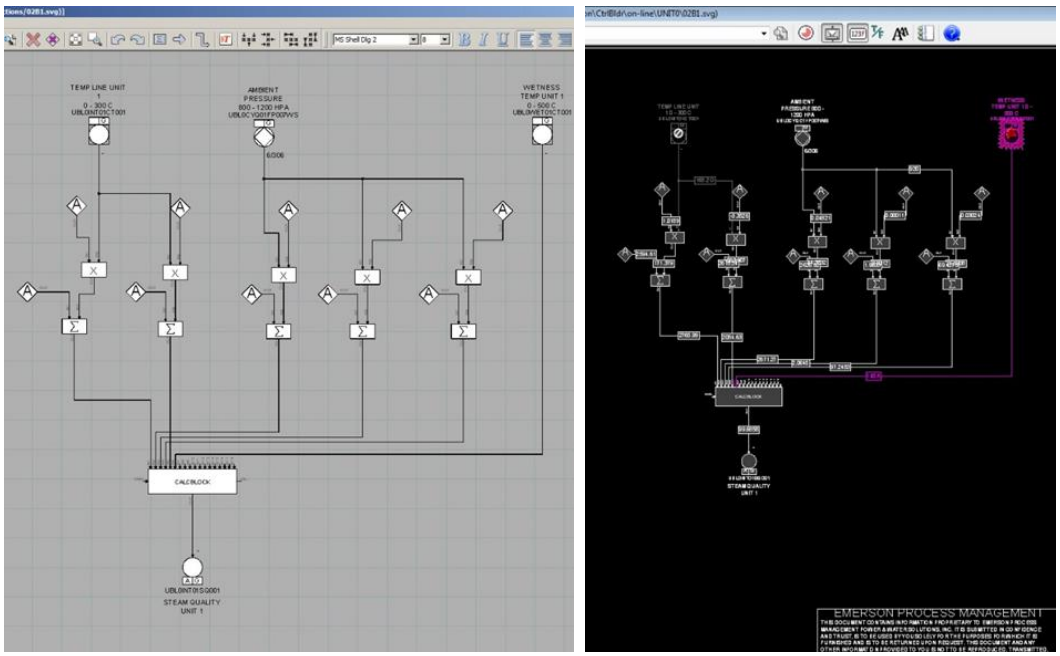

Figure 2: The Ovation Developer and the Signal Diagram of Steam Dryness Calculation.

3.2 Validation of the Calculation Result

Validation is performed to ensure the result of calculation after the modification is correct or acceptable. It is done by comparing the result from manual measurement with automatic measurement at the same time and condition. Data are collected periodically. The results of the comparison show that the difference in measurement results is very small (maximum 0.03%) so it can be concluded that automatic measurement can be used instead of manual measurement.

Table 1: Result of Dryness Measurement.

Manual measurement	Automatic Measurement	% Difference
99.85	99.88	0.03
99.52	99.55	0.03
99.60	99.62	0.02

3.3 Monitoring the Dryness

After the modification and validation have done, the next step is monitoring the dryness on DCS. The new faceplate for dryness monitoring are added to DCS and if it is needed, the change of dryness can be analyze by using trend application. Using trend allow us to look data in graphic and table models. Before the modification, only 4 data of dryness per month but after the medication, in a day, the data of measurement which can be collected are 1440 (data taken per minute).

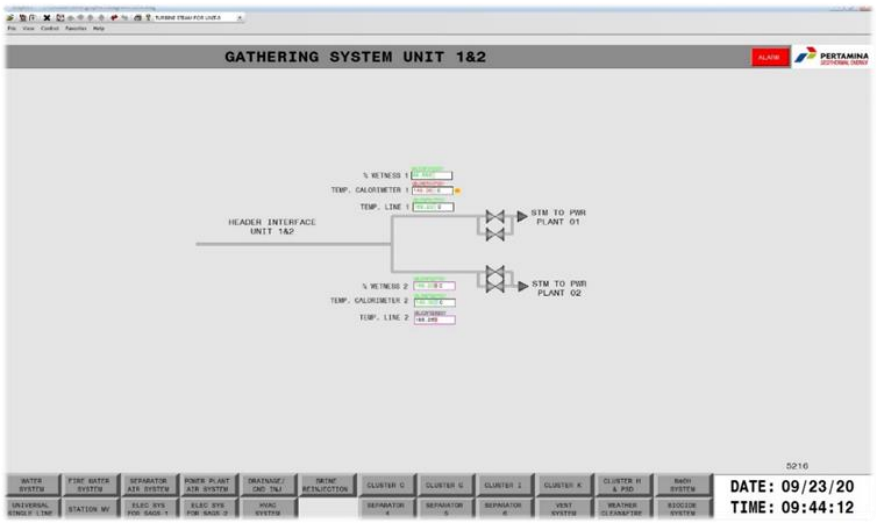

Figure 3: The Faceplate of Dryness Monitoring on DCS.

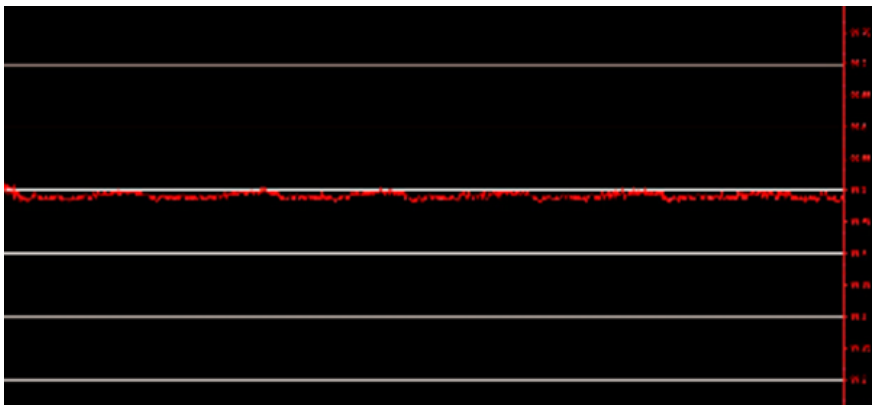

Figure 4: The Trending of Dryness in Graphical Models.

3.4 Alarm

Even though the measurements have been performed automatically and the results can be seen directly on the DCS, it is impossible for the operator in the control room to pay attention to the dryness value all the time. The activity at the power plant is very extensive and numerous, so an alarm is added which will inform the operator that the dryness value has decreased so that appropriate action can be taken immediately.

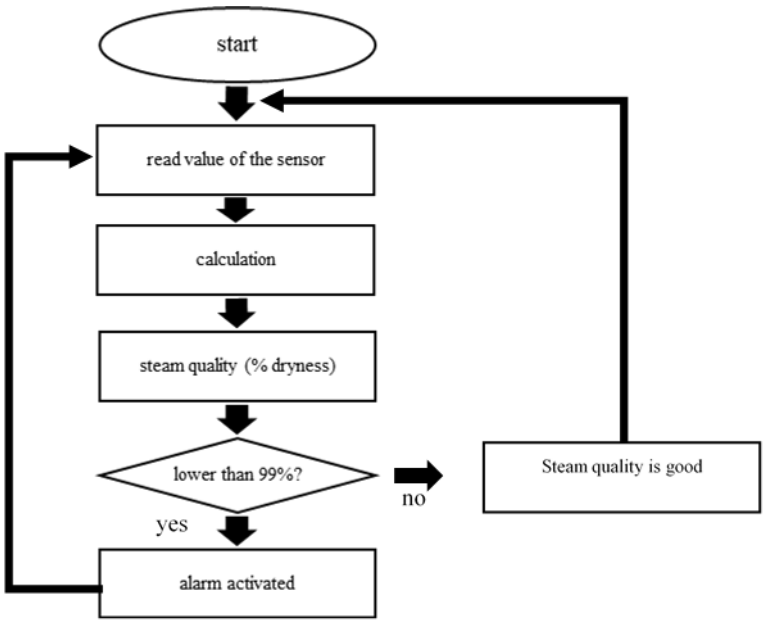

Figure 5: Flow Chart of Automatic Dryness Monitoring.

4. CONCLUSION

Measurement of steam dryness are essential. Steam dryness measurement can be modified from manual to automatic system by substitutes the part of equipment and developing calculation program on DCS. The equation resulting from development of calculation program can be different based on data used on the calculation and parameter units. After the modification, the dryness can be monitored continuously and trended to analysis the change of dryness, whether it decrease or increase so the right action can be taken to maintain the dryness. The modification also provides bank data of dryness for analysis purposes because the data recorded on DCS. The monitoring of dryness cannot be directly changing the dryness of the steam but the initial step to ensure the steam supplied to the power plant meets the expected dryness level.

REFERENCES

Cal Research, Inc.: 900 Series Ellison Steam Calorimeter Operation and Maintenance Manual, (2010).

Hesketh, J.A. and Walker, P.: Effects of Wetness in Steam Turbines, Proceedings, The Institution of Mechanical Engineers Part C-*Journal of Mechanical Engineering Science*, (2005).

Operation Team: Disturbance Report, PT Pertamina Geothermal Energy Area Ulubelu (2019).

YouTube: "Throttling calorimeter|Dryness fraction measurement|To find x|Animation|Limitation|GTU|Calorimeter", uploaded by Mechanical Engineering Management, 5 March 2020. https://www.youtube.com/watch?v=AKJHXAxTiOs

Progress in Research and Development (R&D) of Geothermal Binary Plant in Indonesia

Cahyadi, Suyanto, Riza, and Agus Nurrochim

Balai Besar Teknologi Konversi Energi BRIN
Gedung 620 Kawasan Puspiptek Serpong

cahyadi@bppt.go.id

Keywords: binary cycle, geothermal pilot plant

ABSTRACT

This paper describes the progress of the R&D of geothermal binary plant in Indonesia. The government has been strongly supporting the research in geothermal utilization for power plant. Since 2010, BPPT have been started for geothermal research to develop geothermal power plant with high local content component. Considering the continuously increasing need for electricity in Indonesia, there are strong efforts to further develop the geothermal power capacity. R&D in binary plants accelerate the low enthalpy utilization as well as industrial ecosystem in Indonesia. Based on the evaluation in long term operation of binary pilot plant in Lahendong, the design of binary plant has tremendous potential to replicate in other geothermal fields with low enthalpy steam or available brine water. In term of performance of binary plant is satisfactory compare with worldwide binary plant efficiency. The local content of binary plant still needs to be improved. BRIN coordinate the research with local manufacturers of heat exchanger, dry cooler, and turbine-generator. Knowledge transfer of binary plant must be accelerated to increase the low enthalpy geothermal potency in Indonesia.

1. INTRODUCTION

In Indonesia, total geothermal potential is estimated at 23.9 GWe which is dominated by wet steam fields. Unfortunately, the installed capacity of geothermal power plant amounts to 2.13 GWe, leaving a significant amount of the geothermal potential untapped. (MEMR, 2021). Considering the continuously increasing need for electricity in Indonesia, there are strong efforts to further develop the geothermal power capacity.

The geothermal plant type in Indonesia is dominated by the single-flash plant which directly uses the steam phase from the produced steam-liquid-mixture to drive the turbine. The single-flash steam technology cannot be utilized for low enthalpy geo fluid condition. Binary plants, which transfer the low temperature geothermal heat to a separate working fluid are not many established technologies at Indonesian sites. The commercial binary units in Indonesia locate at Sarulla field since in 2017 and also Sorik Merapi in 2019. Binary power plants can extend the plant capacity at high enthalpy fields but can also be used to exploit low to intermediate temperature geothermal reservoirs and realize small scale geothermal power plants. Binary plants can be implemented at much more sites and increase the geothermal capacity in Indonesia

The government has been strongly supporting the research in geothermal utilization for power plant. Since 2010, BPPT have been started for geothermal research to develop geothermal power plant with high local content component. The pilot plant of flash plant and binary plant have been established. The binary plant has been started with the capacity of 2 kW in Wayang Windu (Bambang et al., 2010). In order to successfully demonstrate geothermal binary power plant technology at an Indonesian site and to intensify the know-how transfer in this technology field, a German-Indonesian collaboration project was initiated in 2013 between GFZ Potsdam (Germany), the Agency for the Assessment and Application of Technology in Indonesia (BPPT) and PT Pertamina Geothermal Energy (PGE). The project was based on a bilateral agreement between the German and the Indonesian Ministry of Research, (Stephanie et.al., 2019).

The pilot plant is located in the Lahendong geothermal area. Technical concept development, component specification, coordination and supervision of the detail planning as well as construction and commissioning were executed by the project consortium under the guidance of GFZ. The operational phase commenced in September 2017. In January 2019 the demonstration plant was handed over to the Indonesian consortium and is now operated and maintained by the Indonesian project partners. Besides commercial operation the plant will be used for demonstration activities and training.

This paper describes the status of the pilot scale of geothermal binary cycle power plant have been developed by BPPT/BRIN in Indonesia. This binary pilot plant paper has successfully introduced an intermediate hot water cycle. Based on, the performance of binary pilot plant since 2017, the binary pilot plant can strongly be replicated in other low temperature steam or other available brine water in geothermal fields.

2. BINARY CYCLE TECHNOLOGY

The binary plant uses a secondary separated system to produce electricity by which a working fluid is preheated and evaporated through transferring heat by making contact with the geothermal heat flow (Braun and Mc CLuer, 1993). DiPippo (2015) previously indicated that binary configurations are mostly appropriate for low temperature geothermal resources (120–150 °C), and that the avoidance of contact between the geo-fluid and power production equipment may prevent scaling and corrosion effects. However, Dickson and Fanelli emphasised that binary system designs can utilise a temperature range between 85 and 170 °C, stating that upper limited temperatures depend on working fluid thermal stability and lower limited temperatures on technical, financial and economic aspects. The secondary fluid (working fluid) in the binary system operates under a conventional Ranking cycle, and as the used working fluid is organic, the binary cycle is also known as the Organic Ranking Cycle (ORC).

The main thermodynamic characteristics of the secondary working fluid in the Organic Ranking cycle are that, at low temperatures (85 and 170 °C), it has a low boiling point and high vapour pressure. Figure 1 illustrates thermodynamic features, pressure-enthalpy and temperature-entropy diagrams are required.

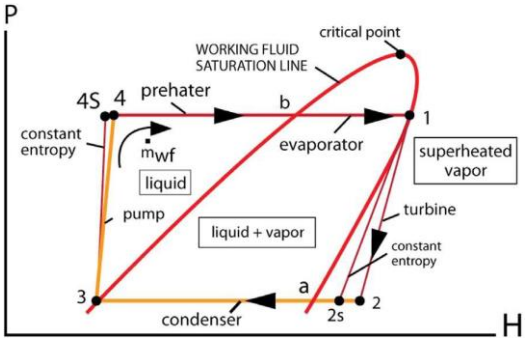

Figure 1: Pressure-enthalpy diagram of a binary geothermal power plant (Dipippo, 2015).

The thermodynamic process starts at state 1 where the working fluid at saturated vapour point enters the turbine expanding and producing work. The generator then generates electricity by using this work. The pressure and temperature of the saturated vapour decrease at the state 2 after turbine expansion. At constant pressure, the working vapour fluid goes into the condenser reducing its temperature and therefore condensing the fluid, at state 3. The cooling process of the working fluid takes place between state 3 and state 4 by using cooling water from the air-cooled cooling tower. This cooling stage changes the state of the working fluid from vapour to saturated liquid. Then, the working saturated liquid fluid is pumped back to the pre-heater (state 5) and evaporator (state 6), and the working fluid emerges as saturated vapour starting the cycle again at state 1 (Dipippo, 2012).

A comprehensive overview on geothermal binary power plants is given by DiPippo (2015). A description of the technical status-quo of binary plant technology can also be found in Bronicki (2013). Geothermal binary plants are in most cases Organic Rankine Cycle (ORC) plants, which are directly driven by the geothermal heat and which are often realized as single-stage and sub-critical processes. Depending on the plant capacity and the site conditions power plants with multiple heat input, multi-stage cycles and cycles with internal heat recovery can be found (DiPippo, 2015; Valdimarsson, 2011; Heberle et al., 2015). Commonly used working fluids are Isobutane, Isopentane, R245fa, R134a, n-Butane and n-Pentane.

Geothermal binary plants use different concepts of site integration. Binary plants complement the direct steam use at a geothermal high enthalpy site by either using the liquid phase from the separator or by utilizing the waste heat from the direct-steam turbine. Geothermal binary plants can also use the complete fluid flow from a geothermal high- or medium-enthalpy field and process the heat contained in the hot water from deep hydrothermal resources.

3. BINARY PILOT PLANT IN LAHENDONG

The pilot plant has been integrated at the Lahendong geothermal field close to the village Pangolombian where geothermal brine with a temperature of about 170 °C corresponding to a separator pressure of 7.9 bara was available. The cooling of the brine should be limited to 140 °C in order to have the possibility for hot brine reinjection close to the production well. The brine composition was reported with a SiO2- concentration between 100 and 500 mg/l, a pH value between 5 and 9 and a TDS-content (total dissolved solids) between 150 and 540 mg/l (Stephanie et.al., 2019).

Considering a broad range of brine compositions and operate the binary plant with variable capacity without changing the brine supply as well as the reliability of evaporator, it was decided to integrate the power conversion cycle by using intermediary closed water cycles for heat supply and heat removal. Aiming for high reliability, a subcritical, single-stage ORC with internal heat recovery was chosen as the conversion cycle. N-Pentane, a well-known working fluid suitable for the heat source temperature at the demonstration site, was selected as the working fluid.

Figure 2 shows the flow diagram of the Lahendong binary pilot plant The binary plant consists of three different cycles, there are hot water cycle, ORC cycle and cooling water cycle. During normal operation, the heat of the brine is transferred to the hot water cycle using the primary heat exchanger. The hot water is then used to heat and evaporate the working fluid inside the ORC-unit. The hot water is continuously circulated by using a centrifugal pump. In order to keep the pressure in the hot water cycle in a defined operating range, an expansion vessel with nitrogen cushion is used. In the ORC-unit the working fluid vapor drives a turbogenerator. After the turbine, the superheated working fluid vapor flows through a recuperator register before getting in touch with the water-cooled tubes. The heat removal in the cooling water cycle is realized with a dry cooler.

The advantage of using the hot water cycle, it was further possible to operate, shut-down and start-up the binary plant without changing the existing operational regime of the brine supply. The used prototype ORC-unit can only be started at low supply temperatures since large temperature differences between hot water and the working fluid can lead to steam hammer in the evaporator. Therefore, an additional dry cooler is necessary to cool down the hot water before restart and the control valves are used to realize a defined temperature ramp. The hot water by-pass pump is implemented to realize modest temperature differences around the primary heat exchanger during restart and to reduce the risk of steam hammer on the brine side.

Another benefit of the hot water cycle is that different priorities can be applied for the heat exchanger design. Regarding the primary heat exchanger, which transfers the heat from the brine to the hot water, the accessibility of the tubes for cleaning procedures and corrosion resistant materials has a high priority. The evaporator design focuses instead on the heat transfer. An advantage of implementing the cooling water cycle is that design and operation of the dry cooler becomes easier due to the well-known single

phase heat-transfer of water. Furthermore, less working fluid is needed to fill the ORC-cycle and the risk of n-pentane leakage is decreased.

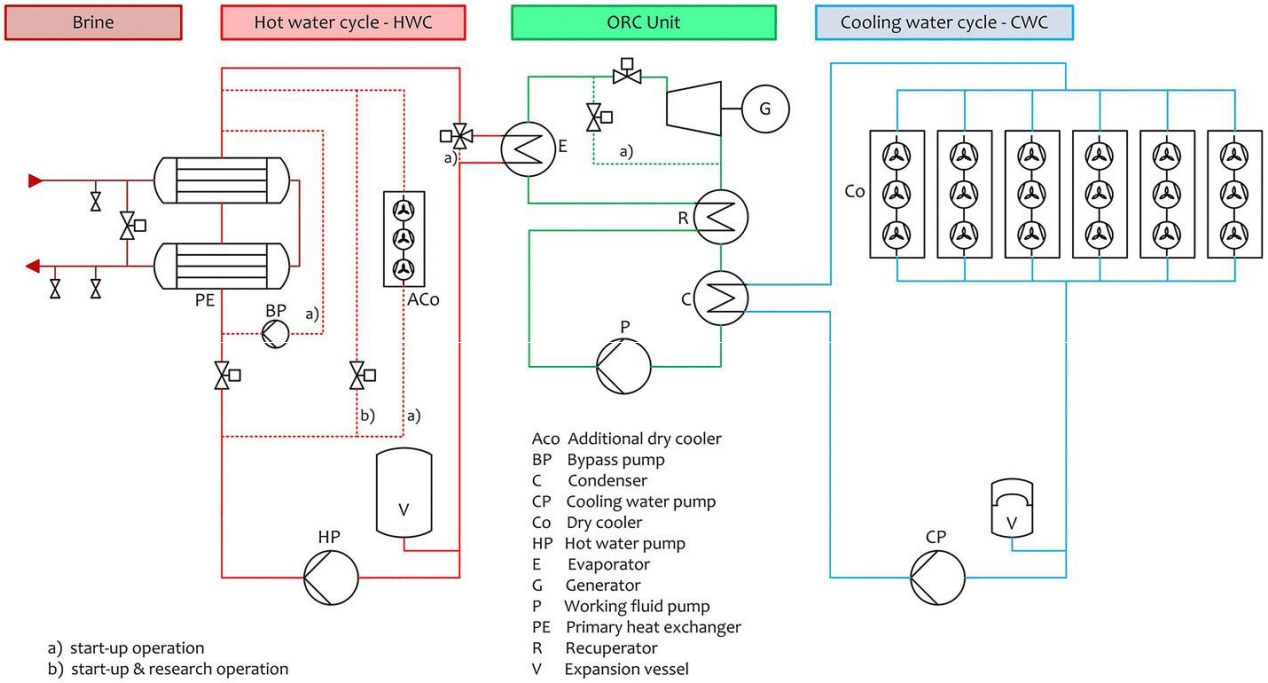

Figure 2: Flow diagram of the Lahendong binary pilot plant (Stephanie et.al., 2019).

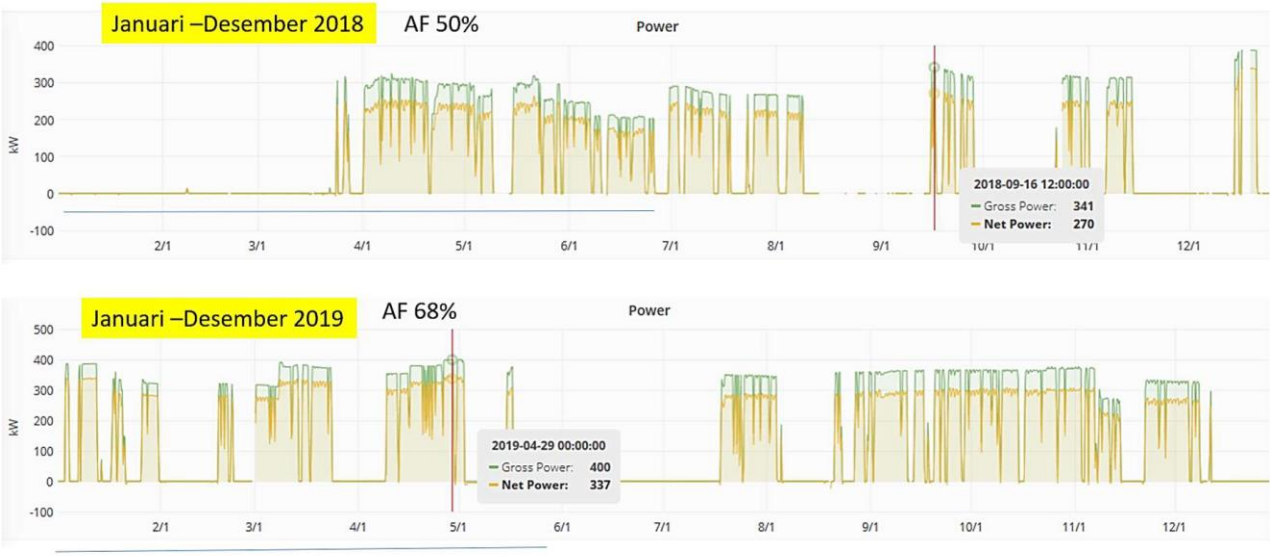

Figure 3: Power generation of the binary pilot plant in 2018 and 2019.

The binary pilot plant has been successfully operating since September 2017 and has produced more than 2.1 GWh gross electricity as of December 2019 and the plant has been connected to 20 kV PLN electricity grids. Figure 3 shows the power generation of binary pilot plant in 2018 and 2019. Since the commissioning several technical modifications have been realized in order to improve the plant reliability and availability. The modifications of the prototype-turbogenerator, the hot water cycle and the plant control were necessary in order to manage frequent starts and stops of the plant which are caused by the electrical grid (mainly power outages, phase failure). The binary plant has been designed for grid-parallel with high reliability and the plant was not equipped with DC system for normal shutdown while the grid outage. Based on the electrical grid quality data that were provided at the beginning of the project, it was not expected to have such a poor grid quality at the used grid connection point. Since September 2017 the plant has experienced more than 150 plant stops and starts as shown in Figure 3. Furthermore, the real brine conditions made it necessary to modify some operating procedures. Instead of pure liquid as assumed for the design, a two-phase flow is supplied to the binary plant. Both the well conditions and the operational regime of the separator have changed since the start of the project.

The plant has operated since 2017. Based on Figure 3 indicated that the availability factor has increased from 50% to 68% as well as the capacity factor from 68% to 80%. The availability factor was mainly affected by a poor grid quality at the used grid connection point. In Figure 4 shows the performance of binary plant efficiency of 9,1% while the plant was generating at 400 kWe. Performance of Lahendong binary plant is satisfactory compare with worldwide binary plant efficiency as shown in Figure 5. Based on the lesson learned of binary pilot plant in Lahendong, the design of binary plant has huge potential to replicate in other geothermal fields with

low enthalpy steam or available brine water. Sustainable collaboration research with National research institution between academic, local manufacturers and the owner of geothermal work area must be maintained. The local content of binary plant still needs to be improved. BRIN coordinate the research with local manufacturers of heat exchanger, dry cooler, and turbine-generator. Knowledge transfer of binary plant must be accelerated to increase the low enthalpy geothermal potency in Indonesia.

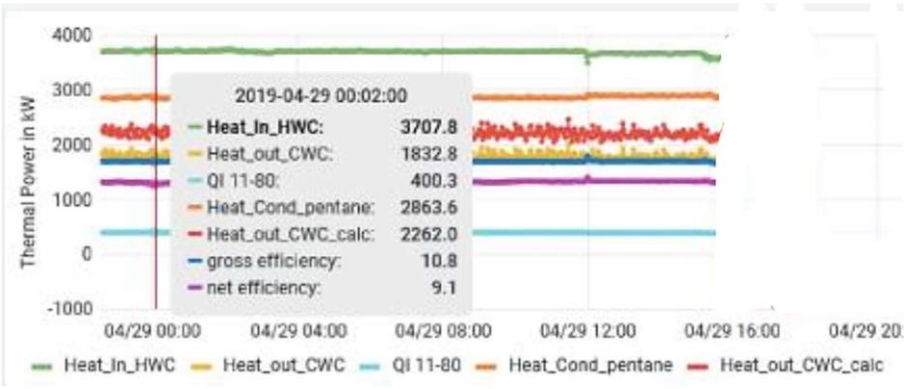

Figure 4 Typical the efficiency of binary pilot plant at 400 kWe.

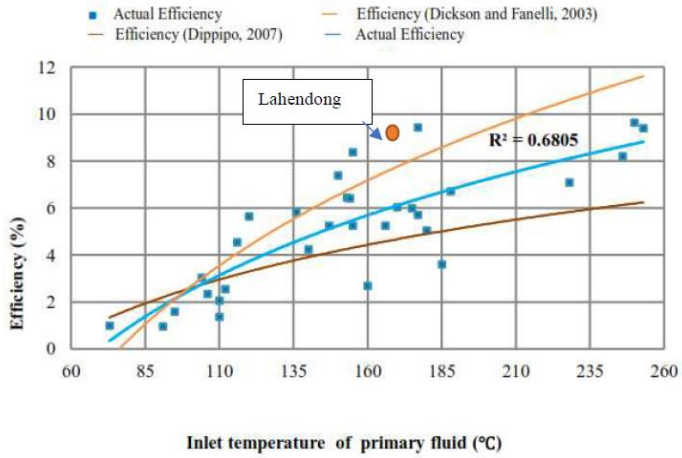

Figure 5: Worldwide binary plant efficiency as a function of geo fluid temperature (Zarrouk, 2014).

The binary plant still needs to be improved for presented technical concept integrates an Organic Rankine Cycle unit using an intermediary hot water and cooling water cycle. However, cost reduction potentials (e.g., decreasing expansion vessel size or using thermal oil instead of water) should be evaluated.

4. CONCLUSION

Based on the evaluation in long term operation of binary pilot plant in Lahendong, the design of binary plant has tremendous potential to replicate in other geothermal fields with low enthalpy steam or available brine water. In term of performance of binary plant is satisfactory compare with worldwide binary plant efficiency. The local content of binary plant still needs to be improved. BRIN coordinates the research with local manufacturers of heat exchanger, dry cooler, and turbine-generator. Knowledge transfer of binary plant must be accelerated to increase the low enthalpy geothermal potency in Indonesia.

5. ACKNOWLEDGEMENTS

We thank the German Federal Ministry for Education and Research (BMBF) for funding this German project under the grants 03G0834A and Pertamina Geothermal Energy (PGE) for the cooperation.

REFERENCES

Bambang, T.P., Himawan, S., Suyanto, Taufan, S., Lina, A., and Ridha Y.: Design and testing of n-Pentane Turbine for 2 kW Model of Binary Cycle Power Plant, *Proceedings*, World Geothermal Congress, (2010).

Braun, G.W. and Mc Cluer, H.K.: Geothermal power generation in United State, *Proceedings IEEE*, (ISSN 0018-9219), vol. 81, (1993), no. 3, p. 434-448.

Dickson, M.H. and Fanelli, M.: Geothermal energy: utilization and technology, Routledge (2013). https://doi.org/10.4324/9781315065786

DiPippo: Geothermal power plants—principles, applications, case studies and environmental impact, 4th edition, Butterworth-Heinemann (2015).

Heberle, F., Jahrfeld, T., and Brüggemann, D.: Thermodynamic analysis of double-stage organic Rankine cycles for low-enthalpy sources based on a case study for 5.5 Mwe Power Plant Kirchstockach (Germany), *In: Proceedings*, World Geothermal Congress 2015, Melbourne, Australia (2015).

Ministry of Energy and Mineral Resources: Huge Potential Untapped, 46 Geothermal Projects Ready to Run, accessed at Sep.11, (2021). https://ebtke.esdm.go.id/post/2020/03/27/2518/potensi.besar.belum.termanfaatkan.46.proyek.panas.bumi.siap.dijalankan

Stephanie Frick, Stefan Kranz, Gina Kupfermann, Ali Saadat, and Ernst Huenges: Making use of geothermal brine in Indonesia: binary demonstration power plant Lahendong/Pangolombian, *Geotherm Energy*, 7, 30, (2019). https://doi.org/10.1186/s40517-019-0147-29

Valdimarsson P.: Short course: Electricity Generation from Low Temperature Geothermal Resources, World Geothermal Congress, Melbourne, Australia vol. 5., (2015).

Zarrouk, S.J. and Moon, H.: Efficiency of geothermal power plants: A worldwide review, (2014). https://doi.org/10.1016/j.geothermics.2013.11.001

This page is intentionally left blank

Unit 2 and Unit 3 Interface Header Separation Optiramp Simulation

Agus Riyadi, Dian Katriya Hadi, Albert Lukman, Asfaari Raasyidah, and Tito Juliasmi

agus.riyadi@starenergy.co.id, dkfi@starenergy.co.id, alukman@optiramp.com, asfaarir@optiramp.com, tjuliasmi@optiramp.com

Keywords: Optiramp, Simulation, Interface, Separation

ABSTRACT

OptiRamp suite is a compilation of solutions, based on comprehensive statistical models, that simulates processes in real time. These solutions identify functional dependencies between various inputs, outputs, and losses in the process operations so that optimization applications may find opportunities for improvement. OptiRamp process model includes detailed and complex sub-models of all components specific to the user's operation. Sub-models (e.g., generator, turbines, piping, valves, feed pumps, cooling towers, condensers, generators, etc.) are then configured to represent complete enterprise. The model simulates mass and energy flow based on real-time process data and control variables to track all losses from the energy source to the final consumer.

As part of I-Field deliverable project, Optiramp has been successfully commissioned in 2012 (Chevron Geothermal and Power Operation Legacy) and continue to support DSC (Decision Support Center) for Operation of Star Energy Geothermal (Darajat and Salak field) to date.

Currently, Darajat Unit-2 and Unit-3 upstream Interface steam supply system is operating with common header mode since January 2015 due to insufficient steam supply from Unit-3 steam gathering production system. Darajat field had just finished to drill five make up wells for Unit-3 as per 2019/2020 Darajat Drilling Campaign program. Two additional production wells (DRJ-44 and 46) have been put online to system. In operating condition, DRJ-44 can produce steam around 20.7 kg/s, while DRJ-46 produce 3.5 kg/s. Objectives of this study is to conduct Optiramp simulation to support Darajat Asset Management Team (DAMT) program to perform split header program to get steam gain 42 kg/s from 1.1 upstream reducing upstream pressure.

Optiramp simulation shows that by changing Unit 2 and Unit 3 interface header operation from common to split header there will be a significant steam flow reduction for approximately 34 Kg/s from shutting off DRJ-22 and DRJ-23 wells. Unit 2 upstream pressure also benefits from the change by decreasing operating pressure for 1.92 barg.

1. INTRODUCTION

OptiRamp is a suite of solutions, based on comprehensive statistical models, that simulate processes in real time. These models identify functional dependencies between various inputs, outputs, and losses in the process operations so that optimization applications may find opportunities for improvement. OptiRamp process model includes detailed and complex sub-models of all components specific to the user's operation. Sub-models (e.g., generator, turbines, piping, valves, feed pumps, cooling towers, condensers, generators, etc.) are then configured to represent complete enterprise. The model simulates mass and energy flow based on real-time process data and control variables to track all losses from the energy source to the final consumer. As part of I-Field deliverable project, Optiramp has been successfully commissioned in 2012 (Chevron Geothermal and Power Operation Legacy) and continue to support DSC (Decision Support Center) for Operation of Star Energy Geothermal (Darajat and Salak field).

As a steam optimization program, Darajat Asset Management Team (DAMT) recommends splitting Unit-2 and Unit-3 from common header to dedicated header (split header) to reduce upstream pressure Unit-2 from 17.03 barg to 16.2 barg and Unit-3 at 17.3 barg (18.13 bara). By split Unit-2 and Unit-3 from common header to dedicated header operation, Unit-2 will get additional steam gain around 43 kg/s from decreasing header pressure 1.1 barg. This study is intended to conduct Optiramp Simulation before implementation for this Unit-2 and Unit-3 steam supply header separation.

2. DISCUSSION AND ANALYSIS

To provide a systematic approach to resolve the issue, we used below methodology during this study:

1. Collect data.
2. Determine assumption.
3. Determine base line of simulation.
4. Conduct simulation as per scenario (what-if).
5. Analyze Simulation result.
6. Conclusion and Recommendation.

2.1 Collect Data

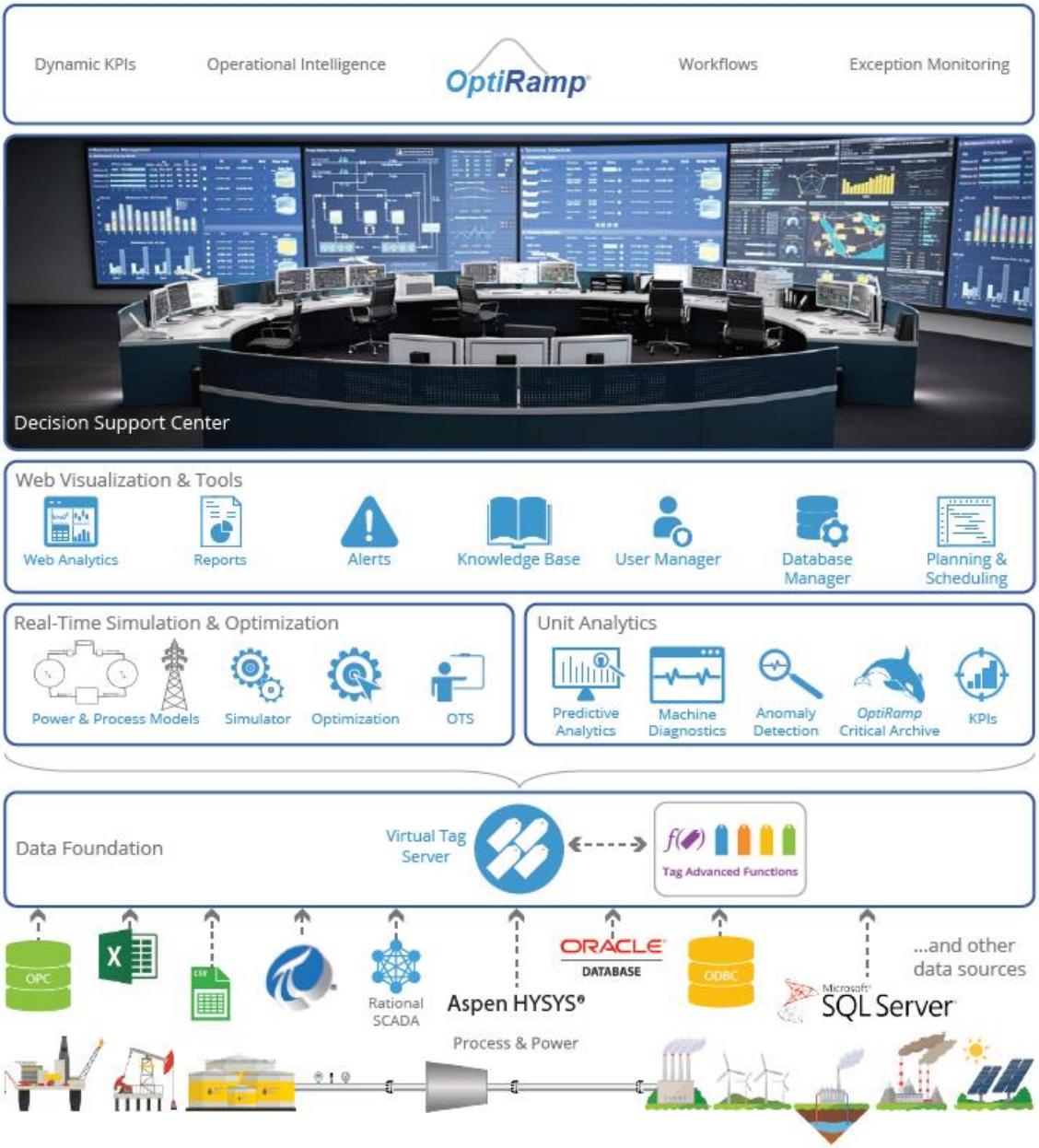

Figure 1: Data Collection Optiramp Overview.

OptiRamp software solutions focus on process and power real-time analytics to optimize operating assets and, in turn, reduce costs and increase reliability. Optiramp system data collection can be divided into five main components:

1. Data Foundation
    - The OptiRamp Virtual Tag Server (VTS) collects data from multiple sources—including Microsoft Excel, CSV files, Rational SCADA, Aspen HYSYS, Oracle databases, Microsoft SQL Server, and OSI PI—using standard OPC and ODBC protocols
    - OptiRamp Tag Advanced Functions (TAF) allows users to create advanced calculations that transform VTS tags and data into actionable key performance indicators (KPIs) and key operating parameters (KOPs)
    - OptiRamp VTS and TAF tags are used in the OptiRamp Simulator and Unit Analytics to simulate and optimize your operation as well as predict future conditions
    - These tags are also visualized in OptiRamp Web Analytics, Alerts, and Reports as various trends, charts, tables, text, and other analytical objects
2. Simulation and Optimization
    - Power and process models represent the total value stream, from producers to consumers
    - These models are used for real-time and offline simulation, auto-tuning, dynamic optimization, and the Operator Training Simulator (OTS)
    - Unit (machine) model are used for Unit Analytics

3. Unit Analytics
    - Unit models use unit data to simulate and auto-tune compressors and pumps and to build respective performance curves
    - Based on these curves and data, anomalies in unit performance are detected
    - Unit Analytics predictive analytics are displayed in OptiRamp Web Analytics, Alerts, and Reports as various trends, charts, tables, text, and other predictive analytics objects.
    - Alerts are generated when performance exceeds configured low and high limits
4. Web Visualization and Tools
    - Decision support is provided across the customer's network (intranet) through a series of interconnected web applications: OptiRamp Web Analytics, Alerts, Reports, Knowledge Base, Security Manager, Database Manager, and Planning and Scheduling
    - KPIs and KOPs are displayed in a manner that allows decisions about operations to be efficiently made
5. Decision Support Center
    - Collaborative workspace
    - Optimize workflows
    - Build and display enterprise KPIs

2.2 Study Assumption

Darajat Optiramp model was developed during project stage and being updated when there's steam facilities change such as developing wells, piping, and any others modification changes. This Darajat model was changed during additional well DRJ-44 development last year. Darajat Optiramp model shall be modified to accommodate additional DRJ-45 and DRJ-46 wells development with followings well properties.

Table 1: DRJ 45 and DRJ-46 Wells Properties.

Well	Height (m)	CWB	PI	WHP (barg)	Q (Kg/s)
DRJ-45	1126	1.17	1.691E-10	19.8	16.76
DRJ-46	1430	0.97	8.600E-12	18.89	3.63

Below are assumptions that we have made during Optiramp simulation

1. Manual data such as Throttle Valves (TV) that we used on this simulation are based on update data from Darajat field that updated on DOR (Daily Operation Report) 28-September-2020 while remaining data are optimized using VTS data points that linked to current real time historian operational data.
2. Scenario was saved from Optiramp scenario on 28 September 2020. Detail report can be found on attachment.
3. Interface PCV Opening was manually simulated as of opening from field reading based on historian data on 28-Sep-2020.
4. Governor opening was manually simulated as of opening from field reading based historian data on 28-Sep-2020.

2.3 Based Line Simulation

2.3.1 Unit 2

Interface Based line data Model- Interface

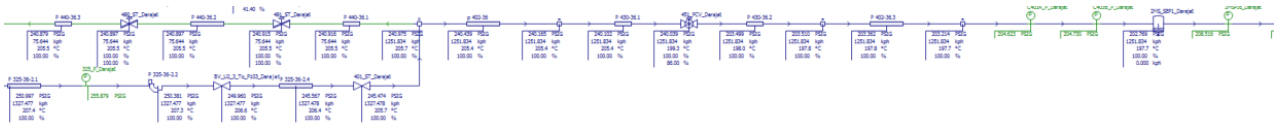

Figure 2: Unit 2 Optiramp Interface Model.

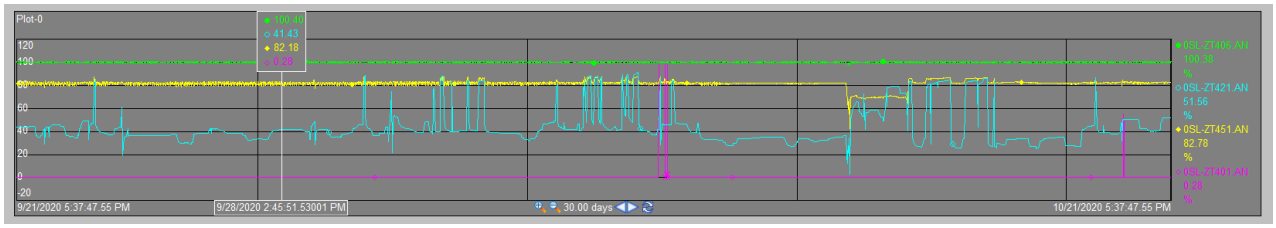

Figure 3: Unit 2 Interface Historian Data.

Optiramp based line data model used optimized Unit 2 model on 28-Sept-2020, the operation data can be found this below picture.

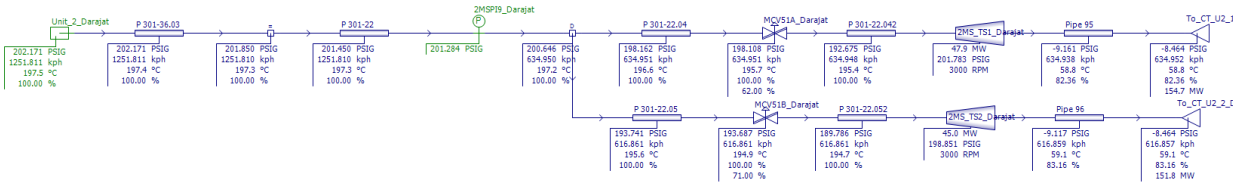

Figure 4: Based Line Data Model for Unit 2.

Table 2: Unit 2 Based Line Performance.

Parameter	Description	Value	Value (Conversion)
M_flow	Steam Flow	1251.810 KPH	157.51 Kg/S
MW	Power Output	92.9 MW	92.9 MW
P_chest	Turbine chest pressure	192.878 PSIG	13.12 BarG
T_inlet	Turbine inlet temperature	195.4 degC	195.4 degC
SQ	Steam quality	100 %	100 %
MCV_51A	Gov RH Opening	66.24%	66.24%
MCV_51B	Gov LH Opening	71.28%	71.28%
P_upstream	Upstream pressure	250.987 Psig	17.03 Barg
P_Interface	Interface pressure 403A	204.623 Psig	13.919 Barg
	Interface pressure 403B	204.730 Psig	13.927 Barg

2.3.2 Unit 3

Interface based line data model – Interface

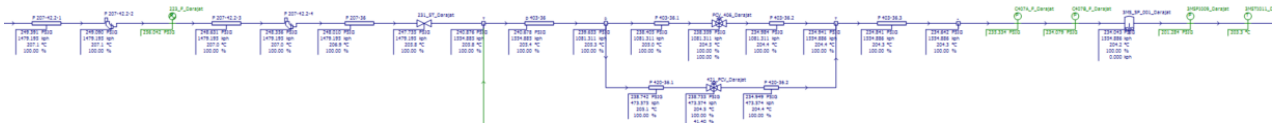

Figure 5: Unit 3 Interface Model.

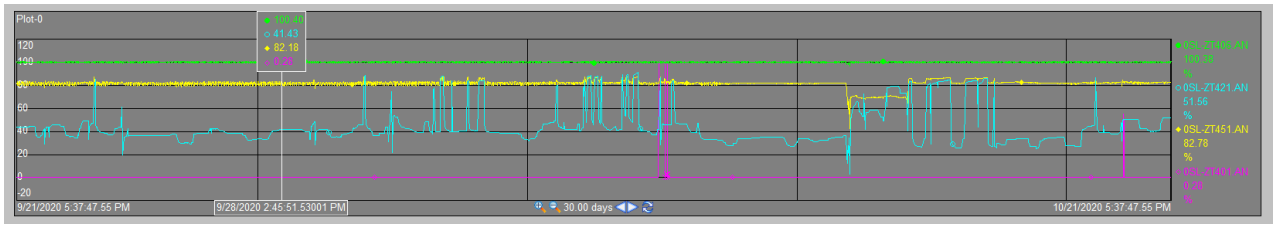

Figure 6: Unit 3 Interface historian Data.

Optiramp based line data model used optimized Unit 3 model on 28-Sept-2020, the operation data can be found this below picture.

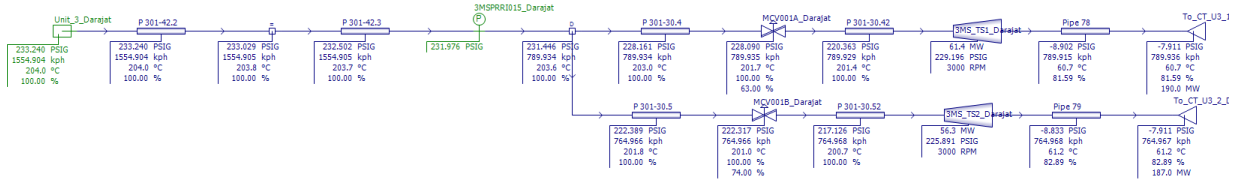

Figure 7: Based line data Model for Unit 3.

Table 3: Unit 3 Based Line Performance.

Parameter	Description	Value	Value (Conversion)
M_flow	Steam Flow	1556.547 KPH	196.12 Kg/S
MW	Power Output	117.6 MW	117.6 MW
P_chest	Turbine chest pressure	220.048 PSIG	14.96 BarG
T_inlet	Turbine inlet temperature	201.7 degC	201.7 degC
SQ	Steam quality	100 %	100 %
MCV_001A	Gov RH Opening	61.84%	61.84%
MCV_001B	Gov LH Opening	73.84%	73.84%
P_upstream	Upstream pressure	249.381 Psig	16.96 Barg
P_Interface	Interface pressure 407A	235.334 Psig	16.009 Barg
	Interface pressure 407B	234.079 Psig	15.923 Barg

From the above data based line vs actual condition is almost same. From this point we can make simulation for splitting interface header between Unit 2 and Unit 3.

2.4 Optiramp Process Simulation

2.4.1 Unit 2 Optiramp Initialization

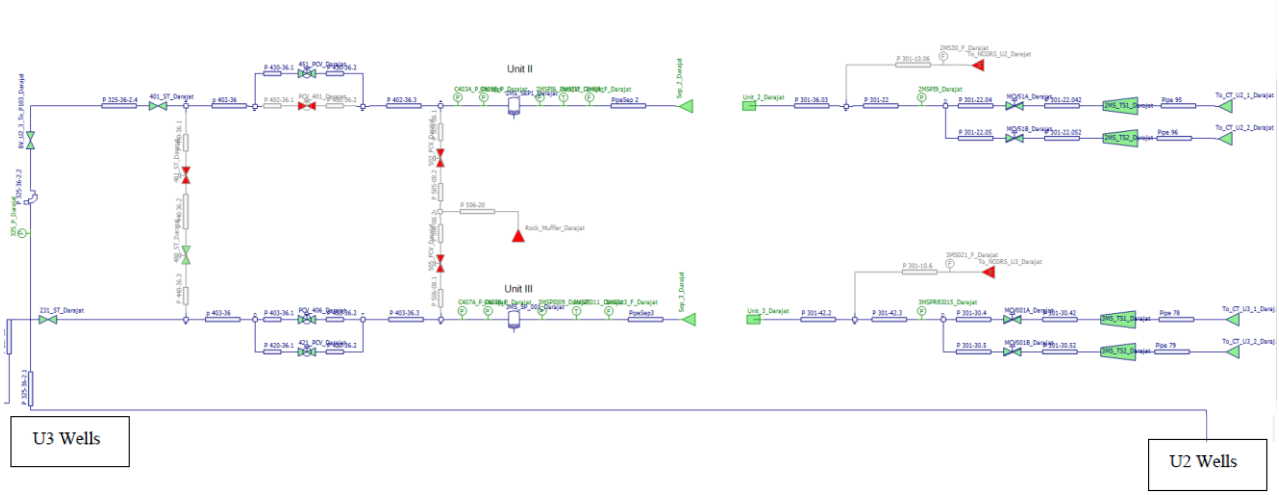

Figure 8: Optiramp Process Model During Initialization.

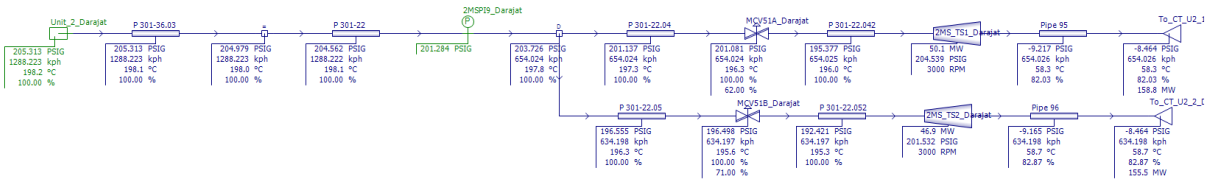

Figure 9: Unit 2 Model After initialization.

Table 4: Unit 2 Optiramp data during initialization U2 and U3 interface header separation.

Parameter	Description	Value	Value (Conversion)
M_flow	Steam Flow	1288.227 KPH	163.07 Kg/S
MW	Power Output	97.0 MW	97.0 MW
P_chest	Turbine chest pressure	196.0 PSIG	13.35 BarG
T_inlet	Turbine inlet temperature	196.3 degC	196.3 degC
SQ	Steam quality	100 %	100 %
MCV_51A	Gov RH Opening	66.24%	66.24%
MCV_51B	Gov LH Opening	71.28%	71.28%
P_upstream	Upstream pressure	255.875 Psig	17.4 Barg
P_Interface	Interface pressure 403A	204.273 Psig	13.893 Barg
	Interface pressure 403B	204.730 Psig	13.927 Barg

2.4.2 Unit 3 Optiramp Initialization

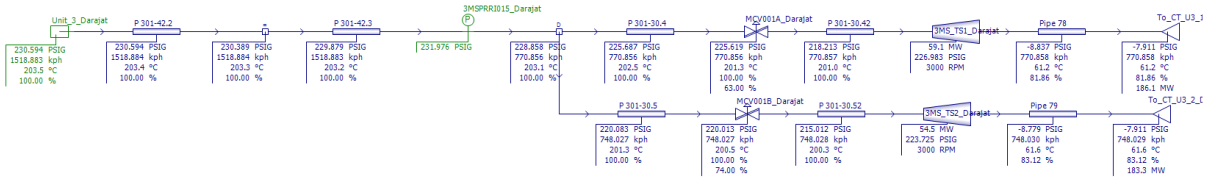

Figure 10: Unit 3 Model After initialization.

Table 5: Unit 3 Optiramp data during initialization U2 and U3 interface header separation.

Parameter	Description	Value	Value (Conversion)
M_flow	Steam Flow	1518.883 KPH	192.264 Kg/S
MW	Power Output	113.6 MW	113.6 MW
P_chest	Turbine chest pressure	218.213 PSIG	14.84 BarG
T_inlet	Turbine inlet temperature	201.3 degC	201.7 degC
SQ	Steam quality	100 %	100 %
MCV_001A	Gov RH Opening	61.84%	61.84%
MCV_001B	Gov LH Opening	73.84%	73.84%
P_upstream	Upstream pressure	246.683 Psig	16.781 Barg
P_Interface	Interface pressure 407A	232.334 Psig	15.805 Barg
	Interface pressure 407B	231.079 Psig	15.719 Barg

2.4.3 Unit 2 Separation After Shutoff DRJ-22 and DRJ-23

Table 6: Unit 2 Optiramp Simulation Result.

Parameter	Description	Value	Value (Conversion)
M_flow	Steam Flow	1246.245 KPH	157.752 Kg/S
MW	Power Output	92.3 MW	92.3 MW
P_chest	Turbine chest pressure	192.247 PSIG	13.07 BarG
T_inlet	Turbine inlet temperature	195.3 degC	195.3 degC
SQ	Steam quality	100 %	100 %
MCV_51A	Gov RH Opening	62.00%	62.00%
MCV_51B	Gov LH Opening	71.00%	71.00%
P_upstream	Upstream pressure	227.518 Psig	15.477 Barg
P_Interface	Interface pressure 403A	202.711 Psig	13.789 Barg
	Interface pressure 403B	202.858 Psig	13.799 Barg

Analysis

Table 6 above simulation result of Unit 2 performance after Unit 2 and Unit 3 interface header separation and shutoff DRJ-22 and DRJ-23 as RM optimization program. Unit 2 generation 92.3 MW and steam mass flow 157.752 Kg/s resulted from Optiramp model are still within operation limit. Both PCV-451 (Lead) and PCV-401 (follower) was operated in 100 % and 45 % to achieve this TOP generation target. LH and RH governors are operated on 62 % and 71 % which is still in good operation performance.

Full load simulation was performed by increasing LH and RH governor valve and PCV follower opening to full load target for 95 MW. This full load setting was finally achieved but Unit 2 was required to be operated in 95 % operation parameter such as PCVlead that was operated in 85 % and both LH and RH governor in 95 %. This is not a recommended operating envelope for PCV and governor valve. PCV delta pressure was observed in 0.571 barg during this full load simulation.

2.4.4 Unit 3 after separation and activate DRJ-45 and DRJ-46

Table 7: Unit 3 Optiramp simulation result.

Parameter	Description	Value	Value (Conversion)
M_flow	Steam Flow	1546.127 KPH	195.712 Kg/S
MW	Power Output	116.7 MW	116.7 MW
P_chest	Turbine chest pressure	219.861 PSIG	14.84 BarG
T_inlet	Turbine inlet temperature	201.3 degC	201.7 degC
SQ	Steam quality	100 %	100 %
MCV_001A	Gov RH Opening	61.84%	61.84%
MCV_001B	Gov LH Opening	73.84%	73.84%
P_upstream	Upstream pressure	249.131 Psig	16.9 Barg
P_Interface	Interface pressure 407A	234.002 Psig	15.918 Barg
	Interface pressure 407B	234.119 Psig	15.926 Barg

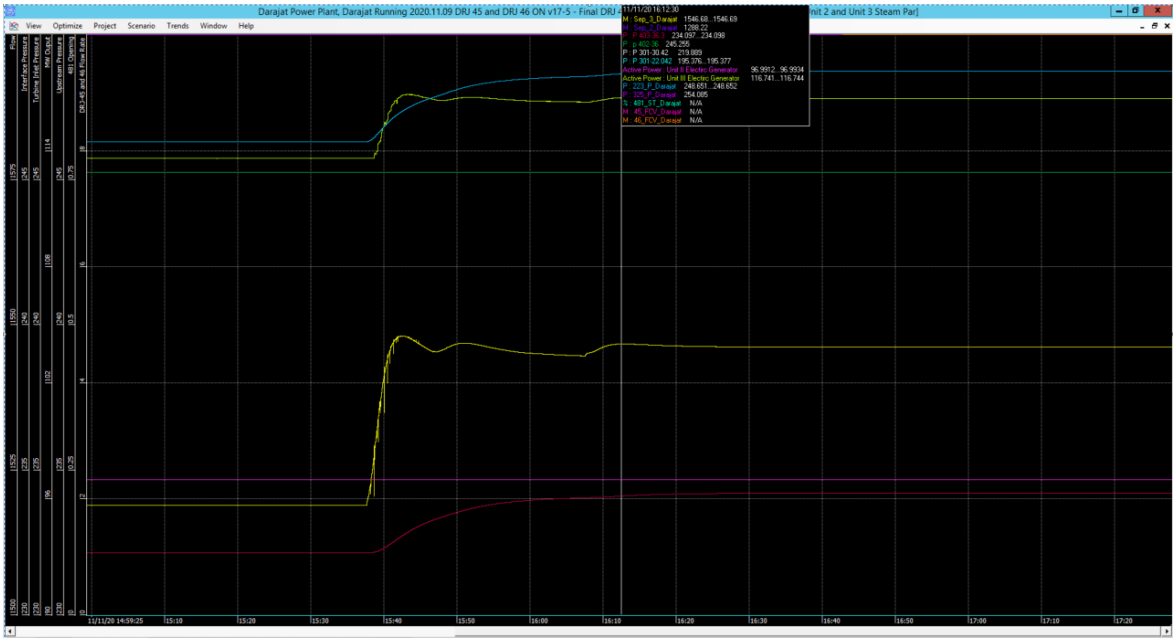

Figure 11: Transient Data Online DRJ-45 and DRJ-46.

Analysis

Simulation of Unit 3 Unit performance for Unit 2 and Unit 3 interface header separation initiated by activating DRJ-45 and DRJ-46 by and resulted flow rate 8 Kg/s for DRJ-45 and 1.45 Kg/s for DRJ-46 (Figure 11). Optiramp simulation result for activating DRJ-45 and DRJ-46 during Unit 2 and Unit 3 interface header separation can be seen on above Table 7. Steam mass flow (M_flow) 195.712 Kg/s and MW output 116.7 MW are observed slightly below TOP (Take or Pay) generation target (117.2 MW). This condition is caused by manual simulation of LH and RH governor still same governor opening with based line data (GV-LH = 61.84% and GV-RH = 73.84 %). The governor opening then need to be simulated manually to determine generation MW output as per previous scenario (TOP and Full load condition).

The LH and RH opening are incremented in simulation to achieve TOP (Take or Pay) target 117.2 MW During manual opening of both LH to 75 % and RH to 70%. During this condition Unit 3 generation to 117.43 MW. PCV lead and follower are in 100 % and 41.4 % opening during condition.

Utilizing the same method with TOP simulation above, full load target 121 MW simulation is performed by increasing LH and RH opening and increasing PCV follower opening. Based on simulation full target simulation could not be achieved even when LH and RH governor opening are set to 100 % and PCV-Follower are set to 75% while PCV-Lead is set to 100%.

3. CONCLUSION

Based on Optiramp simulation for Unit 2 and Unit 3 interface header separation, it is concluded that:

1. By Shutting off DRJ-22 and DRJ-23, Unit 2 is able to generate to TOP (92.3 MW) with all parameters in normal condition and PCV need to be operated in Lead- follower mode with opening 100 % for leader valve and 45 % for follower.
2. By putting online DRJ-45 and DRJ-46, Unit 3 is able to generate to TOP (117.2 MW) with all parameters in normal condition and PCV need to be operated in Lead- follower mode with opening 100 % for leader valve and 41 % for follower.
3. For Unit 2, Full load (95 MW) simulation can be achieved but some critical parameters such as governors opening (GVs) and PCV are operated on higher limit, and this is not recommended since system having bad controllability especially during abnormal condition.
4. For Unit 3, Full load (121 MW) simulation cannot be achieved even when some critical parameters such as governors opening (GVs) and PCV are set in maximum condition.
5. Based on Optiramp simulation of Unit 2, upstream pressure was significant reduced from 17.4 barg to 15.48 barg. There was a 1.92 barg reduction of interface pressure that can be achieved.
6. Based on this simulation, there was a 34 kg/s flow reduction by shutting off DRJ-22 and DRJ 23.

4. RECOMMENDATION

Recommendations for Optiramp simulation for Unit 2 and Unit 3 interface header separation are followings:

1. It is recommended to increase steam buffer for Unit 2 especially during full load condition.
2. It is recommended to increase steam buffer for Unit 3 especially during full load condition due to full load generation could not be achieved using the current steam buffer.

REFERENCES

Bela G. Liptak: Instrument Engineers' Handbook: Process Control 3rd Edition, CRC Press (1999).

Statistic and Control, Inc.: Introducing to Optiramp Student Guide, S&C Press (2018)

This page is intentionally left blank

Grounding and Lightning Protection Issues and Solutions in Darajat Geothermal Power Plant

Nixon Manik[1], Muhammad Ichsan[1], Agustiawan[1], Achmad Arbi[2], and Muhamad Reyhan Savero[3]

[1]Star Energy Geothermal
[2]PT Tesla Daya Elektrika (PT TDE)
[3]Universitas Indonesia

Nixon.manik@starenergy.co.id, m.ichsan@starenergy.co.id, eops@starenergy.co.id,
Arbi@tde.co.id, muhamad.reyhan92@ui.ac.id

Keywords: lightning protection system, electromagnetic compatibility, grounding, geothermal

ABSTRACT

Star Energy Geothermal Darajat II, Ltd. (SEGD) is one of geothermal operating company in Indonesia which operate in the geothermal area at Darajat – Garut. Darajat located on 1473 m average above sea level, about 70-hectare area. Darajat is located near equatorial belt and in the largest tropical archipelago of the world, where lightning activities is high. So that every installation, human resource, and facility in Darajat have a high risk for lightning damages

Lightning is a common problem that occurs in any plant or installation, especially in tropical countries. However, in operating a geothermal plant, the lightning problem can be even worse. Since the first start up in 2007, DRJ Unit III was experiencing 7 times trip after OSL-PCV-406 shut-off when there were heavy lightning strikes. It was also recorded that PCV-401 has the same experience once in Dec 2007. RCA of these incidents led to failure of the spheres Early Streamer's Lightning Protection system installed in Unit II and Unit III which provides the umbrella for the PCV area and the grounding system. Based on investigation of the PCV failure incident, presented the investigation result and came out with a report that PCV repetitive incidents is mainly caused by the additional current flowing through the pair cable of the instruments. The existence of induction charge in this pair cable could be caused by the closed loop current in the shield cable and/or excessive current flows in the armor cable. Excessive current flowing in armor cable followed by a closed loop current shield wire is generated by improper grounding system. The use of isolated grounding cable (yellow green cable) connecting each driven rod grounding, structure, piping, and all metal parts, causes induction of the electrostatic charge on the metal part installed in the plant (pipes, metal structures, etc.) do not straight away flow into the earth but flow among the metal parts, as well as to armor cable and closed loop current shield wire.

Short term solution has reduced the number of incidents from 6 times become 3 times but not adequate yet to totally protect the PCV's from lightning strikes. Long term solution needs to be executed to totally improve DRJ LPS, after improvement the grounding and lightning protection system, no more plant trip failure in DCS remote panel caused by lightning protection until now

1. INTRODUCTION

Lightning is a common problem that occurs in any plant or installation, especially in tropical countries. However, in operating a geothermal plant, the lightning problem can be even worse.

Based on the Lightning Density Mapping System in Indonesia, captured since 2018 until 2020, the lightning density in West Java Province averages 9.51 strikes/ km^2 per year. However, in mountainous and highland areas, where most geothermal plants are located such as Salak, Darajat, Wayang Windu, and Kamojang, the lightning density is much higher at 47.52 strikes/km2/year. Similar phenomena were also found in the Provinces of Banten and Central Java, where lightning density increased significantly in mountainous and highland areas.

Since the beginning of the operation in 2007, DRJ III Darajat Geothermal Power Plant Center – Garut has experienced 13 (thirteen) power plant trips due to 0SL-PCV-406 (Pressure Control Valve) shutoff when a lightning strike occurred. The impact of the events lead to great losses in power production and these events is frequently occurring between the year 2009 to 2010.

Based on the RCA (Root Cause Analysis) conducted by the engineers of Darajat Geothermal, the lightning protection failure leads to the failure of lightning protection tower (monopole) installed in Unit II and Unit III, which are supposed to provide protection for the PCV area and the grounding system. A comprehensive assessment of the external and internal lightning protection system especially on the PCV plant had been done and can be concluded that the main reason of PCV plant shutdown is due to an induced current flowing through the instrumentation cable. Several milliamps of induced current in instrumentation cable pair are able to cause an interference with the measuring system and lead to a misreading that triggered a plant trip.

Based on data collected since 2000, contribution of Grounding and lightning protection issues to overall Disturbances that cause power plant non availability (derating or unit trip) was 19 out 202 equals to 9%.

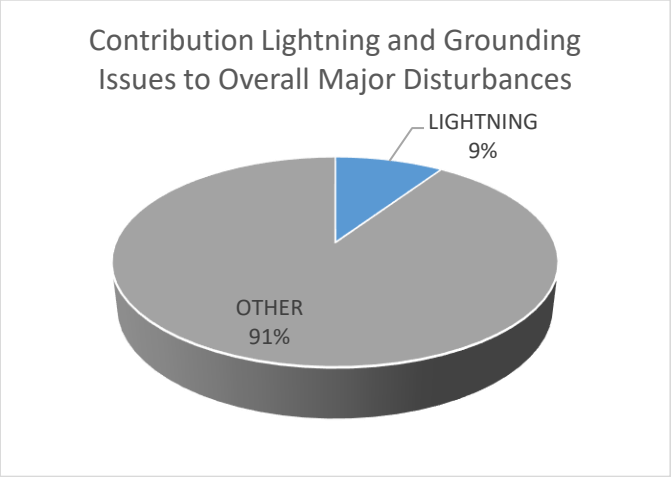

Figure 2: Contribution Lightning and Grounding Issues to Overall Major Disturbances.

Table 1: Record of Plant trip and derating due to lightning strike in Darajat Geothermal.

No	Date	Unit	Trip Causes	Remaks
1	05-Dec-07	Unit-III	PCV-406 fail (close) due to Lightning nuissance	Generator and Turbine Tripped due to PCV-406 fail/closed suddenly by
2	06-Nov-08	Unit-III	0SL-PCV 406 failure by Lightening	Turbine trip by failure of 0SL-PCV 406 due to lightening
3	27-Dec-09	Unit-III	0SL-PCV 406 failure by Lightning	Loss off steam supply caused by 0SL-PCV406 upset due to lightning (0SL-
4	25-Mar-09	Unit-II	External problem, grid line problem by lightning	109.97 MW Gross / Turbine Trip (Black out), due to grid line problem by
5	23-Apr-09	Unit-III	0SL-PCV 406 failure by Lightening	0SL-PCV406 closed due to lightening
6	08-Dec-09	Unit-III	0SL-PCV 406 failure by Lightening	Loss off steam supply caused by 0SL-PCV406 upset due to lightning
7	27-Dec-09	Unit-II	0SL-PCV401 close suddently (fail) caused by lightning	Turbine trip due to 0SL-PCV401 fail and close suddently caused by
8	27-Jan-10	Unit-III	PCV 406 Fail to Close due to lightening strike	PCV 406 fail to close by lightning strike
9	05-Feb-10	Unit III	PCV 406 Fail to Close due to lightening strike	114.5 MW Gross/ PCV 406 fail to close by lightning strike
10	09-Feb-10	Unit-III	PCV 406 Fail to Close due to lightening strike	PCV 406 fail to close by lightning strike
11	10-Feb-10	Unit-III	PCV 406 Fail to Close due to lightening strike	118 MW Gross/PCV 406 fail to close by lightning strike
12	12-Feb-10	Unit-III	PCV 406 Fail to Close due to lightening strike	PCV 406 fail to close by lightning strike and also 0SL PCV 502 & 505 fail
13	16-Oct-10	Unit-II	Trip by Push Button due to 0SL-PCV 401 fail by lightening	0SL-PCV 401 failed due to lightening
14	11-Mar-11	Unit-III	Tripped due to 0SL-PCV-406 failed and closed caused by lightning	0SL-PCV 406 failed and closed due to lightning
15	27-Mar-11	Unit-III	Tripped due to 0SL-PCV-406 failed and closed caused by lightning	0SL-PCV 406 failed and closed due to lightning
16	27-Apr-11	Unit-III	PCV-406 suddenly cloced due to lightning strike	PCV-406 suddenly closed due to lightning strike
17	19-Jan-12	Unit-II	Lighting strike	0SL-PCV 401 fail close due to lightning strike

2. EMC BASED LIGHTNING PROTECTION SYSTEM

Electromagnetic compatibility or EMC for short can be defined as the ability of a device, equipment, or system to operate in its electromagnetic environment without inducing unendurable electromagnetic disturbance to the surrounding environment. Mitigation of electromagnetic interference is crucial and by utilizing the theory of EMC the mitigation can be applied based on the EMC disturbance model.

In principle, electromagnetic compatibility measures for electronic apparatus in instrumentation and control system have the following objectives: Internal immunity (SE), External immunity (SF) complying to electromagnetic requirement and cost constraint, and Disturbance emission level (E), not more than allowable emission.

EMC mechanism involves source, coupling path and victim (sink). Source and victim could be electronic apparatus (see Figure 2) Other type of sources could be nature phenomena, e.g., lightning, electrostatic discharge. Coupling mechanism can occur via wire or field. Galvanic/conductive coupling occurs via wire. Capacitive and inductive coupling arise via capacitive field if electric field E and magnetic field H is dominant, respectively. Radiative coupling occurs via electromagnetic field.

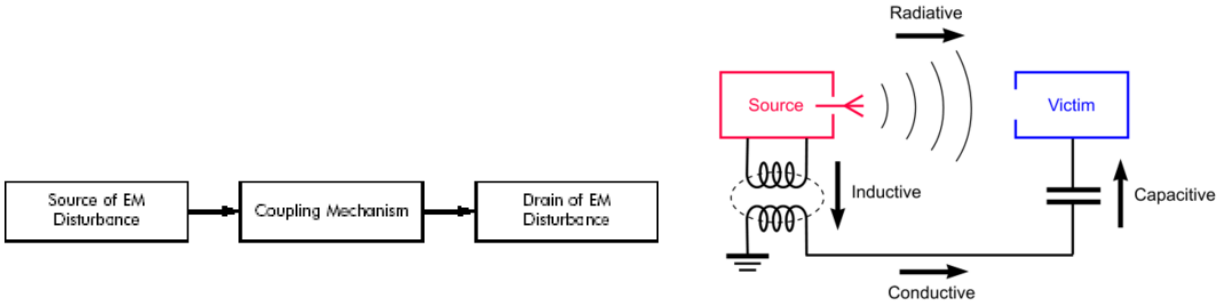

(a) **(b)**

Figure 2: (a) Model of EMC Mechanism (b) Types of Coupling Mechanism.

2.1 Equipotential Bonding Network

The main function of the equipotential bonding network is to prevent hazardous potential drops between all devices/installations inside the LPZs, and to reduce the magnetic field of the lightning. The low inductance equipotential bonding network required is achieved by means of interconnections between all metal components aided by equipotential bonding conductors inside the LPZ of structure.

Enclosures and racks of electronic devices and systems should be integrated into the equipotential bonding with short connections. Protective conductors (PE) and cable shields of the instrumentation lines and data links of electronic devices and systems must be integrated into the equipotential bonding network. The connection in the shape of a star.

Using a star point arrangement S, all metal components of the electronic system must be suitably insulated against the equipotential bonding network. A star shaped arrangement is limited to application in small, locally confined system like in the PCV container room. In this case, all lines must enter the container room at a single point. The star point arrangement S must be connected to the equipotential bonding network at one single earthing reference point (ERP) only. Using spark gap arrester to realize equipotential bonding between PE (protective earth) and IE (instrumentation earth) during overvoltage lightning impulse entering control room.

2.2 Surge Protection

The surge protective device (SPD) required to eliminate surge effect and prevent damage to electrical/ electronic equipment inside the building/structure. It is considered to be a cost-effective approach to mitigate downtime, system and data reliability improvement, and equipment damage prevention due to voltage transients and surges. According to IEC 611634 SPD is classified to several type according to their capabilities and purpose to protect low voltage power supply AC/DC, instrumentation, telecommunication, and information technology (IT) devices.

2.3 Cable Shielding

Cable shields are used to reduce the effect of the electromagnetic interference on the instrumentation active lines, and the electromagnetic interference emitted from active lines to the surrounding systems. From the point of view of lightning and surge protection, attention must be paid to the application of shielded lines. Not only protecting system devices, but cable shielding is also used to increase personnel safety.

2.3 Earthing

Earth electrode is a conductive component or several conductive components in electrical contact with the earth which serves as a discharge line for the fault current to pass through the ground. Earthing systems are a crucial system that is used to protect personnel and electrical system from harm and damage. The earthing system consists of a Surface Earth Electrode, a Driven Earth Rod, and a Natural Earth Electrode.

3. EXISTING LPS IN DARAJAT GEOTHERMAL

3.1 External Lightning Protection

3.1.1 Lightning Protection Mast (Air Terminal)

The picture below shows external lightning protection with an ESE (Early Streamer Emission) air terminal installed in the PCV area. ESE is an unconventional air terminal which was commercially introduced and traded in the world market around 1970. Also known as a lightning attracting air terminal which is claimed to be able to attract lightning strikes with a radius that is farther than conventional lightning rods so that lightning does not strike buildings that are thereby protecting the equipment inside the building. The initial attracting system was in the form of a radioactive air terminal in the 1970s, and then due to much opposition to the use of radioactive, an Early Streamer Emission (ESE) air terminal was introduced in the late 1980s.

(a) **(b)** **(c)**

Figure 3: Lightning protection mast installed in Darajat Geothermal: (a) PCV Area (b) Control Building (c) detail Early Streamer Emission.

Installation of an Air Terminal of the ESE Early Streamer Emission type Dynasphere is the installation of an external lightning protection system that is not based on International Standards (IEC), National (SNI) or National Standards of other countries such as VDE (Germany) or BS (UK). In fact, these inventors from Unconventional Air Terminals (ESE) have never shown their scientific basis for theory. There have never been any published “scientific papers” that have been verified by the independent scientific community. So, to this day the use of these tools is still a controversy among lightning protection experts.

Therefore, it is considered that the ESE Air Terminal works like an ordinary Franklin Air Terminal with a protected corner of the protected area. So that it is still possible for a direct strike to occur on the roof of the building or other objects. Which if the lightning current is not properly channeled to the grounding terminal, an uncontrolled Lightning Ball will occur which is very dangerous for personnel and equipment. Besides that, a lightning strike that hits the air terminal will induce a high electromagnetic field that can interfere with the instrumentation cable, causing misreading and can cause a power plant trip.

3.1.2 Grounding System (Earthing)

Based on the recommendation "Salak and Darajat Steam field Electrical Design Criteria ZP00444-CRT-EL-001" it is stated that for every 200-meter length of pipeline, starting from the outer fence of the power plant, the pipeline is solidly bonded to the ground. Each pipe entering the power plant is bonded to the power plant earthing grid. The earthing grid conductors are planted in the soil to a depth of not more than 60 cm. The recommendation for installing an earthing pipeline every 200 meters has yet to be confirmed, as well as earthing pipes entering the power plant which are connected to the power plant earthing grid.

A surface earth electrode is a grounding electrode that is planted in the ground at a depth of 50 cm to 1 meter. The material used is a round conductor or plate, with a star-type design, ring or meshed earth electrode or a combination thereof., thereby violating its function as a grounding electrode. Lightning currents, both electrostatic induction in the steam pipeline, lightning strike currents at the finials, most of the lightning currents do not go directly to the ground, but flow in the metal construction of the power plant, including flowing in the instrumentation cables.

(a) **(b)** **(c)**

Figure 4: (a) Pipeline (b) surface earth electrode using (c) insulated cable.

With the improper connection of the steam pipeline grounding, which should be grounded every 200 meters of the pipe, and due to the incorrect grounding of the PCV plant area grounding system, the electrostatic induced cloud charge on the steam pipeline and in all parts of the metal construction of the plant, flows mostly to the metal structure and flow on instrumentation cables. The flow of electrostatic induced charges and lightning currents on the instrumentation cable, due to the closed loop current on the cable shield, interference of several milli Amps in the instrumentation cable pair, will have a major effect on the measurement system which can cause "misreading" which triggers a plant trip.

3.2 Internal Lightning Protection

Internal protection in the PCV panels has been installed since the initial construction stage. SPD for LV Network is available, as well as for instrumentation lines. Grounding system messed up between power and instrumentation. TEC (Transient Earth Clamp) is also available although it is not installed properly.

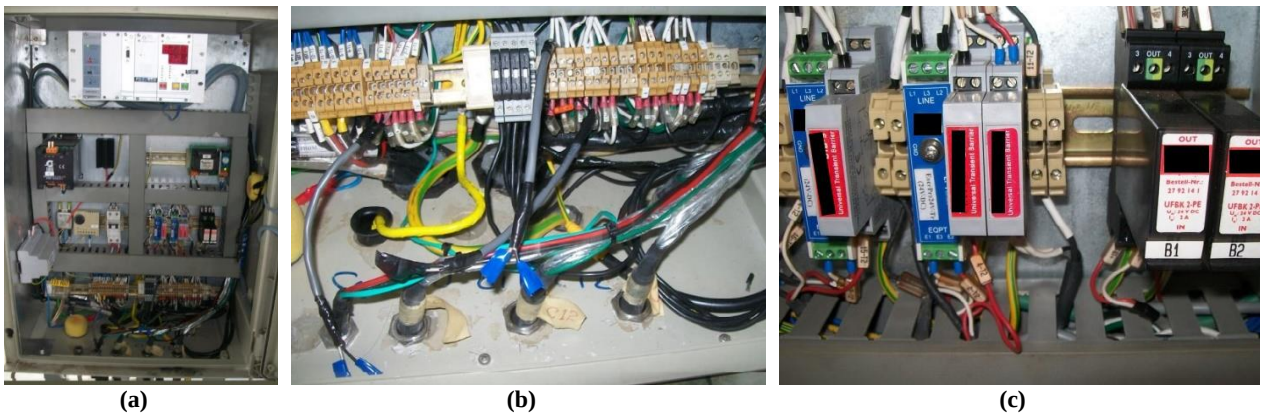

(a) **(b)** **(c)**

Figure 5: (a) Existing internal LPS of PCV Panel (a) Shield wire of instrument cable (c) Surge Protective Device.

The shutdown incident in the PCV is an additional current flowing in the instrument pair cable so that the reading is excessive and causes a trip. The presence of charge induction on the instrument pair cable can be caused by a closed loop current in the shield cable and or an excess current flow in the cable armor. The installed arrester should be of the cascade arrester type with the inductor element as a coupling and have a response time of the order of ns on the suppressed diode and varistor.

Excessive current flowing in the armor cable is accompanied by a closed loop current shield wire, due to an improper grounding system. The use of isolated grounding cable (green-yellow color) that connects each driven rod grounding, structure, pipe and all metal parts in the plant, causes electrostatic induced charges on metal parts in the plant (pipes, metal structures, etc.) not to flow

immediately to earth. however, flows between metal parts in the plant include flowing in cable armor and in closed loop current shield wire.

4. IMPROVEMENT LPS ON PCV DARAJAT GEOTHERMAL AND RESULTS

Improvements have been carried out in several internal stages starting from the end of 2011 until 2013. Improvements covering the areas of PCV 406 (Unit-III), PCV 505 (Unit III), PCV 401 (Unit II), and PCV 502 (Unit II) were carried out gradually because it must adjust to the available shut down plan schedule. Some of the improvements made are described in the subsection below.

4.1 Skin Effect Grounding Installation for Pipeline

The partial lightning currents from the striking point must be through easiest way flow directly to earth without having any damage. The “skin effect grounding”, provided to connect the metal structure with the grounding system, is an effective way to distribute lightning current to earth. Made from thin metal plate with wide dimension compared to the circumference of regular grounding cable, maximized the current flow of high frequency lightning current due to skin effect phenomenon.

4.2 Ring Grounding Installation for PCV Shelter

In order to improve discharging capability of existing meshed grounding, an additional bare conductor ring earthing must be installed encircling PCV area. Purpose of the ring grounding is to capture stray current in the earth from outside PCV due to lightning strike or other fault current. It also serves as equipotential bonding network for protective earth.

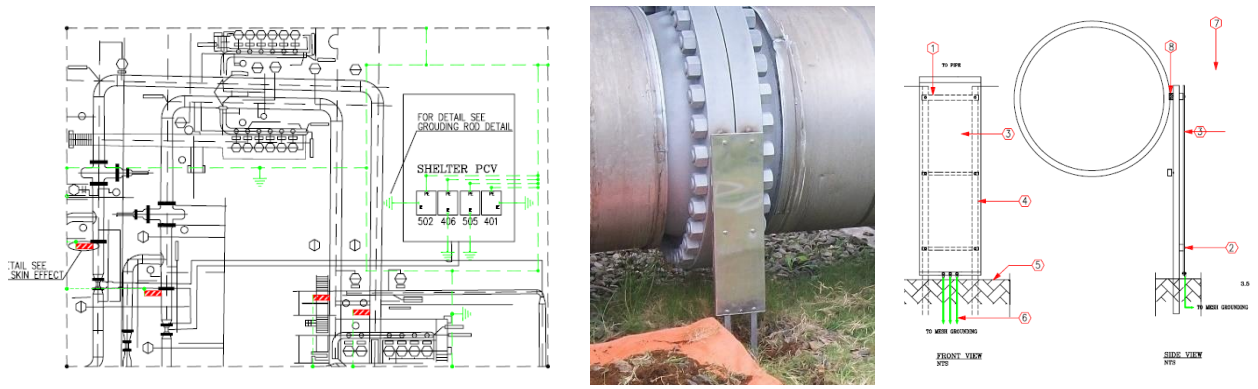

(a) **(b)** **(c)**

Figure 6: (a) Layout PCV shelter with ring grounding and skin effect grounding (b) Skin effect grounding installed (c) detail construction skin effect grounding.

4.3 Internal Grounding Refurbishment and Reroute Instrumentation Shielding Wire

To reduce the interference of charge induction into the instrumentation line, the grounding system in the PCV was reconfigured. Grounding system, which was originally mixed in one bar, is now separated by providing PE (Protective Earth) and IE (Instrument Earth) bars which are isolated from the body panel (see Figure 7). PE bar for grounding of power supply, electronic equipment, and surge arrester. Meanwhile, the IE bar for grounding of shield wire of instrument cables, so it will not be affected by voltage fluctuations that occur in the power system.

Spark gap arrester or transient earth clamp installed between PE and IE bar to prevent dangerous spark due to high potential difference between those bars due to lightning strike. To prevent induced current from junction box in the field to PCV panel, at the ends of the cable in the junction box, the shields are indirectly connected to the earth potential via isolating spark gaps. When EMC interferences such as lightning strikes occur, the isolating spark gap ignites and discharge the interference pulse without consequential damage to the equipment.

4.4 SPD Installation for LV Power Network and Instrumentation Line

To protect the AC electrical power supply of instrumentation control system from lightning impulse overvoltage, a Surge Protective Device for 380 VAC 3 phase install at the entrance of instrumentation panel. The SPD for 24 V DC also installed to protect DC Power Supply system to protect the instrumentation and measuring system of DRJ 3 plant, a Surge Protection Device, Blitzductor with 24V DC voltage is installed on the instrumentation line. Cable armors are directly connected with the PE (Potential Earth) and cable shielding (inner shielding) are directly connected with the instrumentation earthing (IE) at a central point in the control room. Arrester DEHN BXT ML 2 BD 24 install in the measuring junction box which cable shields are earthed at only one end in the control room.

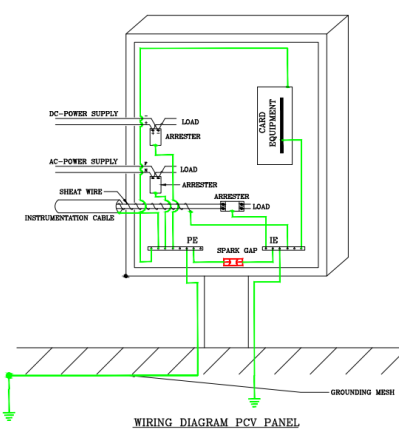

(a)

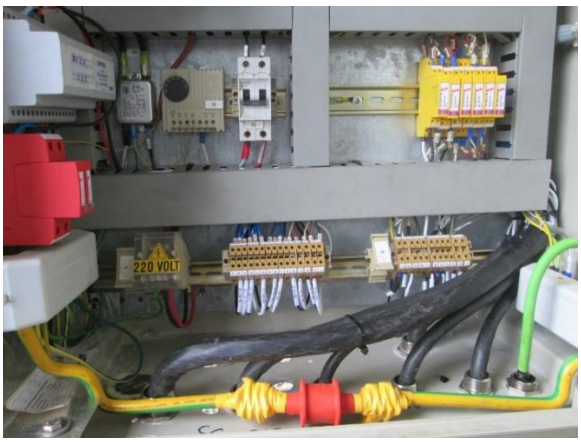

(b)

Figure 7: (a) Design internal protection PCV Panel (b) installation in PCV Panel.

4.5 Improvement Results

After the repairs were completely done, the number of disturbances caused by lightning decreased drastically. From the previous one, it could reach 6 disturbances per year, after the implementation of the improvement, the PCV plants have not found any disturbances until now. The disturbances that occurred in 2018 and 2021 are exceptions because they occur in other areas that have not applied similar methods.

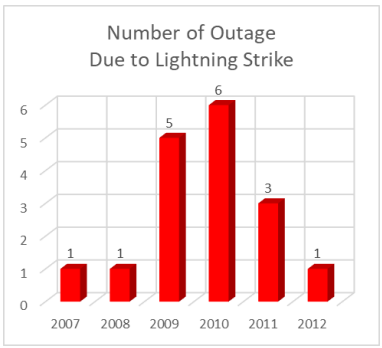

(a)

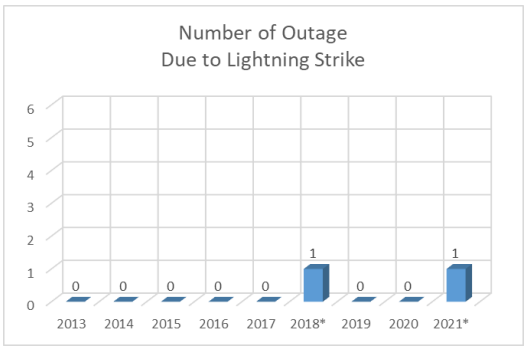

(b)

Figure 8: Number of outage due to lightning (a) before improvement (b) after improvement.

The data above shows that the improvements that have been made have a significant impact on reducing disturbances caused by lightning. To increase confidence, further studies can be carried out by comparing the lightning density data in the Darajat Geothermal area. Although it is quite safe from lightning strikes, maintenance activities need to be carried out periodically to ensure that the installed installation remains in good condition and functioning. Maintenance includes checking bonding connections, measuring grounding resistance, and testing arresters.

REFERENCES

Badan Standardisasi Nasional: Proteksi Terhadap Impuls Elektromagnetik Petir, Bagian 1: Prinsip Umum, (2002).

Dehn+Sohne: Lightning Protection Guide, Neumarkt Germany (2007).

Gadermaier: EMV fuer Planer und Betreiber elektrotechnischer und elektronischer Anlagen. Carl Hanser Verlag, Muenchen Wien (1997).

IEC 62305-3 – Protection Against Lightning: Physical damage to structures and life hazard, (2002).

IEC 62305-4 – Protection Against Lightning: Electrical and electronic systems with structures, (2002).

Kopecky, V.: EMV, Blitz- und Ueberspannungsschutz von A-Z, Huetig & Pflaum Verlag, Muenchen/Heidelberg/Berlin (2001).

PLN Puslitbang: Pengenalan Sistem Deteksi Petir PLN dan Pemanfaatan Data Petir, Webinar, (2021).Trommer, W. and Hampe, E-A.: Blitzschutzanlagen-Planen, Bauen, Pruefen. Huethig, Heidelberg (1997).

Schwab, A.-J.: Elektromagnetische Vertraeglichkeit, Springer-Verlag, Berlin-Heidelberg (1990).

Enhancing Geothermal Power Generation with Binary Technology in Brine Recovery: Exergy's case study in the Philippines, Mindanao 3 Power Plant

Nicola Frascella, Marco Frassinetti, and Chee Aun Kok

n.frascella@Exergy.it, m.frassinetti@Exergy.it, c.kok@Exergy.it

Keywords: Binary Cycle, Radial Outflow Turbine, Exergy International, Real Case Application, Brine Recovery, Reinjection Temperature,

ABSTRACT

Existing steam fields located in Indonesia and in other countries of the Asia Pacific Region mainly use flash steam turbine power generation plants. This power conversion system is well proven and reliable but does not exploit the thermal energy in the geothermal brine. This can be efficiently harnessed to increase the overall power output of the plant without further developments of the wells field and no additional environmental impact.

Using a binary cycle to convert the thermal energy of the brine in additional power has proved to be a very effective and reliable opportunity. This paper will present a real case study of a brine recovery project in the Mindanao 3 flash power plant in the Philippines, with Exergy's advanced binary system based on the unique, highly efficient Radial Outflow Turbine technology.

1. INTRODUCTION

In a world where global warming is threatening peoples, economies and ecosystems, the demand for food, water and energy, linked by the relative nexus, is continuously rising. As long as the human population will grow, the demand for these primary goods will continue to increase, and the possibility to enlarge wealth without exacerbating global warming emissions still seems a paradox. Moreover, issues like global access to electricity and fuel poverty are still waiting to be tackled effectively. In 2019 the global energy consumption has been of 170 PWh (170 million GWh), and it is estimated that by 2035 there will be an increase in energy demand of +35% with respect to such value (Capocelli et al., 2020).

In such context, all main components of society (governments, investors, companies, private citizens) are giving birth to new forms of cooperation capable to deliver effective solutions in the fight against global warming, defined as the most critical challenge of our times. Among these, one of the most relevant is the struggle to decrease the carbon intensity of the energy sector, not only in the electricity generation segment, but also in other activities such as transportation or heating and cooling. However, the exploitation of renewable energy sources for power generation, focusing on PV and wind, is delivering together with clean energy also grid stability issues, caused by the non-dispatchability of these sources. The further development of geothermal energy and biomass usage in first place, together with new resources (tidal energy, wave power, storage systems) and with hydroelectric could solve this problem, guaranteeing a clean energy mix capable of supplying a sustainable base load power generation system.

2. GEOTHERMAL POWER GENERATION

2.1 Geothermal State of the Art

In 2020, the global installed capacity for power production from geothermal energy was about 16 GW, while other thermal usages, either direct (air conditioning, district heating and cooling) or ground-source heat pumps (GSHP), accounted together for more than 70 GW of thermal power (Huttrer, 2020). While the latter can be considered for applications almost anywhere around the globe, as it exploits the Earth average geothermal gradient, electricity generation from geothermal energy requires a combination of factors (heat available close to the crust and water in such reservoir among all) that are currently limiting its use to only a small number of nations. Almost 95% of this installed capacity is present in 10 countries (USA, Indonesia, Philippines, Turkey, Kenya, Mexico, New Zealand, Italy, Iceland and Japan), all places characterized by consistent geological activity. As anticipated, this distribution is surely connected to the availability of the source, but it has been strongly affected also by specific policies that have been driving the market towards desired directions. As an example, the feed-in tariff provided by the Turkish government has been increasing its installed geothermal capacity from 400 MW in 2015 up to 1550 MW in 2020, experiencing the most significant geothermal power increase worldwide for this period (+1150 MW) (Huttrer, 2020).

Over the next five years, geothermal power generation is expected to grow of about +20% (+3.4 GW of installed capacity) (Huttrer, 2020); if compared to the growth of PV, which in the same period is expected to grow of +360 GW (100 times more than geothermal, +60% increase with respect to its 2020 installed capacity), it seems clear that there are some obstacles to the development of this kind of source that must be faced in order to untap a much wider geothermal potential.

2.2 Source Uncertainty, Key Threat to Geothermal Development

Once decided to develop a new geothermal resource, a long and expensive process begins: initial costs are important, as they need to effectively assess the presence of the resource and are required upfront; the first development steps are risky and could lead to disappointing results. For this reason, the cost of capital itself is substantial, because any potential investor is willing to proceed with such risks only if the investment is profitable enough**.** Costs and risks associated to exploration of geothermal energy have been the main threat to the development of new geothermal projects worldwide and strongly affect the price of geothermal electricity (Mulazzani, 2016). Once the resource has been proven and the drilling is completed, the power generation facility needs to be designed, installed, and commissioned before the first revenue stream becomes available. This means that from the beginning of the investment many years have passed. Projects in which this amount of time reaches five years are not uncommon in the geothermal world, especially in green field applications, where also the time required for the site preparation must be accounted for. Finally, also

the stability of the source itself must be investigated in operation, and especially in case of bad or no reinjection, it can decrease over time.

2.3 Flash Cycles, Main Paradigm for Geothermal Power Generation

Flash cycles are the most conventional system used for power generation in geothermal high-temperature applications, mainly because of their simplicity that leads to limited investments per MW. Since most geothermal wells produce fluids which have two different phases, brine and steam (together with non-condensable gases and solid particles), the steam and gases must be split from the heavier components using separators. Then, while the liquid phase is reinjected, the saturated steam enters the turbine, which is coupled with an electrical generator in order to produce power. At the outlet of the turbine, there is a condenser where a cooling fluid achieves the condensation of the steam, taking away its residual heat. Finally, the condensate is usually reinjected together with the cooling fluid and the hot brine. In Figure 3 a simplified diagram of the flash cycle is represented.

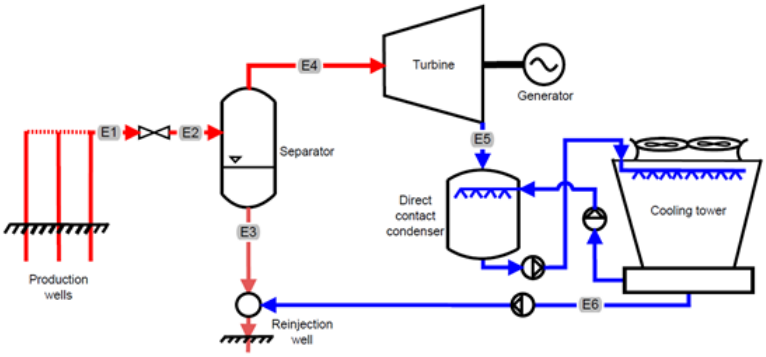

Figure 3: Single Flash Steam Power Plant.

2.3 Binary Plants, ORC Sweet Spot in Geothermal Applications

Binary plants are so called because there are two different fluids which never mix together. The first one is the hot geothermal fluid, either brine or steam, which delivers its heat to another fluid in shell-and-tube heat exchangers and is then completely reinjected at a lower temperature. The second fluid, which usually is an organic fluid with a boiling point lower than water, is evaporated and sent through a proper turbine coupled with its generator, condensed at the outlet (either with water or air as a cooling agent) and then pumped back again with a feed pump. According to case specific issues, such Organic Rankine Cycle (ORC) is then optimized, involving choices like the selection of the working fluid, the cycle configuration (one or more pressure levels, saturated or superheated cycle) or the presence of a recuperator, an internal heat exchanger which usually increases furtherly the conversion efficiency. In Figure 4 an example of a binary cycle is shown.

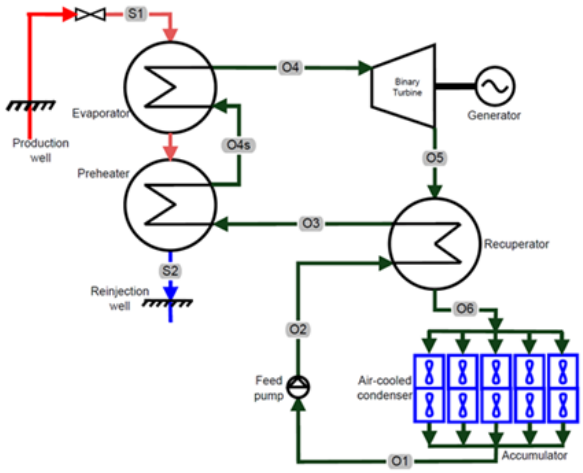

Figure 4: ORC Binary Power Plant, with one pressure level, a recuperator and an Air-Cooled Condenser.

It is worth underlining that the Organic Rankine Cycle just described is a closed loop with no interaction with the geothermal fluid, meaning that all O&M issues related to fouling or corrosion will not affect any of the components of the ORC, but remain limited to the geothermal circuit and the tube-side of the heat exchangers. Other advantages of using an organic fluid in binary plants can be related either to efficiency increase or economic gain. First of all, all organic fluids have a shape of the saturation dome that allows a dry expansion process, meaning that there is no risk of having liquid formation in the turbine, which is on the other hand typical of water steam turbines. In this way, in any off-design condition there is no eventuality of erosion, caused by droplets impacting at high speed against the blades of the expander and resulting in a reduction of the useful life of the turbine. Another advantage is the possibility to avoid any water consumption, especially where this is a precious resource, thanks to the use of an air-cooled condenser; nevertheless, if water and namely condensate is freely available, an indirect water-cooled condenser can be used to increase the cost-effectiveness of the solution. Moreover, the possibility to pick the working fluid across a wide selection of candidates, allows an

overall optimization that can maximize the cost-efficiency of the solution. Finally, the complete reinjection of the geothermal fluid can be pursued, avoiding the release of gases in the atmosphere, and guaranteeing the preservation of the resource.

Binary plants in general, and Organic Rankine Cycles in particular, have a very flexible design structure, where many components can be considered or not, according to the specific features of the project, in order to maximize the conversion efficiency, the economic gain, the O&M activities or a mixture of these. It can be easily understood that, thanks to such a flexible design, these power plants are suitable for working in a very wide range of boundary conditions. However, to exploit the possibilities triggered by this technology, only an appropriate know-how can effectively achieve the maximum satisfaction of the customer's requirement.

As a proof of these advantages towards a more sustainable exploitation of geothermal resources, against an installed capacity of about 25% of the overall 16 GW mentioned earlier, Binary ORC technology accounts for around 65% of the new installed power since 2015, underlining an important trend in the new most recent developments.

3. CASE STUDY: STATE OF THE ART

3.1 Geothermal Exploitation in the Philippines

The Philippines is the third country worldwide for electricity production from geothermal sources, with an installed capacity of almost 2000 MW and an average capacity factor close to 90%. Together with Indonesia, which is the second largest producer and has a similar amount of installed capacity, these are the only two relevant countries in the ASEAN region active in the geothermal power. Despite this, in the 2015-2020 period, only a 12 MW unit has been commissioned in the Philippines, indicating a lacking willingness to continue the segment expansion. However, from the end of 2020 a fresh wave of dynamism has started pervading the sector again, with new investments and an increased attention to the efficient exploitation of the existing resources. For the following five years it has been estimated for the Philippines a potential addition of almost 100 MW of new capacity, while the overall development potential exceeds 4 GW of installed power (Huttrer, 2020).

In both Indonesia and Philippines, most of the existing power plants are single flash units, as the one described before in section 2.3. Moreover, the majority of the reservoirs used are liquid-dominated type, meaning that most of the geothermal fluid is liquid, and it is reinjected hot, immediately after being separated. For this reason, the potential available from cooling down the reinjected brine in a binary plant is extremely attractive, since the source is not only assessed, but also already present and available. In this way, the resultant "Brine Recovery" application has all the advantages of the geothermal energy without the complexities linked to the source uncertainties or to the cost of drilling. In Figure 5 it is shown an example of possible retrofitted integration between a single flash cycle and a binary cycle, however there are many other ways in which their combination is possible.

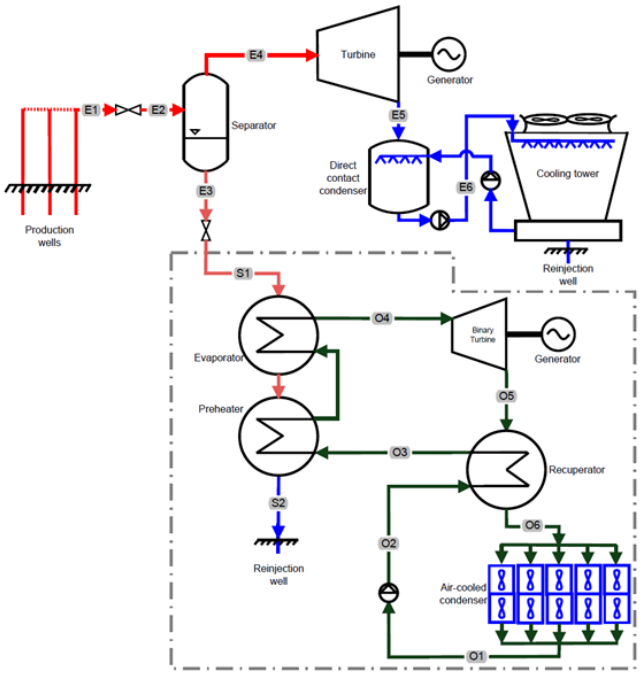

Figure 5: A simplified scheme of a retrofitted combined geothermal configuration, also called a brine recovery plant.

3.2 EDC Existing Power Plants: Mindanao I and Mindanao II

With 45 years of history and more than 60% of the Philippines installed geothermal capacity (EDC, 2021), Energy Development Corporation (EDC) is one of the biggest geothermal operators worldwide and the most important in the Far East region. Among their 1477 MW of installed renewable capacity, 104 MW come from the Mindanao Geothermal field, located close to Mt. Apo in the Mindanao Island. Here, two steam turbines of similar size have been producing electricity from single flash cycles since the last years of the previous millennium. With respect to the Figure 3, after both turbines there is an indirect water-cooled condenser, coupled with the cooling towers. In this way, against a slightly higher investment cost, there is the possibility to use the steam condensate for many different uses, and only a part of it as make-up water for the cooling towers. The first 52 MW unit has been commissioned in 1997, while the second one started its activity in 1999. The reservoir system can rely upon 23 production and 7 reinjection wells, relatively to a liquid dominated hydrothermal system (Trazona et al., 2002). After an initial decrease in the well enthalpy of the order of -8%

occurred during the first years of operation, the reservoir behavior has always remained constant. However, the huge amount of brine reinjected without using it at all, in the new scenario of optimization of the available sources, has lit the possibility to increase the productivity of the geothermal field using a small amount of the hot brine.

Figure 6: Mindanao I and Mindanao II geothermal power plants.

4. MINDANAO III: EXERGY'S CUSTOMISED ORC SOLUTION

4.1 Exergy International: an ORC company with a deep know-how in geothermal power generation

Exergy International srl is the worldwide developer, engineer and producer of Organic Rankine Cycle systems, with the innovative and pioneering Radial Outflow Turbine technology. ORC systems are used for power production from renewable energy sources including geothermal, biomass and concentrated solar power as well as from waste heat. The ORC is the best solution when the enthalpy level of the heat source is low, or if the size of the application is too small for a steam power plant to be an efficient solution. The plant configuration and thermodynamic principles at its basis are the same, but the ORC advantages are based on the differing thermodynamic properties of the single organic fluid. The fluid is chosen to best fit the heat source, thus obtaining higher efficiencies.

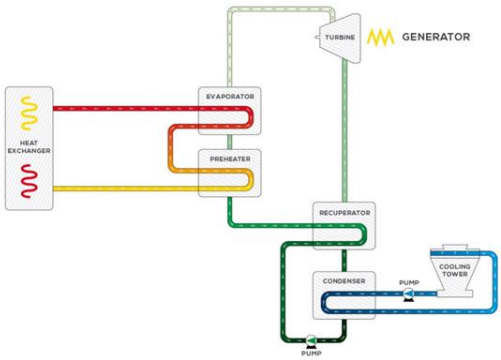

Figure 7: Simplified diagram of a water-cooled Organic Rankine Cycle, with heat delivered from an intermediate circuit.

The advantages of the ORC over the traditional Rankine cycle include:

- Suitable for lower temperature applications
- Low rotation and tip speed in the turbine, together with the absence of liquid in the low-pressure stages
- Phase during expansion lead to a reliable and long-lasting expander, with simple and low-cost maintenance
- Compact and automated, meaning no need for operators
- Design flexibility with the option to utilize the most efficient working fluid available
- Operational flexibility for superior off-design performances
- A no-water consumption option is possible
- High market availability of chemicals /fluids with refilling rarely required
- Low associated costs for foundation and assembly
- Simple and reliable system maintenance made for long product life

Having the unique advantage of operating under diverse conditions, ORC engines perform with greater efficiency and flexibility than traditional Rankine cycle technologies. Exergy undertakes the development and manufacturing process of the ORC turbine and plant internally. This includes in-house R&D, engineering, project management, testing and after-sales service, but Exergy also operate a central control room to provide remote monitoring of the plants of its customers.

Activities are undertaken in a custom-built facility in Varese, to the north-east of Italy. The region is rich in valued partners and a skilled technical workforce due to the traditional presence of mechanical and turbine factories on the territory plus leading Universities

and R&D centers. Inaugurated in 2013, the new facility ensures the engineering teamwork in proximity to the operations and assembly teams. This allows for internal collaboration and controls throughout every step of the process, from initial consultations with the clients, through to the final installation and ongoing service. This supply chain model ensures short delivery times, faster response times and a streamlined end-to-end process.

Exergy is operated by a team of experienced and skilled experts that include energy and mechanical engineers, product managers, technology specialists and designers, sales and marketing professionals, service and quality managers and support staff. Among the about 70 operational people worldwide, most are engineers with many graduates from Politecnico di Milano, the most prestigious technical university in Italy.

With over 30 patents registered in more than 20 countries worldwide, Exergy is a technology company focused on innovative solutions for the global energy sector. Exergy was founded in 2009 with the launch of the Radial Outflow Turbine. In 2011 Exergy became a subsidiary of the Italian Maccaferri Industrial Group, sitting within the SECI S.p.A. Holding. Between 2012 and 2017 Exergy consolidates its know-how and technology and becomes a leader in the ORC sector gaining an important share of the market with more than 30 plants installed with capacity up to 25 MWe, reaching a portfolio of approximately 400 MWe. In 2018 the company sells its first ORC's system for an Oil and Gas application, in a project in cooperation with GE-Baker Hughes. The year later, on the 25th of September 2019 Exergy is acquired by the Chinese Corporation TICA Group, leader in a HVAC sector and thermal energy systems, based in Nanjing and with 10 manufacturing bases worldwide, 3000 employees, over 70 sales offices worldwide. Today Exergy counts 54 power plants in its portfolio for a total capacity of 500 MWe and owns the **s**econd largest geothermal binary fleet worldwide.

4.2 Exergy's core technology: the Radial Outflow Turbine

Designed by Exergy, the Radial Outflow Turbine (ROT) is an innovative technological breakthrough. This technology is covered by current and pending patents and is the first turbine of its kind to be utilized in an ORC system. The Radial Outflow Turbine, different from the axial and radial inflow configuration, can convert the energy contained in the fluid into mechanical power, with higher efficiency than any competing technology present on the market. In 2011 Exergy developed a supplementary Radial Axial configuration suitable for waste heat or biomass engines. The single disk Radial-Axial configuration offers maximum efficiency with an extreme volumetric ratio.

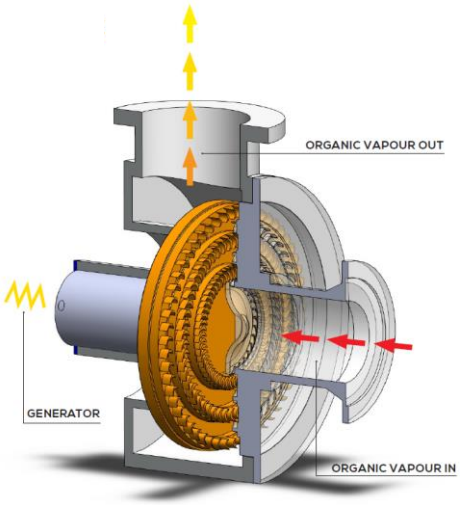

Figure 8: Exergy's Radial Outflow Turbine.

When working with an organic fluid, most of the characteristics of the ROT become advantageous. For example:

- Higher efficiency than an axial turbine
- Multiple pressure admissions possible on a single disk
- Low speed turbine means no gearbox, and therefore higher reliability
- Large increase in volumetric flow achieved without the need for extreme changes in blade height
- Outward movement of fluid leading to minimum 3D effects
- Minimum turbulence, meaning maximum efficiency
- Excellent match between volumetric flow and the cross section across the radius
- No need for partial admission
- Lower tip leakage and disk friction losses
- Low vibrations, meaning longer life on the bearings

All these factors lead to a more compact and efficient machine, rotating at a low speed with minimal noise and vibration.

4.3 Exergy's ORC brine recovery design: Mindanao III

Exergy's Mindanao III ORC power plant is fueled by the brine coming from EDC's Mindanao I and Mindanao II power plants at the temperature of 140°C and, as it will be discussed in the following paragraph, cooled down to 80°C in the high alloy stainless-steel tubes of shell and tube heat exchangers. The thermal power recovered in this way is used to preheat and evaporate a flow of organic

fluid typically used in ORC geothermal applications. This flow enters the Radial Outflow Turbine in saturated conditions and is expanded down to the condensation pressure. The condenser is an indirect shell and tube water-cooled condenser, with the cooling water coming from a cooling tower designed and supplied by Exergy just like all other key equipment. It is interesting to notice that the make-up water for this cooling tower comes from the geothermal steam condensed in Mindanao I and II power plants, highlighting a further degree of integration between the flash and the ORC units. After the condenser two feed-pumps are used to increase the pressure up to the maximum value, to close the loop. The redundancy grade of any element of this power plant has been evaluated in order to allow maximum rates of availability for all the lifetime of the plant, which is expected to work for more than 20 years.

Everything in this cycle has been optimized according to Exergy's know-how and experience. From the smaller details like the electrical wires, threatened by a H_2S rich environment, up to the most impacting equipment like the turbine, the generator, the cooling system, the heat exchangers or the acid dosing system, each component deserved the attention of Exergy's engineering team, that evaluated carefully all possible implications of any design choice in close cooperation with the engineering team of EDC. The outcome, that will start delivering its 3.6 MW of electric power to the grid at the beginning of 2022, will be one of the fastest geothermal power plants to be put in operation in the area (less than 14 months from contract signature), accomplished thanks to a long-lasting cooperation between Exergy, EDC and both their supply chains.

4.4 A critical aspect: the reinjection temperature

The reinjection temperature is a key parameter in the development of a geothermal project, and it can be the crucial factor in determining the success or the failure of the field.
From a purely theorical perspective, the more you cool down the heat source, the more heat you have available for the conversion of thermal energy into electricity, so the first approach will be to take all the thermal input that is possible. However, as a consequence of Carnot's Theorem, one of the most relevant in thermodynamics, the lower is the temperature of the hot source, the lower will be the conversion efficiency. In particular, considering cooling down the brine source from the initial temperature T_{in} to the outlet temperature T_{out}, the maximum conversion efficiency is limited by applying Lorenz's theorem to a trapezoidal cycle, and is according to the following formula:

$$\eta_{Trap,max} = 1 - \frac{\mathrm{Tamb}}{\frac{\mathrm{Tin}-\mathrm{Tout}}{\ln\left(\frac{\mathrm{Tin}}{\mathrm{Tout}}\right)}} = 1 - \frac{\mathrm{Tamb}}{\mathrm{Tml,H}} \tag{1}$$

Where T_{amb} is the ambient temperature, $\eta_{Trap,max}$ is the maximum efficiency achievable ideally from a trapezoidal cycle, while the denominator ($T_{ml,H}$) is the mean logarithmic temperature of the hot source (which has nothing to do with the Logarithmic Mean Temperature Difference – or LMTD – used commonly in heat transfer). In other words, Lorenz generalizes Carnot's theorem for hot sources at variable temperature, while for constant temperature sources (i.e., $T_{in}=T_{out}=T_{hot}$) they converge to the same result.

It is now clear that the lower is the reinjection temperature, the lower the hot source logarithmic temperature and thus the lower will be the power cycle conversion efficiency. As an example, in the picture below it is possible to understand how decreasing the brine outlet temperature, the thermal power available from a hot source increase (at T_{in}=150°C), while the maximum theorical conversion efficiency (alias Lorenz efficiency) decreases. Consequently, the electrical power, calculated as the product between these two factors, has a maximum (at around 40°C in Figure 9); any further decrease in the brine reinjection temperature results in a lower electrical output.

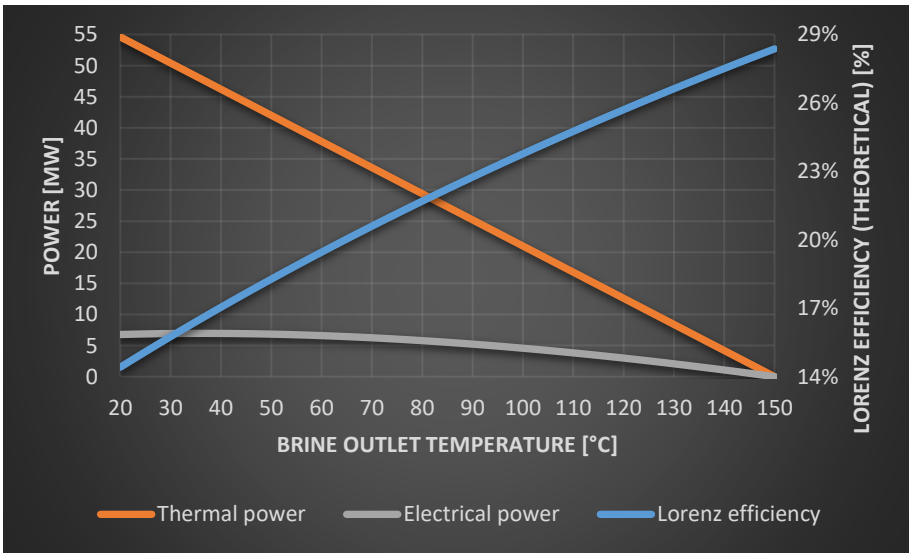

Figure 9: Relationship between brine outlet temperature, thermal power available, Lorenz conversion efficiency and maximum electrical power output available from a brine source at 150°C.

Moreover, many differences occur from a practical point of view that are not considered in the simplified analysis above. As an example, there is a difference between the condensation temperature of the cycle and the ambient temperature, and between the resource and the evaporation, due to the fact that the surface of the condenser is not infinite. The presence of these effects pushes upwards the outlet temperature at which we have the maximum electrical power. Finally, there are also some technoeconomic

considerations so that, unless the price of electricity is very high, the most cost-effective solution will have an optimal reinjection temperature which will be slightly higher than the technical optimum.

Nevertheless, when considering brine recovery geothermal projects, where a flash turbine is present after a separator, such as Mindanao III, the most relevant factor to be accounted for is the deposition of solid substances. This phenomenon called "scaling", can involve many different chemical species, but is particularly relevant in case of silica scaling (but also calcite can be relevant), since once occurred it is almost impossible to solve it and makes it very tough to deal with it. To explain why scaling happens, a very effective similitude is the one of sugar in the cup of coffee: when it is hot, you can add a lot of sugar, and up to a certain threshold, called the solubility limit, it will disappear. However, if you don't drink your coffee soon, it will cool down and some sugar will appear again at the bottom of the cup. This is because the solubility limit depends strongly on the temperature of the liquid, and when the temperature decreases, also the capacity of the coffee to keep the sugar in a homogeneous solution drops down. Silicates are typically present in geothermal brine, and as almost all solid particles, once flashed remain concentrated in the liquid phase. So, when cooling down the brine to recover heat for the ORC cycle, if scaling has not been considered carefully, it is possible that amorphous silica or other chemical component deposit in the shell and tube heat exchangers, jeopardizing the heat exchange process. In Figure 10 the limit of silica saturation is represented against the water temperature; the higher the steam fraction that goes in the flash turbine, the more concentrated will the silica result in the brine.

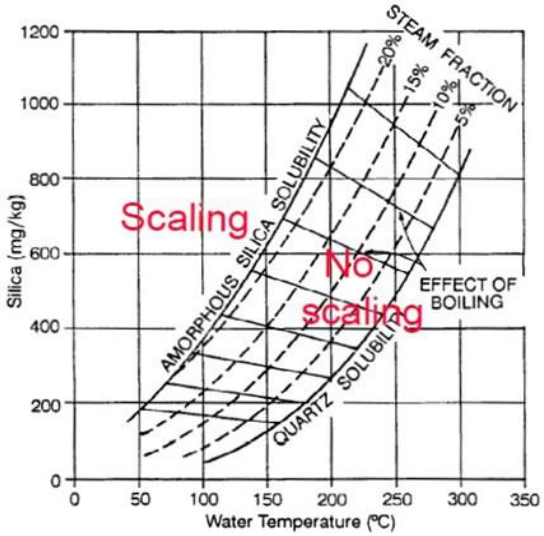

Figure 10: Solubility limit of silica in water.

4.5 Exergy's solution: a customized acid dosing system

In the last decades, the focus has been moving from "IF" silica deposition happens to "WHEN" it materializes concretely. Even in presence of a supersaturated silica solution, there are some factors that can significantly delay the formation of scaling, solving such issue upfront. It is worth mentioning that the residence time of brine in the critical part of ORC heat exchangers and reinjection well is of the order of tens of seconds; for this reason, a system that delays silica deposition of half an hour allows to completely avoid any kind of issue.

Numerical simulations and then experimental tests are essential for a proper selection of the main features of the dosing system.

Among the different possibilities that can inhibit silica scaling, for Mindanao III plant, Exergy focused on an acid dosing system. It is demonstrated in many different studies and applications, that low (acid) or high (alkaline) pH values are one of the most effective system able to achieve such objective. However, acid substances are preferred to alkaline ones, even though steel corrosion is not an issue with alkaline dosing, because of the much smaller operating costs that in the long run are extremely impacting. For this reason, a customized system has been studied, in order to achieve the targeted reinjection temperature (80°C) in the best possible way, keeping in mind all relevant issues that EDC, as a final customer, would experience in the operation of the plant.

Among the many decisions that have been made by Exergy's engineering team during the development of the inhibitor system, the most important are related to the kind of acid (strong vs weak), to the material selection, to the system and process arrangement, to the redundancy of the components and to the positioning of the system itself. Since these kinds of systems are not very widespread yet, each choice considered all possible working conditions without the possibility to rely upon a dominant technical paradigm.

5. CONCLUSIONS

In a scenario of increasing energy demand, pushed by population and economic growth, Mindanao III geothermal plant could be the first of a long series of binary ORC bottoming flash units, extremely diffused in different areas worldwide. This new brine recovery paradigm would overcome one of the most serious barriers to the growth of geothermal energy, alias the uncertainty of the source, since it would rely upon wasted flows already existing and available. Another obstacle addressed and solved by Exergy's and EDC's engineering teams is related to the reinjection temperature optimization and consequent silica deposition. Also, this issue in the past contributed to the technical selection in the development of many geothermal projects, but now the maturity of this technology has reached a turning point, and is ready to be employed anywhere it is required.

REFERENCES

ASEAN Centre for Energy (ACE): Deutsche Gesellschaft für Internationale Zusammenarbeit (GIZ) GmbH, Levelised Costs of Electricity (LCOE) for Selected Renewable Energy Technologies in the ASEAN Member States II, Report, (2019).

Capocelli, M., Moliterni, E., Piemonte V., and De Falco, M.: Reuse of Waste Geothermal Brine: Process, Thermodynamic and Economic Analysis, *Water*, 12, (2020).

EDC: EDC – About, (2021). https://www.energy.com.ph/about/

GlobalData Energy: Global PV capacity is expected to reach 969GW by 2025, (2017). https://www.power-technology.com/comment/global-pv-capacity-expected-reach-969gw-2025/

Huttrer, G.W.: Geothermal Power Generation in the World 2015-2020 Update Report, *Proceedings*, World Geothermal Congress, Reykjavik, Iceland (2020).

Mulazzani, D.: Exergy Geothermal Combined Cycle (ExGCC) power plant for liquid dominated reservoir in the Asia-Pacific Region, *Proceedings*, 4th Indonesia International Geothermal Convention and Exhibition, Jakarta, Indonesia (2016).

Trazona, R.G., Sambrano, B.M.G., and Esberto, M.B.: Reservoir Management in Mindanao Geothermal Production Field, Philippines, *Proceedings*, 27th Workshop on Geothermal Reservoir Engineering, Stanford, California (2002).

Success Story of Scaling Silica Treatment in Brine ORC (Study Case Sorik Marapi Geothermal Field)

Nugraha Y. Arifpin[1] and Ryan Hidayat[2]

[1]Ecolab International Indonesia, Pondok Indah Office Tower 3, 6th Floor, Jalan Sultan Iskandar Muda KavV-TA, Jakarta, Indonesia
[2]KS Orka, Renewable, Recapital Building 5th Floor, Jalan Aditiawaraman Kav 55, Jakarta, Indonesia

nyohanesarif@ecolab.com, ryan.hidayat@ksorka.com

Keywords: Silica, Scaling, Brine ORC

ABSTRACT

The silica oversaturation of geothermal brines is one of the problems in generating an efficient energy recovery in the geothermal power plant. Silica scaling can cause an extensive fouling in the heat exchanger and can reduce injection capacity. This paper presents a success story of silica scaling inhibition program in Sorik Marapi Geothermal Fields. The Sorik Marapi Geothermal field has been commissioned for its first 45 MW plant in 3rd Quarter 2019. New unit of brine ORC installed since January 2021 to support second 45 MW generation phase 2. The utilization of in Brine ORC reduces the temperature of brine from 153˚C to 100˚C, which cause silica to be oversaturated with silica saturation index 2.09 at the ORC outlet. To maintain silica deposition, a proprietary silica scale inhibitor GEO981 is injected to the brine at the inlet line of Brine ORC. Scale monitoring was carried out routinely by measuring differential pressure, monomeric silica concentration and scaling rate from scaling coupon.

1. INTRODUCTION

Sorik Marapi geothermal field has been in operation since 3rd Quarter of 2019 with 45 MW generation in phase 1. In early 2021, a new brine ORC (Organic Rankine Cycle) from Kaishan Group has been installed to generate additional generation 45 MW electricity for phase 2 with a total of 90 MW generation in Sorik Marapi Field. The brine ORC transfers the heat from the brine to the secondary fluid medium which cause the brine temperature to reduce from 153^0 to 100^0 C. With this energy extraction, reduction in temperature, and the chemistry in the brine, the silica saturation index will increase from 1.11 to 2.09 which indicates that silica scaling and deposition potential will increase during the extraction process.

In extracting geothermal energy, particularly in brine ORC system, silica has long been a critical factor that limits the energy extraction from geothermal fluid. Silica deposition forms a highly insulative that reduce the heat transfer. At severe condition, the silica deposition can hinder the fluid flow to the brine ORC system and reduce injectivity in the reinjection well. The layer that formed, apart from being insulative, it also very tenacious and difficult to remove.

The silica deposition occurs because of several chemical reactions and processes that happen simultaneously in the geothermal fluid, which are monomeric silica polymerization, co-precipitation with other minerals and ions (predominantly with metals), and direct deposition of monomeric silica (Gill and Jacobs, 2018). These reactions and processes are controlled by several factors which include chemical and physical conditions, such as silica and other mineral concentration, temperature (Fournier et al., 1983; Setiawan et al., 2019), binary unit design (Grassiani, 2000), acidity (Addison et al., 2015), and others. All the reactions and processes along with all several factors must be controlled simultaneously to prevent silica deposition.

Each geothermal field has a unique chemistry, thermodynamic, and operating condition, thus there is no single solution that can be implemented in all geothermal field. To identify and planned for the solution, a modelling software (Geomizer®) is used to understand the scaling potential as well as to review the available options. From the review, Sorik Marapi geothermal field chose to use silica inhibitor program (GEO981) to mitigate the silica scaling risk. The result of this program will be described further in this paper.

2. PLANT OPERATING CONDITION

The brine ORC plant retrieves the brine from several production wells. The plan diagram can be seen in Figure 1 and the chemistry and thermodynamic properties from each production well can be seen in Table 1.

Table 1: Production Well Properties.

Parameter	Well A-1	Well A-3	Well A-4	Well A-5	Well A-6	Well A-7
Enthalpy (kJ/kg)	1130	1150	1170	1050	1060	1,216
Flow Rate (ton/hour)	174.9	198.7	490.32	535.7	113.4	360.4
Sampling Temperature (^{0}C)	180.8	182.4	178.4	182.4	162.3	181
pH at Sampling Temp	7.9	8.1	8.2	8.2	8.0	8.1
Silica (ppm)	650	690	655	665	685	815

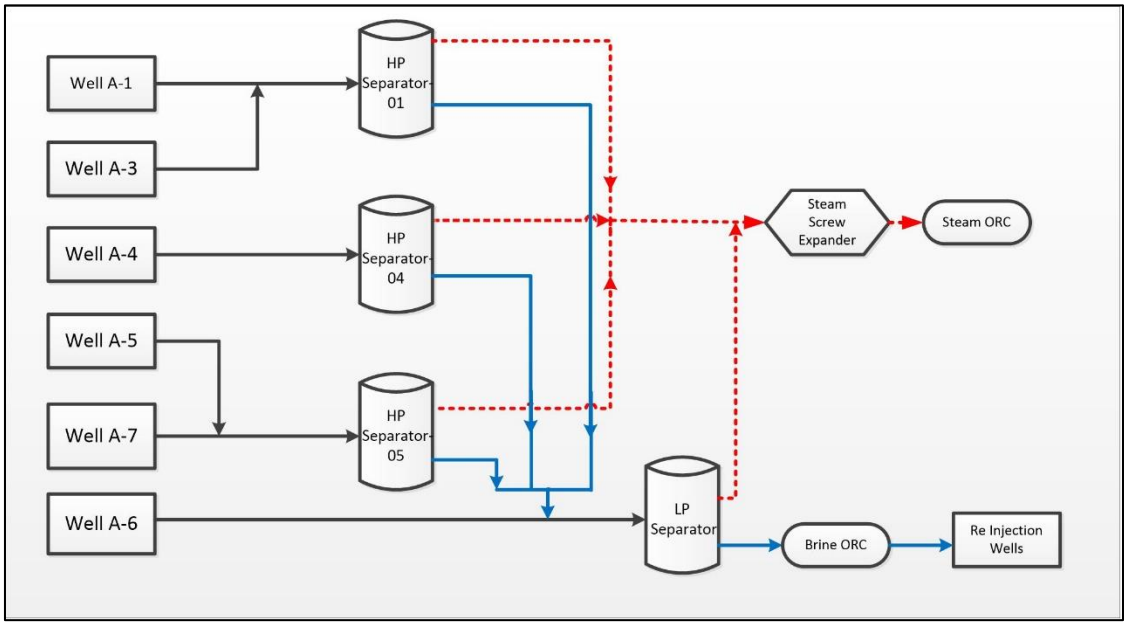

Figure 1: Sorik Marapi Geothermal Field Plant Diagram.

As can be seen in Figure 1, there are three High Pressure separators and one Low Pressure separator. The steam from all HP separators will be combined and sent to Steam Screw Expander. The brine from HP separator combines with two phase fluid from Well A-6 separated once more in LP separator. The brine from LP Separator sent to brine ORC, while the steam goes to Screw Expander and the excess team going to Steam ORC. Based on the operating condition in each separator, the chemical properties and operating condition at the brine ORC inlet can be seen in Table 2.

Table 2: Brine ORC Chemistry and Operating Condition.

Parameter	Brine ORC
Inlet temperature (^{0}C)	153
Outlet temperature (^{0}C)	100
Flow Rate (ton/hour)	1,200
Silica (ppm)	720

Based on the profile temperature in the Brine ORC, Geomizer® is used to simulate the silica saturation index (SSI), to understand the degree of scaling in the system. The result of simulation can be seen in Figure 2.

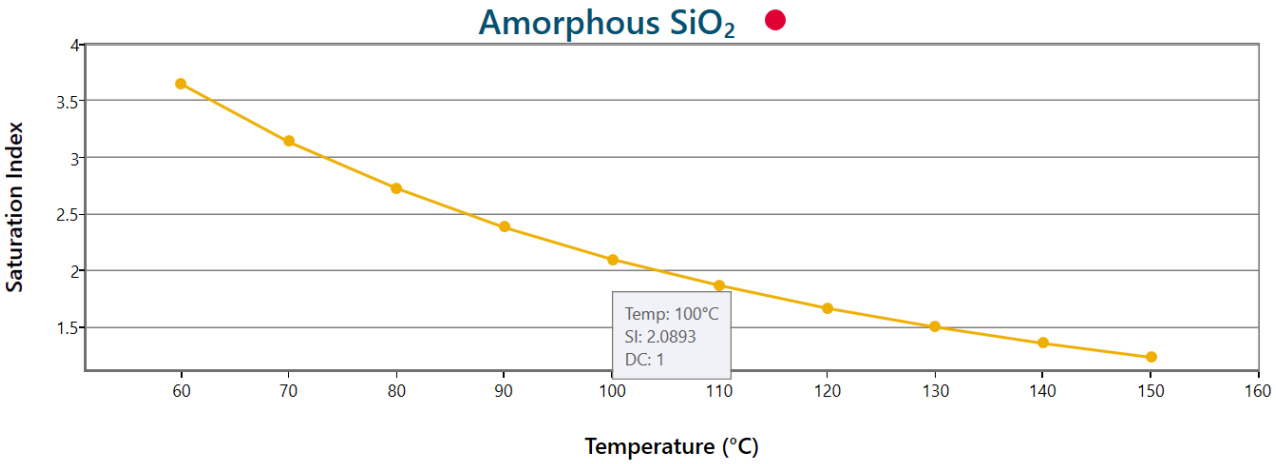

Figure 2: Silica Saturation Index at Brine ORC.

From the Figure 2, it can be seen that the brine at 100^{0}C is in supersaturated condition (SSI 2.09). Therefore, the silica scaling is inevitable and must be mitigated to maintain the heat transfer rate.

3. SILICA INHIBITOR IMPLEMENTATION AND RESULT

Based on the analysis and simulation conducted, the silica inhibitor program that implemented in Sorik Marapi geothermal field is GEO981. GEO981 is a silica inhibitor that used proprietary organic polymer. The polymer has high anionic density charge that able to inhibit silica polymerization by chelation, threshold inhibition, and dispersion. GEO981 reacts in sub-stoichiometric reaction thus the chemical consumption is lesser compare to the acid usage in traditional pH modification. This reaction mechanism eases the logistic complexity onsite. Apart from that, due to its chemical properties, GEO981 offers safer operation compare to acid in pH modification.

GEO981 has been implemented since the commissioning process of the brine ORC. The system is closely monitored to determine the effectiveness of this program. The parameters that monitored are brine ORC differential pressure, monomeric silica at the inlet and outlet of brine ORC (%polymerization), and scaling rate from the coupon. Dosage adjustment is made on regular basis based on the analysis from the parameter that collected to ensure the program performance.

3.1 Brine ORC Differential Pressure

The differential pressure on the brine ORC can be used as an early indicator for the heat exchanger cleanliness. As the differential pressure maintained at constant value, the heat exchanger cleanliness is also maintained. If the differential pressure increase, with combination of monomeric silica data and scaling rate, we can differentiate the root causes of the incremental increase between scaling or other deposition that can be trapped in the heat exchanger.

From data gathered and displayed in Figure 3, we can see that the differential pressure is maintained constant in 0.1-0.2 bar, which indicates that the heat exchanger is maintained at clean condition.

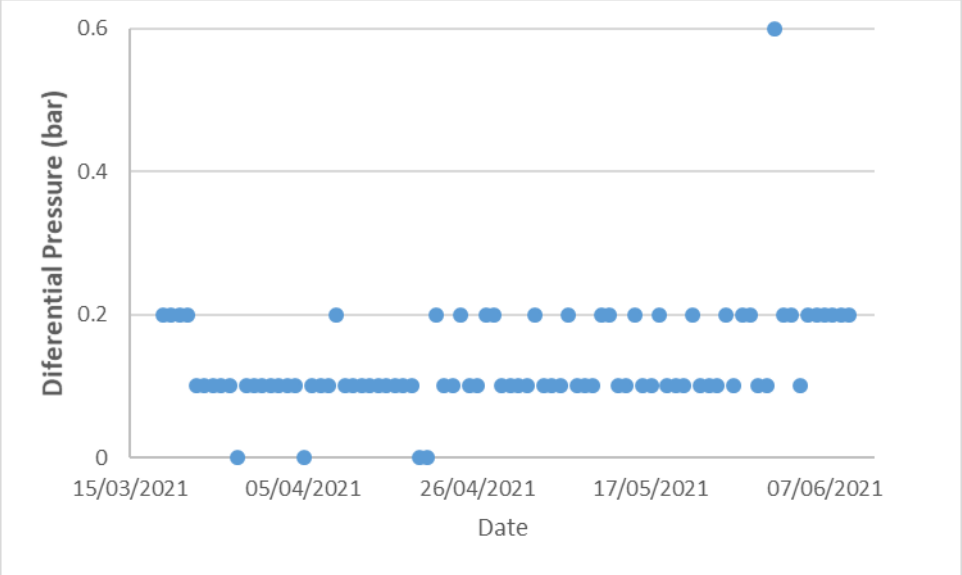

Figure 3: Brine ORC Differential Pressure.

3.2 Monomeric Silica

Monomeric silica analysis can be used to determine the silica deposition rate in the system. If well maintained in the monomeric form, the deposition rate will be minimized in the system. Since it is conducted on site, the monomeric silica analysis can be used to optimize the inhibitor dosage as per requirement. If the monomeric silica at the outlet of brine ORC is maintained at value higher than 90% of the brine ORC inlet silica concentration (<10% polymerization), the inhibitor dosage is considered enough to prevent polymerization. A precaution must be made when conducting silica analysis onsite because there are multiple factors that can intervene the reading such as the reduction in temperature during the analysis (which will increase the rate of polymerization) and the interference from hydrogen sulfide (Berro et al., 2014). The analysis that conducted onsite follows the method described by Berro et al. (2014).

Table 3: Monomeric and %Polymerization Data.

	Monomeric Silica (ppm)		Polymeric Silica (ppm)	% Polymerization
	Inlet	Outlet		
Average	664	642	22	3%
Deviation	13	16	12	2%

From the Table 3 above, we can see that the silica polymerization is maintained below 10%. The result was achieved by optimizing the GEO981 dosage onsite from initial dosage estimation calculate by Geomizer®.

3.3 Scaling Rate

Another parameter that monitored during silica inhibitor implementation is scaling rate from the scale coupon that placed at the brine ORC outlet. The coupon was measured and replaced on monthly basis as an indicator of silica inhibitor program effectiveness. The example scale coupon that has been taken out from the system can be seen in Figure 4, while the scaling rate is displayed in Table 4.

1st April – 1st May 31st May – 2nd July

Figure 4: Scale Coupon at Brine ORC Outlet.

Table 4: Scaling Rate Measurement.

Date		Period	Scaling Rate	
Start	End	(days)	mpy	mm/year
12-Jan	25-Jan	13	2.8	0.073
16-Mar	01-Apr	16	3.26	0.083
01-Apr	01-May	30	1.42	0.036
01-May	31-May	30	2.03	0.052
31-May	02-Jul	32	0.74	0.019

The scaling rate measurement on Table 4 indicate that the silica inhibitor program GEO981 can work as expected to mitigate the scaling potential on Sorik Marapi geothermal field. Having said that, it is critical to keep the performance and operation under control since the chemistry and operation are in dynamic condition. It is important to always records and analyze all associated parameters and adjust the chemical dosage as needed to prevent any deposition.

4. CONCLUSION

Silica inhibitor program GEO981 can work to inhibit silica scale formation in Sorik Marapi geothermal field due to a decrease in temperature from 153˚C to 100˚C due to heat extraction in brine ORC. Calculations using Geomizer® show SSI is 2.09. A close monitoring system and protocol must be implemented to ensure the program performance. Differential pressure, monomeric silica concentration, and scaling rate are the critical parameters that must be monitored closely when implementing silica inhibitor program. Adjustment must be made on regular basis based on the system changes, in both fluid chemistry and operational changes.

REFERENCES

Addison, S.J., Brown, K.L., von Hirtz, P.H., Gallup, D.L., Winick, J.A., Siega, F.L., and Gresham, T.J.: Brine Silica Management at Mighty River Power New Zealand, *Proceedings*, World Geothermal Congress, (2015).

Berro, F., Lelli, M., Minardi, I., and Virgili, G.: A Procedure for Eliminating Sulfide Interference on Silica Colorimetric Analysis, *Mineral Magazine*, 78 (6), (November 2014), 1417-1422. Gill, S.J. and Jacobs, G.: Managing Silica Deposition in Geothermal Power Plants – Pros and Cons of pH Mod versus Silica Inhibitor, *Global Resource Council*, (2018).

Fournier, R.O. and Marshal, W.L.: Calculation of Amorphous Silica Solubilities at 25^0C to 300^0C, *Geochimica et Cosmochimica Acta*, 47, (1983), 587-596.

Grassiani, M.: Siliceous Scaling Aspects of Geothermal Power Generation Using Binary Cycle Heat Recovery, *Proceedings*, World Geothermal Congress, (2000). Setiawan, F.A., Rahayuningsih, E., Petrus, H.T.B. M., Nurpratama, M.I., and Perdana, I.: Kinetic of Silica Precipitation in Geothermal Brine with Seeds Addition: Minimizing Silica Scaling in a Cold Re-Injection System, *Geothermal Energy*, (2019).

Managing Sulfur Deposition and Microbiofouling in Geothermal Power Plant Cooling Tower

Yohannes N. Arifpin[1], Tomy Suryatama[2], Fajar M. Rahman[3], and Fritz Monterozo Earwin[4]

[1,2,3]Ecolab International Indonesia, Pondok Indah Office Tower 3, 6th Floor, Jalan Sultan Iskandar Muda No,05, Jakarta, Indonesia
[4]Nalco Water Philippines, Lower Penthouse, CTP Asean Tower, Asean Drive, Spectrum District, Filinvest City Alabang, Muntinlupa, Philippines

nyohanesarif@ecolab.com, tsuryatama@ecolab.com, fajar.rahman@ecolab.com, fritz.monterozo@ecolab.com

Keywords: Sulfur, Deposit, Biofilm, Sulfur dispersant, GEO966, Purate™

ABSTRACT

Sulfur cycle in the geothermal process has been observed to cause deposition and microbial issues in the geothermal cooling tower powerplant. Sulfur deposit produces from chemical oxidation and biological oxidation process by microbial activity reduce the performance of cooling tower and condenser heat transfer, which ultimately increase steam consumption and reduce the geothermal well lifespan. However, the microbial growth control in geothermal has some challenge as normal oxidizing biocide could results in more deposition while the non-oxidizing has been ineffective on many occasions.

This paper focus on treatment program that focus on synergetic approach in addressing sulfur deposition by implementing sulfur dispersant to prevent deposition, non-oxidizing biocide to control bacteria growth in general, and enzyme inhibitor to control sulfur oxidizing bacteria (SOB) which affects SOB assimilation of either H_2S, elemental sulfur and sulfate as food. The implementation of this approach has helped several geothermal power plants in Indonesia, Philippines, and New Zealand to maintain the efficiency of their power generation that is represented by cooling tower approach temperature and specific steam consumption. In the application of 2 geothermal powerplant located in Southeast Asia, the approach temperature increase was maintained and the specific steam consumption after 1 month of implementation decreased even at increased power generation output.

1. INTRODUCTION

Geothermal water contains a lot of salts, which concentration varies depends on the site location. Mineral and salt component in the geothermal water are subject to chemical reaction which might have adverse impact on geothermal production. Furthermore, these salts serve as critical substrate for bacterial to growth, they are subject of conversion through many microbial metabolism processes (Aditiawati et al., 2009).

One of the chemical components in the geothermal water which could bring some challenge in the plant operation is sulfur. The steam produced at the geothermal wells contains hydrogen sulfide and will be oxidized in high oxygen concentration of cooling water system. Among, the oxidizing reaction product is elemental sulfur that precipitate and forms scale deposits in cooling tower (Sand, 2003).

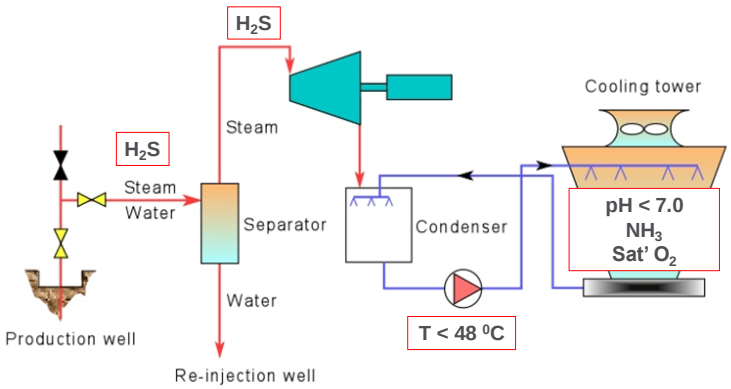

Figure 1: H_2S and Sulfur Oxidation (Ouali, 2017).

The following reactions are deemed to occur in the cooling water system and the formation of the sulfur supposedly depends on the balance between the reactions (Bharathi, 2018).

$$2H_2S + O_2 \rightarrow 2S_{(solid)} + 2H_2O \quad (1)$$

$$2S + 3O_2 + 2H_2O \rightarrow 2H_2SO4 \quad (2)$$

The first reaction could create sulfur deposit in the cooling tower and supplying reactant for second reaction. The second reaction of sulfur oxidation to sulfuric acid is promotes by oxidation potential of the cooling tower and microbial activity of sulfur oxidizing bacteria. Sulfide and sulfur bacterial are both creating acidic metabolic byproducts which are frequently responsible for acid pH excursions in geothermal cooling waters (Relenyi and Rosser, 2019).

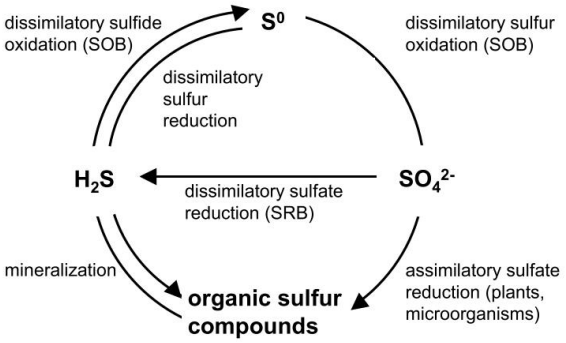

Figure 2: Biological Sulfur Cycle (Kleinjan, 2005).

SOB cover the oxidation of sulfide to sulfate, with reduced sulfur compounds such as sulfur, thiosulfate, and tetrathionate as intermediates. It should be noted that there is a large variety in SOB, of which some species are only capable of covering a specific step in the oxidation of sulfide to sulfate (Kleinjan, 2005).

2. PROBLEM DESCRIPTION

Deposit formation in the cooling tower could block the cooling water spray system or even fouled the fill of the cooling tower. As a result, the performance of cooling tower will be dropped causing higher supply cooling water temperature to the condenser. This will ultimately reduce performance of the condenser.

Furthermore, the corrosive environment due to the microbial activities might results in corrosion and deterioration of plant equipment. Normally, geothermal plant will respond this by injecting caustic to raise the pH of the cooling water. However, as the bacterial population increasing and more sulfate and sulfite are produced, caustic consumption would later increase. This result in caustic having the biggest consumption compare to other chemicals used in geothermal cooling water and rising the chemical treatment cost of geothermal cooling water plant.

Other than the high consumption of caustic other issues that might arise from microbial activities is the formation of the biofilm. Biofilm is generally a slime layer where greater population bacteria are living beneath. The biofilm will hinder the heat transfer in cooling tower the same manner as sulfur deposit or condenser and making the U value much lower compare to the design (Characklis et al., 1981). The deterioration of cooling tower performance and impeded heat transfer in the cooling tower leads to higher specific steam consumption which significantly reduced the life span of geothermal well.

3. FIELD EXPERIENCE

Hidayat et al. (2016) has studied the benefit on implementing sulfur dispersant to disperse sulfur deposition to keep cooling tower clean from sulfur deposit. On the other hand, there are multiple studies to prevent biological oxidation from the activity of sulfur oxidizing bacteria (SOB) (Sarmago and Ho, 2001). Unfortunately, based on observation in several locations, it is critical to prevent sulfur formation from biological oxidation and to disperse sulfur deposition simultaneously. Failed to control one of these factors will cause high sulfur deposition rate which will heavily reduce the total plant performance and increase total cost of operation

The control program strategy that has been implemented in several locations in Indonesia, Philippines, and New Zealand involves the utilization of three main chemistry, which are:

1. GEO966 as a non-foaming sulfur dispersant
2. Purate® as SOB control biocide
3. Isothiazoline as non-oxidizing biocide

The combination of those chemistries is believed to have synergistic impact to prevent SOB growth, reduce sulfur formation from biological oxidation, and dispersing the sulfur deposition that occurs from chemical oxidation.

The performance of the program is reviewed constantly with key parameters follow:

1. Residual dispersant
2. pH of the system
3. Bacteria level
4. Water chemistry
5. Cooling tower approach temperature
6. Specific steam consumption

3.1 Impact on Cooling Tower Approach Temperature

One of the key parameters that can describe the efficiency of the cooling tower is the approach temperature (Lv et al., 2018). Approach temperature serves as a simple indicator of heat transfer that could be done on field, which reflects amount of heat absorbed by air to make it as close as possible to wet bulb temperature. Although its performance could also be affected by cooling water flow and production load reduction, for these cases, we eliminated these possibilities by taking the data when there is no reduction in production load.

During the program implementation at “Site A” and “Site B”, we can see that the approach temperature trend is decreasing at the constant MW production. This phenomenon indicates that the heat transfer in the cooling tower filler that was previously inhibited by the deposition is slightly improving. We suspect that the sulfur dispersant might have some degree of cleaning capability. Figure 3 is the recent data that we collected in “Site A”, while Figure 4 is the past data that we collected in “Site B” last year.

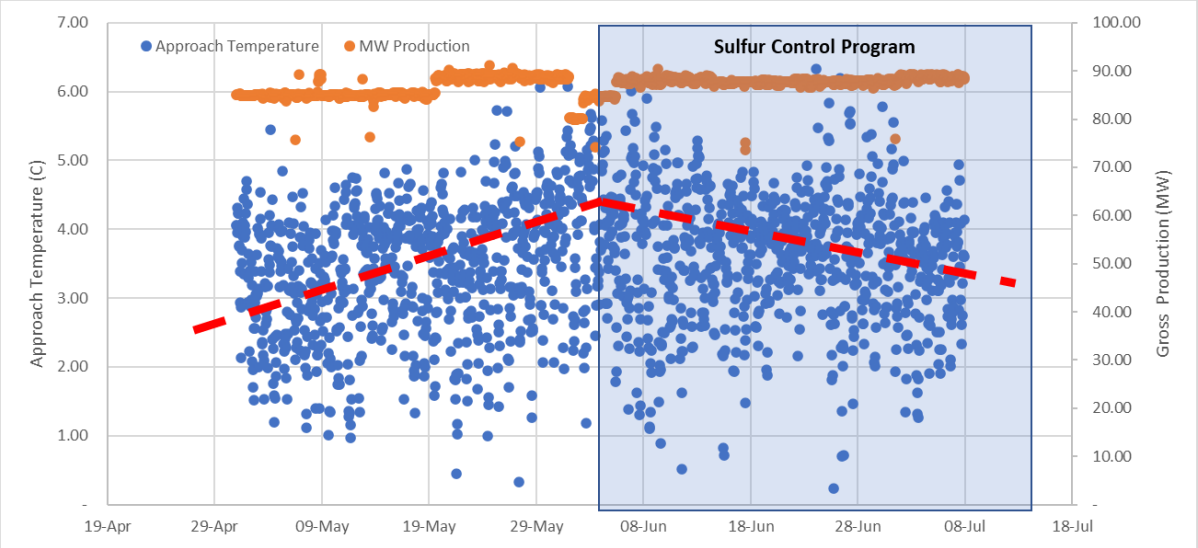

Figure 3: Approach temperature trend of site A.

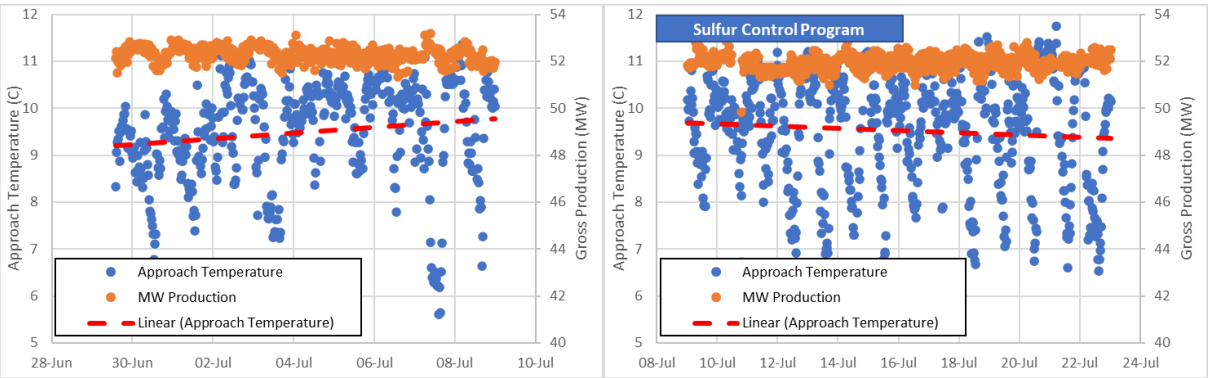

Figure 4: Approach temperature trend of site B.

3.2 Impact on Specific Steam Consumption

During the observation, we also monitor the specific steam consumption since eventually it will be a determining factor that dictate the total operating cost. As mentioned in the previous chapter, there are multiple factors that might affect the specific steam consumption, which include the cooling tower performance.

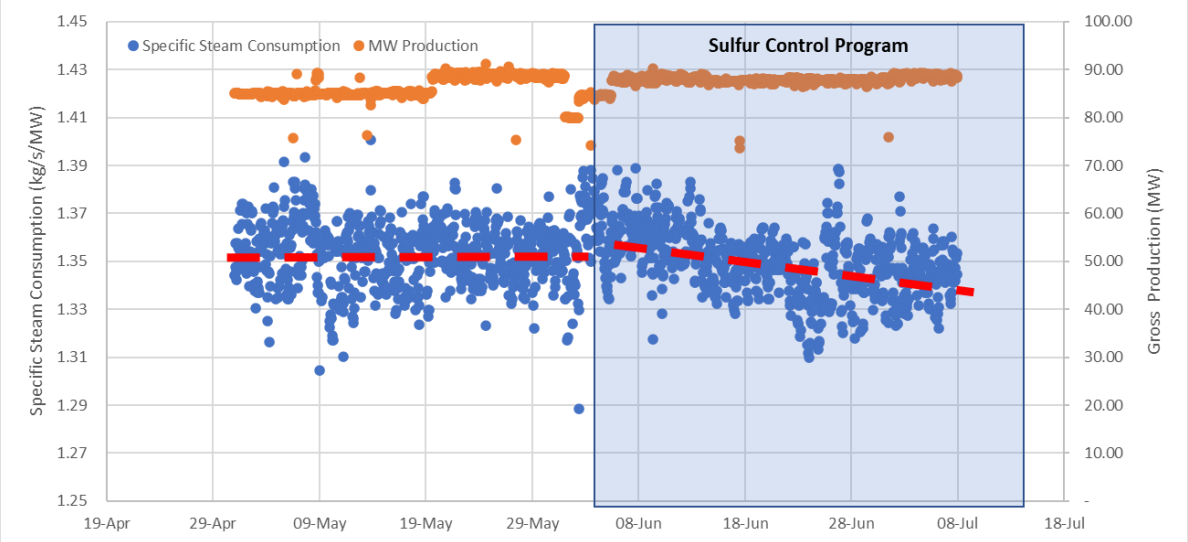

Figure 5: Plant A specific steam consumption and gross production.

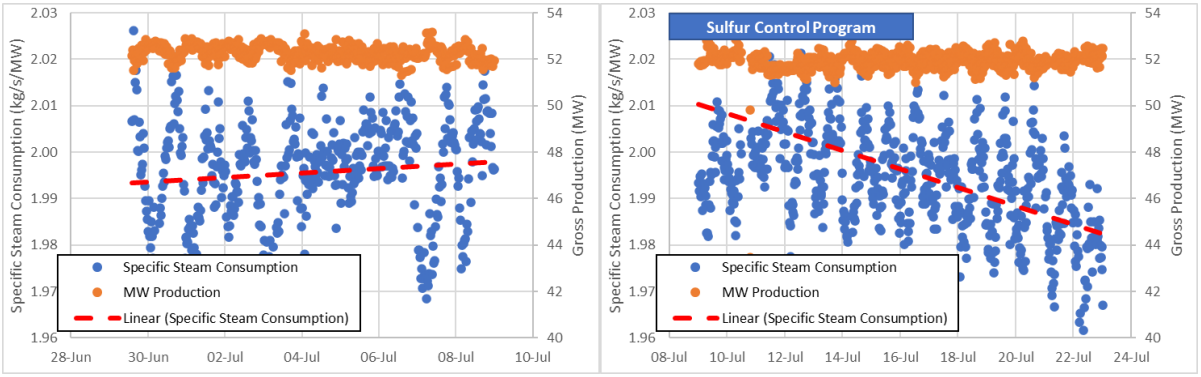

Figure 6: Plant B specific steam consumption and gross production.

Figure 5 displayed "Site A" and Figure 6 displayed "Site B" specific steam consumption against the MW production. As it can be inferred in the graph, there is an improvement on the specific steam consumption at the constant electricity production after sulfur control program is implemented.

Specific steam consumption decreases as more heat from the steam transformed into work by expander/turbine. In this condition higher energy per mass of steam could be transferred to the turbine, as the result of better heat transfer that could happen due to cleaner condenser or better performing cooling tower. From this observation, it can be concluded that the improvement on cooling water performance will help to reduce total plant operating cost by means of reducing specific steam consumption.

3.3 Impact on NaOH consumption

As described in the previous chapter, one of the indicators of uncontrolled SOB growth is the incremental increase of caustic consumption. Caustic consumption accounts for almost 70% of the total cooling water chemical treatment cost in geothermal facilities (Figure 7). It can be inferred that with a proper control of microbio growth in general and SOB growth in specific, the caustic consumption can be maintained and thus will help to prevent any increase of the total chemical cost.

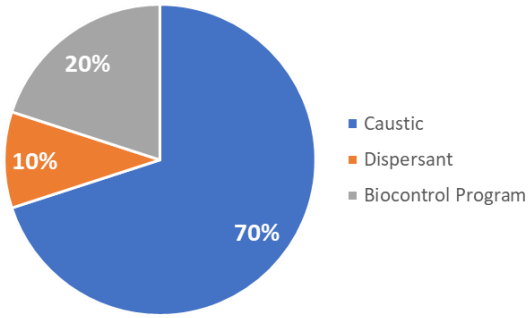

Figure 7: Geothermal chemical cost component distribution.

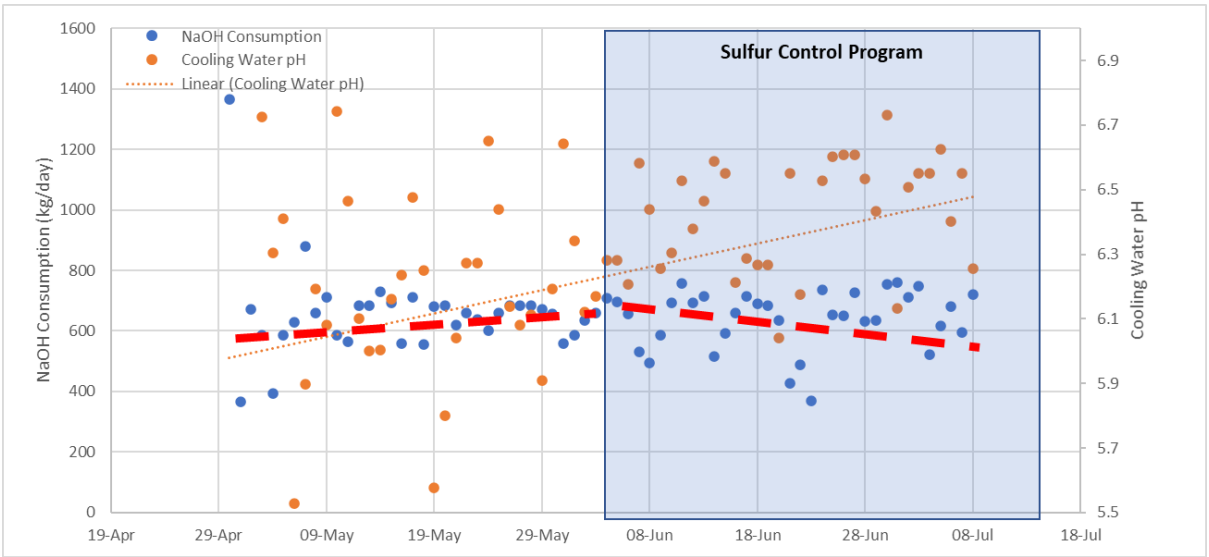

Figure 8: Geothermal chemical cost component distribution.

Figure 8 gives us a caustic consumption trend along with cooling water pH in “Site A”. After new sulfur control program is implemented, the caustic consumption slightly decreases to maintain the pH at higher control range. From this observation, we can conclude that the SOB growth has been suppressed by the chemical program, which caused reduction in acid production from the SOB (Richardson and Addison, 2014) The similar improvement also found at “Site B”, where the total caustic consumption is reduced by 20% after the implementation on new sulfur control program.

4. CONCLUSION

Based on the observation on the sulfur control program (GEO966, Purate®, and Isothiazoline) that has been implemented in several geothermal power plants, we can conclude that:

1. GEO966 can disperse the sulfur deposition formation and to some degree might help to clean the accumulated sulfur deposition in cooling tower filler. Thus, it will help to maintain the heat transfer in cooling tower, maintain approach temperature and specific steam consumption.
2. Combination of Purate® and Isothiazoline can help to maintain the microbio growth in general and SOB growth specifically. With controlled growth, the elemental sulfur formation will be reduced and acid by product from bacteria metabolism will be minimized. These conditions will lead to optimum caustic consumption and heat transfer efficiency to result optimum plant total operating cost.

REFERENCES

Aditiawati, P., Yohandini, H., Madayanti, F., and Akhmaloka: Microbial Diversity of Acidic Hot Spring (Kawah Hujan B) in Geothermal Field of Kamojang Area, West Java-Indonesia, *The Open Microbiology Journal*, (2009), 58–66. http://dx.doi.org/10.2174/1874285800903010058

Bharathi, P.A.L.: Sulfur cycle, Encyclopedia of Ecology, (2018), 192–199.

Characklis, W.G., Nevimons, M.J., and Picologlou, B.F.: Influence of fouling biofilms on heat transfer, *Heat Transfer Engineering*, 3, (1981), 23–37.

Hidayat, I., Kuntoaji, M., and Falah, D.: Increased Generation Performances by Using Sulfur Dispersant in the Cooling Tower at the Wayang Windu Geothermal Power Plant (A Lesson Learned from Wayang Windu Geothermal Power Plant Operation) I, *GRC Transactions*, 40, (2014), 829–838.

Kleinjan, W.E.: Biologically produced sulfur particles and polysulfide ions: effects on a biotechnological process for the removal of hydrogen sulfide from gas streams, (2005), 1-158.

Lv, Z., Cai, J., Sun, W., and Wang, L.: Analysis and optimization of open circulating cooling water system, *Water*, 10, Switzerland (2018), 1-16.

Ouali, S.: Introduction générale, (2018), 1-18.

Relenyi, A.G. and Rosser, H.R.: Sulfur Deposit Removal and Control in A Power Plant Cooling Tower: A Case History from Cerro Prieto, Mexico’s Largest Geothermal Field, *Proceedings*, New Zealand Geothermal Workshop, (2019), 1–9.

Richardson, I., Addison, S., and Addison, D.: Biological control of cooling water in geothermal power generation, *IPENZ Transactions*, 41, (2014), 1–10.

Sand, W.: Microbial life in geothermal waters, *Geothermics*, 32 (4), (2003), 655–667.

Sarmago, W. and Ho, P.: An Innovative Approach to Treating Geothermal Power Generating, *Proceedings*, INAGA Annual Scientific Conference, 5, Yogyakarta (2001), 3-7.

This page is intentionally left blank

Real Time Monitoring of Steam Chemical Composition in Geothermal Plant

Ahmad Marzuki and Ruben Lalamentik

PT Weebz Mandiri

ahmad.marzuki@weebzmandiri.com, ruben.lalamentik@weebzmandiri.com

Keywords: steam chemical composition, analyzer, sampling conditioning system, scaling, corrosion

ABSTRACT

Monitoring steam chemical compositions are important to prevent the damage of Steam Turbine such as scaling and corrosion as well as avoid unplanned shutdown of the plant. Mostly, the sampling in Geothermal Plant still using manual sampling, the result of chemical composition sometimes not represent the actual inside of pipeline due to some components will change at the transportation from field to laboratory as well as it representing the condition when the sample is taken. The preventive action to slow when the steam compositions are change. The improvement monitoring system should be improved to be real time condition.

The real time monitoring is designed carefully. The system will remove H2S and CO2 first before steam chemical analyzed by analyzer. Gas removal system using Nitrogen Sparger Method, Nitrogen comes from air instrument with pressure 80 to 120 psig supplied to the system. The gas H2S and CO2 separated from steam will be analyzed by Gas Analyzers. The steam free from H2S and CO2 contaminant will feed to the steam Analyzers for monitoring. Typically, steam chemical to be monitored are Silica, Conductivity, Natrium, pH and Dissolved Oxygen. Silica and Conductivity monitoring to prevent the Steam Turbine from scaling and abrasive. Natrium monitoring to inform brine carry over after scrubber. pH and Dissolved Oxygen monitoring to prevent Steam Turbine from corrosive.

Real Time Monitoring Steam Composition System in this paper designed to give the high accuracy on measurement, fast preventive action as well as predictive maintenance, simply to operational and cost efficient.

1. INTRODUCTION

Indonesia location in the Ring of Fire Zone it creates many volcanoes actively or not from west until east of Indonesia. This zone make the Indonesia has the largest geothermal resource in the world. The development of this renewable energy more challenging. We are still depending on the fossil energy, high technology requirement, and regulation. The geothermal plant development should consider about the steam chemicals come out from the reservoir to the surface. These chemicals monitoring is important to extend the life of geothermal plant operational. The geothermal operational will disturbed if these steam chemicals monitoring avoided. The main problem caused by scaling and corrosion in the casing production well, steam turbine, pipeline and reinjection well.

Currently, operator sampling the steam manually to measure the chemical composition. The important point to be considered is how this steam sampled represent the actual condition. This sample representative influenced on how to collect the sample, handle the sample and measurement method used. If those concerns avoid the sample collected will not represent the actual condition. The impact, geothermal plant will unplanned shutdown. Designing the right sampling conditioning system and real time monitoring these steam chemicals are the key point to get the highest accuracy of sample measurement and maintain the longer life of geothermal plant. This design installed close with utility facilities such as cooling water and air instrument. The sample tapping point location after scrubber or before inlet steam turbine.

2. SAMPLING CONDITIONING SYSTEM DESIGN

Sampling conditioning system design is the critical point to get the representative chemical measurement and maintain the longer life of analyzers. This sampling conditioning system has the function to control the sample flow rate, sample temperature and sample pressure compatible with analyzer specification. Also, H2S and CO2 removal system added to this design. These H2S and CO2 removal system will maintain sensor analyzer longer life time and create the higher accuracy on the chemical measurement. All components sampling conditioning below will be integrated in one panel modular. See the P&ID sampling conditioning system at Figure 1.

2.1 Isokinetic Probe

The capture of sample from steam pipeline using isokinetic probe type. This isokinetic probe makes the velocity sample to be captured equivalent with velocity steam flowing in the pipeline. The port of nozzle should face the flow of fluid. If the velocity captured lower or higher than velocity flowing inside of pipeline the capture of chemical composition will bias. There are any two types of these isokinetic single port nozzle type or multiple nozzle type. The insertion length of single port nozzle from wall pipeline close with average velocity of fluid inside of pipeline typically this average of velocity at the 0.2R. For multiple port nozzle will capture the velocity sample fully cross section area of pipeline. Each bore diameter of port should be calculated close with velocity sample per segmental within cross section are pipeline. The characteristic of velocity flowing inside of pipeline higher in the center of pipeline and lower close with wall pipeline due to friction contact between fluid and wall of pipeline. The other important point for this isokinetic probe is material selection consideration. Select the material suitable with steam condition to prevent corrosion.

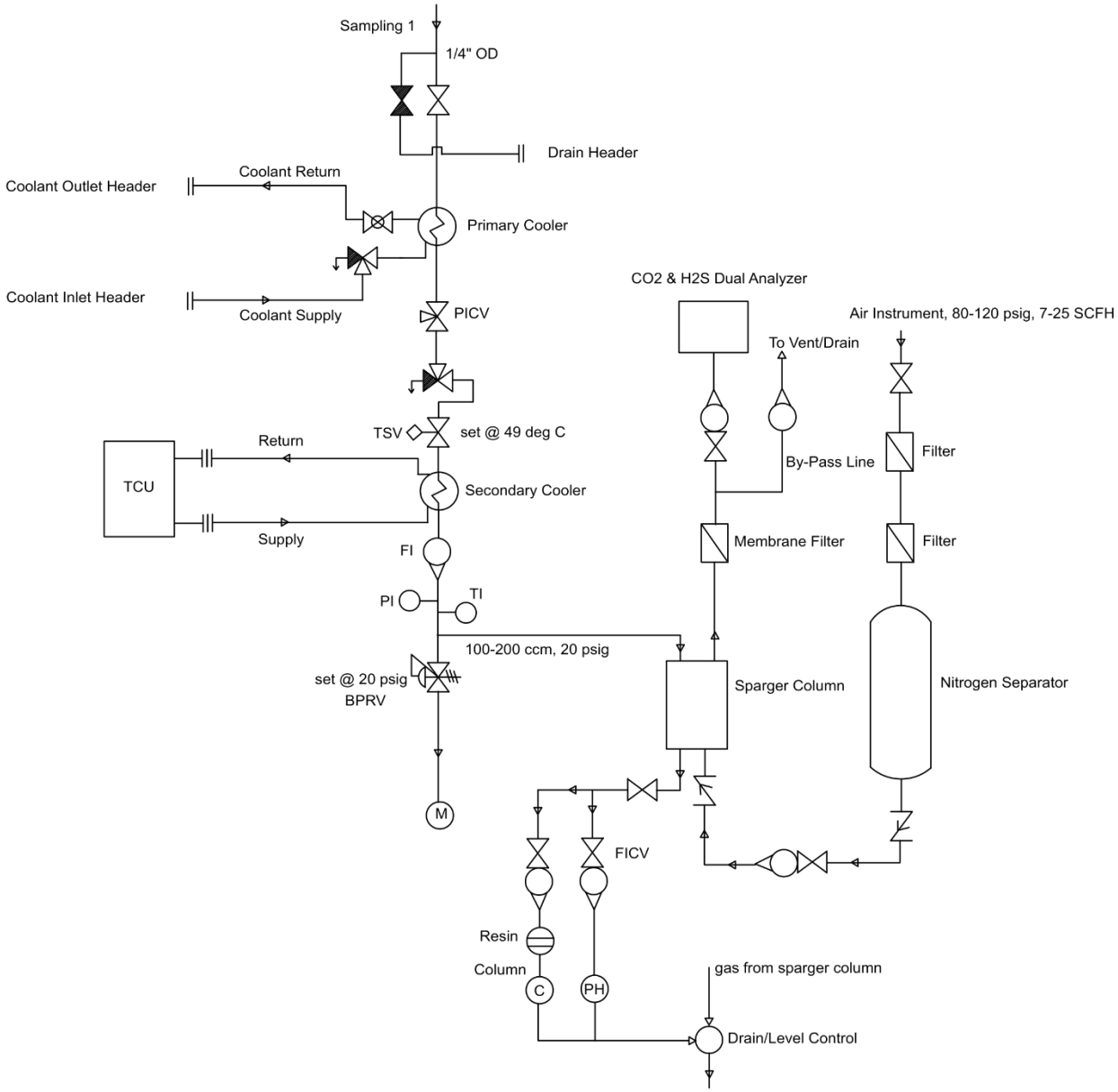

Figure 1: Sampling Conditioning System P&ID.

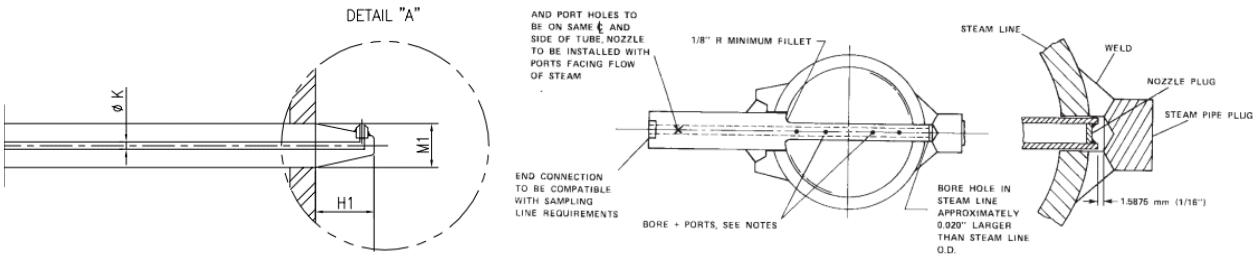

Figure 2: Single port nozzle isokinetic probe (left) and Multiple port nozzle isokinetic probe (right).

2.2 Sample Cooler

The high sample temperature will be cooling down using sample cooler. This sample cooler requires coolant water with temperature 25 deg C or less. Typically, the sample temperature close with coolant temperature at the outlet sample cooler. Coolant flow rate, sample flow rate and coolant operating pressure to be considered to prevent the cavitation inside of sample cooler. If the coolant flow rate too slow the sample fluid will be overheating to its boiling point. If sample flow rate too high the coolant water will be overheating to its boiling point. Then, if coolant operating pressure too slow the sample fluid will boil at a low temperature. This cavitation will create the vibration which can fatigue and ultimately fracture the tubes inside of cooler. The design of sample cooler is counter flow between sample flowing and coolant water flowing, tube surface area and length of spiral tube influence the effectiveness of heat transfer between sample and coolant water. The material selection of cooler to be consider, if the sample fluid or coolant water has

chloride content, we recommend to use Incoloy 625 material instead of 316 SS. This chloride will damage the oxide layer which protect 316 SS from corrosion. If coolant water has temperature more than 30 deg C, we recommend to use secondary sample cooler with coolant water comes from refrigerant or Thermal Control Unit (TCU) with temperature 25 deg C.

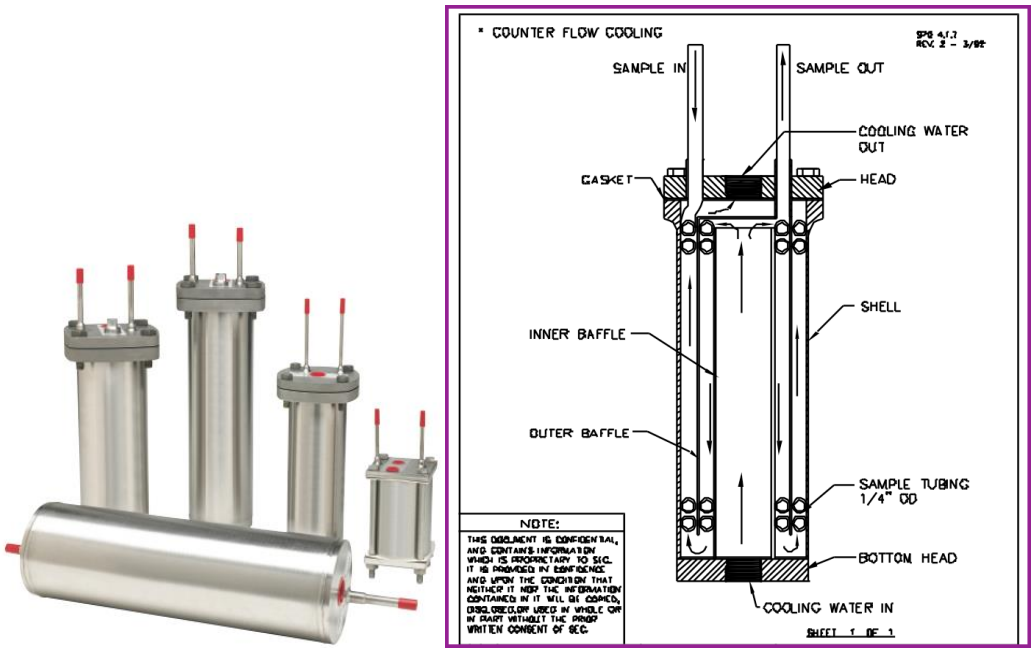

Figure 3: Sample cooler (left) and Counter flow between coolant and sample fluid (right) (Courtesy of Sentry).

2.3 Pressure Reducing

Pressure reducing has the function to reduce sample pressure and to control the sample flow rate. For sample pressure less than 500 psig, needle valve is recommended. The sample pressure should reduce close with analyzer specification.

Figure 4: Needle valve (Courtesy of Swagelok).

2.4 Thermal Shut Off Valve

This thermal shut off valve has function to protect analyzer when the sample cooler fails to reduce sample temperature below set point. In this case the set point is 49 deg C. If the sample temperature more than 49 deg C, TSV will close automatically and require open the valve manually. Before the valve open, operator will check the root problem of why sample cooler failed to reduce sample temperature. The TSV able to indicate the sample temperature higher than set point using local indicator or dry contact to trigger the alarm.

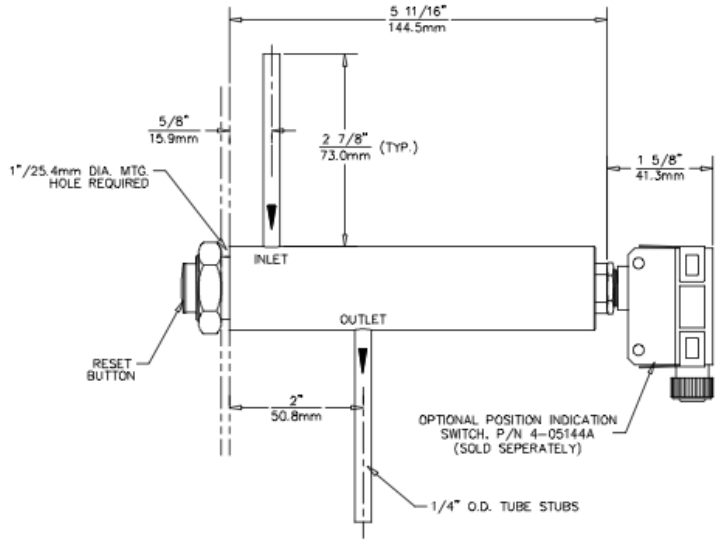

Figure 5: Thermal shut off valve (TSV) (Courtesy of Sentry).

2.5 H2S and CO2 Removal System

The method used in H2S and CO2 removal system is sparger nitrogen. The sample injected by nitrogen to flash the H2S and CO2, the nitrogen is inert and push both of gas using partial pressure following Henry's law. The process inside of sparger column with nitrogen pressure range 80 to 120 psig. The fluid level is maintained half of sparger column to get the effectiveness of process. It requires nitrogen bottle or air instrument utility facility. If air instrument used the air composition (20% oxygen and 78% nitrogen, 2% other components) will separated using membrane fiber. This membrane using thousand fibers enclosed with material. The nitrogen component will be captured by this membrane the separated from others component. The purity of this nitrogen generation up to 99.5% with rating up to 26.5 barg. This nitrogen feed to sparger column to separate H2S and CO2 contents from sample fluid.

Figure 6: Sparger column integrated with nitrogen generator (left) membrane fiber in nitrogen generator (right) (Courtesy of Sentry).

2.6 Back Pressure Regulator and Relief Valve (BPRV)

Back pressure regulator and relief valve are combination function in one item. The item installed at the downstream sampling conditioning system. Back pressure regulator set point is 20 psig and has function to control the sample flow rate and constant pressure 20 psig to the analyzers. If the sample pressure over 20 psi above set point the back pressure regulator release the remain of pressure to be manual sample. If the pressure over 10 psig above set point relief valve working and relief the pressure to be manual sampling.

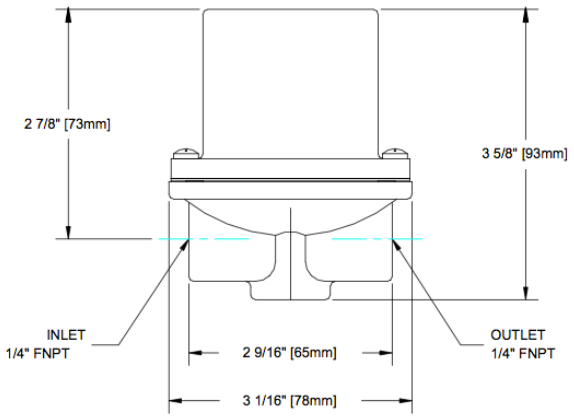

Figure 7: Back pressure regulator and Relief valve (Courtesy of Sentry).

3. ANALYZERS

Analyzer is the one of important component beside of sampling conditioning system. After sample conditioned to the analyzer specification and H2S and CO2 free contamination it feeds to the analyzer to measure the chemical composition in real time or continuously. In this case, the analyzer to be used are pH analyzer and Dissolved Oxygen (DO) analyzer to measure the corrosion content inside of sample, Silica analyzer and Conductivity analyzer to measure the silica particle and ion dissolved in the sample to prevent scaling and abrasive on the steam turbine, Natrium analyzer to measure brine content passing the scrubber. Also, the H2S and CO2 after separated from sparger column will feed to the H2S and CO2 analyzer to measure gas contents. Each of analyzers has specific technology.

3.1 pH Analyzer

pH analyzer will measure pH sample in range 0-14. If pH less than 7.0 the sample in acid condition and pH more than 7.0 the sample in base condition. The technology using electrode to measure the pH content. When the pH reading less than 4.0, operator able to detect the sulphate ion dissolved in their sample if the pH reading more than 7.0, operator able to detect the travertine dissolved in their sample. So, the pH measurement can tell the operator about the corrosion content or contaminant content in their sample.

3.2 Dissolved Oxygen Analyzer

Dissolved oxygen analyzer has the function to measure oxygen content dissolved in the sample. Dissolved oxygen can react with metal to create corrosion. If the dissolved oxygen upset the operator will inject the oxygen scavenger to maintain the dissolved oxygen less than set point. Combination between pH measurement is powerful to tell the corrosion condition in the geothermal plant.

3.3 Silica Analyzer

Silica analyzer will measure the silica content in the sample. Silica is one of the main problems in the geothermal plant due to create plugging or scaling in the pipeline or blade of steam turbine. The geothermal plant will unplanned shutdown. If the silica content upset detected by analyzer, operator will inject the silica inhibitor to prevent scaling and plugging. Technology used in the silica analyzer is colorimeter. The sample will be combined with reagent then measured the silica content by optically.

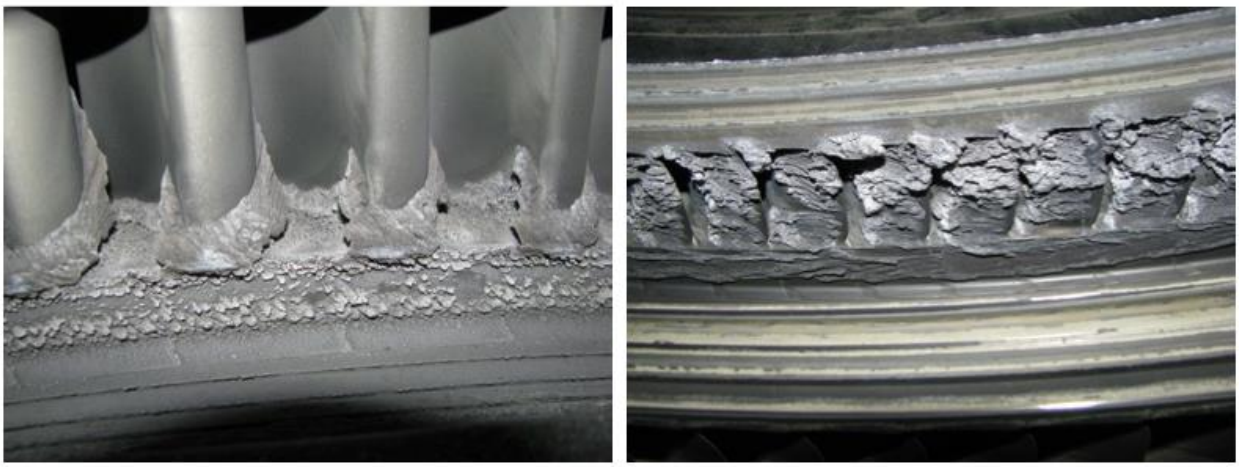

Figure 8: Silica Deposit on the blade steam turbine (Richardson et al., 2014).

3.4 Conductivity Analyzer

Conductivity analyzer has the function to measure the ion contents inside of the steam. This ion contents related to particle dissolved in the steam. CO2 can influent the reading of conductivity because CO2 dissolved in the water can create carbonate ion and bicarbonate ion. So, the contact sample with air directly can influence the conductivity content. The high velocity of steam with high ions content can create the abrasive on the piping, valve or blade of steam turbine. This abrasive can influence the integrity of plant component. Technology used in the conductivity analyzer is electrochemical or membrane technology. Combination measurement with silica analyzer can tell operator about scaling deposition and abrasive potentially in their plant.

3.5 Natrium Analyzer

Natrium dissolved in the brine fluid. Natrium analyzer measure Na+ ion dissolved in the sample. So, the natrium reading can tell the operator that the brine or liquid content pass from scrubber and correlated inform the operator that the scrubber has been saturated and need to be changed. This brine content passing the scrubber will damage the steam turbine.

3.6 H2S Analyzer

H2S analyzer can inform the H2S content inside of sample. The analyzer technology to detect this H2S is tape technology. Tape and H2S can react to create black shadow in the tape. LED can detect this black shadow zone in the tape and correlate with H2S content. The measurement of H2S is important when it is vented to the ambient. H2S is toxic gas and can influence to the environment.

3.7 CO2 Analyzer

CO2 analyzer can inform the CO2 content inside of sample. The analyzer technology to detect this CO2 is infrared technology. Infra-red will be shot to the sample the different intensity of infra-red absorbed correlated to the CO2 content in the sample. CO2 is the odorless and toxic gas; the measurement of CO2 is important when it is vented to the ambient. The CO2 content released to atmosphere should following government regulation about environment.

All the data from each analyzer transmitted to control room using analog output 4-20 mA for continuous monitoring. Also, all the data stored and recorded in real time at the analyzer memory.

4. CONCLUSION

Combination between sampling conditioning system and analyzers can tell the operator about the steam condition in the geothermal plant in real time and representative, the action can be faster to prevent the damage of plant due to chemical attack, reduce operational cost, prevent the unplanned shutdown and increase the steam production.

REFERENCES

ASTM D 1066: Standard Practice for Sampling Steam, (2001), 29.

Environment Minister Regulation No. 21/2008 about source emission quality standard and or for thermal power generation, (2008).

EPRI: Cycling, Startup, Shutdown, and Layup Fossil Plant Cycle Chemistry Guidelines for Operators and Chemists (1015657), Palo Alto, CA (2009).

Richardson, I., Addison, S., and Lawson, R.: Chemistry Challenges in Geothermal Power Generation, *Conference: API Powerchem*, Australia (2014).

Analysis of Cooling Water Flow in the Condenser to Improve the Performance of Dieng Geothermal Power Plant

Arief Surachman

arief.surachman@bppt.go.id

Keywords: Condenser, Cooling tower, Geothermal, Power plant, Renewable energy

ABSTRACT

Currently, geothermal energy has been widely used as a reliable renewable energy and environmentally friendly source of power generation. Indonesia is one of the countries with the largest geothermal potential. There are existing geothermal power plants already built. There are two ways to increase the power output of geothermal power plants. First, build power plants in new areas and the second is improving the thermal efficiency of power plants. This study will discuss the influence of ambient conditions at the Dieng geothermal against the performance of a cooling tower that affects plant performance. This study used a simulation Engineering Equation Solver (EES) program. After the simulation, the optimum pressure separator is 9.9 bar, and the vapor fraction is 0.34, for the maximum working turbines are 27.897 MW. The maximum turbine work is affected by ambient temperature change, the cooling water flowed from the condenser to the cooling tower is 1753 kg/s. Actually, the cooling water that supplies the condenser fluctuates according to changes in ambient temperature, changes in outside air temperature of 15.1 degrees up to 22.2 degrees Celsius The amount of cooling water that supplies the condenser can be controlled by a Variable Frequency Drive (VFD) to adapt the ambient temperature change at which the plant operates.

1. INTRODUCTION

Indonesia is one of the countries in the world traversed by the ring of fire which hence many active volcanoes exist in Indonesia (Nasruddin et al., 2016). The volcanoes spread on the island of Sumatra, Jawa, Nusa Tenggara, Maluku, and Sulawesi, where there are 117 active volcanoes (Hamilton, 1979; Manalu, 1988).

As the results, Indonesia has around 256 potential areas of geothermal energy (Christine, 2012). It is a fact that Indonesia has the largest potential of geothermal energy in the world, which covers about 40% of world's potential or at 28,617 MW, but the utilization is not optimal, especially for geothermal power plants (Sukhyar et al., 2010). The geothermal potential utilized in Indonesia until 2012 was only 4.6% (Ilyas, 2012). The Indonesian government until 2025 has plan to construct of geothermal power plants of 9500 MW (Idral and Mansoer, 2015). One of the objectives of this geothermal power plant is to reduce dependence on fossil energy sources and reduce greenhouse gas emissions (Presidential Regulation of the Republic of Indonesia No. 5, 2006). Generally, the geothermal energy system in Indonesia is the hydrothermal system which produces high temperature over 225 °C, and only a few of hydrothermal systems have a lower temperature between 150-225 °C. The country's geothermal potential and installed capacity status are presented in Table 1 (Mahlia and Yanti, 2010).

In 1978, the first geothermal power plant was built in Kamojang as a pilot project with installed capacity of 0.25 MW (Kementerian Energi dan Sumber Daya Mineral, 2014). In 1983, the geothermal power plant Unit I Kamojang commercially operated with an installed power of 30 MW. Then in 1987, the geothermal power station Kamojang was coupled with Unit II and III with the total capacity of 110 MW. In 2008, the addition capacity of 60 MW at Unit IV developed. Those four units can generate power up to 200 MW (Idral and Mansoer, 2015).

Currently, the geothermal energy in Indonesia that used for power generation is 1,196 MW. It comes from seven plants in different locations: Darajat (260 MW), Dieng (60 MW), Kamojang (200 MW), Mount Salak (377 MW), Sibayak (12 MW), Lahendong (60 MW), and WayangWindu (227 MW) (Sofyan et al., 2010).

There are two ways to increase the power output of geothermal power plants. First, build power plants in new areas and the second is improving the thermal efficiency of power plants (Dwikorianto et al., 2010).

The paper will discuss the influence of ambient conditions at the Dieng geothermal against the performance of a cooling tower that affects plant performance by saving on pumps energy used in the cooling tower.

Table 1: Indonesia's potential geothermal and installed capacity status in December 2012 (in MW) (Christine, 2012).

Island	Potential Energy (MW)			Installed Capacity
	Resources	Reserve	Total	
Sumatra	5,516	7,244	12,760	122
Jawa	3,536	6,181	9,717	1,134
Bali-Nusa Tenggara	777	1,028	1,805	7.5
Sulawesi	1,442	1,602	3,044	80
Maluku	642	4,29	1,071	-
Kalimantan	145	-	145	-
Papua	75	-	75	-
			28,617	1,343.5

2. METHODS

Dieng geothermal power plant located in Banjarnegara and Wonosobo, Central Java which lies to the west of Mount Sindoro and Mount Sumbing. Dieng is an active volcanic region which has some craters. Dieng has a height of about 2,000 m above sea level. Temperatures range from 12-20°C in the day and 6-10°C in the night. The steam in Dieng has two phases: the liquid state and the vapor state, and it is dominated by the liquid which the temperature ranges from 240-333°C (Pambudi et al., 2014). The type Dieng geothermal power plant is a single flash with an installed capacity of 60 MW. There are eight production wells in four locations that supply the plant (Presidential Regulation of the Republic of Indonesia No. 5, 2006). Dieng geothermal power plant began operating at May 14, 1981 (Shulman, 1981) and Dieng is the first plant in Indonesia with water-dominated (DiPippo, 2012). The simple plant scheme of Dieng is given in Figure 1, by assuming a single production well in one separator.

Schematic diagram of this study methodology can be seen in Figure 2. The steam which comes out from the production well is throttled isenthalpic to 9.9 bar. Then steam and water vapor is separated by a separator and cleaned by a scrubber before entering the turbine.

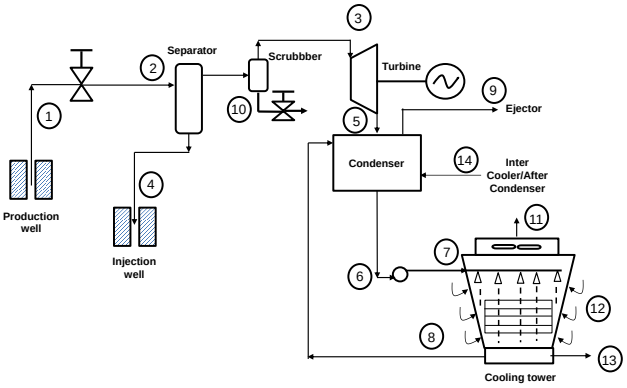

Figure 1: Dieng simple plant scheme.

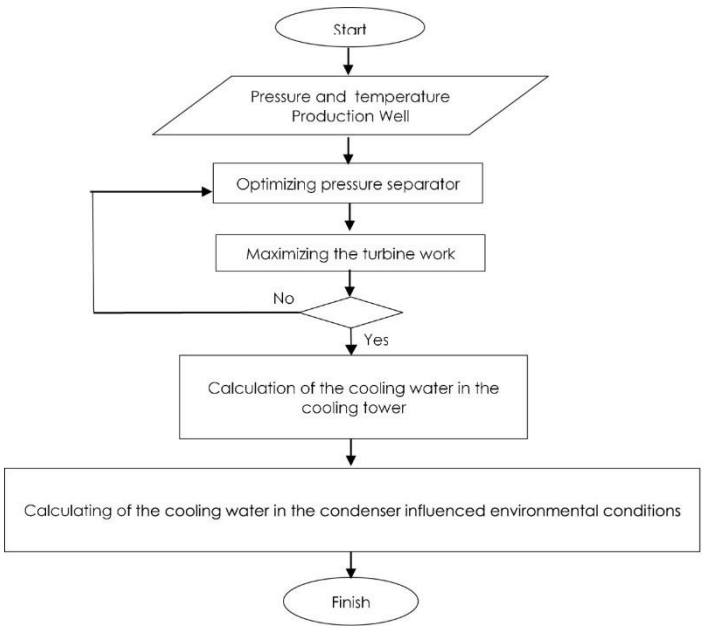

Figure 2: Schematic diagram of the optimization procedure.

Enthalpy of two-phase fluid enters the separator, and in the reservoir its enthalpy is determined by assuming single phase liquid water at specific temperature. The steam fraction in the separator is obtained by:

$$x_2 = \frac{h_2 - h_4}{h_3 - h_4} \quad (1)$$

where x_2 is the steam fractions, h_2 is the fluid enthalpy at the separator inlet, h_3 is the enthalpy of steam at the separator exit, h_4 is the enthalpy of brine. The steam from the separators, flows into the turbine. The steam turbine has isentropic efficiency equation as follow:

$$\eta_{isen} = \frac{h_3 - h_5}{h_3 - h_{5s}} \quad (2)$$

η_{isen} is isentropic efficiency of the turbine, h_{5s} is the isentropic enthalpy from the turbine exhaust. With,

$$\eta_{isen} = 0{,}85 \tag{3}$$

The turbine power is given by:

$$W_{turbine} = \dot{m}_3(h_3 - h_5) \tag{4}$$

Where h_5 is the enthalpy of steam at the turbine exit.

The steam from the turbine, flows to the condenser at a pressure 0.07 bar and the temperature 38°C. The condenser is direct contact type, which steam and cooling water contact directly in a spray system. According to the first law of thermodynamics, the equations of mass and energy balance for the condenser:

$$\dot{m}_5 + \dot{m}_8 + \dot{m}_{14} = \dot{m}_6 + \dot{m}_9 \tag{5}$$

Where $\dot{m}_5$, $\dot{m}_8$ and $\dot{m}_{14}$ is mass flow rate into the condenser from the turbine, cooling tower and inter-cooler condenser respectively, $\dot{m}_6$ and $\dot{m}_9$ is mass flow rate exit from the condenser

and;

$$\dot{m}_5 h_5 + \dot{m}_8 h_8 + \dot{m}_{14} h_{14} = \dot{m}_6 h_6 + \dot{m}_9 h_9 \tag{6}$$

where h_5, h_8 and h_{14} is enthalpy in the turbine, cooling tower and inter-cooler condenser respectively. h_6 and h_9 are enthalpy in the condenser.

The water (condensate) from the condenser flows into the cooling tower. The mass and energy balance equations for the cooling tower:

$$\dot{m}_7 + \dot{m}_{12} = \dot{m}_8 + \dot{m}_{13} + \dot{m}_{11} \tag{7}$$

Where $\dot{m}_7$ and $\dot{m}_{12}$ is mass flow rate into the cooling tower from the condenser and environtment respectively. $\dot{m}_{13}$ and $\dot{m}_{11}$ is mass flow rate exit the cooling tower.

and;

$$\dot{m}_7 h_7 + \dot{m}_{12} h_{12} = \dot{m}_8 h_8 + \dot{m}_{13} h_{13} + \dot{m}_{11} h_{11} \tag{8}$$

Where h_7, and h_{12} is enthalpy in the condenser environment respectively.

The evaporated mass flow rate is:

$$\dot{m}_{11} = \dot{m}_a\,(\omega_{11} - \omega_{12}) \tag{9}$$

Where $\dot{m}_a$, ω_{11} and ω_{12} is mass flow rate dry air, defined as the mass of water vapor (Engkos et al., 2016), humidity ratio wet air and humidity ratio dry air respectively.

In order to calculate inlet and outlet air enthalpy and humidity ratio, cooling tower effectivity equation are given by:

$$Eff\ cooling\ tower = \frac{\omega_{11} - \omega_{12}}{\omega_{11,max} - \omega_{12}} \tag{10}$$

$$Eff\ cooling\ tower = \frac{h_{11} - h_{12}}{h_{11,max} - h_{12}} \tag{11}$$

which $h_{11,max}$ and $\omega_{11,max}$ are the maximum outside air condition which has the same temperature with water inlet, and the relative humidity is 100%.

3. RESULTS AND DISCUSSION

The important properties of the states of the Dieng power plant according to Figure 1 are given in Table 2. In this table, the results of optimization with pressure and the ambient temperature is 0.78 bar and 18°C respectively. The obtained optimum pressure coming into the turbine is 9.9 bar which is shown in Figure 3 with the vapor fraction 0.3473 as in Figure 4 so that the power 27.897 MW is generated by the turbine. The cooling water flows into the condenser so that constant pressure (0.07 bar) is equal to 1753 kg/s.

Having obtained the optimum pressure steam entering the turbine, 9.9 bar, and the flow of cooling water entering the condenser, 1754 kg/s, the plant works at the optimum condition regardless of the ambient temperature in which the plant operates. This study simulates the effect of ambient temperature of the cooling water which flows into the condenser. After the simulation using Engineering Equation Solver (EES), the cooling water supplied to the condenser depending on the ambient temperature in which the plant operates. So that we can control cooling water to condenser according to the outside air temperature, thus we can save cooling water flows into the condenser and save the energy required for the pump, because the cooling water flows into the condenser if without regard the environmental conditions like-pressure and ambient temperature, the cooling water flows into the condenser is 1753 kg/s. The simulation in one day found the cooling water supplied the condenser at 02.00 pm where the temperature 22.2 °C, which amounted

to 1755 kg/s, over the amount of cooling water that enter the condenser during optimum conditions regardless the ambient temperature, amounting to 1753 kg/s, as shown in Figure 5.

Table 2: The parameters for the stages of Dieng power plant.

Stage	Pressure (bar)	Enthalpy (kJ/kg)	Entropy (kJ/kg-ºC)	Mass Flow (kg/s)
1	112.8	1461	3.448	138.9
2	9.9	1461	3.682	138.9
3	9.9	2777	6.589	48.24
4	9.9	761	2.135	90.66
5	9.9	2777	6.589	48.24
6	0.07	2156	6.941	48.24
7	0.95	159	0.5454	4354
8	1.42	460.2	-	1673
9	0.07	-	-	0.7141
10	-	-	-	-
11	0.78	144.8	0.4685	0.0463
12	0.78	467.7	-	2884
13	2.1	113.3	-	88.31
14				8934

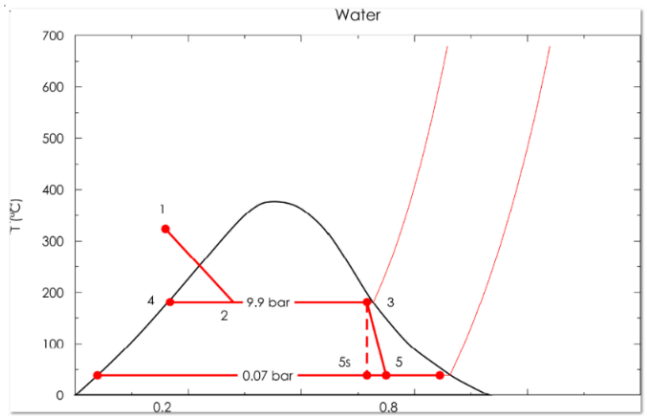

Figure 3: Actual work of turbine and steam fractions as functions of separator pressure/ pressure inlet turbine.

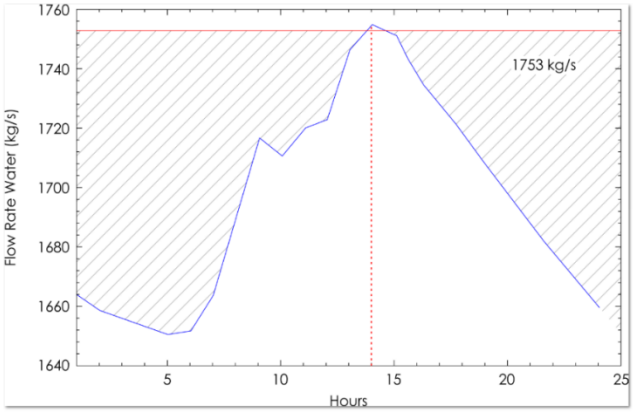

Figure 4: Cooling water flow rate in one day.

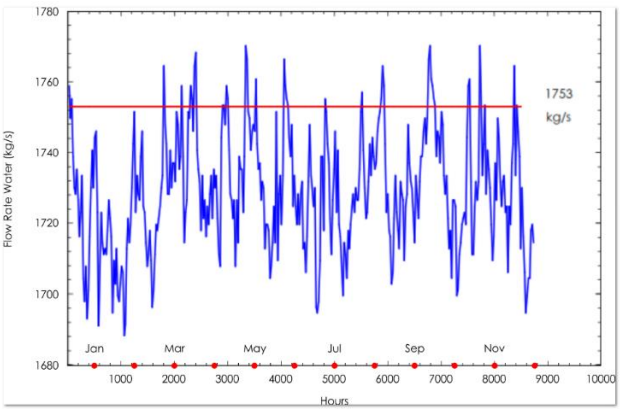

Figure 5: Cooling water flow rate in hours for one year.

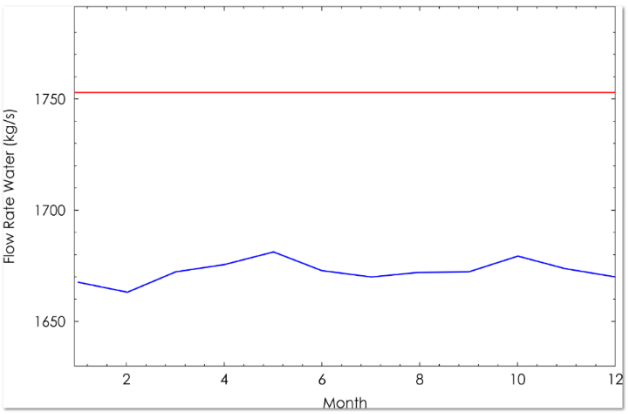

Figure 6: Cooling water flow rate in one year.

In Figure 5, the shaded part is the cooling water that can be saved for the cooling condenser, in which the plant operates for one day, the flow of water entering the condenser below the rate of 1753 kg/s. At these times, the ambient temperature is below the temperature of 18ºC.The amount of cooling water supplied to the condenser in every hour for one year can be seen in Figure 6. In this Figure, it appears that the cooling water to the condenser is generally below the rate of 1753 kg/s. If the result of the calculation of hourly averaged in each month, it is clear that the cooling water entering into the condenser every month under 1753 kg/s as shown in Figure 6.

From the result of all the simulations, it shows that the water flows so the pressure of condenser is constant and the working turbine is 27.897 MW (maximum). The amount of delivered water should be smaller than 1754 kg/s. Thus, the needs of energy to pump the cooling water can be saved.

Automatic Cooling Water System (ACWS)

The parasitic load on the power plant is dominated by the cooling water (Ridwan et al., 2010). The power plant cooling system is highly dependent on temperature and mass of cooling water. In geothermal power plants the cooling water temperature is strongly influenced by ambient air temperature, Because the cooling water after use as coolant in the condenser will be flowed to the cooling tower to be cooled back using the outside air. After cooling water cooled in the cooling tower, the water will be used as coolant in the condenser. The amount of water that flows into the condenser as a coolant is highly dependent on the temperature of the water used. The lower the water temperature used the less amount of water flowed the condenser, and if water temperature is flowing higher so that the amount of water that flows more and more. So the amount of water that flowed into the condenser is greatly influenced by the temperature of the outside air. The amount of cooling water that flows into the condenser varies because the temperature of the outside air in the geothermal power generation area is also constantly changing.

One of the methods to save the supplied cooling water to the condenser is controlling the amount of cooling water to the condenser which is adapted to the ambient temperature in which the plant operates. Controlling the amount of cooling water flow can be done by installing a Variable Frequency Drive (VFD) on the pumps which drain the cooling water from the cooling tower to the condenser.

The configuration of the flow model automatic cooling water system as shown in Figure 7.

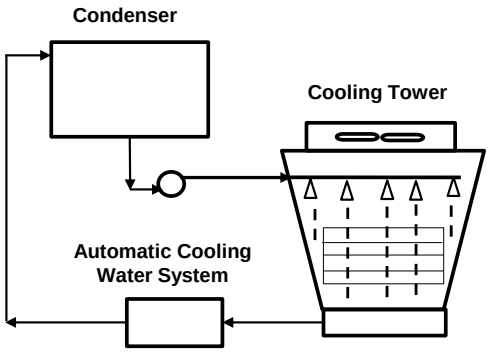

Figure 7: Automatic cooling water system.

4. CONCLUSION

From the simulation, the optimum pressure separator is 9.9 bar, and the vapor fraction is 0.34, so the maximum working turbines are 27.897 MW. To maintain the maximum turbine work regardless of ambient temperature change, the cooling water flowed from the condenser to the cooling tower is 1753 kg / s. Actually, the cooling water that supplies the condenser fluctuates according to changes in ambient temperature. So, the flow of cooling water can be adjusted to the ambient temperature which the plant. The amount of cooling water that supplies the condenser can be controlled by a Variable Frequency Drive (VFD) to adapt the ambient temperature change at which the plant operates.

5. ACKNOWLEDGEMENT

This research is fully supported by Central of Technology Audit System - Agency for the Assessment and Application of Technology.

REFERENCES

Christine Risch EE.: Geothermal Energy: The Economics of West Virginia's EGS Potential, Center for Business and Economic Research, Marshal University (2012).

DiPippo, R.: Geothermal Power Plants: Principles, Applications, Case Studies and Environmental Impact, Butterworth-Heinemann (2012).

Dwikorianto, T., Zuhro, A.A., and Yani, A.: Sustainable Development of the Kamojang Geothermal Field, *Geothermics*, 39(4), (2010), 391-399.

Engkos, A., Kosasih, and Ruhyat, N.: Combination of Electric Air Heater and Refrigeration System to Reduce Energy Consumption: A Simulation of Thermodynamic System, *International Journal of Technology (IJTech)*, 7(2), (2016), 78-85 ISSN 2086-9614. https://doi.org/10.14716/ijtech.v7i2.3004

Hamilton, W.B.: Tectonics of the Indonesian region (No. 1078), US Govt. Print. Off (1979).

Idral, A. and Mansoer, W.R.: Geothermal resources development in Indonesia: a history, *Proceedings*, World Geothermal Congress 2015, Melbourne, Australia, 19 25 April (2015).

Ilyas, Z.: Pemanfaatan Energi Geothermal dan Dampak Perubahan Iklim, Seminar Nasional VIII SDM Teknologi Nuklir, (2012).

Kementerian Energi dan Sumber Daya Mineral: Pengembangan Panasbumi di Indonesia, Direktorat Energi Baru Terbarukan dan Konservasi Energi, Kementerian Energi dan Sumber Daya Mineral Republik Indonesia (2014).

Mahlia, T.M.I. and Yanti, P.A.A.: Cost Efficiency Analysis and Emission Reduction by Implementation of Energy Efficiency Standards for Electric Motors, *Journal of Cleaner Production*, 18(4), (2010), 365-374.

Manalu, P.: Geothermal Development in Indonesia, *Geothermics*, 17(2), (1988), 415-420,

Nasruddin, Alhamid, M.I., Daud, Y., Surachman, A., Sugiyono, A., Aditya, H.B., and Mahlia, T.M.I.: Potential of Geothermal Energy for Electricity Generation in Indonesia: A Review, *Renewable and Sustainable Energy Reviews*, 53, (2016), 733-740.

Pambudi, N.A., Itoi, R., Jalilinasrabady, S., and Jaelani, K.: Exergy Analysis and Optimization of Dieng Single-Flash Geothermal Power Plant, *Energy Conversion and Management*, 78, (2014), 405-411.

Ridwan R.H., Pakpahan P., Fauzi, T.A., Khasani, Zulkarnaen, A.M., Effendi, H., and Nasution, A.: Automatic Main Cooling Water System (aMCWS), *Proceedings*, World Geothermal Congress 2010, Bali, Indonesia, 25-29 April 2010, (2010).

Sekretariat Kabinet: Peraturan Presiden Republik Indonesia Nomor 5 tahun 2006 Tentang Kebijakan Energi Nasional, In: Kabinet S, editor, Sekretariat Kabinet, Jakarta (2006).

Shulman, G.: Geothermal power development in Indonesia, *Trans.-Geotherm. Resour. Counc.*, 5(CONF-811015-), United States (1981).

Sofyan, Y., Daud, Y., Kamah, Y., and Ehara, S.: Microgravity Method to Model Mass Balance in the Kamojang Geothermal Field, *Current Applied Physics*. 10(2), (2010), S108-S112.

Sukhyar, R., Soedibjo, A.W., Ganefianto, N., and Stimac, J.: Geothermal Energy Update: Geothermal Energy Development and Utilization in Indonesia, *In Proceedings*, World Geothermal Congress, (2010).

Spatial Identification and Structure Control on the Distribution of Manifestation in Mountain Ungaran, Semarang, Central Java, Indonesia

Pius Artdanno Bernaldo, Nazwa Khoiratun Hisan, Alviani Permatasari, Ludovicus Damardika Jasaputra, Arhananta, Aditya Rizky Wibowo, and Agung Prayoga

dannobernaldo20@gmail.com, nazwakhoiratunhisan@gmail.com, permatasarialviani@gmail.com
ludovicusdamardika@gmail.com, arhananta@gmail.com, adityarw98@gmail.com, ghoengpryg@gmail.com

Keywords: geothermal manifestations, spatial, structural, Ungaran

ABSTRACT

Investigation on the geothermal manifestations of Mount Ungaran in the period 1996-2019 have been done with various methods. However, during that time, no one has discussed the surface alteration and its integration with geological-geophysical spatial data. This research is located on the southern slope of Mount Ungaran, precisely in the Gedongsongo area and its surroundings, Semarang Regency, Central Java. The research method consists of several stages, processing Landsat and ASTER images with ENVI software to determine the spatial distribution of alteration, processing structural information in the Lineament Density Map to determine the effect of the structure geostatistical, interpretation of Gravity and Geomagnetic data to determine continuity of subsurface structures, field check the manifestation location to understand the thermal manifestation condition and creation of the Ungaran geothermal spatial model. Based on image data processing, there are two types of alteration, namely propylitic (chlorite, epidote, illite) and argillic (clay), with a relatively longitudinal distribution zone of NNW-SSE. The greatest density tends to be in the Gedongsongo valley. Based on the interpretation of geophysical data, it was found that there was a heat source in the North of Gedongsongo, the South Slope of Mount Ungaran and the Manifestation was controlled by a NW-SE trending structure and a circular structure dipping to the South at the North of Gedongsongo. Based on the field check of the research location, there are three variations of lithology, the first is lithology of breccias with andesite, basalt, and pyroclastic fragments. The fractures that become the media for the fluid channel are tension joint in the shear zone with a Northwest strike with a dip direction towards the Northeast which has a NW-SE orientation of right slip fault. Analysis of the shear fracture and gash fracture in the minor fault zone of the right slip fault found that the right slip fault is up with a primary stress 15 degrees from the regional main stress which was interpreted to be an R Shear antithetic fault which controlled the distribution of hot water and alteration.

1. INTRODUCTION

1.1 Background

Ungaran is the only mountain that has geothermal potential in the North - South series of Mount Ungaran - Telomoyo - Merbabu - Merapi (Yudiantoro, 2018). Thermal manifestations are an important element in the geothermal system. One of the geothermal manifestations is hot spring. Besides hot spring, it turns out that knowledge about surface water chemistry is also important to compare with hot spring chemistry. Researches in the 1996-2019 period have discussed the geothermal manifestations of Mount Ungaran in various aspects: Wahyudi (2006), Fujimitsu (2007) discussed geophysics aspects; Setyawan (2009), Phuong (2005), Yudiantoro (2018), and Purnomo (2014) discussed volcanology-geothermal and geochemical aspects; Pertamina (1985) and Thanden (1996) describe stratigraphic, Brehme (2014) investigate the hydrotectonics. Based on previous research focus, the authors feel the need to conduct investigation about spatial identification and structural control relationship of the distribution of geothermal manifestations in Mount Ungaran, Semarang, Central Java, Indonesia.

1.2 Research Area

This research is located on the Southern slopes of Mount Ungaran, precisely in the area of Gedongsongo and its surroundings, Semarang Regency, Central Java with Xmin: 424500, Ymin: 9201500, Xmax: 429000, and Ymax: 9206000.

2. DATA AND METHODOLOGY

The research methods done using image processing software. ASTER image analysis using ENVI software (Version 5.3); IFSAR imagery and geophysical data (TOPEX satellite imagery) processing using Surfer 13 software. ASTER image color and relief with a combination of several bands to determine the distribution of surface lithology and the type of alteration in the study area. Furthermore, using the IFSAR image which is then drawn regional and detailed alignment patterns in the study area. Lastly, processing of geophysical data from radar satellite imagery using the gravity method. After Bouguer correction and terrain correction, a residual and regional anomaly map is obtained. In addition, secondary data analysis in the form of surface temperature survey, geochemical analysis, and petrophysical analysis was also carried out

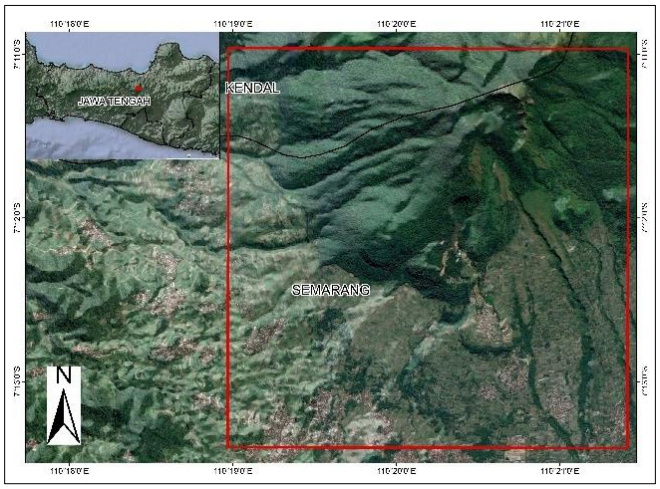

Figure 11: Research Area.

3. REGIONAL GEOLOGY

3.1 Regional Stratigraphy

The stratigraphy of the research area based on the geological map of the Ungaran sheet (Pertamina, 1985) consists of 2 units, namely Gunungapi Termuda Unit composed of lava flows and andesite lava composed of hornblende and augite minerals (Thanden et al., 1996), and the Gunungapi Ungaran Muda Volcano Unit composed of hornblende augite andesite lava flows (Thanden et al., 1996) (Figure 2).

3.2 Regional Structural Geology

The regional geological structure of the study area consists of strike-slip faults in the NE-SW trending plot which intersects Gunungapi Termuda Units and Gunungapi Muda Units. In addition, there is also a relatively NE-SW and E-W lineaments of the lava flow.

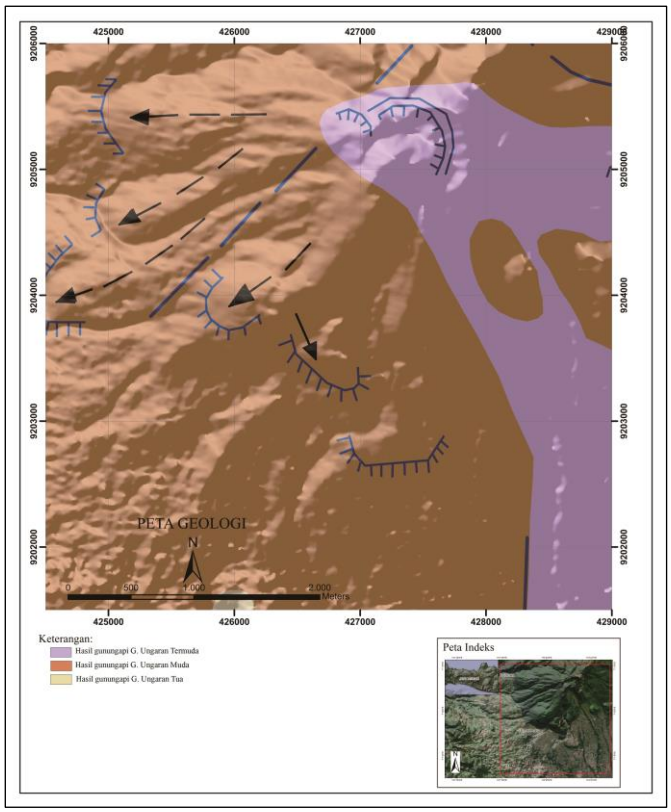

Figure 2: Geological Map of Research Area.

4. RESULT AND ANALYSIS

4.1 ASTER Interpretation

The image used is the ASTER L1T image which was acquired on October 3, 2006, ENVI 5.3. Analysis were carried out using a Spectral Angle Mapper which references Enmember from the USGS spectral library on the VNIR band with a wavelength of 0.52-0.86 µm and SWIR with a wavelength of 1.60-2.430 µm (Gozzard J.R., 2006).

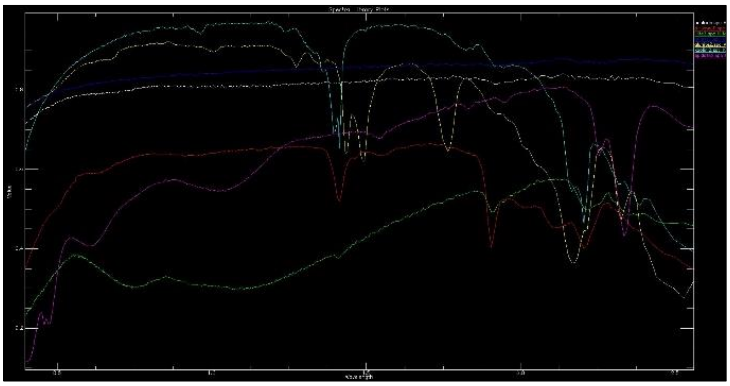

Figure 3: Spectral graph of minerals from the USGS spectral library.

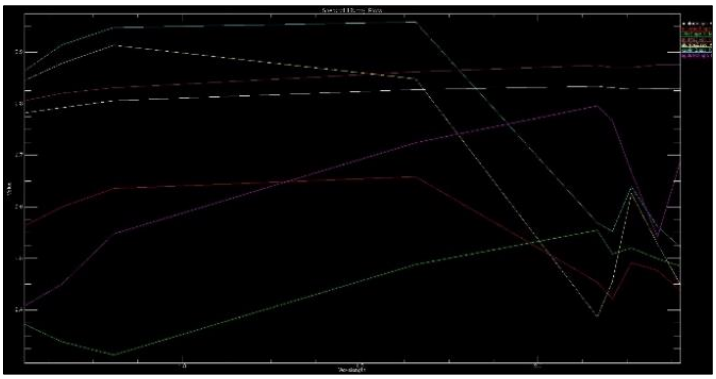

Figure 4: Graph of mineral spectrum resampled to ASTER Image.

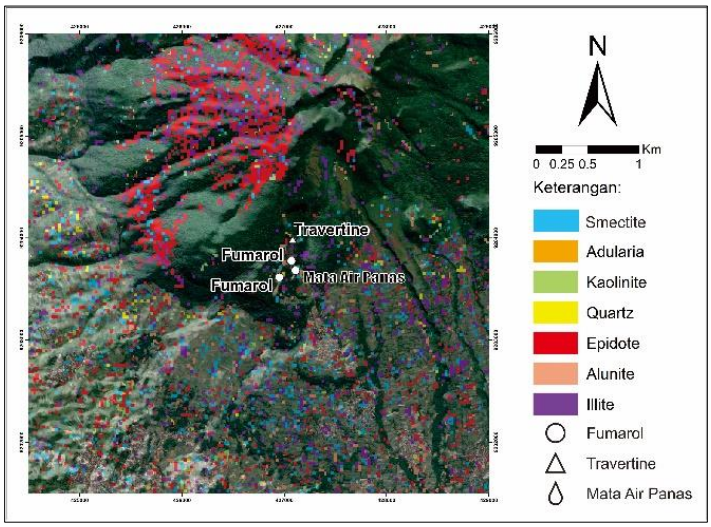

Figure 5: Map of the results of image interpretation of ENVI software 5.3.

Based on the results of ASTER image interpretation in ENVI 5.3 software, the results of mineral distribution are as follows: in the Northern part of the Gedongsongo area there are Epidote, Kaolinite, Smectite, Illite, and Quartz minerals. The Northern part is dominated by Epidote and Illite minerals. In the NE part of the Gedongsongo area there are Epidote, Illite, Kaolinite, and Smectite minerals. The NE part is dominated by Epidote and Illite minerals. In the Eastern area there are Smectite, Illite, Quartz, Adularia and Epidote minerals. The Eastern part is dominated by Smectite, Illite and Epidote minerals. In the SE section there are Illite, Smectite, Alunite, Kaolinite, and Quartz minerals. The SE section is dominated by Smectite, Illite, and Epidote minerals. In the Southern area of the Gedongsongo Region there are Smectite, Alunite, Quartz, Epidote, and Kaolinite minerals. The Southern area is dominated by Smectite and Illite minerals. In the SW area there are the Epidote, Smectite, Kaolinite, and Quartz minerals. The SW area is dominated by Epidote and Smectite minerals. In the West there are Smectite, Illite, Quartz, and Epidote minerals. In the West is dominated by

Quartz, Illite and Smectite minerals. In the NW area there are Epidote, Smectite, Illite, and Kaolinite minerals. The NW area is dominated by Epidote and Smectite minerals. In the central part of the Gedongsongo Region there are Illite, Smectite, Quartz, Epidote and Alunite minerals. The middle part is dominated by Illite, Smectite, and Epidote minerals.

4.2 Surface Temperature Survey

Wahyudi (2006) has conducted ground temperature mapping at a depth of 75 cm so that a ground temperature anomaly map is obtained as shown in the figure 6. From the temperature anomaly map and altered rock map, the heat distribution can be interpreted. The map can be divided into three temperature anomalies clusters found in the Gedongsongo area, one closure near the fumarole and the temperature is high enough that are scattered in the Northwest area of the research area, while the other two are located in the Northeast and South of the research area with lower temperatures.

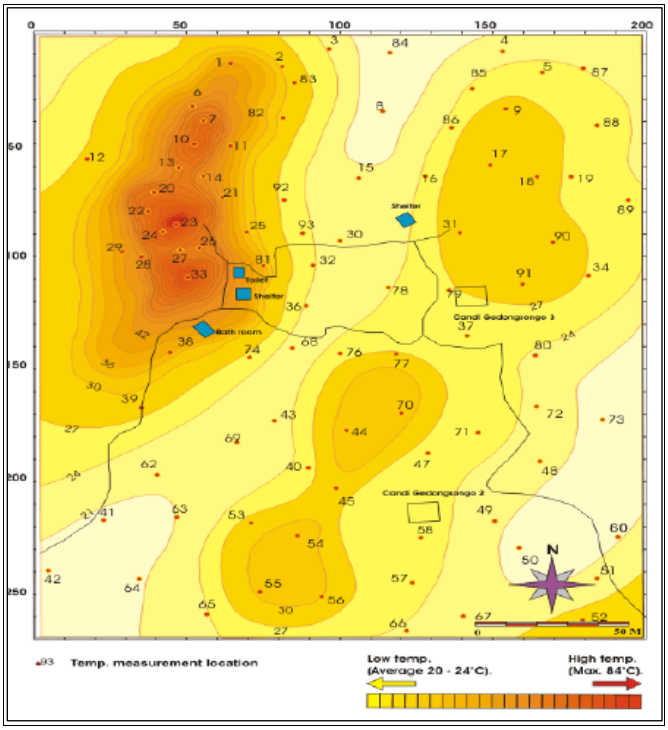

Figure 6: Map of surface temperature survey results with scale 1:4.000 (Wahyudi, 2006).

4.3 IFSAR Interpretation

Image interpretation is carried out to determine the lineaments in the research area. The image used is IFSAR. Based on the results of image interpretation, data obtained is maximum force, minimum force, general shear 1 and 2 directions. At the research location, alignments is obtained with a NW-SE orientation with a value of maximum force: N 315° E, minimum force: N 245° E, Shear 1: N 330° E, Shear 2: N 305° E. From the lineaments, it can be seen that the force working in the research area are NW-SE trending stress.

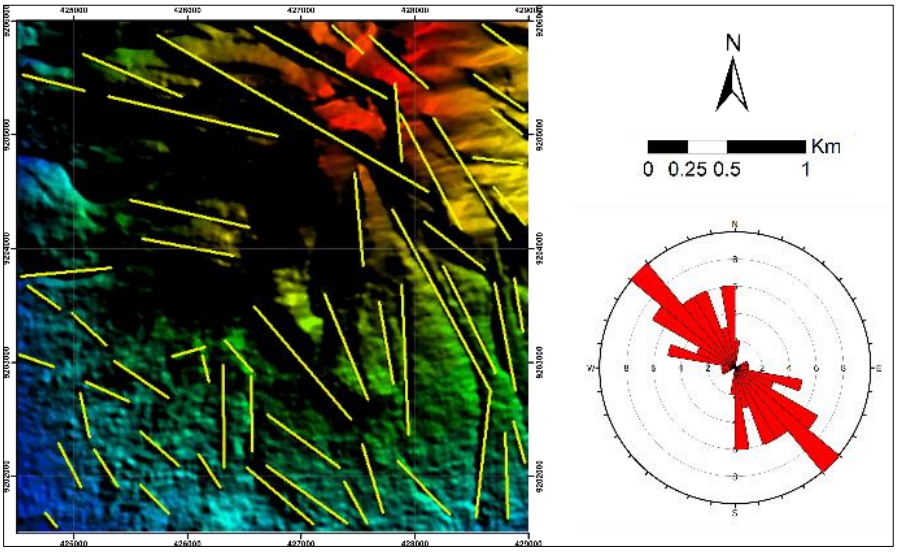

Figure 7: Interpretation map of study area lineaments.

4.4 Gravity Method

Based on the 3-dimensional gravity map model of Mount Ungaran area, there is an anomaly in the area with slope morphology in the South of Mount Ungaran, precisely in the Gedongsongo area and its surroundings. The highest density values ranged from 2-3.5 (mGals), and the lowest density values were -4.5 to -5 (mGals). The highest density value is shown in red which is located in the middle of the Gedongsongo valley morphology. Then the farther away from the center, the density value will be lower, which is shown sequentially with a yellow color of 0.5-1 mGals, the green color indicates a moderate value with a value of -1.5 to 0.5 mGals, the blue color indicates a slightly low value with values of -2.5 to -1.5, and the lowest density values are indicated by purple with values of -5 to -3 mGals.

The results of the residual gravity anomaly map show that the highest density value is an anomaly which is the distribution of heat and conductivity in the geothermal area of Mount Ungaran. The temperature anomaly is thought to be due to the presence of fumaroles, which are the places where hot liquids is upflow to the surface. Based on the interpretation of geophysical data, it was found that there was a heat source in the North Gedongsongo of South Slope of Mount Ungaran and the manifestation was controlled by a NW-SE trending structure and a circular structure dipping to the South at the North of Gedongsongo.

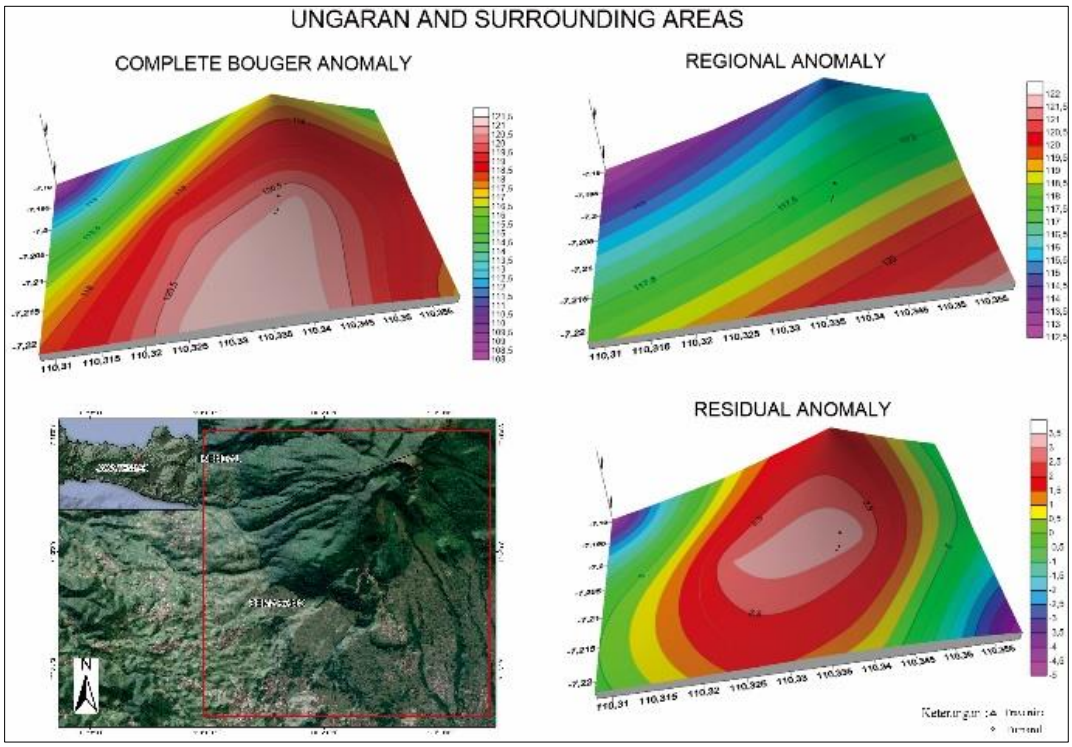

Figure 8: Map of the anomaly gravity of the study area.

4.5 Structural Control

4.5.1 Fault Fracture Density Analysis

The interpretation of the geological structure, which is reflected in the lineaments density, shows that the dominant alignments direction is NW-SE. The calculation of the fault fracture density is then displayed in the form of a lineaments density contour map. It can be seen on the fault fracture density map, the study area can be divided into 5 density classes, namely very high density shown in red in the Southeast and South of the research area, high density shown in yellow in the Southeast, South, Northeast, and East of the research area. Medium densitiy indicated in green color in the South, Southwest, West, and North of the research area, low density shown in blue color in the Southwest and Northwest of the research area, and very low density that shown in purple color in the Northwest of research area. Based on the fault fracture density analysis, the locations with the highest fracture density values are in the Southeast and Southern parts of the study area.

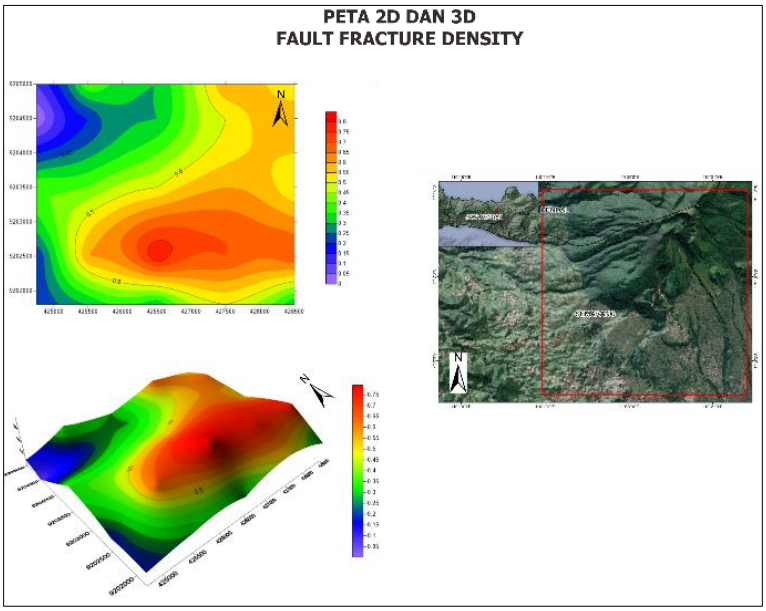

Figure 9: Fault fracture density map of research area.

4.5.2 Structural Geology

In the study area, there were 3 faults in 3 different LP which were analyzed. The results of the first analysis, namely the LP 7 fault analysis, found a fault plane with a position N 189° E / 71° with bearing N 196° E and a rake of 20° with the main stress trending NE-SW. The movement of the fault is the left oblique with the name Normal Left Slip Fault (Rickard, 1972). Then in LP 8, the fault field data was obtained with the position N 175° E/66°. Finally, in LP 10, data on Shear Fracture with a position N 159° E/74°, Gash Fracture with a position N 066° E/57°, and a fault plane with a position N 009° E/84° were found. Then analyzed and obtained data maximum force': 12°, N 073° E, maximum force: 28°, N 043° E, medium force: 55°, N 182° E, minimum force': 30° , N 013° E, minimum force: 34°, N 343° E, Bearing: N 012° E, and Rake: 35° with right oblique direction. The main force is NE-SW. Result of fault analysis using Rickard diagram, 1972 obtained the fault name, namely Reverse Right Slip Fault.

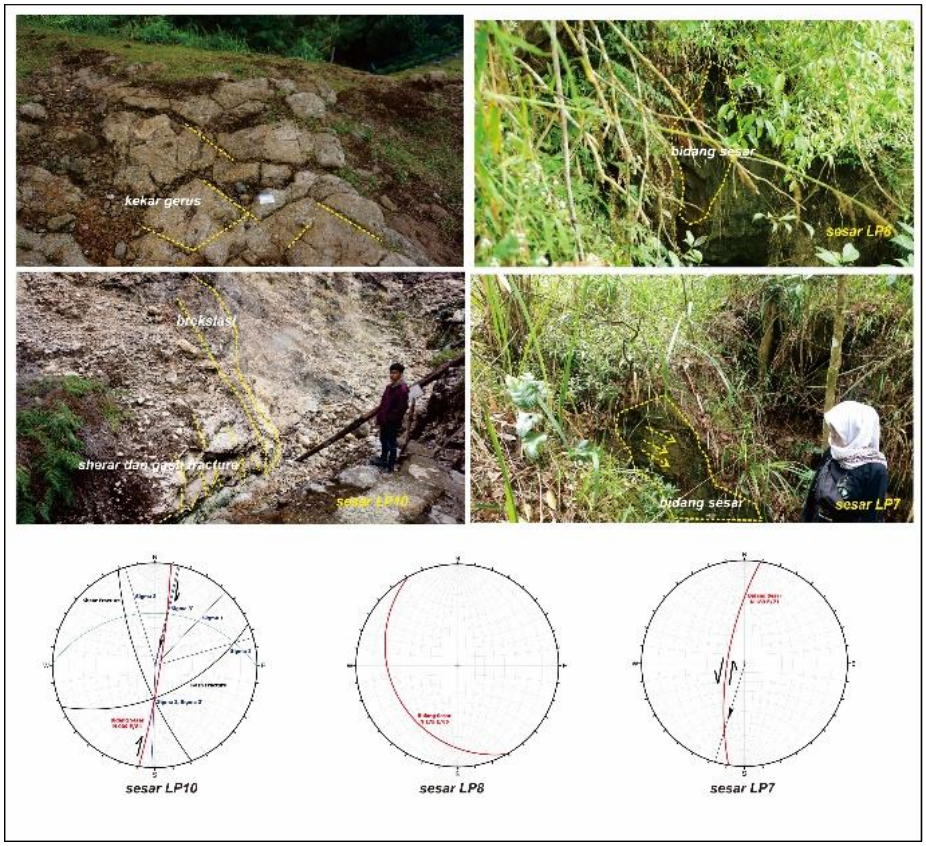

Figure 10: Control of the geological structure of the study area.

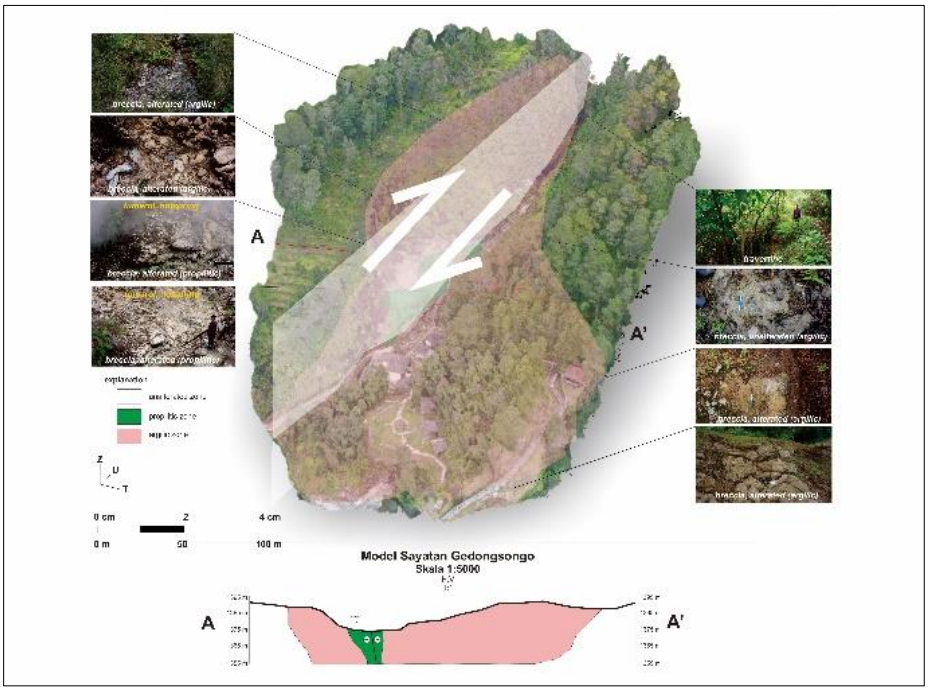

Figure 11: Control model of the geological structure of the study area.

4.6 Geochemical Analysis

Based on previous research by Yudiantoro (2018), the research area is represented by basaltic-andesite volcanic rocks. Considering that Mount Ungaran is part of the alignment of Ungaran, Telomoyo, Merbabu and Merapi Volcanoes, in Yudiantoro (2018) the discussion of the geochemistry of volcanic rocks in the study area is also compared with some volcanic rocks in Merapi. The selected Merapi rocks came from lava which erupted from 1888-1992. Chemically Ungaran volcanic rock has several elements, namely SiO_2 (53.30%), TiO_2 (0.964%), Al_2O_3 (22.00%), Fe_2O_3 (3.30%), FeO (18.49%), MnO (0.221 %), MgO (0.913). %), CaO (7.57%), Na_2O (1.86%), K_2O (3.27%) and P_2O_5 (0.39%). Geochemical data of volcanic rock representing Merapi Volcano has the following characteristics: SiO_2 (50.74-53.78%), TiO_2 (0.65-1.10%), Al_2O_3 (18.36-20.11%), Fe_2O_3 (1.15-1.76%), FeO (6.45-9.89 %), MnO (0.18-0.36%), MgO (2.18-4.40%), CaO (8.64-10.94%), Na_2O (1.66-3.59%), K_2O (1.66-3.59%) and P_2O_5 (0.16-0.95%). Compared to Mount Merapi, Ungaran has a higher content of Fe2O3 which is used to form hornblende. Meanwhile, other elements are relatively lower than Merapi. The chemical elements of Ungaran and Merapi volcanic rocks are presented in Table 1. and can be explained as follows:

Table 1: Chemical elements of ungaran and Merapi volcanic rock samples (Yudiantoro, 2018).

	SiO_2	TiO_2	Al_2O_3	Fe_2O_3	FeO	MnO	MgO	CaO	Na_2O	K_2O	P_2O_5
ML1006	50.74	0.96	18.36	1.26	7.08	0.21	4.16	10.05	3.28	1.60	0.35
ML1992B	51.33	0.84	20.11	1.15	6.45	0.17	4.35	10.64	1.66	1.96	0.17
ML1992L	51.45	0.77	19.97	1.76	9.89	0.16	4.40	10.94	1.68	2.07	0.16
UNG	53.30	0.96	22.00	3.30	7.67	0.22	0.91	7.57	1.86	3.27	0.39
ML1986	53.53	1.10	15.76	1.38	7.75	0.36	2.45	9.39	3.73	2.63	0.38
ML1888	53.78	0.82	18.54	1.37	7.67	0.18	2.77	8.64	3.59	2.48	0.95

Description: UNG: Ungaran ML: Merapi Lava

The results of plotting SiO_2 with total $Na_2O + K_2O$ from the USGS diagram by Tas Le Maitre (1989) in (Yudiantoro, 2018) show that there are several types of volcanic rock, where Merapi volcanic rock consists of basalt, basaltic-andesite, trachy-andesite basaltic, and for the Ungaran sample was basaltic andesite (Figure 12).

While the results of plotting elements of SiO_2 against K_2O show that the Ungaran sample has shoshonitic affinity and the Merapi sample shows a high K-alkaline lime series (Figure 11). The Fe element of the Ungaran volcanic rock has a higher composition compared to the Merapi volcanic rock group. However, the Mg content and alkaline elements of the Ungaran volcanic rock are lower than that of the Merapi volcanic rock (Figure 13).

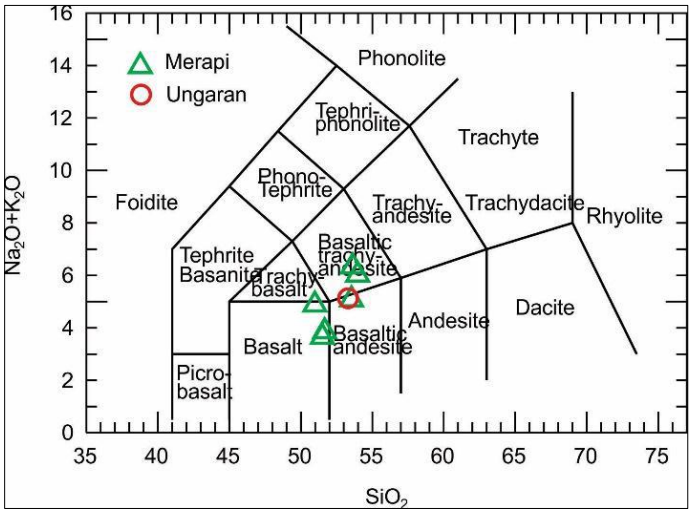

Figure 12: Plot of Ungaran and Merapi volcanic rocks in the USGS (Tas Le Maitre diagram, 1989 in Yudiantoro, 2018).

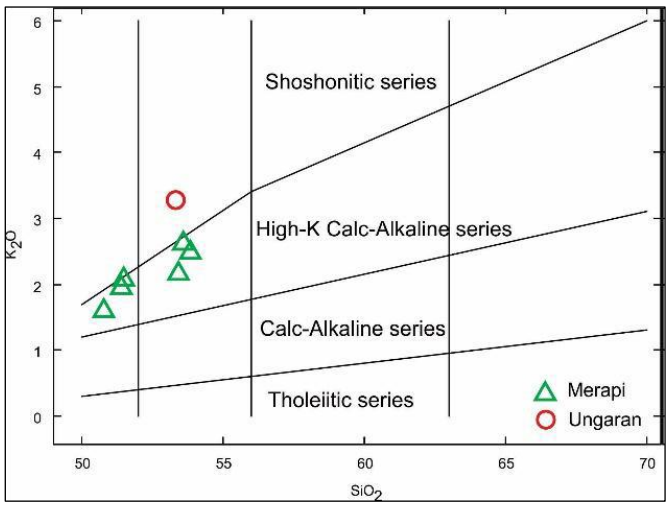

Figure 13: Plot results for K_2O and SiO_2 (Yudiantoro, 2018).

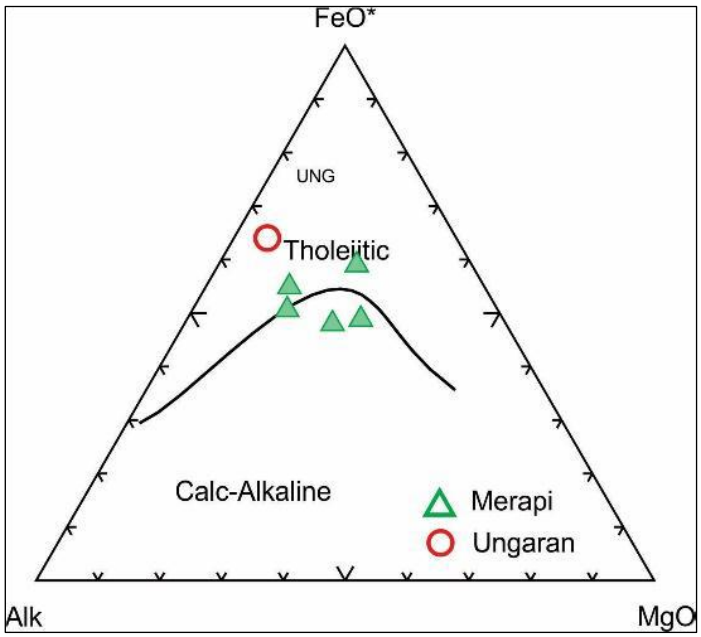

Figure 14: Plotting results of total FeO, MgO and total $Na_2O + K_2O$ (AFM diagram) of the Ungaran and Merapi volcanic rocks (Yudiantoro, 2018).

4.7 Petrophysical Analysis

Yudiantoro (2018) conducted a petrophysical analysis on 5 rock samples, then analyzed the hydrothermal alteration rate, porosity, density and permeability. The hydrothermal alteration rate showed medium levels (25-75%), porosity around 8.43-12.04, density around 1.90-12.04 gr/cc, permeability around 15.78-1145.05 mD or 0.016-1.145 D.

Table 2: Results of petrophysical measurements of samples from the study area (Yudiantoro, 2018).

No	Rock Type	Intensity Alteration	Porosity (%)	Density (gr/cc)	Pemeability mD	Darcy
UN-01	Andesite fragmen	medium	9.89	1.89	152.46	0.152
UN-03	Andesite lava	medium	11.12	1.90	15.78	0.016
DRK-02	Volcanic breccia	medium	12.04	1.92	289.43	0.289
DWK-02	Breccia tuff	medium	8.43	2.26	21.05	0.021
DRK	Travertin	medium	27.24	1.66	1145.05	1.145

5. DISCUSSION

Based on field observations and a digital outcrop model was carried out where the distribution of alteration is controlled by fault alignment with NE-SW direction, then the appearance of manifestations and travertine are still controlled by the same fault alignment. Based on geochemical analysis, it is known that the type of magma in the geothermal system in Ungaran is calc-alkaline. Based on petrophysical analysis, the reservoir rock characteristics in the Ungaran geothermal system interpreted to be a good geothermal reservoir with the porosity around 8.43-12.04, permeability around 15.78-1145.05 mD or 0.016-1.145 D, hydrothermal alteration rate showed medium levels (25-75%), and density around 1.90-12.04 gr/cc which is composed by lithology andesite fragment, andesite lava, volcanic breccia, breccia tuff, and travertine.

6. CONCLUSION

- Based on Corbet (1997), the mineral assemblage in the study area forms a propylitic alteration zone with epidote, smectite, illite and argillic alteration zones characterized by the mineral assemblage of quartz, smectite, kaolinite.
- Based on the map of the surface temperature survey, the research area is divided into three temperature anomaly clusters, one near the fumarole and the temperature is quite high spread in the Northwest area of the research area, while the other two clusters are located in the Northeast and South of the research area with not too high temperatures.
- Based on field survey and geochemical analysis, it is found that the research area that has geothermal potential is in the center of the research area.
- Based on the Google Earth overlay, IFSAR imagery, fault fracture density and gravity, it is found that the areas that have the most structure are in the Southeast and South of the study area.

7. ACKNOWLEDGEMENTS

Thanks to Allah SWT for giving us the strength to finish this paper. To beloved parents who have supported morally and materially, as well as to the Antasena Research Group who has helped in making this research. Hopefully this work can be useful for us and for readers.

REFERENCES

Brehme, M., Moecka, I., Kamahb, Y., Zimmermanna, G., and Sauter, M.: A hydrotectonic model of a geothermal reservoir – A study in Lahendong, Indonesia, *Elsevier: Geothermic*, (2014), pp. 228-239.

Fujimitsu, Y., Setyawan, A., Fukuoka, K., Nishijima, J., Ehara, S., and Saibi, H.: Geophysical investigations of Ungaran Volcano, Central Java, Indonesia, In *Proceedings of the 29th New Zealand Geothermal Workshop*, (2007).

Phuong, N.K., Hendrayana, H., Harijoko, A., Itoi, R., and Unoki, R.: Geochemistry of The Ungaran Geothermal System, Central Java, Indonesia, In *Proceedings Joint Convention Surabaya*, (2005), pp. 64-77.

Purnomo, Budi Joko and Pichler, Thomas.: Geothermal systems on the island of Java, Indonesia, *Elsevier: Journal of Volcanology and Geothermal Research*, (2014), pp. 47-59.

Setyawan, A., Ehara, S., Fujimitsu, Y., and Saibi, H.: Assessment of Geothermal Potential at Ungaran Volcano, Indonesia Deduced from Numerical Analysis, *Proceedings, Thirty-Fourth Workshop on Geothermal Reservoir Engineering Stanford University*, Stanford, California, February 9-11, (2009).

Wahyudi: Kajian Potensi Panas Bumi dan Rekomendasi Pemanfaatannya pada Daerah Prospek Gunungapi Ungaran Jawa Tengah, Kajian Potensi Panas, (2006), pp. 41-48.

Yudiantoro, D.F., Ratnaningsih, D.R., Pramudiohadi, E.W., Kurnianto, A.G.B., Alfian, D.G., Arhananta, and Abdurrahman, M.: Overview of the petrophysical and geochemical properties of the Ungaran Quarternary Volcano in Relation to Geothermal Potential, *IOP Conf. Series: Earth and Environmental Science*, 149, (2018), 012017.

This page is intentionally left blank

Fracture Characterization on the Great Sumatera Fault Zone at Sorik Marapi Geothermal Field

Dhani Sanjaya, Wishnu Triananda, Radhitya E. Pradipta, Haris Siagian, M. Ramos Suryanta Lubis, Christovik H. Simatupang, and Riza G. Pasikki

KS Orka Renewables

dhani.sanjaya@ksorka.com, wishnu.triananda@ksorka.com, radhitya.pradipta@ksorka.com, haris.siagian@ksorka.com, ramos.lubis@ksorka.com, christovik.simatupang@ksorka.com, riza.pasikki@ksorka.com

Keywords: Fracture characterization, Resistivity Image Log, Gamma-Ray, Injectivity Index, GSF, Sorik Marapi

ABSTRACT

The Great Sumatera Fault (GSF) has been identified to play major role in controlling the permeability of the geothermal system in Sumatera Island. In Sorik Marapi geothermal field, most of the wells have been drilled within the GSF zone. In the effort to understand the role of this structure to reservoir permeability, thus resistivity image data were successfully collected from 2 wells that located in the western and eastern sector of the GSF zone.

The Injectivity Index (II) test result that was obtained from 2 completion tests showed significant differences. In general, the western sector well group exhibits higher temperature and higher permeability as compared with the eastern sector well group. Ultimately, the western well is used as production well because of its prolific production potential and the eastern well is used as an injection well because of its deep permeability and higher rock temperature as it penetrates deeper. Based on the resistivity image data, the key findings include discrepancies in fracture trend, fracture conductivity, and fracture aperture even though the fracture density is relatively the same between the two sectors.

The larger aperture in western sector where it is relatively closer to the hypothetical upflow seems to provide better permeability, unlike the eastern sector where it is located in the edge of the GSF. This observation may signify another unique characteristic of a geothermal field that located within the mega fault zone in Sumatera Island.

1. INTRODUCTION

Permeability is one of the key factors in the geothermal system. It accommodates the hydrothermal fluid to flow in the reservoir and preserves a derivable high-pressure and temperature fluid for geothermal energy (Eggertsson et al., 2020). Since most of the geothermal reservoirs are composed of crystalline rocks to volcaniclastic in which the matrix has negligible porosity and permeability, thus fracture network setting is expected to host the permeability.

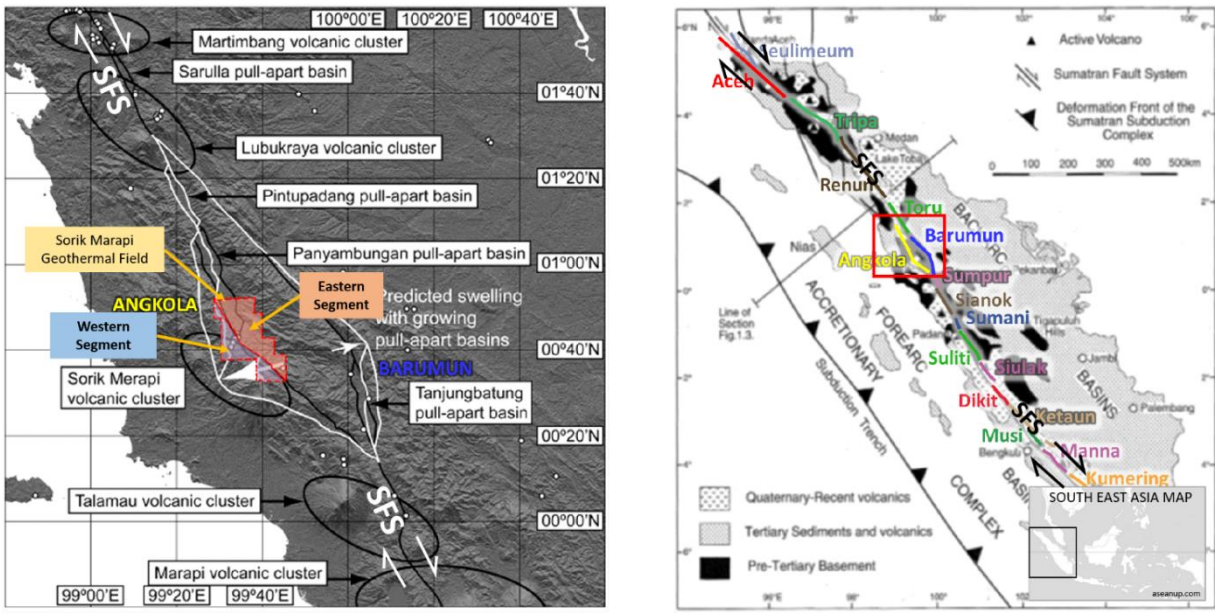

(a) (b)

Figure 1: (a) Map of Regional Tectonic setting of Sorik Marapi located along the Sumatran Fault System after Muraoka et al., (2010). (b) GSF segments by (Sieh and Natawidjaja, 2000).

Sorik Marapi Geothermal Field is located in Sumatra Island, Indonesia. It is situated on the eastern of Mt. Sorik Marapi and on the edge of Panyambungan pull-apart basin of the Great Sumatera Fault in Angkola segment (Figure 1). Surface manifestation consisting of acid crater lake and Solfatara, fumaroles, acid sulphate and bicarbonate springs are distributed fairly from the summit to the slopes and into the graben structure in the eastern area. The boiling Cl springs are observed as far as 17 kilometers towards northeastern area in the Sampuraga lowland indicating the inferred outflow pathways to the east and far to north-northeasterly flow along splays of the Sumatran fault. Those surface thermal manifestation and the drilled wells suggest Sorik Marapi is a volcanic hydrothermal system

with outflow associates with the GSF zone. Temperature as high as 320°C has been encountered from wells that drilled towards the upwelling zone near Mt. Sorik Marapi. It implies that the upflow zone is likely to present beneath the eastern slope of the volcano.

The strike strike-slip deformation along the island is accommodated by a large dextral Sumatran fault, the Sumatran Fault System (SFS), which is influenced by the oblique subduction of the Indo-Australian Plate to the SW of Sundaland since the Mid-Eocene (c.a 45 Ma) (Hall, 2012). In terms of fracture, it is thought that the combination between the volcanic centre, strike-slip, and pull-apart basin will give additional reservoir frameworks for the geothermal resource (Aydin and Nur, 1982; Muraoka et al., 2010).

2. DATA

Data used for the analysis are resistivity image, drilling cuttings, drilling parameters and completion test result of two wells that located in western and eastern of GSF. The western well was logged at 1405 - 1617 mMD / -366 - -539 masl interval in 7-7/8" hole section while the eastern one was logged at 1315 - 2042 mMD / -356 - -945 masl interval in 12-1/4" hole section (Figure 2). The resistivity image is interpreted into structural and lithological information by signifying the sinusoidal features from static and dynamic images and integrating it with gamma-ray log, drilling cuttings and drilling parameters. However, the conclusion from this study may be limited within that particular depth and/or area, hence additional data from different depths and wells would support more robust fieldwide interpretation.

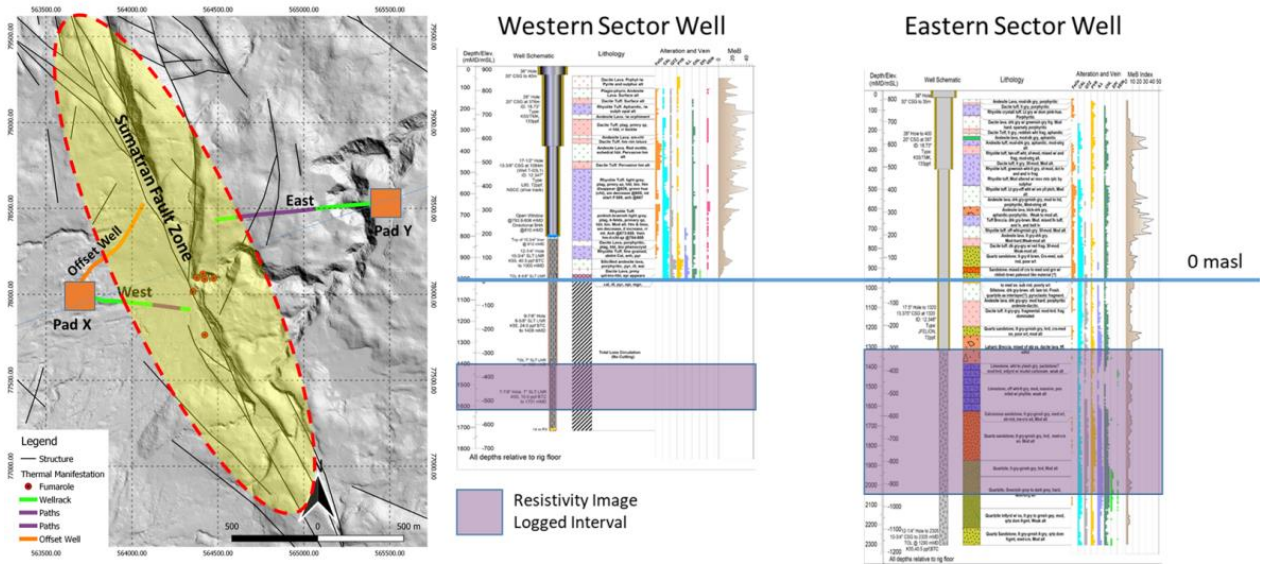

Figure 2: Location and depth showing where the resistivity images were logged.

2.1 Image Facies

The Image facies is defined by integrating the resistivity image log with gamma-ray log and drilling cuttings (Figure 3). The other lithological features such as bedding, foliation, and joint are manually picked from the image log. This data integration is used to create facies model in order to constrain the different fracture development in the two sectors. Since total loss circulation is encountered from 1000 - 1715mMD on the western sector well, therefore the facies model analysis is performed by correlating the logged interval of the resistivity image with the offset wells at relatively the same interval depth (Figure 2). In the case of the eastern well, it showed partial loss circulation during drilling, thus facies model interpretation can be conducted by using its specific borehole data.

2.2 Structure

The fractures are divided into two types based on their appearances on the resistivity images. The fractures that have dark colour on the resistivity images represent conductive fracture. Moreover, the conductive fracture is classified into partially conductive if the dark sinusoid does not continuously appear across the borehole (Figure 4). Since conductivity can be resulted from an invasion of conductive fluid and drilling mud or precipitation of conductive minerals, thus integration with other data sets is mandatory. Meanwhile, a fracture that has a bright colour is categorized as a resistive fracture. This fracture is interpreted as a close fracture due to the filling of resistive minerals namely quartz, calcite, and etc.

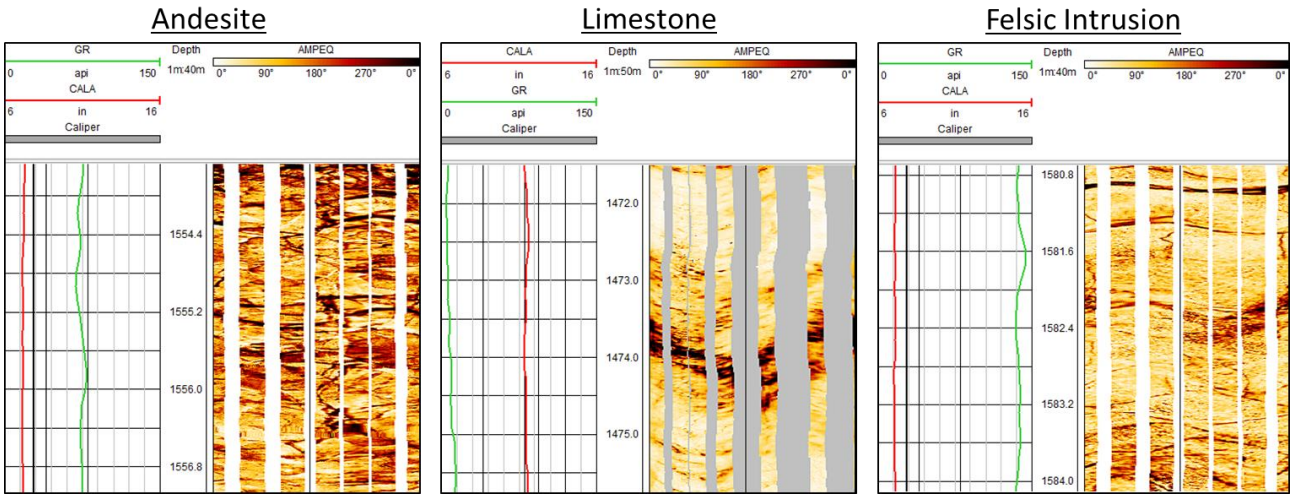

Figure 3: Image facies defines by integrating resistivity image log texture, gamma ray log and drilling cutting description.

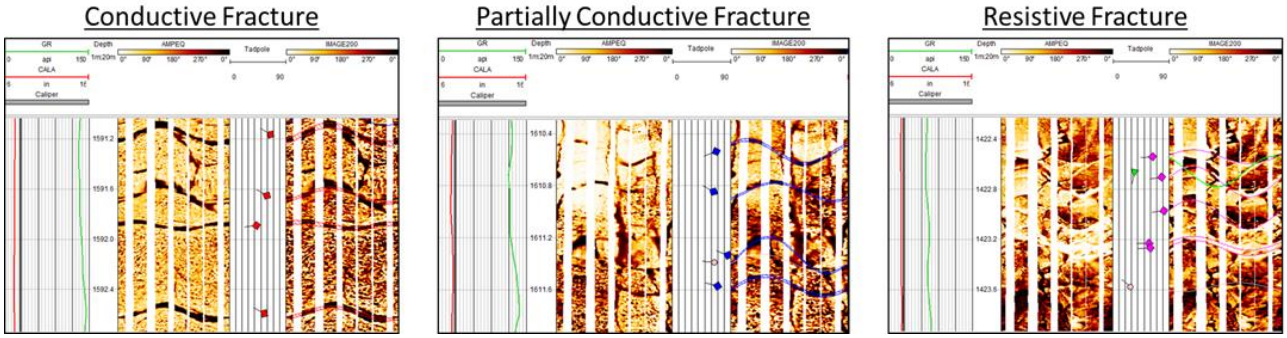

Figure 4: Resistivity image log showing conductive, partially conductive and resistive fractures.

3. RESERVOIR CHARACTERIZATION

3.1 Image Facies Interpretation

3.1.1 Image Facies on Western Sector

The offset wells correlation on the western well exhibits porphyritic alteration associate with andesite, dacite dike, interlayered lava-tuff and breccia with numerous veins. The image at depth 1405-1560 mMD shows relatively gentle dipping sinusoids that interpreted as joint and few interlayered brecciated textures with the gamma ray value ranging from 60-70 API. It suggests that the upper section is composed by andesite with some interlayered breccia (1405-1560 mMD). Meanwhile the bottom section at 1560-1671 mMD shows light pale green-gray felsic porphyry intrusion with quartz, biotite and sparse plagioclase as phenocrysts from the drilling cuttings. It is consistent with the higher gamma ray value 100-150 API that demonstrated by the image log at this interval (Figure 5).

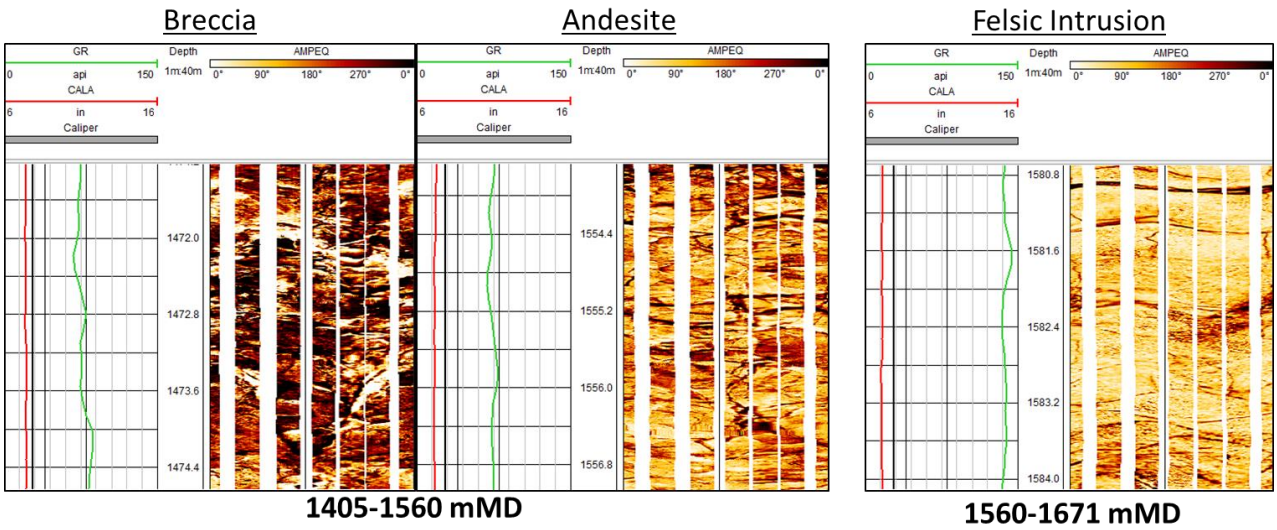

Figure 5: Image facies in the western well consists of breccia, andesite and felsic intrusion.

3.1.2 Image facies on Eastern Sector

On the eastern well, the drilling cuttings at 1315-1385 mMD are composed of tuffaceous lahar, and lesser andesite lava. The resistivity image log at interval 1315-1385mMD shows interlayered and brecciated texture with gamma ray value of 80-95 API. It suggests that the interval consists of laharic breccia. In the next interval at 1385-1595 mMD, the image exhibits planar texture with bright color and low gamma ray value while the drilling cuttings show partially recrystallized limestone. The 1595 - 1875 mMD section consists of clastic sediments and volcanic/volcaniclastic rocks with phyllic alteration while the resistivity image texture showing interlayered planar bedding sinusoids.

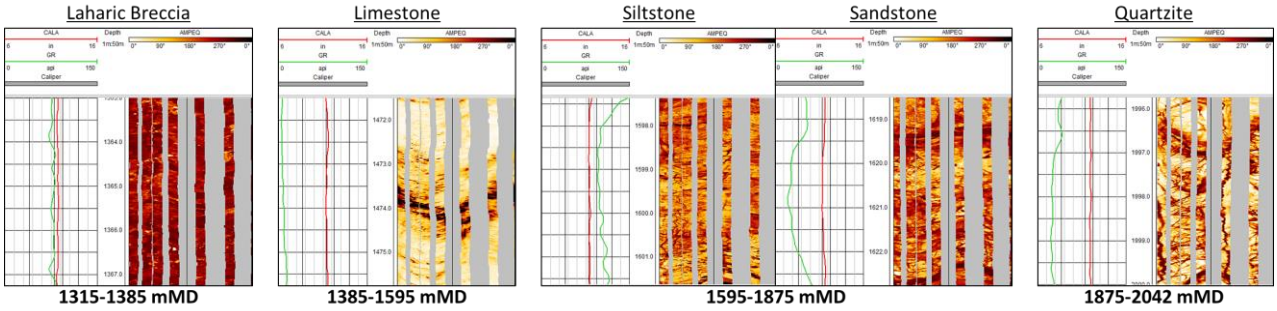

Figure 6: Image facies in the eastern well consists of laharic breccia, limestone, siltstone, sandstone and quartzite.

This planar texture with low gamma ray suggests sandstone bedding while the planar texture with high gamma ray value is interpreted as siltstone. On the bottom section at depth 1875-2042 mMD the cutting consists of quartzite with light grey to greenish light grey color and interlocking grain texture. The resistivity image log shows fracturized texture with gamma ray value ranging from 30-50 API (Figure 6).

3.2 Fracture Orientation

Several fracture orientations are identified along the logged resistivity image interval in both wells. There are at least six lineament trends, namely NW-SE, E-W, N-S, NE-SW, NNE-SSW, NNW-SSE, and WNW-ESE are identified in Sorik Marapi geothermal field with the N-S becomes the major trend (Figure 7 and 8). The differences between the western and eastern sectors of the GSF are the type of fractures. The western sector is predominantly composed of conductive fracture while the eastern sector is associated with partially conductive fracture.

3.2.1 Fracture Orientation on Western Sector

The conductive fractures, which are the common fracture type developed in the western sector show majorly N-S trending strike with a dip magnitude in the range of 50-80 degrees and dip direction to the west. The partially conductive fractures also demonstrate similar N-S trending strike and minor NNE-SSW trending strike with a dip magnitude of 45-90 degrees and dip direction to the west (Figure 7). On the other hand, the resistive fracture trends exhibit more variation. The majority are N-S and NE-SW trends with dip direction to the west, NW. There is minor WNW-ESE trending strike with dip direction to NE. The dip magnitude of the aforementioned is ranging from 40-90 degrees.

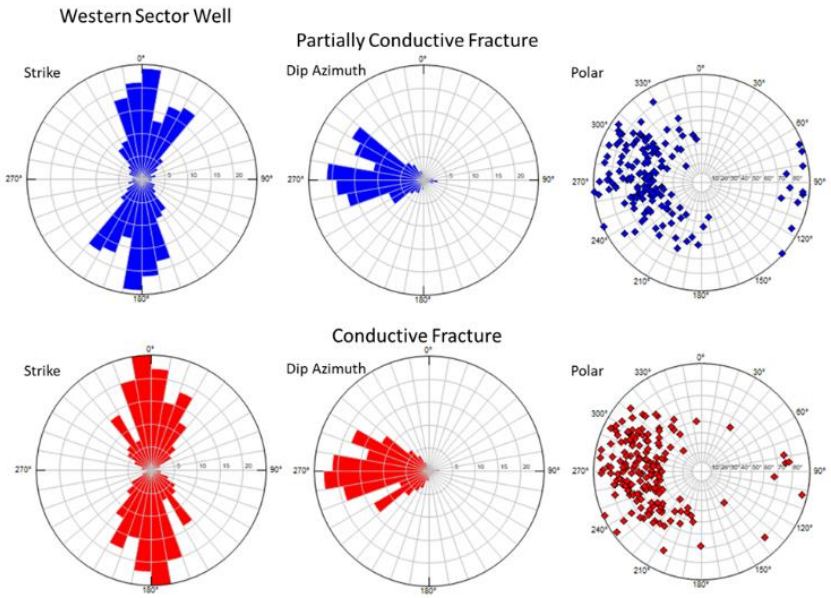

Figure 7: Dip statistic of partially conductive and conductive fracture on the western well demonstrating the fracture strike orientation dominantly in the N-S direction with west dip direction and dip magnitude ranging from 40 to 90 degrees.

3.2.2 Fracture Orientation on Eastern Sector

In the eastern sector well, only partially conductive fractures are well-developed. The majority strike orientation is ranging from NNE-SSW to NNW-SSE with dip direction to the east and dip magnitude in the range of 40-90 degrees (Figure 8). Some west minor orientation is observed with similar dip direction and magnitude. However, some minor conductive fractures are also found with similar trend. Meanwhile, the resistive ones are identified with various strike trends, namely NNW-SSE trends and minor NE-SW, E-W and NW-SE directions with dip magnitude in the range of 50-85 degrees.

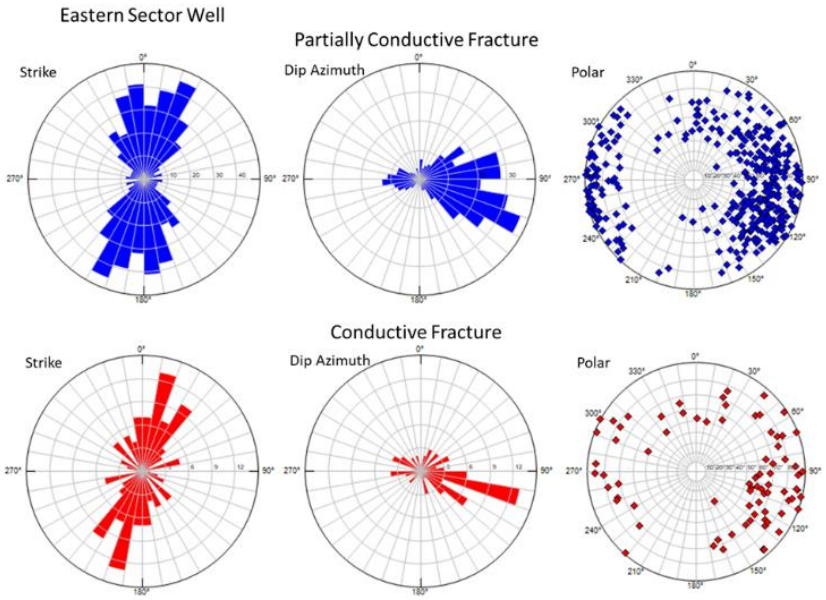

Figure 8: Dip statistic of partially conductive and conductive fracture on the eastern well demonstrating the fracture strike orientation dominantly in NNW-SSE, N-S and NNE-SSW direction with east to south-east dip direction and dip magnitude ranging from 40 to 90 degrees.

3.3 Fracture Density

In order to identify the differences in the permeability patterns of both sectors, the fracture density calculation was only performed on the conductive and partially conductive fractures. This is also intended to give a brief overview of the correlation between fracture development and lithology composition in both sectors.

3.3.1 Fracture Density in Western Sector

Using a cut-off of 4 fractures per meter, there are two zones of high fracture density that identified in the western well at 1520-1555m-MD and 1570-1610m-MD interval (Table 1 and Figure 9). The fractures are developed in the andesite unit at upper section while they are developed in the massive felsic intrusion unit at lower section. Dominantly, both high fracture density zones are composed of conductive fracture that depicted by the continuous conductive sinusoids and clear aperture. The strike of these conductive fractures is relatively N-S to NNW-SSE with the dip direction to west and WNW.

Table 1: Summary of High Fracture Density Zone on Western Sector of GSF.

No.	Depth Interval (mMD)	Lithology	Avg. Fracture Strike/Dip
1	1520-1555	Andesite	N145E/75
2	1570-1610	Felsic Intrusion	N205E/75

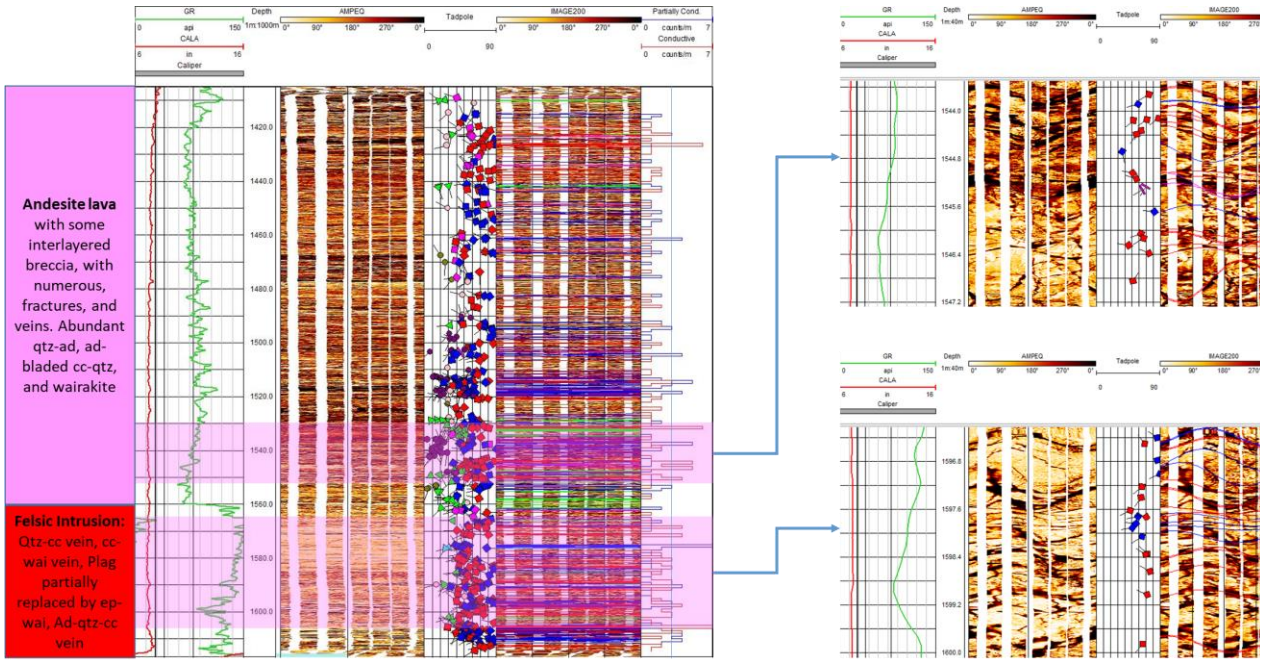

Figure 9: Fracture density of the western well showing a predominance of conductive fractures. Two high fracture density zones are observed: at 1520-1555 m-MD developed in the andesite formation and at 1570-1510 m-MD developed in the felsic intrusion formation.

3.3.2 Fracture Density in Eastern Sector

By using a similar cut-off of 4 fractures per meter, the thickness of the high fracture density zone in the eastern sector is relatively smaller as compared to those in the western sector. They are observed at depth of 1425-1450 m- MD; 1540-1560m-MD; 1585-1595m-MD and 1875-1945m-MD (Table 2 and Figure 10).

Table 2: Summary of High Fracture Density Zone on Eastern Sector of GSF.

No.	Depth Interval (mMD)	Lithology	Avg. Fracture Strike/Dip
1	1425-1450	Limestone	N15E/75
2	1540-1560	Limestone	N327E/80
3	1585-1595	Limestone	N355E/75
4	1875-1945	Quartzite	N213/70

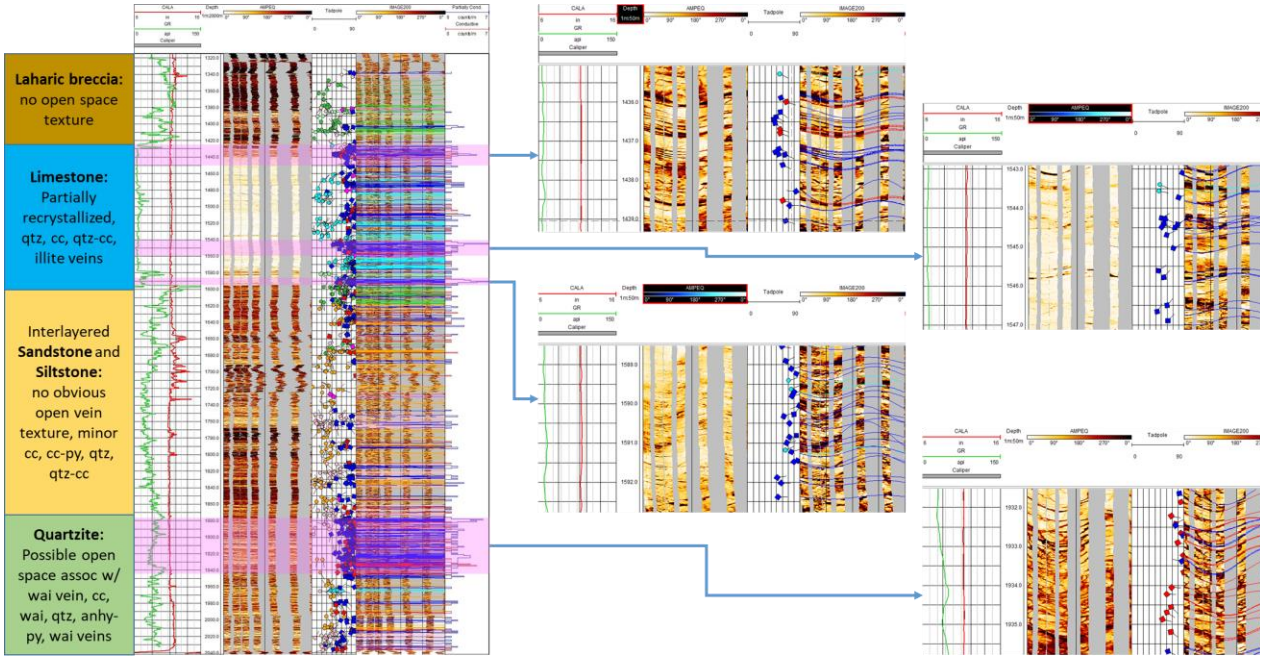

Figure 10: Fracture density of the eastern well showing a predominance of partially conductive fractures. Total four high fracture density zones are observed: at 1425-1450 m-MD (partially); 1540-1560 m-MD (partially); 1585-1595 mMD (partially) developed in limestone formation and at 1875-1945 m-MD (conductive) developed in quartzite formation.

Three intervals of high fracture density are developed on the limestone formation at upper section, while one interval is identified in the interlayered quartzite formation at lower section. The average strike trend of the high fracture density fractures is N-S to NE-SW with the dip magnitude in the range of 70-80 degrees (Table 2). Fractures that developed in the limestone formation are dominantly composed of partially conductive fractures. They are indicated by small to "hairline" aperture size and discontinuity of the conductive sinusoids. Based on the petrography analysis, the limestone unit associates with quartz, calcite and illite filling veins. These data integration possibly indicates that the fractures have been partially filled with secondary minerals. In the other hand, the lower section shows more conductive fractures as indicated by continuous sinusoid with a relatively clearer aperture. This set of fractures is developed in the quartzite formation at 1875-1945 mMD (Figure 10).

3.4 Fracture Aperture

The fracture aperture calculation was performed by calculating the height of the fracture (top and bottom edge) to get the apparent aperture size. It was followed by the correcting the data with hole azimuth, inclination and the fracture strike-dip to obtain the true aperture dimension. The correlation of the fracture aperture and lithology is expected to improve the understanding of the aperture development on the different types of formation and their position relative to the major GSF block. In theory, higher fracture aperture is interpreted to higher permeability.

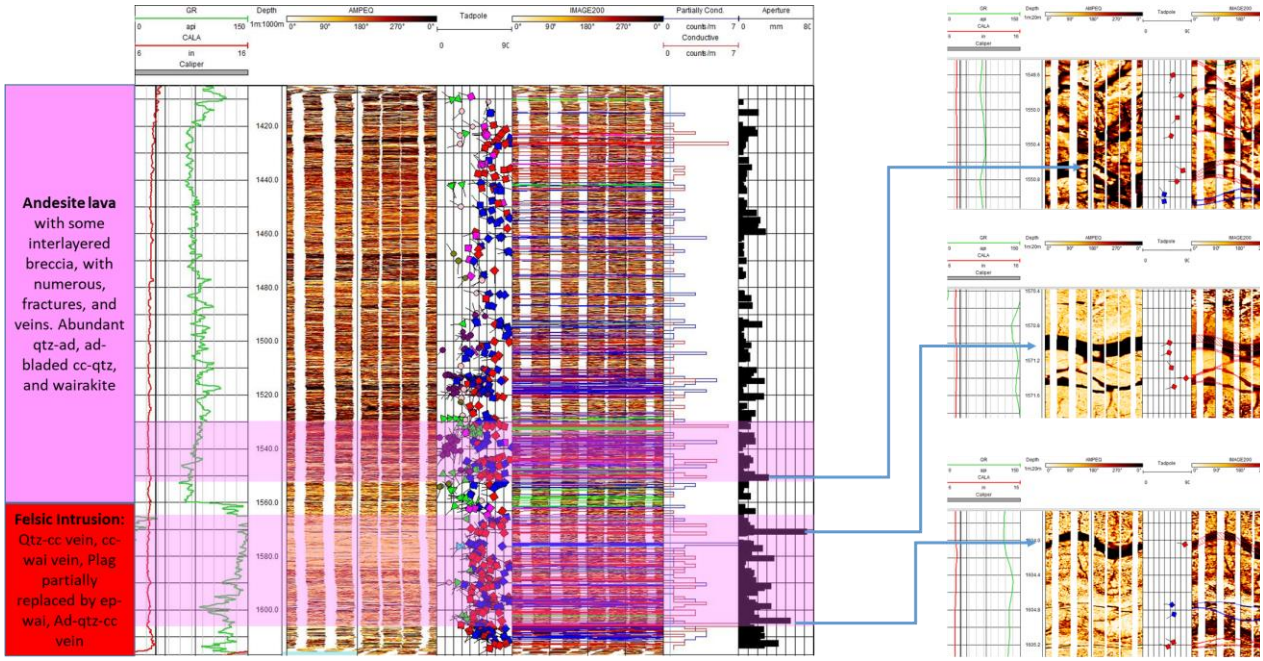

Figure 11: Fracture aperture larger than 30mm was observed in the western sector well. At the andesite formation, the largest aperture is found on conductive fracture at 1550 m-MD has 35mm aperture, while in the felsic intrusion the largest aperture is also found on the conductive fracture at depth 1571 and 1604 m-MD with the aperture of 73 mm and 56 mm.

3.4.1 Fracture Aperture on Western Sector

Several conductive fractures are observed to have apertures larger than 30mm and developed in both andesite and felsic intrusion formations. At depth 1550 mMD, the maximum aperture in andesite formation is ~32 mm while the maximum aperture in felsic intrusion is relatively larger. A fracture aperture of 73 mm is found on the conductive fracture at depth of 1571 mMD and an aperture of 56 mm at 1604 mMD (Figure 11).

The brittle formation of andesite and felsic intrusion is most likely a factor that causes fractures with large apertures to form in the western sector of the GSF. It implies on field development strategy whereas drilling in western sector is suggested to target structures that associates with thick volcanic unit and intrusion that effectively accommodate larger fracture aperture development.

3.4.2 Fracture Aperture on Eastern Sector

In the eastern sector, the maximum fracture aperture is observed significantly smaller as compared to the western sector. It is approximately 29 mm. The fractures with this aperture are found in quartzite formation at depth 1935 mMD and 2020 mMD. Smaller maximum aperture is observed on limestone formation. It is nearly 23 mm at 1438 mMD (Figure 12). The result from aperture interpretation on the eastern sector confirms that fractures are not well developed in the sediment rock units. In addition, the lower fracture aperture on eastern sector is also possibly caused by mineral precipitation. As the result, well targeting in eastern area where this outflow zone is suitable for injection wells may possess higher risk in finding the permeable zones.

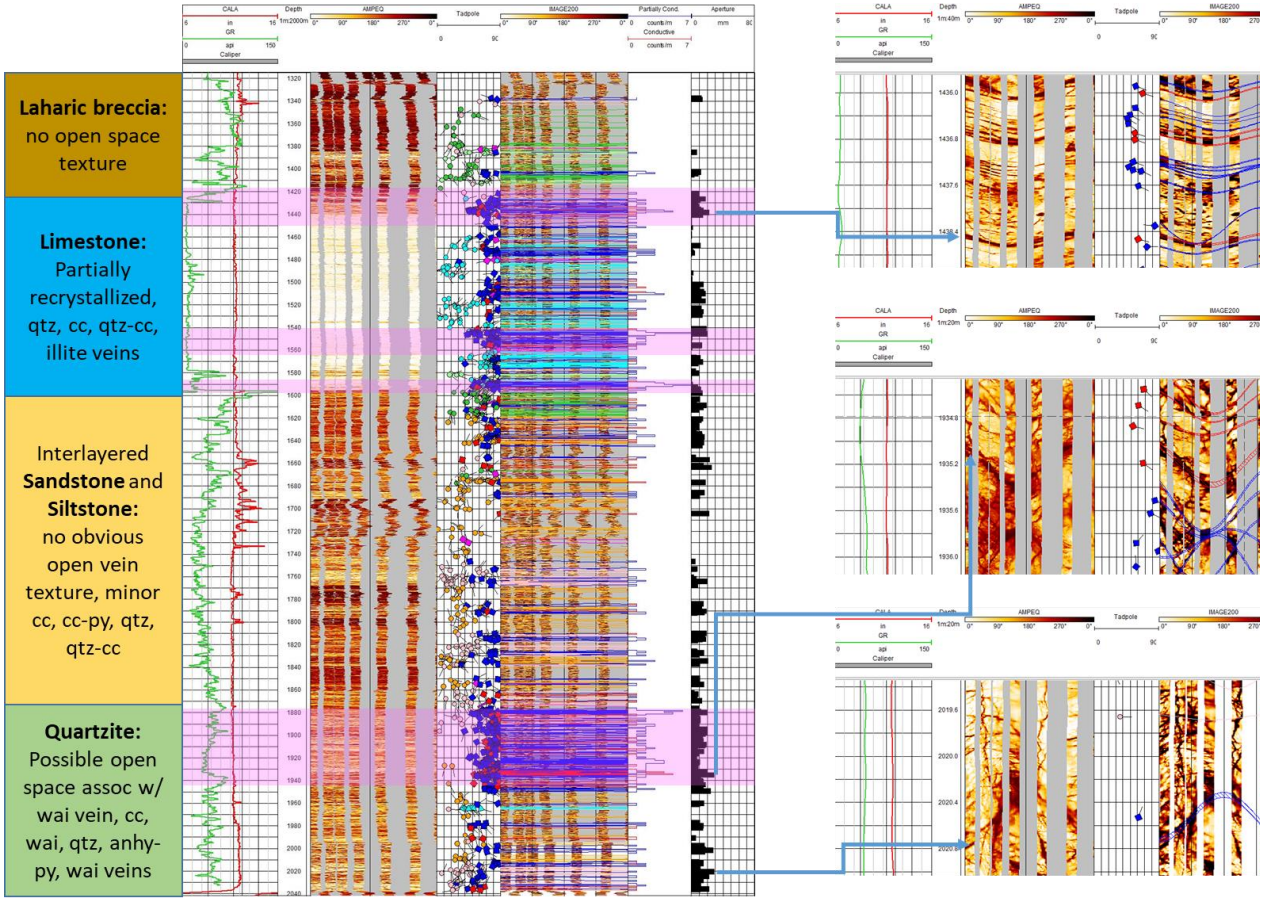

Figure 12: Fracture apertures on eastern sector are smaller as compared to western sector. The maximum aperture of ~ 29 mm is observed on conductive fractures that developed on quartzite formation at depth 1935 mMD, while the maximum aperture of ~ 23 mm is identified on the limestone formation at depth 1438 mMD.

4. COMPLETION TEST RESULT

As part of the completion well drilling procedure, series of well test programs, namely: Injection PTS spinner, II test, pressure fall-off, and static PT are performed. The objectives are to identify the location of the permeable zone, Injectivity Index, and near-wellbore characteristic of both western and eastern wells. The Injectivity Index (II) test result obtained from 2 completion tests showed significant differences. Moreover, the western sector well exhibits higher temperature and higher permeability as compared with the eastern sector well.

Seven permeable zones were identified on the western sector well, with the deep feed zone (below 1420 mMD) comprises of series of fractures (Figure 13a). The presence of big open fracture is supported by the XRMI Image analysis and shown by the evidence of continuous total loss circulation (TLC) until total depth (TD). Based on injection spinner analysis, the total II is not less than 82.4 kg/s/bar, this indicates a highly permeable well. Multirate injectivity test under 5 different injection rates was performed as shown by Figure 13b. As shown in the chart, an insignificant (relative flat) pressure difference was observed, this suggested inflow of fluid to the wellbore from the upper permeable zones. The wellbore pressure due to injection is balanced by incoming fluid from the reservoir. Spinner profile and pressure response during shut-in survey indicate inflow at depth 880-1255 mMD, despite well being injected at 1000 gpm.

Similar to II test, the standard completion test is to conduct the Pressure Fall Off (PFO) test after the multi-rate II test. The test was conducted by shutting off water injection immediately from the initial injection rate of 1200 gpm. However, the downhole pressure increased immediately after injection was stopped due to increased wellbore temperature, which eventually changes the hydrostatic pressure gradient. This quick heat-up is another clear indication of a strong permeable zone.

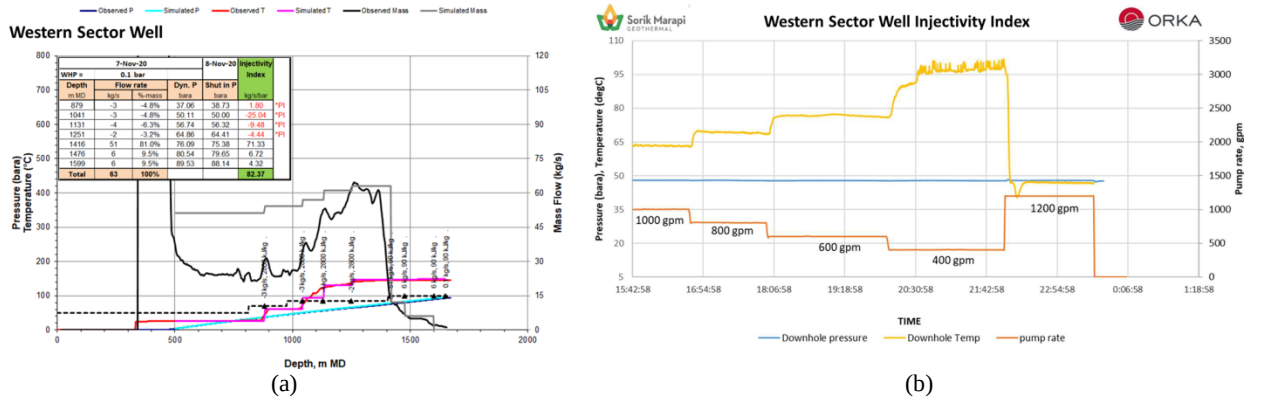

(a) (b)

Figure 13: (a) Injection PTS analysis of western sector well shows seven permeable zones, (b) downhole pressure and temperature of western sector well during multi-rate test showing relatively flat pressure gradient.

Meanwhile, in the eastern sector well, five permeable zones were identified from the PTS-Injection analysis (Figure 14a). Feed zone locations are consistent with the evidence of PLC during drilling and XRMI image log results. According to the multi-rate test, as shown by Figure 14b, the total II estimated by the multi-rate injection test is approximately 1.27 kg/s/bar. PFO analysis results in permeability thickness (kh) of 896 md-ft and skin of -3.95. This low kh value indicates that the eastern sector well has initially tight connectivity to the large natural fracture network, which is consistent with the currently low II value. The negative skin value indicated that there is no near-wellbore formation damage that could create additional resistance to the flow around the wellbore or due to the inherent natural fractures in the vicinity of the wellbore. The current injection capacity of the eastern sector well is in the range of 150 – 200 tph.

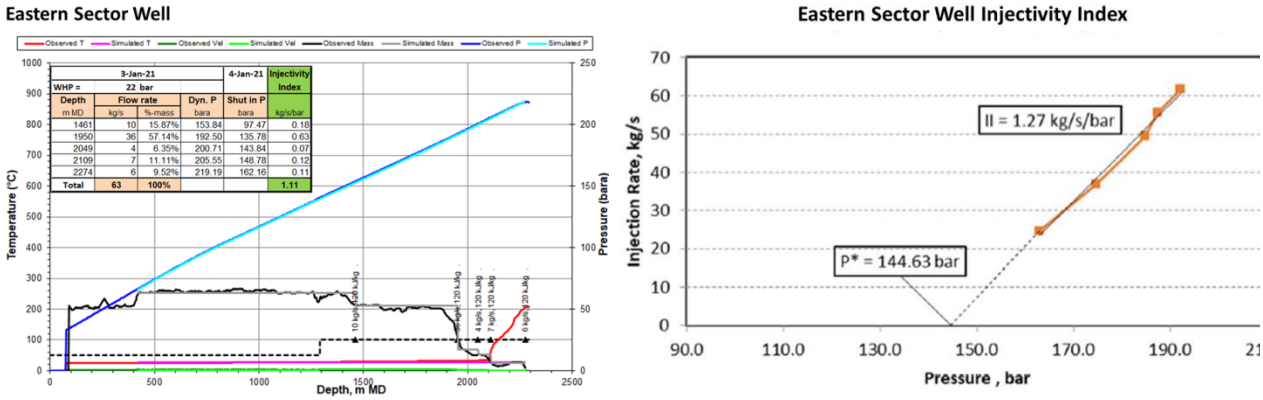

(a) (b)

Figure 14: (a) Injection PTS analysis of Eastern sector well shows five permeable zone, (b) plot of injection rate and downhole pressure at eastern sector indicates II of 1.27 kg/s/bar.

The significantly different completion test results are in agreement with fracture characterization results that discussed in the previous sections. The high injectivity value of 82.4 kg/s/bar on the western sector correlates with high density of conductive fractures and larger apertures, meanwhile the eastern sector has much lower injectivity index. Other factor yielding this discrepancy is higher temperature in the western sector well as compared to the eastern sector well. 1.27 kg/s/bar

5. DISCUSSION

The integration of resistivity image log, gamma-ray log, drilling cuttings, drilling parameters and completion well test data seems to give a reasoning explanation on the different permeability and improve the understanding on the fracture characteristic within Sorik Marapi geothermal fields (Figure 15), such as:

1. In terms of fracture density, both eastern and western sectors have a relatively similar fracture density.
2. In the case of fracture type, the western sector predominantly consists of conductive fracture while the eastern sector mostly consists of partially-conductive fracture.
3. The larger fracture aperture is observed in the western sector as compared to the eastern sector.
4. All the aforementioned are supported by substantial difference on the injectivity index value of about 80 kg/s-bar between the 2 sectors.

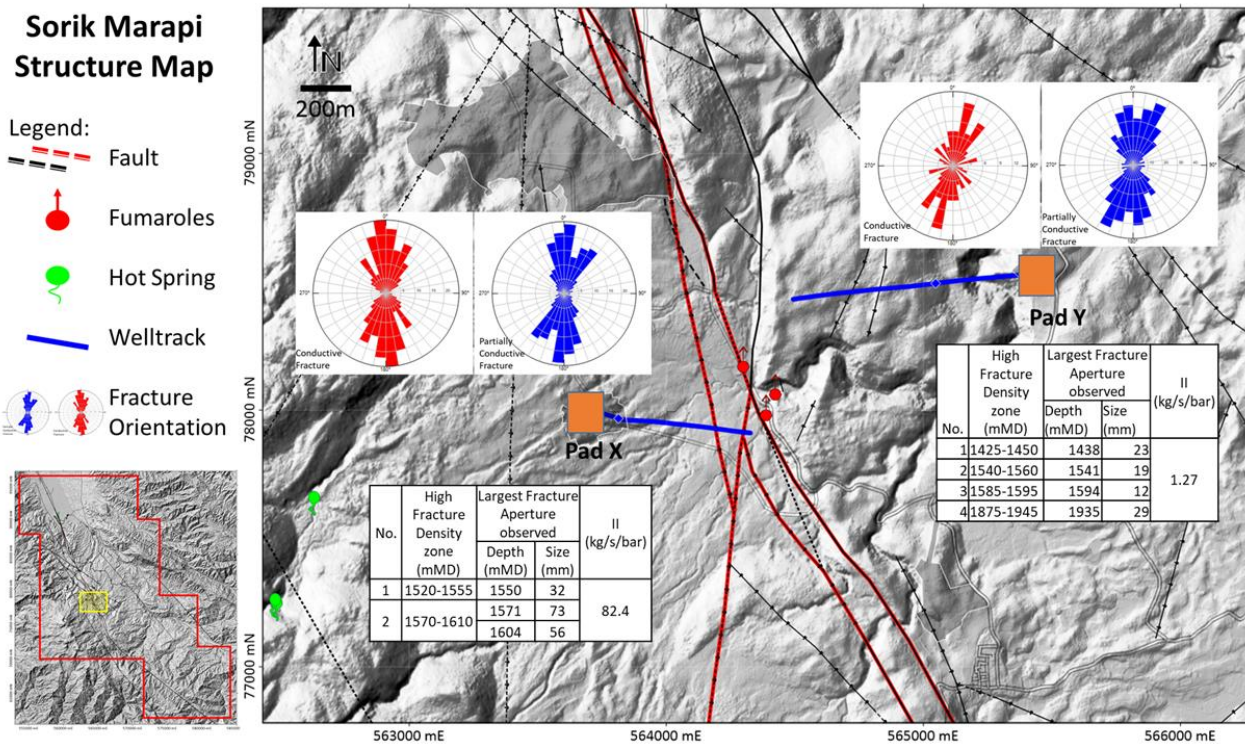

Figure 15: Comparison of fracture characterization on both sectors, namely fracture orientation, fracture density, fracture apertures and injectivity index.

There are 2 possible models that explain the discrepancy of western and eastern fracture characteristics, namely:

1. Basin filling by distal volcanic facies and sediments.
   The position of Sorik Marapi Volcano that slightly outside the pull-apart basin (Figure 16) allows the deposition of distal volcanic facies such as clay-rich deposits to the basin to form impermeable fault cores and less damage zones (Rowland and Sibson, 2004 after Caine et al., 1996 in Sutrisno et al., 2019). This is reinforced by the finding that the high fractures density only observed in limestone and quartzite formation on the eastern sector which is relatively more brittle as compared to the other sedimentary unit that developed on the eastern sector. However, the boundary of the pull-apart basin is still uncertain since it is may have been covered by the younger volcanic products of Mt. Sorik Marapi.

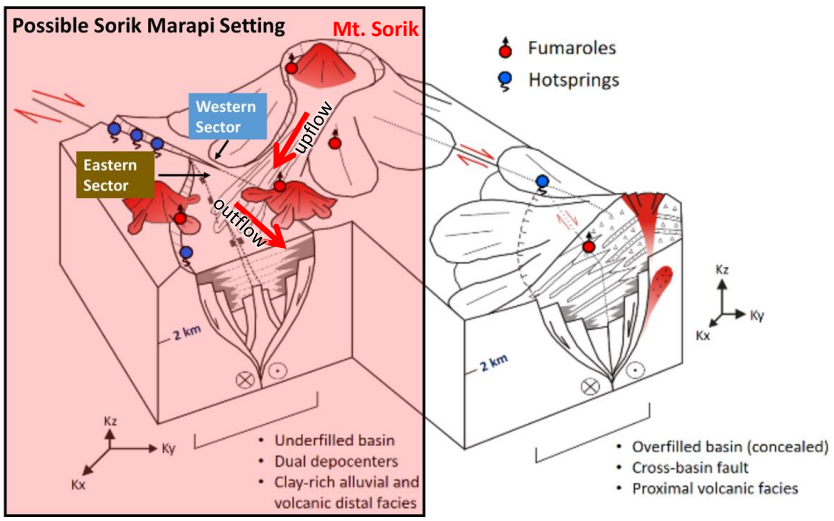

Figure 16: Possible Sorik Marapi setting, volcanic center is located slightly outside the pull-apart basin tends to have underfilled basin and distal volcanic facies deposition which result in and less brittle formation for fracture development and permeability (modified after Sutrisno et al., 2019).

2. Mineral precipitation due to boiling.
   With regards to the fluid flow model of the system, the eastern sector whereas interpreted as the outflow zone may undergo boiling (Figure 16). This common reservoir process may allow the precipitation of secondary minerals within the fractures in the eastern sector. It is evidenced by the presence of minerals such as calcite and silica as vein filling. The precipitation of prograde and retrograde solubility minerals at the same depth is only accommodated by boiling process. In addition, the enormous calcite vein filling observed in the drilling cutting is explained by the calcite dissolution from limestone. It results to calcite oversaturation in the fluid and leads to mineral precipitation at shallower depth as boiling occurs. This hypothesis is supported by petrography analysis (Figure 17).

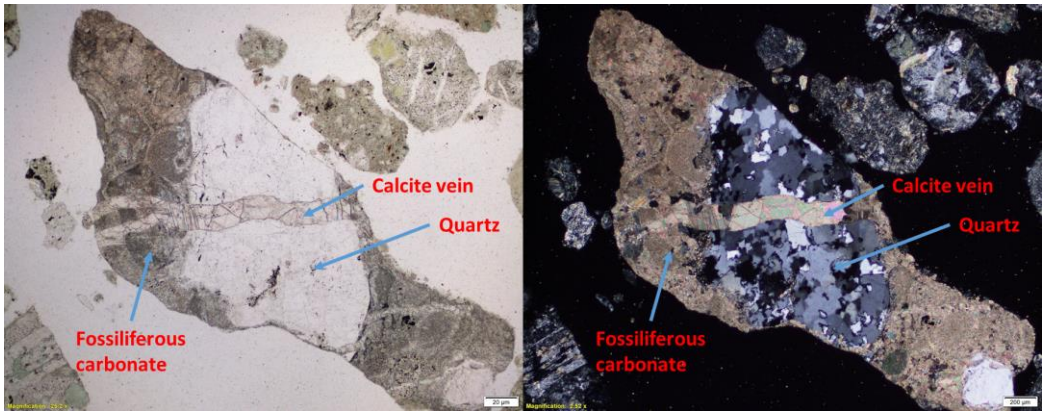

Figure 17: Thin section on parallel (left) and cross nicol (right) on the eastern sector well shows calcite and quartz vein development on the limestone formation.

These 2 competing models need to be narrowed down by additional resistivity image log from different depth and different well, fluid inclusion, and etc. The constrained model is crucial in defining the development strategy of this asset. Placing the production wells and injection wells with respect to permeability difference at western and eastern sectors are critical in ensuring the sustainability of the production. In the meantime, this fracture characterization result is believed to help the subsurface team in developing more effective and efficient well targeting plan.

6. CONCLUSION

Similar stress regime, direction and the inherited basement structures give a more enigmatic story on different permeability on western and eastern sectors. Reminiscing the relatively different lithology between both sectors may reveal the mystery. The western sectors lithology is composed of thick layer volcanics and felsic intrusion rock while the eastern sector is predominantly composed of sediment to metasediment rock. As the result, both sectors experience different rheology and deformation mechanism. The deformation on the western brittle volcanics rocks results to larger fracture aperture meanwhile the active faulting on the eastern sediment only produces smaller aperture. It is interpreted that the fractures with large apertures tend to have a long continuity that allows interconnectivity between the fractures or even connects to the major structure and permit the fluid flow. In the other hand, the smaller apertures possibly tend to be developed near wellbore and disconnected to the major fault and consequently limit the fluid flow. Since eastern sector is located within the outflow zone of the system, thus cooling and boiling of hydrothermal fluid is considerably responsible on its lower permeability. That reservoir process allows the precipitation of silica and calcite as fracture filling and reduced the permeability. This study from Sorik Marapi geothermal field signifies another characteristic of fractures associated with GSF in comparison with the other geothermal fields that located within this mega fault zone in Sumatera Island. It is expected that this result may contribute to the improvement of the understanding on fracture characteristics of the other geothermal prospect along this fault zones.

7. ACKNOWLEDGEMENT

We would like to thank KS Orka Renewables for granting permission to publish this study, especially to Dr. Yan Tang and Kevin Cao for supporting us in making this paper.

REFERENCES

Aydin, A. and Nur, A.: Evolution of pull-apart basins and their scale independence, *Tectonics*, 1(1), (1982), 91–105. https://doi.org/https://doi.org/10.1029/TC001i001p00091

Barber, A. J., Crow, M. J., and Milsom, J. S.: Sumatra: Geology, Resources and Tectonic Evolution, *Geological Society, London*, Memoirs, 31, (2005).

Eggertsson, G. H., Lavallée, Y., Kendrick, J. E., and Markússon, S. H.: Improving fluid flow in geothermal reservoirs by thermal and mechanical stimulation: The case of Krafla volcano, Iceland, *Journal of Volcanology and Geothermal Research*, 391, (2020), 106351. https://doi.org/10.1016/J.JVOLGEORES.2018.04.008

Hall, R.: Late Jurassic-Cenozoic reconstructions of the Indonesian region and the Indian Ocean, *Tectonophysics*, 570–571, (2012), 1–41. https://doi.org/10.1016/j.tecto.2012.04.021

Jafari, A. and Babadagli, T.: Effective fracture network permeability of geothermal reservoirs, *Geothermics*, 40(1), (2011), 25–38. https://doi.org/10.1016/j.geothermics.2010.10.003

Muraoka, H., Takahashi, M., Sundhoro, H., Dwipa, S., Soeda, Y., Momita, M., and Shimad, K.: Geothermal systems constrained by the Sumatran fault and its pull-apart basins in Sumatra, Western Indonesia, *World Geothermal Congress* 2010, April, 25–29, (2010).

Nicholson, K.: Geothermal fluids chemistry and exploration techniques, Springer (1993).

Perdana, T. S. P., Hackett, L., and Roberson-tait, A.: Characterizing Subsurface Structures and Determining In-Situ Stress Orientation Using Fullbore Formation MicroImager (FMI) and Sonic Scanner : A Case Study from FORGE Well 21-31, Fallon, Nevada, USA, *45th Workshop on Geothermal Reservoir Engineering*, (2020), 1–15.

Rowland, J. V. and Sibson, R. H.: Structural controls on hydrothermal flow in a segmented rift system, Taupo Volcanic Zone, New Zealand, *Geofluids*, 4, (2004), 259-283.

Shi, Y., Song, Z., Li, J., Wang, G., Zheng, R., and YuLong, F.: Numerical investigation on heat extraction performance of a multilateral well enhanced geothermal system with a discrete fracture network, *Fuel*, 244, (2019), 207-226. https://doi.org/10.1016/j.fuel.2019.01.164

Sieh, K. and Natawidjaja, D.: Neotectonics of the Sumatran fault, Indonesia, *Journal of Geophysical Research: Solid Earth*, *105*(B12), (2000), 28295–28326. https://doi.org/10.1029/2000jb900120

SMGP: North Sorik Exploration internal report, In preparation (unpublished) (2021).

Sutrisno, L., Bonte, D., Daud, Y., Smit, J., Beekman, F., Wees, J. D. Van, and Purwanto, W.: Assessing the Role of Pull-Apart Basins for High-Temperature Geothermal Resources in Transcurrent Tectonic Setting: Sumatra and California Compared, *European Geothermal Congress*, June, 1–8, (2019).

Zhang, W., Qu, Z., Guo, T., and Wang, Z.: Study of the enhanced geothermal system (EGS) heat mining from variably fractured hot dry rick under thermal stress, *Renewable Energy*, 143, (2019), 855-871. https://doi.org/10.1016/j.renene.2019.05.054

The Important Role of Wairakite at Sorik Marapi Geothermal Field

Ridha Hendri, Stephen Simamora, Haris Siagian, Tio Ferdinan,
Junior Setiawan, Christovik Simatupang, and Riza Pasikki

KS Orka Renewables Pte Ltd.

ridha.hendri@ksorka.com, stephen.simamora@ksorka.com, haris.siagian@ksorka.com, tio.ferdinan@ksorka.com,
junior.setiawan@ksorka.com, christovik.simatupang@ksorka.com, riza.pasikki@ksorka.com

Keywords: wairakite, temperature, epidote

ABSTRACT

The combination of low resistivity anomaly distribution, clay alteration zone, high temperature mineral assemblage, circulation losses during drilling, and temperature measurement from downhole survey have been commonly used to constrain the uncertainty in identifying geothermal Top of Reservoir (ToR).

However, inconsistency between epidote assemblage with measured downhole temperature has been observed from the drilled wells in Sorik Marapi geothermal field. Since epidote is identified as one of the earliest calc-silicate minerals to form in most of geothermal mineral paragenesis, there is chance that other high temperature calc-silicate minerals are potentially to be observed at greater depth where consistency with downhole temperature measurement is exhibited. Petrography analysis from the collected cutting samples have indicated that wairakite could be used as mineral indicator to locate the ToR at consistent depth with Pressure Temperature (PT) survey result. The presence of this mineral at deeper portion in the reservoir is possibly explained by the increasing concentration of Fe^{3+}, decreasing pH and/or temperature.

The correlation of wairakite appearance with vertical distribution of illite, epidote, prehnite, calcite, anhydrite, and silica are believed to constrain the potential model in explaining the role of $Ca_8(Al_{16}Si_{32}O_{96}).16H_2O$ zeolite mineral at Sorik Marapi geothermal field.

1. INTRODUCTION

The Sorik Marapi Geothermal Field is located about 650 km south-southeast of Medan, the capital city of North Sumatra province and situated within the administrative area of Mandailing Natal district. This field (Sorik Marapi) is located on the lower northeast flank of Sorik Marapi volcano and along a major active strand of the Sumatra Fault System in North Sumatra (Figure 1). Sorik Marapi was initially studied by industry and academia in the 1980s and 1990s (Hochstein and Sudarman, 1993). The first comprehensive geothermal assessment of Sorik Marapi was completed in 2011, and involved geology, geochemistry, and geophysics studies, in addition to drilling three shallow slim wells (SKM, 2011). This assessment concluded that up to 4 possible resource areas were present along discrete parts of the SFS of the Sorik Marapi volcanic edifice. Currently Sorik Marapi Geothermal Power (SMGP) has drilled >30 wells in Sibanggor area (southernmost of SKM interpreted area) since 2016 and has proven a ~245° to 325°C and already produced the electricity of 90 MW.

2. GEOLOGICAL SETTING OF SORIK MARAPI FIELD

2.1 Field Overview

Sorik Marapi geothermal (Figure 1) area is a part of Western Bukit Barisan volcanic range which extends along the length of Sumatran Island. This zone forms a volcanic range separated by graben from the late Mesozoic meta-volcanics and meta-sedimentary which was covered by volcanic sediment of Miocene age. It was then overlain by the quaternary volcanic rocks made up of andesitic to dacitic pyroclastics and lava.

The active Sumatra fault zone runs through the whole length of Sumatra, within the Bukit Barisan, from Banda Aceh to the Sunda Strait, and is paralleled by a line of quaternary volcanoes. The overall shape of Sumatran Fault is sinusoidal, the northern half of which is gently concaved to SW, whereas the southern half is concaved to NE. There is an irregularity in the fault geometry termed “bifurcation”. The Bifurcation started near Sibual-buali and Lubuk Raya towards the Southeast into two principal active strands (Figure 2). The two strands are separated from each other (Natawidjaya, 2002). The western branch of bifurcation does not rejoin the eastern branch which continued toward the southeast of Sumatra. Sorik Marapi geothermal field lies at the center of the western branch of Sumatran fault. Most of local fault which parallel to NW-SE major fault trend provide less promising permeability except the NE-SW and N-S trend which are believed to provide good permeability in Sorik systems.

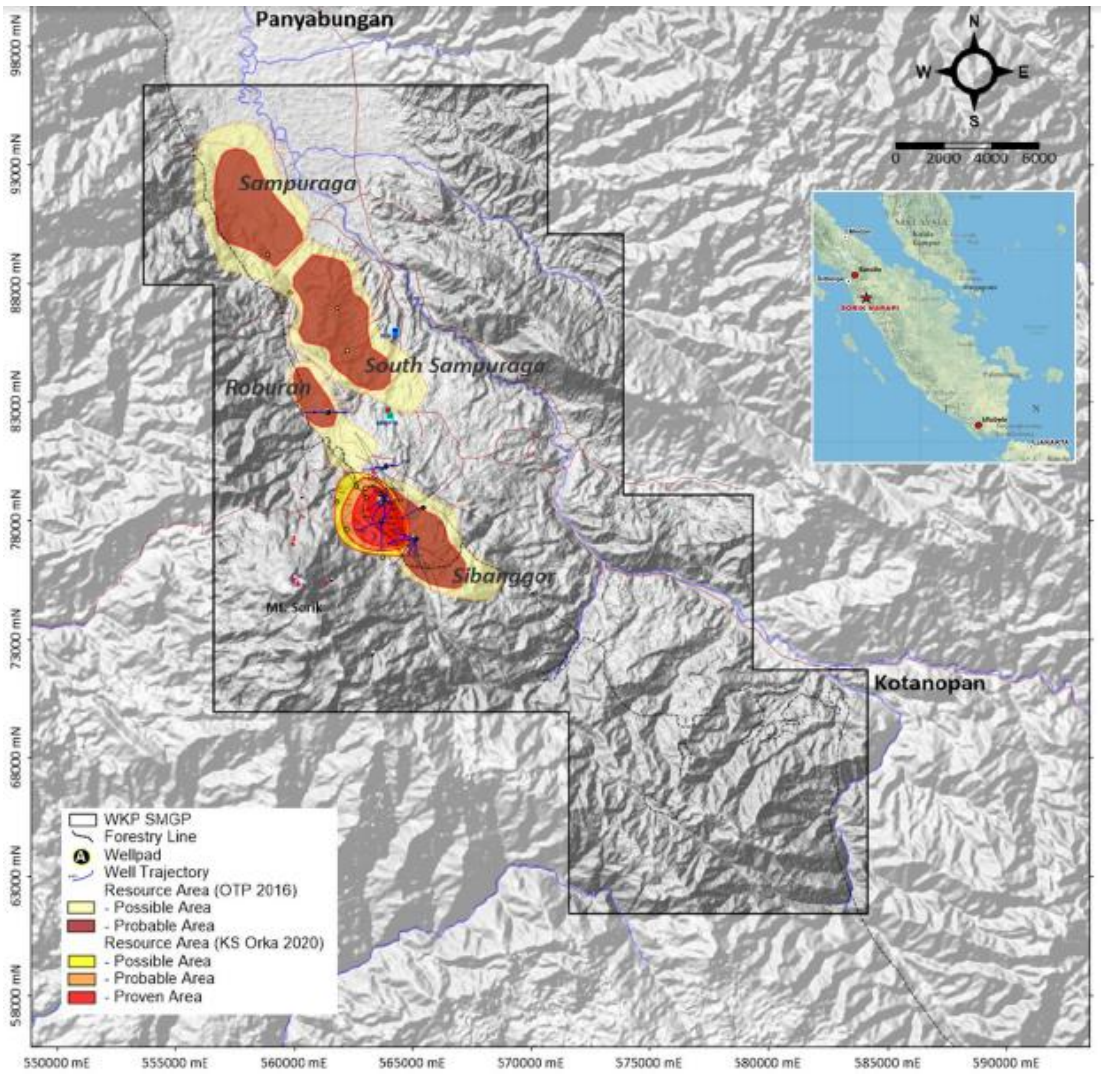

Figure 1: Location map of the Sorik Marapi geothermal prospect on Sumatra.

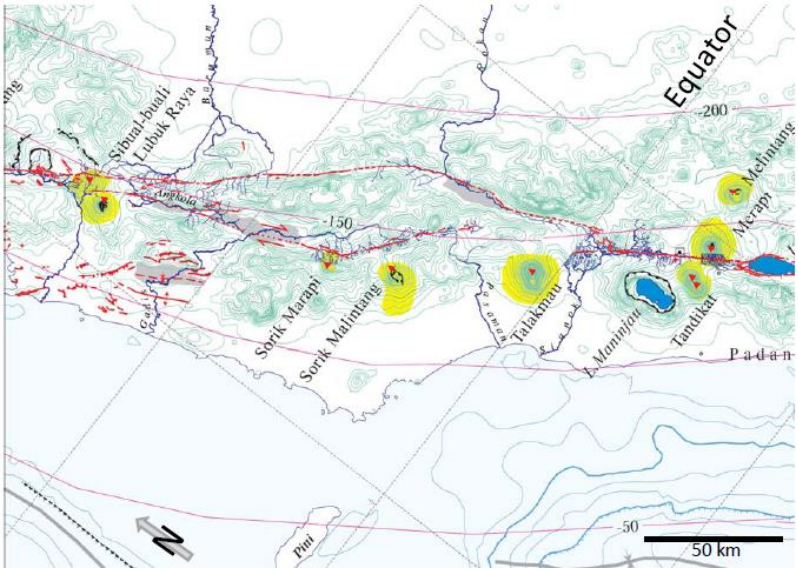

Figure 2: Map of the Sumatran Fault Zone (In red) in the vicinity of Sorik Marapi Volcanic craters and cones are shown in yellow. Contours in red are the top the Benioff-Wadati zone. Detail from Sieh and Natawidjaya (2000).

Lithologic in Sibanggor area of Sorik Marapi were updated based on integrated observations from binocular microscope and petrographic analysis (Figure 3), which resulted in the identification of several new lithologies and grouped into five formations: 1) Quaternary Intrusions, 2) Quaternary-Tertiary Volcanics, 3) Tertiary Sediments, 4) Mesozoic or Paleozoic granite, and 5) Mesozoic or Paleozoic metasediments (Figure 3).

The oldest formations comprise Paleozoic and/or Mesozoic metasediments, which include phyllite, schist, quartzite, slate, and carbonates. The outcrop of this metamorphic units is exposed at NW of Sibanggor area in both deposition and fault contact with overlying QTv. The metasediments are intruded by Paleozoic and/or Mesozoic granite that are present in south of Sibanggor. The tertiary sediments (Ts) overlying the metamorphic rocks and granite and consist of medium to course-grained sandstone and pebble conglomerates. These Miocene sediments are encountered at west and north of Sibanggor, and similar rocks are exposed at east of the Sibanggor or Pad A area (Figure 4). Quaternary to Tertiary age volcanics (QTv), consisting of interlayered felsic to intermediate composition lavas and tuffs rest on the Miocene sediments and volcanics, and older metamorphic rocks. The Qtv is present in all wells and reaches >2 km in thickness. The youngest unit is group of felsic porphyry intrusive rocks (QTi) that is intersected the metasediments and quaternary-tertiary volcanic rocks.

2.2 Geothermal Systems

Sorik Marapi geothermal system has evolved with the drilling of more wells and acquisition of new subsurface data. It becomes more apparent that the Sibanggor area of Sorik Marapi Geothermal system is characterized by heat source which located at flank of Mt Sorik Marapi, Western part of Pad A. It is supported by the highest temperature > 300^{o} C proven by the well that direct to the west. The outflow of this system flow to NE and SW area where it abuts a major strand of SFS. It is assumed that this fault as a boundary between high temperature area western part and low temperature at eastern part. The temperature of P wells (east side of SFS) < 240^{o} C as an indication of this interpretation. The clay cap over the upflow shallow compare to outflow zone. However, the convective area is deeper to upflow than outflow zone.

3. METHOD AND ANALYSES

The resistivity data (MT), MEB analysis, alteration mineral and PT survey data were used to help the analysis of study. The MT supplemented to identify the low conductive which used to translate as clay cap. It is confirmed by the presence of MEB index data that take during drilling operation of each well. The alteration minerals such as anhydrite, wairakite, incipient epidote and crystal epidote were picked and projected in the cross section to understand the distribution. The temperature measurement from PT survey data was used and combined to the model in thermal contour form.

Combination of low resistivity, clay intensity from Meb analysis, high temperature mineral assemblage, location of feed zone and temperature measurement from downhole survey will be used to constrain the geothermal Top of Reservoir (ToR).

The appearance of epidote mineral was become a common practice to identified the ToR during drilling. However, in Sorik Marapi it is observed that the appearance of epidote was not consistent with the down hole temperature. There is calc-silicate mineral which is consistent with downhole temperature data namely wairakite. The correlation of wairakite appearance with other alteration minerals of illite, epidote, anhydrite, calcite and silica are believed to constrain and identify the updated ToR of Sibanggor area

4. HYDROTHERMAL ALTERATION

4.1 Conductive Clay Cap

MeB measurement was conducted during drilling to identify the clay mineral. The mapping of the base of the argillic cap provides the most consistent marker with the low resistivity data < 6 ohm of MT results. The top of the reservoir in this area, coupled with the appearance of chlorite replacement of phenocrysts; this is typical of the argillic to mixed clay (illite/smectite) transition and sometimes with spotted incipient epidote.

The resistivity cross-section runs along SW-NE across Mt Sorik and the Sibanggor Area. This profile shows low resistivity area within Sibanggor Area that overlies high resistivity anomaly positioned at the eastern slope of Mt Sorik Marapi. This feature is often associated with the central part of a geothermal resource, with the presence of a slightly updoming resistivity structure tends to indicate that this area where the main upflow is located. This is consistent with the results of drilling wherein pad T and A wells exhibit the highest temperature based on hydrothermal alteration and downhole measurements that reached > 300 ºC. The drilling of T-09 (reach 320 °C from measured PT survey) directed towards SW close to the eastern slope of Sorik Marapi volcano shed more light on the actual center of the geothermal reservoir.

The zoning of alteration mineralogy in nearby wells and estimated reservoir isotherms have been projected onto the cross-section. Figure 5 shows a very consistent correlation between the clay alteration mineral and resistivity. The low-resistivity cap (resistivity lower than 10 Ωm, typically < 6 Ohm-m) for Sibanggor' base of conductor (BOC), coincides with the smectite zone, which extends to the surface in the well field, and the increase in resistivity with depth very consistently follows the top of the mixed layered clay zone.

Another simplified resistivity cross-section along NW-SE direction of the Sorik geothermal system through 2-prospects area. The conductive layer (vary from 3-6 Ωm) is semi-continuous and thickened toward NW, as shown in Roburan areas, thickness more than 1500 m and related with low gravity anomaly indicates that around this area is affected by the pull-apart basin structure of Panyabungan Graben.

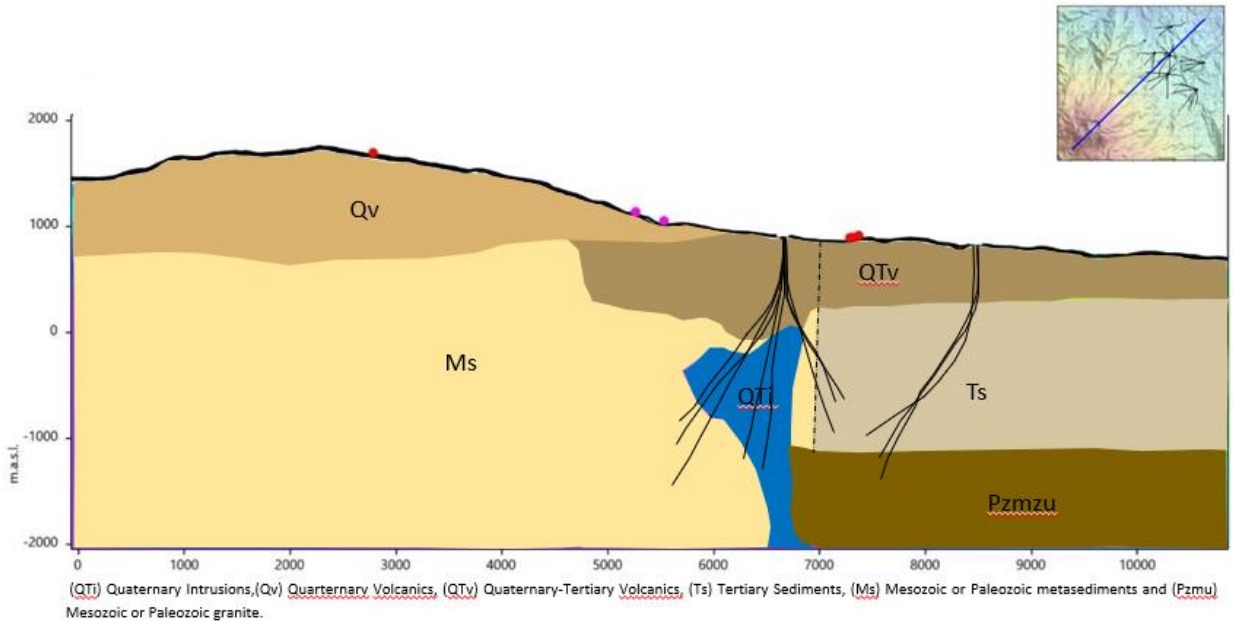

Figure 3: **West-East Stratigraphy Section of Sibanggor area, southernmost of prospect are at Sorik Marapi field.**

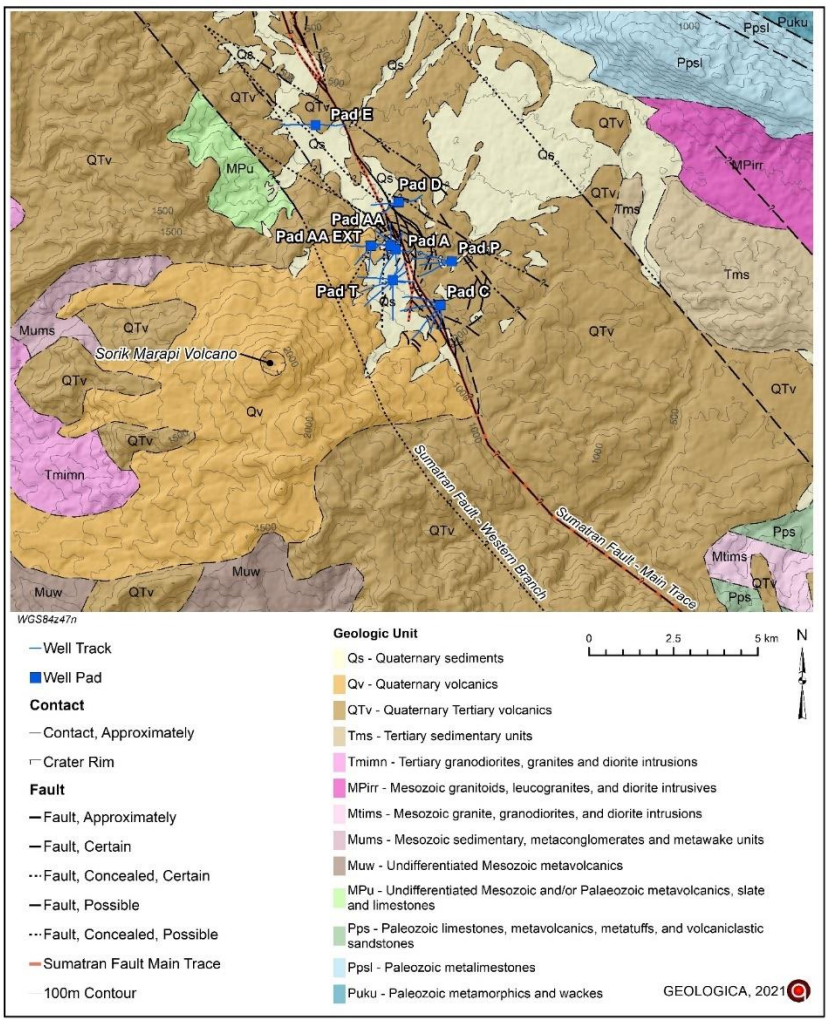

Figure 4: Updated geologic map of the region based on integrating field observations in 2018 - 2019, new drilling data, and original 1:250,000 scale mapping by Rock et al. (1983) (Hinz, 2021).

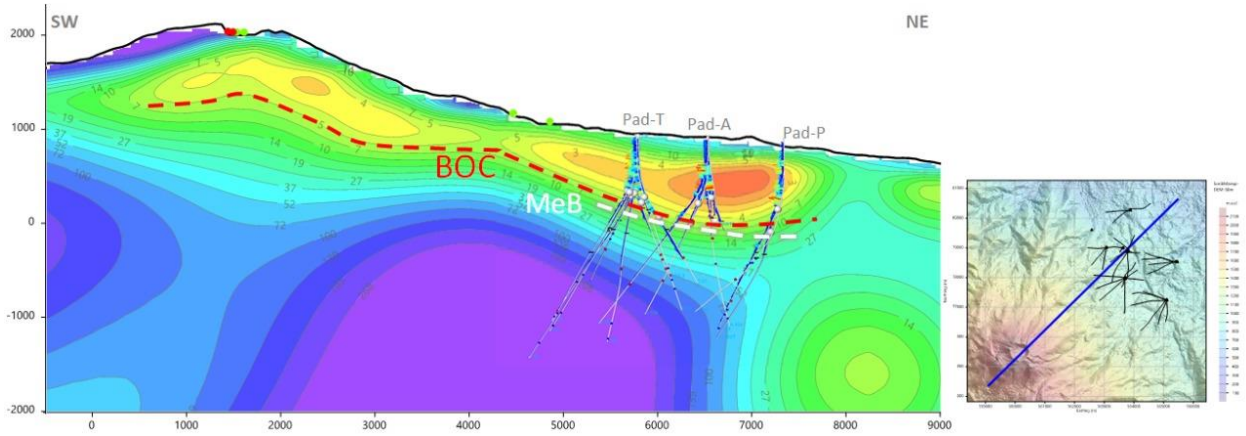

Figure 5: SW-NE cross section of MT data combine with MeB Index (white line), showing that the MeB Index almost similar depth with conductive area.

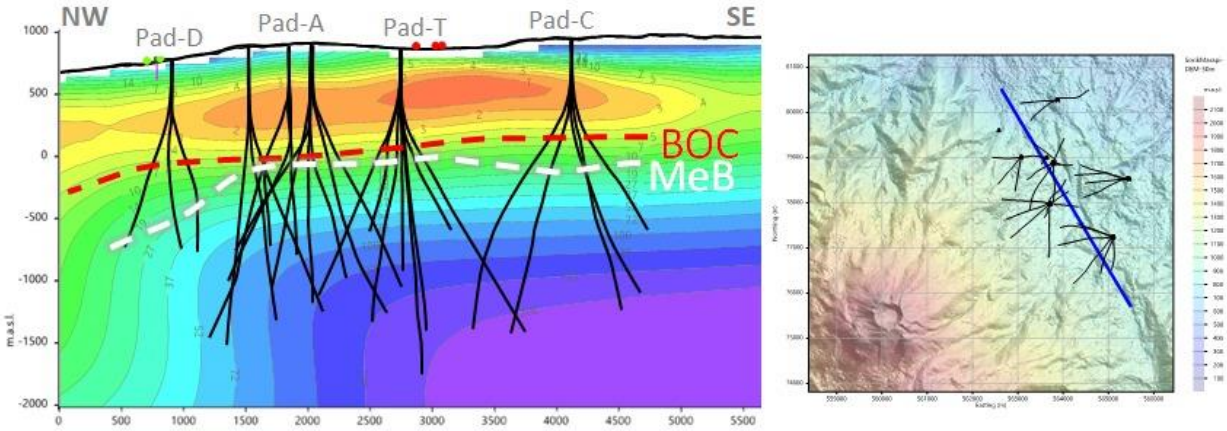

Figure 6: NW-SE cross section of MT data combined with MeB Index (white line), showing that the MeB index slightly deeper than conductive area.

4.2 Alteration zone

Based on the abundance of alteration mineral associations formed in Sorik Marapi, the hydrothermal minerals observed in the studied wells include clays (illite, smectite, and chlorite), silica (quartz), calc-silicate (epidote), zeolite (wairakite), and carbonate (calcite). However, the wairakite intensity is rarely observed or not too dominating. At the first 900 masl, the alteration mineral is dominated by the presence of low to medium temperature clay minerals such as smectite, illite and chlorite. Based on Corbett and Leach (1997), this zone is categorized as the argillic zone (with approximate temperatures of 150°C – 200°C) and is estimated as a caprock zone of the Sorik Marapi geothermal system. Incipient epidote, illite, calcite, chlorite and moderate distribution of anhydrite were found below ±900 masl to ± -1300 masl. Wairakite and epidote in crystalline form present at deeper area, below the anhydrite-incipient epidote zone area.

Although these minerals formed from near-neutral pH fluids, it is estimated that the acidic fluids had been present in the system. It is indicated by the presence of anhydrite. The anhydrite possibly formed as a result of pervasive mineral of condensate fluid.

4.3 Wairakite

As a member of high temperature zeolite mineral, wairakite ($CaAl_2Si_4O_{12}.2H_2O$) indicate neutral-pH condition and formation temperature at least 200 ^{0}C (Morrison, 1997). Wairakite found in Sorik Marapi typically observed as aggregate of subhedral to euhedral crystals with size of 0,1 to 1 mm and pseudo-dodecahedron individual shape. Mohs hardness test usually performed to check its properties, resulting $5<x<6$ in Mohs scale. In Sorik Marapi, this mineral occurs as hydrothermal vein-filling, replacement of primary feldspar and replacement of rock's matrix/groundmass.

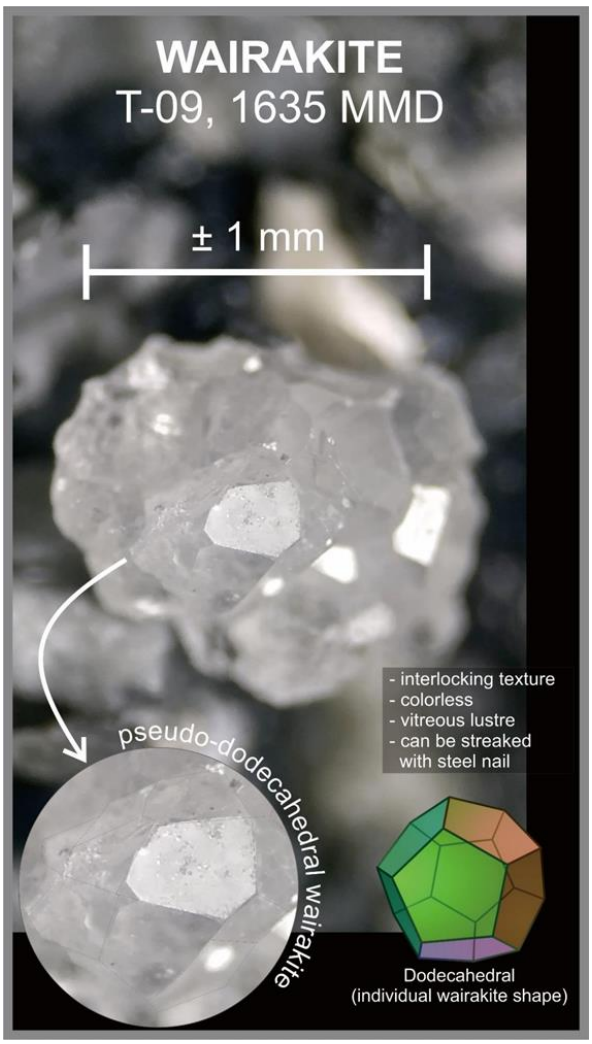

Figure 7: Good example of wairakite mineral observed by binocular microscope when drilling was carried on.

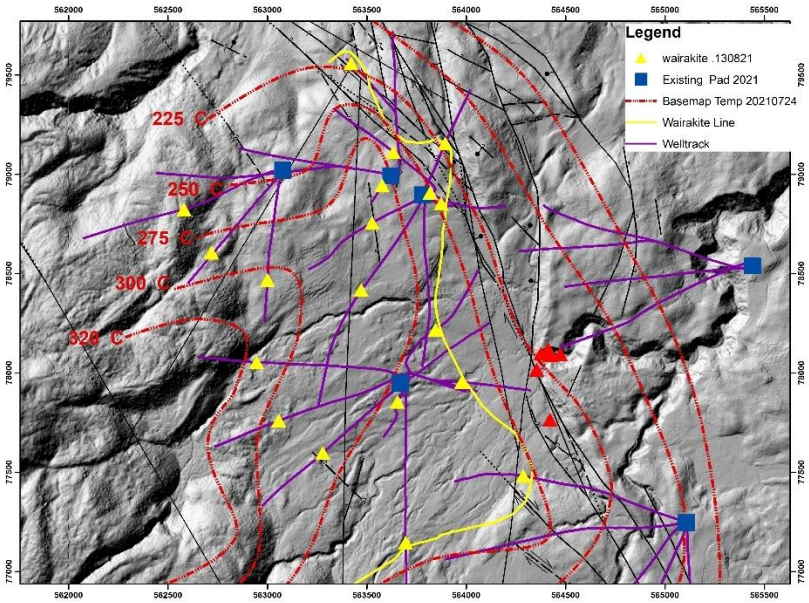

Figure 8: Wairakite distribution map combined with isothermal of present temperature measurement. From this map, it is known that wairakite typically distributed at western side of Great Sumatran Fault.

Based on correlation between PT Shut In survey and formation evaluation, shallowest depth where wairakite was found is at 877 m-MD (26 mSL) in A-104 well, where the downhole temperature is almost 260°C. Meanwhile, the deepest depth of wairakite occurrence is at 1,899 (-733 mSL) m-MD in T-04 well., where the present-day temperature is about ~225°C (Figure 9). These phenomena indicate the thermal and hydrology structures in the Sorik area are quite complex. Generally, the wairakites in Sorik Marapi field are observed on the western part of GSF in which pad A, AA, AAE and pad T located (Figure 8).

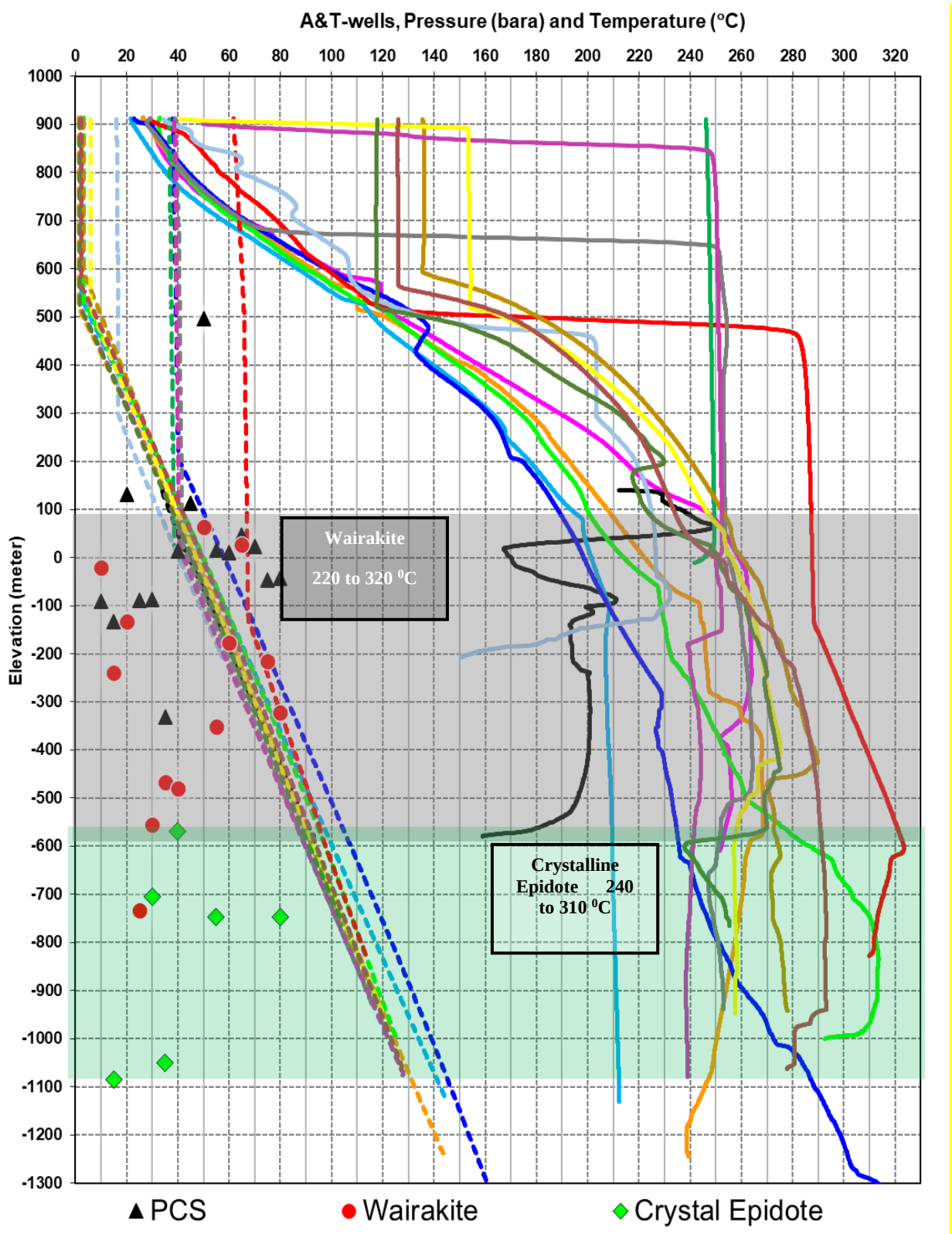

Figure 9: Distribution of top of crystalline epidote and wairakite in several wells of Sorik Marapi, correlated with PT survey.

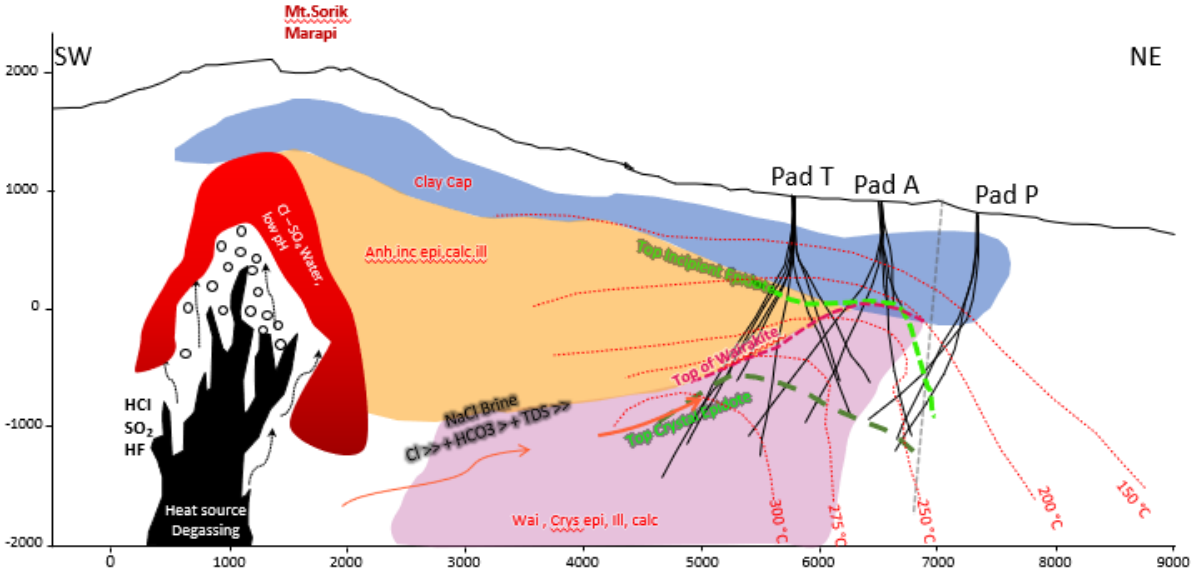

Figure 10: Cross-section model of alteration mineral assemblage in Sorik Marapi. Wairakite growth with crystalline epidote indicate temperature of 250-320 ºC.

Beside indicating high temperature, wairakite also known to indicate permeable zone (Morrison, 1997), especially when occur as euhedral shape and interlocked each other. In fact, occurrence of wairakite in most well is preceded by drusy quartz. As an example, in T-09 wairakite observed at 1632 mMD (-480 mSL), while first loss encountered about a hundred meter below the wairakite occurrence.

5. DISCUSSION

The distribution of hydrothermal minerals gives clues about the past conditions of the system, most notably the thermal conditions. The past thermal structures of the Sibanggor area in Sorik Marapi geothermal system are deduced from the occurrence of temperature-dependent hydrothermal mineral that occurs in the field. These include anhydrite, epidote, and wairakite.

The near-neutral pH fluids of systems could be identified by clays (illite, smectite, and chlorite), silica (quartz), calc-silicate (epidote), zeolite (wairakite), and carbonate (calcite). However, acidic fluids were present in the system. It is indicated by the presence of anhydrite in the production zone. Anhydrite presents sparsely distributed toward Sorik Mountain within range 900 to -1000 mSL. Likely the amount decreased below -1000 mSL.

Apparently at the first stage the ascending steam and gas mix with the ground water and condenses. This produces a condensate layer perched above deeper alkali chloride water. This condensate fluid may descend down through faults to depth at least 1 kilometer and forming the sulfate minerals such as anhydrite and fill the vugs. Second stage of boiling occurred and fluid has been neutralized in this stage, hence the wairakite and crystalline epidote was formed.

Epidote present in two forms: incipient epidote and crystalline epidote, where the first incipient epidote encountered at shallow depth compare to crystalline epidote. Wairakite appeared after first incipient encountered and it continues together with crystalline epidote present at depth area below– 900 masl.

Reyes (1998), mentioned that the crystal epidote occurred at > 280º C and wairakite at 220-310 ºC. Comparing to the pressure temperature (PT survey), wairakite appears where the temperature ranging at 220-320 ºC while crystal epidote found at 250-300 ºC (Figure 9 and Figure 10). From this evidence could be suggested that the presence of wairakite is applicable mineral to use as prominent temperature area in Sorik Marapi field especially in Sibanggor Area.

6. CONCLUSION

The main results of alteration study in Sibanggor Area of Sorik Marapi Geothermal Field, are elaborated below:

- The presence of wairakite together with crystalline epidote provide a reliable data that represent current subsurface temperature (220 to 320 ^{0}C), which validated by at least 17 wells located at the western side of Great Sumatran Field.
- In Sorik Marapi, the permeability can be indicated by wairakite. It is proven by all wells at the western of GSF that encountered the losses after found this mineral.
- Based on alteration mineral, there is an evolution of fluid pH. At the first stage, acidic fluid formed as the result of condensation activity, followed by fluid movement downward resulting precipitation of anhydrite. At the second stage, boiling process occurred and fluid being neutralized which indicated by wairakite and epidote.

REFERENCES

Hinz, N.M.: Conceptual Model Update of the Sorik Marapi Geothermal Prospect, Sumatra, Indonesia, *GRC Transactions*, (2021).

Hochstein, M. and Sudarman, S.: Geothermal resources of Sumatra, *Geothermics*, (1993), pp. 181-200.

Licup, A.S.: Geothermal 3D Subsurface Modelling - A Case Study from Sorik Marapi Field, Indonesia, *Proceedings*, 5th Indonesian International Geothermal Convention and Exhibition, (2017), p.13.

Morrison, K.: Importance Hydrothermal Minerals and their Significance, 7th ed., Geothermal and Mineral Services Division, Kingston Morrision Limited, New Zealand (1997).

Natawidjaya, D.H.: Neotectonics of the Sumatran fault and Paleogeodesy of the Sumatra subduction zone, California Institute of Technology, Pasadena, California (2002).

SKM: Report on Sorik Marapi Exploration, PT SMGP, Indonesia, Internal Report (2011).

This page is intentionally left blank

The Characteristic of 320°C Geothermal Wells at Sorik Marapi Geothermal Field

Ryan Hidayat, Christovik H. Simatupang, M. Ramos Suryanta Lubis,
Junior Setiawan, Haris Siagian, and Riza G. Pasikki

KS Orka Renewables

ryan.hidayat@ksorka.com, christovik.simatupang@ksorka.com, ramos.lubis@ksorka.com, junior.setiawan@ksorka.com, haris.siagian@ksorka.com, riza.pasikki@ksorka.com

Keywords: Sorik Marapi, reservoir characterization, geochemistry, geothermometry, vapor core, geothermal well

ABSTRACT

The Sorik Marapi geothermal field, located within the Great Sumatera Fault (GSF), has commissioned its first 45 MW plant in Q3 2019 and has been supported solely from Pad A wells. The next 45 MW is generated from the pad T wells that are located at the western area of the field. The outcomes demonstrated by the two wells drilled at Pad T exceeded the expectations. These wells exhibited high downhole temperatures up to 320°C and pressure in the range of 80 – 90 barg from the latest shut-in condition.

Despite of drilling fluid and intermittent infield injections, the collected fluid chemistry is still able to indicate a characteristic of wells that have better connection to the upflow of the system. The Na-K-Mg ternary plot shows nearly full equilibrated fluids are being discharged from the two wells. The high H_2S/CO_2 ratio and relatively higher Cl concentration strongly indicate that these 2 wells were drilled toward the upflow zone. In addition, the N_2-CO_2-Ar ternary plot signifies that both wells and the other drilled wells at Pad A and T are still within the productive outflow. In hindsight, there is upside potential to encounter higher temperature reservoir by drilling closer to the hypothetical upflow on the western side of Pad T toward Mt. Sorik.

The elaboration of the characteristics of these high temperature wells reveals another unique characteristic of geothermal fields that located within the mega fault zone in Sumatera Island.

1. INTRODUCTION

The Sorik Marapi geothermal field is located approximately 650 km south-southeast of Medan, the capital city of North Sumatra province and situated within the Mandailing Natal district area. It is currently being operated by PT. Sorik Marapi Geothermal Power (SMGP). The concession area covers nearly 629 km2 with various types of surface thermal manifestations such as solfataras, fumaroles, acid lake, Cl-SO4 springs, SO4 springs, mud pots, and bicarbonate springs. The surface features are distributed from the summit of Mt. Sorik to the depression zone of GSF at lower elevation (Figure 1 and Figure 2).

SMGP has drilled 31 wells at six different pads that aimed to support the generation of 90 MW in 2 stages of development phase. The first 45 MW is supported by six production wells that located at Pad A and the second 45 MW is completed by five wells at pad T. The nine injection wells are designated at Pad P, D and C that conceptually located at the edge of the reservoir (Figure 1 and Figure 2). The well head modular units of screw expander are fed by the steam that separated at each installed separator at Pad A and T, meanwhile the heat from separated brine is extracted through Organic Rankine Cycle (ORC) system. The residual steam from expander unit and brine ORC are still used through steam ORC system to give additional power generation.

In term of geothermal system, Sorik Marapi has similarity with the other geothermal fields that located within or close to the GSF system. The location of the heat source relative to the GSF zone seems to dictate the geothermal reservoir that developed in Sumatera Island. Currently, there are 2 conceptual models in explaining the geothermal system in Sorik Marapi. The first model indicates 2 possible upflows; one located within the Mt. Sorik while another one located on the flank of Mt. Sorik (Haizlip et al., 2020). The second model portrays 1 upflow that associated with Mt. Sorik with neutralization process through mineral buffers (Simatupang et al., 2021). Basically, both models show similar hypothetical heat source location where it is interpreted at western of GSF system. As the result, the area within the pull-apart basin in eastern sector is interpreted as the outflow of the system based on fluid chemistry, temperature, and pressure data. The GSF plays major role in dictating the rock unit and permeability distribution. In term of lithology, the western sector reservoir predominantly consists of volcanic rock at shallower depth with metasediment as the reservoir rock. The permeable zones in the reservoir are associated with fractures due to intrusion or faults. In the other hand, the eastern sector comprises sedimentary rock units as the reservoir rock with metasediment as the basement rock. Most of the permeable zones are related with fractures that developed within the sedimentary rock units and GSF zones.

In the effort on the completion of the second 45 MW power generation, the production wells were mostly drilled at Pad T. T-05 and T-09 were targeted to the westernmost towards Mt. Sorik which eventually exhibit reservoir temperature as high as 320 °C. Aside from their highest temperature, the fluid chemistry and other geoscientific evidences signify the characteristic of wells that close to the upflow of a geothermal system.

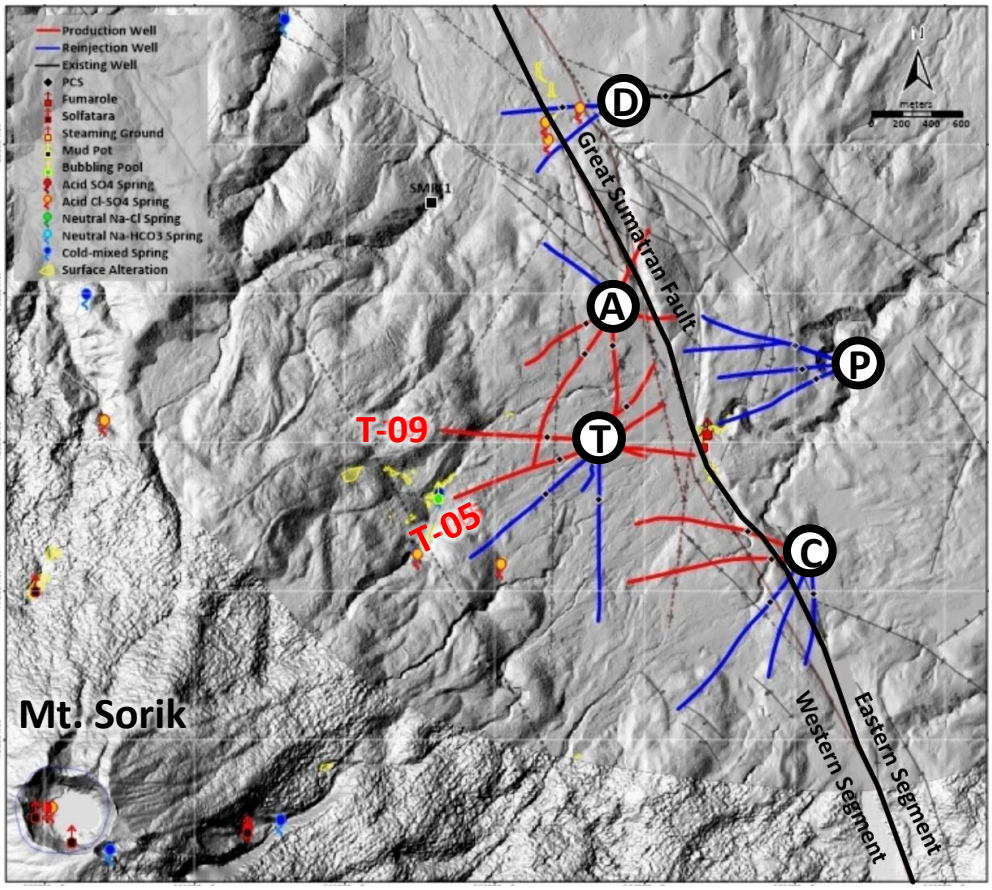

Figure 1: Map of Sorik Marapi geothermal field showing well trajectory, geological features and surface manifestations. The 2 highest temperature wells, T-05 and T-09, were drilled toward Mt. Sorik.

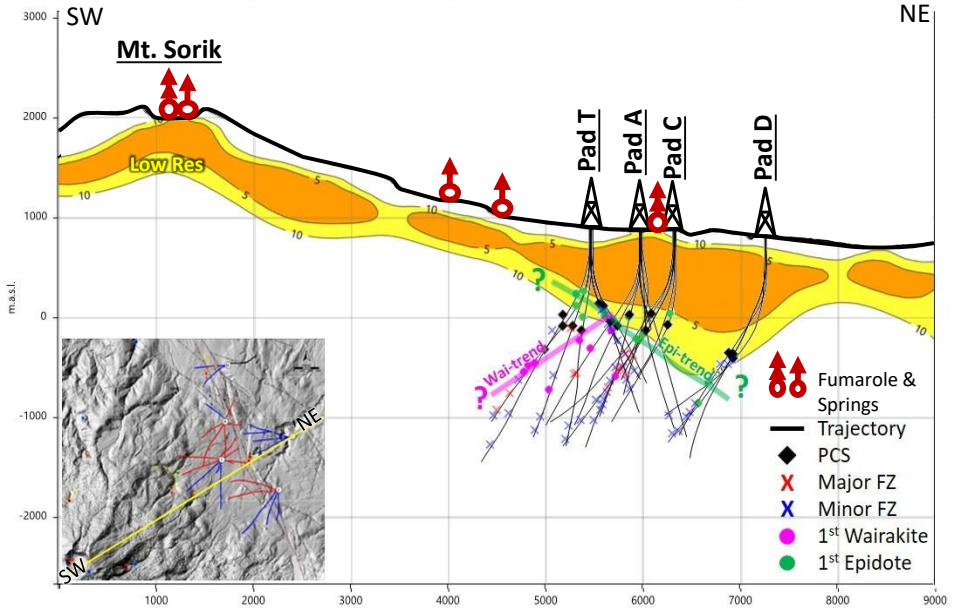

Figure 2: NW-SE cross section showing distribution of mineral markers (wairakite and epidote), low resistivity (<10 ohm.m), and feed zones.

2. CHARACTERIZATION OF T-05 AND T-09 WELLS

In well completion practices of the newly drilled wells, series of flow tests, well surveys and fluid sampling are performed to enable the reservoir characterization and risk mitigation. T-05 test was conducted 189 days after drilling while T-09 test was performed 3 weeks after TD. The results of enthalpy total discharge measurement that derived from James' tube method show 1160 - 1299 kJ/kg for T-05 and 1316 kJ/kg for T-09. Even though the fluid samples from Pad A and Pad T were collected simultaneously with drilling and injection activities at the same pad but the samples are still reliable to reveal the fluid origin. The contamination was identified from $\delta^{18}O$, potassium, chloride, and nitrogen concentrations.

The samples were corrected with total discharge enthalpy and sampling pressure / temperature since the 2-phase fluid is separated with mini separator during sampling at surface. All liquid samples had charge balances less than 3% and all gas samples showed low air contamination < 1% which indicate good quality.

2.1 Lithology and Alteration Minerals

T-05 and T-09 were drilled in the western sector of the GSF zone toward Mt. Sorik. The T-05 well was completed with total depth 2275 mMD, azimuth 248˚ (Figure 1), and Total Lost Circulation (TLC) at 2142.5 mMD (deeper than -1000 m asl) meanwhile the T-09 well was drilled with total depth 2100 mMD, azimuth 274˚, and TLC at 1920 mMD (~ -1000 m asl).

Both wells comprise Miocene to recent volcanic products namely Andesite Lava, Dacite Tuff and Rhyolite Tuffs from surface to sea level and Mesozoic to Paleozoic metasediments such as interlayered Quartzite and Phyllite from sea level to the reservoir section. The observed losses during drilling from these 2 wells consistently associate with the presence of wairakite mineral ($CaAl_2Si_4O_{12}.2H_2O$). Epidote ($Ca_2Al_2(Fe^{3+};Al)(SiO_4)(Si_2O_7)O(OH)$) that commonly used as reservoir indicator only applies on the Pad T wells that drilled to the eastern, Pad A, Pad C and Pad D wells. In addition, the appearance of first epidote from all the wells are only consistent with low resistive anomaly (<10 Ohm-m) but it is not indicative to the top of reservoir at the western sector (Figure 2).

2.2 Liquid Chemistry

The reservoir fluid chemistry from both T-09 and T-05 wells indicates that these wells produce sodium-chloride (NaCl) liquid from a typical benign geothermal reservoir (Figure 3a). The contamination from injection and/or drilling fluid has affected Cl and K concentration of the collected samples at Pad A and Pad T (Figure 3a and Figure 3b). Consequently, the fluid characteristic from Pad A seems to indicate relatively more benign and more equilibrated as compared with the highest temperature wells at Pad T. This finding is important and critical in fluid flow model interpretation. Similar phenomenon is also observed on stable isotope and gas chemistry. However, both T-05 and T-09 still indicate Na/K geothermometry > 300˚C (Figure 3b). This geothermometry is consistent with the measured temperature from well logging survey despite the chemical contamination.

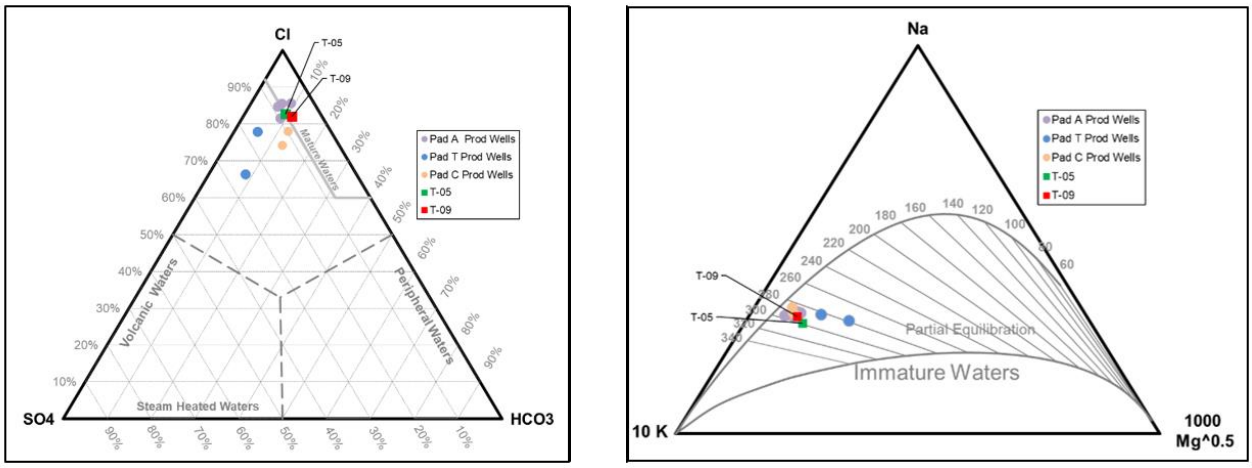

(a) (b)

Figure 3: (a) Cl-SO4-HCO3 ternary showing NaCl type of liquid from a mature system with some factor of dilution. Mixing with drilling/injection fluid have increased Cl concentration at Pad A wells during the flow test. (b) Na-K-Mg ternary indicating nearly full equilibrated geothermal liquid. Mixing with drilling fluid have enriched the potassium (K) concentration which may shift the fluid sample to higher temperature as shown by some Pad A wells.

2.3 Stable Isotopes

Stable isotopes of water and steam are used to identify the origin of geothermal fluids. Isotopes of the reservoir fluid from T-05 and T-09 along with other wells from Pad T and A indicate that the reservoir fluid is originated mainly from meteoric water.

This is typical of geothermal fluid in Sumatera Island where $\delta^{18}O$ is lighter than -6 ‰ (Figure 4). The mixing of meteoric water with magmatic water and water-rock interaction have resulted to a positive $\delta^{18}O$ shift. The heaviest isotope is exhibited by Pad A wells as compared with T-05 and T-09. The lighter isotope at T-05 and T-09 is possibly caused by contamination from the simultaneous injection and/or drilling activity during the sample collection.

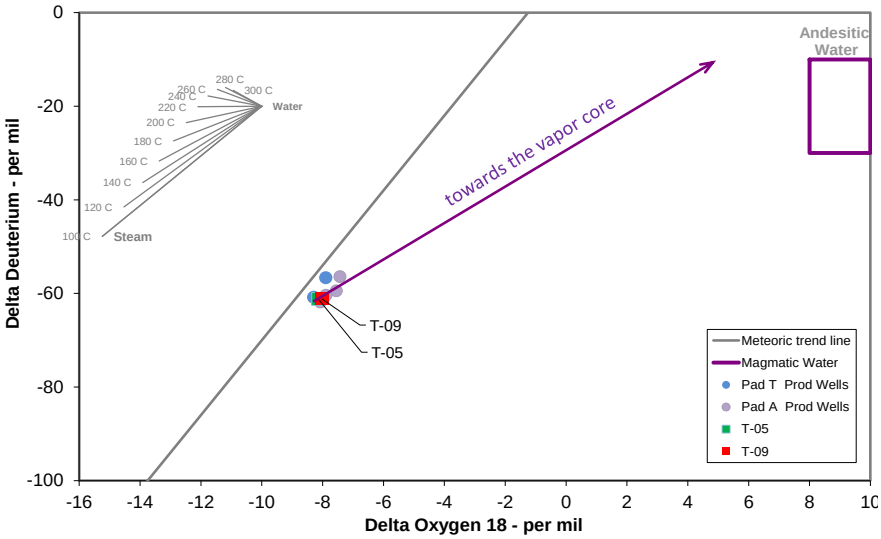

Figure 4: δ18O and δ2H isotopes of Sorik Marapi geothermal wells indicating more meteoric water contribution than vapor core fluids. Mixing with lighter δ18O may shift T-05 and T-09 wells towards meteoric water line.

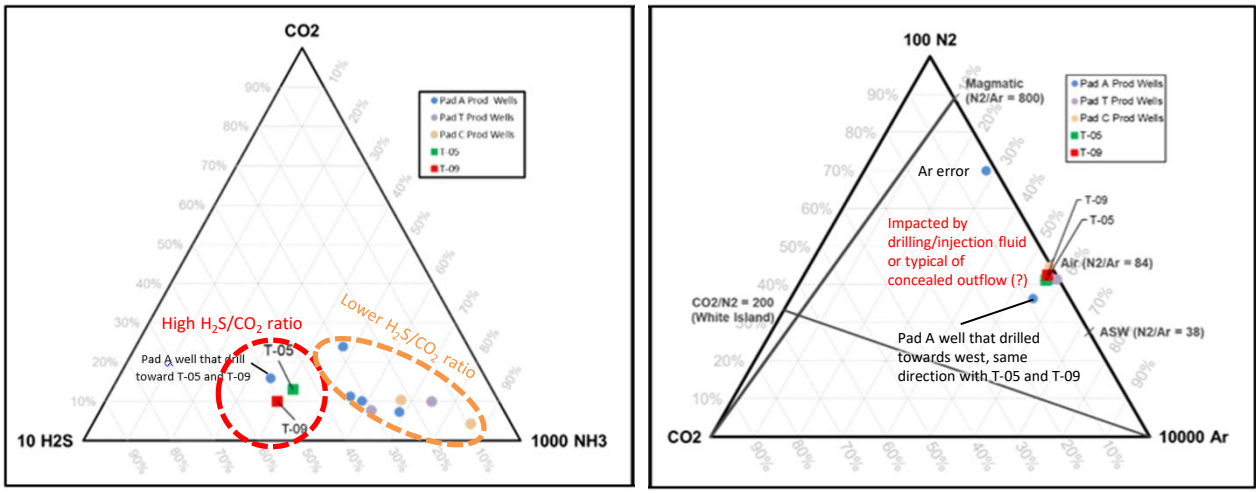

(a) (b)

Figure 5: (a) CO2-H2S-NH3 ternary showing higher H2S/CO2 ratio at T-05 and T-09 and some Pad A wells that drilled toward the western sector. (b) N2-CO2-Ar ternary indicating T-05 and T-09 and some Pad A wells that drilled toward the western sector have lower N2/Ar ratio. It is possibly caused by mixing with drilling/injection fluid or a signature of concealed productive outflow (Simatupang et al., 2021).

2.4 Non-Condensable Gas (NCG)

Reservoir fluids from Sorik Marapi geothermal have relatively low concentration of NCG (< 0.5 wt.%). The gas is primarily dominated by Carbon Dioxide (CO_2) and Hydrogen Sulfide (H_2S), like the common geothermal fluids. An anomalous Nitrogen (N_2) concentration is observed from the collected samples as compared with other geothermal fields. This phenomenon is caused by drilling fluid (Simatupang et al., 2011) or magmatic gases (Simatupang, 2021, pers. comm.). The N_2-CO_2-Ar ternary plot may support the first model but the high H_2S/CO_2 ratio may support the second model (Figure 5a and Figure 5b). The combination of both is also possible. The continuous gas monitoring after drilling activity would help constraining the two models. The fact that T-05 and T-09 relatively have higher H_2S/CO_2 ratio as compared with the other wells may also provide supporting evidence to the one single upflow model (Figure 5a). The N_2-CO_2-Ar ternary plot shows that these two wells and the other drilled wells at Pad A and T are still within the productive outflow with regards to the ability of the well to produce high temperature fluid. In addition, it could also be perceived as the upside potential for the presence of commercially higher temperature reservoir in the western area of T-05 and T-09 wells.

2.5 Temperature

The geothermometry and well survey are the 2 techniques that used in defining the reservoir temperature and the associated reservoir processes. The well survey results are the showcase of T-05 and T-09 wells as the highest temperature well in Sorik Marapi geothermal field. T-09 exhibits reservoir temperature up to 320 °C at -600 m asl while T-05 shows reservoir temp up to 300 °C at -900 m asl (Figure 6a). Since the gas chemistry is suspected to mix with drilling/injection liquid, thus disagreement between some gas geothermometry techniques with liquid geothermometry and well survey temperature is expected (Figure 6b and Figure 6c). Amongst all gas geothermometry techniques, only FT-CO_2 and HAR-CAR that show well data plotted within the grids. However, temperature lower than well survey measurement (< 200 °C) is still demonstrated by FT-CO_2 and HAR-CAR and it is attributed to the

disequilibrium that caused by drilling/injection fluid invasion (Figure 6b and Figure 6c). As the result, equilibrium with specific gas-gas reactions that assumed in all gas geothermometry is not satisfied.

Liquid geothermometry techniques that used in reservoir process evaluation are cation geothermometry and silica/quartz geothermometry. Cation geothermometry is based on the ratios between cations and absolute concentrations of certain cation concentration while silica geothermometry is based on the concentration of dissolved SiO_2 in the brine and liquid-mineral equilibria with various silica minerals. In term of equilibrium rate, cation geothermometry usually equilibrate slower than silica/quartz geothermometry. The highly sensitive of silica to mixing and boiling and the comparison of silica and cation geothermometry techniques with measured temperature from well survey may reveal reservoir processes that the fluid has undergone prior entering the production casing.

The consistency of measured temperature from Pressure and Temperature (PT) shut-in with Na/K Giggenbach geothermometry portrays the equilibrium of fluid and reservoir rock in static condition (Table 1). Meanwhile the measured temperature from PTS flowing shows consistency with quartz adiabatic at T-09 and lower than quartz adiabatic at T-05. Both trends indicate that near wellbore cooling occurs when the wells start flowing with different response from silica at each well (Table 1). The one at T-09 shows re-equilibration of silica while the one at T-05 does not permit such process to occur (Simatupang et al., 2021). This phenomenon is also evidenced by the results of measured temperature from well survey where temperature curve of T-05 still shows lower temperature at depth shallower than -900 m asl while such trend is not observed at T-09 (Figure 6a).

The Na-K-Ca (NKC) geothermometry at both wells exhibit higher temperature as compared with quartz adiabatic and measured temperature from PTS flowing. The trend where NKC is higher than quartz adiabatic and PTS flowing supports the cooling model (Table 1). This cooling is attributed to the hypothesis of the mixing between drilling/injection fluid with the reservoir fluid at T-05, T-09 and the other wells.

Table 1 : Temperature of T-05 and T-09 from selected liquid geothermometry versus the measured temperature from well survey.

Well	Date	Liquid Geothermometry (°C)			Well Survey (°C)			
		Quartz adiabatic	Na-K-Ca	Na/K Giggenbach 1988	Date	PT Shut-in	Date	PTS Flowing
T-05	Jun-20	242	267	299	Jul-20	298	Jul-20	224
T-09	Aug-21	237	264	293	Aug-20	300	Aug-20	240

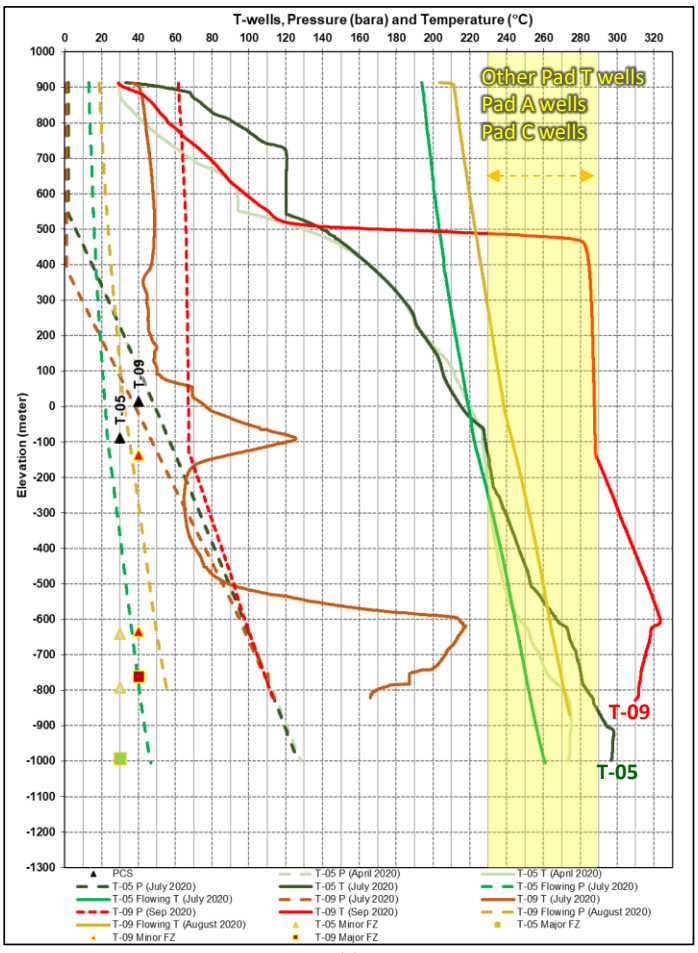

(a)

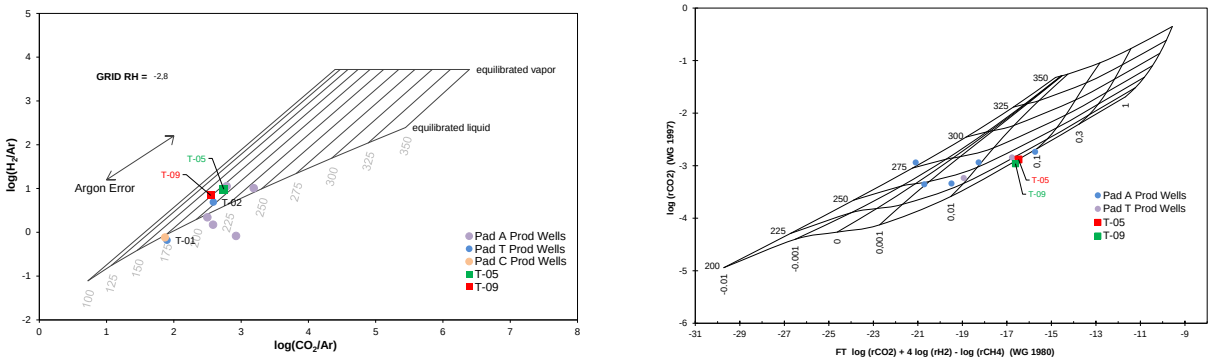

(b) (c)

Figure 6: (a) Pressure and temperature curves showing T-05 and T-09 wells have higher temperature than the other wells in Sorik Marapi geothermal field. T-05 indicating higher temp at deeper reservoir while T-09 demonstrating it at shallower depth (Setiawan et al., 2020) (b) HAR-CAR gas geothermometry shows low temperature < 200 °C (c) FT-CO2 gas geothermometry also exhibiting low temperature < 200 °C. These are the only 2 gas geothermometry that demonstrate the possibility of gas equilibrium since most of the wells are plotted inside the grid. The lower geothermometry is due to mixing with drilling/injection fluid (Simatupang et al., 2021).

2.6 Permeability

These wells feed zones depth is interpreted based on data obtained from series of completion test by doing Injection PTS spinner, multi-rate Injectivity Index (II) test, Pressure fall-off and static PT. The results indicated T-05 has minor feed zone at depth 1779 mMD and 2229 mMD, while major feed zone is located at depth 2157 mMD which coincides with TLC depth. The calculated injectivity index (II) of T-05 is 9.24 kg/s/bar. T-09 has minor feed zone at depth 1190 mMD and 1830 mMD, while major feed zone at depth 2000 mMD (Figure 6a). The calculated injectivity index (II) of T-09 is 30.8 kg/s-bar. T-09 well has the 2nd highest II value and both wells have relatively higher II compared to other wells in the Sorik Marapi geothermal field.

2.7 Fluid Flow Model

Mixing model is an effective tool in all stages of geothermal development. They enable the conceptual understanding of a geothermal field regarding fluid flow interpretation and reservoir characterization. T-05 and T-09 are relatively higher enthalpy and Cl wells as compared with the other wells (Figure 7a). This is typical of wells that drilled towards the upflow zone. This fact is consistent with the H_2S/CO_2 ratio (Figure 5a) where both wells show higher ratio than the other wells. As the fluid flows away from the upflow zone, then decreasing in Cl may occur due to mixing with dilute liquid. It is portrayed by Pad A, Pad C and other wells at Pad T in discharge enthalpy vs Cl cross plot (Figure 7a).

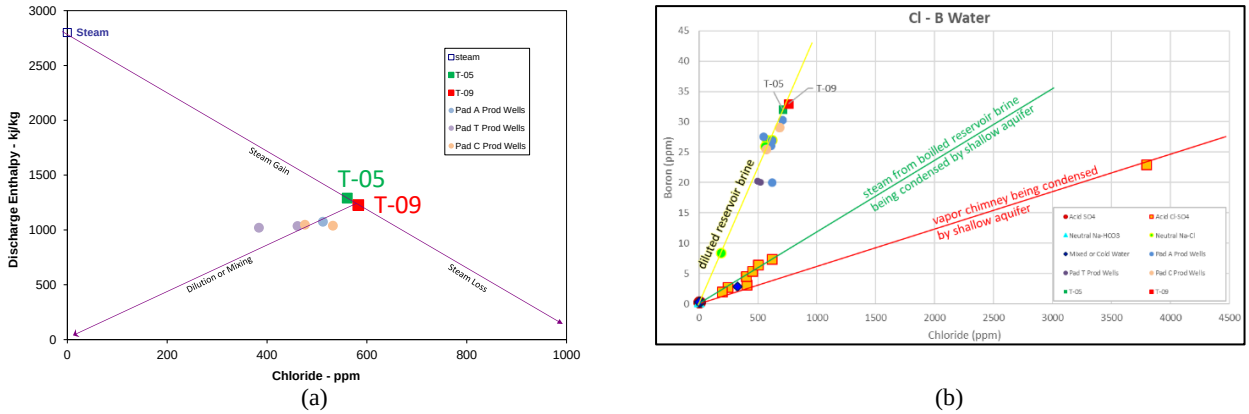

(a) (b)

Figure 7: (a) Reservoir Cl vs Enthalpy from Qtz Geothermometry. T-05 and T-09 have relatively higher Cl and higher enthalpy which are typical of wells that produce an upflow fluid. (b) Three types of fluids have been identified at Sorik Marapi from Cl and B cross plot. T-05 and T-09 wells are plotted at the tipping point of the mixing line which indicate the western wells are typical of upflow well. The 2 wells are also plotted within the same line with the other wells which strongly indicate that all wells are connected. Any drilling or injection activity at nearby wells may affect the other wells (Simatupang et al., 2021).

The fluid chemistry from surface manifestations and wells reveals 3 types of fluid in Sorik Marapi. These 3 fluid types are generated as the fluid flows away from Mt. Sorik to the outflow zone and ascends to the surface by buoyancy mechanism and advective flow (Figure 7b). The reservoir brine is attributed with relatively high Boron and high Chloride. As the reservoir brine flows to lower pressure area and boils off, then the steam ascends to the surface. The steam is then being condensed by shallow aquifer and manifested at surface as Cl-SO_4 springs, SO_4 springs, and mud pools. In the case of steam from vapor core within Mt. Sorik's crater, the HCl is absorbed by near surface liquid and manifested as acid Cl-SO_4 lakes or springs within the summit of Mt. Sorik (Simatupang et al., 2021). T-05 and T-09 wells are plotted on the same Cl-B mixing line and identified as reservoir brine type. Since both of them

are plotted on the tipping point of the mixing line then it is consistent with Cl-H silica cross plot (Figure 7a and Figure 7b). This fact strongly indicates that both wells tap into the upflow zone of the system. In addition, the plotted T-05 and T-09 on the same line with the other wells also imply on the connectivity of all wells in Sorik Marapi geothermal field. Consequently, any drilling or injection activity may affect the adjacent wells.

3. CONCLUSION

Currently, there are 2 conceptual models in explaining the geothermal system in Sorik Marapi. The first model indicates 2 possible upflows; one located within the Mt. Sorik while another one located on the flank of Mt. Sorik (Haizlip et al., 2020). Meanwhile the second model portrays 1 upflow that associated with Mt. Sorik with neutralization process through mineral buffers (Simatupang et al., 2021). Basically, both models show similar hypothetical heat source location where it is interpreted at western of GSF system and associated with Mt. Sorik. The facts that:

- T-05 and T-09 are the two westernmost wells that drilled toward Mt. Sorik
- T-05 and T-09 shows highest temperature as compared with the other wells despite drilling fluid contamination
- T-05 and T-09 has relatively higher permeability as compared with the other wells that drilled within the same sector
- T-05 and T-09 shows deeper top of reservoir as compared with the other wells which is typical of wells that drilled towards upflow in a vapor core setting
- Produced fluid from T-05 and T-09 indicates an upflow fluid type as supported by relatively higher H_2S/CO_2 ratio and Cl

provide strong evidences that the 2 wells are the one that drilled close to the upflow of the system. The characteristics of these wells are consistent with the signatures of other geothermal wells in the other fields with the same geologic setting that drilled closed to the upflow zone.

4. ACKNOWLEDGEMENT

We would like to thank KS Orka Renewables for granting permission to publish this study, especially to Dr. Yan Tang and Kevin Cao for supporting us in making this paper.

REFERENCES

Arnorsson, Stefan and Gunnlaugsson, Einar: New Gas Geothermometer for Geothermal Exploration-Calibration and Application, *Geochim Cosmochimica Acta*, Pergamon Press, Vol. 49, (1985), pp.1307-1325.

Fournier, R.O.: Silica in Thermal Waters: Laboratory and Field Investigations, *Proceedings*, International Symposium on Hydrogeochemistry and Biochemistry, Tokyo, 1970, *Hydrogeochemistry*, Vol 1. Washington DC, Clark, (1973), pp. 122-39.

Fournier, R.O.: Application of Water Chemistry to Geothermal Exploration and Reservoir Engineering, In: Rybach L, Muffler LJP, eds. *Geothermal Systems: Principles and Case Histories*, New York, Wiley, (1981), pp. 109-43.

Giggenbach, W.F.: Geothermal solute equilibria. Derivation of Na-K-Mg-Ca Geoindicators, *Geochim. Cosmochim. Acta*, 52, (1988), 2749-2765.

Haizlip, J., Sussman, D., Hinz, N., and Mason, G.: Geologica Geothermal group: T-05 End of Well report, *KS Orka Internal Report*, (2020).

Nicholson, K.: Geothermal Fluids. Chemistry and Exploration Techniques, Springer- Verlag, Berlin, Heildelberg (1993).

Setiawan, Junior, Sophian, Rudy, and Hidayat, Ryan.: T-05 Well Analysis, *KS Orka Internal Presentation* (2020).

Setiawan, Junior, Sophian, Rudy, and Hidayat, Ryan.: T-09 Well Analysis, *KS Orka Internal Presentation* (2020).

Simatupang, C.H., Golla, G.U., and Molling, P.A.: 'Gas Breakthrough' during Drilling at Darajat and Implications to the Conceptual Model, *IIGCE*, Lampung (2011).

Simatupang, C.H., Siagian, H., Sanjaya, D., and Setiawan, J.: North Sorik Prospect Evaluation, *KS Orka Internal Presentation* (2021).

Simatupang, C.H., Siagian, H., Sanjaya, D., and Setiawan, J.: Sibangor Reservoir Characterization Workshop, *KS Orka Internal Presentation* (2021).

Truesdell, AH. and Fournier, R.O.: Calculations of deep temperatures in geothermal systems from the chemistry of boiling spring waters of mixed origin, *Proceedings*, 2nd UN Symposium on the development and use of geothermal resources, San Francisco, 1, (1975), 837-844.

This page is intentionally left blank

Subsurface Structure Identification from Gravity Modelling of Silangkitang Geothermal Field for Future Injection Well Targeting

Rizal Abiyudo[1], Yunus Daud[1], and Drestanta Yudha Satya[2]

[1] Master Program of Geothermal Exploration, Department of Physic, University of Indonesia, Depok, Indonesia
[2] Sarulla Operation Limited, The Energy Building 7th Floor, SCBD, Jakarta 12190, Indonesia

1rizal.abiyudo@medcoenergi.com, ydaud@sci.ui.ac.id

Keywords: Gravity, Faults, Silangkitang, Fault-controlled, Injection Wells, Well Targeting

ABSTRACT

The injection well has been frequently overlooked by the geothermal developer if compared to production wells. Moreover, the sustainability of reservoir geothermal is determined by the right location of injection wells to provide reservoir pressure support and avoid cooler marginal fluid to enter the reservoir. The robust well targeting of injection wells to hit the major subsurface structures that have a good connection to the reservoir are very important for the reservoir surveillance, one of the geophysical methods to determine the major subsurface structures is a gravity modeling. The objective of this study is to provide geophysics point of view based on a gravity modeling to characterize the faults/structures distribution in Silangkitang in order to identify future make-up well drilling target. A total of 116 gravity stations measured at Silangkitang has passed standard correction such as tide, sensor height, and drift corrections. The spatial corrections such as latitude correction, Free-air correction, Bouguer correction, and Terrain correction were conducted to obtain the Complete Bouguer Anomaly (CBA). The CBA have been filtered to separate the regional and residual anomalies, which associate with deep and shallow anomalies respectively. The result of the CBA, regional anomaly and residual anomaly model enhance the interpretation of the major trend of NW-SE of both Barumun (east) and Angkola (west) faults as identified by the surface geological map. The Forward modeling was also performed to construct the subsurface model of the gravity data. The forward modeling could model the presence of basement rock in the east and west associates with high anomaly while the volcanic-sedimentary product in the center of graben associated with lower gravity response. First Horizontal Derivative (FHD) and Second Vertical Derivative (SVD) from the study also strengthening the kinematic analysis of both Angkola and Barumun faults which associated with normal fault, as indicated by geological study as dextral strike-slip (normal fault with shear component). In conclusion, the study has shown that the gravity study could help to analyst the geological concept in Silangkitang, particularly delineating the extent of major faults/structures and lithological boundary which is very useful to assist the well targeting of future make-up well drilling in Silangkitang.

1. INTRODUCTION

The Silangkitang (SIL) field is a part of Sarulla Geothermal Field which located about 30-km northwest of the town of Sipirok within the Sarulla graben. The reservoir characteristic of Silangkitang is a liquid dominated system with temperature higher than 2800C and relatively moderate gas <1 wt% in reservoir liquid (Simatupang, 2020). The prospect was initially identified by two sets of thermal features: a series of fumaroles on the eastern edge of the valley aligned along a 1.75 km segment of the Great Sumatra Fault, and numerous boiling chloride springs located within the valley in the same vicinity. Further exploration work identified several other characteristics of the prospect that made it even more attractive. These include: a young (120,000 year old) rhyolite lava dome at the southeastern end of the prospect, more boiling hot springs on the western side of the valley, and an area of low resistivity associated with the eastern springs and fumaroles that was identified by geophysical surveys (Hickman et al., 2004). The first systematic exploration study conducted in 1980s by PERTAMINA ranked Silangkitang as one of the attractive projects in Sumatera (Ganefianto et al., 2015). In early 1990s, the extensive exploration program include exploration drilling was continued by Unocal which resulted the reserve confirmation of 80 MWe for 30 years at Silangkitang (Gunderson et al., 2000). In 2017, Sarulla Operation Limited (SOL) has successfully installed 110 MWe capacity in Silangkitang by applying technology optimization of Integrated Geothermal Combined Cycle (IGCCU).

Silangkitang tectonic setting in Sarulla Graben is associated with major right-lateral, strike-slip fault system (Hickman et al., 2004; Gunderson et al., 2000; Satya et al., 2018) which of GSFZ. The GSFZ extend 1650 km long from Aceh to Lampung, the dominating NW-SE faults creates secondary fault structures N-S (extensional fractures), NNE-SSW (synthetic Riedel shears), and NE-SW (antithetic Riedel shears). At Silangkitang the NW-SE orientation act as main permeable zone (Nukman, 2014) which been controlled by the extension of Sarulla Graben perpendicular to GSFZ. SIL lies above a local sub-graben formed between the Tor Sibohi fault and the intersecting Hutajulu fault overlaid by Neogene, Quaternary volcanic and volcanoclastic rocks cap Tertiary sediments (Hickman et al., 2004; Satya et al., 2018). In the east, The Paleozoic Meta-sediments are exposed at the surface east of the GSFZ as the eastern boundary of Silangkitang reservoir.

Satya (2018) has emphasized that the production and injection wells that penetrated GSFZ only obtained good permeability toward the east, which according to detailed mapping shows the main releasing bends and fault steps occur along the Eastern GSFZ within Sarulla Graben. It is likely that the main permeable zone at SIL mainly controlled by fault and fractures of eastern GSFZ or knowing as fault-controlled system, the implication of this structural controlled will limit the natural convection and the reservoir is constraint into structural damage zones as explained by Wallis (2017).

After two (2) years of operation, Simatupang (2020) has acknowledged the chemical response in the production area that indicates an injection breakthrough from injectate liquid without significant enthalpy impact. Most of production and injection wells are drilled perpendicular toward single eastern Great Sumatra Fault Zone GSFZ, while some injection wells drilled away from eastern GSFZ but do not provide adequate injection capacity (Figure 4b). A reservoir optimization study has been conducted to shift the injection wells location further northwest or southeast of the production area, such as geological mapping, geochemistry tracer and reservoir simulation to characterize the main fault/structure which have a good connection for providing pressure support but has sufficient

distance to avoid rapid cooling to the reservoir. The importance of this fault/structure characteristic in Silangkitang needs to study further detail using subsurface tools such as gravity method to enhance the understanding of the subsurface faults/structures of Silangkitang for future well targeting of make-up injection wells. The gravity method is selected since it has good lateral sensitivity and could map the density contrast between low and high-density rocks, perhaps this correlation could identify the eastern boundary of Silangkitang reservoir where the Paleozoic rock outcropping to the surface. This situation juxtaposing the basement rock of different densities in the East compared to the Graben fill product such as volcano-sedimentary rock in the Western area.

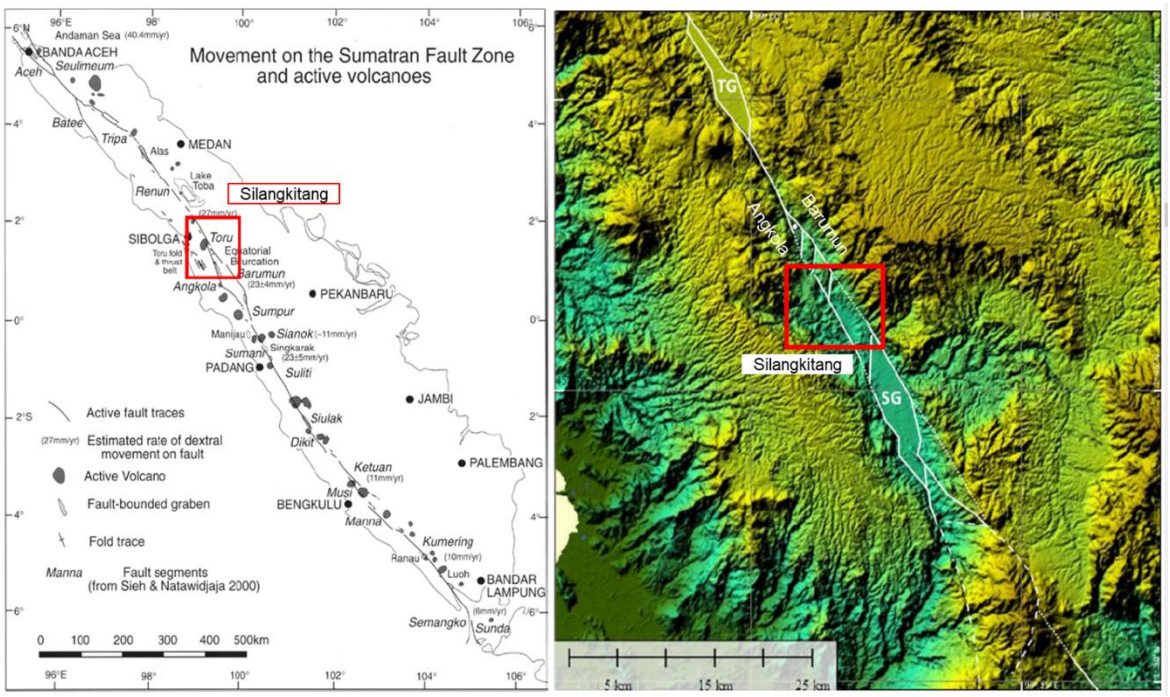

a) b)

Figure 1: (a) Active traces of the Sumatran Fault System identified by their geomorphic expression, fault segments and estimated rates of dextral movement, the location of active volcanoes, lakes and extensional graben (Sieh and Natawidjaja, 2000). (b) Two (2) main Graben Tarutung (TG) in the Northwest and Sarulla (SG) in the Southeast which created from two major segment Barumun and Angkola fault segments.

2. TECTONIC AND GEOLOGICAL SETTING

The SIL geothermal field developed in the northern end of Sarulla Graben is bounded to the east by Barumun Fault and to the west by Angkola Fault (Figure 1). It is in SIL area where the Barumun Fault and Angkola Fault started to diverge, creating a region of tensional stress at its tip, forming the Sarulla Graben. Therefore, the Sarulla Graben probably not a typical pull-apart basin formed by slip interaction of two overlapping fault segment (SOL-UGM, 2020). The Barumun Fault is the most active and the largest throw, as indicated by striking fault escarpment and half-graben geometry in seismic profiles. Hickman et al. (2004) later applied different named for Barumun Fault as the eastern bounded fault, i.e., Hutajulu Fault for northern segment and Tor Sibohi Fault for southern segment.

The oldest rock of unit of SIL is a Metamorphic Rock associated with Paleozoic Age outcropping in the eastern side of GSFZ (Moore et al., 2001). In the west, a relatively younger unit presence in the western side of GSFZ as Simardangiang Pyroclastic Breccia Unit, the volcanism of Simardangiang is presence at Miocene age according to the geology study in NIL (SOL-UGM, 2020). In the middle of Sarulla Graben (SG), the younger of volcanism deposited in SIL is Hopong Volcanic Unit originated from southeast of SIL area (Figure 2). This volcanism was active during the Pleistocene epoch with 9 km diameter of eroded caldera massively truncated by the GSFZ, forming the eastern wall of Sarulla Graben (Hickman et al., 2004). The younger volcanic product of Lapilli Tuff and Clay Tuff Unit filled the Sarulla graben from Northwest to Southeast part of Silangkitang. The latest volcanism deposited in Sarulla Graben is Toba tuff unit, the unconformity is expected in the west due to Toba tuff unit deposited above the Simardangiang Pyroclastic Breccia later followed by alluvium product. The outcrop of oldest rock in the east and west of Silangkitang revealed the tectonic setting of Sarulla Graben (Figure 3).

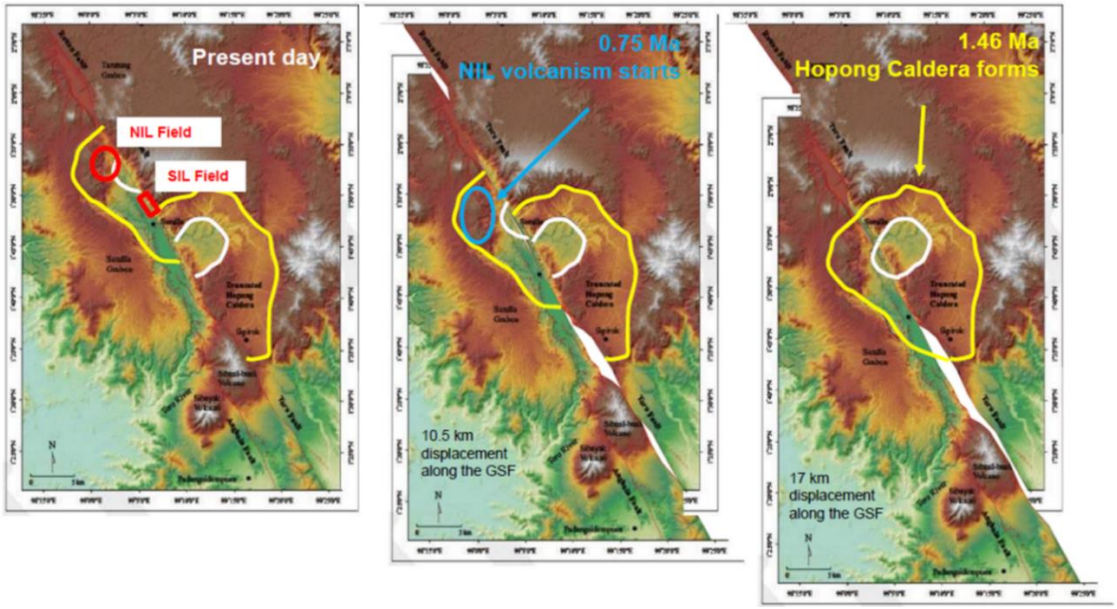

Figure 2: The origin of Toru undifferentiated volcanics that overlay Sarulla Graben (SG) from Hopong Caldera (modified from Hickman, 2004).

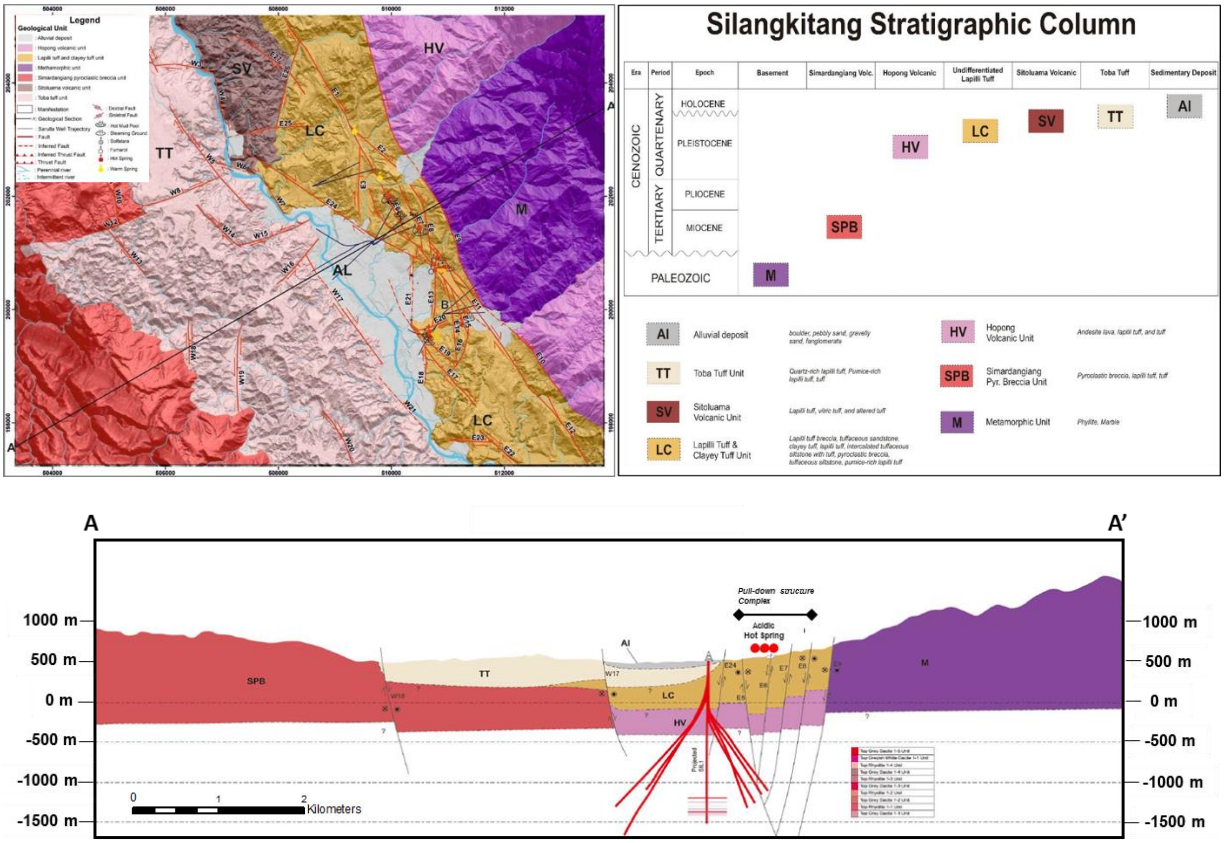

Figure 3: Geological model of Silangkitang.

3. GRAVITY DATA (COMPLETE BOUGUER ANOMALY – CBA)

Gravity survey is a standard best practice of geophysical method to identify the variation of subsurface rock densities for a resource delineation particularly in Sumatra in which the geothermal system dominantly controlled by GSFZ. In Sumatra, most of the preliminary structure mapping for geothermal exploration has been conducted using either open-access satellite gravity data such as Topex or detail gravity survey in the early stage of exploration to reduce the permeability risk of Well Targeting. Unocal collected totally 116 gravity measurement stations at Silangkitang during the exploration in early 1990s the absolute gravity data as the output. The absolute gravity data has been processed with standard correction such as tide, sensor height and drift corrections thus the further correction required is the spatial correction. The spatial correction such as latitude correction, Free-air correction, Bouguer correction and Terrain correction was conducted to obtain the Complete Bouguer Anomaly (CBA), specifically the reduction density of 2.6 g/cc is applied from Parasnis method to calculate the Bouguer correction, and the density calculation is suitable with the dominance of

igneous rocks and metamorphic rock in the Silangkitang area. The gravity data was proceeded and obtained a map of CBA as shown in Figure 4a. The CBA values in the study area varied from -41 mGal to -69 mGal with the high value relatively associated with basement rock in the east (Metamorphic unit) and west (Simardangiang Pyroclastic Breccia unit). On the other hand, the low-density value is located near the center of graben as volcano-sedimentary basin fill products (Hopong Volcanic unit, Lapili Tuff and Clayed unit, Toba Tuff unit, Sitoluama unit, and Alluvial Deposit). The result of CBA map also enhances the interpretation of the major trend of NW-SE of both Barumun (east) and Angkola (west) faults along Great Sumatra Fault Zone (GSFZ) as identified by the surface geological map.

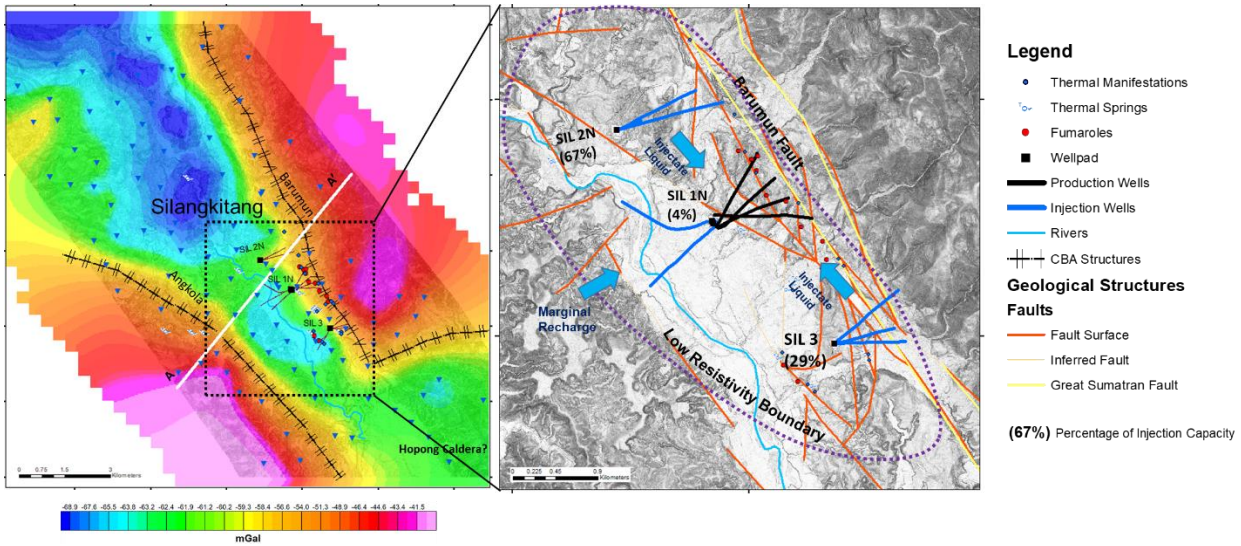

a) b)

Figure 4: (a) The major structural trends from Complete Bouguer Anomaly (CBA) indicates two high-density gradients of NW-SE trend associated with GSFZ. The low density in the southeast of SIL associated with the morphology of Hopong Caldera (cross section A-A' represent the 2D forward modeling line). (b) Map of SIL injectate liquid distribution, marginal recharge occurs from west of Production area and injectate liquid return from northwest and southeast injection wells (modified from Simatupang, 2020).

4. GRAVITY MODELING

After the CBA map is processed from the two steps correction of temporal and spatial, filtering methods were assigned to eliminate the strong regional trend particularly affected by GSFZ. The high-density contrast is produced from the lithology contact between volcano-sedimentary graben fill products with the outcrop of metamorphic unit and pyroclastic breccia unit in the east and west. The result of filtering regional and residual are presented in Figure 5.

Complete Bouguer Anomaly (CBA) data is filtered using the Butterworth filter to separate the regional and residual (shallow) density contrast at certain depth. The residual anomaly is associated with high frequency meanwhile the regional anomaly is associated with low frequency. a Butterworth band-pass filter in a wavenumber domain with the low cut-off about 0.2 rad/km and high cut-off of 0.8 rad/km has been applied to obtain the residual gravity anomaly. Based on the analysis of the power spectrum response, the regional gravity responses the deep Paleozoic and tertiary basement in the Western and Eastern side with depth > 2 km. the residual anomaly map is derived by removing the regional anomaly from the CBA and shows the gravity response density contrast of depth < 2km. Overall the regional and residual shows major trend of NW-SE trend on east and west of SIL, but the residual anomaly map shows the high density anomaly in the northwest probably associated with Namora-I-Langit (NIL) Volcanic complex. This high anomaly gravity of the residual is likely to be caused by volcanic/magmatic bodies rather than deep Paleozoic basement structures since the gravity response of volcanic/magmatic bodies in this location is relatively radial rather than elongating along GSFZ from residual anomaly.

Other methodology used to improve the fault/structure interpretation in Silangkitang are First Horizontal Derivative (FHD) and Second Vertical Derivative (SVD). Rosid and Siregar (2017) has applied FHD to detect a shallow inhomogeneity (fault or lithology contact) contrast based on the horizontal changing of gravity value. While SVD method used to identify a type of fault (normal or reverse) based on the adjacent contrast of high and low anomaly, however shear fault could not be able to detect by using SVD method. The type of fault is defined as a normal fault if the value of g "max > g" min and reverse fault if the g "max < g"min . Figure 6 show the response of FHD and SVD, FHD shows a high-density contrast on both east and west most likely associated with a major structure of Barumun and Angkola faults as identified by CBA, Regional, and Residual anomaly. Based on SVD, the fault kinematic of Barumun and Angkola could be identified by creating a cross section B-B' to analyze g"max and g"min of fault block 1 and fault block 2 (Figure 7). Based on SVD analysis, Fault block 1 and 2 are associated with normal fault, this interpretation supports the fault kinematic of a GSFZ that is a normal fault with Strike-Slip component (Dextral Strike-Slip Fault).

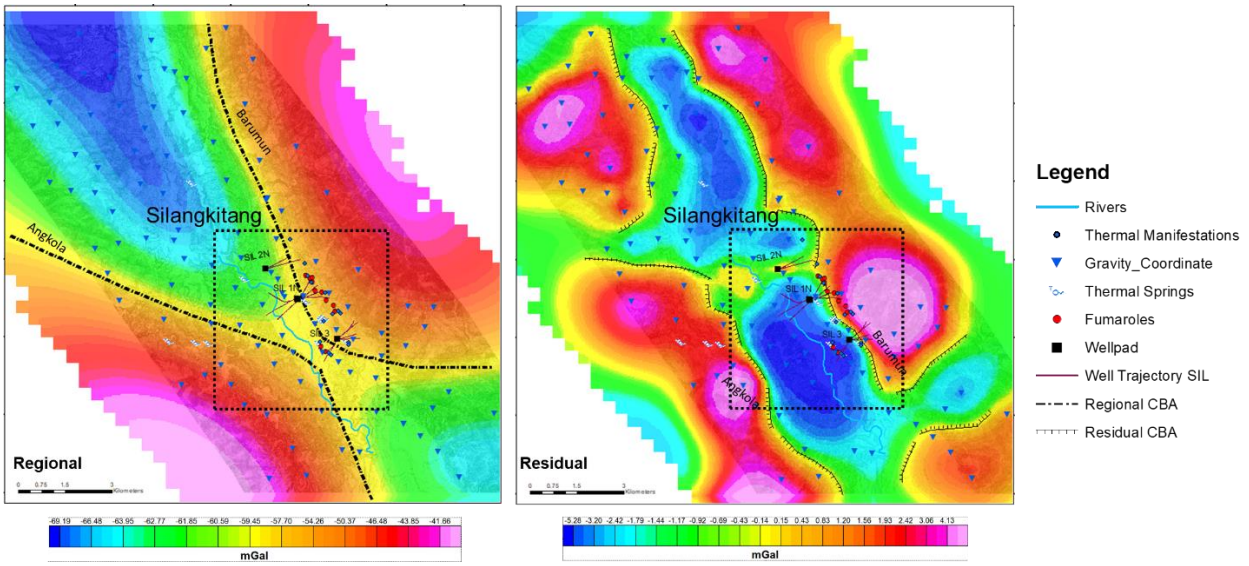

a) b)

Figure 5: (a) Regional anomaly which shows density contrast at depth >2 km with major trend NW-SE (b) Residual Anomaly reveals NW-SE major trend elongating along GSFZ in the middle of SIL field affected by shallow Paleozoic and Tertiary basement outcrop. High-density contrast in the northwest is probably associated with volcanic/magmatic bodies since the trend is relatively radial compared to the other trends.

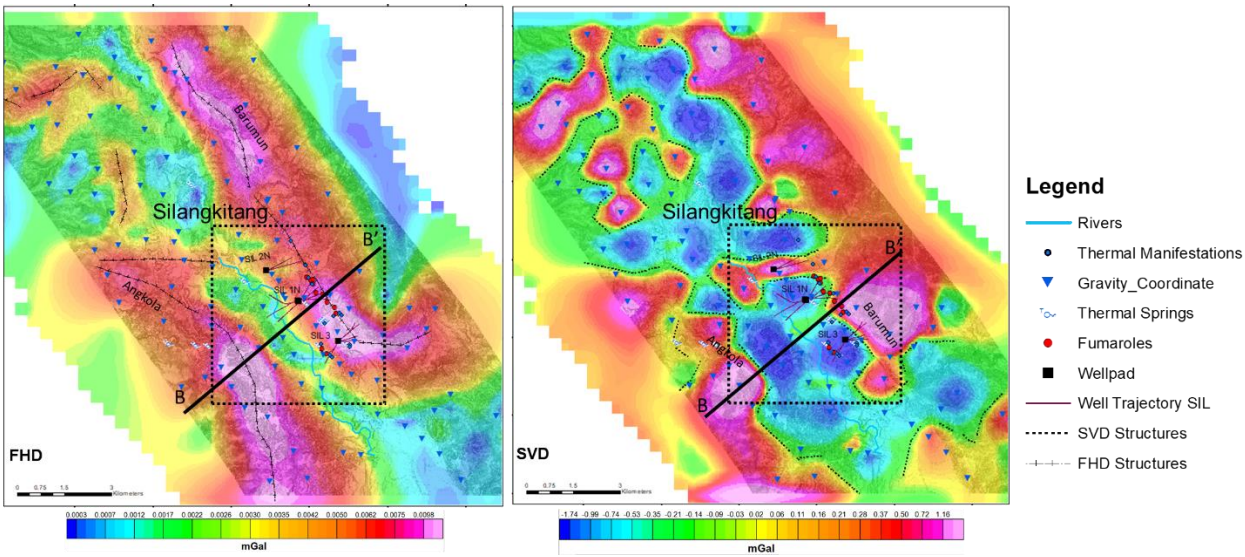

a) b)

Figure 6: (a) Contour map of FHD shows two main high-density contrast on west and east associated with Barumun and Angkola faults. (b) Contour SVD map of Silangkitang.

Forward modeling is performed to construct the subsurface model based on the gravity response. The forward modeling is assumed that the model layers (lithology unit) were homogeneous, constant density and relatively constant thickness. Initially, the model layers are assumed laterally extent to infinite distance although actually the good match could be obtained by extending the layers 50 km in both directions. To test the graben concept of GSFZ in SIL, one (1) profile is constructed to review the gravity and geology model (Figure 8). The objective of this cross section is to prove the consistency of geology concept in Silangkitang where it is associated with Sarulla Graben. The outcropping of Metamorphic rock in the east and Simardangiang Pyroclastic Breccia as tertiary basement rock in the west hint a high-density contrast in both directions. Cross section A-A' (see location on Figure 4) was located across high-low-high density contrast associated with high-density rock, adjacent with Angkola and Barumun Faults. The thickness of the lithological unit was based on the formation log of SIL fields as been modeled by Satya (2018) about geological model of Silangkitang. The Metamorphic unit applied as the 'basement rock' by adjusting its density to 2.8 g/cm3, following that the volcanic-sedimentary product such as Hopong Volcanic, Lapilli tuff and Clayed tuff, Toba tuff and Alluvial unit is assigned in the center associated with lower density value to match the observed model (Figure 8). As explained by McDonald and Gosnold (2014), it should be understood that the modeling of gravity (potential field data) is a non-unique process in that a number of different models could generate similar gravity response. The author has elaborated the geological conceptual model from surface and wells to duplicate a tectonic setting of Silangkitang.

	g" max	g" min	Fault Types
Fault Block 1	4.772	-2.826	Normal Fault
Fault Block 2	3.554	-0.8897	Normal Fault

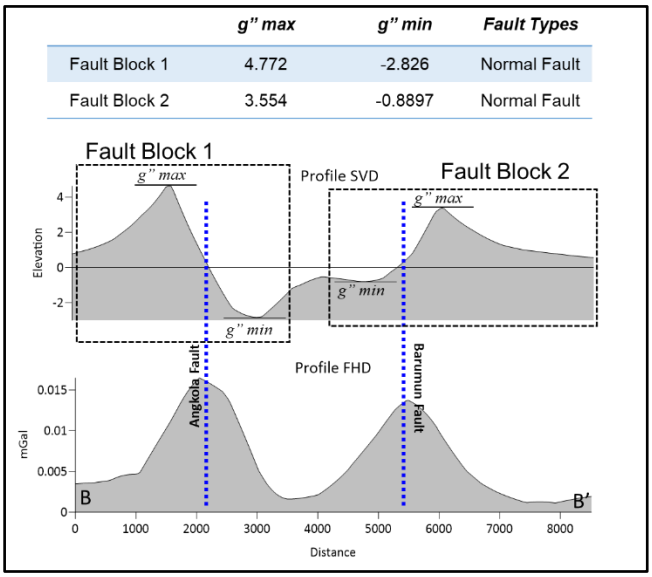

Figure 7: Cross section of line B-B' on SVD and FHD to identify the fault kinematic, both fault block 1 and 2 are associated with normal fault (see cross section line in Figure 6).

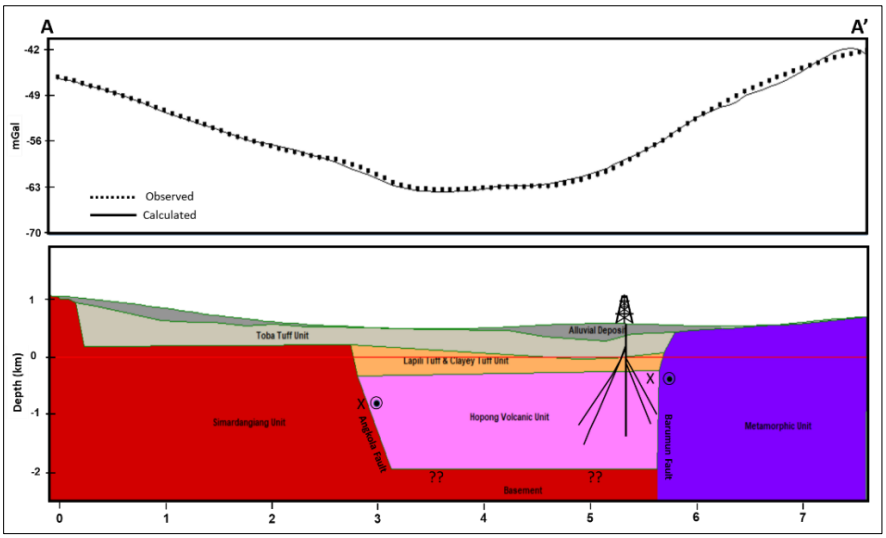

Figure 8: Model profiles and calculated gravity response versus observed values profile A-A' model unfiltered data from Complete Bouguer Anomaly (CBA). Cross section profile in Figure 4.

5. CONCLUSIONS

The study has shown that the CBA, Regional and Residual gravity anomaly can be used to guide the geological concept of Silangkitang, particularly assisting the interpretation of major structure and lithological unit of a geothermal system in Great Sumatra Fault Zone (GSFZ). The gravity model suggests that the gross geologic structure of SIL is consistent as a typical fault-controlled system geothermal system (Satya, 2020). The near vertical faults associated with Barumun block constraint the distribution of geothermal system along the eastern GSFZ, perhaps eastern fault zone has a better connection to a deep magmatic plumed which feeds the high temperature fluid in Silangkitang. This configuration appears to be controlled by a half graben forming which create fault stepping with relatively lower dip angle fault in the west associated with younger lithological unit compare to metamorphic unit in the eastern side. Barumun and Angkola Faults act also as barrier and structural trap that have been proved by the wells drilling in Silangkitang.

Other methodology such as FHD and SVD could further enhance to interpret the shallow horizontal contrast of major faults and determine the fault kinematics that unsurprisingly support the fault kinematic of GSFZ as a normal fault with strike slip components. Since GSFZ is a major fault that extends from shallow to deep anomaly, thus it could be detected in various methodology from CBA, Regional, Residual, FHD, and SVD. Gravity Forward modeling could also perform in constructing Sarulla Graben where the basement rock outcropping in both west and east area and volcanic-sedimentary product in the center associated with lower density value. Again, it should be noted that the gravity (potential field data) is a non-unique process in that a number of different models could generate similar gravity response to duplicate tectonic setting of Silangkitang. However, the gravity forward modeling has replicated the Sarulla Graben setting to support the geological concept of Silangkitang Geothermal Field.

The results of the gravity modeling of CBA, residual, SVD and FHD has coherently revealed the extent of Barumun fault to northwest of Silangkitang (Figure 9). However, the extent of Barumun Fault to the southeast should be interpreted cautiously since it perhaps is associated with low gravity anomaly of Hopong Caldera, the trend of high gravity anomaly contrast shifter to the east of GSFZ creates local low gravity anomaly in the southeast of Silangkitang. Based on the continuation of high contrast gravity anomaly to the northwest that associates with Barumun fault, the future injection wells of Silangkitang should be targeting these locations. The geothermal system in Silangkitang is associated with a fault-hosted system in which the reservoir hosted by one single major fault, the connectivity of injection result significantly expected to support the reservoir pressure since commonly it has limited lateral size. The strong gravity anomaly lineament to the northwest support the potential connectivity reservoir recharge from northwest of Silangkitang along GSFZ for the target of future injection wells.

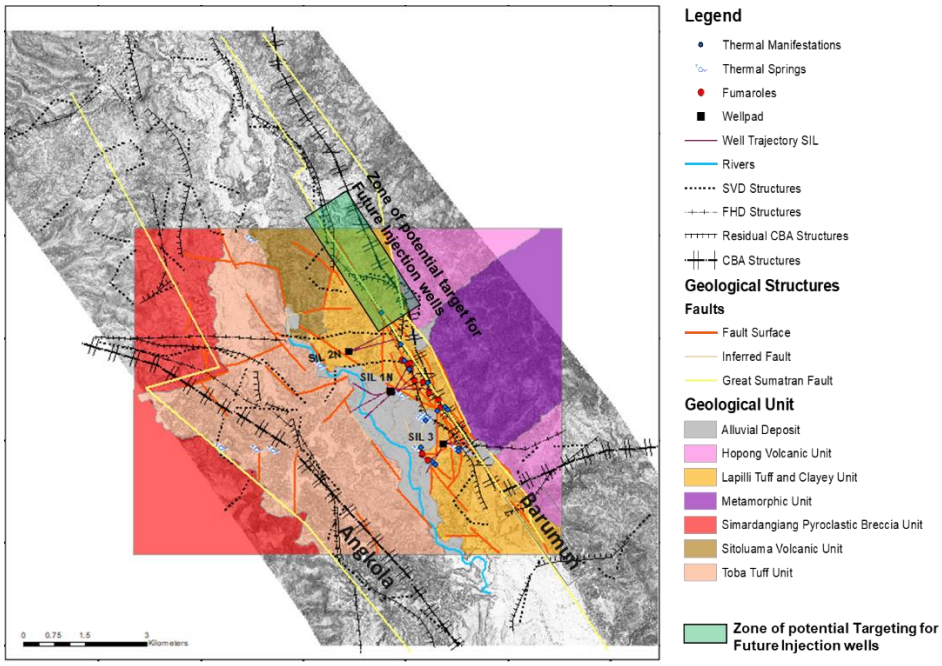

Figure 9: Map integration of all gravity anomaly of CBA, residual, SVD and FHD to determine the extent of Barumun Fault as favorable target of future SIL injection Wells.

6. ACKNOWLEDGEMENTS

I would like to thank the management of Sarulla Operation Limited (SOL) especially Mr. Doddy Astra as VP Subsurface for the permission to publish this paper. I also express special thanks to colleagues of Sarulla technical team who provided technical support for the project of the study area. Finally, I express my sincere for colleagues in Geothermal Exploration Magister Program of University of Indonesia (UI) to provide the support of software, analysis and guidance of this work.

REFERENCES

Blakely, R.J.: Potential Theory in Gravity and Magnetic Applications, Cambridge University Press, Cambridge (1996).

Christi, L.F., Hernawan, A., and Astra, D.: Twenty-Seven Months Performance of Silangkitang Reservoir, Sarulla Geothermal Working Area, North Sumatra, Indonesia, *Proceedings*, World Geothermal Congress Reykjavik, Iceland (2020).

Elkins, T.A.: The Second Derivative Method of Gravity Interpretation, *Geophysics*, 16(1), (1951), 29-50.

Ganefianto, N., Hirtz, P.V., and Easley, E.: A Brief History of the Sarulla Geothermal Field Development, (2015).

Gunderson, R.P., Dobson, P.F., Sharp, W.D., Pudjianto, R., and Hasibuan, A.: Geology and Thermal Features of the Sarulla Contract Block, North Sumatra, Indonesia, *Proceedings*, World Geothermal Congress 2, (1995), 687 – 692.

Gunderson, R.P., Ganefianto, N., Riedel, K., Sirad-Azwar, L., and Suleiman, S.: Exploration Results in Sarulla Block, North Sumatra, Indonesia, *Proceedings*, World Geothermal Congress, (2000), 1183 – 1188.

Hickman, R.G., Dobson, P.F., van Gerven, M., Sagala, B.D., and Gunderson, R.P.: Tectonic and Stratigraphic Evolution of the Sarulla Graben Geothermal Area, North Sumatra, Indonesia, *Journal of Earth Sciences*, 23, (2004), 435-448.

McDonald, M.R. and Gosnold, W.D.: Gravity Modeling of the Rye Patch Known Geothermal Resource Area, Rye Patch, Nevada, *GRC Transactions*, Vol. 38, (2014), 533-539.

Naufal, M.A. and Rosid, M.S.: Structure identification of geothermal field "X" using MLSVD method of gravity data, *IOP Conf. Ser.: Mater. Sci. Eng*, (2017., 854, 012055.

Rosid, M.S. and Siregar, H.: Determining fault structure using first horizontal derivative (FHD) and horizontal vertical diagonal maxima (HVDM) method: A Comparative study, *AIP Conference Proceedings*, (2017), 1862, 030171.

Satya, D.Y., Soeda, Y., Drakos, P., Astra, D., and Lobato, E.M. L.: Building A 3d Earth Model of Silangkitang Geothermal Field, North Sumatra, Indonesia, *Proceedings*, The 6th Indonesia International Geothermal Convention and Exhibition (IIGCE), (2018).

Satya, D.Y., Suryantini, and Astra, D.: Geology Assessment of Permeability Distribution in Silangkitang Geothermal Field, North Sumatra, Indonesia, *IOP Conference Series: Earth and Environmental Science*, Volume 732, ITB International Geothermal Workshop 10-13 August 2020, Bandung, Indonesia (2021).

Simatupang, C., Matsuda, K., and Astra, D.: The Initial State Geochemical Model and Reservoir Response of 2 Years Production at Silangkitang, a Fault-Controlled Geothermal System along the Great Sumatera Fault, *Proceedings*, World Geothermal Congress Reykjavik, Iceland (2020).

SOL-UGM: Structural Geology Mapping of Silangkitang, North Sumatera, SOL Internal Study Material, (2020).

Wallis, I.C., Rowland, J.V., Cumming, W., and Dempsey, D.: The Subsurface Geometry of a Natural Geothermal Reservoir, *Proceedings*, 39th New Zealand Geothermal Workshop, Rotorua, New Zealand (2017).

New Insight into Geothermal System in Field X Based on Reprocessing and 3D Inversion Magnetotelluric Data

Sri Mulyani[1], Yunus Daud[1], Riza G. Pasiki[2], Haris Siagian[2], and Wambra Aswo[3]

[1]Geothermal Exploration Magister Program, Graduate Program of Physical Sciences, Department of Physics, Faculty of Mathematics and Natural Sciences, Universitas Indonesia, Kampus Depok 16424, Indonesia
[2]KS ORKA, Recapital Building, Adityawarman Street 55, Kebayoran Baru, Jakarta Selatan 12160, Indonesia
[3]PT. NewQuest Geotechnology, Pesona Kayangan Estate DC12, Depok 16411, Indonesia

sri.mulyani92@ui.ac.id, ydaud@sci.ui.ac.id, riza.pasikki@ksorka.com, haris.siagian@ksorka.com, wambra.aswo@newquest-geotechnology.com

Keywords: 3D Inversion, Magnetotelluric, Geothermal System, Resistivity, Metronix

ABSTRACT

Geothermal field X located in Sumatra, has been known as high productivity field. Although geothermal exploitation is well-developed, the conceptual model of geothermal system in this field is still has many uncertainties. More data obtained to identify the reservoir characterization and to decide the best strategy to develop this field for sustainable production. In this case, conceptual model of geothermal system that comprehensive play importance role as basic reference for the development plan. In this study, we try to optimize the existing data of Magnetotelluric by doing reprocessing and creating 3D Inversion model. The result will be combined with the latest drilling data that should give better information about the geothermal system. The aim of this study is to get new insight and knowledge about the conceptual model in geothermal field X based on 3D Magnetotelluric Inversion. The new conceptual model can update the existing one and can be used for the next stage. Main input data used in this study is raw MT data with time series format. Additional data used as secondary input while doing the modeling are temperature and lithological data from wells, manifestation of geothermal, and faults distribution. The process started by preparing all of the data and quality check, the selected raw MT data then being reprocessed to get .edi format, then initial resistivity model and input for inversion process being created, finally the 3D inversion being run, and the results can be interpreted. One of the challenges during the process is to deal with metronix data of MT which is less common and need more effort to be used for 3D inversion. The result of this study is 3D resistivity model that can be used to identify the clay cap which shown by low resistivity value, the presence of fault in reservoir zone that indicated by contrast value of resistivity, and the heat transfer which showing Upflow from heat source as well as outflow direction. Basically, by reprocessing the raw MT data should give new knowledge about the overall geothermal system in Field X that might be beneficial for the decision maker and the developer.

1. INTRODUCTION

The Geothermal Power Plant project of geothermal field "X" has several geothermal wells that have been connected to two units and has been known as high productivity field. During this time, the development of geothermal fields is focused on the central part of the geothermal field work area "X" (Figure 1). For the next development, there is planning to develop the production area in the northern part, which is also thought to have geothermal resources based on the presence of manifestations on the surface.

Unlike the central area that is already in the production phase and has a lot of well data, the area in the north has only one exploration well with very limited data. However, there are other sufficient data in the northern part of this geothermal field "X", such as geochemical data from surface manifestations, surface geological data, and geophysical data in the form of gravity and magnetotelluric. Although geothermal exploitation is well-developed, the conceptual model of geothermal system in this field still has many uncertainties. Based on drilling data in the middle of this geothermal field "X", three of the seven wells have very low permeability with a relatively small temperature value compared to other wells (Sarmiento et al., 2017). From this information it is known that the risk of failure of production wells is still quite high in the central geothermal field "X", which can also occur in the northern part. In this case, conceptual model of geothermal system that comprehensive play important role as basic reference for the development plan. In this study, we try to optimize the existing data of Magnetotelluric by doing reprocessing and creating 3D inversion models. The result will be combined with the other geophysics and latest drilling data that should give better information about the geothermal system.

In general, problems that can be formulated for this study include how is the relationship between the permeability and temperature data from existing well to the resistivity value of the magnetotelluric model? and how the distribution of those parameters throughout the geothermal field area "X", which will be shown in the conceptual model of geothermal system in this field. The aim of this study is identifying the correlation between the permeability and temperature values of the well data against the resistivity values of 3D magnetotelluric inversion then interpreting the model which is expected to give new insight about the conceptual model in geothermal field X. The new conceptual model can update the existing one and can be used for the next stage. The limitations of the issues discussed in this study include spatial limitations specified in the research area as well as limitations on the information or data used. The main data of the geophysical methods used are limited to using only magnetotelluric data. There are several interpretations that can be done from resistivity model. For the example, the resistivity value of the magnetotelluric data can be used to indicate rocks with argillic alteration that act as clay cap on geothermal systems (Daud et al., 2019).

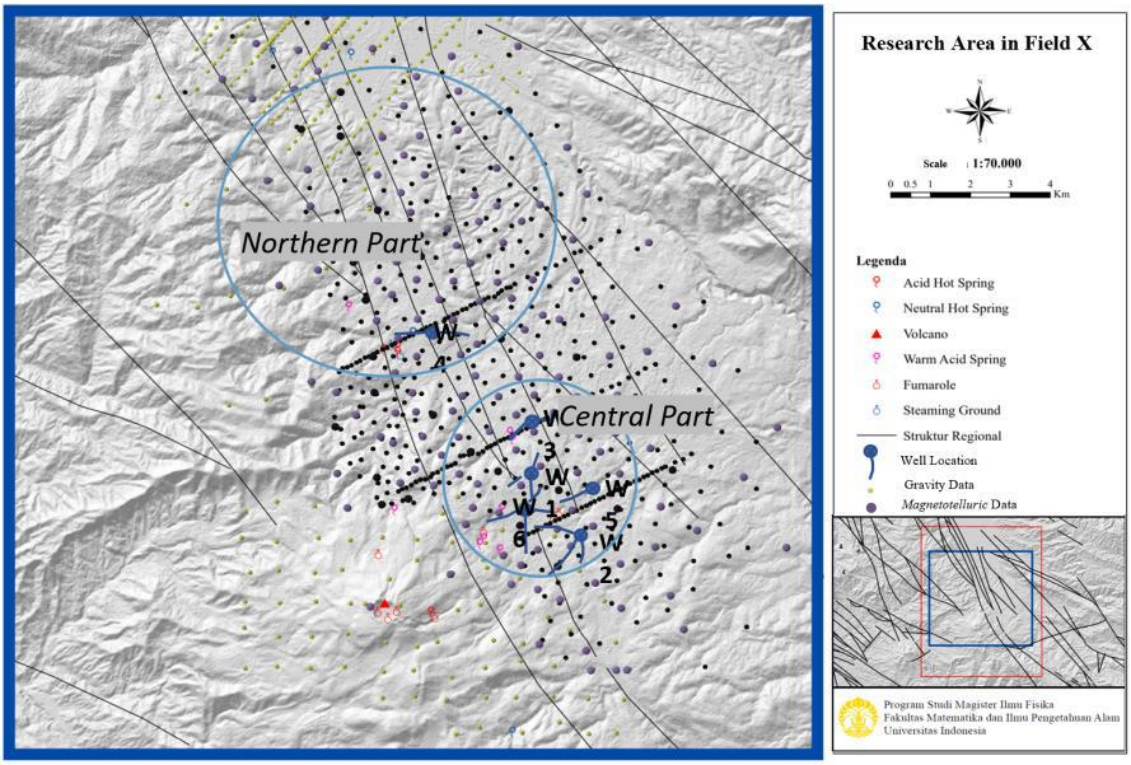

Figure 1: The study area in Geothermal Field X.

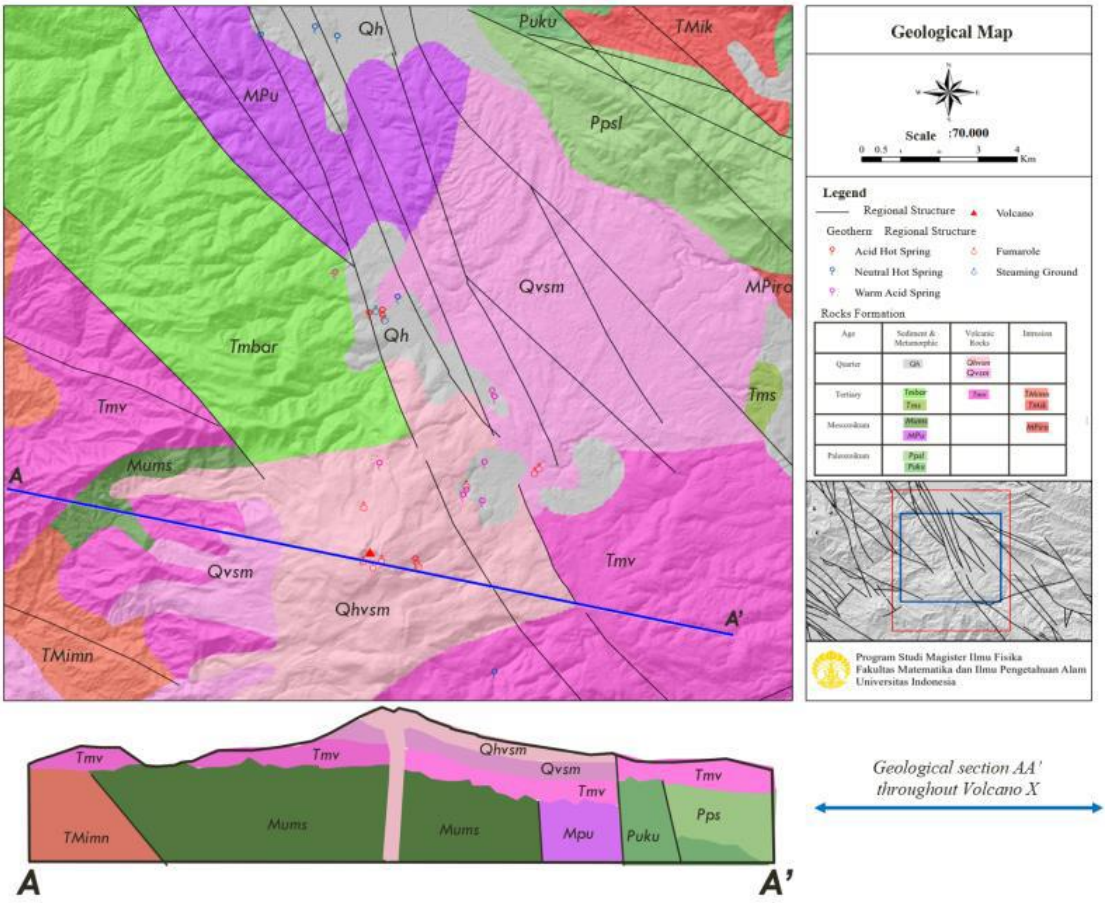

Figure 2: Lateral distribution of rocks formation and Geological Section based on regional geological map (Source: modified from Rock et al., 1983).

2. REFERENCE FIELD

2.1 Geology

The regional geological map at the research area is shown by Figure 2. In general, there are several units of rock that make up this area, with the dominance of volcanic rocks. Based on a regional geological map compiled by Rock et al. (1983), laterally the dominant rock units in research areas consisting of Mpu formations (pre-tertiary rocks), Tmbar (siltstone), Tmv (volcano center), Qhvsm (lava center of volcano X), Qvsm (Volcanoclastic polymictic rock volcano X) and Qh (young Alluvium). Mpu formation is Mesozoic-aged metamorphic rocks, as for Tmbar formations consist of siltstone that belongs to tertiary-aged sedimentary rocks (early Miocene). On top of the formation there is a Tmv formation in the form of polymictic rocks with lithological characteristics as a product of the tertiary-aged volcano eruption center (late Miocene). Next there is the Qvsm formation in the form of polymictic volcanic rocks that vary (Quarter). The youngest rocks are the formation of Qhvsm, which is lava produced by the products of volcanoes X and Qh in the form of alluvial deposits (Holocene).

Vertically, the stratigraphy of this area consists of metasedimentary rocks and various types of Paleozoic-Mesozoic-aged intrusions, Tertiary-aged sedimentary rocks and volcanic rocks, as well as Quarter-aged alluvial deposits and young volcano rocks (Chandra et al., 2016). The geological age difference indicates a non-conformities relationship between the formations. Various metasedimentary rock as the Mpu formation at the study area consist of limestone or marble, quarocytes, slates that generally show the level of greenschist metamorphism and local hornfels. The oldest intrusions (MPiro) consist of granite, microgranite, diorite, syenite with the appearance of foliation due to alteration or metamorphism process. Tertiary-aged sedimentary rocks (Tms) including sandstone, carbonate clay, silt, and conglomerate. Volcanic rocks and intrusions at Tertiary age (Tmv) are dacitic lava, rhyolitic lava, pyroclastic, epiclastic deposits, and volcanic rocks that have undergone alteration. The Quarter-aged rocks (Qh and Qhvsm) in this area are alluvial deposits consisting of sand, silt, and gravels as well as basalt-andesite lava, pyroclastic, epiclastic deposits and lake deposits with high sulfur content (Rock et al. 1983). The geological structure in this area are the regional faults that developed with main direction relatively Northwest–Southeast, with some other structures that have an East-West direction. The distribution of geological structures is affected by the influence of Big Sumatra Fault in the middle of the research area. The existence of the structure is also evidenced by the manifestation of geothermal along the antithetical fault structure (Sarmiento et al., 2017).

2.2 Geochemistry

Surface manifestations in study area in the form of hot springs, fumaroles, and steaming ground. There are three types of hot springs found: acid hot spring, acid warm spring, and neutral hot spring. In general, the manifestations are located at the location of geological structures and near the top of volcano X. Distribution of manifestations that are near the top of the volcano are fumaroles and acid hot springs, while warm acid spring located on the slopes of the volcano. In the Southernmost part of the volcano area is also found neutral hot spring manifestations. Another group of manifestations was also observed in the northern part of the research area in the form of steaming ground, acid hot spring, acid warm spring and neutral hot spring which correlated with regional fault structure (Figure 1). The interpretation of geochemistry in geothermal field "X" used the results of analysis from gas and water samples around the manifestation. In general, there are four types of water outside the mixed or cold-water category that related to geothermal systems (Chandra and Purba, 2016). First is acid chloride sulphate water which generally related to volcanic centers at high elevations (peaks and slopes of the Mountain) where the steam contains volatile magmatic gas (HCl and SO2) indicates the presence of superheated magmatic vapor plume under the active mountain peak. Second water is acid sulphate water that commonly found as steam heated water containing low Cl as indicate a non-magmatic source with low pH (0-3). This water associate with argillic alteration and can form steaming ground on the surface. Third is neutral sodium bicarbonate water that usually derived from the process of steam condensation in groundwater, which is followed by the neutralization process by rock interactions including the dissolving of CO2 that produces HCO3. This water is commonly found in the condensation area of the vapor dominated system and in the marginal part of the liquid dominated system. The last one is neutral sodium chloride water. In liquid dominated system, chloride in this type of water is predicted come from a magmatic source and appear as a hot spring. Because it comes directly from within the reservoir, this manifestation can be used to obtain information about the salinity, pH, and temperature of the reservoir.

Based on the analysis of geochemical data, geothermal field "X" can be divided into 3 types of geothermal activity (Figure 3). They are: acid magmatic system located around the peak and slope of Volcano "X", mature high temperature system that located in the middle of study area on the eastern side of the volcano slope with Upflow zone of the system is estimated to be in the southern part and direction of outflow flows tends to the North and East, the intermediate temperature system in the north of volcano or the northern part of the research area with Upflow zone near sample S04-W and outflow direction to sample S31-W location.

2.3 Gravity Analysis

Interpretation results from gravitational analysis can be used to determine the structure of faults at the research area. In general, there is a large regional structure that has the direction of NW-SE which is likely related to fragments of Big Sumatra faults with a depth below -1500m. As for the residual anomaly map observed some relatively shallow geological structures depth above 1100m from the sea level. In addition, high anomaly areas were observed near the volcano and assumed as shallow igneous rock. The geological structure from geological mapping shows some conformity with the structures observed on both residual and regional gravity maps. The geological structures also observed in SVD that include shallow structures and indicate a location corresponding to the position of surface manifestations that have high permeability. The map of Complete Bouguer Anomaly (mGal), regional anomaly (mGal), residual anomaly (mGal), FHD (mGal/m) and SVD (mGal/m^2) from gravity analysis shown by Figure 4.

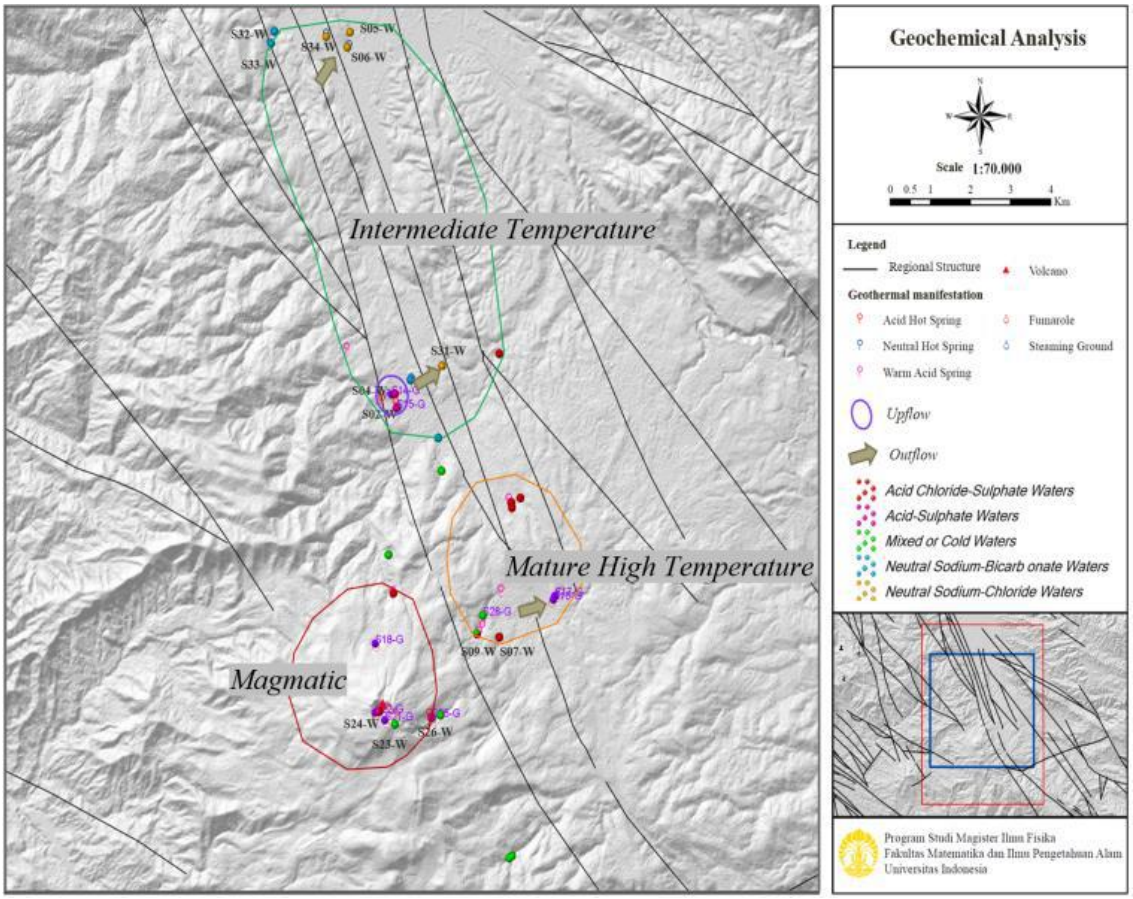

Figure 3: Map of geothermal system classification based on geochemical analysis.

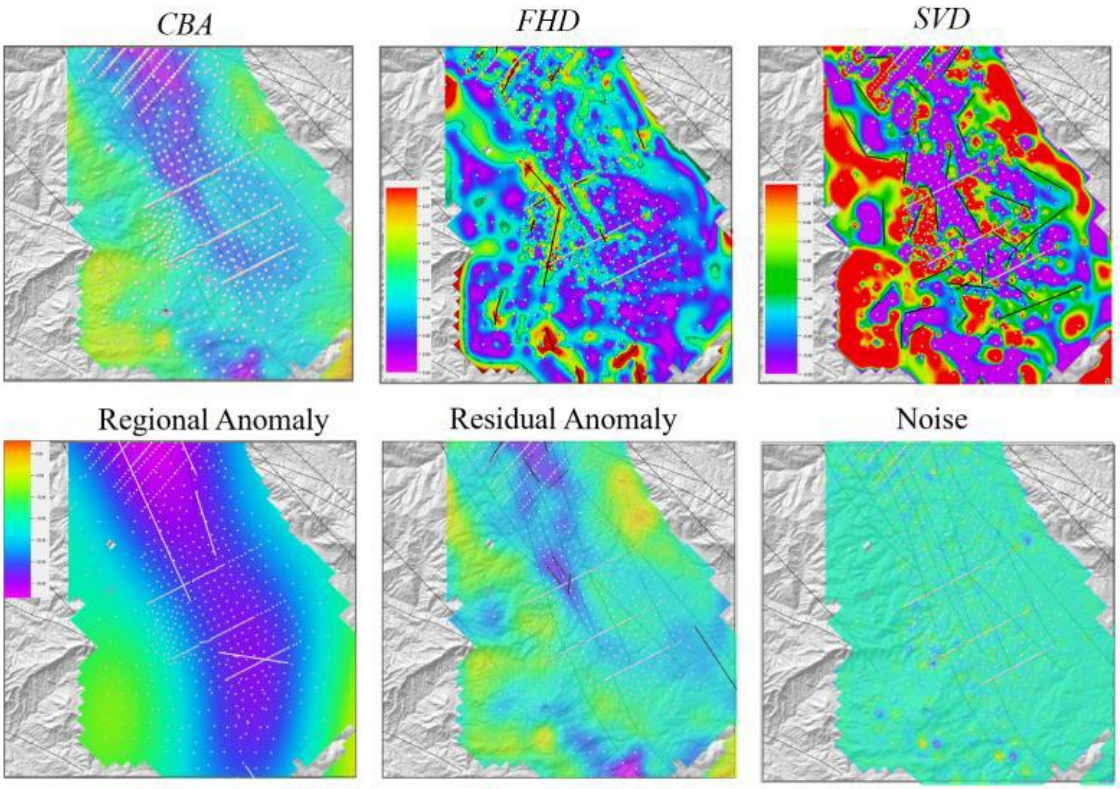

Figure 4: Map of Complete Bouguer Anomaly (CBA), regional anomaly, residual anomaly, FHD and SVD.

2.4 Geothermal System

The research about geothermal systems in Field X were also conducted by Rezky and Hermawan (2015). The results of the study showed that clay cap formed in the volcano complex with impermeable characteristics of *clay cap* in the form of volcanic rocks that have undergone alteration into clay minerals, silica, chlorine, and ore minerals at moderate to strong alteration levels. The magnetotelluric interpretation shows that clay cap rocks correlate with resistivity values <10 Ohm.m with an average conductive zone thickness of 200-300 m at depth 200 m from sea level. The reservoir of the geothermal system is predicted to be below the prospect area with footwall of faults as boundary in the Northwest-Southeast part. The fault is part of Big Sumatra's fault zone that undergoes extension force so that the permeability is high and can store hot fluid in it. The lithology of this reservoir is in the form of volcanic rocks, tuff breccia and lava. The reservoir zones in this field are divided into two and separated by a large structure indicated by MT data. The first reservoir depth reaches 1200 m with a dominated water system and the second reservoir depth is about 900 m with a two-phase system. The heat source of this geothermal system can be a magma pouch (magmatic chamber) in the form of the remaining magma of volcano "X" aged Quarters, or in the form of intrusion of young igneous rocks near the surface. However, predictions of intrusion body as a heat source in this research area were not proven by gravitational data that did not indicate any positive anomalies in the area. Geothermal fluids are identified from Chloride-Bicarbonate hot springs as indications of an outflow zone near the first reservoir zone, and the presence of fumaroles and chloride-sulphate hot springs indicates an up low zone near the second reservoir zone. The recharge area is in a high elevation which is hills which extend to the Northwest-Southeast, with discharge areas in the depression zone at the central and Northern part of research areas.

3. DATA AND METHODOLOGY

The magnetotelluric (MT) method is a geophysical method that utilizes the principle of electromagnetic waves propagation within the earth. The waves interact with media that have certain electrical properties (conductivity) resulting in telluric electric current and secondary magnetic field to be recorded as MT data (Kearey et al., 2002). MT data processing includes several stages: time series inspection, Fourier transform, robust processing, selecting cross power, and static shift correction (Arafat, 2019). Inspections of time series data are useful for verifying the quality of MT data and determining the measurement time range with the best time series. Fourier transformations are performed to convert time series data from time domain to frequency. Robust processing done to eliminate outliers data by involving the least square algorithm in the form of residuals iterative weighting in identifying and removing such bias data (Simpson and Bahr, 2005). Cross power is set of partial data in the form resistivity and phase values paired at the same frequency. Cross power selection is done to select cross power data to obtain the best MT curve trend. According to Cumming and Mackie (2010), static shifts can cause distortion in most resistivity methods that use electrodes so they must be corrected to avoid errors in interpretation. Basically, this static effect is caused by the presence of heterogeneity near the surface, topography, and the presence of vertical contact.

To analyze MT data, the inversion process can be done. Basically, inversion is a mathematical tool for converting observation data into subsurface models to provide information on the properties of physic, geometry and rock depth. On the contrary, predicting measurement results based on known physic parameters is called forward modeling process (Supriyanto, 2007). In MT inversion modeling there are three types: 1D, 2D, and 3D inversions. According to Cumming and Mackie (2010), 1D inversions can provide a rough image of resistivity distribution with undefined boundary. The 2D inversion can give a better picture of resistivity than 1D inversion although the processing requires more precision effort. While 3D inversion is better at displaying the distribution of resistivity in subsurface specially to determine the thickness of clay cap in geothermal systems.

3.1 Classification of Data Quality

There are about 300 MT measurement points at the research area, with data types already in the form of .edi files and some available as time series. Before the data in the form of .edi file is used in the further process, it is necessary to check the quality of the data. The parameters used for MT quality classification are error bar, trend data and minimum frequency contained in the data. Figure 5 shows examples of excellent, very good, good, fair and poor data classification at a minimum frequency of 0.01 Hz and examples of very good data at a minimum frequency of 1 Hz.

From the results of classification process obtained several data that belongs to each category. The distribution of MT data of excellent, very good and good category with a minimum frequency value of 0.01 Hz dominates the research area (Figure 6). However, there are still some time series data that can be reprocessed to get new data of edi files with good quality. The reprocessing results will be added to the data that is already good and ensured that there is no overlay data. Then the selected data will be used as input in the creation of 3D MT inversion.

3.2 Data Reprocessing

Data re-processing was done in the dataset with form of time series from Metronix especially those that have a minimum frequency value 1 Hz. By obtaining edi files that have a minimum frequency value of 0.01 Hz from re-processing, it is expected to produce a good 3D MT inversion for a deeper location. The process of re-processing for time series data was done by using software through several stages. The first step is to set up the configuration system according to the configuration information listed in the xml file. The parameters required in this setting include channel number and type, serial number, and sensor type, as well as a list of bands such as HF, LF1, LF2, LF3, LF4, LF5, or FreeFreq. The next step is importing time series data from each site into the software. In this step the frequency value of data can be checked and displayed as a graph. To get a lower frequency of existing data, a digital filter (1/4) to a frequency of 0.01 Hz has been done. After that, processing started for one site by selecting all bands to be used. The result of processing will show all amplitude plot data and phases against frequency. After that the editing process was done so that it is ready to be exported as edi file. From the results of this processing can be observed that low frequency has a high error bar so that the follow-up process is done with MT software to obtain optimal file edi data results.

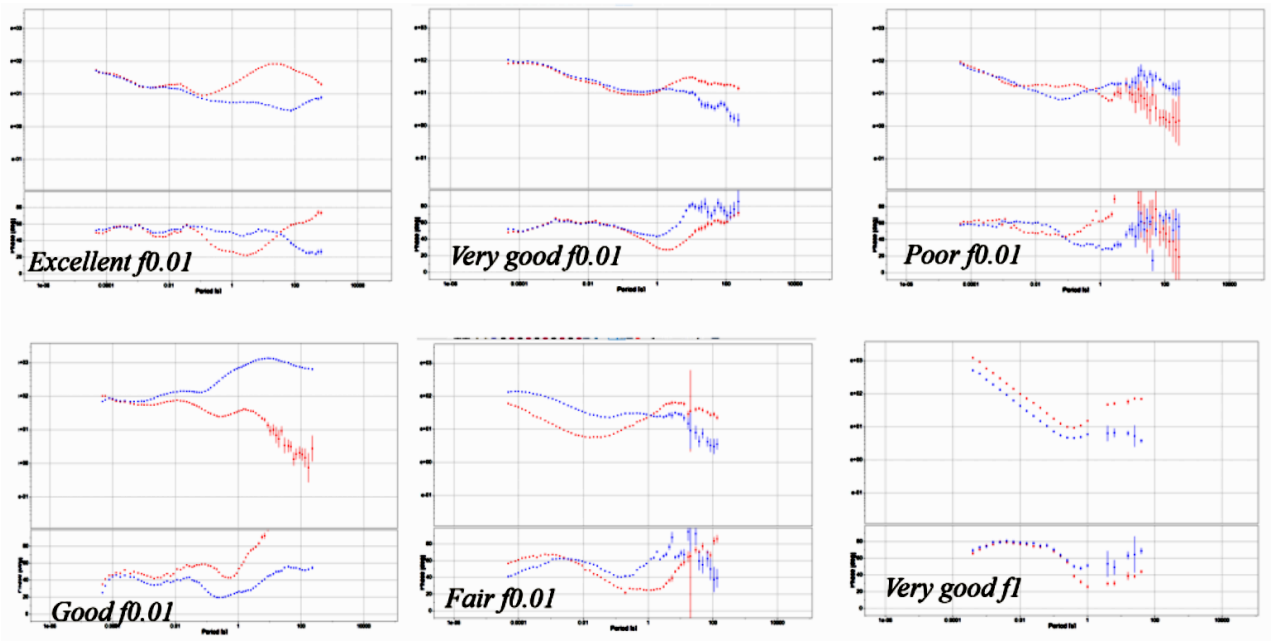

Figure 5: Example of MT data quality classification in the form of edi file.

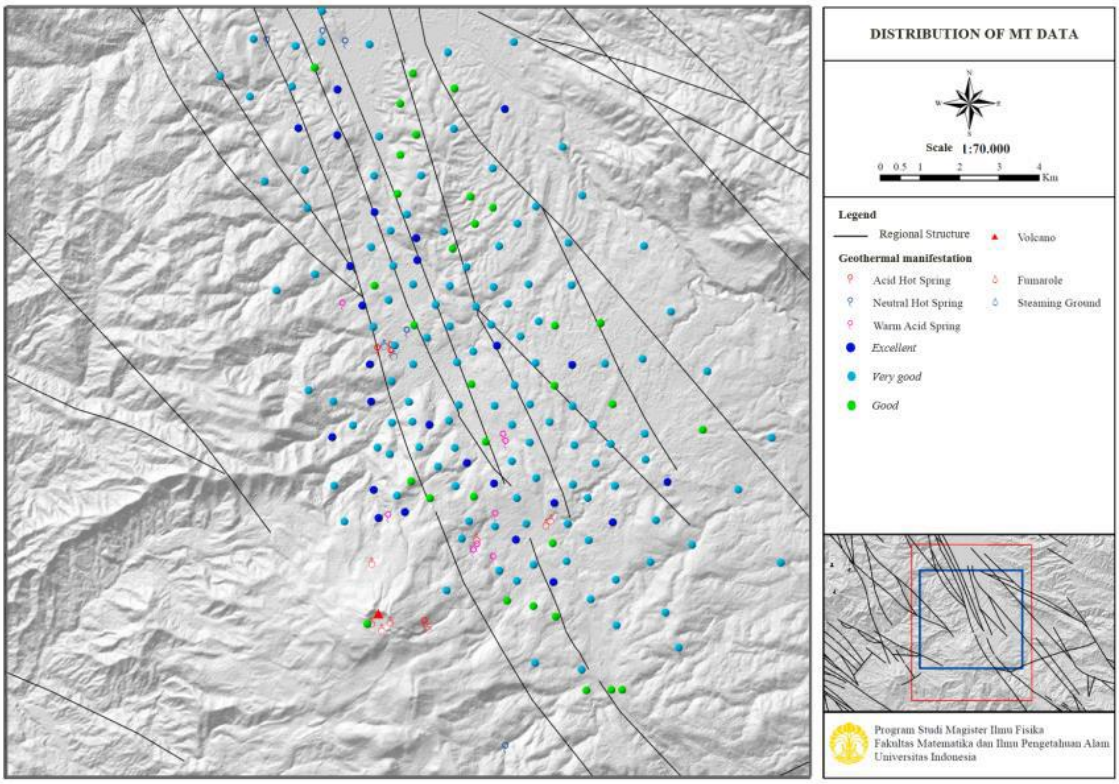

Figure 6: Distribution of MT data with Excellent quality, Very good and good.

3.3 3D Inversion Modeling

The total of 139 MT measurement data used in the inversion 3D modeling. Those points scattered in the area near the "X" volcano and around the geothermal manifestation. The distance between the selected points on average is 500 – 1700 m. The MT data that is ready to use is in the form of apparent resistivity and phase curve from edi files. The next stage is a static correction process for the MT curve in order to eliminate the static shift effect that appears in the form of separate TE and TM curves. In this study, the correction process was carried out using the geostatistical averaging method (Arafat 2019). Prior to the inversion modeling, an initial model was made in the form of a subsurface layering model with a certain resistivity distribution according to the geothermal area in general. This model was made as a benchmark for the next model. In addition, the design of the mesh grid that will be used for the inversion was prepared according to the research area. Then, 3D inversion modeling using the initial model was carried out to obtain cross-sectional shapes and resistivity maps for interpretation stage. The example of a resistivity cross section that passes through the production area is line 1 and line 9 (Figure 7).

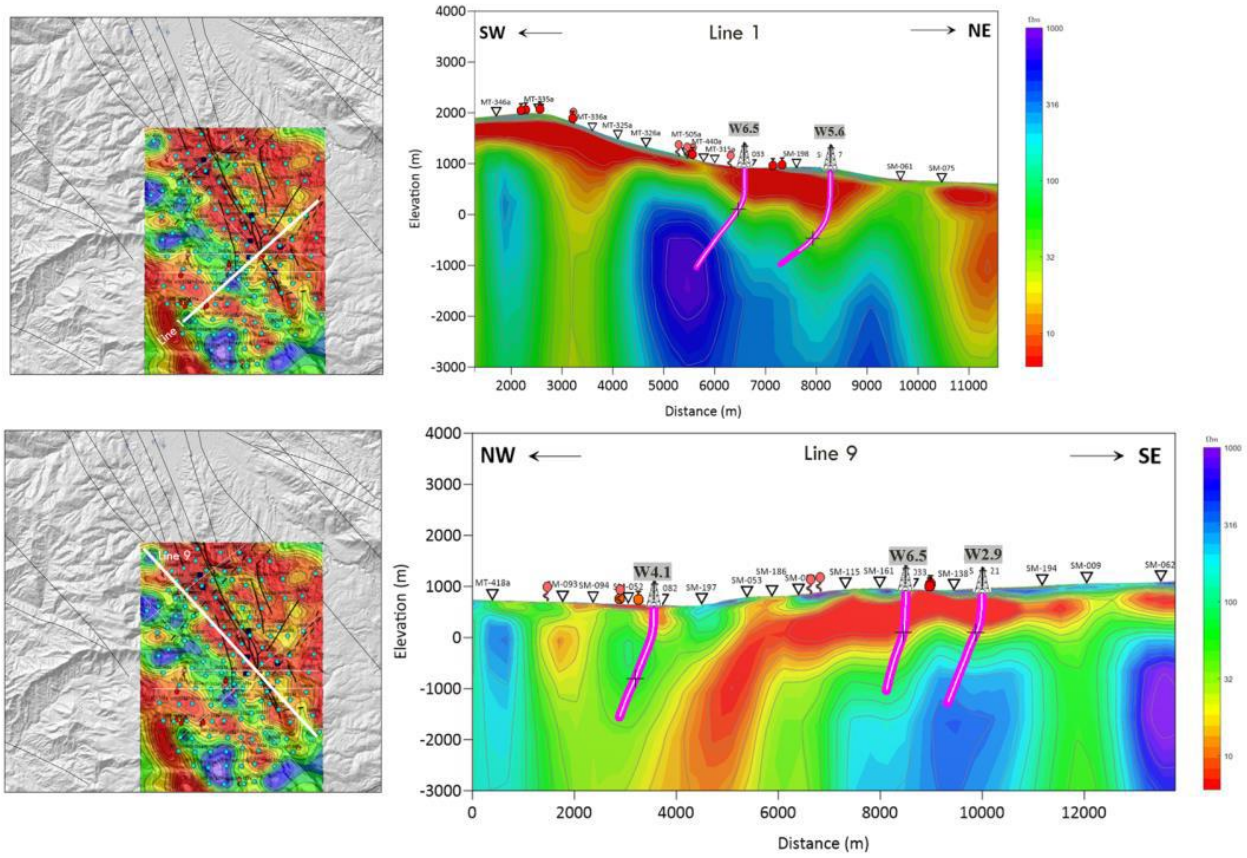

Figure 7: Cross-sectional resistivity of line 1 and line 9 on a 0 m depth resistivity map.

4. RESULTS

Interpretation of the resistivity section was carried out to show the correlation with the presence of fault structures and intrusive rocks (Figure 8). In general, the 3D MT inversion results show good compatibility with the results of Fault Structure modeling in the study area, with features in the form of resistivity values that are laterally contrasting and vertically continuous. In addition, the location of the modeled intrusive rocks generally correlates with the weak zone due to faults in Fault 17 and Fault 15, although there are no special features that characterize these rocks. From line 1, it can be observed that fault 1 is a continuous regional fault in the NW-SE direction. The Fault 17 is shallow fault with a relatively small size. For line 9, the contrast of resistivity values corresponds to the location of Faults 16, 15, 3 and 22 that have been modeled. Fault 3 is assumed to be one of the controls for the low resistivity anomaly which continues downwards. In addition, there is also a fault at the southern part that has not been detected by gravity or geological mapping methods but can be identified by using MT.

Correlation of well data in the form of temperature and location of the feed zone (high permeability zone) to the results of MT modeling and gravity was carried out on sections 1, 7, and 9 as shown in Figures 9a, 9b, and 9c.

The cross section in line 1 (Figure 9a) shows a good correlation between the temperature from the well data and the resistivity data. The temperature distribution of 225^{o}C shows that it corresponds to the contrast of the density values. Where such conformity does not persist at higher temperatures in deeper parts. The permeability indicated by the location of the feed zone and the value of Injectivity Index has a correlation with the resistivity value, but not with the density value. In general, the location of this feed zone is related to the location of the fault structure, which is identified from the gravity method. The cross section of line 7 (Figure 9b) shows a poor correlation between the temperature from the well data and the resistivity data. Based on the well W4.1, there is relatively high temperatures zone in areas with low resistivity. At the end of the well W4.1, the lithology that found is dike, which is an igneous intrusion that may be correlated with high temperatures other than due to overburden heat from the basin filling material. The absence of a permeable zone in the well indicates that the location has low resistivity which can be assumed as a compact sedimentary rock with Fault 2 and Fault 14 acting as sealing faults. The location of Fault 22 which is likely to act as a leaking fault is parallel to this cross section with a slope to the northwest so that it is not observed in the cross section. The cross section of line 9 (Figure 9c) shows a good correlation between the temperature from the well data and the resistivity data, except for the well W1.3. The well has a relatively high temperature in the shallow section, which is interpreted as the effect of an intrusion just below it. The temperature distribution of 250^{o}C shows that it corresponds to the contrast of the density values. Where such conformity does not persist at higher temperatures in deeper parts. The permeability indicated by the location of the feed zone and the value of injectivity index has a correlation with the resistivity value, but not with the density value and the well W1.3.

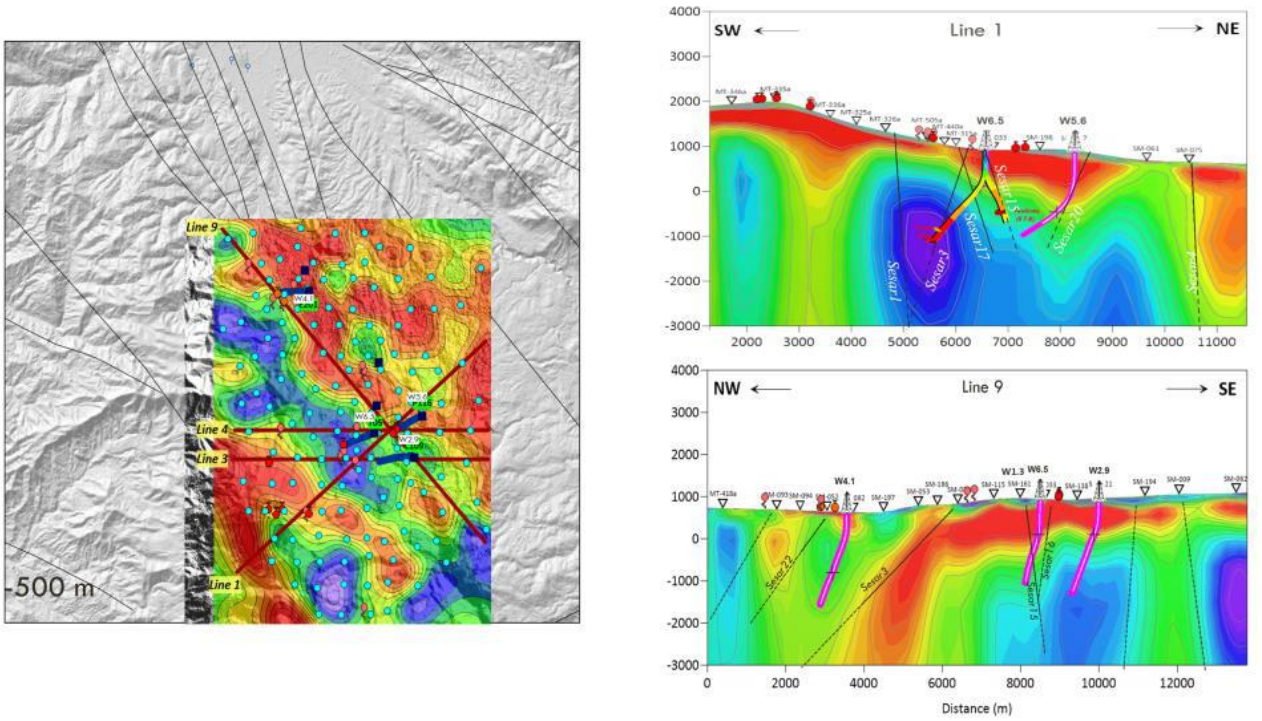

Figure 8: Interpretation of the fault structure (Fault / *Sesar*) on the resistivity section in line 1 and 9.

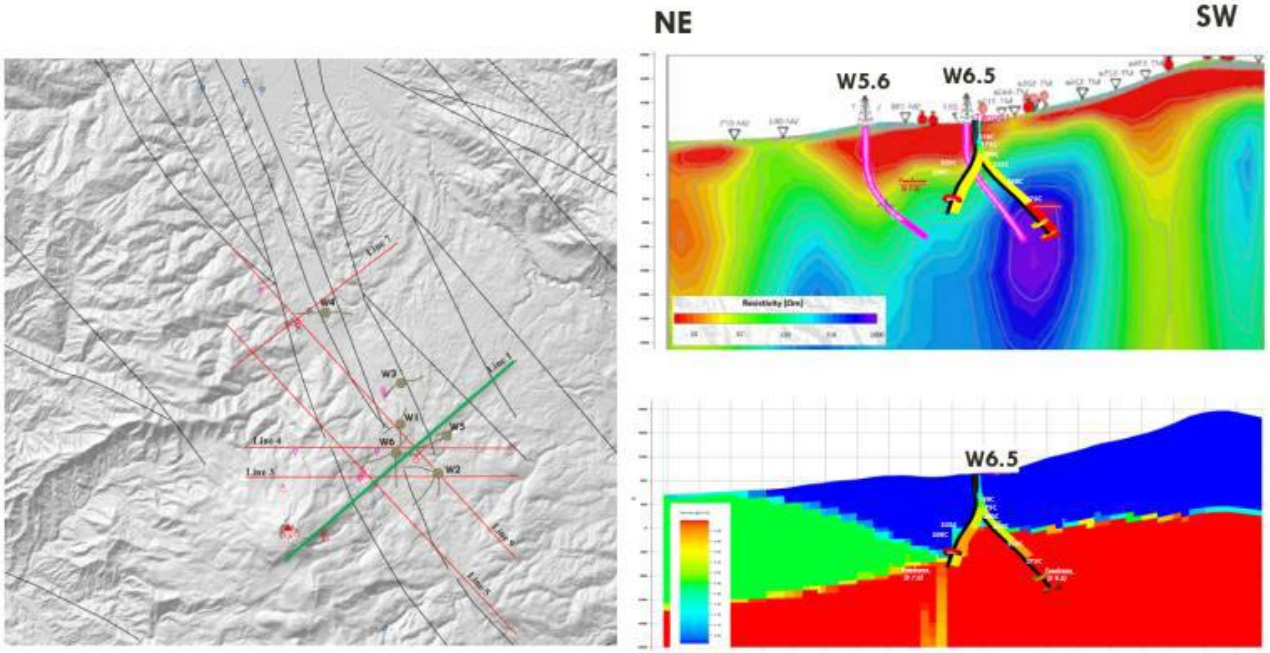

Figure 9a: Cross-sectional resistivity and density on Line 1.

5. DISCUSSION

The interpretation of the temperature values and low permeability distribution is carried out on the resistivity cross-section on lines 1 and 9 as shown in figure 10. The data used as a reference for temperature values is data from drilling wells near the track, which is in the form of wellbore temperature when the shut-in condition so it is expected can represent the reservoir conditions. The temperature distribution pattern is based on the literature on conceptual models of systems controlled by stratovolcanoes and tectonic structures from Goff and Janik (2000). The interpretation of the distribution of permeability, especially low permeability as a characteristic of clay cap is carried out based on the distribution of low resistivity values, which are below 10 Ohm.m. In some locations, low permeability values characterized by low resistivity are also correlated with fault zones or geological features filled with altered rocks or minerals.

The observed temperature distribution from line 1 is the presence of high temperature (275ºC) with high permeability (injectivity index 9.2) located in well W6 and close to the intrusion. In general, low resistivity indicates an area of non-permeability or clay cap

at the top of the reservoir which distributes from around the volcano to the Northwest. The clay cap is relatively thin at the top of the high temperature area, which is in the area between well W6 and the volcano. Based on the conceptual model of the paired liquid and vapor core system according to Reyes et al. (1993), that area is probably a boiling zone. The temperature distribution shown by line 9 shows an Upflow sloping to the Southeast. The location of well W1 is assumed to be in the body of a dike. However, the temperature data in the well shows that the high temperature comes from the Northwest part of that igneous rock. This is also observed in line 1 where the highest temperature is not in the intrusive rock body. So, it can be concluded that this intrusion (dike) acts as a reservoir rock and not as the heat source. It is possible that these rocks are associated with a nearby heat source, because of magma cooling from the same source but the hot zone in the area has moved to the Northwest. The low resistivity indicates an area of non-permeability or clay cap at the top of the reservoir. In the well W1, it is found that there is area with high temperature but has high clay content. This case can be interpreted as the result of Phyllic alteration near the surface. In addition, there are also clay minerals that are likely to fill Fault 3 to the Southeast of the well W4 with a characteristic of low resistivity that continues downward. The temperature distribution shown by Line 7 is limited to the area around the well and nearby fault structures. From the interpretation results, it can be seen that the area with the highest temperature is under the basin zone with low resistivity. The heat flow pattern shows the outflow direction to the Southeast, towards areas with high resistivity which are interpreted as meta-sedimentary rocks. The distribution of low permeability is indicated by a zone with low resistivity in the middle which is very thick, and a thin layer in the Southeastern part of the well W4. In this case, the system that controls the geothermal fluid in this area is a tectonic control system.

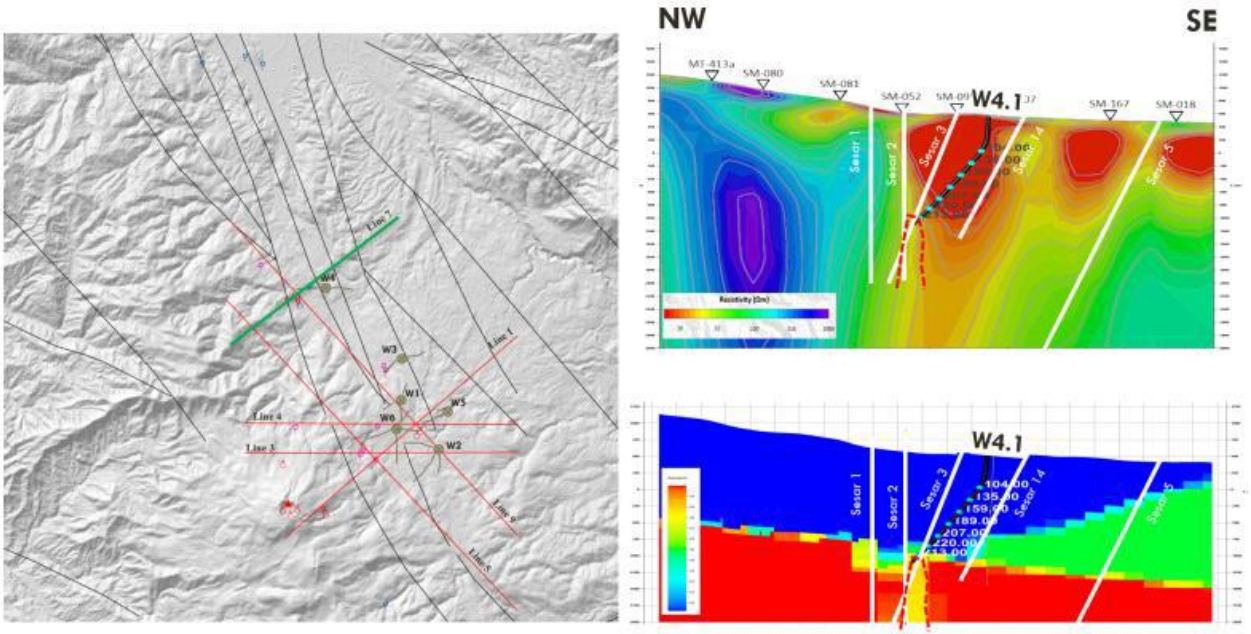

Figure 9b: Cross-sectional resistivity and density on Line 7.

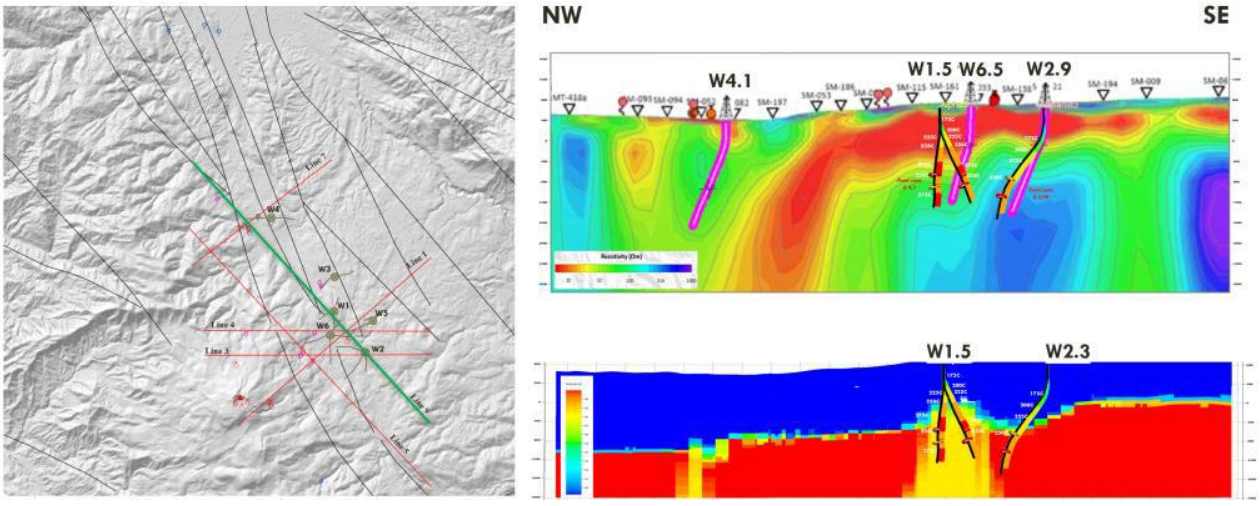

Figure 9c: Cross-sectional resistivity and density on Line 9.

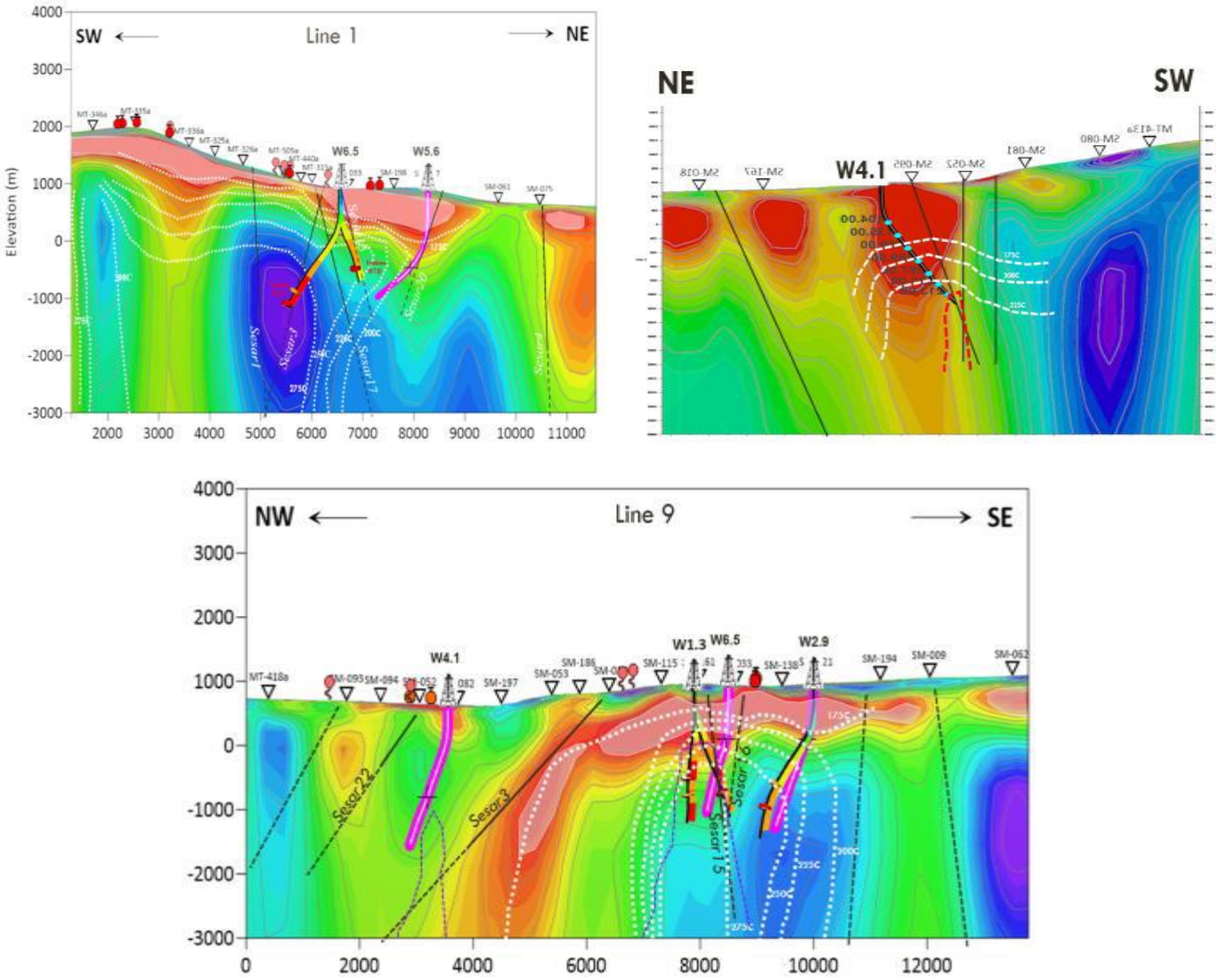

Figure 10: Interpretation of temperature distribution and low permeability on line 1 (top left) and line 9 (top right).

Based on the thorough analysis that has been carried out, it can be concluded that there are two geothermal systems at the research site. The first system is associated with a stratovolcano and it is the location that has been developed at this time, which is in the center of the research area. The second system is a geothermal system that is controlled by geological structures and located in the Northern part of the research location, with limited well data and not much developed yet. Figure 11 shows a map of the existence of the system and its components. From the map, the magmatic system around the volcano maybe related to the heat source for the geothermal system in the center or middle part of research area. In the Northern part, there are several geothermal manifestations which are interpreted as geothermal systems which are also controlled by geological structures, where each manifestation can come from different systems. In general, these manifestations are in the vicinity of the antithetic fault of the main fault which acts as a permeable zone that becomes the path for fluid flow.

5.1 Conceptual Model of Stratovolcano Geothermal System

This geothermal system is a system that is related to the presence of a Quaternary volcano in the vicinity. At the research location, this geothermal system is shown in Figure 12. The conceptual model for this geothermal system consists of several constituent components, which are made based on the reference of paired liquid and vapor core systems (Reyes et al., 1993 in Putra et al., 2020). The heat source is predicted to come from under the "X" volcano which is indicated by the presence of degassing magma below it and is associated with the geothermal system in the east. The reservoir zone consists of meta-sedimentary rocks, intrusions and quaternary volcanic rocks which have secondary permeability from several faults such as fault 1, fault 3, fault 15, and fault 17 as shown in Figure 13. Hot fluid flow in this zone is indicated by location of Upflow which is at the Eastern part of the volcano "X" and the outflow direction is relative to the East and Northeast. The clay cap is formed at the top of the reservoir zone with a thickening geometry towards the volcano and towards the outflow, with a thinning part above the boiling zone. The recharge area is located in the East of the system and may also originate from the Western part of the study area. In general, the modeled temperature reaches 275ºC so it can be classified as high temperature system.

5.2 Conceptual Model of Tectonic Controlled Geothermal System

This geothermal system is a system formed due to the control of the fault structure around it. In this case, the permeable rock that plays an important role as a medium for passing fluids is Fault 22. This fault can be observed in the resistivity section of line 9 and is perpendicular to line 7. The geothermal system controlled by the structure is in the upper section or the Northern part of study area. The position of this system with respect to the system related to the stratovolcano is shown by the resistivity cross-section of line 9 (Figure 14).

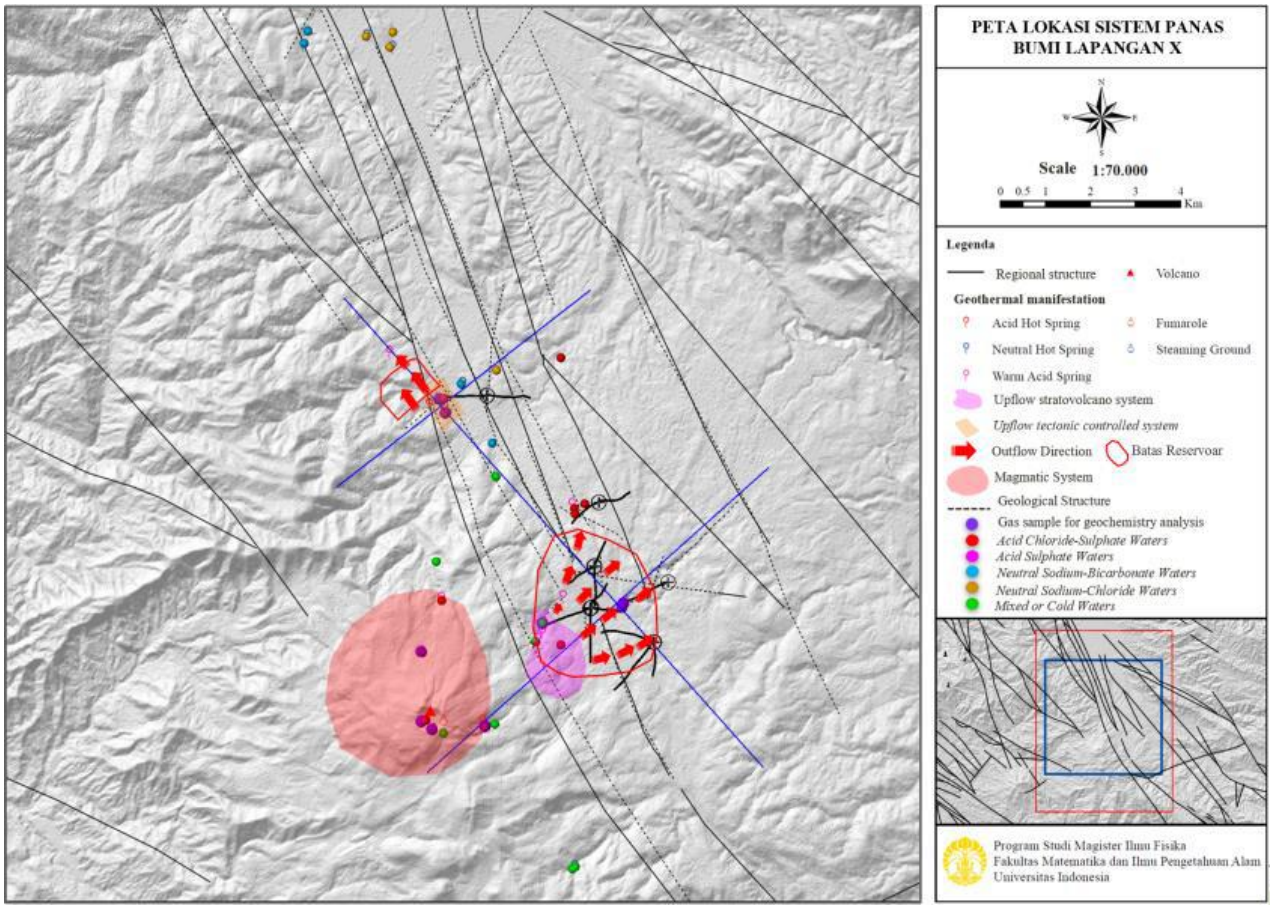

Figure 11: Map of geothermal system location in field "X".

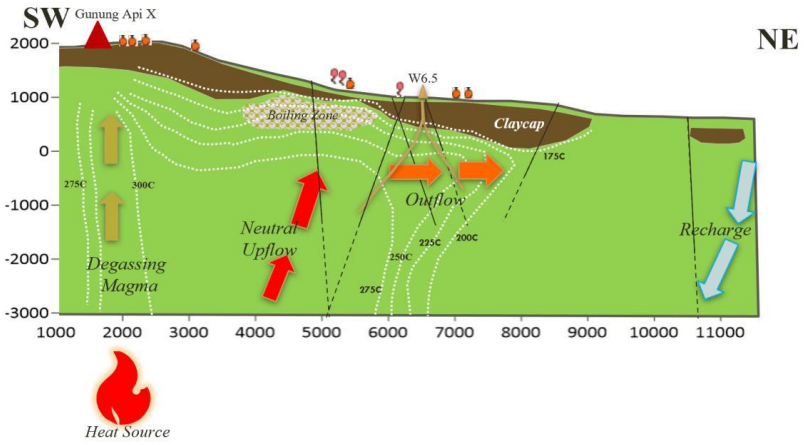

Figure 12: Geothermal system associated with stratovolcano in field "X" (line 1).

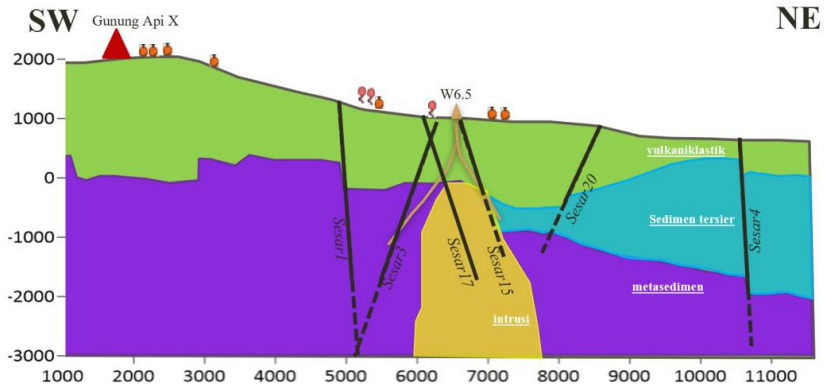

Figure 13: Geological cross section at system associated with stratovolcano in field "X" (line 1).

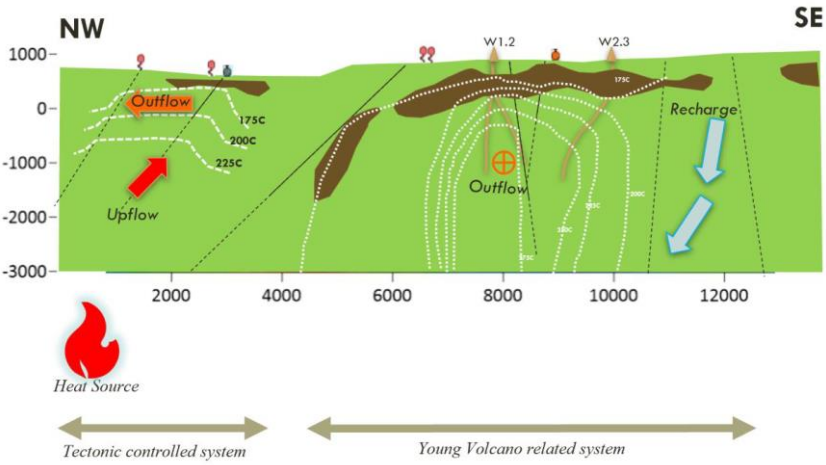

Figure 14: Position of two geothermal systems at the study site (Line 9).

In geothermal systems with geological structural control, the heat source is predicted to come from below Fault 22 which is indicated by the presence of steaming ground at the top. This heat source itself can be in the form of magmatic activity under geological structures where the crust is relatively thin and easily penetrated. The reservoir zone consists of Quaternary volcanic rock which has secondary permeability from Fault 22 as shown in Figure 15. The flow of hot fluid in this zone is indicated by the location of the Upflow under Fault 22 and the outflow direction relative to the Northwest in the direction of the slope of Fault 22. The reservoir zone is also supported by cross-sectional resistivity data on line 7 where there is a high resistivity (light blue) which bounded by metasedimentary rocks and volcaniclastic rocks. A thin clay cap is formed at the top of the upflow zone with a slightly thickened geometry towards the outflow and to the Southeast. The recharge area is likely to be in the Northwest of this system. In general, the modeled temperature reaches 225ºC so it can be classified as a high temperature system.

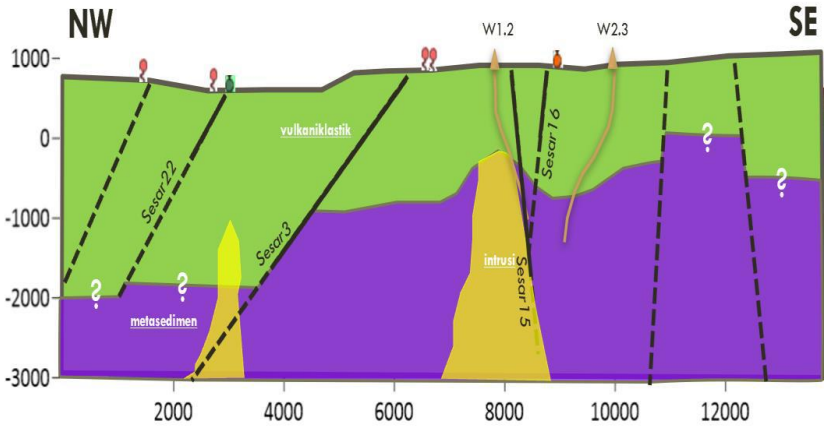

Figure 15: Geological cross section with two geothermal systems at the study site (Line 9).

6. CONCLUSION

The results of this study show that magnetotelluric data have a good correlation with permeability and subsurface temperature data from wellbores. This result can be achieved because the data was processed properly, in this case by conducting 3D inversion of MT. Therefore, at the stage of geothermal exploration when the well data is still limited, the MT data can be utilized. Good data processing can reduce uncertainty in determining reservoir conditions.

Based on the interpretation of the results of 3D inversion MT it is known that the conceptual model of geothermal field "X" shows two geothermal systems: systems associated with volcanoes in the middle of the research site and systems that controlled by fault structures in the northern part of the research site. This can provide a new insight of the conceptual model in Field X as a whole region. So that it can be considered in the planning of the field development.

7. ACKNOWLEDGEMENT

The authors would like to thank for all parties who have contributed to the preparation of this manuscript. Thank you for the permission and support that have been given by University of Indonesia and KS Orka managements. Thank you for the help and technical support from PT NewQuest Geotechnology.

REFERENCES

Arafat, Y.: Inversi 3-D Magnetotelurik dan Koreksi Coast Effects untuk Interpretasi Struktur Bawah Permukaan Lapangan Geotermal Y, Tesis FMIPA UI Prodi Magister Ilmu Fisika, Jakarta (2019).

Chandra, V.R. and Purba, D.: Conceptual Model of Sorik Marapi Geothermal System Based on 3-G Data Interpretation, *Proceedings*, ITB International Geothermal Workshop, (2016).

Cumming, W. dan Mackie, R.: Resistivity Imaging of Geothermal Resources Using 1D, 2D and 3D MT Inversion and TDEM Static Shift Correction Illustrated by a Glass Mountain Case History, *Proceedings*, World Geothermal Congress, (2010).

Daud, Y., W.A. Nuqramadha, F. Fahmi, R.S. Sesesega, Fitrianita, S.A. Pratama, and A.Munandar.: Resistivity characterization of the Arjuno-Welirang volcanic geothermal system (Indonesia) through 3-D Magnetotelluric inverse modeling, *Journal of Asian Earth Sciences*, Elsevier Ltd (2019).

Goff, F. and Janik, C.J.: Encyclopedia of Volcanoes: Geothermal System, Academic Press, (2000), 817-834 pp.

Kearey, P., Brooks, M., and Hill, I.: An Introduction to Geophysical Exploration, Blackwell Publishing, Third Edition, (2002), page 137.

Putra, K., Abiyudo, R., Munazyi, Cumming, W., and Easley, E.: Exploration Risk Assessment of the Mt. Talang Geothermal System, Sumatra, Indonesia, *GRC Transactions*, Vol. 44, (2020).

Reyes, A.G., Giggenbach, W.F., Saleras, J.R.M., Salonga, N.D., and Vergara, M.C.: Petrology and geochemistry of Alto Peak, a vapor cored hydrothermal system, Leyte province, Philippines, *Geothermics*, 22, (1993).

Rezky, Y. and Hermawan, D.: Geothermal System of Sorik Marapi - Roburan - Sampuraga, North Sumatera, Indonesia, *Proceedings*, World Geothermal Congress 2015, Melbourne, Australia, 19-25 April 2015, (2015).

Rock, N.M.S., Aldiss, D.T., Aspden, J.A., Clarke, M.C.G., Djunuddin, A., Kartawa, W., Miswar, Thompson, S.J., and Whandoyo, R.: Peta Geologi Lembar Lubuksikaping, Sumatra, Pusat Penelitian dan Pengembangan Geologi (PPPG), (1983).

Sarmiento, Z. F., Bjornsson, G., Licup, A.C., Esberto, M.B., Indra, T., Baltasar, A.S. J., Maneja, F. C., Omac, X. L., Villareal, M.J.Z., and Chandra, V.R.: Update on the Exploration and Development Drilling at the Sorik Marapi Geothermal Field, North Sumatra, Indonesia, *Proceedings*, The 5th Indonesian International Geothermal Convention and Exhibition (IIGCE), (2017).

Supriyanto: Analisis Data Geofisika: Memahami Teori Inversi, Diktat Kuliah Departemen Fisika Fakultas Matematika dan IPA, Universitas Indonesia (2007).

This page is intentionally left blank

2-Dimensional Modeling of Subsurface Structures Based on Gravity Data Using Multilayer Perceptron Neural Network (MPNN) Method

Supriadi R. Ferrianggoro

rdferrianggoro@ui.ac.id

Keywords: Gravity Method, Artificial Neural Network

ABSTRACT

The application of the Artificial Neural Network method has been used in many fields of engineering and science studies. Artificial Neural Network can also be applied to solve geophysical problems such as gravity data to estimate the shape and depth of rock bodies that cause anomalies below the surface. In this study, the Multilayer Perceptron Neural Network was trained and tested with synthetic data and WGM2012 gravity data. Gravity data is processed to obtain residual anomaly values from the "SM" area which will then be evaluated by the artificial neural network to determine the depth and shape of the rock body that causes gravity anomalies on the surface. In general, the MPNN artificial neural network is able to detect the shape and depth of subsurface rock bodies in the "SM" research test area.

1. INTRODUCTION

In applied geophysics, the ability to process data into results that are close to actual conditions in the field is the key to success in an exploration. Geopotential methods such as gravity have their own difficulties when it comes to subsurface interpretation of existing data. Determining the shape, position, and depth of anomalies caused by subsurface rock bodies is a major challenge in processing gravity data. To solve this problem, there are several methods that can be used such as upward and downward continuation, spectrum analysis, or gradient descent of the gravitational field (Telford et al., 1990). These methods have been proven to be able to solve geophysical exploration problems over the last few decades. However, along with the times, the gravity method requires new breakthroughs to increase the efficiency of the data processing results. Seeing the many studies on artificial intelligence, it is not impossible if this artificial intelligence can be applied in solving geophysical exploration problems.

Artificial neural network or often known as artificial intelligence is a branch of computer science that includes computational algorithms to solve classification problems, parameter estimation, parameter prediction, pattern recognition, filtering, and so on (Brown and Poulton, 1996). Algorithms have a way of working that is almost similar to biological neural networks that humans have, such as the activity of remembering, understanding, storing, and recalling previously learned information. Artificial neural networks are not programmed to produce a specific output. All outputs or conclusions are drawn based on experience during the learning process. This learning process is an important stage in network formation. In the learning process, artificial neural networks can be divided into two types, namely, unsupervised learning and supervised learning (Osman and Albora, 2006). In unsupervised learning, the network does not require output control, so the results are not known in advance. Whereas in supervised learning, the network is given several sets of data as input and output so that the network can learn from the data provided.

Geophysical methods in this case have a great opportunity to be integrated with artificial neural networks. One method that can be applied directly to artificial neural networks is the gravity method. Utilization of artificial neural networks in the gravity method can be done by providing input in the form of gravity data so that the artificial neural network can provide output in the form of rock conditions below the surface. Research on the application of artificial neural networks to gravity data has previously been carried out several times. Like a study conducted by Kaftan et al. in 2011, which evaluated gravity data in the Seferihisar geothermal area, Western Turkey. From their research, Kaftan et al. (2011) used two artificial neural network methods to identify the basin structure in their research area. As a result, the two artificial neural networks were concluded to give results that did not have a significant difference with the inversion results in the trajectory in the research area.

In this study, an artificial neural network that uses the backpropagation algorithm will be trained in supervised learning with synthetic gravity data which will be tested on field data where research has previously been carried out to determine the rock structure below the surface so that the results of the artificial neural network can be compared. With the application of this artificial neural network, it is hoped that it will provide a new method in the world of geophysics that could improve efficiency and accuracy in processing geophysical data.

2. ARTIFICIAL NEURAL NETWORK

Artificial Neural Network or often known as Artificial Intelligence is a branch of computer science that includes computational algorithms to solve classification problems, parameter estimation, parameter prediction, pattern recognition, and more (Brown and Poulton, 1996). this algorithm has a way of working that is almost similar with the biological neural network that humans have, such as the activity of storing and recalling previously learned information.

Figure 2 shown the comparison of artificial neural network and biological neural network. Just like biological neural network, artificial neural network also consists of several interconnected neurons. In biological neural network, incoming information will be received by dendrites which then will be processed in the cell body, named soma and will be delivered to other nerve cells through axon. Like biological neural network, artificial neural network also consists of interconnected neurons, often referred as nodes. This relationship inside artificial neural network is known as weight. Incoming information (input) will be sent with a certain arrival weight. the input will be operated with a propagation formula which will add up the values of all the following weights in vector formats in equation (1) (Shiffman, 2012).

$$y = f(a = \sum_{i=1}^{N} W_I X_I + b \quad (1)$$

Where y is output of neuron, W_I is synaptic weight between the input i, X_I is the input vector, and b is known as bias. Here $f(a)$ represent as the activation function (Kaftan et al., 2011).

Multilayer Perceptron Neural Network (MPNN)

Multilayer perceptron neural networks are one of the most important classes of neural networks and have many application areas ranging from finance to engineering. The network consists of an input layer, one or more hidden layers, and an output layer. The input layer is only responsible for feeding the input data to the neurons of the second layer which is the first hidden layer. The outputs of the second layer are used as the input to the third layer, and so on, for the rest of the complete network.

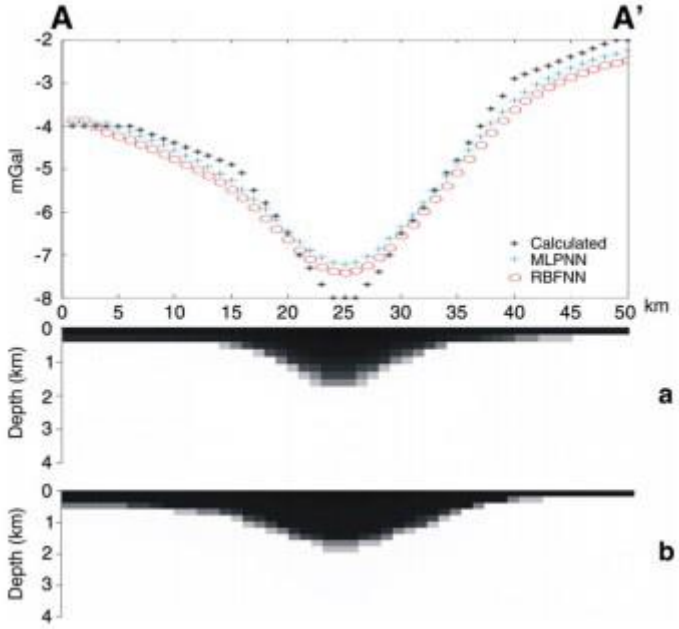

Figure 1: Research Results of Artificial Neural Network Applications on Gravity Data. It has been reprocessed from Kaftan et al. (2011).

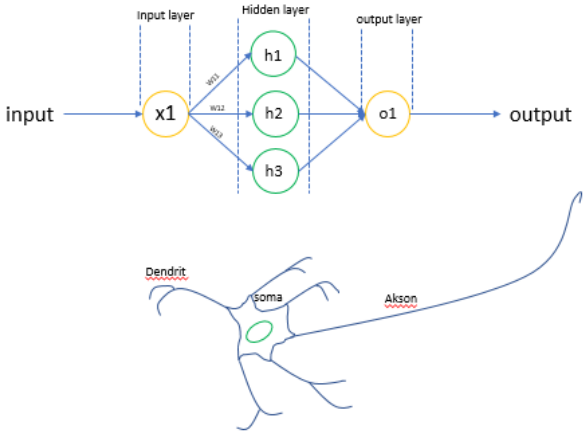

Figure 2: Comparison Illustration of Artificial Neural Network and Biological Neural Network.

3. APPLICATION

The design of the artificial neural network is done by determining the input and output variables used. In this study, the input data for the artificial neural network is in the form of gravity anomaly values and the output data for the artificial neural network is in the form of density values. The artificial neural network needs to be trained to be able to optimize its output. In this study, the neural network was trained with 109 different gravity models such as anticline, intrusion, and syncline. The gravity data generated from the forward modeling will be used as input data from the artificial neural network. While the density value of each square block will be used as output data. The artificial neural network training process used in this study is supervised learning, because data input and data output are fully controlled from data created from synthetic models. In designing the artificial neural network in this study, the algorithm used for the training process is back-propagation. This algorithm automatically updates the bias and weight values for each node during the number of iterations. Bias and weights contained in each node will affect the output value. Iterations are carried out until the comparison of the output and input values is small, in this case the comparison value is usually called a Loss Function. This loss function is used as a reference in determining whether the artificial neural network is optimal or not. The loss function value is obtained from the difference between the target data and the output squared.

3.1 Synthetic Data

The synthetic gravity model was made using the forward modeling method with the concept of Discretized Two-Dimensional Continuous Body developed by Talwani (1959). In this forward modeling method, the two-dimensional model is separated by horizontal and vertical lines to obtain square blocks (Last and Kubik, 1983). Each of these square blocks contains information about the contrast of rock density according to the subsurface geological model. The value of the gravity anomaly that is read at each measurement point will be defined in the following equation.

$$\Delta g_i = 2\gamma\Delta\rho_j \sum_{n=1}^{P} \frac{\beta_n}{1+\alpha_n^2}\left[log\frac{\sqrt{x_{n+1}^2+z_{n+1}^2}}{\sqrt{x_n^2+z_n^2}} - \alpha_n\left(arctan\frac{z_{n+1}}{x_{n+1}} - arctan\frac{z_n}{x_n}\right)\right] \quad (2)$$

Where Δg_i is the response of vertical gravity at each measurement point x_i, P is the number of angles of the polygon. In this study, there are 109 models with various geometric shapes that focus on structures below the earth's surface, different depths, positions, and density variations. The input used in the artificial neural network is residual gravity anomaly data and the output is the density value in each block in the 2D model. The artificial neural network training process is carried out using the sigmoid activation function in all layers and 3000 iterations. The learning rate used in this artificial neural network is 0.001 and the momentum is 0.9. This artificial neural network training process produces a Mean Square Error (MSE) value of 0.0018 and a Mean Absolute Percentage Error (MAPE) value of 7.1201%. In the training process, validation data is used to measure how accurate an artificial neural network is to be able to be tested using data outside of training data. This is because the previously generated Mean Square Error and Mean Absolute Percentage Error value networks are the result of training data and this value will be different if the data used is data that has not been previously trained by the artificial neural network. Therefore, validation data is used to test the accuracy of the artificial neural network before the artificial neural network is used to perform tests on synthetic test data and field data. In the validation data, the artificial neural network training process produces a loss function value of 0.037 and a Mean Absolute Percentage Error value of 20.6402%. The Mean Square Error (MSE) and Mean Absolute Percentage Error (MAPE) values show the value of the square of the deviation of the test data and training data that shows the accuracy of the artificial neural network.

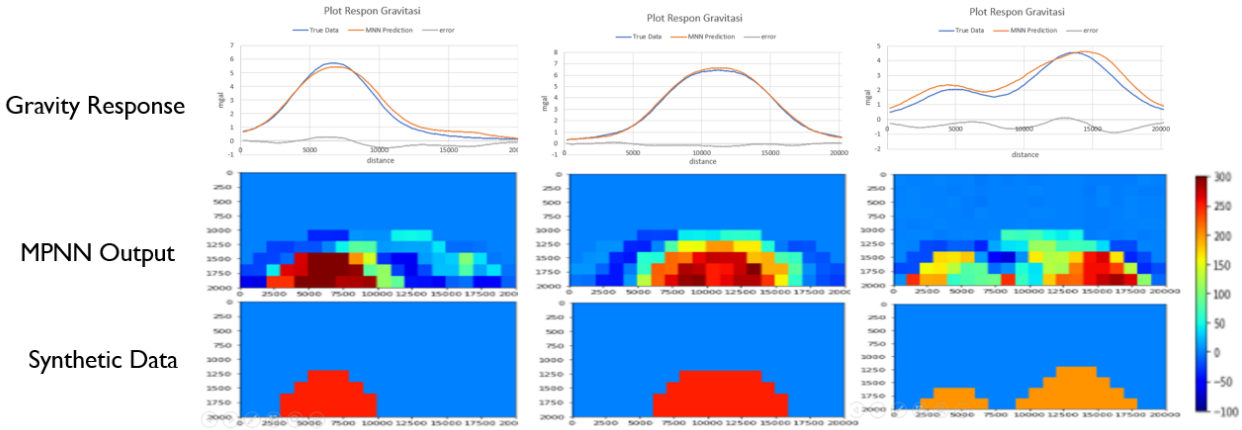

Figure 3: MPNN Output Based on Synthetic Gravity Data.

Figure 2 shows that MPNN is able to provide output in the form of density and geometry and rock density below the surface which corresponds to the synthetic gravity model, especially in the data model that has one anomalous body. However, in data that has more than one anomalous object, MPNN has an output that is not too contrasting, although in general MPNN is able to describe the existence of these two anomalies. This is because the training process for the artificial neural network has less variation on the training data model of two rock bodies.

3.2 Field Data

The artificial neural network testing process in this study uses two gravity data, namely synthetic gravity data for the first test process and secondary gravity data from the 2012 World Gravity Map (WGM2012). WGM2012 gravity data basically provides a Free Air Anomaly Terrestrial value with a fairly high resolution of up to 1 minute. The first test was carried out to determine whether the artificial neural network was able to work well in predicting the density below the surface. The output data of this test is validated using synthetic data that has been created, then comparisons are made. After the first test results have a small loss function, it will be continued to test the WGM2012 gravity data. However, if the loss function value is large enough, then the artificial neural network needs to be repaired again so that the loss function value can be smaller. Field data testing is carried out based on areas that have been carried out in previous research. Panjaitan and Astawa (2010) performed slicing in several tracks in the research area and succeeded in identifying the presence of anticline structures below the surface. The data from the output of the artificial neural network will then be tested with the trajectory traversed by the research and the results will be compared qualitatively. Secondary gravity data from the 2012 World Gravity Map (WGM2012) is then processed to obtain a complete bouguer anomaly value. From the Bouguer anomaly map, it can be seen that there are two dominant anomaly forms in the research area. High anomaly ranging from 65 mgal to 70 mgal indicates the presence of an elevated subsurface structure (anticline). As for the low anomaly ranging from 28 mgal to 40 mgal which may be indicated as a low area of the anticline (syncline). After getting the complete anomaly bouguer value, the gravity data is then separated between the regional anomaly and the residual by using the Radially Averaged Power Spectral. With this method, the regional anomaly value is 6 km deep and the residual is 900 meters deep.

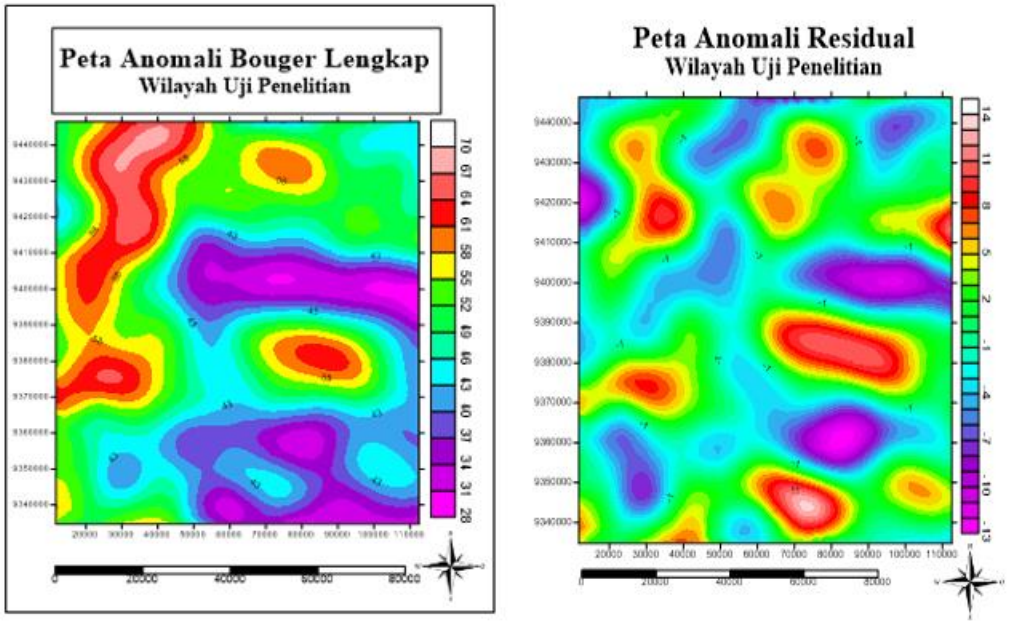

Figure 4: Complete Bouguer Anomaly Map, Residual Gravity Map.

The artificial neural network testing that was carried out on gravity data from the SM field was carried out by slicing the 4 parts of the anomaly which had previously been researched by Panjaitan and Astawa in 2010 to map the condition of the structure under its surface. In this study, Panjaitan and Astawa (2010) were able to map the presence of anticlinal structures along residual anomalies that have high anomalous contrasts. Slicing was carried out in some of the areas studied by Panjaitan and Astawa (2010) along 20 kilometers in areas suspected of having an anticlinal structure that dominates the gravitational anomaly. This will then be compared with the output data of the artificial neural network qualitatively to test whether the artificial neural network is able to model the subsurface rock structure based on gravity data. The slicing performed on the residual anomaly map is depicted in the following map:

3.2.1 A-A’

A-A' slicing was made along the positive anomaly in the study area suspected of having anticline structures. In this trajectory, research conducted by Panjaitan and Astawa in 2010 did not identify subsurface structures. However, this trajectory is thought to still be part of the same anticline as the result of the research identification. In this study, the output of the artificial neural network will be re-modeled in the form of a gravity response and then will be compared and calculated the error value against the observed residual gravity data.

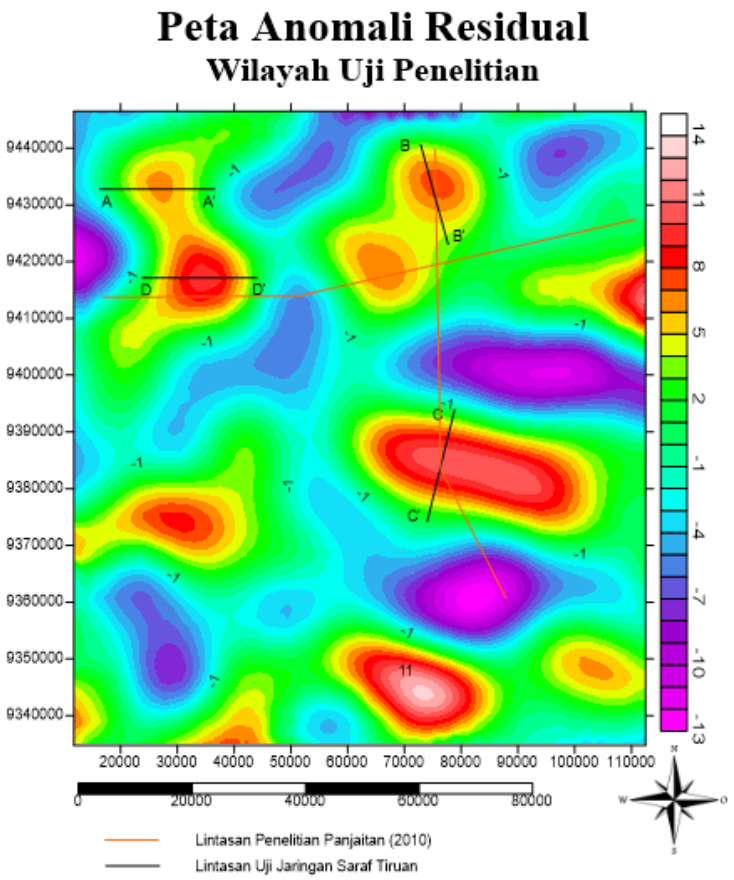

Figure 5: Test Trajectory of Neural Networks on Residual Anomaly Map of Research Area.

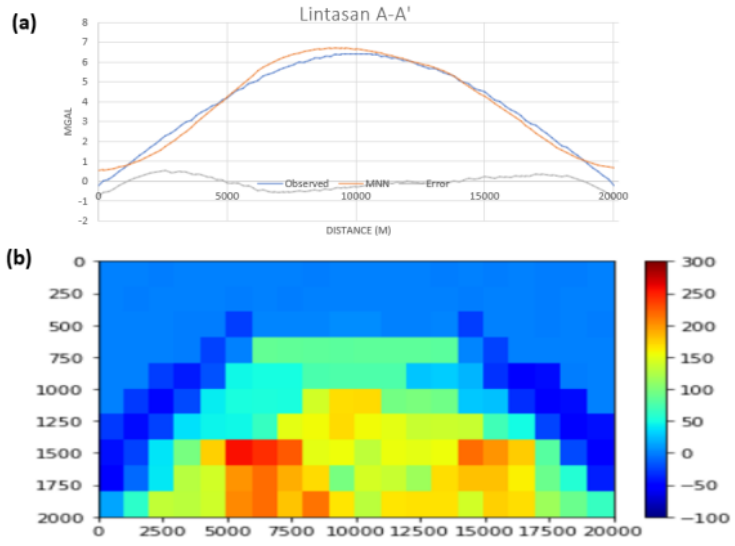

Figure 6: (a) Plot of Observation Gravity Value, Gravity of MPNN Output A-A', and error value (b) Subsurface Structure Modeling MPNN Output A-A'.

The artificial neural network has succeeded in modeling the condition of the anticline structure below the surface with density contrast values ranging from 100 kg/m_3 to 250 kg/m_3 with a density value of 0 kg/m_3 being at a value of 2500 kg/m_3. Based on residual gravity data, this anticline structure has a width of approximately 18 kilometers and is located at a depth of 1000 – 2000 kilometers. Based on this rock density contrast distribution data, forward modeling is then carried out to obtain the gravitational response. The graph in Figure 6 (a) shows that the gravity response from the forward modeling of the artificial neural network has a pattern and value similar to the observed gravity value with an error value ranging from -0.8 mgal to 0.5 mgal. This error value is obtained from the deviation of the artificial neural network gravity data with observational gravity data. This indicates that the artificial neural network is able to model subsurface anticline structures using gravity data, although only in anticline models.

3.2.2 B-B'

B-B' slicing was made along the positive anomaly in the study area suspected of having anticline structures. In this trajectory, research conducted by Panjaitan and Astawa in 2010 identified an anticline structure that is quite dominant in the gravity data anomaly. Based on this research, in the area of the B-B' trajectory there is an anticline structure that extends for approximately 15 kilometers at a depth of 1000 kilometers.

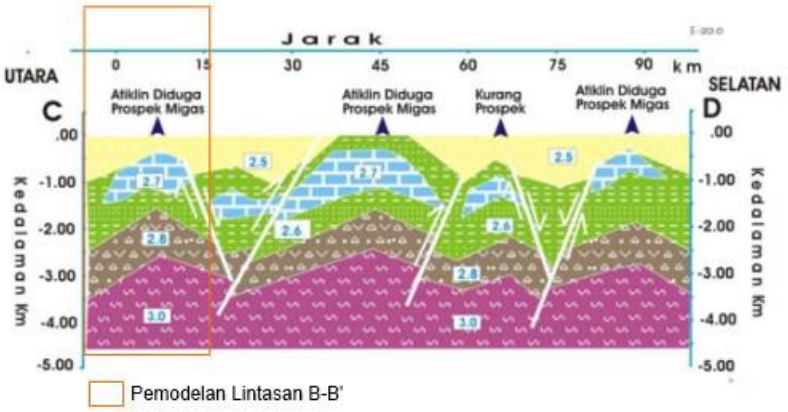

Figure 7: Subsurface Modelling on Research Field (Panjaitan and Astawa, 2010).

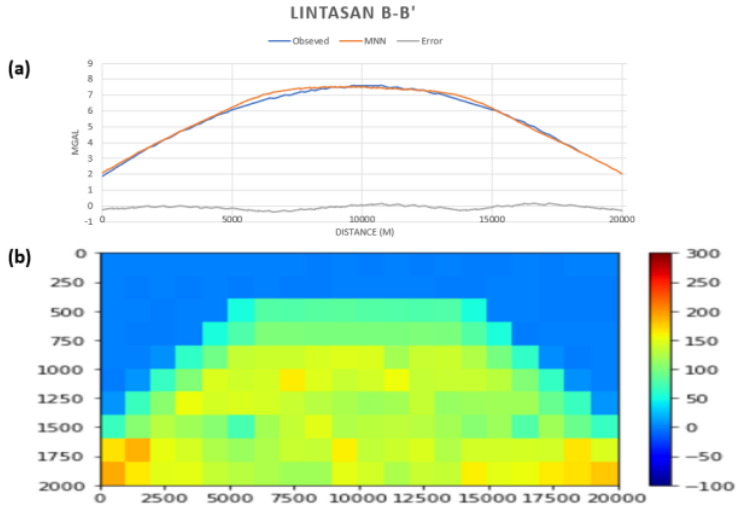

Figure 8: (a) Plot of Observation Gravity Value, Gravity of MPNN Output B-B', and error value (b) Subsurface Structure Modeling MPNN Output B-B'.

The artificial neural network has succeeded in modeling the condition of the anticline structure below the surface with density contrast values ranging from 100 kg/m^3 to 150 kg/m^3 with a density value of 0 kg/m^3 being at a value of 2500 kg/m^3. Based on residual gravity data, this anticline structure has a width of approximately 20 kilometers and is located at a depth of 1000 – 2000 kilometers. The data is then compared with research data conducted by Panjaitan and Astawa (2010), the result is that the output of the artificial neural network provides results that adequately describe the subsurface structure in general. In the modeling conducted by Panjaitan and Astawa (2010), the anticline has an upper limit as deep as 500 meters with a density contrast of more than 200 kg/m^3, similar to that modeled on an artificial neural network, the anticline has an upper limit of 500 meters but with a density contrast value of 150 kg/m^3. This different density contrast value is possible because the data used in this study is satellite data which has a different accuracy with data from terrestrial surveys. Based on this rock density contrast distribution data, forward modeling is then carried out to obtain the gravitational response. The graph in Figure 8 (a) shows that the gravity response from the forward modeling of the artificial neural network has a pattern and value similar to the gravity value of observations with an error value ranging from -0.3 to 0.16. This error value is obtained from the deviation of the artificial neural network gravity data with observational gravity data. This indicates that the artificial neural network is able to model subsurface anticline structures using gravity data, although only in anticline model.

3.2.3 C-C’

C-C’ slicing is made along the positive anomaly in the study area which is suspected to have anticline structures. Based on research conducted by Panjaitan and Astawa in 2010, in the C-C" trajectory area there are two anticline structures. The first structure is a central structure with the upper limit of the anticline reaching a depth of 500 meters to the surface, while for the second small anticline the upper limit of the anticline is at a depth of 1000 meters.

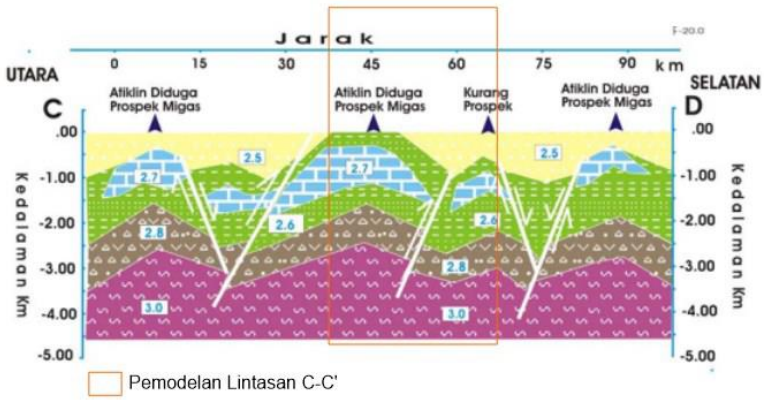

Figure 9: Subsurface Modelling on Research Field (Panjaitan and Astawa, 2010).

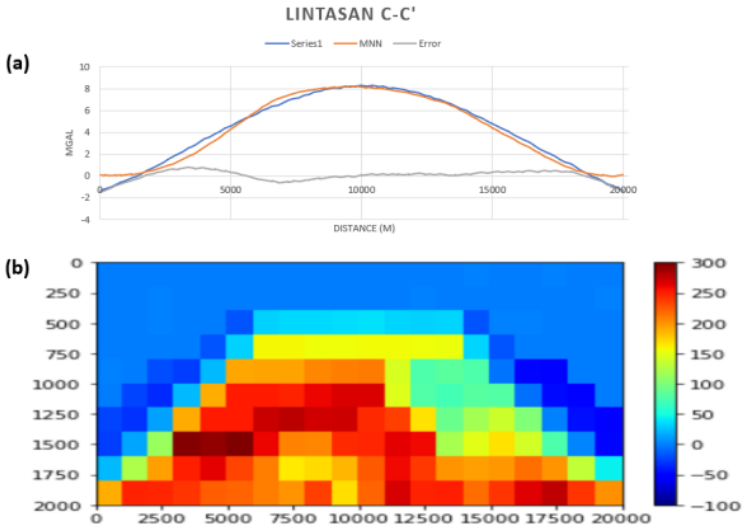

Figure 10: (a) Plot of Observation Gravity Value, Gravity of MPNN Output C-C', and error value (b) Subsurface Structure Modeling MPNN Output C-C'.

The artificial neural network has succeeded in modeling the condition of the anticline structure below the surface with density contrast values ranging from 150 kg/m^3 to 300 kg/m^3 with a density value of 0 kg/m^3 being at a value of 2500 kg/m^3. Based on the output data of the artificial neural network, there are two anticline structures in this trajectory. The first anticline structure has a width of approximately 13000 meters with its upper limit at a depth of 500 meters, while the second anticline has a width of 5000 meters with an upper limit depth of 1500 meters. The data is then compared with research data conducted by Panjaitan and Astawa (2010), the result is that the output of the artificial neural network provides results that adequately describe the subsurface structure in general. In the modeling conducted by Panjaitan and Astawa (2010), on the C-C' trajectory there are also two anticline structures but have different anticline widths. This is possible because of the difference in taking the trajectory from the coordinates used, given that the trajectory was taken manually as well as the trajectory of the previous research which experienced a bend. In addition, the use of satellite gravity data also affects the results of this modeling. Based on this rock density contrast distribution data, forward modeling is then carried out to obtain the gravitational response. The graph in Figure 10 (a) shows that the gravity response from the forward modeling of the artificial neural network has a pattern and value similar to the observed gravity value with an error value ranging from -1.5 to 0.79. This error value is obtained from the deviation of the artificial neural network gravity data with observational gravity data. This indicates that the artificial neural network is able to model subsurface anticline structures using gravity data, although only in anticline model.

3.2.4 D-D’

D-D’ slicing is made along the positive anomaly in the study area where anticline structures are suspected. In this trajectory, research conducted by Panjaitan and Astawa in 2010 identified an anticline structure that is quite dominant in the gravity data anomaly. Based on this research, in the area of the D-D' trajectory there is an anticline structure that extends for approximately 15 kilometers at a depth of 0-500 meters below the surface.

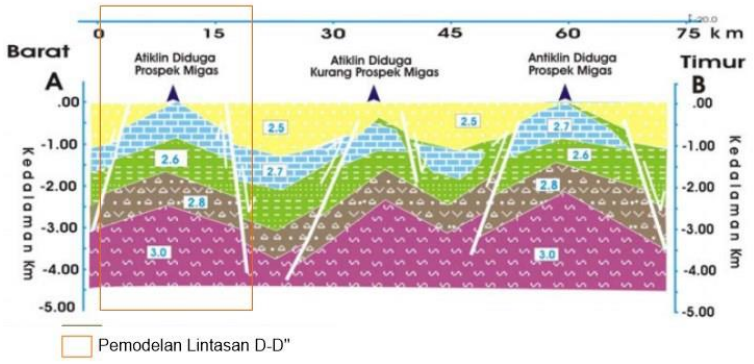

Figure 11: Subsurface Modelling on Research Field (Panjaitan and Astawa, 2010).

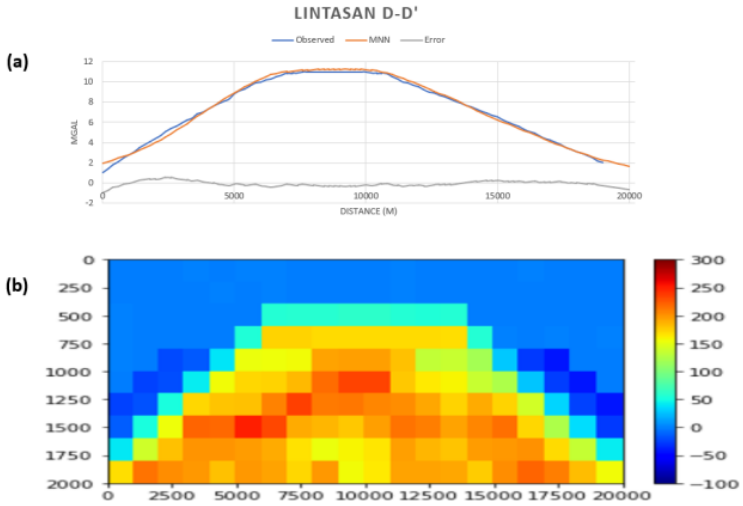

Figure 12: (a) Plot of Observation Gravity Value, Gravity of MPNN Output D-D', and error value (b) Subsurface Structure Modeling MPNN Output D-D'.

The artificial neural network has succeeded in modeling the condition of the anticline structure below the surface with density contrast values ranging from 200 kg/m^3 to 250 kg/m^3 with a density value of 0 kg/m^3 being at a value of 2500 kg/m^3. Based on residual gravity data, this anticline structure has a width of approximately 20 kilometers and is located at a depth of 750 – 2000 kilometers. The data is then compared with research data conducted by Panjaitan and Astawa (2010), the result is that the output of the artificial neural network provides results that adequately describe the subsurface structure in general. In the modeling conducted by Panjaitan and Astawa (2010), the anticline has an upper limit of 0-500 meters with a density contrast of approximately 200 kg/m^3, as well as that modeled on artificial neural networks, the anticline has an upper limit of 500 meters but with a density contrast value. by 200 to 250 kg/m^3. This different density contrast value is possible because the data used in this study is satellite data which has a different accuracy with data from terrestrial surveys. Based on this rock density contrast distribution data, forward modeling is then carried out to obtain the gravitational response. The graph in Figure 12 (a) shows that the gravity response from the forward modeling of the artificial neural network has a pattern and value similar to the gravity value of observations with an error value ranging from -0.9 to 0.5. This error value is obtained from the deviation of the artificial neural network gravity data with observational gravity data. This indicates that the artificial neural network is able to model subsurface anticline structures using gravity data, although only in anticline models.

4. CONCLUSION

In this paper, Multilayer Perceptron Neural Networks (MLPNN) with back propagation learning algorithm have been applied to estimate the structure parameters as location, depth, and density contrasts. The performance of ANN to gravity applications has been analyzed by using two synthetic data and a field data. The artificial neural network was successfully designed to model the subsurface structure in two dimensions which resulted in a Mean Square Error value of 0.0370 and a Mean Absolute Percentage Error of 20.6402% in the validation data of the artificial neural network. The artificial neural network is able to model subsurface structures in two dimensions based on gravity data trained using synthetic data. Subsurface structure modeling using WGM2012 data shows results that are consistent with the geological model. This is shown by the similarity of the model of the artificial neural network to the subsurface model that had previously been researched by Panjaitan and Astawa in 2010. The use of artificial neural networks in this study is still limited to detecting subsurface anticline structures. This is indicated by the success of the artificial neural network in modeling the anticline structure on the paths that have been previously studied. The artificial neural network created in this study is only limited to anomalous areas that have large and not complex density contrasts. So that. it is necessary to develop an artificial neural network with more models and data in order to increase the accuracy of the output of the artificial neural network.

REFERENCES

Blakely, R. J.: Potential Theory in Gravity and Magnetic Application, Cambridge University, New York (1995).

Bonvalon, S., Balmino, G., Briais, A., M. Kuhn, Peyrefitte, A., Vales N., Biancale, R., Gabalda, G., Reinquin, F., and Sarrailh, M.: World Gravity Map. Commission for Geological Map of the World, Eds., BGI-CGMW-CNES-IRD, Paris (2012).

Brown, M. and Poulton, M.: Computational Neural Network for Geophysical Data Processing, Handbooks of Geophysical Exploration: Seismic Exploration, (30), (1996), 219-233.

Haykin, S.O.: Neural Network and Learning Machines 3rd Edition, McMaster University, Canada (2009).

Jaya, H.: Kecerdasan Buatan, Fakultas MIPA Universitas Negeri Makassar (2018).

Jayalakshmi, T. and Santhakumaran, A.: Statistical Normalization and Back Propagation for Classification, *International Journal of Computer Theory and Engineering*, III(1), 2011.

Kaftan, I., Salk, M., and Senol, Y.: Evaluation of gravity data by using artificial neural networks case study: Seferihisar geothermal area (Western Turkey), *Journal of Applied Geophysics*, 75, 4, (2011), pp. 711-718.

Last, B.J. and Kubik, K.: Compact Gravity Inversion, *Geophysics* 48 (6), (1983), 713-721.

Novianto, A., Sutanto, Suhartono, Prasetyadi , C., and Setiawan, T.: Structural Model of Kendeng Basin : A New Concept of Oil and Gas Exploration, Scientific Research Publishing, (2020), 199-214.

Osman, O. and Albora, A.M.: A New Approach for Residual Gravity Anomaly Profile Interpretation: Forced Neural Network (FNN), *Annals of Geophysics*, 49 (6), (2006).

Panjaitan, S. and Astawa, N.: Studi Potensi Migas Dengan Metode Gaya Berat di Lepas Pantai Jakarta, *Jurnal Geologi Kelautan*, Volume 8, No 1., (2010), 23:35.

Parasnis, D.S.: Principle of Applied Geophysics, Chapman and Hall, New York (1986).

Perdana, A., Nasution, D., Wanto, A., Tambunan, F., Said, M., Hasan, M., Ridwan, M., Fadhillah, Y., and Nofriyansyah, D.: Jaringan Saraf Tiruan : Algoritma Prediksi dan Implementasi, Yayasan Kita Menulis (2020).

Pringgoprawiro: Biostratigrafi dan Paleografi Cekungan Jawa Timur Utara, Suatu Pendekatan Baru, Desertasi Doktor : Institut Teknologi Bandung (1983).

Pulunggono, A. and Martodjojo, S.: Perubahan tektonik Paleogen – Neogen merupakan peristiwa terpenting di Jawa, *Proccedings*, Geologi dan Geotektonik Pulau Jawa, (1994), 37-50.

Shiffman, D.: The Nature of Code, California, Creative Commons Attribution (2012).

Talwani, M., Worzel, J.L., and Landisman, M.: Rapid Computation for Two Dimensional Bodies of Arbitrary Shape, *Geophysics*, 25, (1959), 203-225.

Telford, W.M., Geldart, L.P., and Sherif, R.E.: Applied Geophysics Second Edition, Cambridge University Press (1990).

Warsito, B.: Kapita Selekta Statistika Neural Network, Universitas Diponegoro, Semarang (2009).

Van Bemmelen, R.W.: The Geology of Indonesia, Vol IA General Geology of Indonesia and Adjacent Archipelagos, The Haque, Netherland (1949).

This page is intentionally left blank

Application of Multi-Level Second Vertical Derivative (ML-SVD) Method to Identify Subsurface Structure in Mount Endut Geothermal Prospect Area, Indonesia

William Jhanesta and Supriyanto

Laboratory of Geophysical Modelling, Department of Geosciences, Universitas Indonesia

william.jhanesta@alumni.ui.ac.id

Keywords: Geothermal, Mount Endut, ML-SVD, Dip Estimation, Subsurface Structure

ABSTRACT

Mount Endut geothermal prospect area located in Banten province belongs to one of two, from approximately 20 fields, that becomes the first geothermal exploration and development throughout history in Java Island since 1980. This study aims to delineate the subsurface structures correlated with its geothermal system and estimate the slope and dip direction of geological structures using multi-level second vertical derivative (ML-SVD) driven by gravity data. A total of 134 stations were acquired by the Geological Agency of Indonesia in 2014. The interpreted faults obtained from the ML-SVD show a close correlation by the surface faults with nearly NE-SW orientation. The estimation of slope direction is carried out using the oscillations between the minimum and maximum magnitude from SVD values and matched with the zero-value shifting of the ML-SVD result. Based on the estimation from the correlation between the upward-continuation level and the interpreted faults location, the subsurface faults development in this area dominantly has a more than 60° dip angle. This study is expected to enhance the understanding of fault characterization of the Mount Endut geothermal area and support further field development.

1. INTRODUCTION

Banten province has several geothermal energy potentials, namely Mount Karang and Mount Endut geothermal prospect area. Mount Endut is located in Lebak Regency, which is about 30 km from the capital city of Jakarta. Mount Endut was first explored by Pertamina and belonged to one field (roughly 20 prospects) in the second phase of exploration and development in Java Island (Hochstein and Sudarman, 2008). Currently, Mount Endut is still in the advanced exploration stage and is targeted to be one of the targets in the Government Drilling program by the Ministry of Energy and Mineral Resources of Indonesia because this field is believed to meet the electrical energy needs of Banten and its surroundings. Mount Endut is located at the Eurasian and Indo-Australian tectonic plates associated with a diorite intrusion with characteristic steep slopes and high relief (strato-volcanoes) (Hochstein and Sudarman, 2008). Some of the geothermal manifestations in this field include hot springs and altered surfaces (Jhanesta, 2021; Primayudha et al., 2021; Sahdarani et al., 2021) be minor so that further exploration is needed in more detail and proper.

Several studies have been carried out in this field, such as geological studies and surface alteration distribution (Kusnadi et al., 2006; Risman, 2018; Sahdarani et al., 2021), hydrogeochemical and isotope studies (Risman et al., 2019; Jhanesta, 2021; Sahdarani et al., 2021), to gravity measurements (Supriyanto et al., 2018, 2017), DC resistivity (Mustang and Suhanto, 2006; Supriyanto et al., 2019), and 3-D magnetotelluric (MT) inversion (Jhanesta, 2021). However, there remains uncertainty about subsurface faults controlling the system. In addition, information regarding the slope direction and dip angle of geological faults are not well identified (Kusnadi et al., 2006; Risman, 2018; Supriyanto et al., 2017). The subsurface structure is an essential aspect of the geothermal system (Cumming, 2016). The subsurface structure is a pathway for hydrothermal fluids to migrate. Besides that, it acts as a recharge or discharge the medium of the geothermal system (Goff and Janik, 2000).

The gravity method is commonly used for mapping the distribution of subsurface structures. Many subsurface fault studies use the gravity method in geothermal fields globally (Saibi et al., 2008; Nishijima and Naritomi, 2017; Maithya et al., 2020; Pocasangre et al., 2020; Mulugeta et al., 2021). This study aims to delineate the subsurface structures that correlate with the geothermal system, further approximate the slope direction and dip-angle of geological faults with multi-level second vertical derivative (ML-SVD) analysis. The results could reduce the uncertainty during well targeting, from exploration to development drilling, and enhance the interpretation of the geothermal system.

2. FIELD REVIEW

The research area is located in Banten province, Indonesia. Regionally, this area is affected by the subduction activity of the Eurasian Plate with the Indo-Australian Plate on the southern side of the study area. This interaction produces a fairly complex geological structure (Hilmi and Haryanto, 2008). Mount Endut geothermal prospect area is dominated by two regional structural patterns, namely the Meratus suture with a NE-SW orientation and the Sunda suture with a relatively N-S to the NW-SE direction (Pulunggono and Martodjojo, 1994).

The geological map of the Mount Endut geothermal prospect area is shown in Figure 1. The lithologies of Mount Endut were formed since the Middle Miocene until the Pleistocene period (Sujatmiko and Santosa, 1992; Sahdarani et al., 2021). It consists of Middle Miocene sedimentary and andesitic rocks, Pliocene volcanic products, Pleistocene volcanic products, and Holocene surface deposits (Geological Agency of Indonesia, 2006).

The normal fault, with the direction of NE-SW, cuts the formation down to the bedrock and causes sealing in the manifestation of the CKW hot springs. The strike-slip fault was trending NW-SE that intersects preformed rocks and structures. This structure is thought to be the medium that gave rise to the manifestation of the HDL hot springs (Kusnadi et al., 2006).

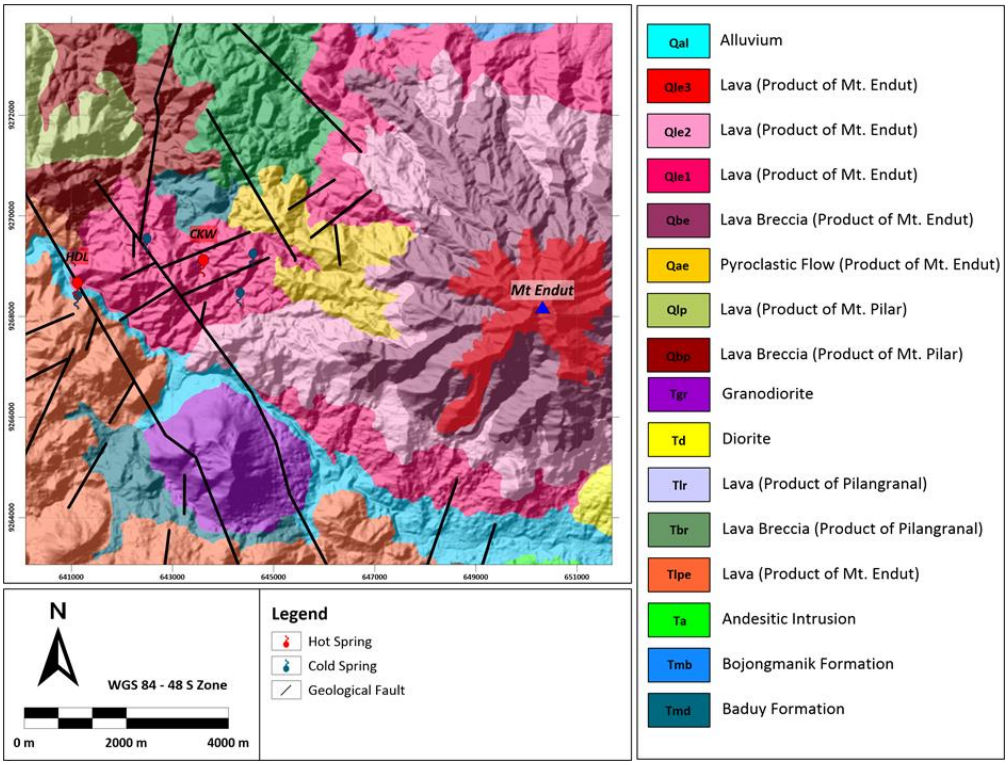

Figure 12: Geological map of the Mount Endut geothermal prospect area modified after Geological Agency of Indonesia (2006). Abbreviations: HDL, Handeuleum hot springs; CKW, Cikawah hot springs.

3. METHODS

The gravity data were acquired by the Geological Agency of Indonesia in 2014 using A Lacoste Romberg gravity-meter with an accuracy of 0.01 mGal with 134 stations. The survey covers an area of approximately 72 km^2. The gravity stations are distributed around the CKW and HDL hot springs, with spacing between points varying from 200 m to 500 m.

Determination of geological boundaries, which are the density contrasts from gravity data, is carried out using the horizontal gradient (HG) method (Cordell, 1979; Saibi et al., 2012). This method shows the maximum amplitude while detecting the geological boundaries with significant changes in density (Maithya et al., 2020). The horizontal gradient caused by a tabular body inclines to cover the boundaries of the body if the boundaries are vertical and well separated (Blakely, 1995). The HG method can be calculated by (Miller and Singh, 1994):

$$HG = \sqrt{\left(\frac{\partial g}{\partial x}\right)^2 + \left(\frac{\partial g}{\partial y}\right)^2} \quad (2)$$

Where $\frac{\partial g}{\partial x}$ and $\frac{\partial g}{\partial y}$ represent the first derivative of gravity anomaly in the x and y directions, respectively. The advantages of the HG method are relatively minimum noise disturbance because it requires two first-order calculations (Phillips, 1998) and could recognize the edges of both shallow and deep structures clearly (Nishijima and Naritomi, 2017).

The multi-level second vertical derivative (ML-SVD) method combines upward continuation and SVD filter (Naufal and Rosid, 2020). It is a novel method proposed by Rosid and Naufal (2019), which estimates the dipping fault by analyzing the shifting of the zero-SVD contour of each upward continuation level. The dip value is then obtained by calculating the arctan from the gradient of the linear regression equation between the fault location (indicated by zero-SVD) and upward continuation level as the x-axis and y-axis, respectively.

4. RESULTS AND DISCUSSION

4.1 Complete Bouguer Anomaly

A series of data correction processes must be carried out before performing a geological interpretation of the gravity data to obtain a complete Bouguer anomaly (CBA), a subsurface gravity anomaly (Abdel, 2011). This study calculates Bouguer density using the F-H method and is estimated to be 2.9 gr/cc. The Bouguer density coincides with the lithological distribution of the Mount Endut area dominated by lavic and pyroclastic products (see the geological map of the study area Figure 1).

The CBA map in Figure 2 illustrates the distribution of subsurface densities and geological features. CBA values varying from 74 mGal to 118 mGal. The high amplitudes (> 102 mGal), distributed in the southwestern part of the study area, are centered around the Tertiary and Quaternary products of Mount Endut. The low amplitudes (< 86 mGal) show an elongated N-NE side of the study area and are thought to be associated with the pyroclastic flow of Mount Endut and Bojongmanik Formation (bituminous claystone, limestone, and sandy limestone).

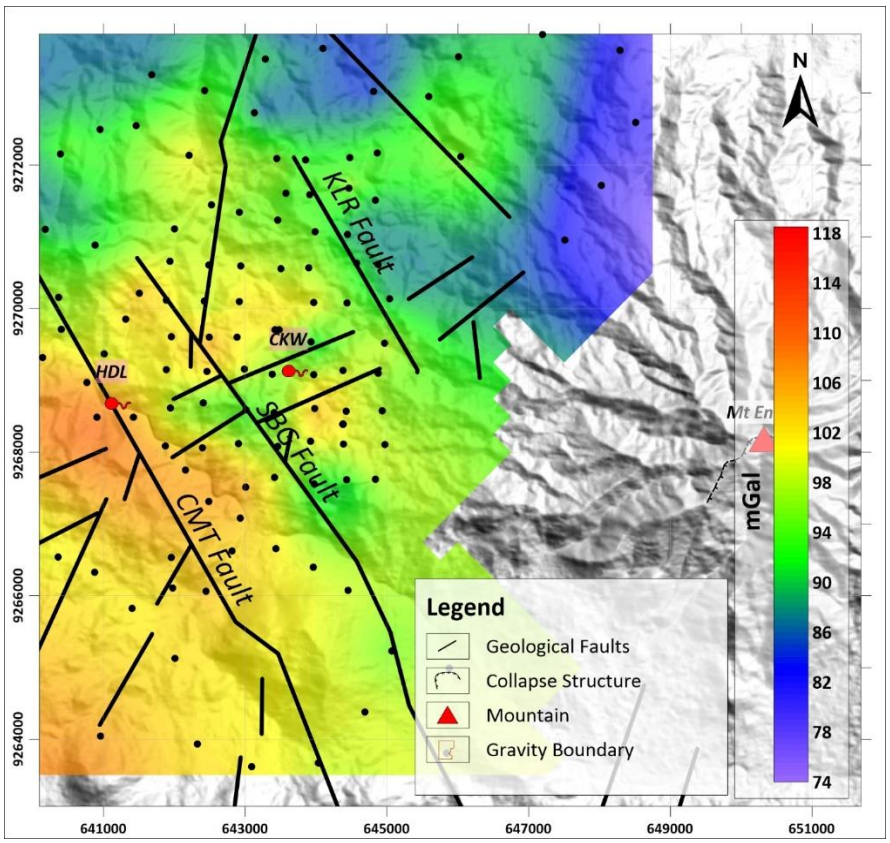

Figure 2: Complete Bouguer anomaly (CBA) of Mount Endut geothermal prospect area with an assumed 2.9 gr/cc density. The black dots show the gravity station.

4.2 Correlation Between HG and ML-SVD

Interpretation of subsurface structures is done by correlating anomalies in HG and ML-SVD. Figure 3 shows the graph of HG and ML-SVD values that have been normalized statistically. The high amplitude on the HG graph and the zero-value shift on the ML-SVD graphs indicate the subsurface structures. The summary of the location and characteristics of the interpreted faults in the study area can be seen in Table 1. Interpretation of the structures on the gravity data is then correlated with the geological structures and the emergence of geothermal manifestations.

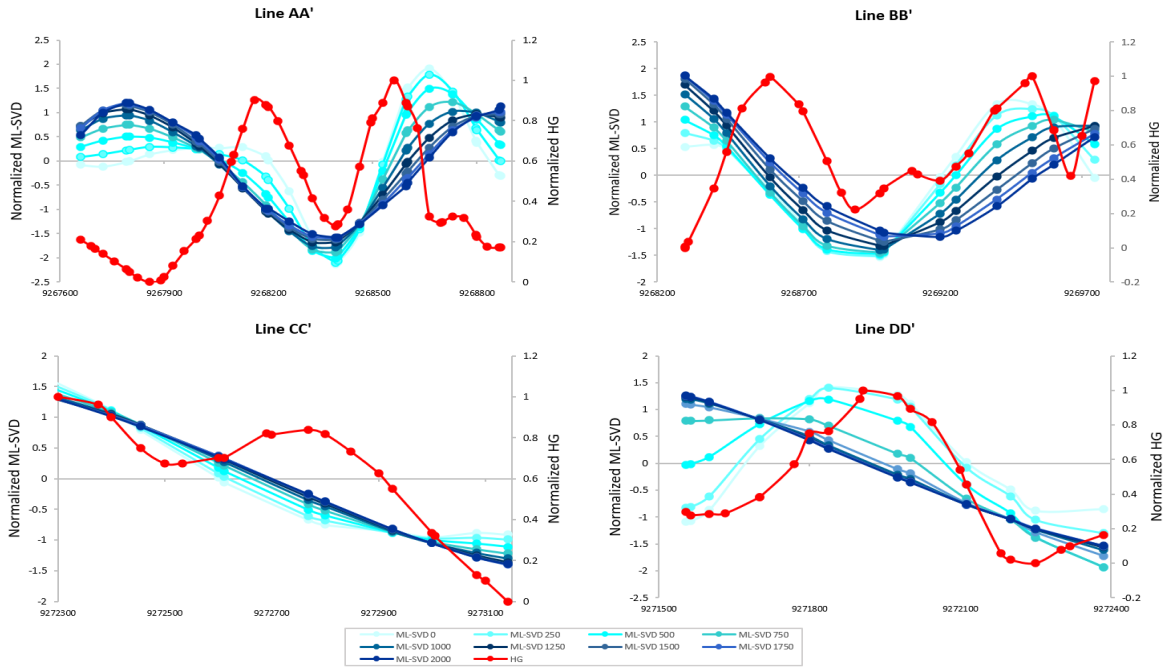

Figure 3: Correlation between HG and ML-SVD graphs.

Table 1: Fault characterization based on ML-SVD calculation.

Upward Continuation	Line AA'	Line BB'		Line CC'	Line DD'
Level	**ML-1 Fault**	**ML-2 Fault**	**ML-3 Fault**	**ML-4 Fault**	**ML-5 Fault**
0	9268520	9268645	9269130	9272685	9272100
-250	9268521	9268610	9269160	9272685	9272125
-500	9268528	9268600	9269200	9272710	9272125
-750	9268537	9268605	9269230	9272730	9272085
-1000	9268550	9268645	9269255	9272750	9272040
-1250	9268565	9268715	9269255	9272750	9272020
-1500	9268570	9268830	9269230	9272730	9272000
-1750	9268560	-	-	9272695	9272000
-2000	9268528	-	-	9272640	9272000
Gradient	21.16	6.33	8.79	1.81	11.63
Slope Direction	NE	NE	NE	SE	NE
Dip Estimation	87.29°	81.02°	83.51°	61.12°	85.08°

4.3 Interpretation of ML-SVD Fault

The upward continuation process is carried out on the gravity anomaly grid with 250 m intervals from 0 m to 2000 m. The results of upward continuation are then processed using an SVD filter which then the zero-value SVD is displayed in Figure 4. The red color indicates the shallowest level of continuity, while the blue color indicates the deepest level of continuity. The Zero-value of SVD indicates the geological boundary that correlates with the subsurface fault location (Naufal and Rosid, 2020). It can be seen that there is a zero-value SVD shift from each depth which indicates the slope direction of the geological fault. From the results of the ML-SVD, an interpretation of the existence of a subsurface fault is carried out, which is then correlated with geological surface fault information.

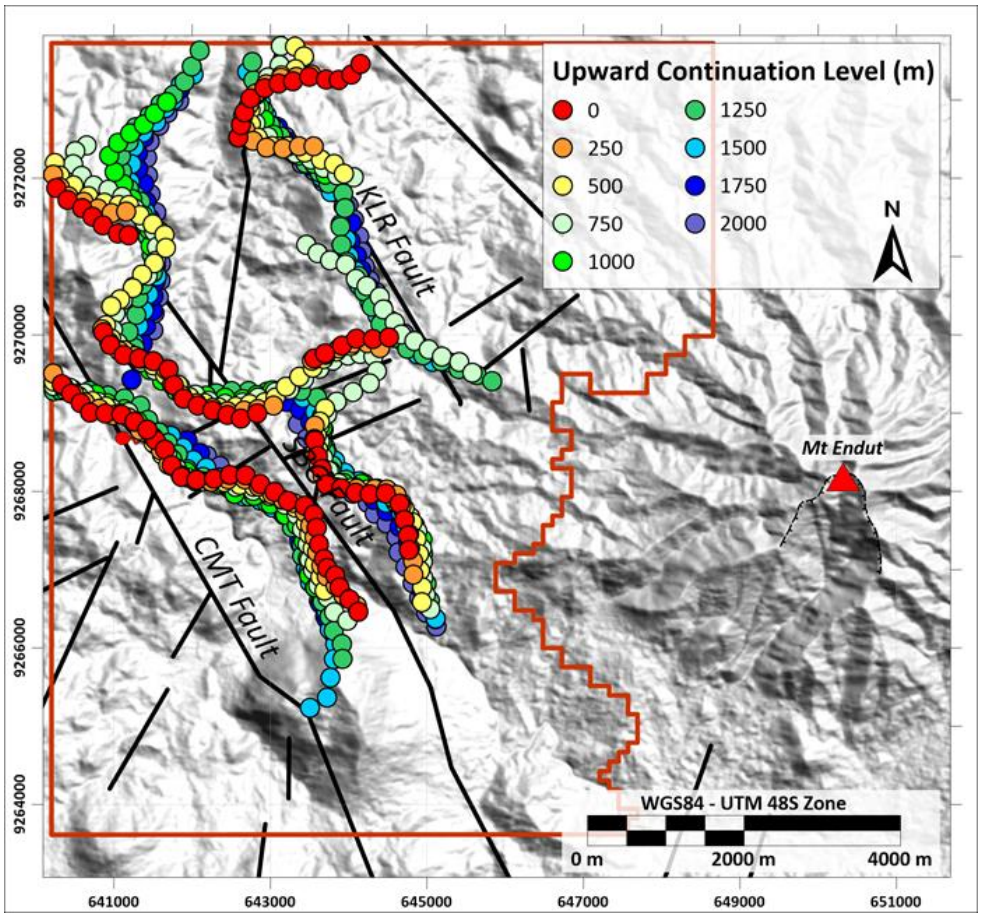

Figure 4: Simplified ML-SVD map. The colored dots indicate the subsurface fault.

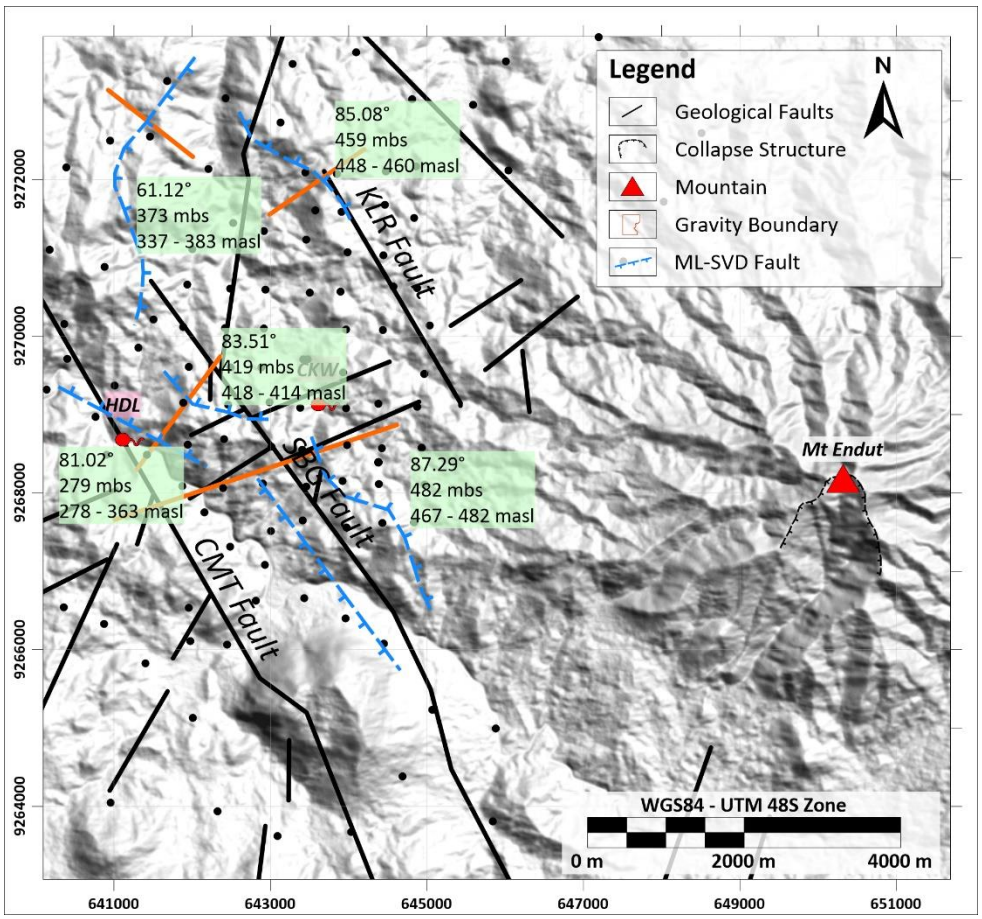

Figure 5: Fault map of Mount Endut geothermal prospect area. Orange lines show the slicing line of HG and ML-SVD. Interpreted ML-SVD faults (blue lines) show a good correlation with geological fault.

CMT Fault, which has a strike direction of N300°-330°E with a normal fault type (PSDG, 2006), was detected in ML-1 Fault with a quite similar orientation. This fault is associated with the Sunda Pattern, which resulted in block faulting in the basement and the formation of a graben (Hilmi and Haryanto, 2008) which later became the center of the Mount Endut geothermal system. The dip calculation for this fault is 81.02°, towards the center of the geothermal system, which is then estimated to control the emergence of the Handeleum hot spring (HDL). This allegation was strengthened by discovering a ground altered with dickite mineral around the CMT Fault (Primayudha et al., 2021).

The ML-2 Fault is considered part of the SBG Fault with an orientation of N60°-80°E, horizontal movement, and normal rejuvenation. This fault is thought to control the emergence of Cikawah hot springs (CKW) (Kusnadi et al., 2006). Calculation of the dip angle is estimated at 87.29°, which leads to the center of the geothermal system. This fault looks discontinuous with the ML-3 Fault and the ML-4 Fault but has relatively the same slope and dip orientation. It is suspected that the ML-3 Fault and the ML-4 Fault are continuations of the SBG Fault. The discontinuity in these two faults is thought to be the effect of the fault type in the form of an oblique strike-slip (Kusnadi et al., 2006; Risman, 2018). ML-SVD is sensitive to density contrast in the vertical direction, thus allowing for undetected fractures.

The ML-5 Fault is estimated to correlate with the KLR Fault with an orientation direction of N315°E. This fault is hardy explainable since it is not associated with geothermal activity. Not much information is obtained about this fault. Still, it is estimated that this fault was formed through the tectonic activity and volcanism of Mount Endut because it separates the Lava Breccia (Tbr) product of Pilangranal and Lava product (Qle1) of Mount Endut. MS-SVD results show that the slope orientation leads to Mount Endut with an estimated dip angle of 85.08°.

The geochemical studies (Risman et al., 2019; Jhanesta et al., 2020; Sahdarani et al., 2021) prove that HDL and CKW hot springs have a diluted bicarbonate-chloride characteristic, which indicates that both manifestations ruled out as the outflow zone. Identification of fault distribution by ML-SVD shows the area that acts as a discharge zone of the Mount Endut geothermal system. The 3-D MT results (Jhanesta, 2021) strengthen that the distribution of the low resistivity anomaly, which is interpreted as smectite clay (Ussher et al., 2000), open (continuously) to the east of the study area. These results substantiate the interpretation that the ML-1 Fault and ML-2 Fault control the manifestations of HDL and CKW in the outflow zone of the Mount Endut geothermal system.

ML-SVD appears to have a relatively well pronounced geological structure (Figure 5), but it cannot be denied that not all geological structures are detected by this method. In addition, field mapping for dip measurement still needs to be carried out to calibrate the dip estimation of the ML-SVD results. Naufal and Rosid (2020) stated that the results of the ML-SVD could not identify the shear fault because it has a relatively insignificant density contrast.

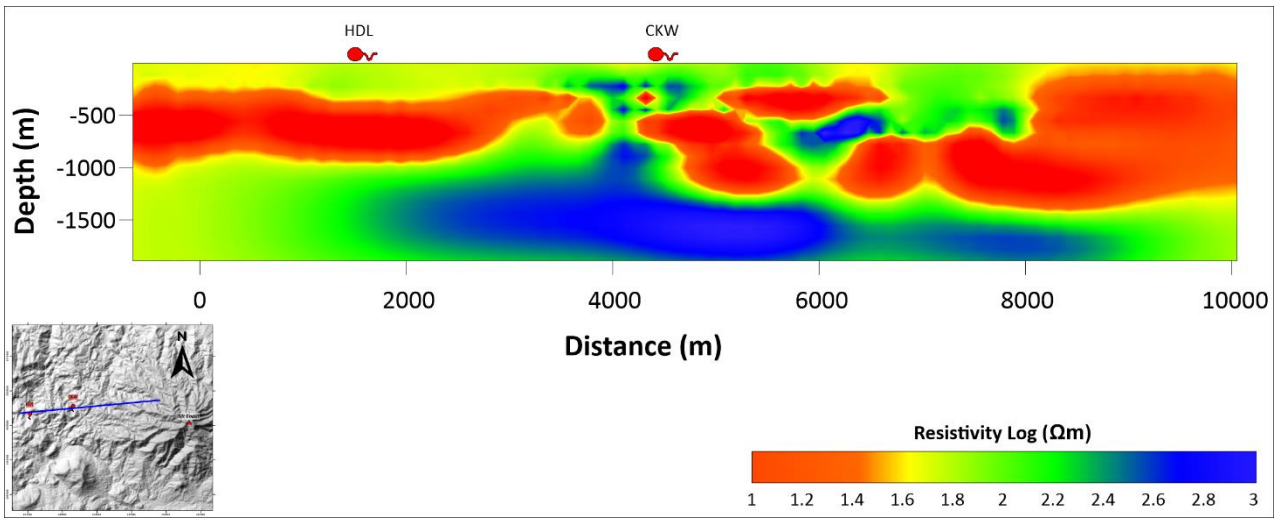

Figure 6: 3D inversion of MT data (Jhanesta, 2021). The red layer shows the distribution of argillic clay, continuing towards the NE (indication center of the reservoir).

5. CONCLUSION

The ML-SVD method can be used to map and characterize the structures related to geothermal systems. The structures detected by ML-SVD are CMT Fault, SBG Fault, and KLR Fault. The dip calculation shows mostly more than 60°, with the direction of the slope being predominantly NE. Integration of geochemical and MT data proves that the detected structures are faults that control the emergence of HDL and CKW manifestations and are manifested in the outflow zone of the Mount Endut geothermal system. However, this method shows several faults undetected due to the slight density contrast of the gravity data. It is necessary to do more simulations by considering the actual data to get more precise results.

REFERENCES

Abdel, Z.M.: Geothermal Exploration and Numerical Modeling at Gulf of Suez, Egypt, Kyushu University (2011).

Blakely, R.J.: Potential Theory in Gravity and Magnetic Applications, Cambridge University Press, New York (1995).

Cordell, L.: New Mexico Geological Society Espanola Basin, New Mexico (1979), 59-64.

Geological Agency of Indonesia: Integrated Studies of Geological, Geochemical, and Geophysical of Mount Endut, Lebak Province, Indonesia, (2006).

Goff, F. and Janik, C.J.: Geothermal System, in: Encyclopedia of Volcanoes, (2000), 817-834.

Hilmi, F. and Haryanto, I.: Pola Struktur Regional Jawa Barat, *Bulletin of Scientific Contribution*, (2008), 57–66.

Hochstein, M.P. and Sudarman, S.: Indonesian Volcanic Geothermal Systems, *Proceedings*, World Geothermal Congress (2015).

Hochstein, M.P. and Sudarman, S.: History of geothermal exploration in Indonesia from 1970 to 2000, *Geothermics*, 37, (2008), 220–266, https://doi.org/10.1016/j.geothermics.2008.01.001

Jhanesta, W.: Conceptual Modelling of Mount Endut based on Integration of Remote Sensing, Hydrogeochemistry, Gravity GGMplus, and 3-D Magnetotelluric Data, Universitas Indonesia, Depok (2021).

Jhanesta, W., Sahdarani, D.N., and Supriyanto: The study of stable isotope 18O as a determination to fluid genesis in Mount Endut geothermal prospect area, Lebak Regency, Banten Province, *Proceedings*, 9th ITB International Geothermal Workshop (2020).

Kusnadi, D., Idral, A., Rezky, Y., Suhanto, E., and Sumardi, E.: Penyelidikan terpadu panas bumi daerah Gunung Endut kabupaten Lebak, Banten, *Proceedings*, Pemaparan Hasil-Hasil Kegiatan Lapangan dan Non Lapangan, (2006), 1-14.

Maithya, J., Fujimitsu, Y., and Nishijima, J.: Analysis of gravity data to delineate structural features controlling the Eburru geothermal system in Kenya, *Geothermics*, 85, (2020), 101795, https://doi.org/10.1016/j.geothermics.2019.101795

Miller, H.G. and Singh, V.: Potential field title-a new concept for location of potential field sources, *Journal Applied Geophysics*, 32, (1994), 213-217, https://doi.org/10.1016/0926-9851(94)90022-1

Mulugeta, B.D., Fujimitsu, Y., Nishijima, J., and Saibi, H.: Interpretation of gravity data to delineate the subsurface structures and reservoir geometry of the Aluto–Langano geothermal field, Ethiopia, *Geothermics*, 94, (2021), 102093, https://doi.org/10.1016/j.geothermics.2021.102093

Mustang, A. and Suhanto, E.: Survei tahanan jenis DC di daerah panas bumi Gunung Endut kabupaten Lebak, Banten, *Proceedings*, Pemaparan Hasil-Hasil Kegiatan Lapangan Tahun 2006, Geological Agency of Indonesia, Bandung (2006).

Naufal, M.A. and Rosid, M.S.: Structure identification of geothermal field "x" using ML-SVD method of gravity data, *IOP Conference Series Material Science Engineering*, (2020), 854, https://doi.org/10.1088/1757-899X/854/1/012055

Nishijima, J. and Naritomi, K.: Interpretation of gravity data to delineate underground structure in the Beppu geothermal field, central Kyushu, Japan, Journal Hydrology: Regional Studies, 11, (2017), https://doi.org/10.1016/j.ejrh.2015.11.022

Pocasangre, C., Fujimitsu, Y., and Nishijima, J.: Interpretation of gravity data to delineate the geothermal reservoir extent and assess the geothermal resource from low-temperature fluids in the Municipality of Isa, Southern Kyushu, Japan, *Geothermics*, 83, (2020), 101735, https://doi.org/10.1016/j.geothermics.2019.101735

Primayudha, F., Sahdarani, D.N., Kadja, G.T.M., and Supriyanto: The relationship of volcanic facies and temperature range derived from the associated clay mineral in Gunung Endut, Banten, *Journal Physics Conference Series*, (2021), 1725, 012073, https://doi.org/10.1088/1742-6596/1725/1/012073

Pulunggono, A. and Martodjojo, S.: Perubahan Tektonik Paleogen dan Neogen Merupakan Peristiwa Tektonik Terpenting di Jawa, *Proceedings*, Geologi Dan Geoteknik Pulau Jawa Sejak Akhir Mesozoik Hingga Kuarter, (1994).

Risman, C.: Geological of Mount Endut, Sobang, Lebak Regency, Banten, Indonesia, Depok (2018).

Risman, C., Sahdarani, D.N., Sihombing, F.M.H., and Supriyanto: Geochemical fluids assessment of Gunung Endut geothermal area, Banten Province, Indonesia, *IOP Conference Series Earth Environmental Science*, (2019), 279, https://doi.org/10.1088/1755-1315/279/1/012045

Rosid, M.S. and Naufal, M.A.: Characterization of Geological Structure Based on Multi Level Second Vertical Derivative (ML-SVD) Gravity Data, *Journal of Geophysical Research*, on progress.

Sahdarani, D.N., Risman, C., Primayudha, F., Sihombing, F.M.H., and Kadja, G.T.M.: Geothermal surface alteration and water chemistry: an updated geochemical data in Gunung Endut geothermal area, Banten, Indonesia, *Proceedings*, World Geothermal Congress, (2021), 1-7.

Saibi, H., Aboud, E., and Ehara, S.: Analysis and interpretation of gravity data from the Aluto-Langano geothermal field of Ethiopia, *Acta Geophysica*, 60, (2012), 318-336, https://doi.org/10.2478/s11600-011-0061-x

Saibi, H., Nishijima, J., Hirano, T., Fujimitsu, Y., and Ehara, S.: Relation between structure and low-temperature geothermal systems in Fukuoka city, southwestern Japan, *Earth, Planets and Space*, 60, (2008), 821-826, https://doi.org/10.1186/BF03352833

Sujatmiko and Santosa, S.: Geological Map of Lewidamar Zona, Geological Map of Java Island with Scale 1:100000. Geological Directorat of Indonesia, (1992).

Supriyanto, Maryadi, M., Sahdarani, D.N., and Zarkasyi, A.: Geoelectrical methods for geothermal exploration in Endut geothermal prospect area, Banten Province, Indonesia, *International Journal Geomate*, 17, (2019), 241-248, https://doi.org/10.21660/2019.63.98151

Supriyanto, Noor, T., and Suhanto, E.: Analysis of gravity data beneath Endut geothermal prospect using horizontal gradient and Euler deconvolution, *AIP Conference Proceedings*, (2017), 1862, https://doi.org/10.1063/1.4991298

Supriyanto, Rokhmatuloh, Sobirin, R., and Suhanto, E.: The effect of gravity measurement distribution points on interpretation of gravity data in the Gunung Endut geothermal prospect area, Indonesia, *International Journal Geomate*, 14, (2018), 60-67, https://doi.org/10.21660/2018.41.07022

Ussher, G., Harvey, C., Johnstone, R., Anderson, E., and Zealand, N.: Understanding the resistivities observed in geothermal systems, *Proceedings*, World Geothermal Congress, (2020), 1915-1920.

This page is intentionally left blank

Initiation of Low Temperature Geothermal System Development in Indonesia: The Potential Challenges

Muhammad Ikhwan[1], Nova Mutiara[2], Asep Purnama[3], Saeful Ghofar Z P[4], and Rendy Maylana P[5]

[1]PT. Pertamina Geothermal Energy, Skyline Building Level 19th, Jalan M. H. Thamrin No.9, Jakarta, Indonesia
[2]Universitas Indonesia, Jl. Margonda Raya, Pondok Cina, Kecamatan Beji, Depok, West Java
[3]Universitas Padjadjaran, Jl. Raya Bandung Sumedang KM.21, Hegarmanah, Jatinangor, Sumedang, West Java
[4]Universitas Gadjah Mada, Bulaksumur, Caturtunggal, Depok, Sleman, Yogyakarta
[5]Universitas Pertamina, Jl. Teuku Nyak Arief, Simprug, Kebayoran Lama, Jakarta

[1]ikhwan.aziz@pertamina.com, [2]nova.mutiara@ui.ac.id, [3]asep18001@mail.unpad.ac.id,
[4]zamianieputra@mail.ugm.ac.id, [5]rendymaylanaputra@gmail.com

Keywords: Low temperature, geothermal, economic, permeability, pump, social

ABSTRACT

In this paper, we present the result of a study investigating the potential challenges of developing a low-temperature geothermal system in Indonesia for indirect use or electricity generation. Our analysis considers various aspects and addresses the technical, operational, social and environmental factors that need considerable attention to initiate the unconventional geothermal development as the alternative way to accelerate the Indonesian energy target. This study compares the existing low-temperature geothermal system worldwide and justifies Indonesia's unique situation that might not agree with anywhere else. The extensive use of literature study combined with our comprehensive analysis and experience enable us to identify the distinctive obstruction that needs to be highly acknowledged.

Characteristics of Indonesia's low-temperature geothermal system and environment are the main focus of our study. The production of a low-temperature system strongly depends on permeability. However, we find the permeability magnitude varies in each Indonesia geothermal system that leads to massive uncertainty in flow mass. The potential outflow area might have low-temperature geothermal system potential mostly occupied with a dense population or allocated for land use such as farms or agriculture. Reflecting on Indonesia's recent unpleasant geothermal risk and accident, the social and environmental resistance might be more complicated than the conventional system as it is mostly developed in further remote areas. The geothermal pump's operational cost and the productivity value of a low-temperature geothermal system also become our consideration to address the low-temperature potential challenges' economic point of view.

1. INTRODUCTION

Indonesia is well known for its abundance of potential renewable energy resources including geothermal. Suharmanto et al. (2015) suggest geothermal energy in Indonesia could dominate 40% of the total geothermal resources in the world. This geothermal energy plays a critical role in meeting the low carbon emission target in 2025 which is stated in Indonesia's National Energy General Plan (RUEN). From the total of 23% in the national renewable energy mix by the end of 2025, geothermal energy holds approximately 7 % in RUEN target 2025 (ESDM, 2019). However, based on the actual renewable energy consumption data in 2020 that is projected to 2025, Indonesia won't meet the RUEN target for renewable energy (Tampubolon, 2020). Especially for geothermal energy, aspects such as technical issues (high-risk resource), operational issues, economic issues (low investment in geothermal), and social-environmental issues might slow the geothermal development in Indonesia.

The focus of Indonesia's geothermal development in power generation so far is on high-temperature resources associated with volcanic areas. However, survey data from Badan Geologi (the geological survey of Indonesia) suggests that a large reserve of medium and low-temperature geothermal resources also exists in the country (Febrianto et al., 2018). In this paper, we define the low enthalpy geothermal resources as the reservoir with temperature <180°C whereas the high enthalpy system in Indonesia mostly comprises temperature >220°C. This low-temperature geothermal system is abundant and spread extensively along the outflow flank of Indonesia's volcanoes, but is not considered worthy to be developed yet.

Many countries utilize low-temperature resources and mainly for purpose of geothermal energy direct use (Thain et al., 2006). Nevertheless, some development of low-temperature geothermal resources were also developed for power generation with sufficient output and lower risk than the conventional high-temperature geothermal system (Febrianto et al., 2018). This invention has been tested by the knowledge, technology, and economic justification that enable development across the world. Such a system seems to promise a concrete alternative way to increase the installed geothermal energy capacity and also accelerating the consumption of renewable energy as the RUEN target.

The low-temperature geothermal system potential in Indonesia must come along with the unique challenges in Indonesia's geothermal system. In this paper, with the extensive use of literature study combined with our comprehensive analysis and experiences, we present the result of a study investigating the potential challenges of developing a low-temperature geothermal system in Indonesia based on its geothermal system, environment, and unique situation compares to low-temperature geothermal system worldwide which is mainly focused on three major aspects, namely permeability, pump, and social environmental issues.

2. PERMEABILITY

2.1 Literature Review

Similar to a conventional high-enthalpy geothermal system, a low-temperature system also uses production and injection wells that are placed separated to maintain the reservoir pressure and temperature (Thain et al., 2006). Both production and injection wells, which are installed with a geothermal pump, needs a sufficient flow rate to make them effectively used. The injection is important to maintain pressure in production areas of low-temperature fields because any pressure drawdown will increase the amount of parasitic pumping power needed to lift the fluid and hence result in a reduction of the net power from the project. High permeability is also necessary for the reservoir to reduce the drawdown seen at the production pumps.

Most of the well-developed low-temperature geothermal system worldwide constrains a great permeability from shallower depth (Kamila et al., 2020). Despite the lower confining pressure factor, permeability in such fields is also mostly associated with the tectonic setting, for instance, the US Basin range or Taupo Volcanic Zone which is strongly associated with rifting mechanism or extensional tectonic setting. The extensional mechanism should create a greater open space for fluid to flow than the compressional tectonic setting that might often be found in Indonesia's high-terrain volcanic geothermal system. In this section, we will compare the published injectivity index, in terms of permeability magnitude, of well-developed low-temperature fields, Steamboat in the U.S, with Indonesia's fields across Sumatra and Java as the most developed geothermal area in Indonesia. These two areas are mainly associated with the compressional tectonic system due to subduction which might affect the permeability magnitude distribution on each field. We believe the tectonic setting plays a critical role to control the permeability together with the geologic condition that results in a range of fluid flow rate variation.

2.1.1 Western US Great Basin Tectonic Setting

The Great Basin segment of the Basin and Range province (Figure 1) is an 800-km wide region of distributed deformation in right-lateral shear and extension, which accommodates ~25% (~11 mm/yr) of the relative motion between the Pacific and North American plates (Faulds et al., 2010). It is separated from the plate-bounding San Andreas transform fault by the 200-km-wide Sierra Nevada–Great Valley microplate, which has remained more or less internally rigid at upper crustal levels since its formation as an arc-forearc pair in Mesozoic time.

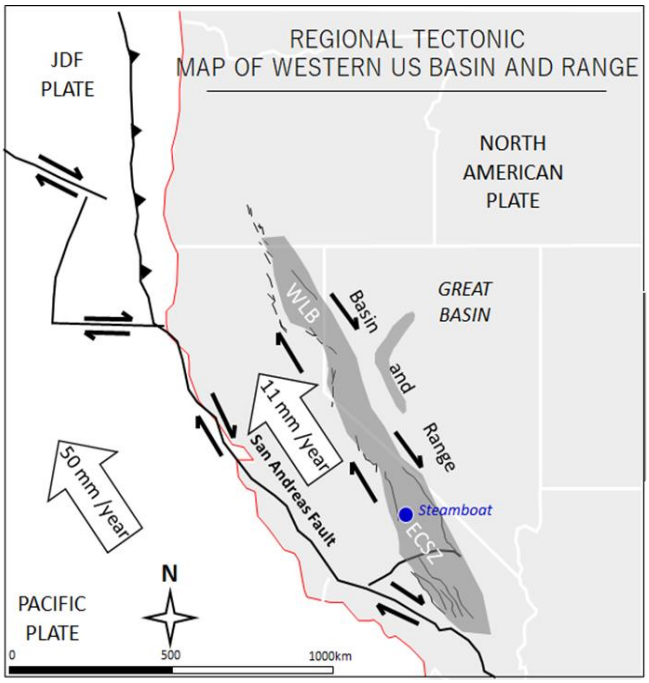

Figure 1: The regional physiography map of Western US Great Basin.

Basin and Range normal faults are dominantly N to NNE striking with E-W to WNW– ESE trending slip vectors (Walsh et al., 2010). Along the western quarter in westernmost Nevada and eastern California, strike-slip faults and pull-apart basin geometries are prevalent, composing a zone of north-northwest right-lateral shear, the WLB or Walker Lane fault system (Wesnousky, 2005) or, where it enters California toward the south, the ECSZ (Fig. 1; Dokka and Travis, 1990; Miller et al., 2001). The WLB-ECSZ accommodates transform motion, which from south to north is progressively transformed into extension. The central and eastern part of the Great Basin is dominated by pure normal faulting; there is some strike-slip faulting in the southern part. The eastern boundary of major Quaternary faulting includes the Wasatch fault system in the northern Great Basin and the Hurricane and Sevier-Toroweap fault systems in the southern Great Basin.

Steamboat

The Steamboat hills project is in South-Reno, Nevada, which is part of spring geothermal areas (Figure. 1A). This location is one of several transverse ridges which divide a major north-south structural trough into separate basins. There are three major structures are identified in this field: The Mud Volcano, Pleasant Valley and Steamboat faults (Walsh et al., 2010). The resource is divided into the upper and lower project, where the lower steamboat has a lower temperature, higher flow rates, and is included in the outflow zone. The reservoir permeability is controlled by deep and high angle fracture under Steamboat Hills for the upper area and shallow with

effective matrix permeability in the combination of faults and mechanical stratigraphy (alluvial formation) in Lower Steamboat (Bjornsson et al., 2014).

2.1.2 Sumatra Tectonic Setting

Tectonically, three major crustal-to-lithospheric scale faults are recognised in Sumatra (Figure 2a). First, the Sunda Trench marks the trace of the subduction thrust interface between the Eurasian and Indian Ocean plates. Convergence is highly oblique with the strike-slip component of plate motion transferred into the overriding plate. Second, the right-lateral strike-slip Sumatra Fault System (SFS) accommodates up to 6 mm/yr of the oblique convergence (Bellier and Sébrier, 1994). The shape of this fault is sinuous, and it extends from Banda Aceh in the north to Lampung in the south. Third, the Mentawai Fault occurs in the forearc and also accommodates a component of strike-slip although its kinematics may be complex (Darman and Sidi, 2000).

The SFS actively affects the entire island of Sumatra from Banda Aceh in the north, through the Bukit Barisan mountains along Sumatra's orogenic axis, to the Sunda Strait in the south. Sieh and Natawidjaja (2000) describe the along-strike segmentation of the SFS and recognise 19 individual segments of approximately 20 km in length based on geomorphic and seismological characteristics. The SFS consists of more than a dozen discontinuities that mostly form right step-overs, but a few contractional bends also occur. This segmentation is sufficient to influence the seismic behaviour of the fault. The SFS also accommodates some of the geothermal systems in Sumatra associated with volcanic structure and topography.

Bukit Daun

Bukit Daun field is one of the geothermal prospects located in Bengkulu province, Indonesia (Figure 2a). It is comprised of the Quaternary stratovolcano complex and is dominated by recent volcanic products that hinder the older deposits and structural trace. Regionally, the Bukit Daun field mapped between the Bukit Barisan and Bengkulu Basin zones in southern Sumatra alongside two other zones, the Mentawai zone, and Jambi-Palembang zone. The impact of such a geological setting is represented in Bukit Daun stratigraphy. Andesite lava and pyroclastic dominates the surface lithology that is derived from geological mapping while more varied lithology found in depth from drilling campaign, such as metasedimentary and siltstone, that indicates the influence of sedimentary process in a particular depositional environment setting. (Ikhwan, 2020)

Lumut Balai

Lumut Balai is located approximately 292 km southwest of Palembang (Figure 2a), around 8 hours of driving from the Palembang airport. Regionally, Lumut Balai lies 60 km east of the Komering Segment, the eastern side of the Sumatra fault. The volcanism in Lumut Balai is closely related to the Sumatra Fault System's activity. Lumut Balai geothermal field itself is located within Old Lumut Caldera, approximately 9 km in diameter (Nurseto et al., 2021).

Ulubelu

Ulubelu geothermal field is located in Lampung province in South Sumatra, Indonesia (Figure 2a). Ulubelu is a liquid dominated system with an average enthalpy of 1100 kJ/kg. It is the largest geothermal power plant in Sumatra with 2×55 MWe capacity from two identical units 1 and 2. Both units have been in operation since September 2012. Another 55 MWe plant was recently introduced in July 2016 which should be followed by a fourth 55 MWe unit in July 2017. (Mubarok and Zarrouk, 2016)

Muaralaboh

The Muaralaboh geothermal prospect is located within the Suliti segment (95 km long) which represents one of the dilatational right offset segments along with the Great Sumatera Fault (GSF) Zones (Figure 2a) (Mussofan, 2018). These offsets along the GSF zones are often the focus of the active volcanic centre. The GSF structure has proven to be the high permeability zones for the existence of such a geothermal system as shown by several well drilling results along with the GSF such as Sarulla, and Ulubelu fields. Besides high permeability zones, the GSF may also provide multiple conduits for magma to rise up and source the geothermal system.

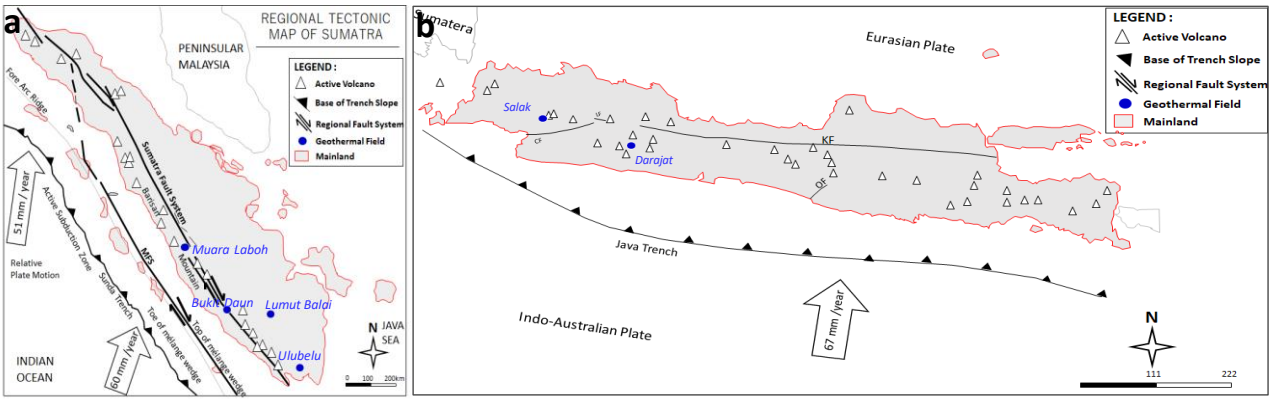

Figure 2: a) The regional physiography map of a) Sumatra showing the SFS which directed relatively parallel with the subduction orientation. b) Java showing the relatively west-east subduction controlled the distribution of volcanic eruption onshore. All maps are attached with the location of the geothermal fields.

2.1.3 Java Tectonic Setting

Java, tectonically comprising a subduction-induced volcano-plutonic arc which classically as the southernmost leading edge of the Continental Sunda plate that overriding the oceanic Indo-Australian plate. (Schlüter, H. et.al 2002) (Figure 2b). The West Java region currently marks the transition between frontal subduction beneath Sumatra, to the west. However, the region has been continuously

active since rifting in the Eocene. The Eocene rifting, as throughout SE Asia, was probably related to the collision between India and Asia (e.g Tapponier et al., 1986). The Oligocene – Recent history is more dominated by subduction-related volcanism and limestone deposition (IAGI, 2000). In general, West Java may be subdivided into the following tectonic provinces: northern basinal area, Bogor Trough, modern volcanic arc, southern slope regional uplift, and Banten Block.

Salak

The Salak (Awibengkok) geothermal field is located in West Java, Indonesia along the Sunda Volcanic Arc (Figure 2b). Salak is a liquid-dominated geothermal system with moderate- to high-temperature (464°-600°F) fracture-controlled reservoir hosting benign and low to moderate non-condensable gas (NCG) fluids. The geothermal reservoir is associated with young volcanism and intrusions in a highland area west of Gunung Salak and east of the Cianten caldera, a collapsed andesitic strato-cone (Satya et al., 2015).

Darajat

Darajat field is situated along the eastern side of a range of volcanic centres (Figure 2b) nearly 30 km in length which includes the active volcanoes Gunung Papandayan (last erupted in November 2002) and Gunung Guntur (last erupted in 1840). Darajat is at an elevation of 1750–2000 meters above sea level and it lies about 9 kilometres southwest of the producing Kamojang geothermal field and 10 km east of Wayang Windu geothermal field (Rejeki et al., 2010).

2.2 Permeability Comparison

To assess the permeability magnitude on each field, we compare the available published injectivity index data related to the interest field. These data compiled from publications about the permeability magnitude in some fields in Sumatra and Java as controlled by compressional tectonic setting include Darajat (Rejeki et al., 2010), Salak (Satya et al., 2015), Bukit Daun (Ikhwan, 2020), Lumut Balai (Firanda et al., 2015), Ulubelu (Mubarok and Zarrouk, 2016), Muara Laboh (Mussofan et al., 2018), and well-developed low-temperature geothermal field in extensional tectonic setting in the US such as Steamboat (Mines, 2016).

Table 1: Injectivity index data *from available published literature.

Geothermal Field	Well	Injectivity Index (t/hr.bar)	Geothermal Field	Well	Injectivity Index (t/hr.bar)
Darajat	Well-A	111.6	Salak	Awi1-9	15.34
	Well-B	72		Awi8-7	17.31
	Well-C	64.8		Awi8-8	19.33
	Well-D	43.2		Awi8-10	43.99
	Well-E	17.28		Awi10-3	21.96
Steamboat	N/A	155		Awi11-4	32.65
Bukit Daun	Well-A	32.7		Awi11-5	13.96
	Well-B	11.4		Awi11-6RD	6.66
	Well-C	15.9		Awi19-2	11.16
Lumut Balai	LMB-X1	154.3	Muara Laboh	Well-A	108
	LMB-X2	22.7		Well-B	97.2
	LMB-Y1	63.8		Well-C	68.4
	LMB-Z1	146.7		Well-D	54
	LMB-Z2	133.3		Well-E	39.6
Ulubelu	UBL-11	99		Well-F	28.8
	UBL-12	51.5		Well-G	14.4
	UBL-14	17.4			

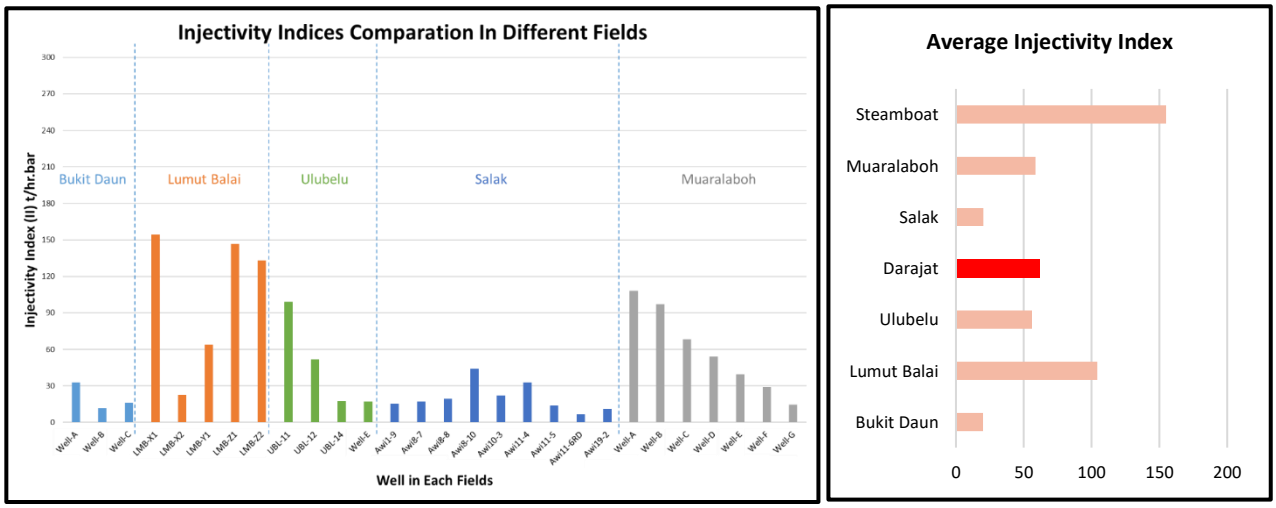

Figure 3: Injectivity index/permeability magnitudes in wells for different fields (left) and average injectivity index comparison in each field.

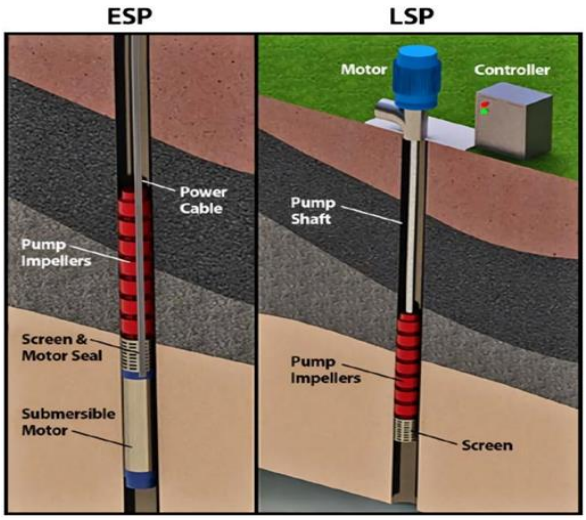

Figure 4: ESP and LSP (NREL,2014).

The challenges of using pumps in Indonesia's geothermal fields are technically and economically. In Indonesia, the lateral outflow of the geothermal field is mostly close-set with local housing, so it is suggested to drill deviated well to avoid contact with the local community on the surface. On deviated wells (inclination more than 4°) and low-temperature reservoirs, ESP installation will more suitable than LSP. Nevertheless, ESP needs routine maintenance, higher operation power, and higher CAPEX.

Based on Indonesia's geothermal resource classification, the reservoir temperature of a low-temperature reservoir is about 100°C – 190°C and it can generate power in the range 850 KWe – 4,175 Mwe (Fauzi, 2015). The power generated from brine with that temperature can economist if the pump produced brine with high flow rates. High flow rates can only reach if the pump has high power output and the reservoir has good permeability, but the higher power output of the pump it will make reduce the run-life of a pump.

Installation of the geothermal pump also needs to examine materials selection for the construction of the impeller, shaft, and body of the pump. Its because geothermal fluids can results corrosion and scaling, which could decrease the lifetime of a pump and productive time. Due to there are no two geothermal sites that are absolute typical, the geothermal fluids could vary across the fields and the pump materials have to be tailored to suit the specific site (Febrianto et al., 2017). Since the specific pump only can be used in specific geothermal fluids, it needs to follow the reservoir temperature, permeability, capacity (areal extent), and pump reliability. There are several key performance indicators (KPI) that are useful to develop the pumped systems across all geothermal settings (Hochwimmer et al,, 2015) (Table 2).

Table 2: Key Performance Indicators Development of Pumped System in Geothermal Fields (Hochwimmer et al., 2015).

Key Performance Indicators	
Depth to Drill to Intersect Target formation	Reservoir Capacity (areal extent)
Temperature of Target Formation	Pump Reliability
Well Productivity and Injectivity	Project Development Size
Reservoir Permeability	Capital Cost and Local Power Price

For a given development size this will dictate the number of wells required and in turn the associated surface fluid gathering and reinjection system. The well productivity can be affected by the impact of neighbour wells so appropriate well spacing is necessary to minimize interference. As we discussed above, permeability plays a critical role to ensure the pump works correctly and fulfil the expected well output. Reservoir capacity also has an impact on the feasibility of the project, so it has to be sufficient to keep the profitable economic aspect on continuous development. Operational run-life is a key factor in AL system selection and can significantly contribute economically (Curkan et al., 2018), simply because pumps with a long operational lifetime will reduce the operational cost. In the end, to develop a low-temperature reservoir using a pump we need to address all the potential and detailed field requirements to know the specific pump needed in the field and also make feasibility higher either in technical aspect or economic aspect.

2.3 Social and Environment

Many of the Indonesia low-medium temperature geothermal systems are found and developed in the outflow zone. In Indonesia, this could be another challenge to though as the lateral outflow zone of the geothermal field is mostly located under people's local housing and/or protected forest that might hold potential challenges such as social and environmental issues. These issues could appear as we need to build the well-pad and drilling infrastructure in the vicinity of the dense area. To ensure the occupancy of the outflow surface condition of the geothermal system in Indonesia, we need to determine the correlation of the geothermal conceptual model and urban condition around the interested geothermal fields. We use the satellite imagery from Google Earth to identify the land usage in some outflow areas of geothermal fields.

2.3.1 Muara Laboh

Dyaksa et al. (2016) describe the geothermal system of the Muara Laboh field. Muara Laboh geothermal system is liquid-dominated with moderate to high temperature (230°C - 310°C). Subsurface investigation proves the reservoir is divided into two different directions that are SW and NE. The outflow zone along NNW has temperature of 160-130°C extending to the Sapan Malulong boiling chloride spring that considered the main outflow of the NE reservoir sector and for outflow from SW reservoir is predicted to the west or relatively to the north near the Muara Laboh spring (Figure 5). This area mostly occupied by farms and rice fields as the main living income for the local community.

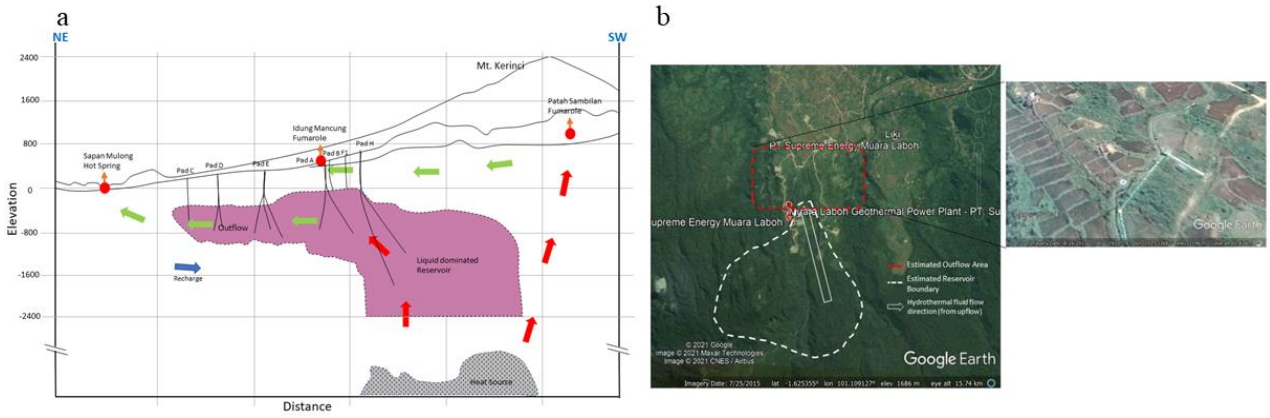

Figure 5: a) 2D Conceptual model of Muara Laboh geothermal field (modified: Stimac, 2019); b) (left) The simple hydrology model of Muara Laboh geothermal system. (right) The highlight image of the outflow zone. Image credit to Google Earth.

2.3.2 Salak

Salak geothermal system is a liquid-dominated and fracture-controlled reservoir (Satya et al., 2015). The commercial reservoir is a medium to high temperature (240°C - 312°C) geothermal resource with high fracture permeability. Reservoir in Salak geothermal system can be divided into some sectors. The principle deep upflows zone with temperatures in the range 275°C - 312°C range is located in the western part of the field. The outflow zones are associated with surface manifestation occurrence. Outflow with lower temperature associated with fumaroles in the east and southeast geothermal field. The Sarimaya (Ciparay) hot spring is located several kilometres to the north of the geothermal reservoir interpreted as the main outflow paths of the system (Figure 6). Cikuluwung hot spring is found about 2 km east of Sarimaya may strongly diluted outflow from either the Salak or Ratu geothermal system. This outflow area has been populated densely and already functioned as a tourist area.

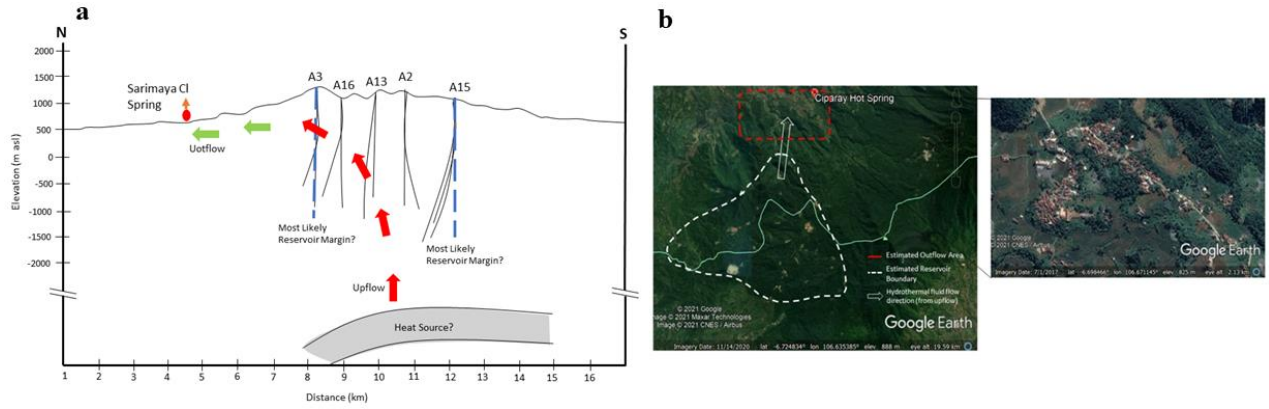

(Previous page) Figure 6: a) 2D Conceptual model of Salak geothermal field (modified: Stimac, 2008); b) (left) The simple hydrology model of Salak geothermal system. (right) The highlight image of the outflow zone. Image credit to Google Earth.

2.3.3 Darajat

Darajat geothermal field is a high-temperature and vapour-dominated reservoir system (Rejeki et al., 2010). This field has a maximum reservoir temperature was measured between 225°C - 245°C with the system upflow believed to be in the north. Geothermal fluids as steam outflows generally flowed towards the south-southeast where the Kawah Manuk, Kawah Darjat, dan Kawah Cipanday in the southeast and sulfate and sulfate-bicarbonate water outflows in the Ciberem and Toblong Spring in the east (Figure 7). This area mostly occupied by farms and rice fields as the main living income for the local community.

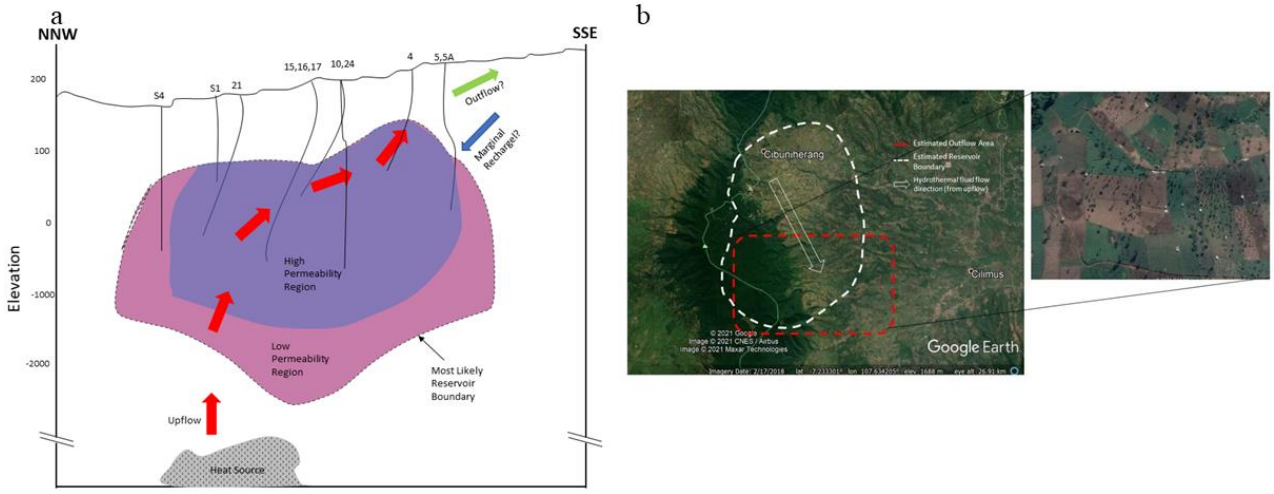

Figure 7: a) 2D Conceptual model of Darajat geothermal field (modified: Rejeki, 2010; Intani, 2020); b) (left) The simple hydrology model of the Darajat geothermal system. (right) The highlight image of the outflow zone. Image credit to Google Earth.

2.3.4 Ulubelu

The conceptual model of the Ulubelu geothermal system discusses in Hochstein and Sudarman (1993) and Siahaan et al. (2015). Ulubelu geothermal field is geothermal water dominated system associated with Great Sumatran Fault. Normal fault with the direction of dominant NW-SE and some structures with NE-SW direction are controlling the geological structure in this area. The presence of these structures also controls the appearance of the manifestation on the west and south of the Ulubelu field. The upflow zone is predicted close to the higher elevation prevalent manifestations of steam-heated groundwater, steaming ground and fumaroles scattered in Pagar Alam, Gunung Tiga and Wayngarip Villages. Meanwhile, the outflow zone is estimated by hot springs with neutral chloride type in the lower elevation zone at Waypanas, the south-eastern part of the upflow (Figure 8).

From the case of Ulubelu, Darajat, Muara Laboh and Salak geothermal fields, outflow zones are mostly located in populated areas and farmland that recorded in satellite imagery which could be another challenge to develop the low-temperature geothermal system in Indonesia. The challenge can involve economically and/or socially due to the presence of another interest on the surface. Land acquisition in the populated area needs more cost than the remote one. The pressure in pricing agreement and negotiation will be much higher compared to the land acquisition process in remote or forestry zone, as the common case in an existing developed geothermal area in Indonesia. Social and environmental is the most sensitive issues that could obstruct the geothermal industry activity. Recently, the rejection of geothermal activity by the local community is often happened in Indonesia and has already become the main concern of the government as the one critical obstacle that slower geothermal development in the country. The perspective that geothermal is green energy is not fully accepted by some people and they tend to presume that the geothermal activity could endanger their land and environment. Unfortunately, such mindset keeps growing as the result of a misunderstanding about how geothermal actually impact the environment and society. Developing an industry in a dense area like this hold a potential challenge and needs more study, not only from a technical factor but also from the economic and social point of view.

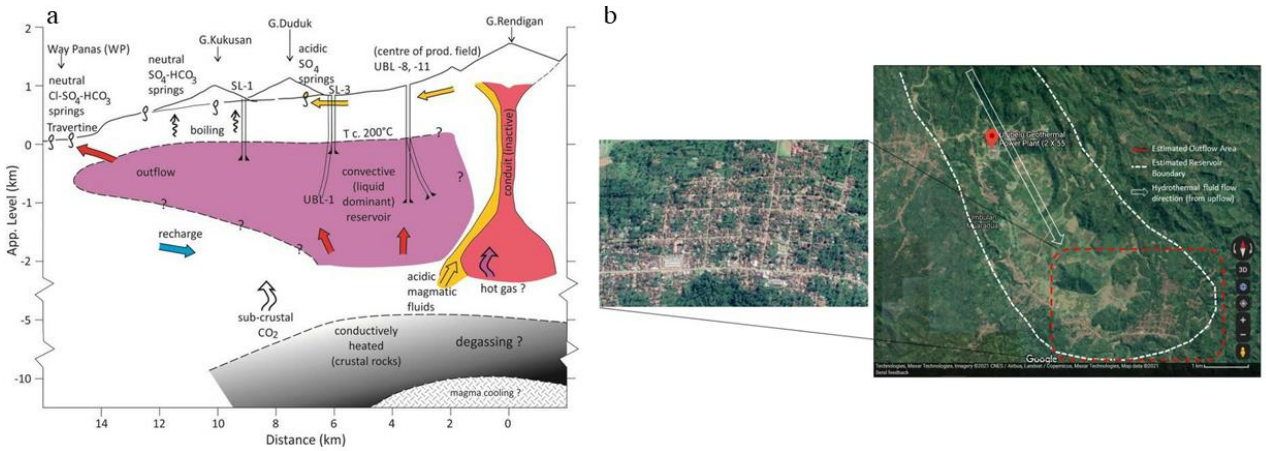

Figure 8: a) 2D Conceptual model of Ulubelu geothermal field (Hochstein and Sudarman, 1993); b) (right) The simple hydrology model of Ulubelu geothermal system. (left) The highlight image of the outflow zone. Image credit to Google Earth.

3. CONCLUSION AND DISCUSSION

The limitation of this study focuses on the available published data that discusses the permeability magnitude, whether in well-developed low-temperature system fields such as Steamboat or the field in Indonesia. No references are mentioning the well injectivity index data in Steamboat, therefore, here we only use the available Steamboat average injectivity index data instead of each well data. Another limitation is only some well's permeability magnitude is available for Indonesia's geothermal field, that uncertain the actual range of permeability magnitude variety. Indonesia's geothermal development has no experience in manage the geothermal well with pump. Accordingly, the challenges here are based on the previous experience from another low-temperature field that might be applied as the lesson learned in the Indonesia system. With abundant geothermal resources along with the country, Indonesia has huge potential to develop a low-temperature geothermal system. Low-temperature system experience and success story in Steamboat field could be an example as another way to accelerate the energy target in the country. However, some challenges exist concerning technical aspects and social environment issues. A low-temperature geothermal system needs a system with great permeability to support the mass supply through the geothermal pump. Due to the tectonic and geological setting, the permeability in Indonesia geothermal systems are varied depends on their structural mechanism or lithology. Moreover, some permeability in the field such as Bukit Daun is mainly controlled by rock matrix that relatively has lower permeability magnitude comparing with the fault or structure. Yet, the average permeability magnitude of Indonesian fields is still lower than the proven low-temperature geothermal field such as Steamboat. More study in geological aspects is needed to certain the permeability control in the hydrothermal system and increase the success ratio in drilling so it could provide sufficient mass in developing a low-temperature geothermal system. The installation of an appropriate geothermal pump is also the key factor to achieve the low-temperature system's success. The geothermal pump needs to adjust correctly with the geothermal well characteristic such as geometry, depth, and fluid temperature. The lifetime of the pump also influences the operational and economic factors in such system as they may be controlled by some operational circumstances depend on well condition. The high terrain geothermal system in Indonesia has the potential of a low-temperature system in its outflow area. Unfortunately, the outflow zone or volcanic flank is commonly populated as a rural or farming area. Construct an industry in such an environment could have huge social pressure and challenges. The local community is usually tough and persistent to keep their land away from the industry, as the impact of the misunderstanding of geothermal industry knowledge on the local community. Moreover, land acquisition in a populated area will need more cost than a remote area or forestry, as the common case for developing the conventional geothermal system in Indonesia.

REFERENCES

Bellier, O. and Sébrier, M.: Relationship between tectonism and volcanism along the Great Sumatran Fault Zone deduced by spot image analyses, *Tectonophysics*, (1994). https://doi.org/10.1016/0040-1951(94)90242-9

Curkan, B., Klaczek, W., and Reede, C.: High Temperature ESPs for Geothermal Production: The Ideal Pump, *Geothermal Resource Council*, (2018).

Darman, H. and Sidi, F. H.: An Outline of the Geology of Indonesia, Indonesian Association of Geologist, Jakarta (2000).

DiPippo, R.: Geothermal Power Plants – Principles, Applications, Case, Studies and Environmental Impact (4th Edition), Elsevier, Amsterdam (2016).

Dyaksa, D.A., Ramadhan, I., and Genefianto N.: Magnetotelluric Reliability for Exploration Drilling Stage: Study Cases in Muara Laboh and Rantau Dedap Geothermal Project, Sumatera, Indonesia, *Proceedings*, 41st Workshop on Geothermal Reservoir Engineering, Stanford University, Stanford, CA (2016), SGP-TR-209.

ESDM.: Rencana Umum Ketenagalistrikan Nasional 2019 – 2038, Sekretaris Kabinet. Jakarta (2019).

Faulds, J.E., Coolbaugh, M., Bouchot, V., Moeck, I., and Oğuz, K.: Characterizing Structural Controls of Geothermal Reservoirs in the Basin and Range, USA, and Western Turkey: Developing Successful Exploration Strategies in Extended Terranes, *Proceedings*, World Geothermal Congress, Bali, Indonesia (2010).

Fauzi, A.: Revision of Geothermal Resource Classification in Indonesia Based on Type of Potential Power Generation, *Proceedings*, World Geothermal Congress, (2015).

Febrianto, R., Bydder, J., Hochwimmer, A., and Ussher, G.: Pumped Well Geothermal Power Generation in the Indonesian Context, *The 5th Indonesia International Geothermal Convention and Exhibition*, (2017).

Febrianto, R., Bydder, J., Hochwimmmer, A., Usher, G., and Libbey, R.: Developing Low Temperature Geothermal Projects In Indonesia Using Pumped Well Technology, *Proceedings*, 7th ITB International Geothermal Workshop, (2018).

Firanda, E., Saputra, M. B., and Silaban, M.: The Effect of Well Elevation on Production in Lumut Balai Field, *Proceedings*, World Geothermal Congress, Melbourne, Australia (2015).

Hochwimmer, A., Urzua, L., Ussher, G., and Parker, C.: Key Performance Indicators for Pumped Well Geothermal Power Generation. World Geothermal Congress, Australia (2015)

Ikhwan, M.: Geological Model and Permeability Framework of Bukit Daun Geothermal Field, Indonesia, Master Thesis of University of Auckland, New Zealand (2020).

Intani, R. G., Golla, G. U., Syaffitri, Y., Paramitasari, H. M., Nordquist, G. A., Nelson, C., and Sugandhi, A.: Improving the conceptual understanding of the Darajat Geothermal Field, *Geothermics*, 83, (2020), 101716.

Kamila, Z., Kaya, E., and Zarouk, S.: Reinjection in geothermal fields: An updated worldwide review 2020, *Geothermics*, (2020).

Mines, G. L.: GETEM User Manual, The INL is a U.S. Department of Energy National Laboratory operated by Battelle Energy Alliance, (2016).

Mubarok, M.H. and Zarrouk, S.J.: Steam-field design overview of the ulubelu geothermal project, Indonesia, *In: Proc.*, 38th New Zeal. Geotherm. Work. Auckland, New Zealand, 23-25 November, (2016).

Mussofan, W., Baroek, M.C., Stimac, J., Sidik, R.P., Ramadhan, I., and Santana, S.: Geothermal resource exploration along Great Sumatera fault segments in Muara Laboh: perspectives from geology and structural play, *Proceedings*, 43rd Workshop on Geothermal Reservoir Engineering, (2018).

Nurseto, S. T., Satriani, R. A. J., Thamrin, M. H., and Suryantini, N.: Productive Structural Geology in Volcanogenic System: A case study of Lumut Balai Geothermal Field, Indonesia, *IOP Conf. Ser.: Earth Environ. Sci.*, 732, (2021), 012013.

Rejeki, S., Rohrs, Dave., Nordquist Gregg., and Fitriyanto, A.: Geologic Conceptual Model Update of the Darajat Geothermal Field, Indonesia, *Proceedings*, World Geothermal Congress, Bali, Indonesia (2010).

Satya, Drestanta., Rejeki, Sri., Golla, Glenn., Waite, Michael., and Aprilina, Nur.: Geologic Modeling Workflow for Volcanic Hosted Geothermal Reservoirs: Case Study from Salak Geothermal Field, (2015).

Setiawan, H.: Geothermal energy development in Indonesia: Progress, challenges and prospect, *Gas*, 1, (2014), 280.

Siahaan, E. E., Sasradipoera, D. S., Silitonga, T. H., Pelmelay, C., Koestono, H., Mubarok, M. H., and Rifki, G.: Success Development Drilling in Ulubelu Green Field in South Sumatra Based on Geological Structure Evidence, Generate 4X55MW, *Proceedings*, World Geothermal Congress, Melbourne, Australia (2015).

Sieh, K. and Natawidjaja, D.: Neotectonics of the Sumatran fault, Indonesia, *Journal of Geophysical Research*, Solid Earth, (2000). .https://doi.org/10.1029/2000JB900120

Stimac, J., Nordquist, G., Suminar, A., and Sirad-Azwar, L.: An overview of the Awibengkok geothermal system, Indonesia, *Geothermics*, 37(3), (2008), 300-331.

Stimac, J., Ganefianto, N., Baroek, M., Sihotang, M., Ramadhan, I., Mussofan, W., and Egermann, P.: An overview of the Muara Laboh geothermal system, Sumatra, *Geothermics*, 82, (2019), 150-167.

Suharmanto, P., Fitria A. N., and Ghaliyah, S.: Indonesian Geothermal Energy Potential as Source of Alternative Energy Power Plant, KnE Energy, (2015), pp. 119-124.

Tampubolon, A: Rencana Umum Energi Nasional (RUEN): Existing Plan, Current Policies Implication, and Energy Transition Scenario, IESR Report (2020).

Thain, I., Reyes, A.G., and Hunt, T.: A practical guide to exploiting low temperature geothermal resources, GNS Science Report, (2006), 76p.

Walsh, P., Martini, B. A., and Spielman, P.: High angle fracture-controlled permeability at upper Steamboat Hills geothermal field, NV. *GRC Trans*, 34, (2010), 833–8.

Wesnousky, S. G.: Active faulting in the Walker Lane, *Tectonics*, 24, (2005), TC3009. doi:10.1029/2004TC001645

This page is intentionally left blank

Managing a Drilling Rig – A KS Orka Experience

Kiki Yustendi, Ashadi, Sentanu W. Reksalegora, Dicky Alamsyah, and Huda N. Ilham

KS Orka, Recapital Building, 5th Floor, Jakarta, Indonesia

kiki.yustendi@ksorka.com, ashadi@ksorka.com, sentanu.wisnuwardhana@ksorka.com, dicky.alamsyah@ksorka.com

Keywords: KS Orka, Drilling Rig, Geothermal Development.

ABSTRACT

KS Orka is a project developer focusing exclusively on the development of geothermal resources. KS Orka currently has three projects in Indonesia, two concession areas and one Study and Exploration (PSPE) area. To support the development of the geothermal projects in Indonesia, KS Orka has decided to own and managing the drilling rig to secure the drilling rig availability and economics. The Drilling Rig was purchased from one of the remarkable Rig Contractor in Indonesia in early 2020 and mobilized to Sorik Marapi. Operation and Maintenance Services was agreed between KS Orka and the Rig Contractor until the Drilling Rig was officially handed over in December 2020. The Drilling Rig has contributed to deliver one of the most economics well in KS Orka. This paper shares challenges and lessons learned in managing the Drilling Rig (i.e., operation, maintenance, spare parts management, and organizational capability).

1. INTRODUCTION

Three main projects that KS Orka owns currently are PT Sorik Marapi Geothermal Power in North Sumatra, PT Samosir Geothermal Power in North Sumatra (PSPE – Study and Exploration), and PT Sokoria Geothermal Indonesia in East Nusa Tenggara.

Figure 1: KS Orka Working Areas ((KS Orka Renewables, 2021).

KS ORKA acknowledges the potential of geothermal energy in Indonesia. Hence, KS Orka is constantly looking for new opportunities to develop and expand in Indonesia. Indonesia's geothermal potentials are located in the ring of fire that is spreading in Indonesia islands.

A drilling rig is required to drill exploration or exploitation well(s). With the growing of the geothermal drilling activities and other land oil and gas drilling, the drilling rig availability in the market becomes more difficult to be obtained. The drilling site location, access road, staging area, and other facility must be prepared before the drilling rig is mobilized to the location. Many geothermal potential locations are located in the conservation forestry area that requires special permits to explore the area. Resistant from local villagers is also one of the challenges. The delayed of the drilling rig mobilization to the location will increase the project cost, for example, when the drilling rig is required to move to the new location that is not ready, standby cost will be applied. To support the KS Orka geothermal development objectives (drilling rig availability and economics), KS Orka has decided to own and manage the "Drilling Rig".

In order to reduce the high cost in geothermal drilling project furthermore, about 40% from the total drilling cost is originated from the rig cost (Purba et al, 2020). Through a careful and efficient drilling rig management KS Orka strives to lower the cost needed to maintain the equipment and to optimize the Drilling Rig performance.

2. THE DRILLING RIG

KS Orka purchased the used Drilling Rig package with the reasonable number of spare parts (1000 HP) from one of the remarkable Rig Contractor in Indonesia in the first quarter 2020. Previously the Drilling Rig has been used in several geothermal drilling in Indonesia with good maintenance record and valid applicable certifications (*Sertifikat Kelayakan Penggunaan Instalasi* – SKPI). The Drilling Rig was completed with all equipment required to drill geothermal wells including top drive system, rig crews' mini camps and base camps, blow out preventers, tubulars and its handling tools. The technical data for every equipment in the Drilling Rig package was mandatory, for example Operating and Maintenance Manual for the Rig Equipment, Spare Parts Manuals for Rig Equipment, history record.

The Drilling Rig was mobilized to the drilling site location after reactivation process carried out in the Rig Contractor workshop. Before hand over the Drilling Rig to KS Orka, the third-party inspection was conducted to ensure major and critical findings (including spare parts readiness) had been closed out. The Drilling Rig was ready to drill the well in Sorik Marapi in end of April 2020.

Managing the Drilling Rig was very challenging, especially KS Orka did not have any experience of running the drilling rig before. Services agreement between KS Orka and the Rig Contractor was made called Operation and Maintenance Contract Service (O&M) to make the transition and knowledge transfer went smoothly. The key points on Rig Contractor responsibility in the O&M Contract Service are as follows:

1. **Provide rig personnel who are familiar with the rig equipment.**

   Rig Contractor supplied KS Orka with the full personnel to operate and maintain the rig equipment, from Jakarta Office based (Operation Manager, HSE Manager, Maintenance Planner, and Rig Manager) to the Field Site Based personnel (Rig Superintendent, Tool Pusher, Driller, Assistant Driller, Derrickman, Floorman, Roustabout, and others). All trainings, complete personal protective equipment, medical check-up, and applicable personnel certifications were provided by the Rig Contractor.

2. **Operating the rig equipment.**

   Executed KS Orka drilling program from rig move, rig up, drilling and completion of the well. Rig Contractor provided health, safety, and environment (HSE) supervisory and monitoring program.

3. **Perform maintenance and repair of the rig equipment.**

   In collaboration with KS Orka drilling team, Rig Contractor performed computerized maintenance management system. Rig engineering support was also included in the event of repair for the rig structure.

4. **Provide certain items, including labor, materials or services as required by KS Orka on reimbursable basis.**

   Managed spare parts inventory and provided spare parts stock report periodically. In collaboration with KS Orka drilling team and supply chain team, reviewed and agreed spare parts purchase as per site requirement and/or inventory maximum-minimum computerized system.

The Drilling Rig SKPI was renewed in November 2020 with the new name in the SKPI letter. The O&M Contract Service had ended in the end of December 2020 after drilling five wells in Sorik Marapi. Considered to have enough knowledge transfer, KS Orka decided to manage on its own the Drilling Rig. Since the Drilling Rig hand over until August 2021, KS Orka has drilled three wells. Currently the rig is undergoing the rig maintenance and overhaul program while waiting on the new pad ready for drilling.

3. DISCUSSION

Managing the Drilling Rig has proved challenging yet rewarding. KS Orka experienced many challenges during the first Drilling Rig mobilization to Sorik Marapi due to COVID-19 pandemic condition. The O&M Contract Service was new to KS Orka, therefore the learning curve was required longer than planned. The highlights during and after the O&M Contract Service will be discussed.

3.1 During the O&M Contract Service

Knowledge transfer and hand over preparation was prepared during the contract duration.

- Key personnel (Rig Superintendent, Tool Pusher, Driller, Chief Mechanics, Chief Electrician, and Warehouse Man) hired by the Rig Contractor was critical at this phase. The objective was to hire the right personnel that are familiar with the rig equipment and can be maintained by re-hiring by KS Orka after the O&M Contract Service completion. Several discussions were made between KS Orka and Rig Contractor regarding the key personnel to satisfy both sides.
- The Rig Contractor HSE system was used with bridging document in place with KS Orka HSE Policy.
- The Drilling Rig maintenance system was performed by the Rig Contractor owned software and computers.
- The Drilling Rig package document and paper work was complete and no issue during SKPI renewal process.
- The Drilling Rig spare parts procurement was performed by the Rig Contractor supply chain at reimbursable plus handling fees. Special parts from overseas Original Equipment Manufacturer were supported by the Rig Contractor principal in the US. Flow process of the spare parts procurement was observed as follows:
  - Material request was issued by rig site personnel,
  - Rig Contractor procurement team searched several vendors for quotation,
  - Quotations were submitted to KS Orka for review and approval,
  - Once approved the delivery was made to Rig Contractor warehouse in Jakarta,
  - Every month trucking was sent to Sorik Marapi,
  - Parts received document at rig site will be signed by rig personnel and KS Orka representatives,
  - Invoice was made based on the actual parts received and complete invoices received from vendors.
- Several times, there were urgent spare parts need. Rig Contractor has the other rig running and can be mitigated by borrowing the parts from the other rig.

3.2 After the O&M Contract Service

Several alternatives to continuously support the Drilling Rig operation and maintenance were considered. KS Orka decided to continue with its own system and adapting several processes as learned from the O&M Contract Service. When drilling the first well KS Orka faced a force majeure situation where the Drilling Rig must be shut down for about one month and required re-activation before recommencing the operation. Mud pumps failure was also contributing to the stuck pipe incident drilling the first well. Lessons learned that can be captured is summarized as follows:

- Hiring the key personnel was difficult to satisfy both sides. Necessary key personnel replacement was made. With the change of the key personnel the adaptation must be restarted.
- Managing own spare parts procurement was challenging during first several months. KS Orka has its own terms and conditions that several parts vendors must adapt. Dedicated spare parts purchaser was hired to accelerate the procurement process.
- Rig equipment preventive and corrective maintenance was conducted manually and left with gaps that several critical equipment required special attention for repair (i.e., mud pumps, engines, etc.).
- Poor Drilling Rig leadership and system was observed, continuous improvement was required to reduce non-productive time rig equipment related and increase rig operability and performance.

Despite several challenges and stuck pipe incident faced by KS Orka when managing its own Drilling Rig, one achievement was also made during drilling the second well by having one of the cheapest well in Sorik Marapi. The spare part cost in average is also cheaper compared to during O&M Contract Service.

To improve more of the Drilling Rig operability, several plans for improvement are addressed as follows:

1. Improve rig site staffing strategy. Position from derrickman to roustabout are all locals. During issue with local community and strike, the local crews were also impacted. Balancing the crews hiring with non-locals will ensure the rig operability to be sustained.
2. Improve team organizational capability and relieve crews. This including hiring rig operation manager, rig engineer and top drive specialist. Site purchaser to bridge between the rig site team personnel and procurement team in Jakarta is also included.
3. Develop own Rig Management System. System that is web based and capable of digitalized rig data from manuals, spare parts part number, maintenance record, preventive maintenance reminder, stock position, spare parts status (request/approval/delivery).
4. Develop long contract of Spare Parts and Services with the OEM and create road map for continuous rig operability improvement. This includes the overhaul and re-certification equipment requirement.
5. Assessment of the obsolete parts/equipment to be replaced with the new equipment. The rig condition is quite old yet still reliable.
6. Assessment of the logistics strategy by having staging warehouse to reduce logistics cost.
7. Prioritize local parts shops near Sorik Marapi area contributing to the local development.
8. Develop alternative plan and source critical equipment parts / back up for any urgent need during drilling operation.

4. CONCLUSION

Praise to God that during the drilling operation activity, KS Orka can achieve zero Loss Time Incident (LTI). One of the KS Orka values is that “We’re personally accountable for our own safety and collectively responsible for each other's safety. In meeting our goals for quality, cost and schedule, we will not compromise safety”.

Managing the Drilling Rig has proven supporting KS Orka to develop the geothermal project in Sorik Marapi. Owning a drilling rig secures rig availability. With the nature of geothermal development that has common challenge on the location permit, like currently KS Orka is facing, standby cost waiting on the location with the Drilling Rig owned by KS Orka has proved to be economics compared to the rig rental. In the long run, managing own drilling rig will help to reduce the cost of drilling the well.

Continuous rig performance and efficiency are work in progress. Despite all challenges, the Drilling Rig managed by KS Orka can achieve one of the cheapest well in Sorik Marapi. With better geothermal project economics, KS Orka and other Geothermal Developer can contribute more to develop geothermal development in Indonesia.

REFERENCES

Purba, Dorman, Adityatama, Daniel, Agustino, Vicki, Fininda, Fikha, Alamsyah, Dicky, and Muhammad, Farhan: Geothermal Drilling Cost Optimization in Indonesia: A Discussion of Various Factors, *Proceedings*, 45th Workshop on Geothermal Reservoir Engineering, Stanford University (2020).

KS Orka Renewables: About Us: Where We Are (2021). https://www.ksorka-sorikmarapi.com/

This page is intentionally left blank

Geothermal Power Plant is Moving to Governor Free Operation, Case Study from Darajat 55 MW Geothermal Power Plant

Sugeng Triyono and Danu Sito Purnomo

sugeng@indonesiapower.co.id, danu.purnomo@indonesiapower.co.id

Keywords: Load limit, governor free, frequency, steam pressure, ejector, condenser vacuum.

ABSTRACT

The 55 MW Darajat geothermal power plant operates as a baseload bearer in the 150/500 KV Java – Bali electricity grid system. This plant is supplied by 5 - 7 geothermal wells, which are depending on the steam capacity of each wellhead. The steam production capacity of each well is generally set at constant steam flow, which leads to delivering MW output capacity at constant 55 MW or following the pre-set target output, and it is not allowed a fluctuation load as per limited by the load limit mode during operation. The change in operating mode from load limit to free governor has experienced a low-pressure alarm on the first and second ejector. The alarm coincided with a fast response on increase capacity output due to the drop 150 KV grid frequency system. If this low ejector pressure continues, there will be a built-up pressure in the condenser which causes the turbine to fail in operation. The free governor mode of operation will mandatory requirement for power plants following regulations from dispatched control, and will be further continuing on LFC "load frequency control" and AGC "automatic generator control", as an anticipating of more penetration on intermittent renewable energy in the grid.

Experienced by Darajat geothermal power plants, the changing mode of operation from load limit to free governor needs strong coordination with the geothermal steam supply, especially when LFC and AGC are applied. Considering the nature of steam production from wellhead is at constant capacity, but there is the need from grid operating system to be able for flexible power plants in responding of fast load response to frequency changed.

The successful change mode of operation Darajat geothermal power plant from load limit to free governor could be duplicated to other geothermal power plants that deliver its electricity through 150 KV Java – Bali electricity grid system.

1. INTRODUCTION

The vapor dominated Darajat geothermal field is located in the West Java province of Indonesia, about 150km southeast of Jakarta. The field is situated along a range of volcanic centers extending nearly 30km in lengths and is adjacent to the Kawah Kamojang and Wayang Windu geothermal fields. Geothermal evaluations at Darajat began in the early 1970's when surface scientific reconnaissance conducted in the area indicated the existence of a vapor dominated reservoir in a hydrological setting similar to the nearby Kamojang field.

Three exploratory wells drilled in 1978-79 verified the geothermal field's existence. Wells drilled into the reservoirs encountered temperature and pressure gradients similar to that of static vapors. Ten years later, Amoseas Indonesia Inc. drilled four additional delineation wells and confirmed a commercial reserve. The first commercial unit has been generating 55 MW of electricity since October 1994. Since then, additional construction of power generation plants with capacity of 90 MW and further the 3rd unit with capacity of 121 MW, adding up to total capacity of 266 MW. Power plant of Darajat 1, belong to PT. Indonesia Power, under steam supply contract with steam field developer. The second and third unit own and operated by steam field operator.

Electricity evacuation from power plants delivered to 150 KV Java – Bali grid. The important role of Darajat power plants among others are to increase voltage drop in 150 KV southern area of Java Island, which is less number of power plants installed in comparison with north sea coastline Java Island. Since Darajat init 1 COD on July 1994, this power plant serves electricity with high availability rate (average 95%). This unit is among the best geothermal unit in Indonesia.

Within operation system, geothermal together with coal power plants is delivering capacity as base loader power plants. Coal power plants is considered as base-loader power plants due to its cheap operation cost, while geothermal on the other side is rigid in fluctuating operation due to less flexible on geothermal steam output from wells. Therefore, the more penetration on intermittency renewable power plants such as solar PV and wind turbine, is leading requirement the grid operating system to be able for more flexible operation, in the event of cloud shedding on PV module or fluctuation on wind speed that spinning the wind blades.

To prevent electricity system that resist to disturbances, units power plants require governor free mode of operation to allow an automatic frequency response by delivering more MW capacity to the grid in the event of frequency drop due to less capacity supply to the grid. The second unit's response is AGC than still give provision on automatic response and then the manual tertiary frequency control within a few minutes if the under-frequency event does not correct itself by governor free and AGC. Tertiary frequency control typically involves the power grid operator manually adjusting the dispatch of some power plants.

During moving from load limit to free governor for Darajat 55 MW geothermal power plants, has experienced a low-pressure alarm on the first and second ejector to response on increasing capacity output due to the drop 150 KV grid frequency system. If this low ejector pressure continues, there will be a built-up pressure in the condenser which causes the turbine to fail in operation. Further coordination between power plants operator and steam field supplying operator can reduce the risk of operation failure because of failing over pressure on condenser due to limited steam to suck non condensable gas built up in the condenser.

2. DARAJAT 55 MW GEOTHERMAL AND ITS CONTRIBUTIONS TO JAVA – BALI ELECTRICITY GRID

The load on a power station varies from time to time due to grid fluctuation demand which are depending on the consumers activities. At any time, a balance between electricity supply and electricity demand is measured by grid frequency such as 50 hz for 150/500 KV Java – Bali grid, as shown in Figure 1. If capacity supply is higher than capacity demand will result an increase of grid frequency, on the flip in the event the big capacity power plants 1000 MW trip, then suddenly grid frequency will drop from normal 50 hz. Normal frequency value for Java – Bali grid is 50 hz ± 0.2 hz. In 2019 grid peak capacity was 27.97 GW.

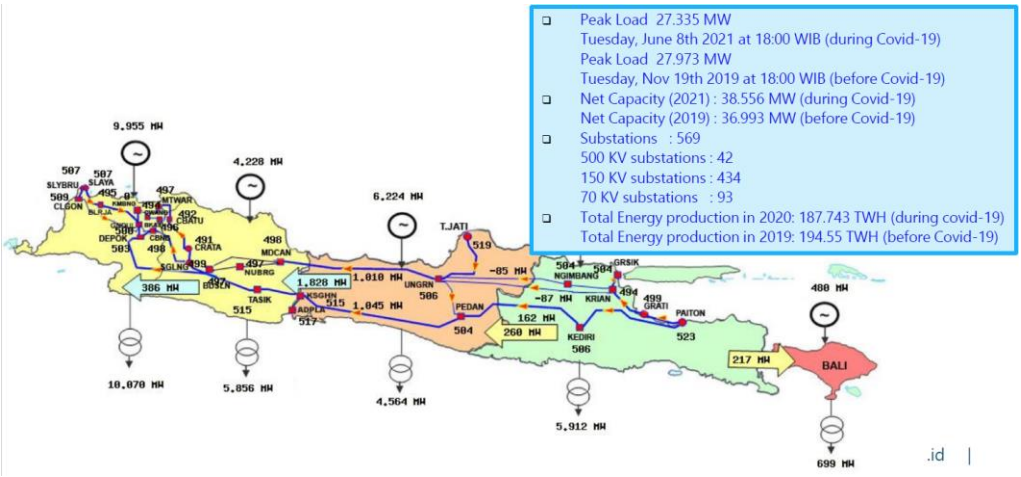

Figure 1: Java – Bali 500 KV grid with 27.97 GW capacity in 2019.

The grid dispatcher manages the minute-by-minute operation based on dynamic load curve forecasting. The dynamic forecasting means that the actual grid demand will always adjust the subsequence of daily load curve. If to be necessary, the revised load forecasting can be done on minute-by-minute on the single day. To be able for keep maintaining quality frequency within standard, unit power plants are required to switch on the free governor facilities, AGC and LFC in order to automatic response whenever the grid frequency fluctuations happen due to imbalance of capacity supply and electricity demand from consumers. Figure 2, shows the governor free status and AGC per July 2021 and grid frequency parameters during normal conditions and load shedding.

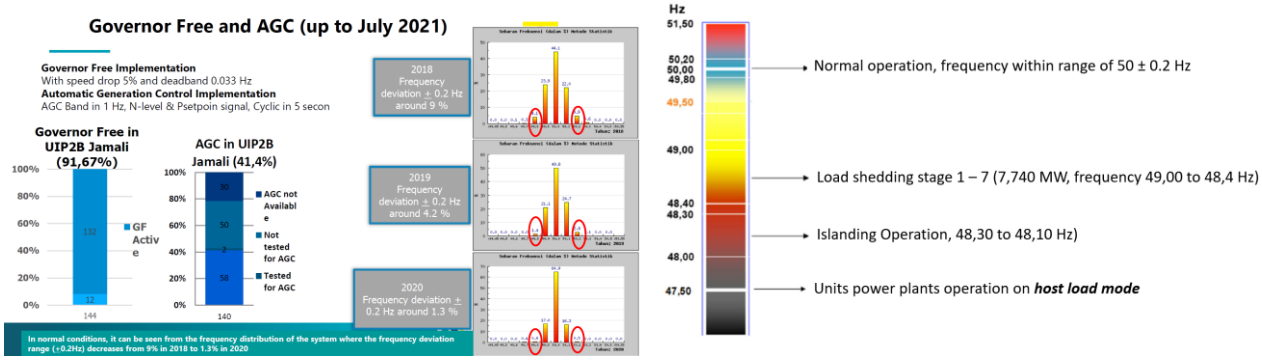

Figure 2: Governor free and AGC of Java – Bali as per July 2021 and Grid frequency normal and load shedding.

Theoretically on ideal conditions, the minimum grid cost is achieved at 50 hz, over frequency will mean that PLN lose money because the power generated is greater than the actual needs which is consumers not used it. On the flip if the grid frequency is below the standard, then consumers will be sacrificing electricity quality that may lead to non-performance of consumers equipment's such as lamp become dimmed due to the voltage drop. This is the essence of free governor facilities in term of automatic capacity response from power plants to match with volatility of consumers behaviors on daily electricity usage.

Within load duration curve, operationally it is common practice to divide into 3 (tree) categories namely, based load unit power plants, medium load unit power plants and peak load unit power plants. Base-loader unit power plants to serve on relatively flat minimum load within 24 hours, as per on the LDC curve, while load follower to provide cyclic operation units to follow the increasing capacity demand usually during ramping up from minimum load to maximum load, and peaker unit power plants are only to provide capacity within around 5 – 6 hours during peak hours only.

Unit base load power plants are come from non-expensive fuel cost such as coal power plants. Geothermal power plants, run out hydro power plants and gas pipe power plants because of less flexibility on fuel supply, then those power plants are operating as base loader power plants. Reservoir hydropower power plants on the other hand has a very good flexibility operation that can be start from stop to on grid very fast, as well as high ramp up to 50 MW/minute, according to water storage in the reservoir, then this dam hydro power plants is operating as peak load units, together with open cycle gas turbine power plants. In between is load follower power plants such as combined cycle gas turbine.

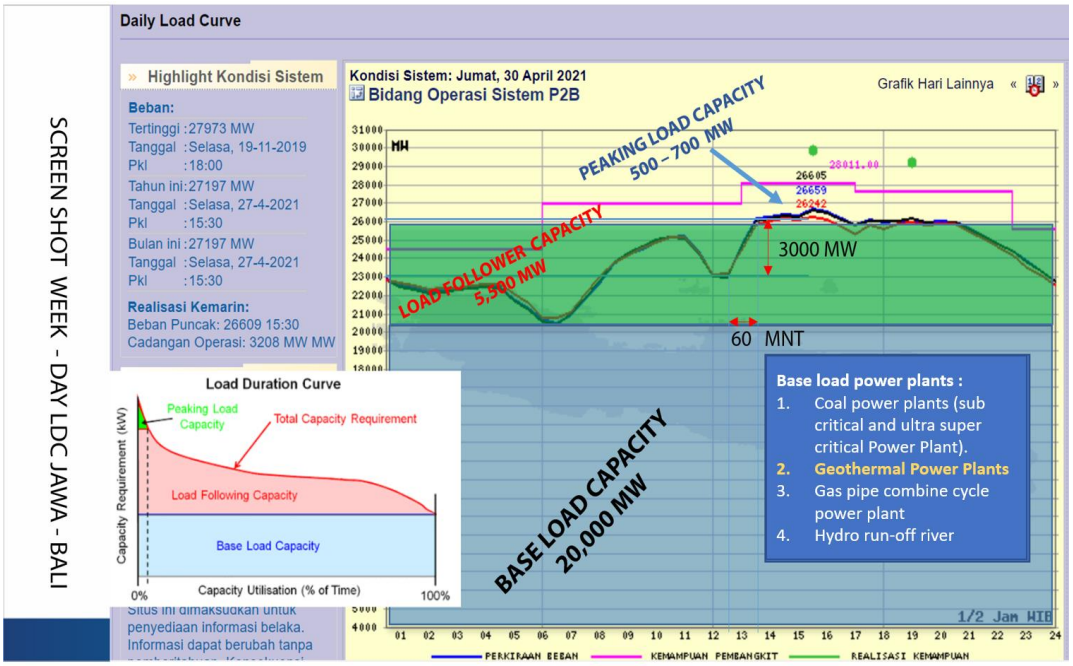

Figure 3: Typical LDC Java – Bali 500 KV and Unit base, intermediate and peak power plants.

Darajat 55 MW geothermal is normally operating for base loader units which fluctuation response is limited by load limit facilities that have very low response on grid fluctuation. Therefore, to anticipate the more penetration of variable renewable energy in the grid system in the future, then Darajat is requested to operate on governor free mode. The experiences shown that alarm of low pressure on primary and secondary steam ejector during unit to response a sudden frequency drop. Initial assessment of alarms indicate that the geothermal steam tends to go for turbine while less steam that go to steam ejector that potentially not able to release non condensable gas in the condenser that could lead to turbine failure.

3. LESSON LEARNED FROM GOVERNOR FREE MODE OPERATION FROM DARAJAT 55 MW

Since 12th May 2020 Darajat 55 MW is requested to contribute on frequency control by activating governor free during operation, which was normal operation on load limit mode. The droop setting was 5% with the dead band frequency 0,03 Hz

A load limit and governor free use to response the power plant MW output with the change of engine speed (rpm). Because of natural inertia force, the increase of engine load will reduce the rpm. At normal grid frequency of 50 hz Java – Bali grid, all power plants have the same speed of 3000 rpm. In case of load demand increase, then for a short period if time, the grid frequency will reduce, similar the power plants sense that the rpm of the engine will slightly below 3000 rpm, similarly if load demand reduce then the frequency of the grid will slightly increase that the power plants will sense the engine speed above 3000 rpm. In order to bring back the grid frequency to normal 50 hz, then the power plant's governor will response either to reduce or to open more fuel, respective the load demand fluctuation.

Mathematical formula for speed drop is defined as:

$$\% \text{ Droop} = \frac{\text{No Load Speed} - \text{Full Load Rated Speed}}{\text{Full Load Rated Sped}} \times 100 \quad (1)$$

Where, No Load Speed is the RPM at which the generator shaft rotates when there is no load attached to it (no torque applied to the output shaft). It is the maximum output speed of the motor. Respectively, Full Load rated Speed is the RPM at which the generator shaft rotates at its MW output rated capacity.

The mathematical formulas for generator MW output response due to the changing of grid frequency are as following:

$$k = \left(\frac{1}{s}\right) . \left(\frac{P_{nominal}}{f_{nominal}}\right) \quad (2)$$

$$\Delta P = -k \, . \Delta f \quad (3)$$

$$\Delta P = P_{generator} - P_{nominal} \quad (4)$$

$$\Delta f = f_{generator} - f_{nominal} \quad (5)$$

Where k, s, $P_{nominal}$, $f_{nominal}$, are response factor in MW/hz, speed drop in%, nominal generator output in MW, nominal generator frequency in HZ.

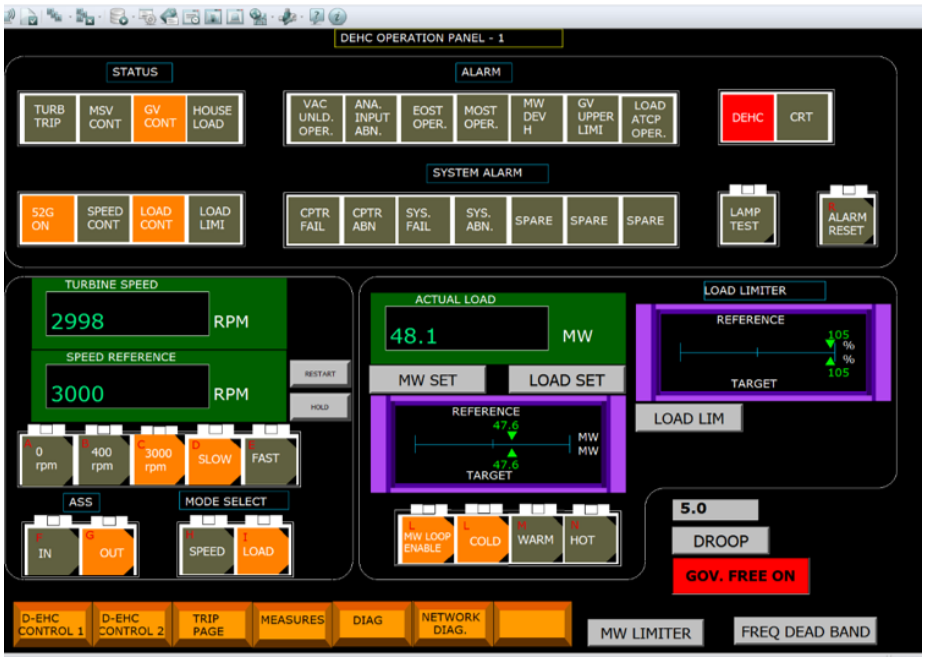

Figure 4: Events of low pressure ejector alarm 6 consecutive times during governor free operation.

If the Darajat Power plants has 5% drop, at engine speed of 2.5 hz above 3000 rpm, or 3150 rpm as considered generator frequency at no load speed and 3000 rpm as full load rated capacity generator rotate.

Speed Droop Governor is normally an indicator of the speed of response from geothermal power plants to increase or decrease the delivery MW output because of frequency fluctuation from the grid, that connected to the power plants. The smaller speed drop is the more responsive of power plant.

Testing of free governor has been carried out at PLTP Darajat unit 1 on March 21, 2021, by PLN P2B (dispatcher) with the test results as shown in Table 1 and shown on Figure 5. Dead band of the governor free is 0.03 HZ.

Therefore, during operation of governor free operation, as shown in Figure 5, that on June 15, 2020 during normal operation occurred 6 times low pressure ejector alarms within about 45 minute period, detailed as shown in Table 2.

Table 1: Result of free governor testing for Darajat 55 MW on March 21, 2021.

No.	Waktu (hh:mm:dd)	Frek (Hz)	Turbin Speed (reference 3000 rpm)	MW Set (bruto)	MW Act (bruto)
1	10:15:01	50,043	3003	47,5	47,0
2	10:15:39	50,000	2999	47,5	47,4
3	10:17:40	49,927	2997	47,5	47,9
4	10:24:48	50,072	3004	47,5	46,6
5	10:24:15	50,097	3005	47,5	46,0
6	10:29:55	50,143	3008	47,5	45,0
7	10:31:00	50,168	3010	47,5	44,0
8	10:31:40	50,190	3011	47,5	43,8
9	10:32:15	50,190	3012	47,5	43,7
10	10:35:00	50,090	3004	47,5	45,6

No.	Waktu (hh:mm:dd)	Frek (Hz)	Turbin Speed (reference 3000 rpm)	MW Set	MW Act
11	10:42:23	49,950	2998	47,5	47,8
12	10:45:40	49,967	2998	47,5	47,6
13	10:46:51	49,946	2997	47,5	48,0
14	10:49:00	49,950	2997	47,5	47,9
15	10:50:15	49,930	2996	47,5	48,5
16	10:51:05	49,912	2995	47,5	48,9
17	10:52:30	49,857	2992	47,5	49,3
18	10:52:45	49,862	2992	47,5	49,5
19	10:54:00	49,849	2991	47,5	50,0
20	10:54:30	49,843	2991	47,5	50,2

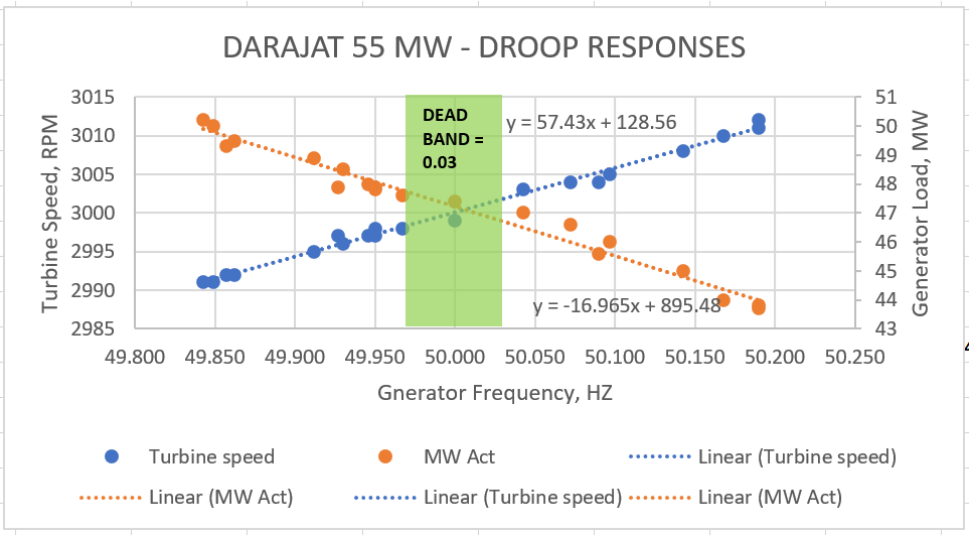

Figure 5: Graph of free governor testing on March 21, 2018.

Table 2: Low Pressure Ejector Alarm during operation of Free Governor.

No.	Parameters	Average Value / Units	TIME DURING ALARM OCCURED						Status
			16:36:01	16:48:07	16:56:00	17:04:40	17:09:09	17:17:53	
1.	Generator frequency	50.03 hz	49.98	49.96	50.00	49.91	49.94	49.95	Generator frequency follow grid
2.	Generator load	47.63 MW	48.05	48.44	47.84	49.22	49.04	48.8	Capacity during normal operation is not at install capacity to allow response for lower grid frequency
3.	Steam pressure after separator	9.35 barg	9.25	9.21	9.35	9.25	9.24	9.32	
4.	Steam pressure before MSV	9.40 barg	9.33	9.28	9.42	9.29	9.3	9.4	
5.	Steam flow–	339 ton/h	340.60	345.62	345.62	350.1	351.7	344.5	
6.	Ejector pressure – barg		9.11	9.09	9.2	9.1	9.09	9.18	Normal pressure is 9.2 barg.
	Ejector Status		ALARM	ALARM	NORMAL	ALARM	ALARM	ALARM	

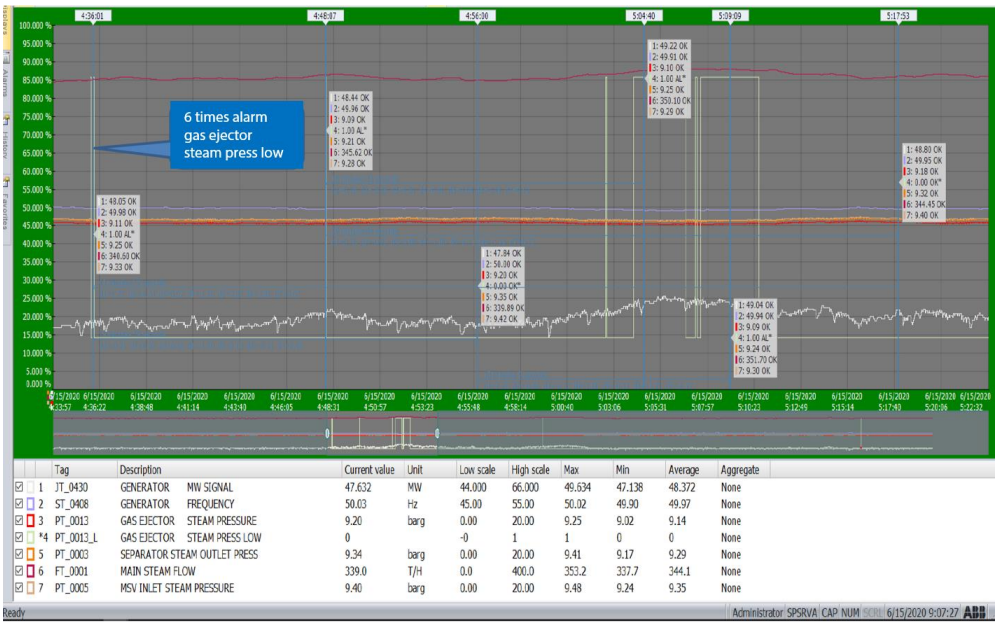

Figure 6: Events of low pressure ejector alarm 6 consecutive times during governor free operation.

Low pressure ejector alarm occurred when grid frequency decrease to 49.8 hz, because of governor free mode than governor valve response by opening more flow of turbine. At this time the generator load is 48.05 MW, while rated capacity of 55 MW, that the meaning of about 7 MW less. Governor valve response is to restore the frequency back to 50 hz that equivalent with 55 MW output from the Darajat power plant. The alarm of low-pressure ejector was because of not sufficient energy of steam inside the geothermal pipeline to for increase MW output from the Darajat. If the low ejector pressure continuous, there will be a risk for pressure built up on the condenser due to geothermal non condensable gas not been release that lead to turbine fail.

Figure 6 shows the picture that indicated grid frequency low, governor valve opening, as a response from Darajat power plant.

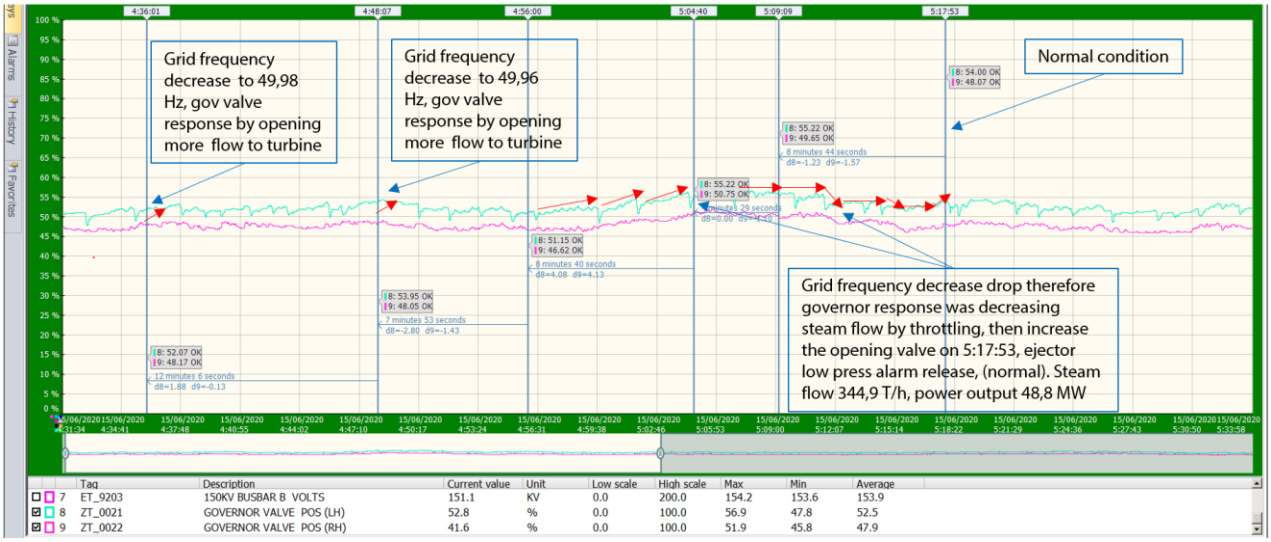

Figure 7: The governor valve response during low ejector pressure of Darajat 55 MW on June 15, 2020.

However, if the available steam on the pipeline is not enough to response the increase MW output, then to avoid ejector pressure low the grid frequency decrease will response by decreasing steam flow by throttling the governor valve, in order to keep main steam pressure goes to ejector on the normal standard value operation, then gradually steam flow increase to increase the increase demand load. To be able for increase steam flow in geothermal pipeline, further coordination between steam supplier and power plants should be manage properly.

Considering equation 1,2,3,4, and 5 to calculate the steam deficit during low pressure alarm, the approach calculation are as following;

- Total design install capacity of Darajat is 55 MW
- Load at 50 hz, free governor mode, power plant load is 47.63 MW. The margin of 55 MW – 47.63 MW is reserved for capacity response due to grid frequency less than 50 hz.
- Total steam flow at 47.63 MW is 339 ton/hr.
- At frequency of 49.61, Darajat power plant will response to increase capacity to maximum design capacity of 55 MW.

Parameters	**Units**
Design Install Capacity	55 MW
Rated capacity at GF	47.63 MW
Normal Frequency	50 hz
Steam flow at 47.63 MW	339 ton/hr
At frequency 49.61 hz *).	55 MW

*). In the event of grid frequency 150 KV drop below 50 hz then the power plant response to increase capacity. At 49.61 hz capacity will be 55 MW

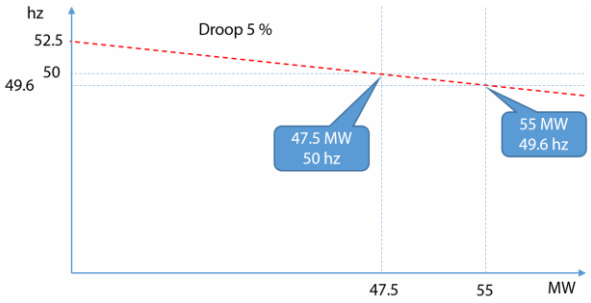

Figure 8: Darajat 55 MW responses on decreasing the grid frequency.

Operation coordination between opening wells valve and generator output is required to avoid insufficient steam flow during ramping up of generator response to increase MW output during decreasing frequency that governor free mode will automatically open more governor valve to increase steam flow to turbine. The maximum steam flow is equivalent with generator output of 55 MW that need steam around 391.4 ton/hr. While during normal operation with free governor mode Darajat power plants is dispatched of 47.63 MW (339 ton/hr steam) at generator frequency of 50 hz. Hence the increase of available steam to meet the maximum rated capacity of 55 MW during low frequency system is 392 ton/hr. – 339 ton/hr. = 52 ton/hr geothermal steam, as per shown in Figure 8. Further correlation between generator frequency and steam flow and generator frequency and generator MW output is shown in Figure 9.

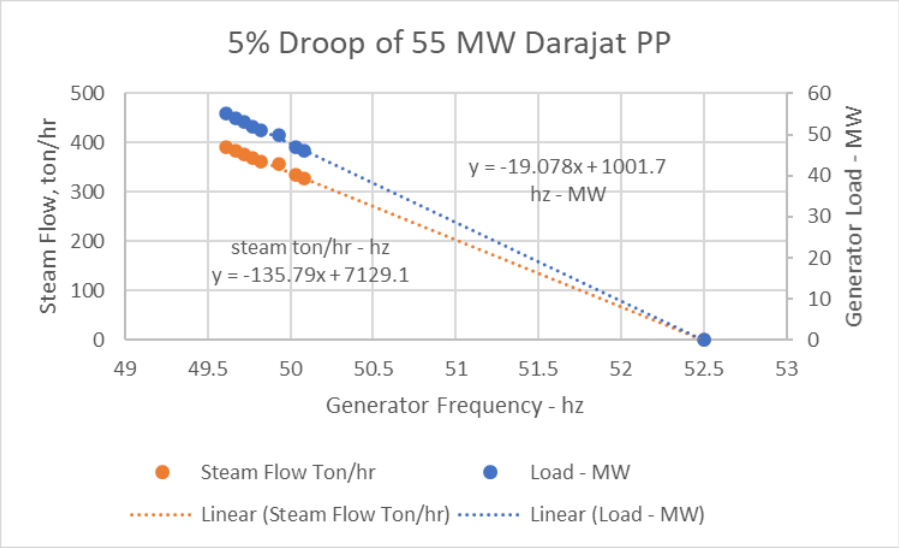

Figure 9: Correlation between steam flow and grid frequency and MW output and grid frequency.

The current steam supply for PLTP Darajat unit 1 55 MW is from Darajat geothermal steam fields that owned and operated by PT. Star Energy Geothermal Darajat (SEGD), as shown in Figure 10. Seven production wells, DRJ 7, 9, 10, 11 locate in the North Sector and DRJ-8, 13 and 34 locate in the South Sector, that steam production rate of about 110 kg/s or around 396 ton/hr gross to produce 55 MW power plant net output. The North Sector provides about 70 kg/s (from wells DRJ-7, 9, 10 and 11) and the South Sector about 40 kg/s (from wells DRJ-8, 13 and 34).

From the steam field operation to support the geothermal steam fluctuation in response to grid frequency ripple because of requirement of Darajat free governor mode, some of the geothermal wells are equipped with an automatic control system - a pressure control valve (PCV) - located on the main pipeline before the interface on the north and south sides. The PCV is serves to regulate the steam pressure and the amount of flow to match with the amount quantity of steam required by the turbine – generator that have an automatic response to increase the MW output during a decrease 150 KV grid frequency network.

The operating history shows that the maximum technical load fluctuation that can still be carried out by PLTP Darajat is 56.5 MW.

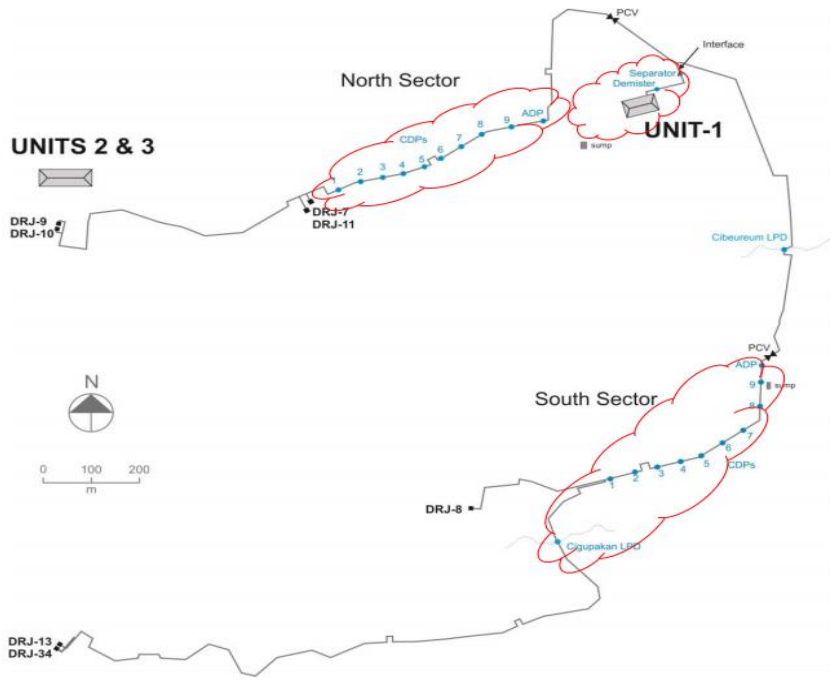

Figure 10: Steam Supply for Darajat 55 MW from geothermal wells located in South Sector and North Sector.

4. DISCUSSIONS AND RECOMMENDATIONS

- The previous geothermal power plants are considered to be based load power plants with load limit operation mode, due to steam flow from geothermal wells considered to be fixed steam flow resulting the relatively fix output of the power plants.
- High penetration on variable renewable energy led to potential instability on the 150 KV grid system, especially within a short period of time the capacity from VRE loses and regain because of its intermittency.
- Darajat geothermal power plants is operated on governor free mode since early 2020 and during operation of have experiences of steam insufficient to response the MW demand load during automatic response of low frequencies.
- To overcome the insufficient steam flow during fast response of the governor free system, the coordination with steam supplier to open more steam flow from wells to avoid the low pressure on ejector steam. Releasing of the excess geothermal steam through steam valve before constant steady flow to turbine. Accumulation of geothermal steam inside the pipeline is monitored by geothermal steam pressure. To overcome the insufficient steam flow is to coordinate with the steam feeder to increase the steam pressure setting from 9.3 bar to 9.7 bar

REFERENCES

Joseph H. Eto, John Undrill, Ciaran Roberts, Peter Mackin, and Jeffrey Ellis: Frequency Control Requirements for Reliable Interconnection Frequency Response, Ernest Orlando Lawrence Berkeley National Laboratory, 1 Cyclotron Road, MS 90R4000 , Berkeley CA 94720-8136, LBNL-2001103 - February (2018).

NERC (North American Electricity Reliability Corporation): Reliability Guideline Primary Frequency Control May 2019 Approved by the Operating Committee, June 4 (2019).

PT. Indonesia Power: Unpublished internal documents, Jakarta (2021).

UCTE Operation Handbook Policy 1: Chapter A: Primary Control, (2004).

Woodward.: Reverence Manual, Governing Fundamentals and Power Management, Manual 26260, Goodward (2004).

Viet Hoang, Ontowiryo Alamsyah, and Jeff Roberts: Darajat Geothermal Field Expansion Performance, *Proceedings*, World Geothermal Congress 2005, Antalya, Turkey, 24-29 April (2005).

Improving The Quality of Preventive Maintenance (PM) Work For FCRS And GPP Equipment With "At Cost Based-Annual Maintenance Contract (AMC) Innovation" at PT PGE Area Lumut Balai

Raka Kautsar Lahia, Azhari Surya Adiputro, Firman Johannes Simanulang, and Angga Hendrawardhana

raka.kautsar@pertamina.com, azhari.surya@pertamina.com, firman.simanulang@pertamina.com, angga.wardhana@pertamina.com

Keywords: Geothermal Power Plant, FCRS, equipment, maintenance

ABSTRACT

Lumut Balai Unit-1 Geothermal Power Plant PT Pertamina Geothermal Energy is one of the mainstay power plants in the South Sumatra, Indonesia region. With a generating capacity of 55 megawatts, there are more than 6000 pieces of equipment, including Geothermal Power Plant (GPP) and the Fluid Collecting and Reinjection System (FCRS) equipment. All equipment, especially critical equipment in GPP and FCRS, must be always in good condition, have good mechanical availability, and have good reliability to achieve the electricity generation target. In maintaining availability and reliability, PT Pertamina Geothermal Energy has prepared a reliability-centered maintenance strategy and put it into the Computerized Maintenance Management System (CMMS). The strategy that has been made well must be executed properly as well. This paper will describe how the Maintenance division of Pertamina Geothermal Energy Lumut Balai developed an innovation called "At cost based-Annual Maintenance Contract", a maintenance contract scheme that ensures all Preventive Maintenance (PM) programs are executed well as scheduled in the CMMS. This is a new fresh Innovation that has not been implemented before in any of the Geothermal areas owned by PT Pertamina Geothermal Energy and has been proven to improve the quality of Preventive Maintenance activities on GPP and FCRS equipment.

1. INTRODUCTION

PT Pertamina Geothermal Energy Area Lumut Balai (PGE LMB) is one of the areas owned by PT Pertamina Geothermal Energy. Located in Muara Enim, South Sumatera province, PGE LMB currently has a generating capacity of 55 megawatts. generated by PLTP Unit 1 that belongs to PT Pertamina Geothermal Energy. The Contract that is owned is an Electricity Purchase Agreement. PGE Lumut Balai has been operating since 2019.

The Lumut Balai Geothermal Area is the most remote area owned by PT PGE. With the remote condition, an on-off work system is applied for workers in the Lumut Balai area. There are many challenges with this remote condition, one of which is the challenge of maintaining the reliability of the Geothermal Power Plant and FCRS equipment owned by PT PGE Lumut Balai. PGE already has a lot of experience in managing the maintenance of GPP equipment and its FCRS. However, with the conditions of field workers with a daily work system, not an on-off system. In this paper, the author will describe the strategy of the maintenance function in running the Preventive Maintenance (PM) program optimally with an on-off work system.

2. INNOVATION PROCESS AND RESULT

As a company that has experience in the field of geothermal energy generation, PT PGE has prepared a maintenance strategy for GPP and FCRS equipment. The cycle in performing maintenance on this equipment can be seen in the scheme below.

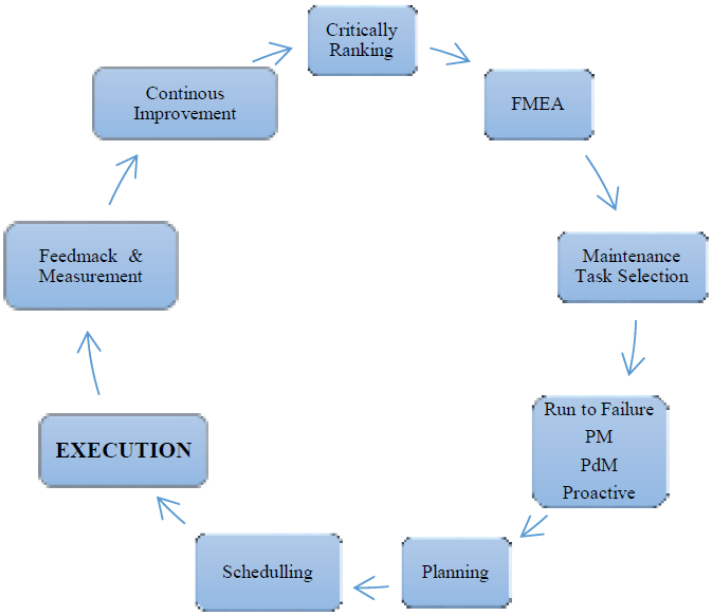

Figure 1: Maintenance Strategy Process PT PGE.

PT PGE's revenue is strongly influenced by the reliability and availability of PLTP and its facilities. Maintaining availability and reliability requires an effective maintenance execution strategy. Optimization of manpower in the implementation of PM and CM is needed so that PGE workers can stay focused on analyzing equipment so that availability and reliability are maintained for long-term operations. In this paper, the author will focus on the execution stage where this execution step is the responsibility of the maintenance area division.

2.1 Planning

As an initial step, the author conducted a SWOT analysis of the situation on PT Pertamina Geothermal Energy Area Lumut Balai.

Table 1: SWOT Analysis.

STRENGTH	WEAKNESS
1. Already have a Reliability Centered Maintenance-based PM strategy 2. Using CMMS (My SAP) 3. Have experienced workers in the implementation of PM	1. Still relying on Supporting Manpower Contract ("TKJP") for PM implementation 2. TKJP is a lump sum contract that does not have a PM completion target/KPI.
OPPORTUNITY	**THREAT**
1. There is no other system apart from relying on TKJP for PM activities. 2. Support the company's efficiency program 3. Improving operational excellence to carry out the mission and achieve the company's vision	1. The location of the area is very remote. 2. Limited capability of the surrounding human resources.

In 2020, there were 2,928 maintenance items or equivalent to 12,044 working hours for each work center (rotating, non-rotating, electrical, instrument, and operation). With this amount, a minimum of 12 additional personnel is needed for PM activities for a year. With the needs of these 12 people, two alternative solutions can be done:

1. Using the TKJP system (Lum Sump-Based Supporting Manpower Contract)
2. Using a performance-based Annual Maintenance Contract system.

The study was carried out with the following results:

Table 2: Study Results.

Parameter	TKJP (Existing) Lum sump-Based Supporting Manpower Contract	AMC (Innovation) Performance-based Annual Maintenance Contract system
Work- Supervision	The workforce is directly under the supervision of PGE workers	The workforce is under the supervision of a contractor who reports to PGE workers
Safety-Supervision	Safety Monitoring by PGE internal Safety Officer	Safety Monitoring day by day carried out by the Contractor's Safety Officer
Implementation	Easy	Difficult (never done before at PGE)
Activity Report	Simple Report	Daily, Weekly, and Monthly Reports by the contractor
Payment	Monthly/fixed wages, not dependent on work orders	Wages according to work realization/number of work orders

With the various advantages provided by the AMC system, AMC was chosen to be implemented in the Maintenance Division with this structure:

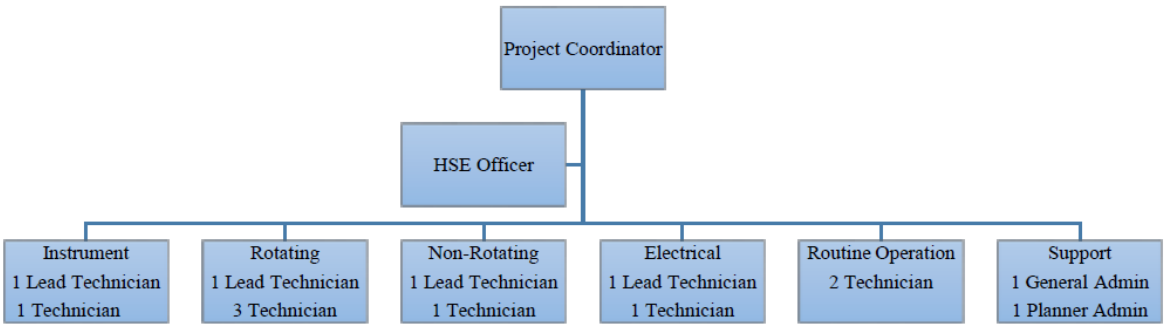

Figure 2: Annual Maintenance Contract Organization Structure.

After developing the organization structure, we develop a formula of the man-our tariff as a basis of the Annual Maintenance Contract. We obtain the formula with the following steps:

1. Calculate the total man-hour needed for annual contract maintenance.
2. Calculate the total manpower needed
3. Calculate total cost for all manpower needed
4. Determine man-hour rate by dividing the total cost (point 4) with the total man-hour (point 1)
5. Man-hour tariff is obtained. Used as the basis of the man-hour value/tariff in the AMC contract.

The flow process of the Annual Maintenance Contract is as follow:

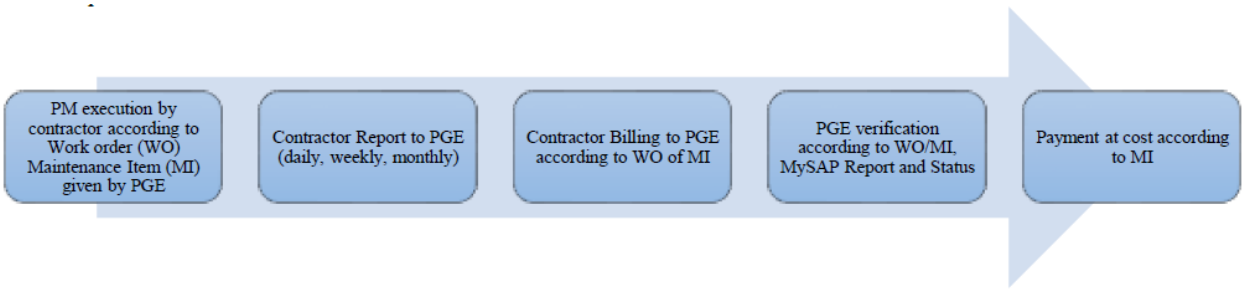

Figure 3: Annual Maintenance Contract Work Flow.

2.2 Implementation

The innovation of annual maintenance contract has already been implemented at PT PGE Lumut Balai since May 2020.

No.	Activity	Photo
1.	Preventive and Corrective Maintenance Activity	
2.	Report Of PM and CM Activity	

3. CONCLUSIONS

From the explanation above, it can be concluded that the implementation of the Annual Maintenance Contract is quite effective in improving the quality of Preventive Maintenance works. From the graph below we may see that completion of work orders in 2020 was 95% for PM and Overall, 91% for both Preventive Maintenance and Corrective Maintenance. This innovation could be adopted in any geothermal field, especially for remote fields with an on-off working system to make sure all of the Planned work is executed on time and well.

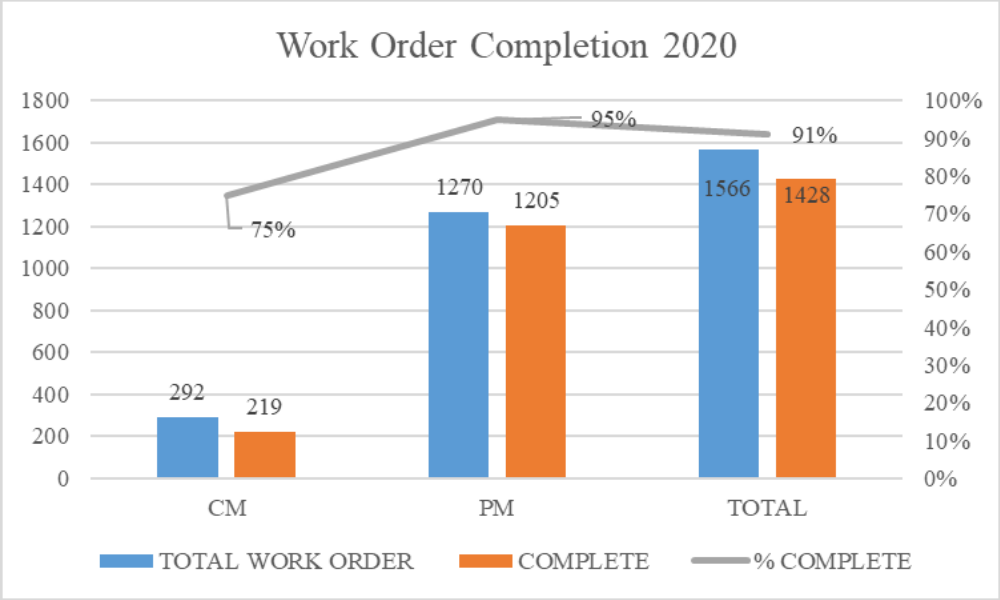

Figure 4: Work Order Completion PT PGE Lumut Balai Year 2020.

REFERENCES

PGE: Maintenance Lumut Balai.: Laporan Monthly PM Activity, PGE Lumut Balai (2020).

PGE: Maintenance Lumut Balai.: Laporan Tahunan Fungsi Maintenance, PT PGE Lumut Balai (2020).

SWOT Analysis for Geothermal Enhanced System (EGS) As New Technology for Geothermal Development in Indonesia

Sulistyorini Widi Hastuti, Andi Novita Mama Anugrah, Konita Nafista, and Ashabul Kahfi Ilham

Petroleum Engineering Department, Faculty of Mineral Technology, UPN Veteran Yogyakarta

sulistyoriniwh88@gmail.com

Keywords: drilling technology, enhanced geothermal system (EGS), environmental attribute, geothermal, reservoir development, SWOT

ABSTRACT

Geothermal systems are usually associated with volcanic systems formed along island arcs due to plate movement on the earth's surface, which causes volcanoes and becomes a source of geothermal energy. The vast source of geothermal energy as an alternative to renewable energy gives Indonesia have the opportunity to convert energy into environmentally friendly energy, such as geothermal. Based on a survey conducted by the Directorate of Vulcanology and Pertamina, with the assistance of the France and New Zealand governments, there are about 256 geothermal prospects in Indonesia. At the same time, only 46 projects have been utilized, or 8.9%. Technology related to geothermal energy is currently developing from conventional to non-conventional methods, namely the dynamic geothermal system (natural geothermal system), beginning to move towards the Enhanced Geothermal System (EGS). Enhanced Geothermal System (EGS) is a non-conventional method in engineering reservoirs on barren, hot dry rocks. It includes hydrothermal sources of low permeability or low fluid saturation of the surrounding rock. EGS is done by injecting high-pressure fluid to form more permeability, and heat can be lifted to the surface. Conditioning of low permeability reservoir is done by creating hydraulic fracturing in a large volume to allow more significant and more effective heat transfer. This paper will discuss the strategy of an enhanced geothermal system in Indonesia to study the components of EGS resource, technology for EGS Reservoir Development, development of EGS drilling technology, and environmental attribute of the EGS power project. The methodology used is a SWOT analysis by examining the potential for developing an enhanced geothermal system through four dimensions: strengths, weaknesses, opportunities, and threats. The results of this study, namely the presence of EGS technology in Indonesia, the geothermal potential is likely to be increased more than five times or more. In addition, it is expected to provide understanding and description of EGS technology in geothermal development by taking into account environmental, economic, and ecological issues so that geothermal utilization can be carried out optimally for the future.

1. INTRODUCTION

Heat stored within and flowing through the earth's crust is an energy source that can be explored and exploited in almost all locations. Based on the type of exploitation, geothermal systems can be divided into traditional geothermal (hydrothermal) systems and enhanced geothermal systems (EGS). Conventional geothermal power systems have been developing for approximately 100 years; therefore, power generation technology is mature. Meanwhile, EGS is a new technology developed to access heat by creating artificial fractures in the hot rock and injecting the liquid. Currently, geothermal technology applied to a dynamic geothermal system (natural geothermal system) moves towards an Enhanced Geothermal System (EGS) in sedimentary basins and hot dry rocks. Enhanced Geothermal Systems (EGS) is an energy source that can be used in almost any location. The heat in the earth's crust is extracted by circulating hot air or fluids in artificially engineered fracture systems in hot rock. Applying this system requires an area with dry and scorching rock so that its application is of commercial value. Based on the studies that have been carried out, the western Indonesian basin is a possible area for the development of EGS. It can produce energy up to 110 MW/km with the most extensive theoretical potential (Hendrawan and Draniswari, 2016). EGS is expected to be a clean and renewable energy source because it emits few greenhouse gases (USGS, 2012). In addition, EGS has the advantage that the utilization of this system will continue as long as the hot rock in the reservoir can still be drilled and broken so that the heat contained in the stone can be extracted and used sustainably.

Objectives

This study aims to identify and discuss strategies for improving the geothermal system in Indonesia with EGS technology. In addition, it can find out the components that make up the EGS resource, EGS reservoir development technology, EGS drilling technology development, and environmental attributes of the EGS power plant project. Using SWOT analysis can see the potential for EGS development in Indonesia.

2. METHODOLOGY

To answer the problems and objectives of this study, the authors chose the SWOT analysis method to see all the factors of the enhanced geothermal system technology in the form of strengths, weaknesses, opportunities, and threats. The results of this analysis are expected to be a new technology that is effective and efficient in geothermal management. The data used in this study are secondary qualitative data related to SWOT from various works of literature and opinions from previous authors and the views of multiple sources regarding conditions in exploration and exploitation of geothermal energy in Indonesia.

SWOT analysis

SWOT analysis is a problem-solving technique to assess the performance, competition, risk, and potential of the variables we consider. This analysis aims to understand Indonesia's development of an enhanced geothermal system regarding strengths, weaknesses, opportunities, and challenges. Hence, we conduct a SWOT analysis by observing every political, economic, social, technological, ecological, and environmental aspect.

Table 1: SWOT Analysis of Enhanced Geothermal System (EGS).

Strength	Weakness
● EGS emits little to no greenhouse gases and carbon neutral ● Has great potential as a sustainable energy source ● The economic lifetime of 20–30 years using current technology ● Baseload resource that can generate power 24 hours/day ● State revenue potential with this technology	● Upfront costs of project development are very high ● A significant amount of water used ● Limitations of experienced professionals in the industry, government, and research sectors ● Limited records in the long-term operation of EGS projects and technology ● Difficult to maintain the economic flow
Opportunity	**Threat**
● EGS has the potential to be an essential contributor to clean and renewable energy sources ● Public demand for low emission carbon ● Advanced EGS technologies are young and still underdeveloped. EGS has been successfully realized on a pilot scale ● Carbon sequestration potential with CO_2 based EGS technology ● Development of national and global policies to reduce fossil fuel usage ● Knowledge developed from experimental, theoretical, and numerical research work	● Social license to operate may be threatened by hydraulic fracturing ● EGS investment is considered unprofitable because there is a risk of return ● Uncertain market conditions due to inconsistent energy policies ● Perception in marketing assumes that EGS technology is high risk ● During fracturing, there is a potential for induced seismicity

3. RESULT AND DISCUSSION

The following are the results and discussions related to enhanced geothermal system (EGS) technology, namely swot analysis EGS, the component of EGS resource, technology for EGS reservoir development, development of EGS drilling technology, environmental attribute of EGS power project, the impact of EGS implementation.

3.1 SWOT analysis

Based on SWOT analysis of Enhanced Geothermal System (EGS) can be summarized as:

3.1.1 Strength

Based on the analysis carried out, it can be seen that the power of EGS is feasible anywhere. In hot dry rock reservoirs, when the air is injected into the well, it will be heated faster and produce steam with high intensity so that it has the potential to generate electricity. In addition, because geothermal is one of the renewable energies, energy availability has a cycle so that the supply of steam is maintained. The EGS treatment system as a renewable energy source to produce electrical energy involves the extraction of hot water from the ground and converting the thermal energy into electrical energy, where only the power plant is located on the surface, the rest of the distribution line is underground. This condition is favourable, where there are no greenhouse gases or other emissions and wastes that come out into the air. The absence of greenhouse gas production will indirectly reduce global warming and climate change.

The application of EGS technology makes geothermal wells have a longer life of about 20-30 years; this is because the reservoir rock is a hot dry rock that is quite close to the geothermal source. The rock is predicted to produce heat continuously. Using this technology to produce power plants can fulfil electricity supply because geothermal can provide electricity 24 hours per day. By looking at the strength of EGS technology, it offers many benefits when applied to geothermal wells with hot dry rock characteristics. Thus, geothermal projects can be used massively in Indonesia.

3.1.2 Weakness

Based on the SWOT analysis, it can be seen that EGS has a weakness. To overcome this weakness, the thing that can be done is to make the EGS project attractive so that investors are attracted to invest so that initially expensive costs can be overcome. In addition, policies can also be made for business schemes in EGS, especially in the exploration stage. The business scheme that is implemented will certainly benefit both parties, namely investors and related companies. According to the U.S. Department of Energy (DoE), the large-scale development of EGS, the operation and establishment of unique technology can be a strategic tool to improve EGS performance (Ziagos et al., 2013). This technological breakthrough will later minimize the uncertainty that is often encountered in EGS investments. Can facilitate reservoir performance in the long term so that production can be of economic value. In addition, it is worth noting that considering the current state of technology and industry challenges, involvement of the private and public sectors in innovative research is recommended to overcome the existing restrictions. Furthermore, gaining public and understandable acceptance and providing financial and political incentives will lead to safe, environmentally friendly and commercially viable EGS technologies (Kumari and Ranjith, 2019).

EGS requires a lot of water to produce steam from hot dry rock. The large consumption of water in the reservoir can lead to contamination due to the injection of additional chemicals and noise and disturbance associated with drilling (Evans et al., 2012). So that before exploration, a site survey related to the availability of water in the area can be carried out. Then, several injection wells were carried out for water supply when production activities were carried out. Meanwhile, due to limited human resources and technology, this is still relatively new, so there is a need for training from experts in the EGS field. The movement will certainly increase our knowledge of the use of EGS technology because most failures in this technology are caused by a lack of professionals and experts in their fields. The most important thing before carrying out the project is determining the long-term planning of what actions will be taken to keep the wells producing optimally.

3.1.3 Opportunity

Key opportunities in the development of the EGS system are seen in the environmental impact of fuel. Replacement of fossil fuels and other energy sources affected by emissions or reduced efficiency such as air-based heat pumps and chillers and biomass-based heating. Heating and cooling provided by the same system are also seen as an asset for future investment and national support legal framework that is in line with climate change mitigation and environmental protection policies. By utilizing EGS in peak power supply, able to take advantage of the political push for electrification of heat demand and integrated heat/energy systems.

Opportunities that are carried out to reduce CO2 emissions can be reached with technology that can capture and store carbon (CCS). CO_2 as fluid for combined carbon storage and geothermal extraction in the Enhanced Geothermal System (EGS). The characteristics of CO_2 as a working fluid were compared from a thermophysical and thermodynamic perspective, and the solubility of CO_2 in reservoir fluids with different ionic strength, pressure, and the temperature was analyzed. N.S. the effect of artificial stimulation on the permeability of the EGS reservoir is described. The experiment of supercritical alternating water heat extraction CO2 (SC CO2) Cycle injection analysed the effect of CO2 -liquid-rock interaction on reservoir structure and mineral dissolution and precipitation on geological CO2 storage (Wu and Li, 2020).

EGS has been successfully realized on a pilot scale in Europe and is now in three DOE-funded pilot projects in the U.S. in 2013. Extending the life of unproductive wells using new technology is one example of this innovation. EGS technology uses directional drilling and pressurized water to improve flow paths in subsurface rock and create new reservoirs, capturing energy from previously uneconomical or unrecoverable resources. With an increased injection rate of up to 1500 gpm, well stimulation at Desert Peak generates new revenue, greater resource reserves and production certainty, increasing investor confidence. The success of Desert Peak demonstrates that EGS technology is within reach, supporting research and development investments across the Department of Energy's renewable energy and oil and gas portfolio. American companies like Ormat Technologies are now leveraging this untapped resource. (Ormat Technology, 2013)

By looking at the EGS opportunities that several developed countries have carried out, it can be concluded that EGS-based geothermal projects can be developed massively in the future. Provided, opportunities in carrying out future strategies should also be actively promoted at all levels of public activity to increase general awareness of EGS. Shallow geothermal energy should be implemented in national and local energy plans. Legislative procedures should be harmonized and simplified.

3.1.4 Threat

Several threats have been identified. Arguably, the sector's biggest danger is that the social license to operate could be jeopardized by hydraulic cracking due to fracturing that does not occur naturally. Any industry, especially those still in the early stages of technology development, faces threats to successful operations in the market. Inadequate exploration and characterization of resources can result in a high failure rate for trying and unfavourable options for investors. However, it is not unique in terms of energy system control regulation; it is a serious problem for the widespread deployment of EGS technology. Ultimately, the most serious threats arise from untested or immature technologies, with high capital costs and high-risk perceptions in financial markets. So far, geothermal energy has failed to attract investment due to inconsistent energy policies, so the sector will languish and be unable to deliver cost-effective technology deployments.

To overcome this problem, what can be done is to provide incentives that can attract investors to develop geothermal energy by developing comprehensive policies that provide clarity for investors to invest in the geothermal sector. Perform technological breakthroughs that minimize uncertainty over EGS development and facilitate long-term reservoir performance to ensure that production levels remain economical.

3.2 Component of EGS resource

Several EGS resources are located in rock formations dominated by basement rocks with low permeability by considering several things, namely heat flow, geothermal gradient, thermal conductivity, temperature, fracture rock volume, fracture spacing, and fracture surface area.

3.2.1 Heat flow

In terms of geology, EGS is composed of granite with the assumption of uniformity of rock types. From a more practical point of view, lithology can affect the flow of heat in radioactive content and the flow of heat generated. Areas of high radioactivity will have a more increased heat flow and have a high temperature as well.

3.2.2 Thermal gradient

The thermal gradient of the EGS reservoir in the sediment section can be found by dividing the heat flow by the thermal conductivity, as shown in the following Figure 1.

An extensive BHT (Bore Hole Temperature) data set is used, a new feature of the heat flow and temperature maps with the analysis used in previous studies. This additional data improves the definition of areas that qualify for further EGS evaluation.

3.2.3 Thermal conductivity

Calculate temperature EGS at a depth of vertical thermal conductivity ordered by depth in one or two layers. This value-based is on median bedrock values from the regional heat flow database.

3.2.4 Temperature

The rate of heat extraction from rock depends on the difference between the temperature of the rock and the circulating air temperature at any point in the reservoir. In an EGS reservoir, the heat extraction rate must be equal to the product of the mass flow rate and the specific enthalpy difference between the liquids produced by reinjection.

3.2.5 Fractured rock volume

In EGS wells, a configuration can be done in various ways, namely with one manufacturer for each injector (doublet), two manufacturers for each injector (a triplet), or four manufacturers for each injector (the classic five-point pattern used in Enhanced recovery oil operations). The stress regime in the rock volume will determine the fracture pattern and direction, which will influence the optimal injector and producer settings.

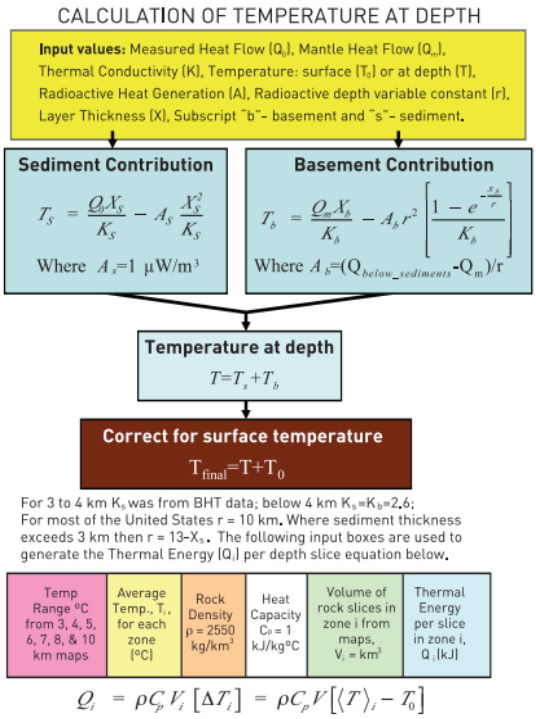

Figure 1: Flow chart for calculation of temperature and heat content at depth (Systems, 2006).

3.2.6 Fracture spacing

Based on the research conducted by Sanyal and Butler in 2005, it is known that the crack volume has the most significant influence on the recovery factor from the parameters studied, the fracture distance in the EGS reservoir has a measurable effect because it is part of the determination of the active reservoir volume.

3.3 Technology for EGS Reservoir Development

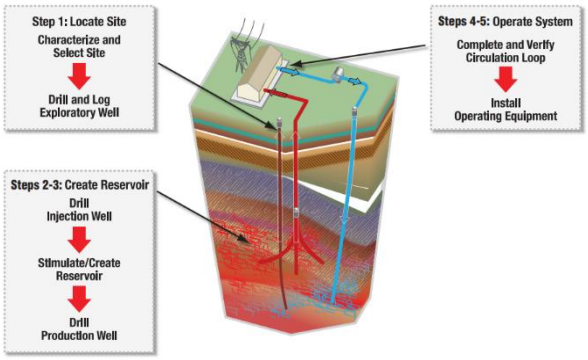

Figure 2: EGS Development Sequence (DOE, 2008).

Based on a study conducted by MIT (Massachusetts Institute of Technology), EGS technology is carried out with a solid basis for evaluating available technologies from various fields to estimate their usefulness for EGS applications. In assessing this technology, EGS reservoir development has been represented as a multi-step decision process. The goal of this process is to create an economic EGS reservoir with the logical steps that must be taken to complete the EGS economy, which are:

3.3.1 Finding the site characterization

The first step in creating an EGS reservoir is to determine the exact location. Determination of the area must be carried out appropriately by considering the characterization of the site based on temperature gradients and heat flow, stress fields, lithology and stratigraphy, structures and faults, in situ fluids and geochemistry, geological history, seismic activity, proximity to transmission, land availability, and demographics.

3.3.2 Exploratory well and reservoir characterization

This stage should be carried out on exploration wells, either boreholes or full-scale injection wells. Wells such as these to measure and confirm reservoirs do not have to be part of the final EGS reservoir. In determining the location of exploration wells and reservoir characterization, observations can be made based on a short time, namely:

- Subsurface conditions
  The stress measurement is based on the breakdown of natural rock in the wellbore wall and "mini-frac" with the technological status, direction, and magnitude of stresses estimated from limited test capabilities.
- Conduct flow tests

Performing flow tests, pressure, temperature, and fluid flow gauges are technologically state-of-the-art, with downhole instrumentation suitable for standard flow tests available up to 200ºC.

- Perform stress measurements
  Micro-frac track and borehole measurements with the most advanced technology available for low-temperature applications and lack zone isolation capabilities.
- Interpret data to plan stimulation
  In this stimulation model, the availability of technology predicts the effect of stimulation on the formation and growth, with the technology being ineffective in the geothermal environment.

3.3.3 Injection well

After the initial characterization activities are completed, reservoir development can be continued with the initial injection well drilling. Drilling planning begins with collecting reservoir rock information data (e.g., temperature, stress field, lithology, and structure). After that, it will be continued by discussing the adequacy of drilling technology flows for EGS applications, including reducing rock, steer direction well, complete well, isolating zones during drilling, logging wells, monitoring well parameters, and interpreting data to plan stimulation.

3.3.4 Stimulation

Based on MIT's (Massachusetts Institute of Technology) research, what needs to be done for reservoir stimulation is to create large volumes of rock cracks. Fracture fluids must be pumped at high pressures and flow rates and a high-precision seismic monitoring network for stimulation. Reservoir stimulation aims to provide an abundant fluid flow path between the injection well and the production. These flow paths must have a minimum impedance to reduce pumping power requirements, but the residence time and surface area must be adequate to maintain hot liquid production.

3.3.5 Completion well field

After the initial volume is stimulated by opening and creating a new fracture, circulation can be carried out by drilling production wells. In production well drilling, directional drilling is required to cut the fractures during initial well stimulation. Measurement of the acoustic signal generated by the stimulation is used to describe the fracture zone.

3.3.6 Operating and maintenance reservoir

EGS technology is intended to produce energy over a long period without resorting to expensive repairs. Operationally, the EGS well must function at high pressures and flow rates with injection and production modes for many years.

3.4 Development of EGS drilling technology

Several technologies deemed necessary for the development of EGS drilling are expected to be more related to general capabilities in the EGS well construction process. The technology in EGS indeed uses more complex technology than conventional geothermal drilling.

3.4.1 High-temperature technology

Some applications for high-temperature drilling technology in geothermal well drilling. Some of the technologies used in EGS are more complex than geothermal drilling in general.

- The electronic component (>200ºC)
  In EGS with hot dry rock, a technology used in well drilling is essential. Higher temperature geothermal applications usually prevent their use due to the device's temperature limitations (Polsky et al., 2009). Regardless of the specific function (sensor modality), some supporting components are required to operate all downhole tools. Some elements allow drilling EGS and logging tools at high temperatures, such as processors, muti chip modules (MCMs), Higher bit converters, field-programmable gate array, large memory arrays, batteries, and oscillators. The use of the tool should be considered in the context of whether it is suitable for hot dry rock geothermal formations, potential problems with log interpretation, and how information and well construction improve EGS implementation.
- Complicated rock directional drilling tools
  Ultra series motor with MWD tool is one of the directional drilling technologies based on keeping electronic components cool through drilling mud circulation. The implementation and development of targeted drilling need to be discussed to assess and promote the implementation of EGS. Directional tools, steering tools, and measurement while drilling tools have been improved for use at higher temperatures and are in everyday use in geothermal drilling (Systems, 2006).
- Production and service isolation tools
  The isolation capability of the zone is currently considered critical for EGS production and intervention practice. The application of existing tools in geothermal applications is mainly influenced by the temperature limits of the elastomeric components, differential pressure capabilities, and maximum inflation diameter.
- Pumps
  A high-temperature submersible pump will be required to facilitate the production of the EGS liquid. Although significant improvements have been developed to this technology, most of them are evident in the large, wellbore, high-temperature environments expected for EGS. There is a need for research to advance this technology to meet the needs of EGS.

3.4.2 Logging tools

A 300 °C geothermal well monitoring tool is being developed to support EGS (enhanced geothermal system) drilling. The logging used is an analog device designed to monitor the pressure and temperature of 3 different circuit topologies and software development and supporting surface electronics (Normann et al., 2015). The main component is the cable used to connect the analog device to the surface. Logging trucks equipped with high-temperature lines are now more common, but not without additional costs (Tester et al., 2006).

3.4.3 Thermal expansion of the casing

In hot dry rock drilling with high temperature so that it’s possible to occur. Thermal expansion can cause casing buckling and casing collapse, thus requiring costs. At EGS, Full casing cementing and surface expansion spools can be used in this temperature range

with confidence above 260°C (500°F) operating temperatures. More outstanding care must be taken to accommodate thermal expansion or contraction effects. In addition, expandable tubular is used to primarily mitigate telescoping effects by reducing the magnitude of diameter change between intervals (Polsky et al., 2009).

3.4.4 Drilling fluid

Surface mud coolers are typically used to reduce the drilling fluid temperature before being pumped back into the well. A slurry cooler should be commonly used if the return temperature exceeds 75°C (170°F), as the high mud temperature is an explosive hazard to rig personnel.

3.4.5 Drill bit for increasing ROP

Drilling through complex formations needs to be upgraded with new bearings, improved heel row designs, improved carbides, and polycrystalline diamond coatings. Conical roller bearing bits prove to be quite effective on complex formations. However, the rate of cutting structure wear in cracked and abrasive formations can still be a problem, and bit life in deep geothermal drilling is still limited to less than 50 hours in many applications.

3.5 Environmental attribute of EGS power project

The EGS geothermal power plant operates in a closed-loop. The circulation also provides environmental benefits by having minimal greenhouse gases and emissions. Geothermal, like other renewable resources, can reduce dependence on imports of fossil fuels because it allows for real help that can be geothermal even at high storage levels does not require storage or reserves.

- No greenhouse gas emissions during operations
  The development of EGS is considered environmentally friendly because the process uses circulating water as a conductor of hot steam from hot dry rock. In addition, the geothermal power plant built on top of the EGS reservoir uses a "closed-loop" cycle so it will not emit carbon dioxide (CO_2). So that the closed-loop process does not have greenhouse gas emissions.
- Modest use of land
  The land use of the Enhanced Geothermal System (EGS) plant is much less than that of fossil fuel, nuclear, or solar power plants. The land used is also not fully occupied by wells because it can also be used for agriculture and livestock. In addition, these EGS plants do not have to be tied to hydrothermal areas, so locating them within populated and industrial districts is much more possible with clear advantages over fossil or nuclear plants.
- Possible sequestration of CO_2

  CO_2 as a heat transfer fluid reservoir at high-pressure levels. Considering CO_2 has chemical and thermal properties that can be used as a heat transfer medium—in an EGS plant, using water as the fluid can cause water loss in commercial operations. Still, in an already running plant, CO_2 failure can result in geological absorption of CO_2, which can be a secondary benefit. Besides being able to store CO_2 in the reservoir, another benefit of CO_2 as a fluid for EGS is that the actual heat flow rate from the reservoir can be five times greater than the heat flow rate using formation brine as the working fluid. CO_2 is not an ionic dissolution product, so it does not cause significant dissolution/precipitation problems. The comparison between CO_2 and water as a working fluid in an EGS geothermal power plant can be seen in the following Table 2.

Table 2: The comparison between CO2 and water as a working fluid in an EGS geothermal (Pruess, 2006).

Fluid Properties	CO_2	H_2O
Chemical	Not an ionic dissolution product. No mineral dissolution/ precipitation problems	Anionic dissolution product. Serious problems of mineral dissolution/precipitation.
Fluid circulation in wells	High compressible and expandable	Low compressibility. Moderate expandability
Ease of flow in the geothermal reservoir	Low viscosity and density	High viscosity and density
Heat transmission	Low specific heat level	High specific heat level
Fluid losses	Could result in beneficial geological storage of CO_2	A hindrance to the development of geothermal reservoirs. Costly.

- Low overall environmental impact
  EGS has an impact comparable to that of a binary hydrothermal plant operating with closed-loop circulation. Because it is the only area that can ultimately reach the reservoir target before drilling or stimulation if using the geoscientific method. Considering all the existing technologies to generate large amounts of electric power and a social, environmental impact, EGS is the best technology because it can increase or create geothermal resources in hot dry rock (HDR) through various stimulation methods.

3.6 Impact of EGS implementation

Applying EGS in different geological settings, various and site-specific issues must be evaluated, from environmental, socio-economic impacts, geological and technology problems. (Figure 3).

3.6.1 Environmental

EGS technology is environmentally friendly because no greenhouse gases or other emissions are produced, there is no intrusion into the soil or waste to be disposed of and stored. However, due to the bottomless water injected into the ground, and the restricted zone, the potential of EGS to influence the hydrogeological regime and effects of thermochemical diagenesis also needs to be considered. In addition, the problem that must be considered when the EGS reservoir is stimulated is the micro-seismic that causes the existing cracks to reopen, which is called a minor earthquake. These events are monitored as acoustic emissions determine the extent to which

the reservoir is stimulated. So, a thorough assessment of the existing environmental impacts must be carried out with the planned EGS project.

3.6.2 Socio-economic

The impact of social acceptance of EGS technology brings many benefits to the community, such as employment opportunities, local development (agriculture, tourism, etc.). On the other hand, many opinions from the public and aversion to change increase in building large industries. The critical problem with EGS power plants is cost. Factors that become the problem are divided into capital costs (exploration and drilling, stimulation, and distribution facilities), operating and maintenance costs over the projected lifetime of each existing facility. According to Sanyal et al., 2007, these costs for 2050 are based on minimal data obtained to date from crucial installation areas. It was found that for a reservoir of at least 5 billion cubic feet (about 0.14 km3), which is homogeneous and isotropic as sub-horizontal and for a system, the electricity production capacity is several hundred M.W. However, there are likely to be significant developments in EGS technology over the next 40 years, making the technology more efficient as reservoirs more substantial than 5 billion cubic feet. Therefore, there is a good possibility for the electric EGS technology to be commercialized in the following year.

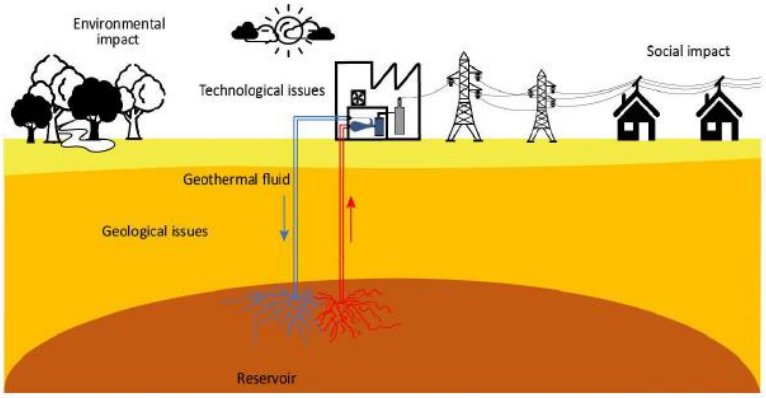

Figure 3: Graphical overview of enhanced geothermal systems implementation and integration (Bilic et al., 2018).

3.6.3 Geological and technology issues

Most of the heat energy is in the "basement" rock beneath the sediment. It is considering that the basement is an area of metamorphic rock or igneous rock with very varied composition and lithology. The quantification of favourable rock composition and structure in the development of EGS remains to be done. Some experimental EGS sites are in granite in bulk composition but still have some intrinsic permeability and porosity. Modelling by Nalla and Shook (2004) indicated that even a small amount of inherent porosity and permeability increases heat extraction efficiency. These types of rocks may be better EGS hosts than true granite. Thus, there is a natural path from hot gas reservoir stimulation and production to EGS reservoir development in both technology and location.

4. CONCLUSION

The strategy for improving the geothermal system in Indonesia with Enhanced Geothermal Systems (EGS) technology. From a SWOT analysis of Enhanced Geothermal Systems (EGS), it can be seen that EGS can be a strategy for improving geothermal systems in Indonesia. The components that make up the EGS include heat flow, thermal gradient, thermal conductivity, temperature, the volume of fractured rock, and fracture distance. Reservoir technology development includes Finding the Site Characterization, Exploratory Well and Reservoir Characterization, Injection Well, Stimulation, Completing the Well Field, and Operating and Maintenance Reservoir. Meanwhile, development is carried out from drilling technology with High-Temperature Technology, Logging Tools, Thermal expansion of casing, fluid or drilling mud, Drill bits to increase ROP. Environmental attributes of the EGS power plant include No greenhouse gas emissions during operation, Moderate land use, the Possibility of carbon dioxide sequestration, Low overall ecological impact. The SWOT analysis that EGS has carried out can be developed in Indonesia by considering environmental, socio-economic, and geological conditions and based on the availability of EGS technology in Indonesia.

REFERENCES

Bilic, T., Rajšl, I., Ilak, P., Raos, S., Šadek, S., Krajcar, S., Debrecin, N., Genter, A., and Leoutre, E.: Overview of techno-economic issues of enhanced geothermal systems implementation and integration, *IET Conference Publications*, (2018), (CP759). https://doi.org/10.1049/cp.2018.1872

DOE: An Evaluation of Enhanced Geothermal Systems Technology, *U.S: Department of Energy*, (2008), 1–37. papers2://publication/uuid/05E2BD91-8E8D-46D7-BF78-1ACE08256F93

Evans, K.F., Zappone, A., Kraft, T., Deichmann, N., and Moia, F.: A survey of the induced seismic responses to fluid injection in geothermal and CO2 reservoirs in Europe, *Geothermics*, 41, (2012), 30–54. https://doi.org/10.1016/j.geothermics.2011.08.002

Hendrawan, R.N. and Draniswari, W.A.: The Possibility of Enhanced Geothermal System in South Sumatra Basin, August, (2016).

Kumari, W.G.P. and Ranjith, P.G.: Sustainable development of enhanced geothermal systems based on geotechnical research – A review, *Earth-Science Reviews*, 199, (2019), 102955. https://doi.org/10.1016/j.earscirev.2019.102955

Normann, A.R.A., Llc, P.W., and De-fg-go, G.: Developing 300 ° C Analog Tool for EGS, (2015), 1–44.

Polsky, Y., Blankenship, D., Mansure, A.J., Swanson, R.J., and Capuano, L.E.: Enhanced geothermal systems well construction technology evaluation, *SEG Technical Program Expanded Abstracts*, *28*(1), (2009), 4331–4332. https://doi.org/10.1190/1.3255790

Pruess, K.: Enhanced geothermal systems (EGS) using CO2 as working fluid-A novel approach for generating renewable energy with simultaneous sequestration of carbon, *Geothermics*, *35*(4), (2006), 351–367. https://doi.org/10.1016/j.geothermics.2006.08.002

Sanyal, S.K., Morrow, J.W., Butler, S.J., and Robertson-Tait, A.: Cost of Electricity from Enhanced Geothermal Systems, *Thirty-Second Workshop on Geothermal Reservoir Engineering*, 11, (2007). https://pangaea.stanford.edu/ERE/pdf/IGAstandard/SGW/2007/sanyal1.pdf

Systems, E.G.: The Future of Geothermal Energy, In *Technology: Vol. I'm* (Issue November), (2006). http://www.eere.energy.gov/geothermal/pdfs/structure_outcome.pdf

Tester, J.W., Anderson, B.J., Batchelor, A.S., Blackwell, D.D., and DiPippo, R.: The Future of Geothermal Energy - Impact of Enhanced Geothermal Systems (EGS) on the United States in the 21st Century, *MIT - Massachusetts Institute of Technology*, (2006), 358. www1.eere.energy.gov/geothermal/pdfs/future_geo_energy.pdf

US Department of Energy: "What is an Enhanced Geothermal System (EGS)?", September (2012). http://energy.gov/eere/geothermal/enhanced-geothermal- systems-0 (accessed July 30, 2021).

US Department of Energy: “Enhanced Geothermal Systems Demonstration Projects”, April (2013). https://www.energy.gov/eere/geothermal/enhanced-geothermal-systems-demonstration-projects (accessed, September 11, 2021).

Wu, Y. and Li, P.: The potential of coupled carbon storage and geothermal extraction in a CO2-enhanced geothermal system: a review, *Geothermal Energy*, 8(1), (2020). https://doi.org/10.1186/s40517-020-00173-w

Ziagos, J., Phillips, B.R., Boyd, L., Jelacic, A., Stillman, G., and Hass, E.: A technology roadmap for strategic development of enhanced geothermal systems, *Proceedings*, The 38th Workshop on Geothermal Reservoir Engineering, Stanford, CA, (2013), 11–13. https://pangea.stanford.edu/ERE/db/GeoConf/papers/SGW/2013/Ziagos.pdf

Opportunity of Geothermal Energy Direct Use for Agriculture in Indonesia

Rizki Edi Nugroho, Iqbal Ipmawan Yogatama, and Andri Wibowo

UPN "Veteran" Yogyakarta
Jalan SWK Jalan Ring Road Utara Nomor 104, Kecamatan Depok, Kabupaten Sleman, Daerah Istimewa Yogyakarta

andriwibeww@gmail.com

Keywords: geothermal, direct use, agriculture

ABSTRACT

Indonesia is a country with one of the largest geothermal energy resources in the world, with a potential of more than 23.9 GW. As a country with high potential of geothermal resources, Indonesia focusing the development of geothermal energy for electricity. However, Indonesia also takes advantage of geothermal resources in other sector which can be applied for direct use applications such as tourism, aquaculture, agriculture, greenhouse, etc. In general, the geothermal resources in Indonesia are located in mountainous areas with agricultural lands which need heat for their activities. This is a perfect situation for the geothermal energy direct use to be developed. Unfortunately, at present the direct use of geothermal energy in Indonesia is very low. Based on Center for Research and Development of Electricity Technology, Renewable Energy, and Energy Conservation (P3TKEBTKE) direct geothermal utilization in Indonesia is still relatively low, less than 5% of the existing potential. Therefore, the development of geothermal energy must continue to be improved especially in the agricultural sector, considering that Indonesia is an agricultural country.

1. INTRODUCTION

Indonesia is located along the ring of fire because three tectonic plates collide underneath which consists of the Eurasian, Indo-Australian and Pacific plates. Therefore, Indonesia has many active volcanoes which make Indonesia have a large geothermal energy potential. Geothermal locations in Indonesia are scattered in various areas such as Sumatra, Java, Bali and Nusa Tenggara, Maluku, Sulawesi, Borneo and Papua. Based on Directorate General EBTKE Ministry of ESDM, the total of geothermal potential in Indonesia is about 23,965 MW spread over various islands including Sumatra 9,679 MW, Java 8,442 MW, Bali and Nusa Tenggara 1,363 MW, Borneo 182 MW, Sulawesi 3,068 MW, Maluku Islands 1,156 MW, and Papua 75 MW.

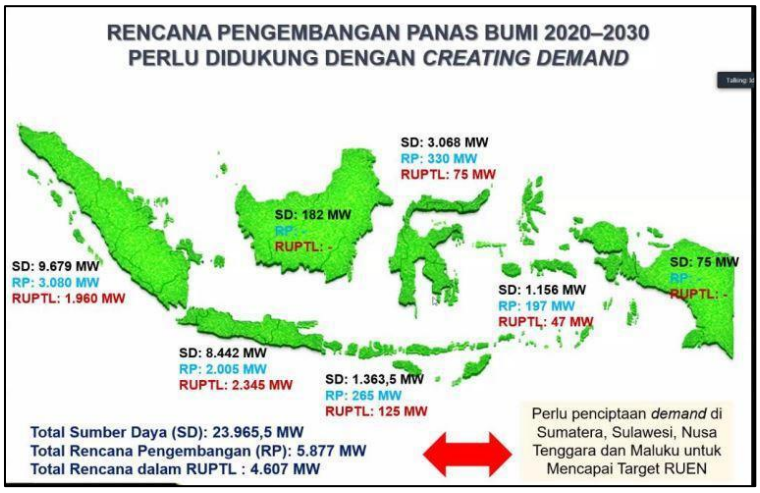

Figure 1: Geothermal Development Plan 2020-2030. (Directorate General EBTKE Ministry of ESDM).

According to the Indonesia Geothermal Law (UU No. 21/2014), that geothermal energy is an environmentally friendly energy that has great potential and its utilization is not optimal so that it needs to be encouraged and improved in a planned and integrated manner in order to reduce dependence on fossil energy. This is due to several factors such as high investment costs, high risk of failure, community rejection, incomplete resource data, and insufficient technology and human resources. Besides that, geothermal areas located in mountainous areas are mostly in protected forest areas, which makes licensing and access difficult.

The development of geothermal direct use in Indonesia is still being carried out and continues to be improved. Such as in the agricultural sector which has progressed. Geothermal direct use in agriculture is one of the best choices because most people in the area are peasant by profession. For example, in Indonesia precisely in the Bandung regency West Java, there is the use of geothermal energy to help the mushroom cultivation process. By utilizing this technology will help farmers to increase their economic income and support the economic development. So, the development of geothermal energy is very important to continue to be improved considering the benefits are so great to help advance the Indonesian economy, especially in the field of agriculture.

2. GEOTHERMAL DIRECT USE

Direct Utilization is an activity of exploiting geothermal directly without converting heat energy and fluid into other types of energy for non-electrical purposes. (UU No. 21/2014 chapter 1). Geothermal direct use dates back thousands of years, when people began using hot springs for bathing, cooking food, and loosening feathers and skin from game. Meanwhile, for now direct use has been

applied in various other ways such as space heating, agricultural cultivation gardens, aquaculture ponds, drying of materials in industry and others. In Indonesia, the use of geothermal energy is used more indirectly than directly. This is due to many factors, one of which is the direct use of geothermal energy that can only be done near the location of geothermal sources.

In general, the direct use of geothermal energy can be divided into 2 groups, namely parallel use and serial use. The hot fluid supply can be channeled into 2 or more parallel lines that operate for different purposes, each of which requires a heat intake at a relatively the same temperature. In series utilization, geothermal fluid is extracted heat at different temperature ranges. After the fluid has been extracted for application at a higher level, the lower temperature waste fluid is used in processes that require a temperature equal to or lower than the previous stage waste temperature.

The Lindal diagram is a diagram that illustrates how the application and utilization of geothermal energy matches the temperature range of the heat source. Geothermal utilization directly according to the Lindal diagram has a small medium time and temperature range (except for utilization in the industrial sector) which is 20-120^{o}C. The Lindal diagram had a generic design and was all encompassing providing insight to people from varied backgrounds. It showed a range of well-established applications, such as de-icing and soil warming; fish farming; swimming pools and balneology; space heating of buildings and greenhouses; organics drying, evaporation and food caning; as well as the digestion of paper pulp and refrigeration by ammonia absorption. Recent versions of the diagram are no longer limited to direct-use applications and expanded to include electrical power production from dry steam, flash steam and binary power cycles. It can be redesigned to include specific applications that are usually not seen outside particular industries for example oil and gas or mining projects. See below a modification of the Lindal for mining applications.

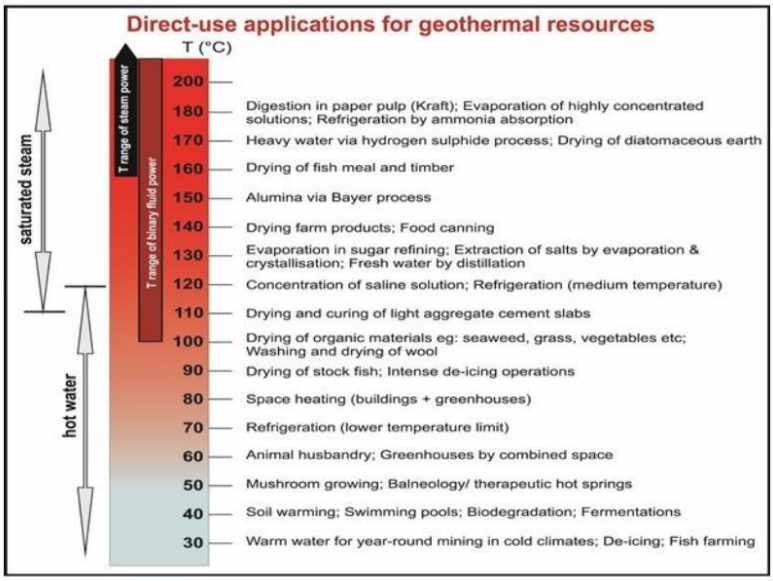

Figure 2: Diagram Lindal (Australian Academy of Science, 2018).

2.1 Hot Spring

The common usage of geothermal energy in Indonesia is for bathing and heated swimming pools. According to the estimation by Lund et al. (2005), the use for bathing and swimming in Indonesia is 2.3 MWt in capacity with an annual energy use of 42.6 TJ/yr. However, it is believed that the exact number is still unknown because there is no accurate data on the total utilization and national capacity because there are many hot springs in remote areas. So, very difficult to measure. For example, swimming pool from geothermal hot springs located in Cipanas, West Java Province.

Figure 3: Hot Water Swimming Pool (Surana et al., 2010).

2.2 Food Drying

The nature of agricultural products, has a tendency to rot easily if not consumed or processed directly. Drying is one of the most effective ways to prevent spoilage. Geothermal can be used in the process of drying agricultural products so that the water content of the food is reduced and the microorganisms that cause the decay process do not have a medium to breed. For example, geothermal energy is used to dry coffee in Garut and Bandung Regencies, West Java. By using a dryer, farmers now don't have to bother drying coffee in the hot sun anymore. The drying process is also much faster.

Figure 4: Geothermal Coffee Dryer (Pabumnews, 2018).

2.3 Greenhouse

Greenhouse agriculture is a growing trend around the world, and crops grown under these conditions are in high demand. Greenhouse has several advantages such as providing cultivators with the ability to accomplish significantly higher yields than open field production, using less land area compared to open field production and using water resources efficiently. Using geothermal energy for greenhouse heating reduces operating costs and enables operation in cold weather areas. Moreover, greenhouses enable a higher quality of products s, it needs less labors than open field production and allows extending period of the crop production. Some plants that can be grown in a greenhouse include roses, carnations, lilies, tomatoes, lettuce, cucumbers, hydroponic plants, and potted plants.

2.4 Space Heating

Space heating can be provided by means of pumped wells or through the use of downhole heat exchangers. Space heating can be provided on a building or increasingly via a district heating network that supplies the needs of multiple consumers via an underground piping network connected to one or multiple wells or downhole heat exchangers. A small space heating in Indonesia is applied in the Patuha Geothermal Field, however detailed information on the exact size and capacity is difficult to find.

Figure 5: Geothermal space heating (Surana et al., 2010).

2.5 Aquaculture

Geothermal aquaculture aims to heat water to the optimum temperature for aquatic species. This involves the raising of freshwater or marine organisms in a controlled environment to enhance production rates. Generally, when the breeding processes, fish need a warm and maintained temperature. Indonesia currently only has one place aquaculture facilities that utilize geothermal fluids, namely traditional freshwater fisheries in Lampung province, with natural geothermal hot water mixing with fresh water from the river to grow large catfish. Based on observations, fish grow better in a mixture of geothermal fluids and fresh water.

Figure 6: Geothermal Direct Use for Large Catfishes Growing (Surana, et. al., 2010).

3. GEOTHERMAL AGRICULTURE

Agriculture is the activity of utilizing biological resources by humans to produce food, industrial raw materials, or energy sources, as well as to manage their environment. Agriculture consists of several sectors including food crops, plantations, forestry, and livestock. The use of geothermal energy is now slowly starting to become more prevalent in the agriculture. Geothermal energy is proven to help improve agricultural products so that they are more effective and efficient. Utilization of geothermal energy in Indonesia in agriculture includes distillation of vetiver into essential oils in Kamojang field, palm sugar production in Lahendong field, mushroom breeding in Kamojang field, drying of copra and cocoa in Way Ratai field, and the use of a tiered system in Wayang Windu field.

3.1 Distillation of Vetiver into Essential Oil in Kamojang Field

The idea of using geothermal fluid for vetiver distillation arose considering that the Garut area has a large potential for vetiver. Judging from its location, Garut is not far from the Kamojang field. The use of geothermal energy for distillation of vetiver is used to replace the role of other fuels because it is more environmentally friendly. In simple terms, the concept of vetiver distillation begins with geothermal steam entering a heat exchanger. Then the water is pumped into the heat exchanger so that the pressure and temperature drop. After that, the steam is put into a distillation tank which already contains dried vetiver roots and distillation is carried out to form a mixture of steam and oil. The mixture is cooled in a condenser and after condensation the mixture is separated in a separator tank. Based on research, the use of geothermal is proven to improve the quality of vetiver oil. However, until now there is no geothermal well that can be utilized by vetiver distillers in Garut.

Figure 7: Vetiver Production (Saptaji, 2020).

3.2 Palm Sugar Production in Lahendong Field

Lahendong geothermal field surrounded by palm trees extensive sugarcane plantations. There are facilities for direct use of large-scale geothermal energy for palm oil sugar production by utilizing flashed steam from separated hot water. The two-phase fluid from the well is flowed into the separator to be separated into a vapor phase and a liquid phase. The steam from the separator is used to generate electricity while the water is sent to the flasher. The steam from the flasher is routed to a production facility to produce palm sugar. The use of geothermal fluids is proven to accelerate the palm sugar production process compared to the use of conventional combustion.

Figure 8: Palm Sugar Production Factory (Saptaji, 2020).

3.3 Mushroom Breeding in Kamojang Field

BPPT (Agency for the Assessment and Application of Technology) in collaboration with Pertamina Geothermal Energy utilizing geothermal energy for mushroom cultivation in the Kamojang field. The facility consists of a steam generator heat exchanger, an autoclave, a freshwater tank, an inoculation room, incubation rooms and production rooms. Small capacity dry steam is directed at the steam generator to heat fresh water and is used to sterilize the mushroom growing medium and to heat the incubation chamber to keep it warm. While geothermal steam is used to replace fossil fuels to be economical and more environmentally friendly. So that mushroom can be obtained at a cheaper price by the community due to cutting production costs by geothermal energy.

Figure 9: Mushroom Breeding (Saptaji, 2020).

3.4 Drying of Copra and Cocoa in Way Ratai Field

Way Ratai is an undeveloped geothermal field in Lampung Province, located in coconut plantation area. The facility consists of downhole heat exchanger, drying room, pump, and freshwater tank. The fluid flow diagram schematic begins by placing a downhole heat exchanger in a geothermal well and fresh water flows into it. After the fresh water is heated, it is then flowed into the drying chamber and dried. The quality of the copra produced in this facility is much better compared to the conventional one because there is no smoke contamination on it.

Figure 10: Drying Copra and Cocoa (Suntoro et al., 2018).

4. CONCLUSION

Indonesia has many active volcanoes which makes Indonesia has a large geothermal energy potential. Geothermal resources in Indonesia are generally located in mountainous areas with agricultural, forestry, and plantation land so that it is very potential for various kinds of direct use application. The application of direct use of geothermal energy is currently commonly used in various activities such as hot springs, food drying, green houses, space heating, and aquaculture. Besides that, several agricultural applications are already developed such as distillation of vetiver into essential oil, palm sugar production, mushroom cultivation, and drying copra cocoa.

REFERENCES

Fahmy, F., Atia, D., El Madany, H., and Farghally, H.: Greenhouse Heating System Based on Geothermal Energy, *International Journal of Energy*, (2016), Volume 10.

Ragnarsson, Árni: Geothermal Energy in Aquaculture, Short Course VI on Utilization of Low and Medium Enthalpy Geothermal Resources and Financial Aspects of Utilization, Reykjavík, Iceland (2014).

Saptadji, N.M.: Teknik Geothermal, ITB Press, Bandung, Indonesia (2020), 102-107.

Surana, T., Atmojo, J.P., Suyanto, and Subandriya, A.: Development of Geothermal Energy Direct Use in Indonesia 2010, *Proceedings*, World Geothermal Congress 2010, Bali, Indonesia (2010).

UU Republik Indonesia Nomor 21 Tahun 2014 tentang Panas Bumi, (2014).

ISSN 2829-9671

Asosiasi Panasbumi Indonesia (API)
Apartemen Menteng Square, BR-9 Tower B
Jl. Matraman No 30 E, Jakarta Pusat - 10320 Indonesia
Email: api.inaga@yahoo.co.id